MAGNETIC SENSORS

and MAGNETOMETERS

Second Edition

Pavel Ripka
Editor

Magnetic Sensors and Magnetometers

Second Edition

Magnetic Sensors and Magnetometers

Second Edition

Pavel Ripka
Editor

ARTECH HOUSE
BOSTON | LONDON
artechhouse.com

Library of Congress Cataloging-in-Publication Data
A catalog record for this book is available from the U.S. Library of Congress

British Library Cataloguing in Publication Data
A catalog record for this book is available from the British Library.

ISBN-13: 978-1-63081-742-8

Cover design by Charlene Stevens

685 Canton St.
Norwood, MA

10 9 8 7 6 5 4 3 2 1

Contents

Preface to the First Edition xiii

Preface to the Second Edition xvii

Acknowledgments xix

CHAPTER 1

Basics 1

1.1 Magnetic Units and Basic Rules 1

1.1.1 Basic Laws 2

1.1.2 Magnetic Field and Matter 3

1.1.3 Magnetic Circuits 3

1.2 Magnetic States of Matter 4

1.2.1 Diamagnetism and Superconductivity 4

1.2.2 Paramagnetism 5

1.2.3 Ferromagnetism, Antiferromagnetism, and Ferrimagnetism 5

1.2.4 Superparamagnetism 6

1.3 Magnetic Anisotropy 6

1.3.1 Magnetocrystalline Anisotropy 7

1.3.2 Shape Anisotropy and Demagnetization 7

1.3.3 Induced Anisotropy 9

1.3.4 Anisotropy in Magnetic Wires 12

1.4 Magnetostriction 12

1.5 Domain Structure 14

1.6 Magnetization Process 16

1.6.1 Magnetization Curve 17

1.7 Magnetic Materials 20

1.7.1 Soft Magnetic Materials 20

1.7.2 Hard Magnetic Materials 22

1.8 Sensor Specifications 22

1.8.1 Full-Scale Range, Linearity, Hysteresis, and Temperature Coefficient of Sensitivity 23

1.8.2 Offset, Offset Temperature Coefficient, and Long-Term Stability 24

1.8.3 Perming 24

1.8.4 Noise 24

1.8.5 Resistance Against Environment (Temperature, Humidity, and Vibrations) 25

1.8.6 Resistance Against Perpendicular Field and Field Gradient 26

1.8.7 Bandwidth 26
1.8.8 Other (Power, Radiation Immunity, and Cost) 27
References 27

CHAPTER 2
Induction Sensors 29

2.1 Air Coils 30
2.1.1 Voltage Sensitivity at Low Frequencies 32
2.1.2 Thermal Noise 33
2.1.3 The Influence of the Parasitic Capacitances 34
2.1.4 Current-Output (Short-Circuited Mode) 35
2.2 Search Coils with a Ferromagnetic Core 37
2.2.1 Voltage Output Sensitivity 37
2.2.2 Thermal Noise of the Cored Induction Sensor (Voltage Output) 41
2.2.3 The Equivalent Circuit for Cored Coils 41
2.2.4 Cored Coils with Current Output 42
2.3 Noise Matching to an Amplifier 42
2.4 Design Examples 43
2.5 Other Measuring Coils 43
2.5.1 Rotating Coil Magnetometers 43
2.5.2 Moving Coils: Extraction Method 44
2.5.3 Vibrating Coils 46
2.5.4 Coils for Measurement of *H* 46
2.5.5 The Rogowski-Chattock Potentiometer 46
References 48

CHAPTER 3
Fluxgate Sensors 51

3.1 Orthogonal-Type Fluxgates 52
3.2 Core Shapes of Parallel-Type Fluxgates 55
3.2.1 Single-Rod Sensors 55
3.2.2 Double-Rod Sensors 56
3.2.3 Ring-Core Sensors 56
3.2.4 Racetrack Sensors 57
3.3 Theory of Fluxgate Operation 58
3.3.1 The Effect of Demagnetization 59
3.4 Core Materials 62
3.5 Principles of Fluxgate Magnetometers 63
3.5.1 Second-Harmonic Analog Magnetometer 63
3.5.2 Digital Magnetometers 65
3.5.3 Nonselective Detection Methods 67
3.5.4 Auto-Oscillation Magnetometers 69
3.6 Excitation 69
3.7 Tuning the Output Voltage 69
3.8 Current-Output (or Short-Circuited) Fluxgate 72
3.8.1 Broadband Current-Output 73

3.8.2 Tuning the Short-Circuited Fluxgate 75
3.9 Noise and Offset Stability 75
3.9.1 Zero Offset 78
3.9.2 Offset from the Magnetometer Electronics 79
3.9.3 Other Magnetometer Offset Sources 79
3.10 Crossfield Effect 80
3.11 Designs of Fluxgate Magnetometers 80
3.11.1 Portable and Low-Power Instruments 80
3.11.2 Station Magnetometers 81
3.12 Miniature Fluxgates 81
3.12.1 Miniature Wire-Wound Sensors 82
3.12.2 Devices with Flat Coil (CMOS or Other Technologies) 82
3.12.3 PCB-Based Sensors with Solenoid Coils Made of Tracks and Vias 83
3.12.4 Sensors with Microfabricated Solenoids 84
3.13 AC Fluxgates 85
3.14 Multi-Axis Magnetometers 85
3.14.1 Three-Axial Compensation Systems 86
3.14.2 Individually Compensated Sensors 87
3.15 Fluxgate Gradiometers 89
References 90

CHAPTER 4
Ferromagnetic Magnetoresistive Sensors 99

4.1 AMR Sensors 100
4.1.1 Magnetoresistance and Planar Hall Effect 100
4.1.2 Magnetoresistive Films 103
4.1.3 Linearization and Stabilization 105
4.1.4 Sensor Layout 109
4.1.5 Crossfield Sensitivity of the AMR Sensor 112
4.1.6 AMR Magnetometers 114
4.2 GMR and TMR (SDT) Sensors 115
4.2.1 GMR Effect Basics 117
4.2.2 Tunnel Magnetoresistance (Spin-Dependent Tunneling) 122
4.2.3 GMR/TMR Sensor Design 123
4.2.4 Magnetoresistance Sensor Applications 127
4.3 Operating Parameters of Magnetoresistive Sensors 128
4.3.1 Noise 128
4.3.2 Field Range and Linearity 129
4.3.3 Offset, Offset Drift, and Hysteresis 130
References 131

CHAPTER 5
Hall-Effect Magnetic Sensors 135

5.1 Basics of the Hall Effect and Hall Devices 136
5.1.1 The Hall Effect 137

5.1.2 Structure and Geometry of a Hall Device 140
5.1.3 Main Characteristics of Hall Magnetic Field Sensors 141
5.1.4 Other Problems 143
5.2 High Electron Mobility Thin-Film Hall Elements 143
5.2.1 InSb Hall Elements 144
5.2.2 InAs Thin-Film Hall Elements by MBE 146
5.2.3 Deep Quantum Wells (DQW) and Application to Hall Elements 148
5.2.4 GaAs Hall Elements 150
5.3 Integrated Hall Sensors 150
5.3.1 Historical Perspective 151
5.3.2 CMOS Hall Elements 153
5.3.3 Hall Offsets 154
5.3.4 Excitation 157
5.3.5 Amplification 159
5.3.6 Geometry Considerations 159
5.3.7 Vertical Hall Elements 162
5.3.8 Packaging for Integrated Hall Sensors 162
5.3.9 Applications and Trends 163
5.4 Nonplate-Like Hall Magnetic Sensors 163
5.4.1 The Vertical Hall Device 164
5.4.2 Two-Axis Vertical Hall Device 166
5.4.3 Three-Axis Hall Devices 167
5.5 Hall Devices with Integrated Magnetic Concentrators (IMCs) 168
5.5.1 Rotary Sensor with IMC 170
5.5.2 3-Axis Sensor with IMC 171
5.5.3 Integrated Current Sensor [55] 173
5.5.4 Stray-Field Robust Gradiometric Sensors [56] 173
5.5.5 IMC Technology 175
References 175

CHAPTER 6
Resonance Magnetometers 179

6.1 Introduction to Magnetic Resonance 179
6.1.1 Historical Overview 179
6.1.2 Absolute Reproducibility of Magnetic Field Measurements 181
6.2 Proton Precession Magnetometers 182
6.2.1 The Mechanical Gyroscope 182
6.2.2 The Classic Proton-Free Precession Magnetometer 185
6.2.3 Overhauser Effect Proton Magnetometers 193
6.3 Optically Pumped Magnetometers 197
6.3.1 Alkali Metal Vapor Magnetometers 197
6.3.2 The Metastable He^4 Magnetometer 202
References 207

CHAPTER 7

SQUID 211

7.1 Introduction 211
7.1.1 Superconductivity 211
7.1.2 Meissner Effect 212
7.1.3 Flux Quantization 213
7.1.4 The Josephson Effect 214
7.1.5 SQUIDs 216
7.2 SQUID Sensors 217
7.2.1 Materials 217
7.3 SQUID Operation 220
7.3.1 The RF SQUID 221
7.3.2 The DC SQUID 222
7.3.3 SQIFs 222
7.3.4 Fractional-Turn SQUIDs 223
7.3.5 The Bi-SQUID 224
7.4 Noise and Sensitivity 224
7.4.1 White Noise 225
7.4.2 Temperature Dependence 226
7.4.3 Field Dependence 227
7.4.4 $1/f$ Noise 227
7.5 Control Electronics 228
7.6 Limitations on SQUID Technology 229
7.7 Input Circuits 231
7.7.1 Packaging 231
7.7.2 The SQUID as a Black Box 231
7.7.3 Sensitivity 232
7.7.4 Detection Coils 233
7.7.5 Gradiometers 235
7.7.6 Electronic Noise Cancellation 236
7.8 Refrigeration 238
7.8.1 Dewars 238
7.8.2 Closed Cycle Refrigeration 240
7.9 Environmental Noise (Noise Reduction) 240
7.9.1 Gradiometers for Noise Reduction 241
7.9.2 Magnetic Shielding 242
7.10 Applications 243
7.10.1 Laboratory Applications 246
7.10.2 Cryogenic Current Comparators (CCC) 249
7.10.3 Geophysical Applications 250
7.10.4 Nondestructive Test and Evaluation 252
7.10.5 Medical Applications of SQUIDs 253
References 256

CHAPTER 8
Magneto-Optical Sensors and Other Principles 261

8.1 Magneto-Optical Sensors 262
8.1.1 Faraday Effect and Optical Sensors of the Magnetic Field 262
8.1.2 Magneto-Optical Kerr Effect and Observation of Domains 264
8.2 Magnetoimpedance and Magnetoinductance 265
8.2.1 Principle 265
8.2.2 Materials 267
8.2.3 Sensors 268
8.3 Magnetoelastic Field Sensors 270
8.3.1 Fiber-Optic Magnetostriction Field Sensors 270
8.3.2 Magnetostrictive-Piezoelectric (Magnetoelectric) Sensors 270
8.3.3 Shear-Wave Magnetometers 272
8.4 Lorentz Force Magnetometers 273
8.5 Biological Sensors 274
8.5.1 Magnetotactic Bacteria 274
8.5.2 Magnetic Orientation in Birds 274
References 275

CHAPTER 9
Applications of Magnetic Field Sensors and Magnetometers 279

9.1 Biomagnetic Measurements 279
9.2 Navigation 282
9.3 Military and Security 287
9.3.1 Unexploded Ordnance (UXO) 287
9.3.2 Target Detection and Tracking 289
9.3.3 Antitheft Systems 289
9.4 Automotive 290
9.5 Nondestructive Testing 290
9.6 Magnetic Marking and Labeling 292
9.7 Geomagnetic Measurements: Mineral Prospecting, Object Location, and Variation Stations 292
9.8 Space Research 297
9.8.1 Deep-Space and Planetary Magnetometry 298
9.8.2 Space Magnetic Instrumentation 300
9.8.3 Measurement of Magnetic Fields Onboard Spacecraft 302
References 307

CHAPTER 10
Testing and Calibration Instruments 313

10.1 Calibration Coils 313
10.1.1 Coils as Sources of the Magnetic Moment 320
10.2 Field Compensation Systems 320
10.3 Magnetic Shielding 321
10.3.1 Magnetic Shielding Theory 322
10.3.2 Transverse Magnetic Shielding 322

10.3.3 Axial Magnetic Shielding 324
10.3.4 Flux Distribution 326
10.3.5 Annealing 326
10.3.6 Demagnetizing 327
10.3.7 Enhancement of Magnetic Shielding by Magnetic Shaking 327
10.3.8 Magnetic Shielded Rooms 328
10.4 Calibration of 3-Axial Magnetometers 328
10.4.1 Vectoral Calibration of 3-Axial Magnetometers 329
10.4.2 Scalar Calibration of 3-Axial Magnetometers 329
References 329

CHAPTER 11
Magnetic Sensors for Nonmagnetic Variables 333

11.1 Position Sensors 333
11.1.1 Sensors with a Permanent Magnet 334
11.1.2 Eddy-Current Sensors 335
11.1.3 Linear Transformer Sensors 341
11.1.4 Rotation Transformer Sensors 343
11.1.5 Magnetostrictive Position Sensors 344
11.1.6 Wiegand Sensors 345
11.1.7 Magnetic Trackers 345
11.2 Proximity and Rotation Detectors 346
11.3 Force and Pressure 347
11.4 Torque Sensors 349
11.5 Magnetic Flowmeters 355
11.6 Electric Current Sensors 355
11.6.1 Magneto-Optical Current Sensors 356
11.6.2 Current Transformers 357
11.6.3 Fluxgate Current Sensors 361
11.6.4 Rogowski Coils 362
11.6.5 Sensors with a Gapped Core 364
11.6.6 Coreless Current Sensors 366
11.6.7 Current Clamps 368
11.6.8 Magnetometric Measurement of Hidden Currents 369
References 369

Acronyms and Abbreviations 375
About the Editor 379
List of Contributors 381
Index 385

Preface to the First Edition

In recent years, several valuable books and review papers on various types of magnetic sensors, magnetometers, and their applications appeared, but there is no up-to-date text fully covering this important, complex, and exciting field.

The most comprehensive of the existing sources is, undoubtedly, *Magnetic Sensors*, edited by R. Boll and K. Overshott [1]. Many parts of this book are still very valuable; it covers most of the sensor types (except for resonance sensors and superconducting quantum interference devices (SQUIDs), but not many of the problems of the magnetometers and their applications. *Solid State Magnetic Sensors*, written by Roumenin [2], covers only semiconductor sensors and SQUIDs. This book is oriented toward interesting but often rather impractical devices, such as magnetotransistors and carrier-domain magnetometers. *Hall Effect Devices*, written by R. S. Popovic [3], is still valuable, but very specialized.

The recent and most valuable review papers were written by Gibbs and Squire [4], Heremans [5], Rozenblat [6], Lenz [7], and Popovic et al. [8].

Although magnetic sensors are usually only briefly mentioned in books on sensors in general, such as [9–11], these books give important comparisons to the properties of other sensor types; also a lot of discussed problems with, for example, sensor construction, thermal stability, interfacing, and signal processing are common to various sensor groups.

The authors have the ambition to make the present book useful as a tool; they have tried to keep a realistic, comprehensive, and practical approach.

1. *The realistic approach:* The book does not concentrate on exotic methods and techniques often appearing in numerous conference papers, but sometimes having no or little practical impact. The performances of individual sensors and magnetometers are compared (both the reported laboratory prototypes and commercially available devices) in relation to the various application areas.
2. *The comprehensive approach:* The book covers not only sensors, but also magnetometers including multichannel and gradiometric systems. Special problems, such as cross-talk and crossfield sensitivity, are discussed. Problems of testing and calibrating of magnetic sensors are covered in Section 1.4 and Chapter 11.
3. *The practical approach:* The theory serves for understanding the working principles of real devices. The book gives information, which helps selecting the sensor suitable for a particular application, or to start the development of a customized device.

It aims at the following reader groups to explain the basic principles, available device parameters, and application rules and give extensive reference for further reading:

- University teachers and students (including postgraduates) mainly in the field of physics, geophysics, electrical engineering, and measurement and instrumentation;
- Instructors and participants in courses for the military (navigation, bomb location, and weapon and vehicle detection);
- Users and designers of industrial sensors;
- Marketing and consulting in the field of sensor systems and industrial automation;
- Integrators and programmers of systems containing sensors.

We assume that the reader has a general education in physics (at an undergraduate level).

Chapter 1 could have been entitled "Basics of Magnetism Revisited." The text does not replicate the introductory chapter on magnetism, which can be found several times on the bookshelf of every physicist and electrical engineer. Instead, the aim is to recapitulate these parts, which are, or once were, already familiar to the reader, in a new light. For more conventional and detailed introductions to magnetism, electromagnetics, and magnetic materials, we recommend several excellent textbooks [12–14].

This book may look inconsistent; the world of magnetic sensors is not very consistent itself. While some of them (e.g., fluxgates) have been developed over more than half a century, the others (e.g., magneto-optical or GMI sensors) are rather fresh. Although it is tricky, we decided also to cover these fast-developing areas. We even discuss the sensors, which we consider not particularly prospective with the aim just to show their principles and point out disadvantages. Some sensors (such as magnetoresistors and Hall sensors) are available on the market and the user has a lot of support from the manufacturer in the form of reference brochures and application manuals. In such a case, this book explains the principles and applications rather than the details of the manufacturing process. Contrary to that, induction and fluxgate sensors are usually sold only as a part of magnetometers; it makes sense to develop these sensors custom-made, for a specific application and this book may partly serve as a "cookbook."

The term magnetometer has two meanings: (1) most commonly, the magnetometer is a device for measurement of the magnetic field; and (2) a magnetometer is also an instrument for the measurement of magnetic moment (for example, a rotating or vibrating sample magnetometer). There is no danger of confusion, as the type of the instrument is usually specified (for example, a proton magnetometer measures the magnetic field).

The term magnetic sensor has two meanings: (1) the wider definition is magnetic sensors work on magnetic principles; and (2) and sometimes these are just sensors measuring the magnetic field. Although this book mainly concentrates on magnetic field sensors and magnetometers, magnetic sensors for the measurement of nonmagnetic variables are covered in Chapter 12.

One of the most important applications of precise magnetometers is in geophysics. For further reading, we may recommend an excellent basic book *Applied Geophysics*, written by Telford et al. [15], and an extremely useful handbook on magnetic measurements and observatories by Jankowski and Sucksdorff [16].

Finally, we briefly mention two trends in the development of magnetic sensors: miniaturization and the use of new materials. Microtechnologies are already in use for the fabrication of nonsemiconductor sensors: fluxgates and induction position sensors. High-aspect ratio structures such as multilayer micromachined coils can be made using current micromachining technologies [17]. The applications of amorphous tapes and wires to all kinds of magnetic sensors is reviewed in [18]. The use of multilayers in GMR magnetoresistors is discussed in Chapter 4.

References

[1] Boll, R., and K. J. Overshott, (eds.), *Magnetic Sensors, Vol. 2: Sensors*, Veiden, Germany: VCH, 1989.

[2] Roumenin, C. S., *Solid State Magnetic Sensors*, New York: Elsevier, 1994.

[3] Popovic, R. S., *Hall Effect Devices*, Bristol, U.K.: Adam Hilger, 1991.

[4] Gibbs, M. R. J., and P. T. Squire, “A Review of Magnetic Sensors,” *Proc. IEEE*, Vol. 78, 1990, pp. 973–989.

[5] Heremans, J., “Solid State Magnetic Sensors and Applications,” *J. Phys. D*, Vol. 26, 1993, pp. 1149–1168.

[6] Rozenblat, M. A., “Magnetic Sensors—State-of-the-Art and Trends,” *Automation and Remote Control*, Vol. 56, No. 6, 1995, pp. 771–809.

[7] Lenz, J. E., “Review of Magnetic Sensors,” *Proc. IEEE*, Vol. 78, 1990, pp. 973–989.

[8] Popovic, R. S., J. A. Flanagan, and P. A. Besse, “The Future of Magnetic Sensors,” *Sensors and Actuators A*, Vol. 56, 1996, pp. 39–55.

[9] Norton, H. A., *Sensor and Analyzer Handbook*, Upper Saddle River, NJ: Prentice Hall, 1982.

[10] Fraden, J., *AIP Handbook on Modern Sensors*, New York: American Institute of Physics, 1993.

[11] Pallas-Areny, R., and J. G. Webster, *Sensors and Signal Conditioning*, New York: John Wiley & Sons, 1991.

[12] Jiles, D., *Introduction to Magnetism and Magnetic Materials*, London: Chapman & Hall, 2016.

[13] Kraus, J. D., *Electromagnetics*, 2nd ed., New York: McGraw-Hill, 1984.

[14] Crangle, J., *Solid State Magnetism*, Edward Arnold, 1989.

[15] Telford, W. M., L. P. Geldart, and R. E. Sheriff, *Applied Geophysics*, Cambridge: Cambridge University Press, 1990.

[16] Jankowski, J., and C. Sucksdorff, *Guide for Magnetic Measurements and Observatory Practice*, Warsaw: IAGA, 1996.

[17] Ohnmacht, M., V. Seidemann, and S. Büttgenbach, “Microcoils and Microrelays — an Optimized Multilayer Fabrication Process,” *Sensors and Actuators*, Vol. 83, 2000, pp. 112–124.

[18] Meydan, T., “Application of Amorphous Materials to Sensors,” *J. Magn. Magn Mater.*, Vol. 133, 1995, pp. 525–532.

Preface to the Second Edition

Twenty-one years after the first edition, we decided to substantially upgrade this book. Some of the research trends we described turned into the mainstream industrial technologies, but many disappeared.

Chapter 1 was completely rewritten to be more concentrated on the sensor-related effects such as shape anisotropy and magnetostriction. With the advance of smart grids, renewable energy resources, and electric vehicles, the importance of electric current sensors increased. We therefore substantially enlarged the corresponding section in Chapter 11.

We made a lot of small upgrades and added more recent references, but we mainly focused on the following milestones in magnetic sensors technology that happened in the past two decades:

- Integrated fluxgate single-chip magnetometer appeared on the market.
- Orthogonal fluxgates reached noise level below 1 pT.
- AMR 3-axial integrated compass chips dominated gadgets such as mobile phones and smart watches.
- GMR sensors penetrated the automotive market, especially for end-of-shaft angular sensors.
- Linear TMR sensors reached the market.
- GaAs Quantum-Well Hall integrated circuit reached 200-nT resolution and high offset stability.
- Vertical Hall sensors and sensors with integrated ferromagnetic concentrators are two competing technologies that both brought 3-axial single-chip Hall ICs on the market.
- Digital fluxgate magnetometers were introduced for both satellite and ground-based applications.
- All-optical resonant magnetometer based on the coherent population trapping effect has reached approval for space applications.

Acknowledgments

We thank our colleagues and professional friends for reading parts of the manuscript and for valuable comments. We express particular gratitude to O. V. Nielsen, J. Hochreiter, P. Kejík, R. Schneider, and V. Mosser for their comments and suggestions. We also thank to our families for their support and patience.

CHAPTER 1

Basics

Pavel Ripka and Karel Záveta

This chapter begins with definitions of magnetic units and an overview of rules and effects important for magnetic sensing. After a short summary about magnetic states of matter, we treat in more detail magnetocrystalline and shape anisotropy, domain structure, and the magnetization process. We also provide a short outline of magnetic materials for sensor applications. The last section of the chapter examines the basic sensor specifications. More about magnetism and magnetic materials can be found in books by Jiles [1] and Coey [2]. Technical magnetic materials are well described in the book by Hilzinger and Rodewald [3]. A comprehensive book on magnetic materials was written by Krishnan [4]. A book series on magnetic materials edited by Buschow and later by Bruck has 27 volumes [5]. Engineering design methods for magnetic circuits (reluctance method and finite element method) are described in the book by Brauer [6] and magnetic measurement methods are explained in a book by Tumanski [7].

1.1 Magnetic Units and Basic Rules

Magnetic field strength (or magnetic field intensity also called just magnetic field H) H (A/m) is defined as a field caused by electric current I flowing in a long straight conductor at the distance of r

$$H = \frac{I}{2\pi r} \tag{1.1}$$

The vector $\mathbf{H}$ is perpendicular to both $\mathbf{I}$ and $\mathbf{r}$ (see Figure 1.1). Magnetic flux density $B(T)$ (also called magnetic induction or magnetic field B) is another quantity describing magnetic field.

In a vacuum:

$$B = \mu_0 H \tag{1.2}$$

where μ_0 is the permeability of free space $\mu_0 \cong 4\pi \cdot 10^{-7}$ H/m (after the 2019 redefinition of SI this is no longer defined as an exact value).

The SI definition of Tesla is through the magnetic part of Lorentz force

$$\mathbf{F} = I(\mathbf{l} \times \mathbf{B}) \; ; \; \mathrm{F} = I \cdot l \cdot \mathrm{B} \tag{1.3}$$

where l is the length of the conductor with current I, which is constantly moved in the field B.

Former centimeter-gram-second (cgs) units are still found in literature. Table 1.1 lists the main conversion factors from cgs to SI.

In this book, we will use SI units.

There is a wide range of magnitudes of magnetic fields in the universe. In order to give a feeling of the variety of tasks with which we are confronted during the measurement of the magnetic field, some examples illustrate the full scale of flux densities that we meet in everyday life, in the laboratory, and in outer space:

- Biomagnetic fields (brain, heart): $B \approx 10$ fT … 1 pT;
- Galactic magnetic field: $B \approx 0.25$ nT;
- Interplanetary magnetic field at Earth orbit: $B \approx 4$ … 10 nT;
- In the 1-m distance from the electrical household appliance: $B \approx 600$ nT;
- Earth's magnetic field (magnetic south is near geographic north): $B \approx 60$ μT;
- Electrical power machines and cables (in 10-m distance): $B \approx 0.1$ … 10 mT;
- Permanent magnets at their surface: $B \approx 100$ mT … 1T;
- Electromagnets: $B \approx 2$T;
- NMR tomography (superconducting magnets): $B \approx 1.5$T … 4T;
- Superconducting magnets for nuclear fusion: $B \approx 10$T … 20T;
- Pulse fields by coils: $B \approx 60$T … 100T;
- Surface of neutron stars: $B \approx 100$ MT.

1.1.1 Basic Laws

Ampère's law is:

$$NI = \oint_s \boldsymbol{H}\, d\boldsymbol{s} \tag{1.4}$$

where the ring integral of $\boldsymbol{H}$ over a closed path $\boldsymbol{s}$ is equal to the sum of currents surrounded by s, also called a magnetic voltage; for multiturn winding, the magnetic voltage is expressed by Ampère-windings (N conductors with current I). This law forms a basis for contactless sensors of the electric current (Chapter 11). A direct consequence is that the field along the axis of a long cylindrical coil (having N turns, length l, and diameter $d << l$) is $H = NI/l$.

Table 1.1 Conversion of cgs Units to SI Units

Quantity	*cgs-to-SI Conversion*
Magnetic field intensity H	1 Oe (Oersted) = $10^3/4\pi$ A/m
Magnetic flux Φ	1 Mx (Maxwell) = 10^{-8} Wb (weber)
Magnetic flux density B	1 G (Gauss) = 10^{-4} T
(volume) Magnetization M	1 emu/cm^3 = 10^3 A/m
(mass) Magnetization σ	1 emu/g = 1 A·m^2/kg
Polarization J	$J_{cgs} = J_{SI}/4\pi$
Permeability μ	$\mu_{cgs} = \mu_{SI}/\mu_0$
Susceptibility κ	$\kappa_{cgs} = \kappa_{SI}/4\pi$

Faraday's induction law is that if the induction changes with time t in an area A enclosed by N turns of a conductor, a voltage V is generated:

$$V = -N\frac{d\Phi}{dt} = -\ NA\frac{dB}{dt} \tag{1.5}$$

supposing that B is has the same value in the coil area A. Otherwise, we should write for the magnetic flux φ:

$$\Phi = \iint_A \boldsymbol{B}\, d\boldsymbol{A} \tag{1.6}$$

The unit of magnetic flux φ is Weber (Wb = Vs). From this equation, it is clear why the magnetic field B is also called flux density.

The magnetic field of real coils used for compensation and testing is analyzed in Chapter 10. The magnetic field can be visualized by lines of force. The tangent of these lines gives the local field direction and their density (distance) determines the field strength. This is illustrated by Figure 1.1 for Ampère's law.

1.1.2 Magnetic Field and Matter

Inside magnetic material of infinite dimension

$$B = \mu H = \mu_r \mu_0 H = \mu_0 H(1+\kappa) = \mu_0 H + J = \mu_0 (H + M) \tag{1.7}$$

where J is magnetic polarization, M is (volume) magnetization, $J = \mu_0 M$, and relative permeability, $\mu_r = 1 + \kappa = \mu_0/\mu$ with κ being susceptibility.

1.1.3 Magnetic Circuits

The concept of magnetic circuit is simplification useful for the first design. Serial direct current (DC) magnetic circuit consists of k segments, which are assumed to

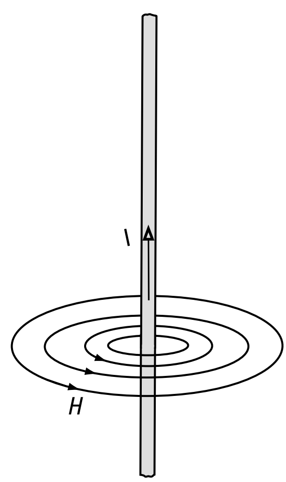

Figure 1.1 Magnetic lines of force H of a conductor with current I.

be always in the direction of H and B. Reluctance method is based on simplified Ampère's law (1.4):

$$NI = \oint_s \boldsymbol{H}\, d\boldsymbol{s} = \sum_k \boldsymbol{H}_k \boldsymbol{l}_k = \sum_k \frac{\Phi_k}{\mu_k \boldsymbol{S}_k} \boldsymbol{l}_k \tag{1.8}$$

where $\mathfrak{R}_k = \boldsymbol{l}_k / \mu_k \boldsymbol{S}_k$ is called reluctance [6].

The total reluctance of the serial magnetic circuit is

$$\mathfrak{R} = \sum_K \mathfrak{R}_k \tag{1.9}$$

Reluctance for alternating current (AC) circuits become complex to include eddy currents in metal parts of the circuit.

The reluctance method can be used in case that the stray fields can be neglected. Much more precise results can be obtained by finite-element modeling (FEM) [6].

1.2 Magnetic States of Matter

The effect of a magnetic field on matter is rather diverse. We will only touch diamagnetism and paramagnetism, and we shall deal in more detail with the most important phenomena of magnetically ordered media: ferrimagnetism and ferromagnetism.

1.2.1 Diamagnetism and Superconductivity

Diamagnetic materials exhibit small negative susceptibility (i.e., their relative permeability μ_r is slightly smaller than one, which means that their magnetic moment induced by the applied magnetic field is oriented against field direction). Diamagnetic contribution to magnetic moment occurs in all materials, but in nondiamagnetic materials it is masked by other, stronger effects. The values of the susceptibility κ are thus negative and usually very small ($|\kappa| \approx 10^{-5}$). Langevin explained diamagnetism by the reaction of the fictitious current loops in individual atoms on the applied external magnetic field. The diamagnetic moment is linear in the magnetic field and the diamagnetic susceptibility is thus constant.

The noble gases, most semiconductors, pure water, and many metals (Cu, Zn, Ag, Cd, Au, Hg, Pb, and Bi) belong to diamagnetic materials. Some of the latter ones are used for the design of mechanical parts of the devices, which must not disturb the magnetic field to be measured.

The magnetic behavior of superconductors (see Chapter 7) can be described as a strong form of diamagnetism. Due to the Meissner-Ochsenfeld effect, the inside of an ideal superconductor is completely shielded by nondissipative surface currents ($B = 0$ inside the superconductor) below a critical temperature and a critical applied field, and, thus, $\kappa = -1$ in this case [1]. If the material consists of nonsuperconducting parts (e.g., grain boundaries, inclusions) or the applied field locally exceeds the critical value, B penetrates the material and $|\kappa|$ decreases. This is also the case of type-II superconductors such as the high-temperature superconductors [1].

1.2.2 Paramagnetism

Paramagnetic materials have small positive susceptibility (i.e., relative permeability slightly higher than 1). Paramagnetic atoms or ions have unpaired electrons, whose magnetic spin moments prefer orientation in parallel with the external magnetic field. Thus, the effect of the thermal motion trying to randomize these atomic (ionic) moments results in the simple dependence of paramagnetic susceptibility on temperature expressed in the Curie law:

$$\kappa = \frac{C}{T} \tag{1.10}$$

where T is the absolute temperature and C is the Curie constant. For low temperatures and/or very high magnetic fields, the (paramagnetic) magnetization has a tendency to saturate. The magnetization of paramagnetic materials may play a non-negligible role at a low temperature.

Oxygen is paramagnetic, unlike the other gases present in air, which is the principle of the magnetic oxygen sensor. Paramagnetic metals are, for example, Mg, Al, Ti, V, Mo, Pd, and Pt. Iron oxide (FeO as mineral called siderite) is also paramagnetic.

Paramagnetic materials are used for sensor applications in electron spin resonance (ESR) magnetometers (see Chapter 6).

Under normal conditions, the magnetizations of both diamagnetic and paramagnetic materials are approximately linear with the magnetic field (i.e., their susceptibility is constant).

For unlocalized electrons, as, for example, in conducting metals, which are well described by a band scheme, there exists a paramagnetic contribution to the magnetic moment, which is practically independent of temperature and also linear with the magnetic field. This susceptibility is connected with the changes of energy levels in the bands with external magnetic field and is called Pauli paramagnetism.

1.2.3 Ferromagnetism, Antiferromagnetism, and Ferrimagnetism

Solid state matter can exhibit a unique feature in special cases of atomic neighborhood order: spontaneous magnetization (i.e., magnetic moment in zero external magnetic field). Due to the quantum-mechanical exchange coupling of electrostatic origin, the energy of two neighboring atomic moments may depend on their mutual orientation and either parallel (ferromagnetic coupling) or antiparallel (antiferromagnetic coupling) orientation is preferred. In a three-dimensional (3-D) system of moments, this leads to spontaneous ordering. In order to realize the antiferromagnetic case, the system must possess two equivalent interpenetrating sublattices whose magnetic moments are equal and oriented antiparallel: the spontaneous moment equals zero.

In the case that the sublattices are not equivalent (they have different number of sites or the sites are nonequivalently occupied), the resulting moment given by the algebraic difference of the sublattice moments is not zero and such material is called ferrimagnetic [8] and behaves in many respects similarly as a ferromagnet. The situation in real cases may be more complicated by the fact that not only nearest-neighbor interactions are present and, in various types of magnetic structures, nonparallel configurations of moments are realized. These possibilities of spin alignment are shown in Figure 1.2.

Ferromagnetic and ferrimagnetic materials have nonlinear dependence between *B* and *H*, which is called the BH loop or hysteresis loop, as *B* depends on the magnetic history. The main parameters of the hysteresis loop are coercivity H_c for which $B(H_c) = 0$ and remanence *Br* for which $H(Br) = 0$. Other parameters of the hysteresis loop are described in Section 1.6.1.

1.2.4 Superparamagnetism

If the magnetic particles are small, usually in the nanometer size, they are formed by one magnetic domain and their moments are exposed to the randomizing effect of the thermal motion similarly as the atomic moments in paramagnetism. If the thermal energy is comparable to the energy of the anisotropy of the particle, be it magnetocrystalline or shape, the orientation of the moment of the particle changes its direction and the behavior closely resembles the paramagnetic one. The (system of) particles are in the superparamagnetic state or regime. This is true for temperatures above the blocking temperature of the particles; below this temperature, they display standard behavior. The value of the blocking temperature is increasing with the particle size.

Let us stress that the superparamagnetic state depends on temperature and the time scale over which the magnetic moment is averaged during the measurement. The times range from seconds for the DC magnetic measurement to 10^{-9} s, for example, nuclear magnetic resonance (NMR) or Mössbauer spectroscopy. It is thus incorrect to speak about superparamagnetic nanoparticles without stating the temperature and time window of observation.

Similarly, as in the paramagnetic case, the magnetization measured to high fields follows the Langevin curve, and if the temperature dependence of the low-field susceptibility is analyzed, the role of atomic moments of paramagnets is played here by the moments of the superparamagnetic particles.

1.3 Magnetic Anisotropy

A body is magnetically anisotropic if its magnetic properties (e.g., permeability or ease of magnetization) depend on the direction of the applied magnetic field. The main contributions to the anisotropy are magnetocrystalline anisotropy and shape

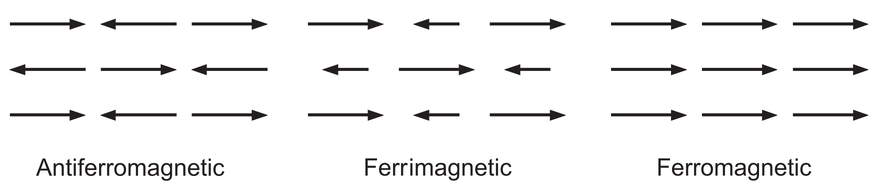

Figure 1.2 Spin alignments due to exchange coupling: (a) antiferromagnetic, (b) ferrimagnetic, and (c) ferromagnetic.

anisotropy; particularly in a noncrystalline system, a significant role is played by the induced anisotropy. Another constituent of anisotropy may lie in the magnetoelastic coupling. As a resulting outcome, in a certain direction, it is easier to magnetize the object than in other ones: these directions are called easy directions or easy axes of magnetization.

1.3.1 Magnetocrystalline Anisotropy

In a single crystal, the magnetic properties may differ along various directions with respect to the crystallographic axes. The free energy of the magnetic crystal must not depend on the change of the sense of magnetization to an antiparallel one; the expression for energy may thus only contain even powers of directional cosines of angles describing the orientation of magnetization with respect to the crystallographic axes. For cubic crystal, the first 2 terms of energy density are usually written as

$$f_{\mathrm{mgcr}} = K_1\left(\alpha_1^2\alpha_2^2 + \alpha_2^2\alpha_3^2 + \alpha_3^2\alpha_1^2\right) + K_2\alpha_1^2\alpha_2^2\alpha_3^2 + \ldots \tag{1.11}$$

where K_1 and K_2 are the anisotropy constants and α_i are the directional cosines.

For the hexagonal symmetry, it is usual to describe the direction of magnetization by its angle ϑ with the hexagonal axis and the lowest term has the form:

$$f_{\mathrm{mgcr}} = K_1' \sin^2\vartheta + \ldots \tag{1.12}$$

The anisotropy constants K have the dimension of energy density and the anisotropy energy is thus $K\cdot V$, where V is the relevant volume. It is useful to introduce the anisotropy field, which, for the uniaxial case (1.10), is

$$H_{\mathrm{mgcr}} = \frac{2K_1'}{M_s} \tag{1.13}$$

Magnetocrystalline anisotropy is usually macroscopically averaged for polycrystalline materials, but it still exists in microscale and affects the material properties such as permeability.

1.3.2 Shape Anisotropy and Demagnetization

When the ferromagnetic body of a finite size is inserted into a homogeneous magnetic field H_0, the magnetic field inside the ferromagnetic body H is smaller than the external field H_0. (In general, the direction of the H vector may also be different from the direction of H_0, but we will not consider this case here.) This difference is called the demagnetization field DM, which acts against the external field:

$$H = H_0 - DM \tag{1.14}$$

where D is a dimensionless demagnetization factor (in the general case, it is a tensor and in our simplified case it is a number between 0 and 1), and $M = \kappa H$ is the magnetization.

The demagnetization field is homogeneous only in bodies with a shape of an ellipsoid (or in limiting case of a thin sheet or a long wire). The magnetic field inside a ferromagnetic sphere in homogeneous magnetic field is shown in Figure 1.3: $H < H_0$, $B > B_0$.

For an ellipsoid, D is constant within the volume of the ferromagnetic body but depends on the direction.

For the general case of an ellipsoidal body with 3 various axes, the demagnetization factor has three principal components, whose sum is equal to 1:

$$D_x + D_y + D_z = 1 \tag{1.15}$$

Directly from that relation, we receive that the demagnetization factor of a sphere must be 1/3.

For the extreme cases of:

1. An infinitely long magnetic wire: the demagnetization factor $D = 0$ along its length $H = H_0$, $B = \mu H_0$ and according to (1.15) in the direction perpendicular to its length D equals ½ and consequently $H = H_0 - ½M$, $B = \mu_0 (H_0 + ½M)$.
2. A thin sheet: $D = 0$ in the sheet plane and thus from (1.15) follows $D = 1$ for H_0 perpendicular to the sheet plane and $H = H_0/\mu$, $B = B_0$

For every case between these extremes, B is larger than B_0 and H is smaller than H_0.

For long strips, one can use an estimate for the magnitude of the demagnetization factor

$$D = \frac{t}{(t + w)} \approx \frac{t}{w} \tag{1.16}$$

where w is the width and t is the thickness of the strip [9].

For all shapes different from an ellipsoid, D depends on the position within the body volume. It is also practical to define demagnetization for the whole body by averaging. Two such definitions can be found in the literature:

1. Ballistic or local demagnetization factor D_{local}, which is calculated from the average magnetization in the body's midplane, corresponding to measurement with a very short search coil in the middle of the body;

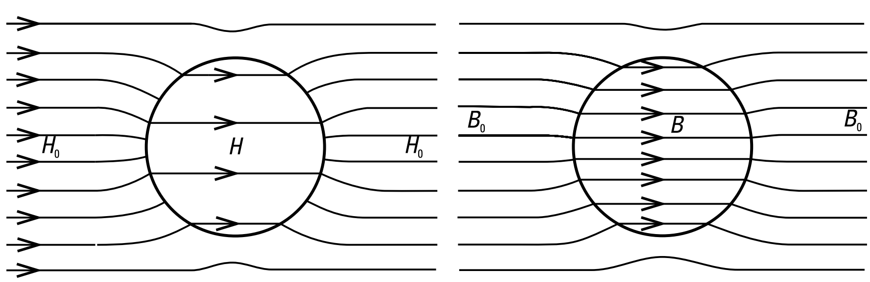

Figure 1.3 Ferromagnetic sphere in the homogeneous magnetic field.

2. Global (magnetometric) demagnetization factor D_{global}, which is calculated from the average magnetization in the whole volume of the body, corresponding to the measurement with a long search coil that surrounds its whole volume.

Ideally, D does not depend on permeability. For real shapes, both the local and global D calculated by FEM and verified by measurement depend slightly on material permeability [9].

From (1.14), we can also write:

$$H = \frac{H_0}{1 + D\kappa} = \frac{H_0}{1 + D(\mu_r - 1)} \tag{1.17}$$

and

$$B = \mu_r \mu_0 H = \frac{\mu_r \mu_0 H_0}{1 + D(\mu_r - 1)} = \mu_0 \mu_A H_0 \tag{1.18}$$

where μ_A is apparent permeability,

$$\mu_A = \frac{\mu_r}{1 + D(\mu_r - 1)} \tag{1.19}$$

For $\mu >> 1$, this relation is simplified to

$$\mu_A = \frac{\mu_r}{1 + D\mu_r} \tag{1.20}$$

Demagnetization factors of long cores are analyzed in Chapter 2, as these are used for induction sensors. The demagnetization of ring cores and racetracks is discussed in Chapter 3, as these core shapes are typical for fluxgate sensors.

The various values of demagnetization factors along different directions give rise to the shape anisotropy. This anisotropy may be also characterized by means of the anisotropy field; let us give an example of a prolate rotational ellipsoid with a demagnetization factor D along the long direction. Then the demagnetization factor in the perpendicular directions equals $(1 - D)/2$ and the anisotropy field stemming from the shape is proportional to the difference of the demagnetization factors in these two directions and equals

$$H_{\mathrm{sh}} = \frac{1}{2}\mu_0 M_{\mathrm{s}}(1 - 3D) \tag{1.21}$$

1.3.3 Induced Anisotropy

The interaction between the crystal lattice or, more generally, the atoms in equilibrium positions and the atomic magnetic moments gives rise to magnetocrystalline anisotropy via the spin-orbit interaction. This interaction is also responsible for the induced anisotropy [2]. If we change the external force, usually the magnetic field, the atomic system approaches the new thermodynamically equilibrium state with a characteristic relaxation time τ, whose temperature dependence is typically given by the Arrhenius relation

$$\tau = \tau_\infty \exp\left(\frac{E_a}{kT}\right) \tag{1.22}$$

where E_a is the activation energy of the process.

At this point, let us stress that the driving agent for inducing anisotropy is the magnetization and the applied magnetic field only changes its spatial distribution and thus this mechanism is only operative below the Curie temperature (T_C) of the material. In order to attain equilibrium at a reasonably short time, according to (1.22), the temperature has to be increased and thus the procedure is called field annealing, although the term magnetization annealing would be more proper.

The equilibrium state of the atomic systems including defects of all types and local order or disorder leads to an easy direction coinciding with the direction of local magnetization; the anisotropy is uniaxial and may be thus described by a relation analogous to (1.11). In the volume of the domain, the induced anisotropy is constant, and in the domain wall, the spatially changing directions of local magnetization stabilize the position of the wall by forming an additional force when the wall is moved by an external field from its stabilized position [10].

For the resulting magnitude of the induced anisotropy, not only the annealing temperature, but also the time dependence of the temperature changes, including the cooling rate, is decisive. This is particularly important when the temperature of the magnetic annealing (i.e., in a magnetic field) is higher than the Curie point; the process of atomic changes leading to the induced anisotropy is here mainly restricted to the cooling range below the Curie temperature.

The effects connected to the induced anisotropy may be roughly divided according to the relaxation time of its changes with respect to the time of observation at the temperature of the experiment. If the former one is much longer, then the induced anisotropy may be treated as constant and constitutes just a contribution to the effective anisotropy.

The magnetization process then essentially depends on the direction of the magnetizing field with respect to the easy axis. Magnetization reversal with external magnetic field in the easy direction proceeds either by one jump at H_c or by the motion of the domain walls, if the critical field for domain walls formation is smaller than H_c. However, when the external field is perpendicular to the easy axis, the magnetization process is realized by reversible rotation without hysteresis and remanence and for $H < H_a$, the susceptibility is constant and equal to M_S/H_a. For a system of particles with the random distribution of easy axis, the resulting magnetization curve is given by the summation or integration over all directions as described by the Stoner-Wohlfarth model [1, 2]. The stabilization of the domain wall position leads to various peculiar shapes of hysteresis curves: the constricted or perminvar hysteresis loops.

If the relaxation time is smaller than the time of observation at the temperature of the experiment, we may observe changes of the observed quantity with time. The most dramatic expression of these changes is the disaccommodation of permeability due to gradual stabilization of the domain walls in new positions after demagnetization or a rapid change of the magnetic field. The complementary effect is the magnetic viscosity: the creep of magnetization to its equilibrium value at the changed field due to destabilization of domain walls after the field change. These effects can be observed, for example, in current transformers.

We may also observe a gradual change of hysteresis loop with time (e.g., forming of the perminvar loop produced by stabilization of the positions of the domain walls).

The frequency dependence of the complex AC permeability displays a decrease of the real part and a maximum of its imaginary part when the relaxation time at the temperature of measurement is equal to the inverse frequency. Similar effects are seen in the temperature dependence of the complex permeability at constant frequency were the coincidence of the relaxation time with the $1/f$ is reached by its change with temperature according to (1.22).

Induced anisotropy may also be caused by fabrication (deposition, drawing, casting, rolling), or it can be created by annealing under stress. Creep-induced anisotropy in amorphous [11] or nanocrystalline magnetic tape is created by stress annealing. Here the direction of the easy axis depends on the sign of magnetostriction. If the easy axis is perpendicular to the tape length, the resulting permeability is very linear, with very small coercivity. This is used to produce core materials for low-noise fluxgate sensors (Chapter 3) and DC-tolerant current transformers (Chapter 11). Anisotropy in anisotropic magnetoresistance (AMR) sensors is induced by deposition in a magnetic field high enough to saturate the whole volume. The measured field is then applied in the hard direction, in which the magnetization process is purely rotational, resulting in low noise and small hysteresis [11].

Anisotropy in magnetic sensor materials is usually uniaxial. Uniaxial anisotropy has a single easy axis corresponding to a minimum energy state. Without the external field, the magnetization M_s of each domain is in the easy direction. If the magnetization is declined by angle θ from the easy direction, the associated anisotropy energy E_u (per unit volume) may be written in the first approximation as

$$E_u = K_u \sin^2 \theta \tag{1.23}$$

where K_u is the constant of uniaxial anisotropy and θ is the angle between M and the easy direction.

Anisotropy is also characterized by the anisotropy field H_a

$$H_a = \frac{2K_u}{M_s} \tag{1.24}$$

where M_s is saturation magnetization.

H_a is equal to the external field needed to rotate magnetization M to the hard direction (which is perpendicular to an easy direction). If the external field applied in the hard direction is smaller than H_a, the component of magnetization in the hard direction is

$$M_h = \frac{M_s H}{H_a} \tag{1.25}$$

Two uniaxial anisotropies with anisotropy fields H_{a1} and H_{a2} result in a uniaxial anisotropy in the same plane. If they have the same direction, the resulting characteristic field $H_a = H_{a1} + H_{a2}$.

For $\varepsilon = 90°$, the angle α is either 0° or 90° depending on which anisotropy is stronger and $H_a = H_{a1} - H_{a2}$. For $H_{a1} = H_{a2}$, the anisotropies are cancelled and the material is isotropic.

In the general case when the easy axes are declined by an angle ε, the direction of the resulting anisotropy is inclined by α from H_2:

$$\alpha = \frac{1}{2}\arctan\frac{H_{a1}\sin 2\varepsilon}{H_{a1} + H_{a2}\cos 2\varepsilon} \tag{1.26}$$

and the resulting anisotropy field H_a is [12]:

$$H_a = \sqrt{H_{a1}^2 + H_{a2}^2 + 2H_{a1}H_{a2}\cos 2\varepsilon} \tag{1.27}$$

1.3.4 Anisotropy in Magnetic Wires

Magnetic wires are used for giant magnetoimpedance (GMI) and fluxgate sensors. The axial M_z and circular M_φ magnetization components are given by:

$$\begin{pmatrix} M_z \\ M_\varphi \end{pmatrix} = \begin{pmatrix} \kappa_{zz} & \kappa_{z\varphi} \\ \kappa_{\varphi z} & \kappa_{\varphi\varphi} \end{pmatrix} \begin{pmatrix} H_z \\ H_\varphi \end{pmatrix} \tag{1.28}$$

The diagonal components of the susceptibility tensor correspond to axial and circular magnetization loops. The M_z-H_φ loop is related to the inverse Wiedemann effect and the M_ϕ-H_z loop to the Matteucci effect. These two effects appear only in the presence of helical magnetic anisotropy caused by stress and strain induced by applied torque or torsion annealing [13].

1.4 Magnetostriction

The magnetoelastic phenomena and, in particular, magnetostriction, are based on the fact that the emergence of spontaneous magnetization leads to a change of interatomic distances in the condensed matter. This spontaneous magnetostriction s

$$s = \frac{\Delta l}{l} \tag{1.29}$$

(sometimes also called exchange magnetostriction [13]) may be either positive (e.g., iron) or negative (e.g., nickel). The strong temperature dependence of this magnetostriction may lead to the invar effect, where the thermal expansion is compensated by the decrease of the (spontaneous) magnetostrictive strain resulting in an effective thermal dilatation coefficient equal to zero in a certain temperature range.

Let us for the moment neglect the magnetocrystalline anisotropy and consider an isotropic case; the situation is then schematically illustrated in Figure 1.4.

Figure 1.4(a) shows the undeformed paramagnetic domains, Figure 1.4(b) shows the deformed ferromagnetic domains with random orientation in the demagnetized state, and Figure 1.4(c) shows magnetization to saturation by an external magnetic field. In each isotropic domain, the strain e varies with angle θ from the direction of spontaneous magnetization

$$e(\theta) = \frac{\Delta l}{l}(\theta) = e\cos^2\theta \tag{1.30}$$

The spontaneous magnetostriction λ_o due to the existence of spontaneous magnetic moment in the demagnetized state is then given by the integration of $e(\theta)$ over the angle θ, which gives for homogeneously random distribution

$$\lambda_o = \frac{\Delta l}{l} = \frac{e}{3} \tag{1.31}$$

Let us remark that the magnetostrictive strain must not depend on the sense of magnetization but only on its direction so that it is only changed by the rotation of magnetization and reversing the sense of magnetization does not change the strain.

The length of a material is changed in the external magnetic field

$$\lambda = \frac{\Delta \mathrm{l}}{l} \tag{1.32}$$

and the relative change of the length along the direction of the field λ is called Joule magnetostriction. If the magnetized samples are elongated, we define magnetostriction as positive. It reaches a saturated value λ_s at magnetic saturation. If in the

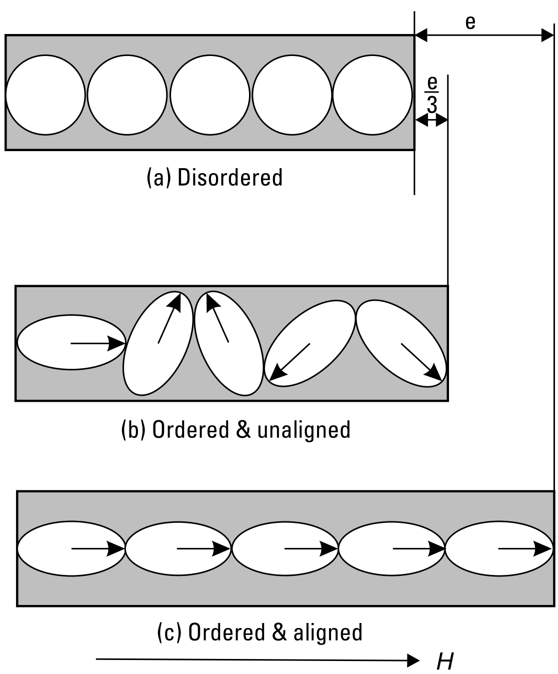

Figure 1.4 The origin of magnetostriction. (*After:* [1].)

external field the volume is not changed, the strain in the direction normal to the external field equals $\lambda_{\perp} = -\lambda/2$.

The measured λ_s may have different values depending on the initial conditions: the saturated state always corresponds to the spontaneous magnetization in the domains aligned along the external field, but the distribution of the magnetization directions, even in the demagnetized state with $M = 0$, may be essentially different from the homogeneous randomness assumed in Figure 1.4. Only those volumes contribute to the magnetostrictive strain λ, where magnetization is rotated to the field direction. In the limiting case that the domains in the demagnetized state are oriented along the external saturating field, the strain is equal to 0. However, if in the initial state, the magnetizations in domains are perpendicular to the external field, the saturated strain is maximum and equal to 3/2 λ_o. A metallic glass is an example of isotropic material, in particular, without magnetocrystalline anisotropy, where the only anisotropy may be the shape anisotropy holding magnetization in the ribbon plane.

If the magnetostriction is anisotropic, it may be characterized (e.g., for a cubic symmetry) by two different constants λ_{100} and λ_{111} that may even have a different sign. The magnetostriction of a polycrystalline material reflects this anisotropy of its constituting grains and the resulting magnetostriction may be approximated, under some conditions, by the linear combination of the two mentioned constants [14].

While iron and nickel have saturation magnetostriction λ_s of units or tens of parts per million (ppm), the largest magnetostriction constant at room temperature of 2,000 ppm was achieved for Terfenol-D alloy in a 160-kA/m field (the name shows that it is essentially an alloy of terbium and iron, invented at the Naval Ordnance Laboratory and it is doped by dysprosium). This large magnetostriction is utilized mainly in actuators.

Inversely, magnetostrictive materials change their properties by stress. This effect, inverse to the Joule magnetostriction, is called the Matteucci effect. Applying the uniaxial stress σ to an isotropic material with magnetostriction λ_s results in a uniaxial magnetoelastic anisotropy with

$$E_{\text{mel}} = K_{\text{mel}} \sin^2\theta, \text{ with } K_{\text{mel}} = -\frac{3}{2}\lambda_s \cdot \sigma \tag{1.33}$$

whose sign depends on the sign of the product $\lambda_s \cdot \sigma$. If we apply tension to a material with a positive λ_s, the direction of the stress becomes the easy axis, just the same as applying uniaxial compression to a material with negative λ_s. However, if the stress and λ_s have different signs, an easy plane of magnetization is induced normal to the stress. This magnetoelastic anisotropy constant has to be added to the effective uniaxial anisotropy constants of the crystalline, induced, or shape origins.

1.5 Domain Structure

In the preceding section, it was assumed that a ferromagnetic body exhibits spontaneous magnetization. However, only some hard magnetic materials appear macroscopically magnetized in the absence of an applied field. If the sample were magnetized with M_s, the demagnetizing stray field energy W_D would be very high, as discussed above. Therefore, M_s occupies the available easy directions, given by the magnetocrystalline and strain anisotropy energy minima in order to reduce the pole strength and herewith H_d and, consequently, W_D as shown in Figure 1.5.

The volumes, magnetized uniformly with M_s in an easy direction, are the magnetic domains, divided by the domain walls. These walls also need energy to be established, which yields a lower domain size limit. The wall energy consists mainly of magnetocrystalline anisotropy and exchange energy (the contributions of stray fields are usually neglected).

The wall thickness is a trade-off to minimize the wall energy, the exchange energy trying to extend the wall thickness, and the anisotropy pressing it down.

Domain structures and domain walls can have a very complex nature, caused by magnetostriction (both inner and applied stresses) and microscopic stray fields [10]. For instance, the domain structure of Figure 1.5 is only favorable if the magnetostriction is very low and no strain occurs. Otherwise, a compromise structure like in Figure 1.5(e) is established.

Furthermore, the domain walls should provide a steady normal component of M_s, but in small volumes this law can be violated in order to reduce inner stray fields and stresses. The orientations of the easy directions may also differ for each crystal grain or they can be totally random in amorphous materials where crystal order and consequently magnetocrystalline anisotropy are missing. A typical width of a domain is 10 … 100 μm and a typical wall thickness is 10 … 100 nm, but much larger domains may exist in grain-oriented materials, thin films, or wires. Figure 1.6 shows a simplified 1800 Bloch-type domain wall where the magnetic moments are gradually rotated from one easy direction to the antiparallel one with the axis of rotation normal to the wall plane.

The Bloch wall is accompanied by stray fields, where it intersects the surface of the ferromagnet. In thin films, the Bloch walls become energetically disadvantageous because of these stray fields and a Neel wall is realized where the moments

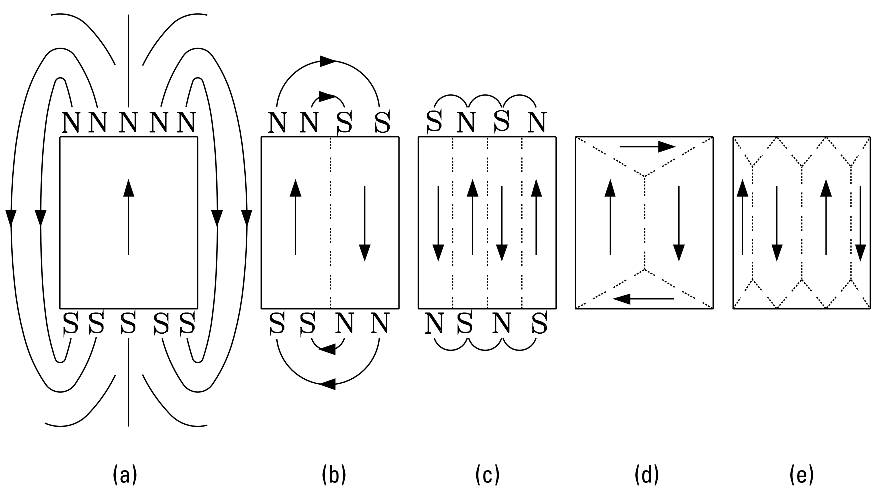

Figure 1.5 (a–c) Reduction of stray fields by orienting the electron spins in domains, magnetized uniformly in easy directions; (d) $\lambda_s \approx 0$; and (e) compromise structure, $\lambda_s > 0$.

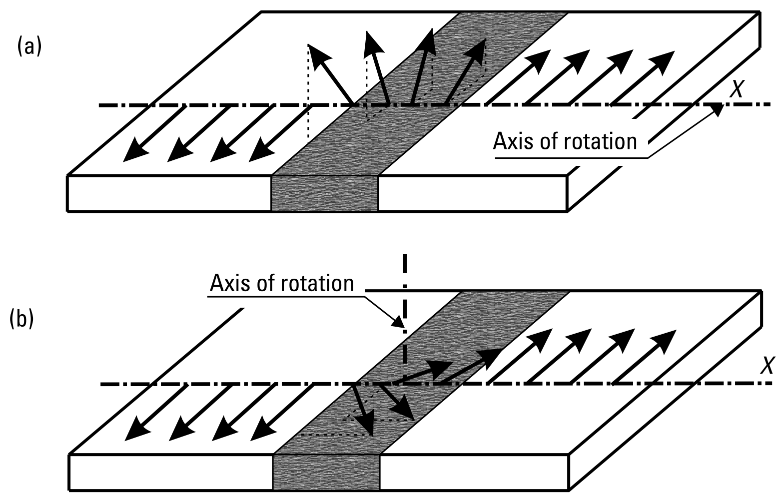

Figure 1.6 Spin rotation within: (a) a Bloch wall and (b) a Neel wall between antiparallelly magnetized domains. (*After:* [2].)

in the wall are rotating along the axis normal to the thin film and no stray fields above the film surface are formed.

1.6 Magnetization Process

Figure 1.7 shows schematically the process of increasing the macroscopic magnetization by applying a field on a ferromagnetic material. In absence of H, the spin moments are equally distributed along the four easy directions in this example. At weak fields, the domain walls are moving in order to increase the volume of the domains with a magnetization component closer to H at the expense of the others. This motion is caused by the torque acting on the magnetic moments within the volume of the wall, where exchange energy and anisotropy energy are in a fine balance. These easy domain wall displacements are the reason of the high permeability of soft magnetic materials and determine their technical applications. Several magnetic sensor concepts are based on the behavior of domain walls, as the well-known Wiegand sensors (see Chapter 8).

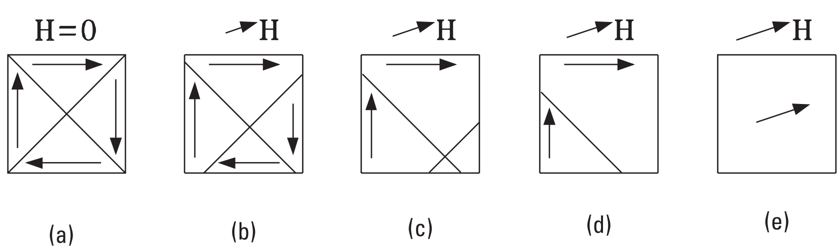

Figure 1.7 The effect of an applied field on a simplified domain structure; the rotation of the domain's magnetization starts before the end of the wall displacements only if a strong stray field can be avoided.

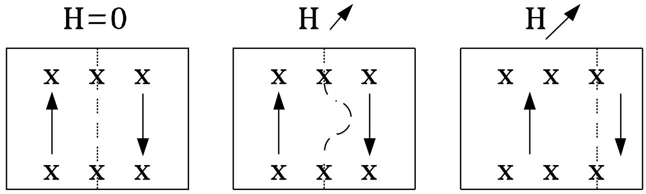

Figure 1.8 Reversible (a → b) and irreversible domain wall displacements (b → c).

The increase of bulk magnetization by domain wall displacements in an applied field (energy W_H) is balanced by the shape anisotropy energy W_D and hindered by local stray fields and magnetostriction, for example. If W_H is large enough to compete with the magnetocrystalline anisotropy energy, the domain's magnetization is rotated towards the field direction, tracing the minima of the total energy $W_T = W_c + W_s + W_D + W_H$. This simplified magnetization process is the basis for calculating magnetization curves of anisotropic materials.

In the case of nonideal material structures with defects such as grain boundaries, nonmagnetic inclusions, or cracks, the domain walls are pinned, reducing the stray fields of these pinning sites when covering as many imperfections as possible. Figure 1.8 illustrates the mechanism of irreversible[1] domain wall displacements.

Pinned at two imperfections in this case, the wall is moving reversibly at low H. Further field increase forces the wall to jump until it is pinned again by other impurities.

The path of the domain wall differs for each cycle and these irreversible Barkhausen jumps are energy dissipative due to spin relaxation, magnetomechanical interaction, and microscopic eddy currents. Furthermore, the induction within the moving domain wall's volume because of spin rotation gives rise to the Barkhausen noise. Therefore, we find that the magnetization process depends on the magnetic history experienced by the material.

1.6.1 Magnetization Curve

The initial (virgin) magnetization curve is obtained when a field is applied to a previously completely demagnetized sample. Starting with the reversible domain wall displacements at weak fields and proceeding with irreversible Barkhausen jumps, the saturation M_s[2] is finally reached by processes of magnetization rotation against the anisotropy energy. After reducing H to zero, the sample remains magnetized at the remanence M_r. The magnetization becomes zero at the coercive field strength $H = -H_{cJ}$. The upper branch of the major hysteresis loop is completed at $M = -M_s$

[1]Rotation processes can also be irreversible in the case of materials with restrained domain structure (permanent magnets, fine particles, thin films).

[2]The saturation magnetization is almost identical to M_s. It differs from the spontaneous magnetization only by the effect of the field on aligning the magnetic moments against the thermal disorder, which is very small at technical field values and at temperatures far below T_C.

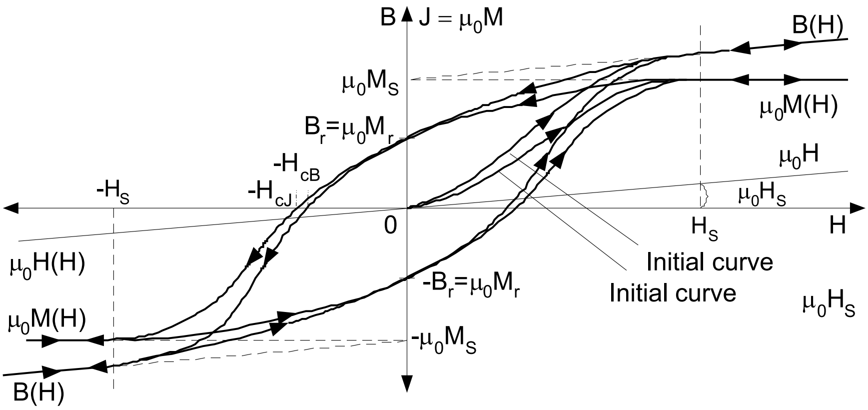

Figure 1.9 Hysteresis of $J = \mu_0 M$ (H) and B(H).

and the lower branch is obtained by an analog procedure (Figure 1.9). The $B(H)$ hysteresis curve is similar in soft materials (the difference is only $\mu_0 H$), and $B = 0$ is reached at H_{cB}.

Demagnetization can be accomplished by several methods that yield different results. Heating the sample over T_C in a zero magnetic field leads to a perfect erasure of the magnetic history. Applying an AC field with decreasing amplitude is the most usual way of demagnetization (see Figure 1.10), but it does not yield the desired random distribution of the domain magnetizations over the easy directions. An improvement is the demagnetization by a decreasing rotating AC field; this technique is used in geophysics. Demagnetization by mechanical shock waves happens

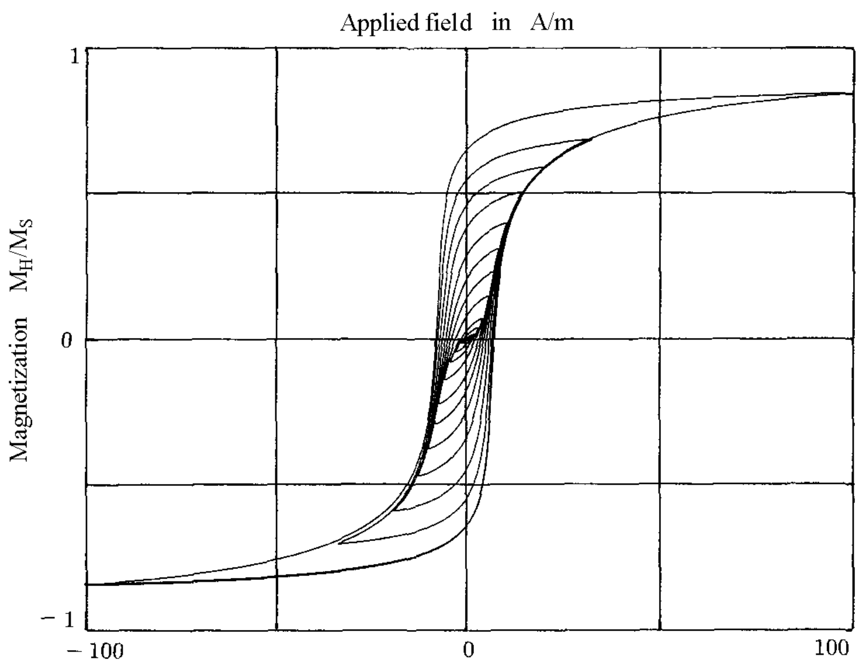

Figure 1.10 Demagnetization by applying an AC field with decreasing amplitude.

sometimes accidentally to permanent magnets (decaying stress oscillations change the easy directions, which cause domain wall displacements of decreasing amplitude).

The total (relative) permeability or amplitude permeability depends on the operation point B_t, H_t.

$$\mu_a = \frac{B_t}{\mu_0 H_t} \tag{1.34}$$

Important types of permeability are the initial permeability, which is represented by the tangent line on $B(H)$ at the origin

$$\mu_i = \lim_{H \to 0} \frac{B}{\mu_0 H} \tag{1.35}$$

the maximum permeability that is the slope of the tangent line from the origin to $B(H)$

$$\mu_{max} = \max(\mu_a) \tag{1.36}$$

the incremental permeability

$$\mu_\Delta = \frac{\Delta B}{\mu_0 \Delta H} \tag{1.37}$$

and the differential permeability, which is the derivative of the $B(H)$ curve.

$$\mu_{diff} = \frac{dB}{\mu_0 dH} \tag{1.38}$$

Often parameters of the minor loops are also important, such as reversible permeability, which is the limit of the superposition permeability for small AC fields at the operation point B_t, H_t. Reversible permeability is the slope of the small minor loop and it is smaller than the differential permeability at the same working point. Minor loops are used for magnetic circuits with DC bias and a small AC working signal.

The energy loss W_L per unit volume and cycle, which is finally converted to heat, corresponds with the area of the hysteresis loop.

$$W_L = \int \boldsymbol{H} \, d\boldsymbol{B} \tag{1.39}$$

To obtain the power loss, one has to multiply W_L by the frequency f. Losses are divided into static hysteresis losses and frequency-dependent losses. The latter are distinguished between normal (due to bulk dB/dt) and anomalous (due to additional dB/dt of large domain wall displacements) eddy-current losses.

In order to reduce the effects of hysteresis, in particular remanence and coercivity, the magnetization curve can be idealized by superposing an AC field of higher frequency (see Figure 1.11), averaging the magnetization by tracing the centers of the minor loops. This is called magnetic shaking, a technique successfully used for improving the parameters of magnetic shielding (see Chapter 10).

Magnetization curves can be measured inductively at a ring-core sample with different windings, evaluating (1.4) and (1.5) for H and B, respectively. If the sample

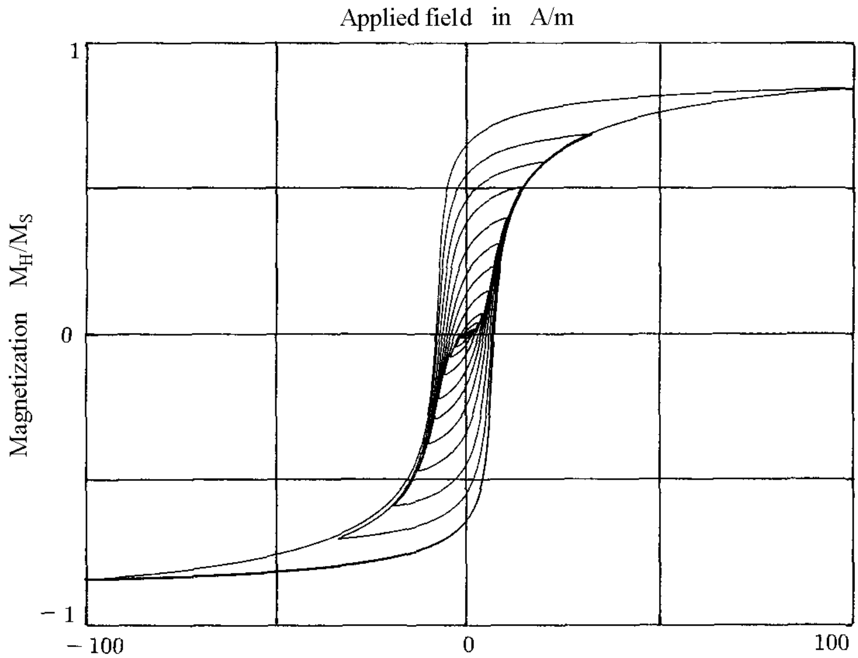

Figure 1.11 Minor loops and their permeability by applying a small AC field with a variable bias.

is an open magnetic circuit, the demagnetizing field causes a flattening of the curve by decreasing the material permeability to the apparent permeability (1.17). Modern techniques of magnetic measurements are described in detail in a comprehensive handbook by Tumanski [7].

The nonlinearity of magnetization curves is utilized in fluxgate sensors (see Chapter 3). Simulating the magnetic behavior of sensors, the calculation of hysteresis loops is a very complex task and several models have been developed [15, 16].

1.7 Magnetic Materials

In this chapter, we shortly characterize magnetic materials that are used in magnetic sensors: soft magnetic materials are mainly used as functional materials in ferromagnetic magnetoresistors and fluxgates or as field concentrators for all types of sensors. Magnetically hard materials are mainly used as a source of field for positions sensors and some torque sensors or for biasing of magnetoresistors. Semiconductors are nonmagnetic materials, and we discuss them as basic materials for Hall sensors in Chapter 5.

1.7.1 Soft Magnetic Materials

Crystalline, amorphous, and nanocrystalline magnetically soft materials are used as functional materials for many magnetic sensors (with the exception of Hall sensors and semiconductor magnetoresistors).

Soft magnetic alloys are also used in flux concentrators to increase the sensitivity of Hall sensors and magnetoresistors and also as cores of induction coils (Chapter 2). Magnetically soft magnetic shields are used in giant magnetoresistance (GMR) sensors, and large ferromagnetic shieldings are used for sensor testing (Chapter 10). Yokes for electric current sensors are another application of soft magnetic materials (Chapter 11).

The requirements on soft magnetic materials are usually a large saturation field B_s, a minimum coercivity H_c, high or constant permeability with minimum temperature dependence, high electrical resistivity, and small magnetostriction λ_s. Small B_s is an advantage for fluxgate sensors, and large λ_s is required for magnetoelastic devices [17]. Some sensors such as proximity switches utilize materials with square hysteresis loops.

Many sensors still use traditional polycrystalline FeNi high-permeability materials (permalloy, Supermalloy, Mumetal), which require annealing. Also being used are FeCo (highest saturation), FeSi (increased resistivity, decreases eddy currents), and FeAlSi (Sendust, mechanically hard).

Amorphous alloys are produced by fast solidification from the melt in a form of tapes or wires. Cobalt-based amorphous alloys such as Vitrovac 6025 may have zero magnetostriction and low coercivity, but they have low saturation field of typically $B_s = 0.7$T. These materials are popular for the cores of fluxgate sensors. Fe-based amorphous alloys may have $B_s = 1.6$T. Sensor applications of amorphous magnetic materials were reviewed in [18].

Nanocrystalline soft magnetic alloys are made by recrystallization of the amorphous master alloy. They are used mainly for current transformers [19] (Chapter 11). The 16% Si nanocrystalline Finemet was used in [20] for a high-temperature fluxgate sensor. The material has a Curie temperature of 600°C compared to 210°C for the commonly used amorphous Vitrovac 6025.

Soft ferrites are cheap, but at low frequencies they do not achieve comparable performance as metallic materials. The advantages of ferrites are high electrical resistivity (frequency limit up to 5 GHz), absolutely no oxidation, and the possibility of arbitrarily shaped cores. The main disadvantages are the lower saturation magnetization ($B_s \approx 0.5$T) compared to ferromagnets and only moderate permeability.

All the mentioned materials are used in bulk form and as thin films made by sputtering, electroplating, or laser deposition. Bulk materials are produced mainly in the form of a thin tape or wire. The magnetic properties of the bulk material are usually better than those of thin films: minimum achieved coercivity for an electroplated permalloy was 280 A/m [21], while coercivity of tapes can be under 1 A/m.

The most common sensors based on thin-film soft magnetic alloys are AMR sensors, which usually use sputtered permalloy and work up to 225°C (Chapter 4). A thicker layer of similar material is used for microfluxgate sensors (Chapter 3).

Many sensors are making use of magnetic multilayers: giant magnetoresistance (GMR) and tunneling magnetoresistance (TMR) sensors (Chapter 4) and also some giant magnetoimpedance (GMI) sensors (Chapter 8).

Amorphous glass-coated microwires with positive magnetostriction have bistable magnetization characteristics. The critical field at which a transition from one direction of magnetization to the opposite one takes place, the switching field, is sensitive to temperature and mechanical stress, which allows the use of these microwires as sensors [22].

1.7.2 Hard Magnetic Materials

Permanent magnets are often used as targets or field sources for position and velocity sensors. The most popular are cheap ferrite magnets, but stronger NdFeB magnets or more temperature stable, SmCo magnets are also being used. For temperatures above 350°C, the only solution is AlNiCo. Unlike the other magnetically hard materials, coercivity of ferrite magnets increases with temperature. This means that they are not suitable for low-temperature applications, as they can be more easily demagnetized at low temperatures.

Polymer-bonded magnetic materials are used for magnetic scales: multipole magnetic patterns are created by pulse magnetization during or after the production, which is mainly made by injection molding. These scales are used for rotational and linear position sensors [23]. Spray-coated magnetic rings from polymer-bonded semihard magnetic material are used for polarized-band torque sensor (Chapter 11).

Hard magnets are also used as biasing magnets; in this case, the temperature stability is critical parameter. They also serve as a field source for MEMS magnetic field sensors based on Lorentz force (Chapter 8).

If we pay special attention to the two main characteristics of the hysteresis loops (permeability and coercivity), we may use an oversimplified but helpful approach. Notwithstanding the exact mechanism of the magnetization process (motion of domain walls, turning of spontaneous magnetization of domains to the direction of applied field), it comes out from the rigorous treatment of various models that the relative permeability is inversely proportional to the effective anisotropy. Similar consideration of the process of magnetization reversal results in the conclusion that again, without details of the system (multidomain or single-domain systems, coherent or incoherent modes of rotation of magnetization, or the various mechanisms of wall pinning and/or wall formation), the coercivity is proportional to the effective anisotropy.

This is illustrated in the Figure 1.12, where log of relative permeability is plotted against the logarithm of coercive field. The slope of −1 in this representation shows that the above-mentioned general relation is valid over 8 orders of magnitude from magnetically extremely soft to the hardest known materials.

Let us add a remark that is a consequence of the above-mentioned relation between (static) permeability and coercive field: the high permeability in soft and extremely soft magnetic materials is maximum at fields $H_{\mu\max}$ that are of the order of coercive fields and are limited $H_{\mu\max} < M_s/\mu_r$.

1.8 Sensor Specifications

Besides the well-known parameters for other sensors and instruments, magnetic sensors have specific peculiarities given by nonlinearity of materials and complex effects used. We also mention the basic problems associated with the sensor calibration. The calibration instruments, especially the shieldings, are described in Chapter 11.

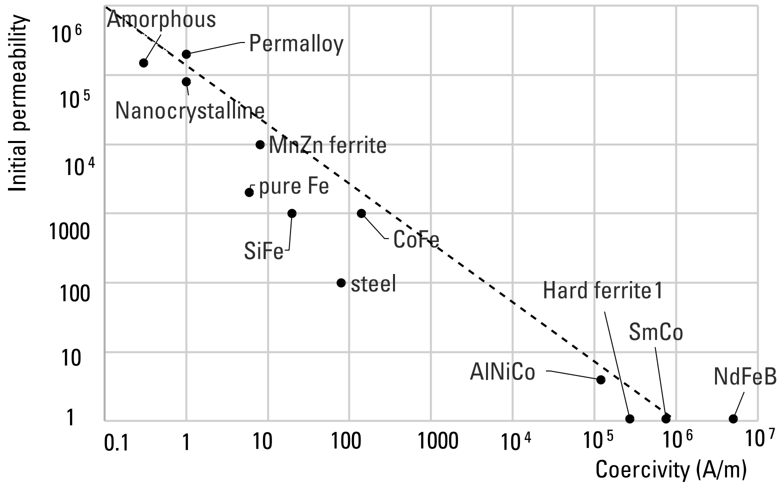

Figure 1.12 Relative permeability versus coercivity for various magnetic materials. (*After:* [1].)

The manufacturers' datasheets sometimes give only the sensitivity or resolution, but fail to mention temperature stability of the sensitivity and offset, perming, hysteresis, and other tricky parameters. In general, all the absolute specifications should be given in the units of the measured field, the sensitivity should be referred to the sensor output, and the measuring conditions should be specified.

1.8.1 Full-Scale Range, Linearity, Hysteresis, and Temperature Coefficient of Sensitivity

These characteristics can be measured in calibration coils (e.g., a Helmholtz coil pair). The coils should be far from ferromagnetic objects, which could cause nonlinearity, and they should be much larger than the tested sensor to ensure that the field is homogenous in the sensor location. The disturbing fields should be small; the ideal calibration coil is located in a thermostated nonmagnetic house far from the sources of the magnetic pollution (see Figure 7.20(b)). Nighttime (especially on weekends) is the ideal time for precise measurements because of low traffic and urban activity. The worst disturbing fields are caused by DC current from electric trains, streetcars, and the subway. Simultaneous monitoring of the Earth's field is recommended; it may prevent invalid calibration due to the daily variation of the Earth's field and especially during magnetic storms. The uncertainty may be reduced by averaging.

If precise calibration of the sensor sensitivity is required, the testing coil should be calibrated against a high-accuracy scalar magnetometer (usually a resonance magnetometer) and special care should be taken to align the sensor sensing axis to the direction of the testing field.

DC current magnetic sensors are usually calibrated by field steps of both polarities to correct eventual changes of the sensor offset and the background field. The field steps should have sufficient duration as the time constant of the sensor and also the time constant of the calibration coil may be long. The current into the coil should be measured synchronously with the sensor output. The calibration current may heat the testing coil and this effect may change its constant; the coil temperature should be monitored by measuring the voltage drop.

1.8.2 Offset, Offset Temperature Coefficient, and Long-Term Stability

Offset and offset stability are ideally tested in multilayer magnetic shieldings (Section 10.6). It is important to keep the residual field, which is usually caused by remanence, low. If necessary, ferromagnetic shieldings can be demagnetized. Good cylindrical shieldings have an axial rest field below 10 nT and a radial rest field below 2 nT. Sensor offsets are measured by averaging the sensor reading from 2 opposite sensing directions (or more directions equally distributed), since it corrects for the remanent field. The offset can be measured with a precision of 0.1 nT by this technique. It should be mentioned that some sensors cannot measure zero field; the typical example are the resonance sensors (Chapter 7).

Temperature changes of offset are tested by the thermostat inside the magnetic shielding. The thermostat should be made of nonmagnetic material and also electrically insulating material; otherwise, thermoelectric currents generated by temperature gradients in the testing device may cause disturbing magnetic fields. There should be good temperature insulation between the thermostat and the shielding so that the shielding temperature is constant. Some setups use a flow of, for example, N_2 gas for the temperature control of the magnetic sensors within the shielding. In general, the temperature changes should be slow enough: the magnetic sensor offset is often more sensitive to temperature gradients than slow changes. The reason is that temperature gradients cause large mechanical stresses due to different dilatations of the sensor structure.

It is also necessary to check if the offset changes with temperature are reversible and reproducible. Irreversible changes often occur at higher temperatures. The offset temperature coefficient is usually given in nT/°C. In many cases, offset temperature coefficient changes with temperature and also piece-to-piece, so typical or maximum values are often given. Offset interval in a given temperature range is more convenient value than the temperature coefficient, especially for large temperature intervals.

1.8.3 Perming

Perming is the change of the sensor offset due to a magnetic shock. It is similar to hysteresis, but the applied field may be much higher than the full-scale range. All the sensors containing ferromagnetic material are susceptible to perming. The only solution is periodical remagnetization of the sensor, which ensures the defined magnetic state. In case of fluxgate sensors (Chapter 3), the remagnetization is performed by the excitation current; if the excitation amplitude is high enough, no significant perming is observed. Ferromagnetic magnetoresistors can be flipped to reduce the perming and crossfield responses. Perming may appear also at semiconductor sensors with ferromagnetic flux concentrators.

1.8.4 Noise

Noise is a random variation of the sensor output when the measured value is zero. Ultralow-frequency noise is a part of long-term stability: the fluctuations of zero are usually referred to as noise, and the trend is referred to as time drift. The noise properties are characterized by its power spectrum. Power spectrum density $P(f)$

at a given frequency f can be used to compare the noise properties of sensors. If the peak-to-peak value of the noise or rms value is given, the frequency range from f_L to f_H must be specified.

The magnetic-sensor noise is usually something between the ideal white noise and the ideal $1/f$ noise. White noise has a power spectrum density P independent of frequency; for noise of $1/f$ character, $P(f) = P(1)/f$ [nT^2/Hz], where $P(1)$ is the power spectrum density at 1 Hz. In the case of $1/f$ noise, the precise specification of f_L is much important than f_H. Sensor data like noise peak-to-peak (or rms) value from DC current to 10 Hz have sense for sensors with only white noise, which is rare.

Although the peak-to-peak noise value may be tricky and it is usually not precisely defined, it is very convenient and of practical value to characterize the sensor performance.

The low-frequency limit f_L is often simply taken as the inverse value of the observation period; f_H is often taken as the corner frequency of the lowpass filter in the signal path. RMS value can also be calculated by integration of the power spectrum density over the required frequency range (from f_L to f_H); in digital processing, the integration is replaced by summation.

$$N_{\text{rms}} = \sqrt{\int_{f_L}^{f_H} P(f)\,\mathrm{d}f} \tag{1.40}$$

in case of the white noise

$$N_{\text{rms}} = \sqrt{P(f_H - f_L)} \tag{1.41}$$

in case of the $1/f$ noise

$$N_{\text{rms}} = \sqrt{P(1)\ln(f_H/f_L)} \tag{1.42}$$

The noise spectrum density is often given in the units of nT/√Hz or pT/√Hz. The conversion is straightforward: for example, 9 nT^2/Hz corresponds to 3 nT/√Hz, often written as 3 nT/sqrt(Hz). For $1/f$ noise, the $\sqrt{P}$ value decreases with $\sqrt{f}$: in our example, if the noise is 3 at 1 Hz, it is $3/\sqrt{10} = 0.95$ at 10 Hz, and $3\cdot\sqrt{10} = 9.5$ nT/√Hz at 0.1 Hz.

If we sum the noise contributions N_i from several (independent) sources or several (nonoverlapped) bandwidths, we can calculate the total noise N

$$N^2 = \sum_i N_i^2 \tag{1.43}$$

1.8.5 Resistance Against Environment (Temperature, Humidity, and Vibrations)

Temperature range is often limited by package technology. In Table 1.2, the maximum and/or typical values are given.

Also, permanent magnets have a limited operation temperature: NdFeB up to 100°C, and SmCo works up to 300°C; ferrites and AlNiCo magnets can be used over 400°C.

Table 1.2 Temperature Range of Magnetic Sensors

Sensor Type	*Minimum Temperature*	*Maximum Temperature*
Silicon Hall	1.5K < −40°C	150°C (up to 400°C)
InSb/GaAs		300°C
InSb magnetoresistor	−60°C	200°C
AMR		85°C (potentially up to 200°C)
GMR		150°C
Fluxgate (as tested for space applications)	−150°C	200°C
SQUID	<1 μK	−180°C

Humidity destroys high-temperature superconducting quantum interference device (SQUID) sensors (Section 7.7.1). Self-capacitance of the coils increases with moisture; sensor coils may be impregnated, but most of the impregnation processes worsen the coil temperature stability. A number of high-temperature SQUID sensors fail if they are wet from condensed moisture. One solution is to keep the sensor either at liquid nitrogen temperatures or in a sealed package with desiccant.

1.8.6 Resistance Against Perpendicular Field and Field Gradient

Vector magnetic sensors that contain ferromagnetic material such as ferromagnetic magnetoresistors and fluxgates are also sensitive to fields perpendicular to their sensing direction. The crossfield effect is nonlinear so it cannot be easily corrected. The errors of this origin are small for the Earth's field: 20-μT perpendicular field in horizontal direction may cause 1-nT to 10-nT errors in fluxgate sensor reading (Section 3.10) and similar errors for GMR and AMR sensors. Large perpendicular fields may cause gross errors; the sensor characteristics may be distorted or even reversed and, in the case of magnetoresistors, the error may remain after the perpendicular field disappears. Similar to the perming effect, the sensor should be remagnetized.

Resonance magnetometers fail in large field gradients: the broadening of the resonance curve causes a decrease of the signal, which may cause a decrease in the accuracy or even a false reading. Thus resonance sensors cannot be used for measurements inside buildings in the close vicinity of ferromagnetic objects. Precisely defined field gradients are used in NMR tomography.

1.8.7 Bandwidth

The sensor bandwidth is usually given for a specified decrease in sensitivity (e.g., −3 dB, −10%), phase characteristics are usually not specified. Increasing the sensor bandwidth usually causes increase in the N_{rms}.

When testing the bandwidth, care should be taken to check the frequency characteristics of the testing coils and monitor the testing current. Also, eddy currents in conducting structures may cause false calibration.

1.8.8 Other (Power, Radiation Immunity, and Cost)

1.8.8.1 Power

Sensor power is critical for battery-operated devices. Lowering power usually means compromises with sensor noise and stability. In the case of AC-excited sensors, the power consumption can be decreased by lowering the operation frequency, but the bandwidth would be reduced.

The semiconductor sensors are the most susceptible to radiation, but they withstand a much higher dose than the typical computer memory.

The sensor cost is often an important parameter. Simple Hall sensors cost below $1, but the price is growing quickly with performance: highly linear calibrated Hall sensors may cost $1,000, and some SQUID sensors can exceed $10,000/channel.

High-performance sensors are often not sold alone, only as a part of the magnetometer. This is usually the case of resonance sensors and high-performance fluxgates.

References

[1] Jiles, D. C., *Introduction to Magnetism and Magnetic Materials*, Third Edition., Boca Raton, FL: CRC Press, 2016.

[2] Coey, J. M. D., *Magnetism and Magnetic Materials*, Cambridge, U.K.: Cambridge University Press, 2010.

[3] Hilzinger, R., and W. Rodewald, *Magnetic Materials: Fundamentals, Products, Properties, Applications*, New York: John Wiley & Sons, 2012.

[4] Krishnan K. M., *Fundamentals and Applications of Magnetic Materials*, Oxford, U.K.: Oxford University Press, 2016.

[5] Buschow, K. H. J., and E. Bruck, (eds.), *Handbook of Magnetic Materials*, Vols. 1–27, London, U.K.: Elsevier, 1980–2019.

[6] Brauer, J. R., *Magnetic Actuators and Sensors*, 2nd ed., New York: John Wiley & Sons, 2014, p. 400.

[7] Tumanski, S., *Handbook of Magnetic Measurements*, Boca Raton, FL: CRC Press, 2011.

[8] Néel, L., "Théorie du traînage magnétique de diffusion," *J. Phys. Radium*, Vol. 13, No. 5, 1952, pp. 249–264; and "Anisotropie magnétique superficielle et surstructures d'orientation," idem 15(1954)225, see also [2]

[9] Kubík, J., and P. Ripka, "Racetrack Fluxgate Sensor Core Demagnetization Factor," *Sensors and Actuators A: Physical*, Vol. 143, No. 2, May 16, 2008, pp. 237–244.

[10] Hubert, A., and R. Schaefer, *Magnetic Domains: The Analysis of Magnetic Microstructures*, New York: Springer, 2008.

[11] Nielsen, O. V., et al., "Metallic Glasses for Fluxgate Applications," *Anales de Fisica*, Vol. B86, 1990, pp. 271–276.

[12] Tumanski, S., *Thin Flm Magnetoresistive Sensors*, IOP, 2001.

[13] Knobel, K., M. Vázquez, and L. Kraus, "Giant Magnetoimpedance," in K. H. J. Buschow, (ed.), *Handbook of Magnetic Materials, Vol. 15*, New York: Elsevier, 2003, pp. 497–563.

[14] du Tremolet de Lacheisserie, E., D. Gignous, and M. Schlenker, (eds.), *Magnetism: Fundamentals*, New York: Springer Science, 2005.

[15] Bertotti, G., *Hysteresis in Magnetism*, San Diego, CA: Academic Press, 1998.

[16] Jiles, D. C., and D. L. Atherton, "Model of Ferromagnetic Hysteresis," *Journal of Magnetism and Magnetic Materials*, Vol. 61, 1986.

[17] Jiles, D. C., and C. C. H. Lo, "The Role of New Materials in the Development of Magnetic Sensors and Actuators," *Sensors and Actuators A: Physical*, Vol. 106, No. 1-3, September 15, 2003, pp. 3–7

[18] Morón, C., et al., "Magnetic Sensors Based on Amorphous Ferromagnetic Materials: A Review," *Sensors*, Vol. 15, No. 11, November 2015, pp. 28340–28366.

[19] Draxler, K., and R. Styblikova, "Use of Nanocrystalline Materials for Current Transformer Construction," *Journal of Magnetism and Magnetic Materials*, Vol. 157/158, May 2, 1996, pp. 447–448.

[20] Butvin, P., et al., "A Relax Type Wide Range Field Sensor Using Finemet," *Sensors and Actuators A: Physical*, Vol. 106, No. 1-3, September 15, 2003, pp. 22–25.

[21] Yi, J. B., et al., "Study of the Grain Size, Particle Size and Roughness of Substrate in Relation to the Magnetic Properties of Electroplated Permalloy," *Journal of Alloys and Compounds*, Vol. 428, No. 1-2, January 31, 2007, pp. 230–236.

[22] Varga, R., et al., "Magnetically Bistable Microwires: Properties and Applications for Magnetic Field, Temperature, and Stress Sensing," in A. Zhukov, (ed.), *High Performance Soft Magnetic Materials*, Springer Series in Materials Science, Vol. 252, New York: Springer, 2017.

[23] Grönefeld, M., "Permanent Magnets: Sensor Applications," in J. Buschow, (ed.), *Encyclopedia of Materials: Science and Technology*, New York: Elsevier, 2007.

CHAPTER 2

Induction Sensors

Pavel Ripka

The basic description of induction sensors starts from Faraday's law:

$$V_i = -\frac{d\Phi}{dt} = -d\frac{\left(NA\mu_0\mu_r(t)H(t)\right)}{dt} \tag{2.1}$$

where V_i is the voltage induced in a coil having N turns (instantaneous value), Φ is the magnetic flux in this coil, $\Phi = B\ A$, A is the core cross-sectional area, H is the magnetic field in the sensor core, and $\mu_r(t)$ is the sensor core relative permeability (the core may be ferromagnetic or air).

Thus, we can write the general equation for induction sensors as:

$$V_i = \frac{NA\mu_0\mu_r dH(t)}{dt} + \frac{N\mu_0\mu_r HdA(t)}{dt} + \frac{NA\mu_0 Hd\mu_r(t)}{dt} \tag{2.2}$$

Basic induction or search coils are based on the first term of (2.2). The middle term describes rotating coil sensors (Section 2.5), where $A(t)$ is the effective area in the plane perpendicular to the measured field. The last term is the basic fluxgate equation (fluxgate sensors are covered in Chapter 3).

Induction magnetometers were reviewed by Tumanski [1] and Coillot and Leroy [2]. A typical induction coil magnetometer consists of a multilayer solenoid. We will start our description with air coils (Section 2.1). They are very stable and linear, but their sensitivity is limited. Typical optimized air coils have a large diameter and they are relatively short. Coils with a ferromagnetic core (Section 2.2) have larger sensitivity, but they are less stable. They should be long and thin to have low demagnetization. Modern low-noise induction coils are usually working in the current-output mode. A low-noise voltage or current preamplifier is usually mounted in proximity to the induction coil, and it should be considered part of the sensor. Induction sensors are, in general, passive, and they should be distinguished from inductance sensors (Section 11.1), which are based on the change of the sensor inductance and which need excitation.

Here we briefly mention some applications of induction magnetometers (more about applications in Chapter 9): in geophysics ([3] and also Section 7.10.3), they serve to measure micropulsations of the Earth's magnetic field (1-mHz to 1-Hz frequency range). Magnetotelluric exploration is the measurement of secondary magnetic fields caused by induced currents under the Earth's surface at frequencies up to the audio range. The field source is the natural variation of the Earth's field caused by solar wind and lightning.

In space research, induction coils are used in plasma experiments (Section 9.8). Magnetic antennas serve for navigation (Section 9.2) and underwater communication. Important are induction velocity sensors and position detectors (Section 11.1). One of the most important applications is the electro-magnetic compatibility (EMC) measurement: extremely low-frequency (ELF) magnetometers measure the magnetic field in the frequency range of 30 to 300 Hz, which includes the power frequency (50 or 60 Hz) and its several harmonics. They are designed to measure the fields from electric appliances and power lines. They often have also wideband rms (root mean squares) value output, which covers typically the 20-Hz–50-kHz frequency range and very low-frequency (VLF) rms output (2–50 kHz). The correct rms field value must be calculated from the time-dependent field modulus $B(t)$, which is a result of instantaneous orthogonal values, measured by three orthogonal coils as:

$$B(t) = \sqrt{B_x(t)^2 + B_y(t)^2 + B_z(t)^2}$$

Air-cored coils, together with an integrator (fluxmeter), are used to map the DC current induction B by an extraction method (Section 2.5.2) and also to measure field intensity H (Section 2.5.4). It is very important to properly calibrate each individual induction coil. The coil constant can be reliably calculated only for very simple air coils with well-defined geometry. The techniques for calibration of sensitivity are explained in Section 10.1.

In this chapter, we cover induction coils and magnetometers, which are used to measure AC magnetic fields. Position and distance sensors based on induction principle are described in Section 11.1.

2.1 Air Coils

Air coils (or loop antennas) contain no nonlinear magnetic materials, and so they have linear amplitude characteristics and their parameters are very stable in time. Their frequency characteristics are linear in a certain frequency range: at low frequencies for voltage output and at middle frequencies for current output. The temperature coefficient of the sensitivity depends mainly on the thermal expansion of the used materials, so it can be made very small and predictable. A typical application for air coils is precise sensing of magnetic fields in accelerator physics [4].

Any air coil, which serves for the generation of magnetic fields (such as Helmholtz coils), can also be used as a pickup coil. Pickup coils may not only measure the outside field, but they are also used for measurement of the magnetic moment of objects located inside them, and that is the principle of rotating sample magnetometers.

The distributed coil capacitances of multiturn coils, together with their high inductance, cause resonances at relatively low frequencies; the output voltage response at higher frequencies is thus nonlinear. The parasitic capacitances may be temperature-sensitive, so that the frequency characteristics change with temperature. Current output is more convenient: short-circuiting the coil inductance L with a small serial resistance R using a current-to-voltage converter suppresses the effect of the parasitic capacitance C. While the ideal induced voltage V_i is proportional to the frequency, the output current response is flat for $f >> R/2\pi L$.

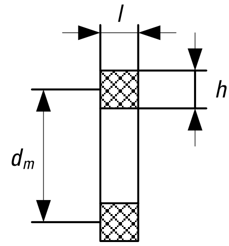

Figure 2.1 Geometry of the air coil.

The geometry of the induction coil is shown in Figure 2.1. Increasing the coil diameter d_m increases the sensitivity, and the R/L factor depends on the amount of copper; the number of turns and the wire thickness are selected to match the input noise characteristics of the amplifier. A disadvantage of the large area induction coils is their vulnerability to vibrations that change the effective coil area and, thus, in the presence of a DC current field, cause noise. It is therefore necessary to construct them to be mechanically stable and mount them securely.

While the cylindrical coils measure the average field over their volume, then the ideal spherical coil measures the field value at its center [5]. Inversely, a current into the spherical coil generates an internal homogeneous field. A good approximation of the spherical coil was used for the Compact Spherical Coil (CSC) fluxgate magnetometer (Section 3.14.1).

If the measured field is not homogeneous, the designer should also consider the sensitivity to field gradients. Axially symmetric coils are insensitive to all even gradients. In the case of cylindrical coils, the sensitivity to odd gradients (spatial harmonics) is minimal for a length-to-outside diameter ratio of 0.67. It is possible to construct coils insensitive to third-order and fifth-order gradients and having very small sensitivity to seventh-order gradient [4]. If we want to measure AC field gradients, it is possible to construct gradiometric induction coil systems that are insensitive to a homogeneous field (harmonic coils): the simplest type is a Helmholtz coil pair connected antiserially (Helmholtz coils are a popular source of a magnetic field; see Chapter 10).

Proper shielding and grounding of the induction coils and their cables are important in order to prevent capacitive couplings (i.e., sensitivity to electrical fields). Sensor shielding must not create any short-circuited turns. Copper is a common material for coils, but where weight is critical, aluminum coils can be used. As shown in Table 2.1, the density of aluminum is 3 times lower than that of copper. Although aluminum has higher resistivity, an aluminum coil has only 45% the weight of a copper coil, having the same voltage sensitivity and noise [6].

High-frequency coils are sometimes wound from *litz* (stranded) wire in order to reduce the effect of eddy currents. Some search coils are made by printed circuit board (PCB) technology. PCB fabricated coils can be flexible and they have a well-defined geometry. However, the achievable number of turns is limited [4]. Coils made by thin-film or CMOS technology have the disadvantage of higher resistance. Coils can be also printed by inkjet printer [7]. Microfabricated solenoids for fluxgate sensors are described in Section 3.12.4.

Table 2.1 Basic Parameters of Wire Materials

Parameter	*Copper*	*Aluminum*
Density	8.9 g/cm^3	2.7 g/cm^3
Specific electrical resistivity	0.0178*10^{-6} Ωm	0.027*10^{-6} Ωm
Temperature coefficient of resistance	0.39%/°C	0.4%/°C
Coefficient of linear expansion	16.6 ppm/°C	25 ppm/°C

2.1.1 Voltage Sensitivity at Low Frequencies

If the parasitic capacitances are negligible and the average turn area is A, we may write for the induced voltage:

$$V_i(t) = -\frac{NAdB(t)}{dt} \tag{2.3}$$

Let us suppose that the measured field B is periodical with period $T = 1/f$. After integration between two zero crossings t_1 and t_2:

$$\int_{t_1}^{t_2} V_i(t)\,dt = NA \cdot \Delta B = NA\left(B_{\max} - B_{\min}\right) \tag{2.4}$$

because B reaches its maximum and minimum values at the time when $V_i(t)$ goes through zero. The arithmetic mean value of the induced voltage will be:

$$V_{\text{mean}} = \frac{2}{T}\int_{t_1}^{t_2} V_i(t)\,dt = 2fNA\left(B_{\max} - B_{\min}\right) \tag{2.5}$$

(as we know that V_i has no DC current component). Usually $B_{\max} = -B_{\min}$ and if the coil is cylindrical and has a mean diameter of d_m

$$V_{\text{mean}} = 4fNAB_{\max} = fN\pi d_m^2 B_{\max} \tag{2.6}$$

Here we notice that, at low frequencies, where we can neglect the parasitic capacitances, the voltage sensitivity is proportional to field frequency. Equation (2.6) is valid for any arbitrary antiperiodical waveform of B. (*Antiperiodical* means that the positive and negative parts of the waveform are symmetrical, that is, there are no even harmonic components.)

In order to find the peak value of a nonsinusoidal field, the induced voltage must be measured by a voltmeter measuring the arithmetic mean value (rectified average value), not by a true rms voltmeter. Knowledge of the signal frequency is necessary for the calculation. If the waveform of the magnetic field is requested, the induced voltage must be integrated by an analog integrator or, after the sampling and analog-to-digital conversion, numerically integrated.

If B is a sinewave, we may write the peak (maximum) value of the induced voltage:

$$V_p = 2\pi fNAB_{\max} = \frac{Nd_m^2 fB_{\max}\pi^2}{2} \tag{2.7}$$

or, for its rms value, the well-known formula

$$V_{\text{rms}} = 4.4NAfB_{\max} = 1.11N\pi d_m^2 fB_{\max} \tag{2.8}$$

The coil DC current resistance can be calculated as

$$R_{\text{DC}} = \frac{4\rho N d_m}{d_w^2} \tag{2.9}$$

where ρ is the coil wire specific resistivity (see Table 2.1), d_w is the wire diameter, and d_m is the mean coil diameter.

We can also easily derive the coil winding mass:

$$m_w = \frac{\pi^2 \gamma N d_m d_w^2}{4} \tag{2.10}$$

where γ is the density of the winding wire (usually copper, rarely aluminum; see Table 2.1).

2.1.2 Thermal Noise

The coil produces thermal noise, which has (in the frequency band of Δf) the rms value

$$V_{N\text{rms}} = \sqrt{\left(4k_B T R_{\text{DC}} \Delta f\right)} \tag{2.11}$$

and the noise density is

$$V_N = \sqrt{\left(4k_B T R_{\text{DC}}\right)}\ \left[\text{V}/\sqrt{\text{Hz}}\right] \tag{2.12}$$

where T is the absolute coil temperature [K] and k_B is Boltzmann's constant.

Let us recalculate the coil thermal noise to the equivalent noise density of the measured field. Using (2.7) and after some calculation, we obtain, in agreement with [6]:

$$B_{N\tau} = \frac{8\sqrt{k_B T \rho}}{\pi^2 f} \frac{1}{d_{\text{W}}\sqrt{N d_m^3}} \tag{2.13}$$

and, for an equivalent field thermal noise $B_{N\tau}$ as a function of the coil winding mass, we may derive:

$$B_{N\tau} = \frac{4\sqrt{k_B T \rho \gamma}}{\pi f} \frac{1}{d_m \sqrt{m_{\text{W}}}} \tag{2.14}$$

An important design rule is this: the thermal noise depends only on the coil winding mass and diameter, not on the wire diameter. The air coil diameter should be as large as possible. The noise voltage is of the white type, but because the voltage sensitivity is proportional to f, the field noise is proportional to $1/f$. Another important factor is the input noise of the preamplifier. Because the amplifier noise depends on the coil resistance and also on frequency, design rules become complex and lead to an optimum wire diameter (Section 2.3). We should also keep in mind that, in real thick coils, the turn diameter is not constant.

2.1.3 The Influence of the Parasitic Capacitances

Distributed capacitance, inductance, and resistance of the coil cause several resonant frequencies. The main parasitic capacitance (parallel to the coil terminals) is responsible for the first (bottom) resonant frequency f_{r1}. Because f_{r1} is the basic limiting frequency, a simple equivalent circuit is sufficient for the description (Figure 2.2).

The coil inductance can be estimated from the following empirical formula for short coils with a large mean diameter d_m (the optimum shape for an air coil) [8]:

$$L = \frac{\mu_0 d_m N^2}{2} \ln\left(\frac{4d_m}{\sqrt{l^2 + h^2}} - 0.83\right) \tag{2.15}$$

At high frequencies, L decreases because of the eddy currents, which produce a magnetic field decreasing the main field [6]. However, for most cases, L can be considered to be constant. R_s consists of the DC resistance and AC losses caused at higher frequencies by skin effects, proximity effects, and eddy currents in the shielding and in other parts of the sensor. The skin effect is stronger for thick wires: the R_{AC} is 2% of R_{DC} if the penetration depth δ is equal to the wire radius. For a 0.1-mm copper wire, that happens at approximately 200 kHz, and for a 1-mm wire, it happens at 18 kHz. In the case of densely wound multiturn coils, the proximity effect may be stronger than the basic skin effect.

The parasitic capacitances of coils are discussed and derived in [9]. In solenoids, the self-capacitance is proportional to

$$C \sim l\left(\frac{d_m}{h}\right)\log\left(\frac{c}{d_w}\right) \tag{2.16}$$

where c is the wire pitch.

From (2.16), it follows that short disk coils have a lower capacitance than long solenoids for the same number of turns and mean diameter. The parasitic capacitances can then be reduced by using thicker wire insulation, layer spacing, or special winding techniques (wild winding, cross winding). A good technique is to divide the solenoid into n sections, connected in series (split coil). For a sufficiently large section spacing, the capacitance is reduced by $1/n^2$.

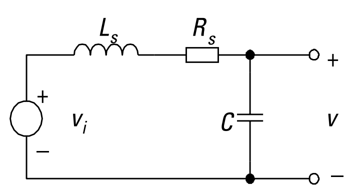

Figure 2.2 Equivalent circuit of the voltage-output induction coil.

Figure 2.3 Frequency characteristics of the thick air solenoid with voltage output.

The actual value of the coil capacitance highly depends on the winding geometry, so the deviation from calculated results may be large. The actual value can be calculated from the resonant frequency. The resonant frequency f_r can easily be measured if the coil is voltage-driven from an audio generator: with increasing frequency, the coil current decreases, as the ωL component of the impedance dominates. At f_r, the current reaches its minimum; if the frequency is further increased, the current increases because the total impedance has a capacitive character. The general rule is that the coil can be used without special care for frequencies up to $f_r/5$.

The typical frequency characteristics of the sensitivity for the voltage-output induction coil of the thick solenoid type is shown in Figure 2.3. The Q factor of the resonance is determined by the coil resistance and losses in the parasitic capacitances. Sometimes a parallel damping resistor is added to decrease Q and linearize the characteristics so that the coil can be used closer to f_r.

2.1.4 Current-Output (Short-Circuited Mode)

If the equivalent circuit of the induction coil equivalent circuit (Figure 2.2) is connected to the current-to-voltage converter (Figure 2.4), the capacitance of the coil is virtually short-circuited and thus effectively eliminated. The useful frequency range of the induction coil is then considerably expanded.

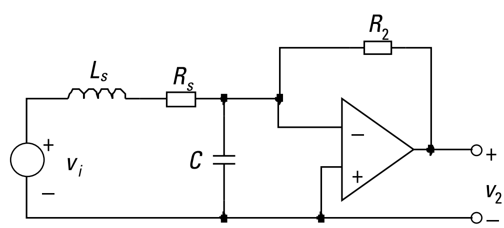

Figure 2.4 Short-circuited induction coil.

If, for a sinusoidal waveform, we express the maximum value of the induced voltage using the formula $V_p = 2\pi f NAB_m$, from (2.7), the output voltage of the current-to-voltage (I/V) converter with the feedback resistor R_2 can be found as

$$V_2 = \frac{R_2}{\sqrt{(2\pi f L_S)^2 + R_S^2}} 2\pi NAB \tag{2.17}$$

The frequency characteristics are shown in Figure 2.5. At higher frequencies, where $2\pi f L_s >> R_s$, the output voltage is independent of frequency:

$$V_2 = \frac{R_2}{L_S} NAB, \ I = \frac{NA}{L_S} B \tag{2.18}$$

As we suppose a sinewave shape of B, then (2.17) and (2.18) are correct for instantaneous, peak, rms, and mean values; it is just necessary to use the same value on both sides. If B is expressed as a maximum value, V_2 will also be a maximum value.

If we suppose that $d_m >> l, h$, then $L \sim N^2 d_m$ and the current sensitivity depends on d_m/N; here the sensitivity is not dependent on the wire diameter d_w. The short-circuited induction coil can be used for observing nonsinusoidal fields, because (2.18) can be rewritten in the time domain, so that I and V_2 follow the waveform of B for $f >> f_1 = R_s/L_s$. Furthermore, $R_s \sim Nd_m/d_w^2$, so that $f_1 \sim 1/Nd_w^2$, and the only way to decrease f_1 without decreasing the sensitivity is to increase the wire diameter d_w (with the already mentioned limitations from skin effects and increase of coil weight).

Some frequency compensation may be necessary to guarantee the stability at higher frequencies and also possibly linearize the characteristics at low frequencies. The simplest method is to use a serial capacitor at the input. The approximate low-frequency limit of the frequency-independent current-output induction magnetometer is the coil corner frequency f_1. The upper frequency limit is usually determined by the I/V converter.

The air-core induction coil should be designed according to the required frequency range and noise properties. In general, current-output mode and a large coil diameter are preferred. The number of turns should be fitted to match the amplifier input. The design of a 3-axis search-coil magnetometer is well documented in [8], where the coil parameters are (largest coil): $d_m = 0.33$m, $l = 17$ mm, $h = 21$ mm, $N = 4{,}100$ turns, $R = 1{,}560\Omega$, $L = 11.9$H, and $f_c = 20$ Hz. The frequency range is 20

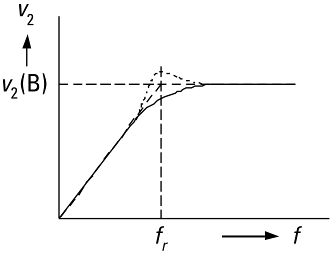

Figure 2.5 Frequency characteristics of the current-output induction sensor. The dotted line shows the (over)compensation by a serial capacitor.

Hz–2.5 kHz (–1 dB, after compensation at a low-frequency corner), and the current output sensitivity is 34 mA/mT.

Extending the frequency range requires the reduction of turn numbers. Cavoit developed a single-turn coil connected to the current transformer [10]. The frequency range is 100 kHz–30 MHz, and for 20-cm diameter coil the noise in this frequency band is 0.2 fT/√Hz.

The voltage output is suitable for measurements at ultralow frequencies such as slow variations of the geomagnetic fields, but for such applications induction coils with ferromagnetic cores (which are often working in the short-circuited mode) or fluxgate magnetometers are preferable.

Air coils can be tuned in order to increase the sensitivity in the narrow frequency band, which finds application in biomagnetic methods such as magnetic induction tomography or magnetic resonance imaging [11].

2.2 Search Coils with a Ferromagnetic Core

In the design of an induction sensor with a ferromagnetic core, the demagnetization effects cannot be neglected. Due to this, H in the sensor core is substantially lower than the measured field H_0 outside the sensor core. Therefore, we must write for the flux density within the core:

$$B = \frac{\mu_0 \mu_r H_0}{\left[1 + D\left(\mu_r - 1\right)\right]} = \mu_0 \mu_a H_0 \tag{2.19}$$

where D is the effective demagnetizing factor and μ_a is the apparent relative permeability.

In the following analysis, we suppose that the measured fields are small and thus μ is constant. Figure 2.6 illustrates the geometry of an induction sensor with ferromagnetic core.

2.2.1 Voltage Output Sensitivity

After inserting the ferromagnetic core, the voltage sensitivity is increased by μ_a:

$$V_i = \frac{NA\mu_a dB(t)}{dt} \tag{2.20}$$

The apparent permeability can be measured by comparing the inductance L of the coil with the core and L_0 with the core removed. The first estimate is $\mu_a = L/$

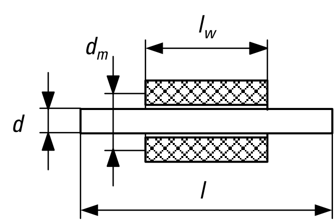

Figure 2.6 Geometry of the induction sensor with ferromagnetic core.

L_0, but a more precise analysis has to take into consideration the different cross-sectional areas of the core and the coil. The analysis of the demagnetization effect D and of the inductance L may be found in [12–14] and references listed therein. For rotational ellipsoids having the length/diameter ratio m, the demagnetization factor D does not depend on μ_r, and it can be precisely calculated using Stoner's formula:

$$D = \frac{1}{m^2 - 1}\left[\frac{m}{\sqrt{m^2 - 1}}\ln\left(m + \sqrt{m^2 - 1}\right) - 1\right] \tag{2.21}$$

For long ellipsoids, this can be simplified to

$$D = \frac{\left(\ln 2m - 1\right)}{m^2} \tag{2.22}$$

The effective demagnetization factor for long rods ($m = l/d > 10$) was approximated for $\mu_r = \infty$ by the Neumann-Warmuth empirical formula, which gives similar numerical results:

$$D \approx \frac{\left[2.01\log(m) - 0.46\right]}{m^2} \tag{2.23}$$

For finite permeability D is decreased. Demagnetization factors for cylinder wires are plotted versus m in Figure 2.7 [15]. Demagnetization values for rods were calculated with 0.1% accuracy in [16].

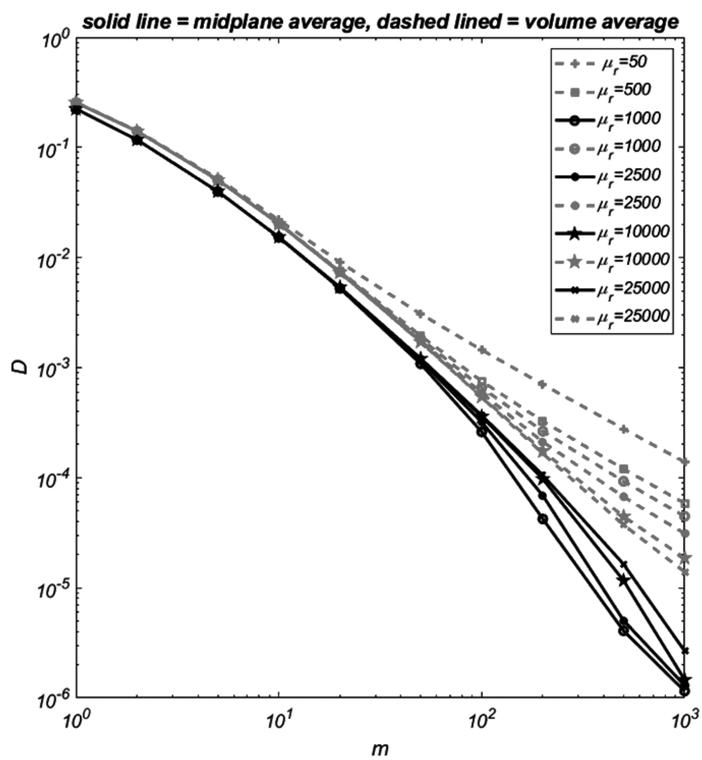

Figure 2.7 Demagnetization factor (fluxmetric solid line, magnetometric dashed line) of a ferromagnetic wire. (*After:* [15].)

Ferromagnetic cores in sensors should generally be long and thin. The use of ferromagnetic cores has serious drawbacks. The core permeability is changing with time and temperature and after the sensor is subjected to stress or vibrations. The permeability also changes if the core is DC-magnetized; it may happen if it is exposed to the Earth's field. The permeability is dependent on amplitude and frequency of the measured field; that dependence may cause sensor nonlinearity and distortion. Thus, it is important to design the sensor so that its constant is not very sensitive to changes of the core material permeability μ_r. If the material permeability is high, the apparent permeability μ_a is mainly given by the core geometry. That approach is illustrated by Figure 2.8. If m is extremely high such as m = 1,000, μ_a is very high for a high value of relative permeability (e.g., μ_r = 100,000), but in the case of μ_a, it is very sensitive to a variation of μ_r. However, if we use a high permeability core (for example, having μ_r larger than 50,000 for the whole temperature range) and moderate m (for example, 100), we may reach a moderate value of μ_a = 2,500, which is relatively insensitive to variations of μ_r. Moderate values of μ_a also keep the core DC magnetization caused by the Earth's field low. A permalloy core with μ_a = 20,000 would be saturated even by the Earth's field of 50 μT.

In other words, good design should satisfy the condition $\mu_r D >> 1$, so that (2.20) is simplified and $\mu_a \cong 1/D$ becomes practically independent of μ_r. If that is satisfied, and we estimate D from (2.22) and substitute $A = \pi d^2/4$ and $m = l/d$ into (2.20), we obtain the following for the output voltage:

$$V_i \cong N\frac{\pi}{4}\frac{l^2}{\ln(2l/d) - 1}dB/dt \tag{2.24}$$

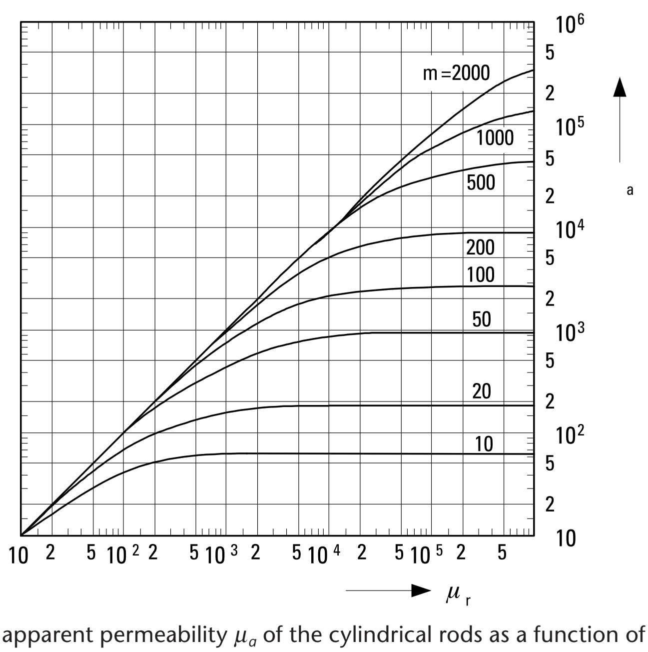

Figure 2.8 The apparent permeability μ_a of the cylindrical rods as a function of the length-to-diameter ratio m and the material relative permeability μ_r. (*After:* [14].)

If the measured field is sinewave-shaped with a frequency $\omega = 2\pi f$, then we can write for the ideal frequency-normalized voltage sensitivity

$$S_{/f} = \frac{V}{Bf} = \frac{\pi^2 l^2 N}{2\ln(2l/d) - 1} \tag{2.25}$$

That formula fits well the measured sensitivities of sensors having m between 20 and 100.

Now let us discuss the optimum core diameter if the sensor maximum length is given. Figure 2.9 shows the situation for a 2-m-long core with a 1-m-long winding of 100,000 turns [17]. Increasing the core diameter to more than 20 mm brings an increase of the core and winding weight, but almost no increase in sensitivity (due to the demagnetization).

The coil length should be less than the core length in order to avoid the edge effects. The voltage sensitivity at the core ends may drop down to 10% of the maximum sensitivity in the middle part. However, a short coil with the same number of turns has a longer wire and thus a higher DC resistance; other parameters such as parasitic capacitance and ac resistance may also be worse. The reported coil lengths are between 50% and 90% of the core length; values between 75% and 90% may be recommended. Other coil shapes than solenoids have shown no significant advantages.

Another technique to increase magnetic amplification is to use magnetic concentrators at the ends of the ferromagnetic core. These concentrators can increase apparent permeability by 30% [18] or even threefold [19, 20].

In any case, the induction sensors with ferromagnetic cores should be field-calibrated. This is usually done in a calibration system, which has to be either much larger than the calibrated coil, or corrections for the calibration field nonhomogeneity should be done. For very large stationary coils, calibration is usually performed by

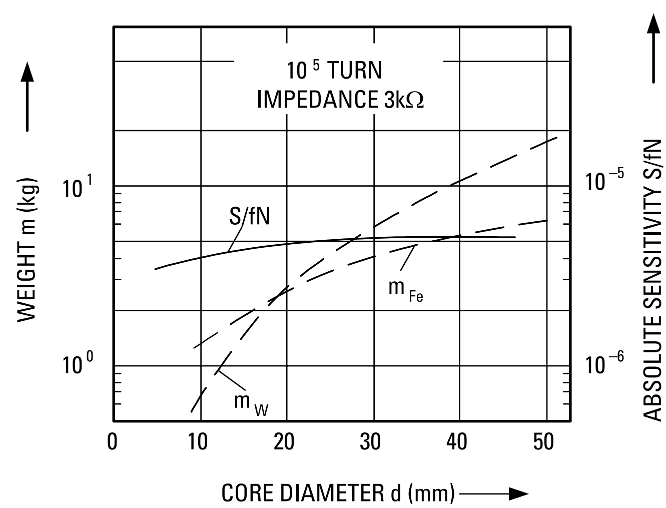

Figure 2.9 The absolute sensitivity S/fN (normalized to 1 turn, solid line), core weight m_{Fe}, and winding weight m_w (dashed lines) of a 2-m sensor as a function of the core diameter. The 100,000 turns winding is 1m long. (*After:* [17].)

comparing them with calibrated air coils using the Earth's natural field variations. An alternative calibration method is to use a small field source (calibrated coil or rotating permanent magnet) at a large and known distance.

2.2.2 Thermal Noise of the Cored Induction Sensor (Voltage Output)

We should take into consideration that the mean coil diameter d_m is larger than the core diameter d and also that the voltage sensitivity of a cored solenoid is increased by a factor of μ_a according to (2.20). By similar calculations to those that we did for the air coil, we obtain for the equivalent field thermal noise $B_{N\tau}$ as a function of the coil mass:

$$B_{N\tau} = \frac{4\sqrt{k_B T \rho \gamma}}{\pi f} \frac{d_m}{\mu_a d^2 \sqrt{m_W}} \tag{2.26}$$

Again, in this simplified model, the noise does not depend on the wire diameter or the number of turns, but only on the weight of the winding. It is also clear that the coil mean diameter d_m should be kept low by tight winding. The dependence on the core diameter is not simple, as it is related to μ_a. If we increase d, then we should substantially increase l and thus the core weight in order to keep μ_a constant.

We should keep in mind that the coil thermal noise voltage is only one component of the magnetometer noise, which represents the theoretical low limit (for noiseless amplifier). The calculations show that a sensor containing 2.5 kg of copper and 2.5 kg of magnetic material having $\mu_r = 10{,}000$ and a length/diameter ratio of 100 has a theoretical noise limit of 30 fT/√Hz at 1 Hz [6], which is 15 times lower than realistic values achievable with up-to-date real sensors having the same weight, and 1 m length (Table 2.2). The influence of the amplifier noise will be discussed in Section 2.3. Magnetic noise of the core is usually considered to be negligible [18].

2.2.3 The Equivalent Circuit for Cored Coils

The inductance of induction coils having short windings ($l_w << l$) in the middle of the long high-permeability cores was evaluated in [13] to be

$$L = \frac{N^2}{2} \frac{\mu_0 \pi l}{\ln 2m - 1} \tag{2.27}$$

If we suppose that $\mu_a = 1/D = m^2/(\ln 2m - 1)$ according to (2.22), we get

$$L = N^2 \frac{2\mu_0 \mu_a A_{\text{core}}}{l} \tag{2.28}$$

Notice that this is twice the value derived in [22] for long windings on a core with effective length l.

If the winding is not short, the inductance is lower [6]. For a winding having 50% of the core (physical) length, the inductance is 90% of the ideal value; for 100% length, the inductance drops to 50% of the ideal value calculated from (2.28).

Lukoschus [23] determined and experimentally verified the empirical formula for l_w/l in the range of 0.1 to 0.8:

$$L = N^2 \frac{\mu_0 \mu_a A_{\text{core}}}{l} \left(\frac{l_w}{l} \right)^{-2/5} \tag{2.29}$$

The self-capacitance of coils with an electrically conducting core cannot be easily calculated, especially in the case of shielded coils as capacitances between the shielding, core, and winding become dominant. The resistance R_s is increased by losses in the core: eddy-current losses ($R_e \sim f^2$) and hysteresis losses ($R_h \sim f$). Eddy-current losses are suppressed by using laminated cores. Ferrite cores have very small eddy-current losses, but they are less effective for low and middle-frequency coil cores, because they have only a low permeability (initial relative permeability μ_i maximum, 10,000) compared to that of permalloy (where μ_i may be ~100,000). Cobalt-based amorphous materials have some advantages over permalloys. They do not need to be annealed, they are not so sensitive to vibrations, and their eddy currents are lower because they have higher resistivity; the disadvantage is their low saturation magnetization B_s. Excellent materials for this application are nanocrystalline alloys; they have a large B_s, and they can be annealed to have a large constant permeability so that high linearity can be obtained.

The cored induction coils optimized for voltage output usually have a large L and a small C (because of the split winding) and often a high Q-factor, which results in a large step-up near the resonance frequency f_r. A parallel damping resistor R_d is sometimes used to lower Q and linearize the frequency characteristics.

2.2.4 Cored Coils with Current Output

We may substitute L from (2.28) into (2.18) for the output voltage of the I/V converter (for sinewave B, $f >> f_1 = R_s/L_s$), we obtain:

$$V_2 = \frac{R_2}{L} N A_{\text{core}} \mu_a B = \frac{R_2 l}{2N\mu_0} B \tag{2.30}$$

and for the short-circuited current:

$$I = \frac{N A_{\text{core}} \mu_a}{L} B = \frac{l}{2N\mu_0} B = \frac{l}{2N} H \tag{2.31}$$

Notice that this is half of the short-circuited current of the very long, zero-resistance solenoid used as a search coil (as ideal zero-resistance short-circuited coil perfectly compensates the measured field by its field $H = NI/l$). It appears as if the output current does not depend on the core parameters, but remember that this is true only for long, high permeability cores.

2.3 Noise Matching to an Amplifier

The amplifier noise usually plays an important role in the induction magnetometer design. As both the input current and voltage noise are frequency-dependent, it is not possible to globally optimize the magnetometer performance over the whole frequency range. The usual procedure is to fit the required noise level at two or three fixed frequencies. A good start for the design is to fix the sensor length and weight. Several iterations using numerical simulation tools are always necessary. Also, the selection of the amplifiers is not trivial, because they differ in the values and frequency dependencies of the input current noise I_{na} and voltage noise V_{na}.

The best modern low-noise operational amplifiers suitable for voltage amplification have a very low V_{na} but a rather high I_{na}. These are two reasons why the coil resistance should be kept low; $R_{DC} \cong 100\Omega$ is recommended in [6], which contrasts with the traditional induction coils having huge N and R.

It should be clearly stated that the general trend is the current-output mode except for the geophysical induction magnetometers working at ultralow frequencies (from 100 μHz). Some of these instruments use magnetic feedback; the voltage amplifier output is fed back through the feedback resistor into a compensation winding [6]. The resulting characteristic is similar to that of the current-output coil (i.e., the influence of the parasitic capacitance is suppressed, and the sensitivity is constant in a certain frequency range). However, at ultralow frequencies, the sensitivity drops. The use of a feedback coil separate from the sensing coil gives another degree of freedom in the magnetometer design. If the size and weight of the low-frequency magnetometer are strictly limited such as in the case of satellite instruments, fluxgate magnetometers (Chapter 3), which also measure the DC component, are preferable for the measurement of the ultralow frequencies. The crossover is somewhere between 1 Hz (Cluster mission) and 6 Hz magnetospheric multiscale (MMS) mission [24]. Hybrid magnetometers are trying to combine fluxgate with an induction magnetometer into a single device, but up to now, the noise of these devices is, at best, 30 pT/√Hz at 1 Hz [25].

2.4 Design Examples

A detailed comparison of geophysical induction magnetometers can be found in [26]. An overview of space induction magnetometers is made in [2], and an example of such a magnetometer is shown in [27]. An overview of commercial induction magnetometers is shown in Table 2.2, and several design examples of induction coil with ferromagnetic core taken from literature are given in Table 2.3.

2.5 Other Measuring Coils

2.5.1 Rotating Coil Magnetometers

If the effective coil area A_0 (i.e., perpendicular to the direction of B) is changing by rotation, $a(t) = A_0 \cos \omega t$, then the induced voltage according to (2.1) will be:

$$V_i = -BNA_0 \omega \sin \omega t \tag{2.32}$$

Rotating coil magnetometers based on this principle were once popular but suffered from poor reliability due to moving parts. A sophisticated pneumatically

Table 2.2 Commercial Induction-Coil Magnetometers

Type	*Frequency Band (Hz)*	*Noise Frequency (pT/√Hz at 1 Hz)*	*Length (m)*	*Core Diameter (mm)*	*Weight (kg)*	*Producer*
Air-cored						
Bell 4190 3-axial magnetometer	30 Hz–2 kHz	10-nT resolution	0.12	—	0.18	F.W. Bell, fwbell.com
Geophysical with ferromagnetic core						
Low-frequency	0.1 mHz–1 kHz	0.1 pT at 1 Hz, 0.01 pT at 100 Hz	1.3	85	5.7	LEMI, lemisensors.com
Middle frequency	1 Hz–70 kHz	5 pT at 1 Hz, 5 fT at 10 kHz	0.35	42	1.7	
MGC-1	5 Hz–10 kHz	0.5 pT at 10 Hz, 0.1 pT at 100 Hz, 20 fT at 1 kHz	0.25	—	1	MEDA, Meda.com
MGCH-2	10 Hz–100 kHz	2.5 pT at 10 Hz, 0.1 pT at 100 Hz, 10 fT at 1 kHz, 4 fT at 10 kHz	0.325	—	0.715	
MFS-06e	0.1 mHz–500 (chopper on) 10 Hz–10 kHz (chopper off)	11 pT at 1 Hz, 0.11 pT at 10 Hz, 1 fT at 1 kHz (chopper off)	1.14	75	—	Metronix, Metronix.de
SHFT-02e (3-axial)	1–300 kHz	50 fT at 1 kHz, 8 fT at 10 kHz, 6 fT at 100 kHz	0.19	0.17	5.5	

powered magnetometer with air bearings and mercury contacts was described in [30]. A 20-mm diameter coil spinning at 20,000 rev/min gave a resolution of 10 pT and an offset below 100 pT. Rotating coil magnetometers are presently used only in special applications such as precise measurement of high magnetic fields in accelerators [31].

2.5.2 Moving Coils: Extraction Method

Small search coils connected to an electronic integrator may be used to measure B. The induced voltage is integrated while the coil is extracted from the measuring location M with the field B to place with zero field B_z [32]:

$$\int V_i \, dt = -NA\left(B_Z - B_M\right) \tag{2.33}$$

This technique can be used for precise mapping of the magnetic fields in accelerator magnets. The coil movement is computer-controlled, and after scanning each row, the coil is returned to the null position to check the integrator drift. The alternative to this mapping technique is to use a precise Hall sensor.

Table 2.3 Design Examples of Induction Coils with Ferromagnetic Cores

Type	*Frequency Band (Hz)*	*Sensitivity*	*L (H)*	*k (Ω)*	*Noise*	f_r *(Hz)*	*N Turns*	*l (cm)*	*d (mm)*	*Weight (kg)*	*Reference or Producer*
Ferromagnetic-core coils											
Example		3,200 V/(T*Hz)	70	3	5 pT/√Hz at 1 Hz	4.2 kHz	10 kHz	35	6	—	[6]
UC	1 Hz–10 kHz	50 mV/nT	500	2	0.8 pT/√Hz at 1 Hz		45 kHz	60	16	2.5	[28], current output
DEMETER 3-axial magnetometer	1 Hz–20 kHz	86 mV/nT	12.6	1.3	4 fT/√Hz at 6 kHz	8 kHz	12,200	17	10	0.43	[29]
SCM 3-axial	1 Hz–6 kHz	—	—	—	11 pT√Hz at 1 Hz, 2 pT/√Hz at 10 Hz		>10,000	10	—	0.21	[27]
	0.02 Hz–2 kHz	—	—	86	14 pT/√Hz at 1 Hz	250	160,000	6	30	0.21	[19]

The DC-magnetic induction in the specimen or part of the magnetic circuit can be measured by wrapping around it several turns of wire connected to the input of the integrator (fluxmeter). Another possibility is to use a sliding search coil. The magnetic moment of a permanent magnet can be measured using a Helmholtz coil connected to a fluxmeter by the flux change produced after the magnet is inserted into the coil [33].

2.5.3 Vibrating Coils

Vibrating coils are used to measure field gradients. Their main application is in the measurement of magnetization of samples. The coil is in the vicinity of the sample and measures the field difference between two positions. Periodic excitation allows the extraction of weak signals by a synchronous detector. In general, vibrating sample or rotating sample magnetometers are the preferred solutions, but some types of samples (such as liquids, dusts, or brittle solids) are sensitive to vibrations and acceleration, so vibrating or rotating coils are used instead.

2.5.4 Coils for Measurement of *H*

Coils in connection with an analog integrator (or, in the AC case, a voltmeter measuring the mean value) may also be used for the measurement of $H \times l$ or the magnetic potential drop (voltage) U in amperes. H-coils are flat coils, which serve to measure H near the surface of a ferromagnetic material. They are based on the fact that the tangential component of H does not change across the material boundary. H-coils are used in single-sheet testers (devices for the measurement of hysteresis loops of electrical steels and other soft magnetic materials). H-coils are sometimes doubled to compensate for the linear decrease of H with distance from the sample surface. One coil is close to the surface and the second coil is slightly displaced; the value of H inside the sample is extrapolated. H-coils are also sometimes used for measuring the parameters of magnetically hard materials in electromagnets [33].

2.5.5 The Rogowski-Chattock Potentiometer

The Rogowski-Chattock potentiometer (also called Rogowski coil) measures the magnetic potential drop (voltage) U in amperes between two points. It consists of a long slim coil wound on a nonmagnetic and nonconducting core. The typical shape is a semicircle with the ends of the coil lying in one plane. If the potentiometer lies flat on the surface of a ferromagnetic material (Figure 2.10), and there is no electric current flowing inside the semicircle, we may write

$$\oint H \, dl = 0 \tag{2.34}$$

and so

$$\int_X H_{\mathrm{Fe}} \, \mathrm{d}l = \int_Y H_{\mathrm{air}} \, \mathrm{d}l = U_{\mathrm{AB}} \tag{2.35}$$

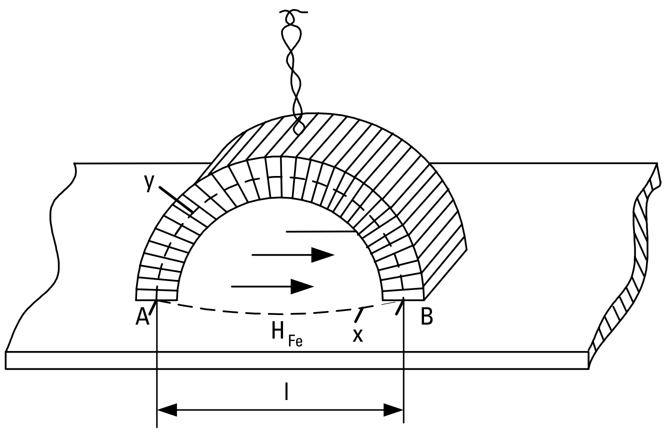

Figure 2.10 The Rogowski-Chattock potentiometer.

where H_{Fe} and H_{air} are the field intensities inside the specimen and in the air, respectively.

For a short path, we may write $U_{AB} = H_{Fe} l_{AB}$. If the winding density is high and constant, we may write for the coil flux of the potentiometer:

$$\sum_N \Phi_i = \mu_0 A \sum_N H_i \cong \frac{\mu_0 A}{l} \int_A^B H\,dl \qquad (2.36)$$

Semicircular potentiometers are used for the measurement of H in ferromagnetic samples. In the case of an AC magnetization, the induced voltage is measured (mean value, if nonsinewave) and eventually integrated (if also the waveform is required). The DC value of H can be measured if we integrate the induced voltage while the coil is removed from the sample surface to a sufficiently large distance, where the stray field is negligible.

A straight potentiometer (potential coil) together with an integrating fluxmeter is used for measuring the magnetic potential drop between two points. The induced coil output voltage is integrated while one coil end is moved between two points; the other coil end is supposed to be at zero or constant field. The influence of the Earth's field can be compensated for by another coil having the same coil constant but a smaller size, attached to the far end of the potentiometer and connected anti-serially. This technique is used for mapping H in permanent magnet structures as an alternative for using precise Hall sensors.

Potentiometers are made as single-layer solenoids with a very small area. A large number of turns is necessary to obtain sufficient sensitivity. The winding uniformity is very important. Potentiometers should be calibrated as their sensitivity constant cannot be calculated from the dimensions with sufficient precision.

Circular Rogowski coils of the ring shape are used to measure large AC and transient currents (Chapter 11). The device contains no magnetic material, so it is extremely linear; the uniformity of the winding is critical.

References

[1] Tumanski, S., "Induction Coil Sensors: A Review," *Measurement Science and Technology*, Vol. 18, No. 3, March 2007, pp. R31–R46.

[2] Coillot, C., and P. Leroy, "Induction Magnetometers Principle, Modeling and Ways of Improvement," in K. Kuang, (ed.), *Magnetic Sensors*, London, U.K.: Intech, 2012, pp. 45–63.

[3] Kearey, P., M. Brooks, and I. Hill, *An Introduction to Geophysical Exploration*, New York: John Wiley & Sons, 2013.

[4] Buzio, M., "Fabrication and Calibration of Search Coils," *CERN Accelerator School*, 2009.

[5] Brown, W. F., and J. H. Sweer, "The Fluxball: A Test Coil for Point Measurements of Inhomogeneous Magnetic Fields," *Review of Scientific Instruments*, Vol. 16, No. 10, 1945, pp. 276–279.

[6] Dehmel, G., "Induction Sensors," *Magnetic Sensors*, VCH, 1989.

[7] Shilyashki, G., et al., "3D-Printed Detector Band for Magnetic Off-Plane Flux Measurements in Laminated Machine Cores," *Sensors*, Vol. 17, No. 12, December 2017.

[8] Macintyre, S. A., "A Portable Low-Noise Low-Frequency 3-Axis Search Coil Magnetometer," *IEEE Transactions on Magnetics*, Vol. 16, No. 5, 1980, pp. 761–763.

[9] Welsby, V. G., *The Theory and Design of Inductance Coils*, 2nd ed., New York: John Wiley & Sons, 1960.

[10] Cavoit, C., "Closed Loop Applied to Magnetic Measurements in the Range of 0.1–50 MHz," *Review of Scientific Instruments*, Vol. 77, No. 6, June 2006.

[11] Pellicer-Guridi, R., et al., "Towards Ultimate Low Frequency Air-Core Magnetometer Sensitivity," *Scientific Reports*, Vol. 7, May 2017.

[12] Primdahl, F., et al., "Demagnetizing Factor and Noise in the Fluxgate Ring-Core Sensor," *Journal of Physics E-Scientific Instruments*, Vol. 22, No. 12, December 1989, pp. 1004–1008.

[13] Kaplan, B. Z., "A New Interpretation of the Relationship Existing Between Demagnetizing Factor and Inductance," *IEEE Transactions on Magnetics*, Vol. 30, No. 5, September 1994, pp. 2788–2794.

[14] Bozorth, R. M., and D. M. Chapin, "Demagnetizing Factors of Rods," *Journal of Applied Physics*, Vol. 13, 1942.

[15] Ripka, P., V. Grim, and M. Mirzaei, "The Apparent Permeability and the Amplification Factor of Magnetic Wires and Wire Arrays," *Journal of Magnetism and Magnetic Materials*, Vol. 527, June 2021.

[16] Chen, D. X., E. Pardo, and A. Sanchez, "Fluxmetric and Magnetometric Demagnetizing Factors for Cylinders," *Journal of Magnetism and Magnetic Materials*, Vol. 306, No. 1, November 2006, pp. 135–146.

[17] Saito, T.,"Development of New Time-Derivative Magnetometers to Be Installed on Spacecrafts (in Japanese)," *Bull. Inst. Space Aeronaut. Sci Univ. Tokyo*, 1980.

[18] Coillot, C., et al., "Magnetic Noise Contribution of the Ferromagnetic Core of Induction Magnetometers," *Journal of Sensors and Sensor Systems*, Vol. 4, No. 1, 2015, pp. 229–237.

[19] Paperno, E., and A. Grosz, "A Miniature and Ultralow Power Search Coil Optimized for a 20 mHz to 2 kHz Frequency Range," *Journal of Applied Physics*, Vol. 105, No. 7, April 2009.

[20] Grosz, A., and E. Paperno, "Analytical Optimization of Low-Frequency Search Coil Magnetometers," *IEEE Sensors Journal*, Vol. 12, No. 8, August 2012, pp. 2719–2723.

[21] MEDA, Inc., http://www.meda.com/.

[22] Primdahl, F., et al., "The Short-Circuited Fluxgate Output Current," *Journal of Physics E-Scientific Instruments*, Vol. 22, No. 6, June 1989, pp. 349–354.

[23] Lukoschus, D. G., "Optimization Theory for Induction-Coil Magnetometers at Higher Frequencies," *IEEE Transactions on Geoscience and Remote Sensing*, Vol. 17, No. 3, 1979, pp. 56–63.

[24] Fischer, D., et al., "Optimized Merging of Search Coil and Fluxgate Data for MMS," *Geoscientific Instrumentation Methods and Data Systems*, Vol. 5, No. 2, November 2016, pp. 521–530.

[25] Shi, H. Y., et al., "A Dumbbell-Shaped Hybrid Magnetometer Operating in DC-10 kHz," *Review of Scientific Instruments*, Vol. 88, No. 12, December 2017.

[26] Korepanov, V., and V. Pronenko, "Induction Magnetometers—Design Peculiarities," *Sensors & Transducers Journal*, Vol. 120, No. 9, September 2010, pp. 92–106.

[27] Le Contel, O., et al., "The Search-Coil Magnetometer for MMS," *Space Science Reviews*, Vol. 199, No. 1-4, March 2016, pp. 257–282.

[28] Labson, V. F., et al., "Geophysical Exploration with Audiofrequency Natural Magnetic-Fields," *Geophysics*, Vol. 50, No. 4, 1985, pp. 656–664.

[29] Seran, H. C., and P. Fergeau, "An Optimized Low-Frequency Three-Axis Search Coil Magnetometer for Space Research," *Review of Scientific Instruments*, Vol. 76, No. 4, April 2005.

[30] Prihoda, K., et al, "MAVACS—A New System for Creating a Non-Magnetic Environment for Paleomagnetic Studies," *Geologia Iberica*, No. 12, 1988.

[31] Arpaia, P., et al., "A High-Precision Miniaturized Rotating Coil Transducer for Magnetic Measurements," *Sensors and Actuators A: Physical*, Vol. 274, May 2018, pp. 37–49.

[32] Jiles, D., *Introduction to Magnetism and Magnetic Materials*, Boca Raton, FL: CRC Press, 2015.

[33] Tumanski, S., *Handbook of Magnetic Measurements*, Boca Raton, FL: CRC Press, 2011.

CHAPTER 3

Fluxgate Sensors

Pavel Ripka and Werner Magnes

Fluxgate sensors measure the magnitude and direction of the DC or low-frequency AC magnetic field in the range of approximately 10^{-11} to 10^{-3} T. The basic sensor principle is illustrated by Figure 3.1 [1]. The soft magnetic material of the sensor core is periodically saturated in both polarities by the AC excitation field, which is produced by the excitation current I_{exc} through the excitation coil. Due to this, the core permeability is changing and the DC flux associated with the measured DC magnetic field B_0 is modulated. Gating of the flux, which occurs when the core is saturated, gave the device its name. Figure 3.2 shows the simplified corresponding waveforms. The device output is usually the voltage V_{ind} induced into the sensing (pickup) coil at the second (and also higher even) harmonics of the excitation frequency, which is proportional to the measured field.

A similar principle was used earlier in magnetic modulators and magnetic amplifiers, but, in these cases, the measured variable was a DC electrical current flowing through the primary coil. The first patent on the fluxgate sensor (in 1935) is credited to H. P. Thomas [2]. Aschenbrenner and Goubau worked on fluxgate sensors from the late 1920s, and in 1936 they reported 0.3-nT resolution on the ring-core sensor [3]. Sensitive and stable sensors for submarine detection were developed during World War II. Fluxgate magnetometers were used for geophysical prospecting, for airborne field mapping, and later for space applications. Since the *Sputnik 3* in 1958, thousands of triaxial fluxgate magnetometers have been launched (Section 9.8). Fluxgate magnetometers worked on the Moon [4] and in deep space. From the 1980s, magnetic variation stations with fluxgates supported by a proton magnetometer are used for observing the changes in the Earth's magnetic field [5]. Fluxgate compasses are extensively used for aircraft and vehicle navigation; see Section 10.3. Foerster [6] started to use the fluxgate principle for the nondestructive testing of the ferromagnetic materials. The fluxgate principle is also used in current sensors and current comparators [7]. Compact fluxgate magnetometers are used for navigation, detection, and search operations; for the remote measurement of DC; and for reading magnetic labels and marks. Magnetic sensor applications are discussed in Chapter 9.

Fluxgate sensors are solid-state devices without any moving parts working in a wide temperature range. They are rugged and reliable and typically have low energy consumption. They can reach 10-pT resolution and 1-nT long-term stability; 100-pT resolution and 10-nT absolute accuracy are standard in commercially produced devices. Many DC fluxgate magnetometers have a cutoff frequency of several hertz, but, when necessary, fluxgates may work up to kilohertz frequencies. Fluxgates are temperature-stable: the offset drift may be 0.1 nT/°C and sensitivity temperature coefficients are usually around 30 ppm/°C, but some fluxgate magnetometers are compensated up to 1 ppm/°C. Most of the fluxgate sensors are working in the feedback mode, so that the resulting magnetometer linearity is typically 30 ppm.

Fluxgates are the best selection if nano-tesla resolution and bipolar measurement of field with good offset stability is required. While they do not have the sub-pT sensitivity levels of superconducting quantum interference device (SQUID) sensors (Chapter 7), their ability to operate in the Earth's field environments with full dynamic range and room-temperature operation makes them the choice for pT and higher-level measurements. For higher fields, fluxgate competitors are the magnetoresistors, especially anisotropic magnetoresistance (AMR) sensors (Chapter 4). While commercially available AMR magnetoresistors have a resolution poorer than 10 nT and also poor offset stability, they are smaller and cheaper and consume less energy than fluxgates.

Review articles on fluxgate sensors were written by Gordon and Brown [8] and Primdahl [9] and also one of the authors of this chapter [1]. A remarkable advanced fluxgate magnetometer was designed for the *Oersted* satellite launched in 1999 to map the Earth's magnetic field; construction details about this instrument can be found in [10, 11]. Modern fluxgates were described in book chapters by Janosek [12] and Butta [13]. Fluxgate space magnetometers have been described in a book by Musmann and Afanassiev [14].

The typical modern low-noise fluxgate magnetometer is of the parallel type with a ring-core sensor; however, double-rod sensors also have a lot of advantages. A phase-sensitive detector extracts the second harmonic in the induced voltage, and the pickup coil also serves for the feedback. Other designs are used for specialized purposes, such as miniature rod-type sensors for nondestructive testing, position sensing, or magnetoelastic torque sensors. For the latter application, simple fluxgate sensors with a single coil are used. Fluxgate sensors have also been microfabricated (Section 3.12).

3.1 Orthogonal-Type Fluxgates

Figure 3.1 shows the configuration of the most widely used parallel type of fluxgate, for which both the measured and the excitation fields have the same direction. There is also another type called the orthogonal sensor with an excitation field perpendicular to the sensitive axis of the sensor, which is identical to the ideal axis of the sensing coil. This type of magnetometer was first described in a patent by Alldredge [15] and in an important paper by Palmer [16]. Orthogonal fluxgates were described in a book chapter by Butta [13] and also in a book by Weiss and Alimi [17].

The gating mechanism of orthogonal fluxgate was first explained by Primdahl [18] and later considering anisotropy by Butta and Ripka [19]. Without an external DC axial field along the sensitive axis, the core is magnetized in circumferential direction and there is no axial field detected by the pickup coil. When the DC axial field is present, the core magnetization is deflected from circumferential direction and the pickup detects the AC field of the second harmonics of the excitation frequency. Two orthogonal sensor configurations are shown in Figure 3.3: they have a core in the form of a ferromagnetic wire (Figure 3.3(a)) or a tube (Figure 3.3(b)).

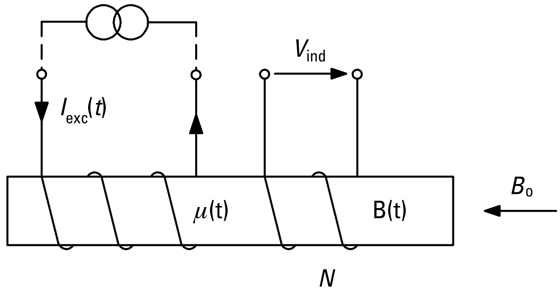

Figure 3.1 The basic fluxgate principle. The ferromagnetic core is excited by the AC I_{exc} of frequency f into the excitation winding. The core permeability $\mu(t)$ is therefore changing with $2f$ frequency. If the measured DC field B_0 is present, the associated core flux $\Phi(t)$ is also changing with $2f$ and voltage V_{ind} is induced in the pickup (measuring) coil having N turns. This principle is valid for the parallel fluxgate. (*After:* [1].)

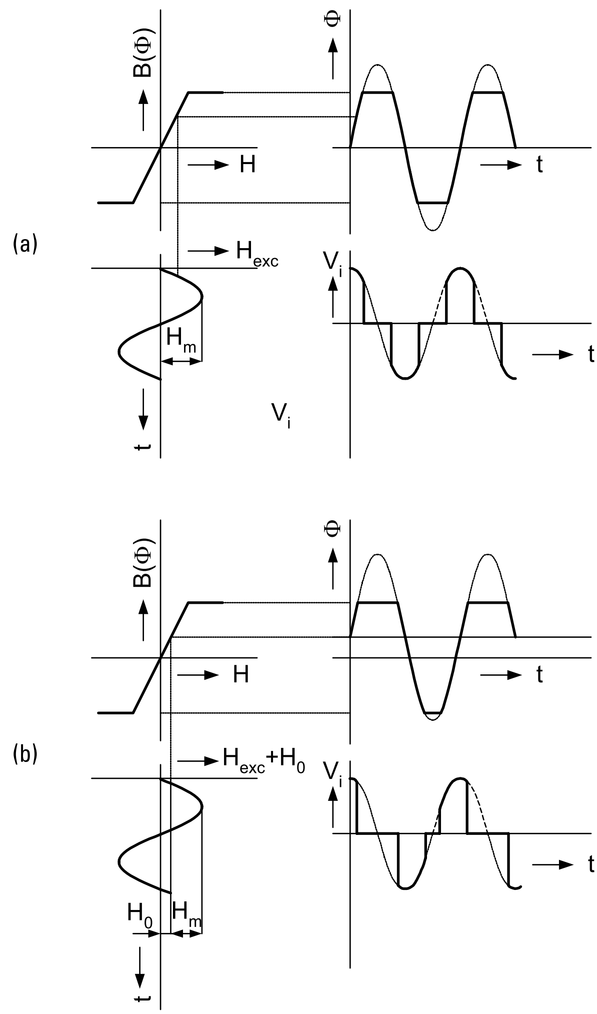

Figure 3.2 Simplified parallel fluxgate waveforms: (a) in the zero field; and (b) with the measured field H_0.

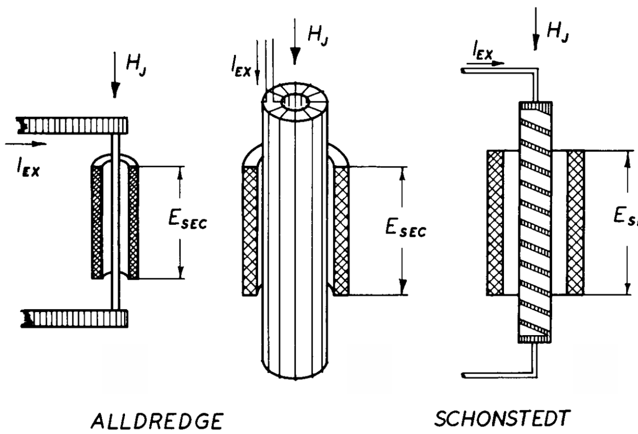

Figure 3.3 Two orthogonal-type fluxgates: (a) with wire core; (b) with tube core; and (c) helical core. (*From:* [18].)

A current through the core excites the first type: such a configuration has the principal disadvantage that the excitation field in the center of the core is zero, which causes problems with sensor remanence. The second type is excited by a single wire in the tube or by a toroidal coil.

The miniature planar sensor described by Seitz [20] is also of the orthogonal type. Another orthogonal sensor made from permalloy film electrodeposited on a solid copper rod was reported by Gise and Yarbrough [21] and later in [22]. The advantage of this sensor is that most of the excitation current flows through the copper core, so that the permalloy layer is deeply saturated, which erases the remanence. The copper core can be even insulated by glass layer so that no current is flowing through the permalloy shell [23]. Helical anisotropy causes the second harmonic field to also appear in the radial direction. This allows to detect it as a voltage across the core terminals. Such sensor is called a coil-less fluxgate [24–28].

Some orthogonal fluxgates work in the fundamental mode invented by Sasada [29]. This means that their excitation current has a DC component so that the core is saturated only in one polarity. The output of such a sensor is at the excitation frequency. Orthogonal fluxgates have large offsets, which can be effectively suppressed by flipping the excitation bias; 0.7-nT stability within a 60°C range was shown in [30]. However, this technique tends to increase the noise, which was shown to be up to 3 pT/√Hz at 1 Hz.

Orthogonal fluxgates in a unipolar fundamental mode achieved 0.75 pT/√Hz noise at 1 Hz, which is the lowest noise reported for a solid-state vectorial magnetic sensor [31, 32]. The sensor core is a folded Unitika 125AC20 amorphous wire of 125-μm diameter, with the chemical composition $(Co_{0.94}Fe_{0.06})_{72.5}Si_{12.5}B_{15}$. The disadvantage of this type of sensor is rather high offset temperature drift of the sensor without flipping the bias; the initial drift of the as-cast core of 15 nT/K was reduced by annealing to 2.5 nT/K, but this is still a large value compared to parallel fluxgates.

A mixed orthogonal-parallel sensor was constructed from the helical core formed by a tape wound on a tube [33], as shown in Figure 3.3(c). A helical anisotropy of the sensor core can also be induced by twisting the wire core [34] or annealing the core tape or wire under torsion [26].

In this chapter, we will concentrate on parallel type fluxgates, which generally have better offset stability. So, if the fluxgate type is not explicitly specified, we always have in mind the common parallel-field type.

3.2 Core Shapes of Parallel-Type Fluxgates

The basic single-core design is used mainly in magnetoelastic devices and some current sensors. The main problem is the large signal on the excitation frequency at the sensor output, because the device acts as a transformer. Thus, double cores (either double rod or ring-core) are normally used for precise fluxgates. The basic parallel-type fluxgate configurations are shown in Figure 3.4.

3.2.1 Single-Rod Sensors

Sensors with a single open core (Figure 3.4(a)) are used for magnetometers using time-domain detection (the device described by Sonoda and Ueda [35] and Blazek [36] being a typical example), and it is often used for auto oscillation or magnetic multivibrator (or self-oscillating) sensors, such as in [37]; the principles of these devices are described in Section 3.5.4. Single-rod open cores can also be used with a single coil serving for excitation, pickup, and eventually feedback simultaneously. Multiple single-coil fluxgates can also be connected in series to measure the field in several directions or measure the field gradient or to provide increased spatial averaging of the measured magnetic field and common-mode rejection. This is often used in magnetoelastic torque sensors.

Single closed cores are also used for fluxgate electric current sensors described in Section 11.6.

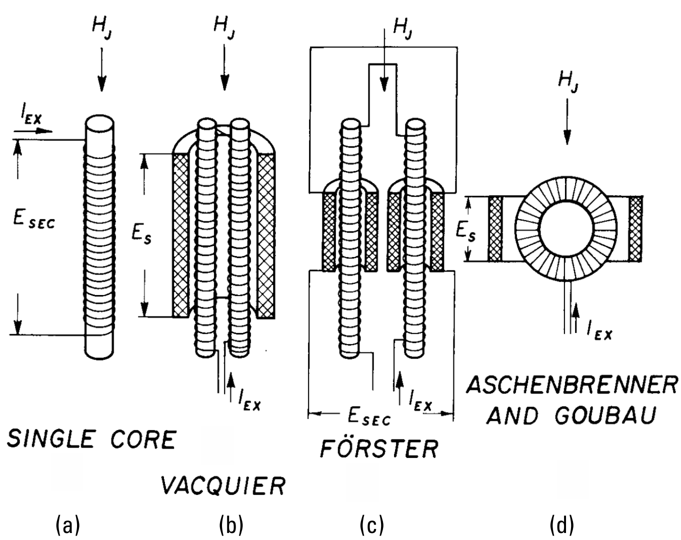

Figure 3.4 Parallel-type fluxgates: (a) single-rod sensor; (b) double-rod sensor of the Vacquier type; (c) double-rod sensor of the Förster type; and (d) ring-core sensor. (*From:* [18].)

3.2.2 Double-Rod Sensors

Most magnetometers use the conventional method of evaluating the second harmonics of the output signal; in such a case, great difficulties may arise from the presence of a large signal at the excitation frequency and odd harmonics, caused by the transformer effect between the excitation and sensing windings. The large part of this spurious signal is eliminated in the two-core sensor consisting of symmetrical halves excited in opposite directions, so that the mutual inductance between the excitation and measuring coils is near zero. Figure 3.4(b) shows the double-rod sensor with a common pickup coil (Vacquier type). Such a sensor was developed by Moldovanu et al. for the INTERBALL satellite instrument [38] and later tested with different kinds of core materials [39]. Foerster [6] used two individual identical pickup coils connected serially; such a configuration, as shown in Figure 3.4(c), allows easier matching of the cores and adjustment of the sensor balance by moving the cores with respect to their coils. A 50-cm-long fluxgate of this type with 10-pT resolution was constructed for a geophysical observatory [40].

The large geometrical anisotropy is the main advantage of the rod-type sensors: large sensitivity and resistance against perpendicular fields. There are also important disadvantages: Sensor cores with open ends are usually noisier and their offset is less stable with temperature and time than the closed-core sensors. The open rods are more difficult to saturate, so these sensors are also more energy-consuming and more susceptible to perming effects (i.e., offset change after a shock of a large field).

3.2.3 Ring-Core Sensors

The widely used ring-core sensor is shown in Figure 3.4(d). The excitation coil is in the form of a toroid (or, more precisely, a torus), while the pickup coil is a solenoid. Ring-core sensors may be regarded as a form of a balanced double sensor: the two half-cores are the parts of the closed magnetic circuit. The core usually consists of several turns of thin tape of soft magnetic material. The ring-core sensor design was used as early as 1928 by Aschenbrenner and Goubau [3]. Sensors made from sheets in the shape of flat rings or racetracks have been also reported [41, 42]. Although the ring-core sensors have, in principle, low sensitivity due to the demagnetization, ring-core geometry was found to be advantageous for the low-noise sensors because of several possible reasons:

1. It allows fine balancing of the core symmetry by rotating the core with respect to the sensing coil.
2. The possible mechanical stress in the core is uniformly distributed.
3. The open ends usually accompanied with the regions of increased noise are absent. Possible tape ends play only a minor role.

The size of the core affects the sensor sensitivity as analyzed by Gordon et al. [43]. Although the problem is complex due to the demagnetization effect and nonlinearity, the sensitivity is generally increasing with the sensor diameter. The demagnetization factor of fluxgate ring-cores is analyzed in [44–46]. With the given diameter, there is always an optimum of other dimensions for the best performance; usually, it must be found experimentally. The core dimension and number of excitation and

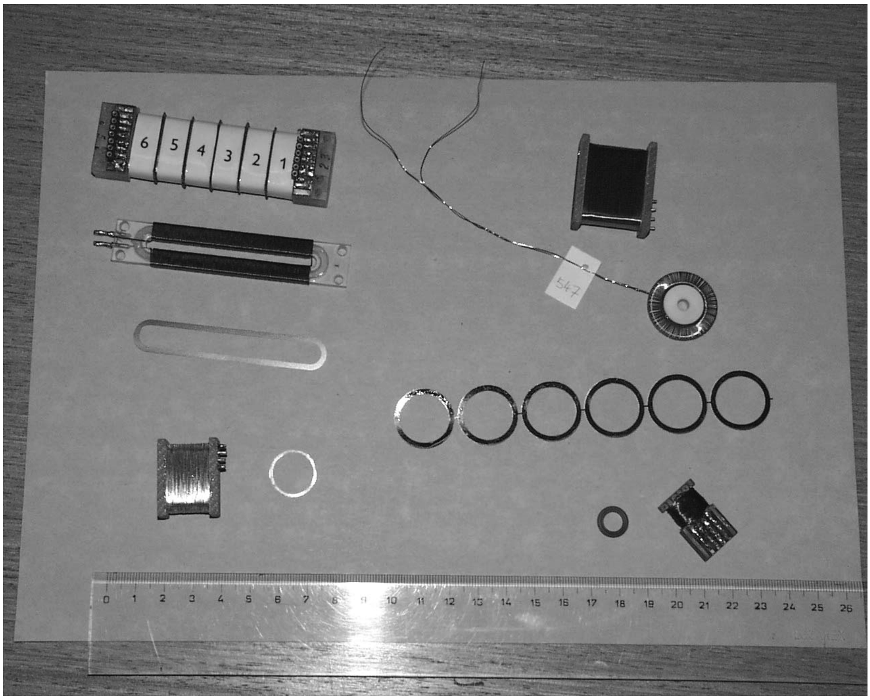

Figure 3.5 Elements of ring-core and racetrack sensors.

measuring turns also play a crucial role in matching the excitation and interfacing electronic circuits. A typical low-noise sensor size is a 17–25-mm-diameter ring-core wound from 4 to 16 turns of 1–2-mm-wide tape of 25-μm thickness.

An original mechanical design was used for the sensors developed by Nielsen et al. for the *Oersted* satellite [10]. The amorphous tape is wound in the groove in the inner surface of the ceramic support ring (bobbin). The tape is kept in position by its own spring force, but in order to increase the pressure and make it uniform, Nielsen later used an additional nonmagnetic stainless-steel spring of a complex shape.

In order to reach high sensor symmetry, the excitation coil should be wound with high uniformity. This is a difficult task even if using numerically controlled winding machines. A good technique is to keep the wire turns dense at the inner diameter of the bobbin.

3.2.4 Racetrack Sensors

A racetrack (oval) sensor is shown in Figure 3.5. This core geometry has a lower demagnetization factor than that of the ring-core, so the sensor sensitivity is higher and the sensor is less sensitive to perpendicular fields. The demagnetization factor of a racetrack is analyzed in [47]. Racetracks still have the advantages of closed-type sensors. Racetrack sensors wound from tape were reported already by Gordon and Brown [8] and later by the Schilling group, which achieved 2 pT/√Hz at 1 Hz noise [48]. Such sensors have a potential problem with offset temperature stability caused by the higher tape stress in the corners.

Sensors made of etched sheets of racetrack shape have been reported in [49]. The core is made of 8 layers of 35-μm-thick amorphous ($Co_{67}Fe_4Cr_7Si_8B_{14}$) material. Some of these sensors have 8 pT rms noise in the 50-mHz to 10-Hz band, corresponding to 2.6 pT/√Hz at 1 Hz noise density. The core length was 70 mm, the core width was 12 mm, and the track width was 2 mm.

3.3 Theory of Fluxgate Operation

The classical description of the fluxgate principle is given in [43]. Many other papers are based on idealized magnetization characteristics $B(H)$ of the sensor core and excitation field waveform $H(t)$. The validity of such a semigraphical description was verified by Primdahl [18] observing the B-H curves on a two-core sensor. A similar description for the ring-core sensor from [50] is shown in Figure 3.6. An idealized hysteresis loop of one-half of the sensor (Φ_1 versus H_{exc}) is identical to the characteristics of the magnetic material as long as the magnetic circuit is closed, as shown in Figure 3.6(a). When the external measured DC magnetic field is present, the characteristic curve is distorted as shown in Figure 3.6(b). For some critical value of H_{exc}, that half of the core, in which the excitation and the measured fields have the same direction, is saturated. At this moment, the reluctance of the magnetic circuit rapidly increases (as the flux is gated), and the effective permeability of the other half-core is decreased. In addition, the characteristic is shifted by the

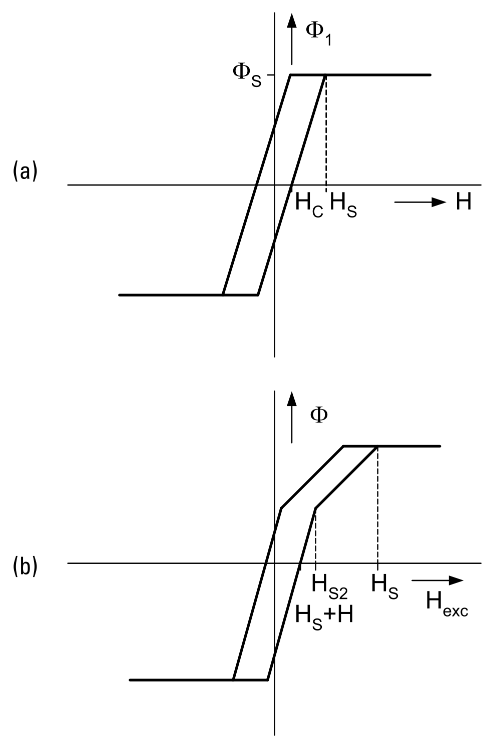

Figure 3.6 Ring-core fluxgate model: magnetization characteristics of the half-core: (a) without the external field; and (b) with the external DC field H_0. (*After:* [1].)

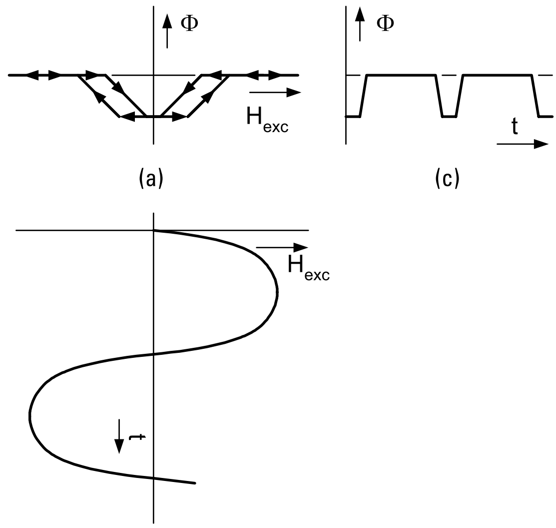

Figure 3.7 Ring-core fluxgate model, derivation of the pickup coil flux: (a) transfer function Φ versus H_{exc}; (b) excitation field; and (c) pickup coil flux. (*After:* [1].)

external field along the H axis. The characteristic for the second half-core is symmetrical with respect to the Φ axis. By summing up these two loops, we obtain the transfer function (i.e., Φ versus H_{exc} characteristic), which is shown in Figure 3.7. The height of the transfer function (which corresponds to the peak-to-peak (p-p) change of the pickup coil flux) increases with the measured field. The mentioned dependence is linear up to high field intensities, for which the whole sensor becomes saturated. This principle has also been used for the evaluation of the sensor output by integrating the induced voltage and measuring the p-p value of the waveform obtained this way. Figure 3.8 shows the actual shape of the dynamical hysteresis loop and the transfer function measured at 1 kHz with an oval-shaped core from amorphous material. So, if we know the excitation field waveform and transfer function, we may construct the flux waveform, and by taking its derivative, we obtain the waveform of the induced voltage.

3.3.1 The Effect of Demagnetization

If we assume a constant pickup coil area in the general induction sensor equation (2.2), we have:

$$V_i = \frac{NA\mu_0\mu_r dH(t)}{dt} + \frac{NA\mu_0 H d\mu_r(t)}{dt} \tag{3.1}$$

We see that the basic induction effect (first term) is still present in fluxgate sensors. In some cases, it can cause interference, but sometimes it can be used simultaneously with the fluxgate effect to measure the AC component of the external field (Section 3.13). However, here we concentrate on the fluxgate effect, second term

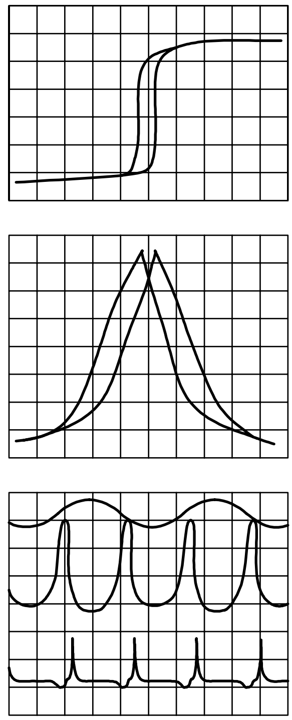

Figure 3.8 Measured ring-core fluxgate waveforms: (a) dynamic hysteresis loop; (b) transfer function; and (c) time dependences of the excitation field, flux, and induced voltage. (*After:* [1].)

in (3.1). The time dependence of the core permeability is caused by the periodical excitation field. The given formula may be used for long rod-type sensors. For the more often used ring cores, we should consider the demagnetization effect (i.e., recognize that H in the core material is substantially lower than the measured field H_0 outside the sensor core). Thus, we must write for the flux density within the core:

$$B = \frac{\mu_0 \mu_r H_0}{\left[1 + D\left(\mu_r - 1\right)\right]} = \mu_0 \mu_a H_0 \tag{3.2}$$

where D is the effective demagnetizing factor (as seen from the pickup coil) and μ_a is the apparent permeability, $\mu_a = \mu_r/[1 + D\ (\mu_r - 1)]$, for very large μ_r, $\mu_a \rightarrow 1/D$.

If we consider the demagnetization, the equation for the fluxgate output voltage becomes more complex:

$$V_i = NA\frac{dB}{dt} = NA\mu_0 H_{\text{ex}} \frac{(1 - D)}{\left\{1 + D\left[\mu_{\text{r}}(t) - 1\right]\right\}^2} \frac{d\mu_r(t)}{dt} \tag{3.3}$$

The detailed analysis of the demagnetization effect can be found in [51] and references listed there. A good estimate for the effective demagnetization factor of tape-wound ring cores is

$$D = \frac{kT}{d} \tag{3.4}$$

where T and d are the core thickness and diameter and k is constant depending on the pickup coil geometry and other factors, but not on core permeability and excitation parameters.

As we see, D approximately does not depend on the tape width w; that holds for $w >> T$.

Primdahl measured $k = 0.22$ for 17-mm diameter ring cores wound on 1-mm-thick tape. The pickup coil was wound on the 23 × 23 × 5.7-mm bobbin. The typical values he measured on a 10-wrap core were $D = 0.0032$, $\mu_r = 33{,}000$ and $\mu_a = 300$ for no external DC field and zero excitation.

If we substitute these values into (3.3), we obtain for zero excitation:

$$V_i = \frac{10^{-4} NA\mu_0 H_0 d\mu_{\mathrm{r}}(t)}{dt} = 10^{-4} NA\mu_0 H_0 \left(\frac{d\mu_{\mathrm{r}}(t)}{dH_{\mathrm{exc}}}\right)\left(\frac{dH_{\mathrm{exc}}}{dt}\right) \tag{3.5}$$

A is the core cross-sectional area and N is the number of turns of the pickup coil, which suggests that the sensitivity of the ring-core sensor is 10,000 times lower than that of a very long rod core. The real situation is much better: for zero excitation current, the core permeability is constant so that $d\mu(t)/dH_{\mathrm{exc}} = 0$ and therefore V_i is zero regardless of the core shape. The fluxgate effect appears at the moment when the core becomes saturated, and then the permeability is decreasing and the effect of demagnetization is lower: for $\mu(t) = 1{,}000$, the ring-core sensor sensitivity is only 0.6 of the ideal rod sensor. The local distribution of the demagnetizing field in the ring-core was theoretically analyzed in [52]. The demagnetization factor of fluxgate ring cores was further discussed in [44–46] and demagnetization factor of racetrack was analyzed in [47]. Finite-element simulations (FEM) were used in these calculations. FEM is also a convenient tool for the design of coil shape.

The given formulae show that the analytical description of the voltage-output fluxgate mechanism is very complex. Further analysis by the Fourier transformation may follow to calculate the sensor sensitivity as was done by Nielsen et al. [53]. Another analytical model for sinewave excitation was made by Perez et al. [54]. A computer simulation of the fluxgate magnetometer using PSPICE and the Jiles-Atherton model of the hysteresis loop was performed in [55]. However, such descriptions have limited practical use. The general practical rules for achieving high sensitivity can be deducted from (3.3) and also from practical experience rather than complex theoretical models:

1. Voltage sensitivity is increasing with N (for high N, sensitivity is limited by other factors such as coil parasitic capacitance).
2. Sensitivity monotonically decreases with D.
3. For given D, sensitivity increases with T for small T, but this dependence saturates for big T.
4. The core material should have a steep change of permeability when coming into saturation.
5. The preferred excitation current waveform is squarewave.
6. Voltage sensitivity is increasing with excitation frequency (because $dH_{\mathrm{exc}}/dt \sim f$), until parasitic effects (such as eddy currents and parasitic capacitances) become important.

In real applications, the voltage output is tuned, either intentionally to utilize parametric amplification or unintentionally by parasitic pickup coil capacitance (Section 3.7). Also, the real excitation current waveforms are very different from the ideal shapes (such as sinewave, squarewave, or triangle), which further limits the practical applicability of the voltage-output fluxgate theory. In contrast, the current output fluxgate description (Section 3.8) is quite simple and matches the reality much better.

3.4 Core Materials

It is difficult to discuss the selection of the core material generally, as it depends on the type and geometry of the sensor, on the type of processing of the output signal, and also on the excitation frequency and required temperature range. However, there are general requirements for the material properties:

1. High permeability (permeability may be further intentionally reduced by thermomagnetic treatment to reduce the noise);
2. Low coercivity;
3. Nonrectangular shape of the magnetization curve (points 2 and 3 are equivalent to the smallest possible area of the B-H loop);
4. Low magnetostriction;
5. Low Barkhausen noise;
6. Low number of structural imperfections, low internal stresses;
7. Smooth surface;
8. Uniform cross-section and large homogeneity of the parameters;
9. Low saturation magnetization;
10. High electrical resistivity.

All known studies of core material compositions and processing parameters have shown that the minimum noise is achieved for near-zero magnetostriction alloys. Although the magnetostrictive core tapes are susceptible for offset instability, there is no simple direct mechanism for generation of second harmonic signal by magnetostriction. Offset and noise are caused by variation of local core properties and mechanical stresses together with magnetoelastic coupling [56].

The material traditionally used for the sensor cores is high permeability low magnetostriction permalloy (or Mumetal) in the form of a thin tape. The permalloy 81.6 Ni 6 Mo developed by the Naval Ordnance Laboratory [57] for a low-noise NASA magnetometer, which was later produced by Infinetics as S1000, is still the superior material with 3 to 6 pT/√Hz at 1-Hz noise. The aims to reproduce these 2.5-cm-diameter rings resulted only in 6 to 12 pT/√Hz at 1-Hz rings developed by Miles et al. [58].

Electrodeposited permalloy [59] and ferrite [9] were also used for the sensor core, but, in general, with worse results. The same applies for sputtered Permalloy. However, material deposition should be used in integrated sensors. Fluxgate effects were also reported in high-temperature superconductors [60].

Amorphous magnetic materials are magnetic glasses produced by rapid quenching. They started to be used for fluxgate cores in the early 1980s. A study concerning the noise of the amorphous magnetic materials was performed by Shirae [61]. He found that:

1. Low-magnetostriction Co-based alloys are suitable for fluxgate applications.
2. Room-temperature noise decreases with Curie temperature.
3. Annealing of the tape may further decrease the noise level.

Narod at al. [62] tested a number of alloys and observed the $1/f$ characteristics of the noise spectrum as was already known for crystalline materials. The minimum noise level for annealed Co-based alloy was 10^{-4} nT^2/Hz (= 10 pT/√ Hz) at 1 Hz. The measured sensor was a 23-mm ring-core. Nielsen et al. used stress annealing of the tape to produce a creep-induced anisotropy with the ribbon axis being a hard direction. In materials having this type of anisotropy, the rotational magnetization process dominates over the domain wall movement, which reduces the Barkhausen noise [63]. For 17-mm-diameter ring-core sensor, the lowest noise level was 11-pT rms (64 mHz–12 Hz) and the noise density was 1.8×10^{-5} nT^2/Hz (or 4.2 pT/√Hz) at 1 Hz [64]. Amorphous wires are used for the cores of both parallel and orthogonal fluxgates. The amorphous core properties may be further improved by chemical etching and polishing [65] and also by annealing [66, 67].

Nanocrystalline alloys were also tested for fluxgate cores, but until now they have exhibited higher noise values [68]. Their potential advantage is higher stability at elevated temperatures up to 250°C [69].

3.5 Principles of Fluxgate Magnetometers

The second-harmonic detection of the output voltage is still the most frequently used; the classical fluxgate magnetometer working on this principle will be described as an introduction. Besides that, a number of other principles for the processing of the sensor output voltage appeared, which are used mainly to reduce the power. The fluxgate output is often tuned to enhance the sensitivity. Problems with output tuning are discussed in Section 3.7. Fluxgates may also work in the short-circuited mode; current output is analyzed in Section 3.8.

3.5.1 Second-Harmonic Analog Magnetometer

In this section, a block diagram of a typical magnetometer working on the second-harmonic principle is described and crucial parts of the magnetometer electronics are discussed. The sensor output is amplitude-modulated by the measured field and the phase-sensitive detector (PSD) demodulates it back to DC or near-zero frequency. As the sensor itself has a linear range limited to typically 1 μT, fields larger than that usually have to be compensated. Figure 3.9 shows the block diagram of the feedback magnetometer. The analog feedback loop has a large gain, so that the sensor works only as a zero indicator. The output variable is then the current into

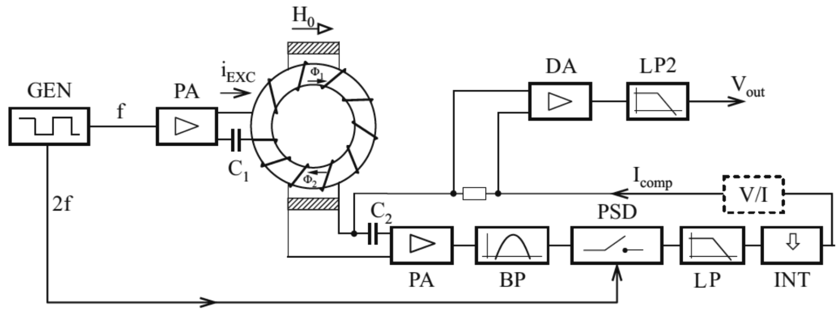

Figure 3.9 Block diagram of the second-harmonic fluxgate magnetometer. GEN produces the excitation frequency *f* and the reference frequency 2*f* for PSD.

the compensation coil. The sensor nonlinearity and the nonstability of its sensitivity are suppressed by the feedback gain. The sensor is excited by the generator (GEN) working on the frequency *f*. The preamplifier is often just a totem pole-connected pair of low, on-resistance Hexfet transistors. The generator circuits also produce the 2*f*-squarewave signal as a reference for the PSD. Proper phase shift of this signal must also be performed. The pickup (detection coil) for the voltage output typically has 2,000 turns. The first harmonic and other spurious signals at the sensor output are sometimes too high for the PSD, so preamplification and sometimes also filtration has to be performed in a bandpass filter (BP). To obtain a sufficient amplification, an integrator (INT) is introduced into the feedback loop. The loop signal is fed back to the feedback (compensation) coil. Additional feedback current generated by the digitally controlled low-noise and stable current source may be added to increase the range of the instrument. The dynamic range of the basic analog feedback magnetometer may be 120 dB, which is sufficient for most of the applications; it allows for the construction of an instrument with 100-μT range, making it possible to measure the Earth's field with 0.1-nT resolution. The compensation current is usually measured as a voltage across the highly stable sensing resistor; two principles of analog-to-digital converters (ADCs) are used for this application: (1) delta-sigma (ΔΣ) ADCs may have resolution of 16 to 32 bits and their speed or resolution may be software configured; and (2) integrating (e.g., dual slope) converters are slower, but they better suppress the power-line frequency.

The excitation generator produces a sinewave or a squarewave frequency between 400 Hz and 1 MHz; 5 to 20 kHz are typical for crystalline core materials, and 1 MHz is typical for integrated fluxgates. An increase in the frequency increases the sensitivity to some point, at which eddy currents in the core material become important. Thus, sensors made from thin tape or layer with large electrical resistance may be operated at higher frequencies. Increasing the excitation frequency accelerates the dynamical performance of the sensor; this will be discussed in Section 3.13. The excitation current should have a large amplitude and a low second harmonic distortion, which may cause a false output signal. The excitation circuit can also be tuned; see Section 3.6.

An increasing number of turns of the pickup coil increases the sensor sensitivity, but there are limitations caused by parasitic self-capacitances, which create a resonant circuit. The voltage output is often tuned to increase the sensitivity (see Section

3.7). The preamplifier has to be decoupled by the serial capacitor C_2 to prevent any DC from flowing through the pickup coil, causing sensor offset. The feedback current source should be of large output impedance to prevent short-circuiting of the sensor output, which would lower the sensitivity.

In simple magnetometers, the pickup coil also serves for the feedback, but this requires some trade-offs. The pickup coil should be close to the sensor core in order to keep the air flux low. The feedback field should be homogeneous and therefore a large feedback coil is required. Thus, in precise magnetometers, the two coils are separated. However, even in this case, the impedance of all connected circuits must be kept high to prevent decrease of the sensitivity, as the interaction between the two coils is high. On the contrary, the mutual inductance between the excitation and the pickup coil is very low, so that the output impedance of the excitation generator has no direct influence on the sensitivity.

Classical analog magnetometers measure only the second harmonic. If we use a gated integrator or digital detector instead of a classical PSD, we can use also the higher even harmonics, which may increase the sensitivity and lower the noise.

3.5.2 Digital Magnetometers

In a digital fluxgate magnetometer, the field extraction from the sensor output and the calculation of the feedback signal are done in the digital domain. This replaces the analog (bandpass) filter after the preamplifier, the phase-sensitive detection, the lowpass filter, and the analog integrator blocks of Figure 3.9 by digital circuitry. An ADC of the sensor output signal is required right after the preamplification and a digital-to-analog converter (DAC) circuit is used for the generation of the analog feedback (Figure 3.10). The field detection within the sensor is still in the analog domain.

The digital fluxgate magnetometer with its reduced number of analog parts:

- Is more robust against changes of electronics temperature and supply voltages, which can cause offset drifts due to phase shifts of potential error signals;

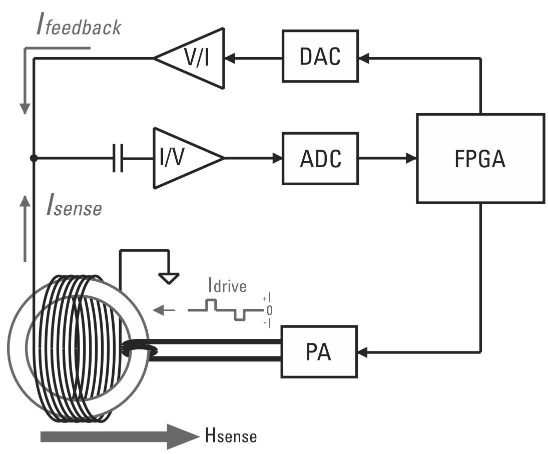

Figure 3.10 Generic block diagram of a single-axis digital fluxgate magnetometer with the digital computing within a field programmable gate array. (*From:* [87]. CC BY license.)

- Is less sensitive to electromagnetic disturbances (e.g., the routing of the $2f$ reference signal to the PSD, which can easily cause an additional offset, is not needed);
- Features higher flexibility of the instrument operation since no analog range switching is needed for a modification of the dynamic range and the reference signal can have an arbitrary shape so that it can perfectly match the measured signal.

The feasibility of direct digital processing of the fluxgate output was first shown by Primdahl et al. in [70]. It is based on a matched filter processing for the field extraction, which requires a sampling of the amplified sensor output at $16f$ or higher. A closed-loop version with a digital signal processor as the central processing chip is described in [71] and it was flown aboard the Swedish *Astrid-2* satellite [72].

The first real-time fluxgate magnetometer was reported by Auster et al. [73]. Their design reduces the sampling rate to $4f$, which is required as a minimum for the monochromatic detection of the field proportional $2f$ signal. The feedthrough signal at odd harmonics of the excitation frequency is well attenuated by a simple accumulation of the digitized samples. This kind of digital fluxgate instrument has been developed for various space missions such as Rosetta [74], THEMIS [75], and BepiColombo [76], and it is also used in ground-based instruments.

Another approach for a digital fluxgate magnetometer is based on combining the control loops of a conventional analog fluxgate magnetometer with the control loop of a $\Delta\Sigma$ modulator. When comparing ADC principles, the $\Delta\Sigma$ technique is the one with the highest resolution and the smallest bandwidth, which fits well for the fluxgate application. Kawahito et al. [77] developed a micro-fluxgate magnetometer based on this working principle with sensor and readout electronics fully implemented in silicon microtechnology. Magnes et al. [78] followed a similar approach with the integration of just the sensor readout circuits on a mixed-signal application-specific integrated circuit (ASIC) for space application. The ASIC contains three 2–2 cascaded $\Delta\Sigma$ modulators with modified first stages, which are directly connected to the sense and feedback coils of a triaxial fluxgate sensor. The fourth-order $\Delta\Sigma$-fluxgate modulators enable a signal-to-noise ratio of 89 dB at an output data rate of 128 Hz. The power consumption of the ASIC, which is in use for two space missions [79–80], is 60 mW. A drawback of this design is its limited dynamic range ($<\pm 2{,}000$ nT) because of the single-bit feedback into the fluxgate sensor, which causes nonlinearity at large fields. Similar designs that are also based on second-order $\Delta\Sigma$ modulators are presented in [81–83].

Different digital fluxgate magnetometer concepts are reviewed in [84]. In general, ADCs with an effective number of at least 14 bits are required for a proper detection of the magnetic field in the forward path of digital fluxgate magnetometers. This is well established and no specific problems have been reported in literature. Much more attention has been placed on the feedback path with the DACs as the central circuit block. It is key for the overall accuracy and stability of the measurement, especially when a dynamic range of $\pm 65{,}000$ nT is required for the measurement of the Earth's magnetic field. A 24-bit digital resolution and >20-bit signal-to-noise and distortion ratio are the goals to be achieved. Single-chip solutions, which are radiation-tolerant enough for space application, are practically not available on the market.

Forslund et al. combined a pulse width (PWM) with a ΔΣ modulator [85]. The DAC features a linearity that corresponds to 16–17 bits. It could be further improved by avoiding $2f$ content in the feedback signal [86]. Miles et al. [87] combined two 10-bit PWMs that were overlapped by 2 bits with ultrahigh stable resistors in the attenuator and summing network. The 24-bit resolution is achieved by digitizing the remnant field with a 14-bit ADC. Nonlinearity problems are reported but not quantified. The feedback of the magnetometer in [88] is composed of two industry-level, radiation-tolerant 16-bit DACs. Again, 24-bit digital resolution is achieved but the linearity is driven by the precise matching of the two DACs. A hybrid version of the same design has first been flown on the South Korean GEO-KOMPSAT 2A satellite [81]. A new ASIC design is claiming DAC performance with 20 effective numbers of bits [89]. The 20-bit resolution, ±5-ppm linearity, and 0.03 ppm/√Hz at 1-Hz noise were achieved by PWM DAC described in [90].

3.5.3 Nonselective Detection Methods

Although the PSD of the second-harmonic component of the sensor output voltage is the most usual method, several other detection methods have appeared on processing the output signal in the time domain.

The peak detection method is based on the fact that, with an increasing measured field, the voltage peaks of the sensor output are increasing in one polarity and decreasing simultaneously in the opposite polarity. The difference between positive and negative peak value is zero for the null field and may be linearly dependent on the measured field within a narrow interval. Probably the best magnetometer based on this principle was constructed by Marshall in 1971 [91]. He used a 4-79 Mo permalloy ring-core and reached a 0.1-nT resolution with a portable instrument.

The principle of the phase-delay method is illustrated by Figure 3.11. We assume the simple magnetization characteristics without hysteresis and a triangle waveform of the excitation current. For the time intervals t_1, t_2 between two succeeding output voltage pulses, we may write

$$\begin{aligned} t_1 &= \frac{T}{2} - 2\Delta t = \frac{T}{2} + T\frac{H_0}{H_m} \\ t_2 &= \frac{T}{2} + 2\Delta t = \frac{T}{2} - T\frac{H_0}{H_m} \end{aligned} \tag{3.6}$$

where T is the period of the excitation current, H_m is the excitation field maximum value, and H_0 is the measured field.

These relations were used by Heinecke in a digital magnetometer described in [92]. The time intervals t_1, t_2 were measured by a counter with the reference frequency n times higher than the excitation oscillator frequency. If the time $(t_2 - t_1)$ is equal to N periods of the reference oscillator, then we may write

$$t_1 - t_2 = 2T\frac{H_0}{H_m} = \frac{NT}{n} \tag{3.7}$$

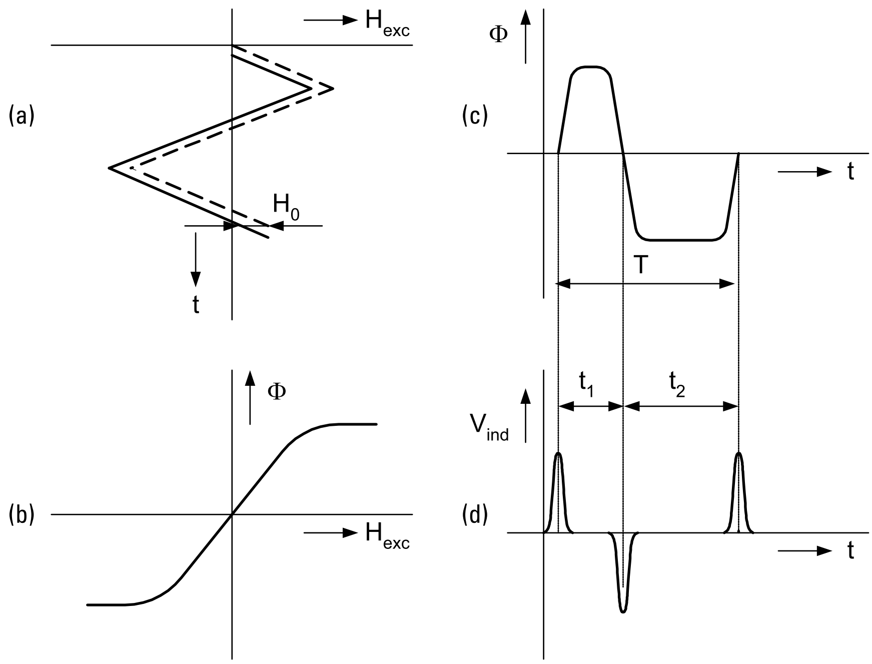

Figure 3.11 Phase-delay method: (a) excitation field with DC shift by measured field H_0; (b) magnetization characteristics; (c) flux; and (d) induced voltage. (*After:* [1].)

$$H_0 = \frac{H_m N}{2n} \tag{3.8}$$

The resolution of this method is limited by the maximum counter frequency. Heinecke reached a 2.5-nT resolution with a 10-MHz basic oscillator. The resolution was improved to 0.1 nT by summing 100 time intervals, but this caused a significant limitation of the sensor's dynamic response as the excitation frequency was only 400 Hz. The complications with noise from fast digital signals of the counter and other drawbacks limit the performance of the magnetometers based on this method. Residence times difference fluxgate magnetometer are based on a similar principle [93].

The relaxation-type magnetometer uses a single core saturated by unipolar pulses and measures the length of the relaxation pulse after the excitation field is switched off. The instrument has ±200-μT range, 5% linearity error, and about 0.5-nT p-p noise [36].

3.5.3.1 Sampling Methods

The sampling method was used by Son [94]. The instantaneous value of the excitation current at the time of zero-crossing of the core induction depends on the measured field. In an ideal case, the sensitivity is not dependent on the excitation frequency, amplitude, or waveform. Son reached 0.1-nT resolution and 5-μV/nT sensitivity using two open 4-mm-long cores made from amorphous water-quenched Vitrovac 6030. The magnetometer works in an open loop, but the linearity error is only 0.02% in the 400-μT range; stability data was not given. A similar principle was used by Sonoda and Ueda in their feedback magnetometer employing a single-rod sensor [35].

3.5.4 Auto-Oscillation Magnetometers

Auto-oscillation magnetometers are considered a separate group, although most of them are similar to the previously mentioned ones. A magnetic multivibrator constructed by Takeuchi and Harada [37] consists of a single-core sensor, capacitor, and operation amplifier forming the oscillating circuit. The multivibrator duty cycle depends on the amplitude of the measured field. The 0.1-nT resolution of this very simple device was reported, although no information was given on the device stability (often the missing information of many fluxgate papers; poor stability is a weak point of simple fluxgate magnetometers). Other auto-oscillation magnetometer designs have the oscillator frequency as the output variable. Such a principle is used in PMI's fluxgate compass sensors (although the manufacturer calls them magneto-inductive sensors and claims that they are not based on fluxgate technology).

None of the nonselective or auto-oscillation methods has reached the parameters of the best low-noise and long-term stable magnetometers based on the conventional second-harmonic principle. Nevertheless, they may find application in simple low-cost and low-power instruments used for various indication and search purposes.

3.6 Excitation

The excitation current has to be free from any distortion at the second harmonic (and other even harmonics if they are evaluated), as this may leak into the sensor output, through the inductive coupling caused by a nonideal balance of the sensor or capacitance coupling, and cause a false signal. The amplitude of the excitation current must be large enough to deeply saturate the sensor core in each cycle in order to remove any remanent effect. As the excitation field is attenuated in the central part of the core by the eddy currents, and as some magnetically harder regions in the material may exist, the excitation current peak value has to be 10 to 100 times higher than required for the technical saturation. High narrow peaks of the excitation current may be achieved by using a tuning capacitor either parallel to the excitation winding (for current-mode or high-source impedance) or connected serially (for voltage-mode excitation) as shown in Figure 3.12. The typical tuned current waveform is in Figure 3.13 (upper trace). Tuning may also decrease the second harmonic distortion of the excitation. The nonlinear resonance in the excitation current is described in [95].

3.7 Tuning the Output Voltage

In the case of voltage-output sensors, the parasitic self-capacitance and the inductance of the pickup coil form a parallel resonant circuit. We can find the multiple resonant peaks by changing the excitation frequency. Because of the nonlinear

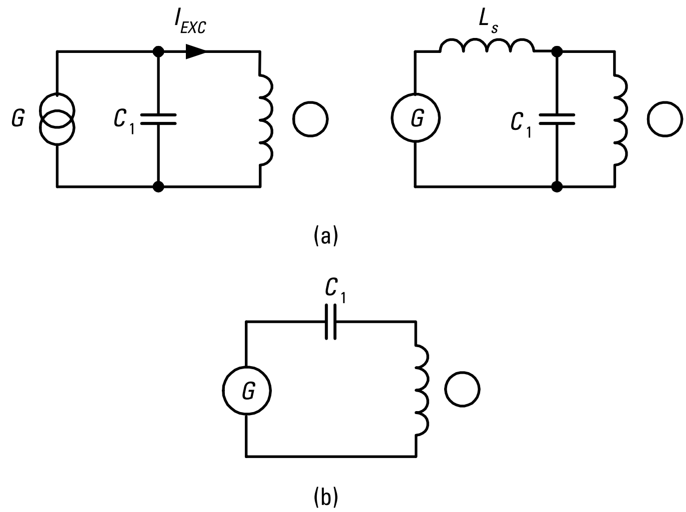

Figure 3.12 Tuned excitation circuits: (a) parallel; and (b) serial.

characteristics of the circuit, the resonance frequency depends also on the excitation amplitude. Sometimes the circuit is unstable (i.e., it oscillates at some harmonics even without any external field). In general, this kind of resonance is unwanted as the coil self-capacitance is both unstable and temperature-dependent. Splitting the pickup coil into separate sections lowers the self-capacitance. Many studies on fluxgate sensitivity are influenced by such resonance, so they are valid only for the particular pickup coil and their results should be generalized only with great care.

Some of the fluxgate magnetometers intentionally use parametric amplification by tuning the sensor voltage output by a parallel capacitor. Gains of as high as 50,000 are achievable, but the circuits are extremely sensitive to parameter variations and have a narrow bandwidth. An increase in the sensitivity by the factor of 10 to 100 is reasonable; for a high-quality factor (low pickup coil resistance), the

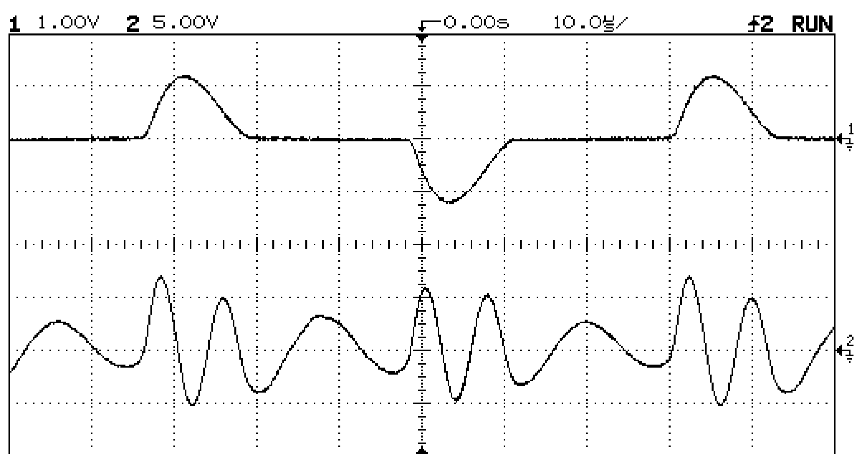

Figure 3.13 Excitation current (upper trace, 1A/div) and the untuned voltage output (lower trace) of the ring-core sensor in an 5-μT uncompensated measured field.

circuit may again become unstable. This situation arises more often for very sensitive fluxgates, for example, racetrack core sensors. Parametric amplification helps to suppress the influence of the preamplifier noise and also to suppress the spurious signals at the sensor output.

Figure 3.13 shows the unloaded output voltage of a racetrack fluxgate sensor for the measured field of 5 μT. Higher even harmonics are dominant due to parasitic self-resonance of the pickup coil. Figure 3.14(a) shows the same sensor tuned into an unstable mode by a parallel capacitor with $C_2 = 11$ nF. The large amplitude oscillations are present even for the zero measured field. The sensor may be stabilized by damping resistor either in series, or parallel to the tuning capacitor. Figure 3.14(b) shows the same sensor stabilized by a serial resistor of 10Ω. It should be noted that the value of the damping resistor necessary to stabilize the sensor is small compared to the DC resistance of the pickup coil, which is 45Ω.

Ring-core sensors are less sensitive than the racetrack sensors due to their higher

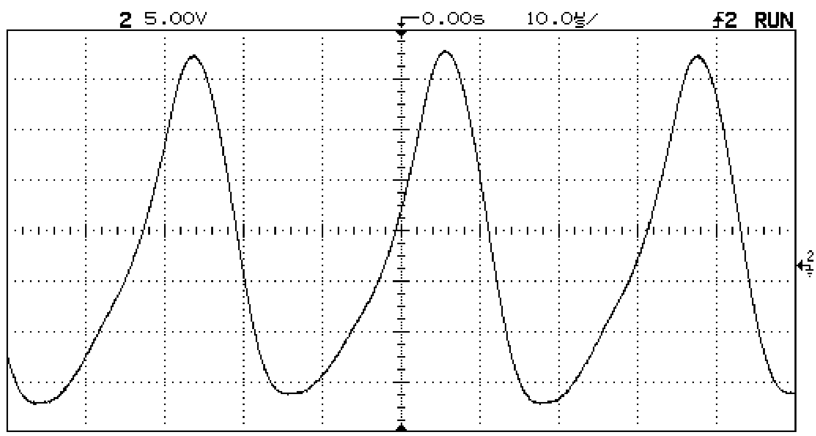

(a)

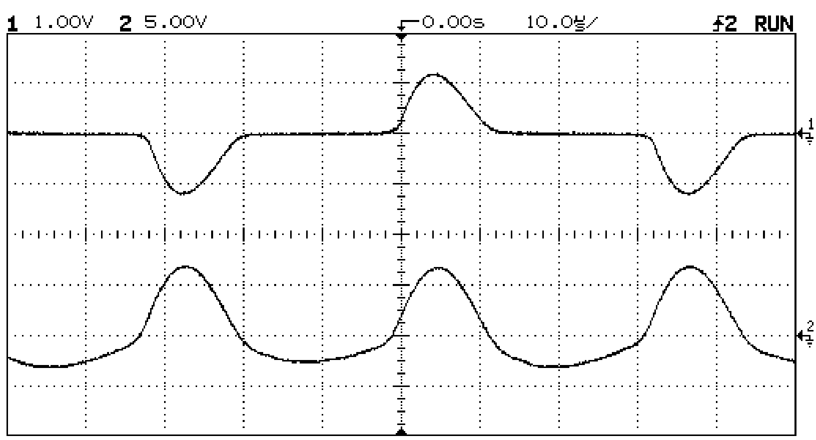

(b)

Figure 3.14 (a) Oscillations at the output of the unstable tuned sensor; and (b) stabilized sensor tuned to the second harmonic, output voltage for the 5-μT measured field.

demagnetization factor. If their pickup coil is wound of thin wire, they are usually unconditionally stable (for each value of the tuning capacitor and measured field and any excitation parameter).

Although the resonating circuit is very simple, the precise analytical description is complex, as the effect is again strongly nonlinear. Since the first study by Serson and Hannaford [96], parametric amplification and its stability have been analyzed by many authors [97]. Primdahl and Jensen [98] pointed out some disadvantages of the parametric amplification. The sensor performance degradation they observed is most pronounced when being close to the stability limit. Some authors observed that proper moderate tuning of the sensor output increases the sensor sensitivity (typically 10 times), but also suppresses the magnetometer noise to about one-half. They explained this fact to be that the tuning concentrates the broadband output power to the second-harmonic frequency [99]. They also concluded that moderate tuning does not degrade the temperature stability of the sensor offset.

3.8 Current-Output (or Short-Circuited) Fluxgate

In the conventional fluxgate magnetometer, the output of the pickup coil is connected to an amplifier with a large input impedance, so that the voltage induced into this coil forms the output of the sensor. Primdahl et al. [100] short-circuited the pickup coil by the current-to-voltage converter with a very low input impedance and used the current-output mode of operation. The amplitude of the current pulses was shown to depend linearly on the measured field. Low input impedance of the electronics eliminates problems with the stray capacitance of the coil and cable, and the design of the low-noise input amplifier is simplified. Primdahl et al. [101] showed that by using the gated integrator (controlled rectifier of the switching type with an adjustable gate width), the maximum sensitivity is achieved for a specific phase delay and the width of the reference voltage, when the shape of the pulse is best fitted. Because that principle uses the information from all even-harmonic components (the weight of each given by the spectrum of the reference), it is not possible to use a classical bandpass input filter. The demands on the PSD circuit (Figure 3.9) are very high in the case of current output, as very small signals have to be processed in the presence of large overcoupled disturbing signals. There are two main sources of feedthrough: (1) air mutual inductance between the excitation and pickup coils, and (2) flux leakage from the core. These two contributions cannot be simultaneously nulled, as shown in [102].

The sensitivity of the short-circuited fluxgate increases with increasing sensor length and cross-section (the latter dependence saturates for thick sensors because of the demagnetization) as usual for voltage-output sensors, but decreases with the increasing number of turns with certain practical limitations. The sensitivity of the 17-mm toroidal core sensor was about 40 nA/nT compared with about 20-μV/nT sensitivity, which can be reached for an untuned voltage-output sensor of the same dimension. Although the short-circuited fluxgates have shown practical advantages, they have, in general, very similar parameters as the traditional voltage-output design.

3.8.1 Broadband Current-Output

The circuit diagram of the current-output fluxgate is shown in Figure 3.15. The pickup coil is short-circuited by the current-to-voltage converter with the feedback resistor R. The capacitor C is used to prevent any DC input current of the op-amp from flowing through the pickup coil (such a current would cause a sensor offset). In the traditional broadband case, C is very large, but it can also be used for tuning (Section 3.8.2).

The current-output fluxgate model based on circuit analysis was presented in [101, 103].

The basic equation for the circuit in Figure 3.15 is:

$$\frac{d\Phi}{dt} + i(t)r_{Cu} + \frac{1}{C}\int i(t)\,dt = 0 \tag{3.9}$$

In order to incorporate the measured DC field B_0 into the circuit equations, we replace its effect by the equivalent coil current i_{EQ},

$$i_{EQ} = \frac{l}{\mu_0 N} B_0 \tag{3.10}$$

The total pickup coil flux is

$$\Phi = \left[i_{EQ} + i(t)\right]L(t) \tag{3.11}$$

The effective length of the coil is defined here as $l = \mu_0\ NI/B_0$, where B_0 is an external field, which is canceled by a DC compensation current I into the pickup coil. We suppose that l is only dependent on the coil geometry, not on the sensor core properties or on the mode of the excitation. The value of l is higher than the physical length of the coil and may also be determined from the inductance of the pickup coil with a removed (or completely saturated) core [51].

The apparent permeability μ_a is defined as $\mu_a = \mu_0 B/B_0$, where B is the magnetic field inside the core. Apparent permeability is lower than the core material permeability because of the core demagnetization. It is dependent on the core size and properties and mode of excitation, but also on the geometry of the pickup coil.

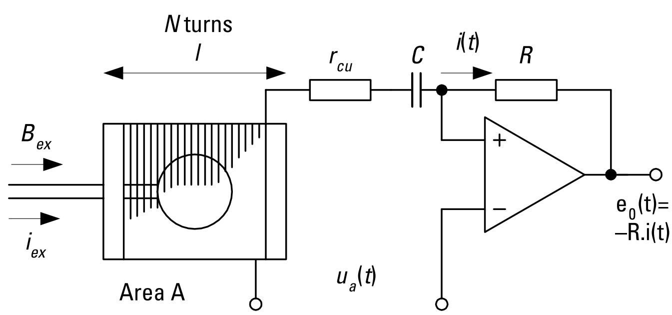

Figure 3.15 Circuit diagram of the current-output fluxgate.

After substitution of (3.10) and (3.11) into (3.9), we obtain:

$$i_{\mathrm{EQ}} \frac{dL(t)}{dt} + \frac{d}{dt}\left[i(t)L(t)\right] + i(t)r_{Cu} + \frac{1}{C}\int i(t)\,dt = 0 \tag{3.12}$$

Here $L(t)$ is a periodic function of frequency $2f$, for which

$$L(t) = \mu_0 \frac{N^2}{l} A\mu_a(t) \tag{3.13}$$

where l is the effective length of the coil, A is its cross-sectional area, N is the number of turns, and $\mu_a(t)$ is the (modulated) apparent permeability of the sensor core.

In the untuned case, where $C \to \infty$, we have:

$$\frac{d\Phi}{dt} + i(t)r_{Cu} = 0 \tag{3.14}$$

If the coil losses are small, then the copper resistance r_{cu} may be neglected, as discussed in [100]. Then (3.14) is simplified to $d\Phi/dt = 0$, or

$$\Phi = \left(i_{\mathrm{EQ}} + i(t)\right) \cdot L(t) = \text{constant}$$

and from that

$$i(t) = -i_{\mathrm{EQ}} + \frac{\Phi}{L(t)} \tag{3.15}$$

The output current cannot have any DC component, that is, it has a zero time average, $\langle i(t)\rangle = 0$:

$$0 = -i_{\mathrm{EQ}} + \Phi\left\langle \frac{1}{L(t)} \right\rangle \Rightarrow \Phi = i_{\mathrm{EQ}} \cdot L_{G0} \tag{3.16}$$

where L_{G0} is the geometric mean value of the pickup coil inductance

$$\frac{1}{L_{G0}} = \left\langle \frac{1}{L(t)} \right\rangle \tag{3.17}$$

and from this, we have the basic short-circuited fluxgate equation:

$$i(t) = i_{\mathrm{EQ}}\left[\frac{L_{G0}}{L(t)} - 1\right] \tag{3.18}$$

It was shown that in practical cases the core permeability, and thus, also the pickup coil inductance is rapidly changing between two values, $L_{\max}$ for the linear part of the hysteresis loop and $L_{\min}$ for the saturated sensor core. Thus, the ideal short-circuited current is a squarewave. The p-p value of the output current was derived in [101] as:

$$i_{p-p} = i_{\mathrm{EQ}} \frac{L_{G0}}{L_{\max}}\left(\frac{L_{\max}}{L_{\min}} - 1\right) \tag{3.19}$$

The actual waveforms of the current output sensor are shown in Figure 3.16. The current impulses decay because of ohmic losses and the waveform is also distorted by the feedthrough from the excitation.

3.8.2 Tuning the Short-Circuited Fluxgate

The current-output fluxgate can also be tuned by a serial capacitor as shown in [103]. The sensitivity was increased 5 times, while the level of the spurious feedthrough remained the same. Serial tuning is easily made only by decreasing the value of the input decoupling capacitor. The simplified analytical description was shown to fit the measured parameters well. If the pickup coil is well tuned, we can limit the solution only to the second-harmonic output current:

$$i(t) \cong i_a \cos(2\omega t) + i_b \sin(2\omega t) \tag{3.20}$$

The circuit analysis performed in [104] leads to the matrix equation:

$$\begin{bmatrix} \dfrac{r_{cu}}{2\omega L_0} & \dfrac{-L_4}{2L_0} \\ \dfrac{-L_4}{2L_0} & \dfrac{r_{cu}}{2\omega L_0} \end{bmatrix} \cdot \begin{bmatrix} i_a \\ i_b \end{bmatrix} = \begin{bmatrix} 0 \\ \dfrac{L_2}{L_0} \cdot i_{\mathrm{ex}} \end{bmatrix} \tag{3.21}$$

and the stability condition is $r_{cu} > \omega L_4$, where L_2 and L_4 are second-order and fourth-order Fourier components of $L(t)$ and L_0 is a zeroth-order Fourier component, which is the arithmetic mean value $L_0 = \langle L(t) \rangle$.

The current-output fluxgate resonance condition is

$$C = \frac{1}{(2\omega)^2 \cdot L_o} \tag{3.22}$$

Notice that the arithmetic mean value, L_0, differs from the geometric mean value L_{G0}, which is important for the untuned current-output equations.

An example of tuned current-output fluxgate waveforms is shown in Figure 3.17 for the same sensor as in Figure 3.16. Also, here the ideal sinewave is distorted by feedthrough from excitation. The second-harmonic sensitivity was increased only by the factor of 5, which shows that the damping is much higher than in the case of tuning the voltage output.

3.9 Noise and Offset Stability

The important factor affecting the precision of the fluxgate magnetometer is the stability of the sensor zero. The changes of the offset are usually divided into two components (although they may be caused by similar effects): (1) noise as a relatively fast variation, and (2) long-term offset stability.

Sensor noise was investigated by many authors starting from the classical study by Scouten [104]. It was demonstrated that the noise level may be decreased using

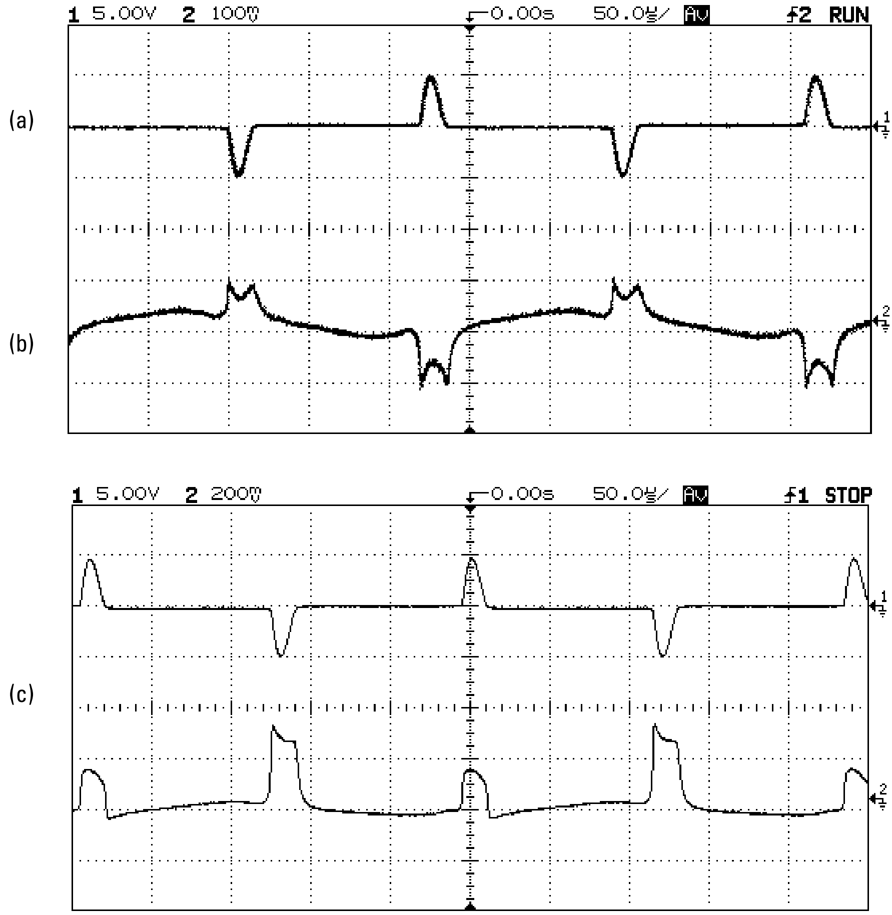

Figure 3.16 Waveforms in the broadband current-output fluxgate: (a) excitation current (0.5 A/div); (b) output current for $B_0 = 0$ (20 μA/div); and (c) output current for $B_0 = 5$ μT (40 μA/div).

high peak value of the excitation current [105]. This was interpreted as if there existed small volumes inside the material that are more difficult to magnetize than the rest, and so they are not necessarily saturated during each period of the excitation field. The uncertainty of magnetization of these regions is one of the sources of the sensor noise and offset. These regions are often associated with structural (such as dislocations or inclusions) or surface imperfections of the core; it was shown that improving the structural and surface quality by annealing and etching or polishing reduces noise. Another mechanism is associated with magnetostriction; as the magnetostriction itself does not generate fluxgate offset signal, the noise mechanism is probably associated with inhomogeneous magnetoelastic coupling of the local stresses to magnetization [106, 107].

Sensor noise depends mostly on the core material, but the geometrical aspect is also important; the demagnetization factor determines how the material noise is calculated to the effective noise value on the sensor input. Primdahl et al. [51]

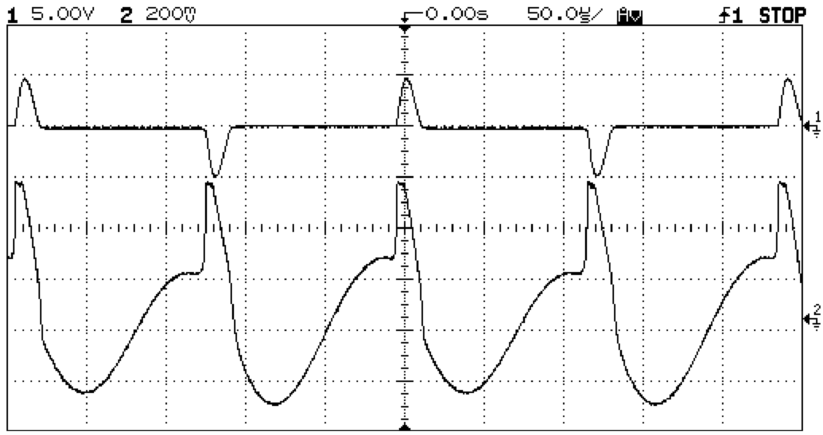

Figure 3.17 Output current for the tuned current-output fluxgate for $B_0 = 5$ µT (lower trace, 40 µA/div). The sensor is the same as for Figure 3.16. The upper trace is the excitation current.

observed that the internal noise in the ring-core is practically independent of the core cross-section, that is, the magnetic noise within the core is well correlated, and thus, it makes no sense to increase the core volume and expect averaging of the noise.

Decrease in the sensor noise with increasing temperature was observed first for low Curie point alloys. With increasing temperature, the core permeability was increasing and the saturation magnetization was decreasing simultaneously. A similar effect was observed for low-noise permalloys. The effect of decreasing the room-temperature noise with Curie temperature was also observed for amorphous alloys [62]. Shirae [61] reported 2.5-pT rms (100 mHz ... 16 Hz) for cobalt-based amorphous alloy with a Curie point $T_C = 50$°C.

The techniques used for measuring the spectrum of the sensor noise are described in Chapter 11. Fluxgates have a noise of $1/f$ nature from millihertz up to kilohertz frequencies (i.e., $P(f) = P(1)/f$ [nT^2/Hz], where $P(1)$ is the power spectrum density at 1 Hz. The rms level of the noise N_{rms} in the frequency band from f_L to f_H is then given by the expression

$$N_{\text{rms}} = \sqrt{\int_{f_L}^{f_H} P(f)\,df} = \sqrt{P(1)\ln\left(\frac{f_H}{f_L}\right)} \tag{3.23}$$

More often the noise spectrum density is given in nT/√Hz or pT/√Hz. The conversion is straightforward, for example, 9 pT^2/Hz corresponds to 3 pT/√Hz, as explained in Section 1.8.4.

Primdahl et al. [64] found that the fluxgate noise p-p level is typically approximately 6 times larger than the rms value in the same frequency band.

Figure 3.18(a) shows the noise spectrum for the sensor with a permalloy low-noise core produced by Infinetics for NASA (type S1000-C31-JC-2239C). The measurement was performed by an HP 3566A digital spectrum analyzer using overlapping averaging from 1,000 samples to smooth the plot and remove the distortion caused by the time window. The noise spectral density was 3.8 pT/√Hz at

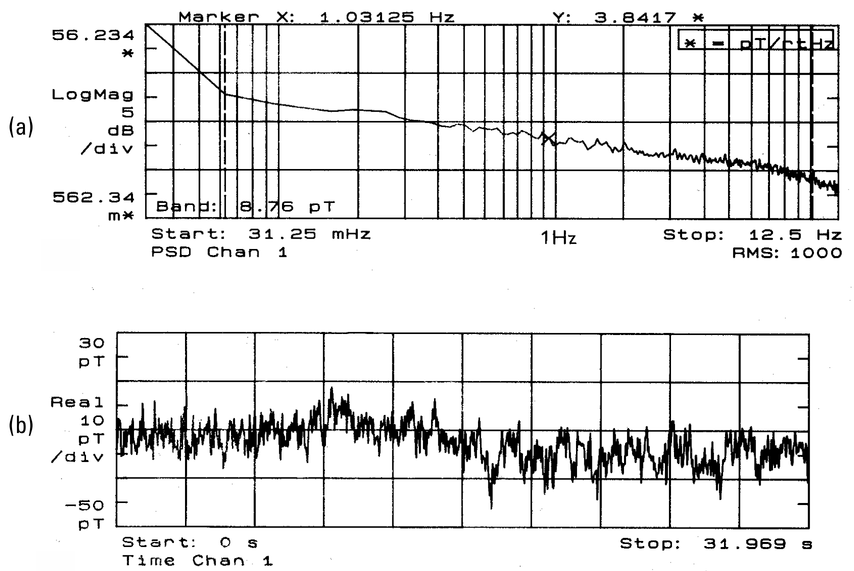

Figure 3.18 (a) Noise spectrum for the superior sensor, and (b) time plot. (*From:* [1].)

1 Hz and the rms value calculated from the measured spectrum was 8.76 pT (64 mHz to 10 Hz). The time plot of the last one of the 1,000 (overlapping) 32-second time intervals is in Figure 3.18(b). The rms value calculated from the estimated $P(1)$ using (3.23) is 8.81 pT, which is close to the measured value.

For ring-core and racetrack sensors, the noise level reaches its minimum at a certain low value of the cross-sectional area. Low-noise Vacquier-type sensors should have the excitation coils longer than the cores, and the detector coil shorter than the cores. Moldovanu et al. showed that a 65-mm-long sensor with cores of 1-mm-wide, 25-μm-thick stress-annealed Vitrovac 6025 has the same 11-pT rms (64 mHz to 10 Hz) level of noise as a 17-mm diameter ring-core sensor from the same material [108].

Koch and Rozen [109] reported noise of 1.4 pT/√Hz at 1 Hz on a wire core biased by DC flowing through the core, but this value was not confirmed by independent measurement.

3.9.1 Zero Offset

Zero offset of the sensor and its changes may be partially caused by some of these factors:

1. Magnetically hard regions already mentioned;
2. Thermal and mechanical stresses;
3. Inhomogeneities of the core and winding together with changes in the magnetic properties of the core material, the parameters of the excitation field, and temperature.

To increase the temperature and long-term stability of both the sensor offset and sensitivity, it is useful to match the thermal expansion coefficient of all the sensor parts to reduce internal stresses. Nonmagnetic metal Inconel 625 or ceramics (corundum or machinable Macor) are used for the bobbin. For permalloy cores, which need to be annealed at higher temperatures, bobbins are made from corundum ceramics. Gordon and Brown [8, 57] have measured zero offset changes less than ±50 pT within 24 hours and temperature shift less than 100 pT from −40°C to +70°C using 81 Mo permalloy for the sensor core. More recently, the long-term stability of magnetometers on magnetic observatories was compared during the geomagnetic observatory workshops organized by International Association of Geomagnetism and Aeronomy (IAGA) [110]. Drift less than 1 nT/year may be achieved using presently available instruments in a temperature-controlled room. The temperature coefficient of the compensation field may be as low as 2 ppm/°C using quartz coil frames. This corresponds to approximately 0.1 nT/°C temperature dependence while measuring the Earth's field.

The best temperature offset stability reported for amorphous sensors was 1 nT in the −20°C to +60°C range [10].

3.9.2 Offset from the Magnetometer Electronics

A very useful tool for distinguishing between the offset contributions is to incorporate switches into critical magnetometer points [53, 107]. For example, reversing the excitation coil will reverse only the offset from excitation. Simultaneous flipping of the pickup coil and feedback coil will change the polarity of all the offsets except those generated in the processing circuits. The offset of the processing circuits is given not only by the offset of the DC-coupled amplifiers (starting after the PSD), but also by the second-harmonic distortion of the AC amplifiers (before the PSD), and the dynamic distortion caused by the finite slew rate of the amplifiers and finite switching time of the switches in PSD (see also Section 3.5.1). An efficient technique for offset reduction is the adjustment of the reference phase [111]; the magnetometer offset drift caused by the change of the excitation resonant tank was reduced by factor of 7 to ±0.5 nT in the temperature range (−13°C to +60°C). Fluxgate characteristics at temperature range −160°C to +200°C were studied by Nishio et al. [112]. A BepiColombo magnetometer achieved offset stability of ±1 nT in the temperature range −100°C to +180°C [113].

3.9.3 Other Magnetometer Offset Sources

Temperature gradients in conducting materials close to the sensor induce DC, which may generate magnetic fields. Some materials in the supporting mechanical structures and connectors may be magnetic; a remnant field looks like a magnetometer offset. Also, some electronic components are magnetic (tantalum capacitors and some ceramic chip carriers). Temperature measurement close to the sensor can also be a source of offset. Some relays and electric motors contain strong permanent magnets. Also, DC may cause offsets; a good technique is to use twisted conductors to minimize the current loops and keep the current far from the sensor. While the magnetic field at the distance d from a permanent magnet is decreasing with $1/d^3$, the field created by current conductor is dropping only with $1/d$. The magnetometer on the *Oersted* satellite was mounted on a boom, 6 m off the satellite body in order to suppress the interference especially from the solar cell currents [10]. Practical guides for magnetic cleanliness are [114, 115].

3.10 Crossfield Effect

Many of the vector magnetic field sensors have a nonlinear response to magnetic fields perpendicular to their sensing direction (crossfields). The crossfield effect is dramatic in anisotropic magnetoresistors, but it may also be found in fluxgate magnetometers. In general, the crossfield effect may be suppressed by core shape (in rod-type or racetrack sensors) or by total compensation of the measured field, not only the component in the sensing direction (as in the Compact Spherical Coil (CSC) design described in Section 3.14).

Crossfield effect errors of more than 20 nT in the Earth's field were observed in ring-core fluxgates. Brauer et al. showed that a variation in magnetic susceptibility along the core might result in a nonlinear perpendicular field response [116]. It was also shown that the crossfield response is temperature-dependent: errors as high as 2 nT/°C in the Earth's field were observed on low-cost sensors, which should be compared with their 0.1 nT/°C offset drift [117]. The crossfield effect may be the dominant source of error when making 3-axial measurements in the presence of the Earth's field. Crossfield can be reduced by making the core more homogenous, decreasing the ring-core diameter, or selecting another core geometry such as race-track or rod [118]. It should be mentioned that Fornacon et al. reported that no crossfield effect could be measured on their ring-core sensors [119]. The identical sensor was flow on Double Star as inboard sensor [120].

3.11 Designs of Fluxgate Magnetometers

Fluxgate magnetometers can be made very resistant against environmental factors such as vibration, radiation, and temperature. Sensors developed for deep drilled wells work up to 200°C. There are many fluxgate designs for specific purposes: the two extremes are simple low-power, low-cost instruments, and precise, stable, low noise, and expensive station magnetometers.

3.11.1 Portable and Low-Power Instruments

An ultralow-power 2-axis magnetometer was developed for vehicle detection [121]. The instrument power consumption was 0.72 mW, linearity 5% in the 80-μT range, noise 1.5 nT p-p, but huge temperature offset drift of 6 μT existed in the −40°C to +70°C range. The offset drift was reduced to the order of nT/°C when the power consumption was increased to 5 mW.

A 3-axis vector portable analog fluxgate magnetometer is described in [122]. The instrument has 300-mW consumption from ±6-V source and a range of ±100 μT with 0.01% linearity. The effective resolution is 1 nT and the response time to a large field step is 4 ms. Innovated sealed ring-core fluxgate sensors made of etched rings ensure high resistance against vibrations and mechanical shocks.

A book by Weiss and Alimi is devoted to low-power fluxgate sensors with wire core [17].

Most fluxgate systems developed for magnetoelastic torque sensors (Chapter 11) have a range of approximately ±500 μT with approximately 50-nT resolution. Their power consumption of the analog electronics is approximately 240 mW when powered from a 12-V source. They typically have less than 400-nT drift and 0.25% variation in gain across the full range of −40°C to 125°C. As the driving electronics can be moved away from the sensor located in higher temperature regions, the sensors can be made to handle extremely high temperatures, such as greater than 200°C.

3.11.2 Station Magnetometers

Together with a proton magnetometer (Chapter 6), a single-axis fluxgate magnetometer mounted on top of a nonmagnetic theodolite telescope is the standard instrument for absolute measurements at magnetic observatories. The fluxgate theodolite is routinely used for the measurement of the magnetic declination D and inclination I. The procedure is described in detail in [123].

Three-axis fluxgate magnetometers are also used for the recording of magnetic variations. Long-term and temperature stability of these instruments are critical. The coils are often wound on quartz tubes, which may improve their temperature coefficient to 2 ppm/°C. The sensor head is mounted on a pillar in a thermostated nonmagnetic chamber. Marble is often used for supporting structures as it is a dimensionally stable, nonmagnetic, and electrically insulating material that is also easily machinable and cheap. The possible pillar tilting may be corrected for by suspended sensors. The best fluxgate magnetometers for observatories have long-term offset stability of 1 nT/year. Periodical calibration by absolute measurements further reduces the absolute error of the observatory records to 1 nT. Comparisons and testing results of station magnetometers were performed at observatory workshops [110]. Observatory fluxgate magnetometers are made by GEM, EDA, Narod Geophysics, Dowty, Scintrex Thomson-Sintra, Danish Meteorological Institute, Magson, Shimadzu, and other companies.

Battery-powered sea floor triaxial gimbaled fluxgate magnetometers are described in [124–126].

3.12 Miniature Fluxgates

Many applications, including magnetic ink reading, safety and security sensors, and sensor arrays, require very small sensor size. The process of the fluxgate sensor miniaturization is rather complicated as the magnetic noise dramatically increases with decreasing sensor length. Small-size fluxgates are made of open or closed cores from amorphous or permalloy wires, tapes, and deposited structures. Up to now, the quality of sputtered or electrodeposited permalloy has not been sufficient for low-noise fluxgate applications, so patterns etched of amorphous tape are often used for the sensor core.

3.12.1 Miniature Wire-Wound Sensors

A number of simple multivibrator-type fluxgate magnetometers was reported from Japan (see Section 3.5.5). A 15-mm-long hairpin sensor was made up of a strip with helical anisotropy [127]. This sensor has 5-nT/√Hz noise (averaged in the 64-mHz to 10-Hz band) and 4 nT/°C temperature drift in the 25°C to 50°C interval. Orthogonal fluxgates with magnetic wire core and wire-wound solenoid pickup coil and coil-less orthogonal fluxgates also belong to this category.

3.12.2 Devices with Flat Coil (CMOS or Other Technologies)

Probably the first fluxgate sensor with all the coils made by planar technology was developed by Vincueria et al. [128]. The sensor has two parallel cores of 24-mm-long amorphous strips, and the flat coils for excitation and sensing are 10 μm thick. Figure 3.19 shows how the magnetic field of the sensor core strip can be sensed by a pair of flat coils. A CMOS fluxgate sensor with sputtered core and integrated electronics was developed by Kawahito et al. [129]. The sensor core is in the form of two serially configured 1.4-mm-long strips of sputtered 2-μm-thick permalloy film. The flat excitation coil saturates the strips in opposite directions, the differential flux is sensed by two antiserially connected flat pickup coils. The maximum sensitivity of 73 V/T was reached for a 1-MHz/150-mA p-p excitation current.
An orthogonal fluxgate with flat excitation and pickup coil was developed by Kejik et al. [130, 131]. The sensor 10-mm-diameter ring-core is also etched from Vitrovac 6025 amorphous ribbon. The sensor resolution is 40 nT and the linearity error in the 400-μT range is 0.5%. A parallel-mode 2-axis integrated fluxgate magnetometer by the same group was developed for a low-power watch compass [132]. The sensor is shown in Figure 3.20. The 4 × 4-mm large sensor chip has power consumption of 10 mW, which was achieved by using short excitation pulses. The noise is 10

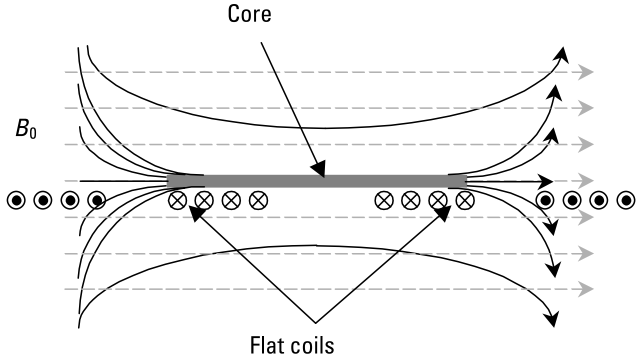

Figure 3.19 Planar fluxgate with a pair of flat pickup coils. (*From:* [129].)

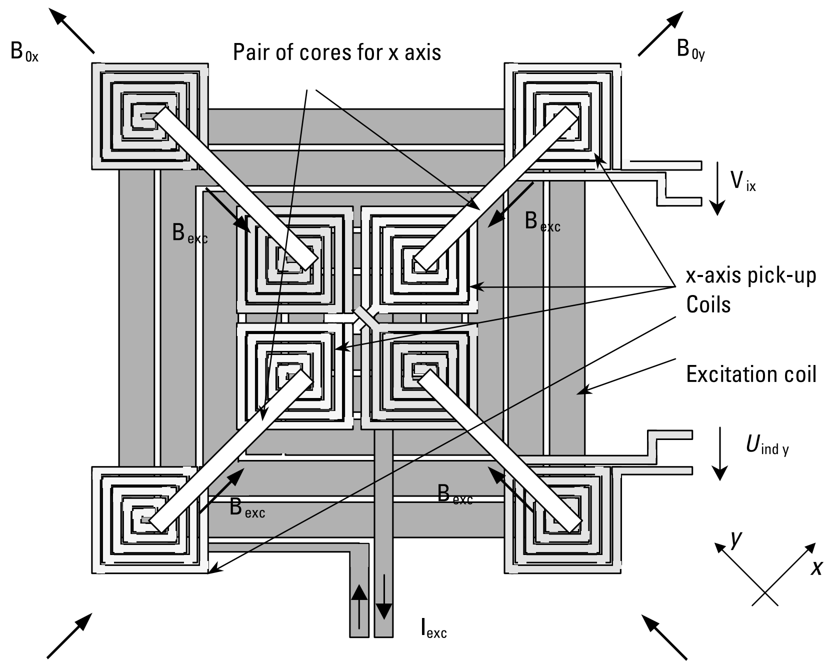

Figure 3.20 Planar fluxgate compass sensor. (*From:* [130].)

nT/√Hz at 1 Hz. Similar sensors with sputtered 1-μm-thick amorphous Vitrovac cores achieved 7.4 nT/√Hz at 1 Hz [133, 134].

A 2-axis fluxgate sensor with multilayer flat coils was fabricated by using the printed circuit board (PCB) process and a silver-ink dispenser. The sensor core is made of two amorphous strips. Sensitivity enhancement was achieved by stacking PCB layers without enlarging the element planar size. Compared to sensors with a single-layer sensing coil of the same pattern, the sensitivity of the three-layer sensor increased from 895 V/T to 2496 V/T [135]. For an excitation current of 500 mA at a frequency of 50 kHz, the sensor showed nonlinearity below 5% in the range of 0–80 μT.

A common weak point of integrated flat coils is that they cannot sufficiently saturate the core to erase the perming effect. The two reasons are: (1) the weaker coupling to the core than in the case of solenoid coil, and (2) that low metallization layer thickness results in high coil resistance and low current amplitude. High coil resistances are also the reason that the sensor cannot be tuned, neither in the excitation nor at the output. One possible improvement is a double-side core structure, which has an almost closed magnetic circuit [136].

3.12.3 PCB-Based Sensors with Solenoid Coils Made of Tracks and Vias

A simple PCB-based construction of the 15-mm-long fluxgates is described in [137]. The annealed core made of amorphous foil is sandwiched between two PCB layers, which have outer metal layers forming the halves of the winding. The layers are then connected by electroplating. PCB fluxgates with a racetrack core achieved low noise and good temperature stability with 20 nT in the −20°C to +70°C temperature range, but the minimum size for this technology is approximately 10 mm [138]. The power consumption of these sensors can be decreased by using pulse excitation and corresponding signal processing [139]. As the number of turns of the pickup coil is low, PCB fluxgates can be operated in the current-output mode [140]. An advanced magnetometer using 5-layer PCB fluxgates has been described in [141]. While the open-loop sensor linearity was 0.5%, feedback-compensated linearity was 0.01%. Long-term stability was 1 nT in 9-hour period, and the temperature coefficient of sensitivity decreased to 50 ppm/K by using a controlled excitation current. The sensor noise was typically below 20 pT/√Hz at 1 Hz.

3.12.4 Sensors with Microfabricated Solenoids

The two-layer metallization process can form a solenoid around the electrodeposited core [137, 142]; the noise was 40 nT p-p for a 5-mm-long sensor. A similar sensor was developed at the Fraunhofer Institute and became a part of a CMOS-integrated magnetometer [143].

Microfabricated fluxgates have been developed at several laboratories. The Guo Group at Shanghai Jiao Tong University claimed a noise floor of 36 pT/√Hz at 1 Hz with their 8-mm-long amorphous racetrack sensor, but this value was not verified by independent testing. The time-domain noise was 1-nT p-p, which corresponded to 150 pT/√Hz at 1 Hz [144]. In any case, this sensor probably has superior performance for an integrated sensor application. The dynamic range is 1 mT and the perming error below 0.4 μT with an excitation current amplitude of 70 mA at 500 kHz.

The DRV425 integrated fluxgate sensor manufactured by Texas Instruments is a feedback-compensated sensor with on-chip excitation and signal processing circuits [145]. The advantage of this sensor is its high excitation frequency, which gives a wide bandwidth of 47 kHz, a small sensor size of 4 × 4 mm, and a wide dynamic range of ±2 mT, compared to ±100 μT of previous micro-fluxgate designs, which were limited by CMOS technology [132]. The sensor has a temperature-dependent offset drift of 5 nT/°C, which is high compared to classical fluxgates, but small compared to similar size AMR (20 nT/°C) and Hall sensors (5 μT/°C). The crossfield error is below 10 nT, the noise is 5 nT/√Hz at 1 Hz, and the temperature dependence of the sensitivity is 7 ppm/°C. The perming error for a field shock of 10 mT (500% FS) is 5 μT.

The advantages of miniature fluxgate sensors (besides the small size) are light weight, high geometrical selectivity, low cost in mass production, and the possibility of integration of on-chip electronics. They have a fast response, thanks to the high operation frequency. The sensitivity and the stability of miniature fluxgates are higher than that of any semiconductor sensors, but their competitors are AMR sensors. AMRs of the same size working in the flipping mode (see Chapter 4) may have similar parameters, including power consumption.

3.13 AC Fluxgates

There are three basic approaches to increasing the frequency range of the fluxgate: (1) increasing the excitation frequency, (2) exploitation of the direct induction effect in the pickup coil, and (3) using the AC error signal of the DC loop [146, 147].

Ioan et al. reached a 3-kHz bandwidth even with feedback [148]. Integrated fluxgate DRV 425 has excitation frequency of 500 kHz and bandwidth of 47 kHz [145].

AC fields can be also measured by induction coils (Chapter 2), which are generally more simple devices. Still, there may be a good reason to use a fluxgate for AC field measurements: either in case that the fluxgate magnetometer is already a part of the system, or for weak fields, where fluxgate transforms the signal spectrum to a higher frequency where the noise of the input amplifier is lower. In general, the fluxgate is more sensitive for frequencies below a few hertz [149], dependent on the size of the induction coils. A method for merging search coil and fluxgate data is described in [150].

3.14 Multi-Axis Magnetometers

The typical application of a 2-axial fluxgate magnetometer is for a magnetic compass. The ring-core sensor with double cross-shaped pickup coil may measure the field in two directions simultaneously, as shown in Figure 3.21(a). Such sensors are used in simple magnetic compasses for automotive applications [151–153] and also in some precise space magnetometers (Section 3.14.2).

If a 2-axis compensated sensor is used as a magnetic compass, the short-time angular accuracy may be 5 minutes of arc. Figure 3.21(b) shows the tubular core sensor, which measures all three components of the field. While in the x and y directions, the parallel fluxgate effect is used, the z-output works as a perpendicular fluxgate. Afanasiev and Bushev suggested making the core in the form of loops of tape, which results in a sensor having similar sensitivity in all 3 directions [154]. Single-core configurations have an advantage in low power and small dimensions of the sensor head, but the long-term and temperature stability is limited by coil dimensional stability.

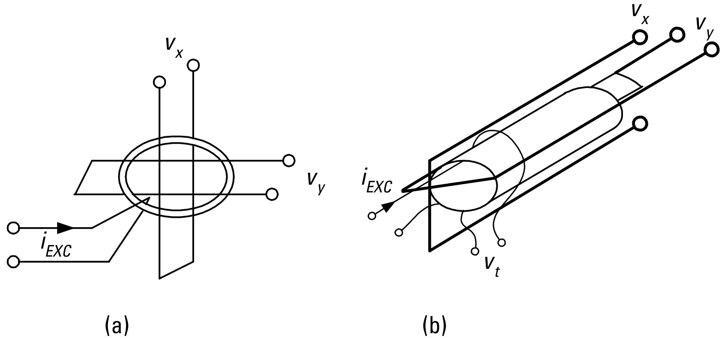

Figure 3.21 (a) Single-core dual-axis ring-core fluxgate sensor, and (b) 3-axis tubular sensor.

3.14.1 Three-Axial Compensation Systems

Three-axial fluxgate magnetometers usually have three single-axis sensors mounted perpendicularly in the sensor head. Large 3-axial feedback systems creating complete magnetic vacuum are preferred to three separate coils compensating the measured field only in one direction for each sensor. Three orthogonal circular or rectangular Helmholtz coils, or more complex coil systems of both circular and rectangular shapes, are frequently used for the compensation system (see Chapter 10). Primdahl and Jensen [155] constructed a spherically shaped 3-axial coil system for rocket and satellite applications, where the size of the sensor is strictly limited. The three coils have identical center points; each of them consists of nine sections approximating the ideal spherical coil, which generates a uniform field (Figure 3.22). Although the outer diameter of the CSC is just 90 mm, the homogeneity was proved to be sufficiently high for 40-mm-long sensors. The main advantage of keeping all three orthogonal sensors of the magnetometer in the center of the 3-D feedback system is that the sensors are kept in a very low field. This is important for long-term stability and low-noise operation, but the main advantage is that the system is free of errors caused by the crossfield effect (Section 3.10). The measuring axes are defined only by the feedback coil system (the exact position of the individual sensors is not critical) and thus may be easily determined and kept very stable. The CSC system was successfully used for the Oersted, CHAMP, and SWARM satellite magnetometers. The coil support is made from epoxy filled with glass microballoons and carbon fibers. This material has a thermal linear expansion coefficient of only 32 ppm/°C, while the density is just 750 kg/m^3. The temperature coefficients of the sensitivity in 3 axes were 31 to 36 ppm/°C, well corresponding to the expansion coefficient of the coil support material. Later, the structural stability was even improved by using

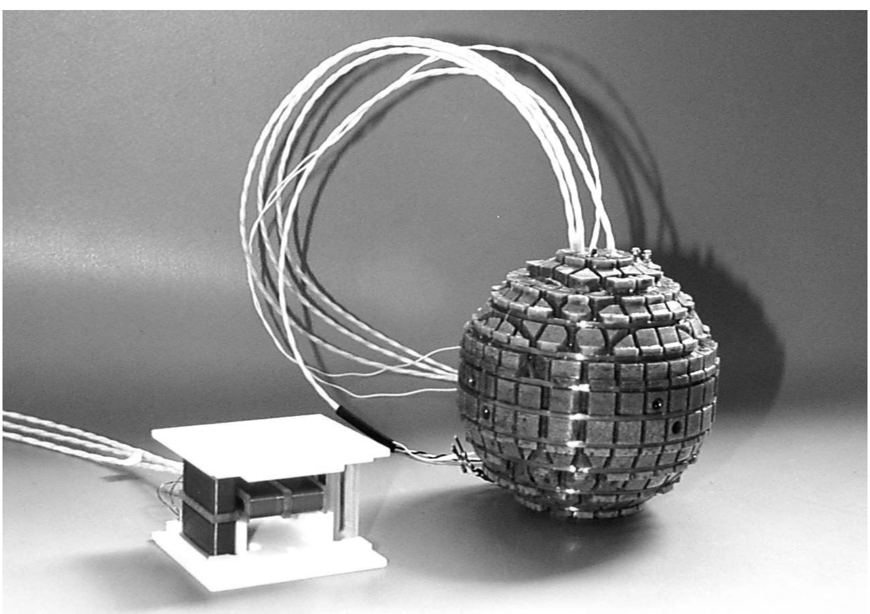

Figure 3.22 CSC sensor. (Courtesy of the Danish Technical University.)

C-SiC material for the supporting shell. C-SiC is a compound quasi-ceramic material with low electric conductivity and high thermal conductivity [156]. It has excellent dimensional stability and low thermal expansion (2 ppm/°C at room temperature, near zero at 150°C). The temperature sensitivity coefficient of the CSC was then further reduced to 10 ppm/°C. The Oersted fluxgate magnetometer linearity was found to be below 1 ppm in the Earth's field, the temperature coefficient of the deviation angles was 0.07 arcsec/°C. The in-flight calibration of the Oersted CSC magnetometer has shown the instrument's stability for a 47-day period, the scatter was 0.3 nT for the offsets, less than 10 ppm for the scale values, and less than 1.5 arc-sec for the nonorthogonalities.

3.14.2 Individually Compensated Sensors

Although the CSC system is known to be the technically best solution, it is considered to be rather exotic because of its complexity and high price (for example, some of the 27 coils should be wound after mounting the three sensors inside the sphere). Simple and cheaper are systems consisting of sensors with individual feedback coils; however, some of these systems can have problems arising from the crossfield effect.

Three-axial systems also can face problems from the crosstalk between the sensors. The vicinity of other sensor cores might change the feedback coil sensitivity as the sensor core represents a region of higher magnetic conductivity for the neighboring sensor. However, all these problems can be avoided by careful design.

The sensor head geometry and the temperature stability of its dimensions are very important. Sensors with individual feedback should be mounted symmetrically and at a maximum distance. Figure 3.23 shows the possible sensor arrangement. The z sensor should have a larger distance to the other(s), in order to keep the sensor sensitivities alike. The magnetic path of the z sensor includes the core of the x sensor in low demagnetization direction, while all the other couplings are much weaker. The sensors are usually excited from the same generator. If the excitation amplitude allows, the excitation coils are simply connected serially. In the Oersted magnetometer, the excitation generator output was stepped up by a transformer, which also allowed the use of a balance drive, which reduces the capacitive couplings [10].

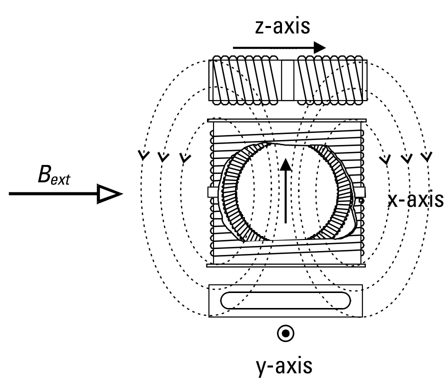

Figure 3.23 Three-axial sensor head (sensors compensated individually). (Courtesy of the Danish Technical University.)

The very precise MAGSAT satellite instrument had three single-axis compensated sensors [157]. Later, a three-axial magnetometer was developed for the Swedish satellite *Astrid-2*, which has three closely mounted 17-mm ring-core fluxgates. The magnetometer construction and the test results are documented in [158]. All the critical mechanical parts are made of machinable ceramics MACOR. The dimension of the sensor head is 32 × 47 × 55 mm. Close vicinity of the sensors increases the nonlinearities caused by the crosstalk and crossfield effect up to 8 nT p-p in the 60,000-nT range. Due to the low temperature expansion of MACOR (9.4 ppm/°C), the temperature drift of the sensitivity for the individual sensors is between 10 and 13 ppm/°C. The offset drift was 0.01 and 0.02 nT/°C for the x and y axes, respectively, but degraded to 0.45 nT/°C for the z axis, which was explained by the fact that this axis is more magnetically coupled to the other sensors due to the holder geometry. This effect is again caused by the crossfield sensitivity and may be suppressed by increasing the sensor distance as already mentioned or decreasing the core diameter. The temperature drift of the angles between the sensors was in the range of arcseconds: 0.17, 0.33, and 0.5″/°C [159]. However, it should be mentioned that reports on a similar sensor for a different low Earth orbit (LEO) mission did not mention such crossfield sensitivity [160].

Other implementations of 3-axial magnetometers utilize two cores: the first one with two perpendicular pickup coils measures two orthogonal x and y components, and the second one measures the remaining z component. Such a magnetometer was developed by TU Braunschweig and has already been used for many missions (e.g., THEMIS [75], see also Figure 9.14). Another two-core 3-axial magnetometer was developed by UCLA [80].

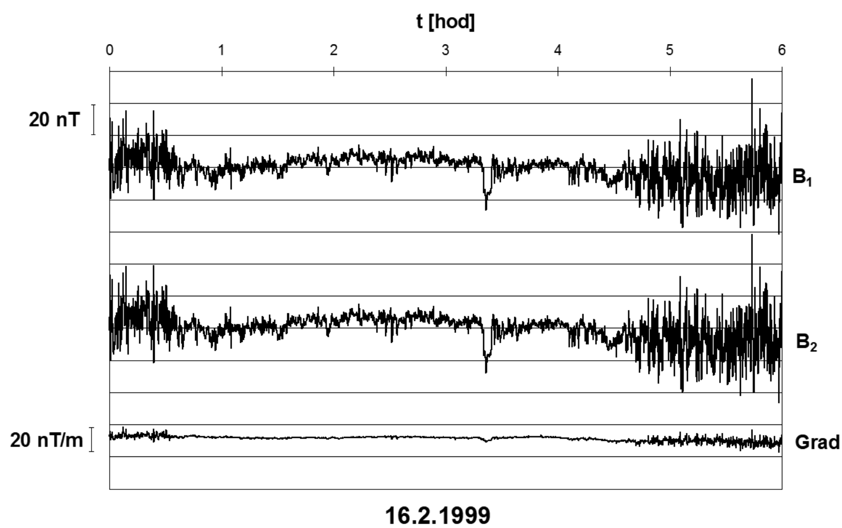

Figure 3.24 Magnetic field in the laboratory located in the city. Subway (underground) and trams do not operate between 0:30 and 4:30. B_1 and B_2 are the outputs of two fluxgate sensors measuring in the same direction in 50-cm distance. Grad is their difference recalculated to magnetic gradient, in nT/m.

Table 3.1 Fluxgate Sensors and Magnetometers

Producer or reference	*Core/Type*	*Noise (pT/√Hz at 1 Hz)*	*Linearity (ppm)*	*Offset Temperature Coefficient (nT/K)*	*Range (μT)*	*Gain Drift (ppm/K)*	*Max. Sensor Size (mm)*
Bartington MAG13-Q	Rod	5	15	0.3 to 1.8	60 to 1,000	15 to 200	203*
Billingsley HFM500	Ring-core	10	70	1	500	100	154*
Billingsley DFM28G	Ring-core, digital output	3	15	0.5	65	20	305*
Magson MGF-1S	Ring-core	15	—	—	65	17.5	67***
Magson MACM	Ring-core	200	250	2.5	120	—	138*
LEMI-029		6	—	—	78	—	62*
TI	Rod, microfabricated	5,000	1,000	5	2,000	7	4#
Nielsen [10]	Ring, amorphous	6	4	Compensated (±0.5 nT in 80°C range)	65	10	90**
Ripka [42]	Racetrack	2.5	8	0.5	50	40	70#
Janosek and Butta [32]	Wire. orthogonal, fundamental mode	1.5 (0.75 open loop)	—	2.5	25	—	70#
Auster [75]	Ring-core	10	—	0.05	25	22	70***
Miles [77]	Ring-core	10	50	—	65	—	70***
Russell [80] DFG	Ring-core	<8	30	0.01	0.65	60	50***

#: single-axis, size includes electronics; ##: single-axis, electronics separate form sensor; *3-axial magnetometer, size includes electronics; **: 3-axial magnetometer, compact spherical feedback coil; and ***: 3-axial sensor, electronics separate from sensor.

3.15 Fluxgate Gradiometers

The traditional way to measure the field gradient is using two sensors and subtract their reading. The sensor distance is called the gradiometric baseline. The gradient is thus approximated by the difference. Error arises when higher-order gradients are present. The measurement of the gradient is often used when the measured field source is at a short distance. In such a case, the disturbing fields from distant sources that are more homogeneous (such as the Earth's field) and their variations can be effectively suppressed as shown in Figure 3.24.

Gradiometric nondestructive sensors are used for biomagnetic measurements, detection and location of ferromagnetic objects, magnetic, testing, and other applications. The dual-sensor gradiometer can have a single feedback controlled by the master sensor so that the compensation current is the same for both sensors. In such a case, the slave sensor works in the open loop, and its output is directly the field difference. The alternative is to use one long solenoid for compensation of both sensors. Another possibility is to compensate the sensors individually and subtract their reading (preferably numerically). The disadvantage of the analog processing is that the compensation coils should have exactly the same constant and their axes should be perfectly aligned, which is difficult to guarantee in a wide range of temperatures. Digital processing needs two ADCs, but the adjustment for the sensitivity mismatch can be made automatically. The latter configuration requires a larger sensor distance to avoid interference between the sensors. Arrays of low-noise fluxgate sensors are used for detection systems for military and security applications. The sensor signals are processed numerically to compensate for the crosstalks, individual sensitivities, and temperature coefficients.

Racetrack single-core fluxgate gradiometers are described in [161, 162]. Precise single-axis [163] and 3-axial fluxgate gradiometers were built by Merayo et al. [164]. If the individual sensors are in close distance, it might be a good idea to feedback-compensate the gradient [165]. A full-tensor gradiometer was described by Sui et al. [166, 167] and Janosek et al. [168].

References

[1] Ripka, P., "Review of Fluxgate Sensors," *Sensors and Actuators A: Physical*, Vol. 33, No. 3, 1992, pp. 129–141.

[2] Thomas, H. P., *Direction Responsive System*, 1935. U.S. pat. 2,016,977, 1935.

[3] Aschenbrenner, H., and G. Goubau, "Eine Anordung zur registrierung rascher magnetischer Storungen," *Hochfrequenztechnik und Elektroakustik*, Vol. 47, 1936, pp. 177–181.

[4] Dyal, P., and D. I. Gordon, "Lunar-Surface Magnetometers," *IEEE Transactions on Magnetics*, Vol. MAG9, No. 3, 1973, pp. 226–231.

[5] INTERMAGNET, *INTERMAGNET Technical Manual*, February 8, 2019, https://www.intermagnet.org/publication-software/technicalsoft-eng.php.

[6] Foerster, F., "A Method for the Measurement of d-c Field Differences and Its Application to Nondestructive Testing," *Nondestruct. Test.*, Vol. 13, 1955, pp. 31–41.

[7] Moore, W. J. M., and P. N. Miljanic, *The Current Comparator*, London, U.K.: Peter Peregrinus, 1968.

[8] Gordon, D. I., and R. E. Brown, "Recent Advances in Fluxgate Magnetometry," *IEEE Transactions on Magnetics*, Vol. MAG8, No. 1, 1972.

[9] Primdahl, F., "Fluxgate Magnetometer," *Journal of Physics E-Scientific Instruments*, Vol. 12, No. 4, 1979, pp. 241–253.

[10] Nielsen, O. V., et al., "Development, Construction and Analysis of the 'OErsted' Fluxgate Magnetometer," *Measurement Science and Technology*, Vol. 6, No. 8, 1995, pp. 1099–1115.

[11] Primdahl, F., et al., "Design, Calibration and Testing of Precise Magnetometers," *Proceedings of the IEEE Sensors 2003, Vols. 1 and 2*, 2003, pp. 466–467.

[12] Janosek, M., "Parallel Fluxgate Magnetometers," in A. Grosz, M. Haji-Sheikh, and S. Mukhopadhyay, (eds.), *High Sensitivity Magnetometers*, New York: Springer, 2017.

[13] Butta, M., "Orthogonal Fluxgate Magnetometers," in A. Grosz, M. Haji-Sheikh, and S. Mukhopadhyay, (eds.), *High Sensitivity Magnetometers*, New York: Springer, 2017.

[14] Musmann, G., and Y. Afanassiev, *Fluxgate Magnetometers for Space Research*, Books on Demand, 2010.

[15] Alldredge, L., "Magnetometer," U.S. Patent Office, 1958.

[16] Palmer, T. M., "A Small Sensitive Magnetometer," *Proc. of Institution of Electrical Engineers-London*, Vol. 100, No. 77, 1953, pp. 545–550.

[17] Weiss, E., and R. Alimi, *Low-Power and High-Sensitivity Magnetic Sensors and Systems*, Norwood, MA: Artech House, 2019.

[18] Primdahl, F., "Fluxgate Mechanism. 1. Gating Curves of Parallel and Orthogonal Fluxgates," *IEEE Transactions on Magnetics*, Vol. MAG6, No. 2, 1970.

[19] Butta, M., and P. Ripka, "Two-Domain Model for Orthogonal Fluxgate," *IEEE Transactions on Magnetics*, Vol. 44, No. 11, Pt. 2, 2008, pp. 3992–3995.

[20] Seitz, T., "Fluxgate Sensor in Planar Microtechnology," *Sensors and Actuators A: Physical*, Vol. 22, No. 1-3, March 1990, pp. 799–802.

[21] Gise, P. E., and R. B. Yarbrough, "Improved Cylindrical Magnetometer Sensor," *IEEE Transactions on Magnetics*, Vol. 13, No. 5, 1977, pp. 1104–1106.

[22] Ripka, P., et al., "Orthogonal Fluxgate Effect in Electroplated Wires," *2005 IEEE Sensors, Vols. 1 and 2*, 2005, pp. 69–72.

[23] Butta, M., et al., "Bi-Metallic Magnetic Wire with Insulating Layer as Core for Orthogonal Fluxgate," *IEEE Transactions on Magnetics*, Vol. 45, No. 10, 2009, pp. 4443–4446.

[24] Atalay, S., P. Ripka, and N. Bayri, "Coil-Less Fluxgate Effect in (Co0.94Fe0.06)(72.5) Si12.5B15 Amorphous Wires," *Journal of Magnetism and Magnetic Materials*, Vol. 322, No. 15, August 2010, pp. 2238–2243.

[25] Atalay, S., et al., "Coil-Less Fluxgate Effect in CoNiFe/Cu Wire Electrodeposited Under Torsion," *Journal of Magnetism and Magnetic Materials*, Vol. 323, No. 22, November 2011, pp. 2818–2822.

[26] Butta, M., et al., "Magnetic Microwires with Field-Induced Helical Anisotropy for Coil-Less Fluxgate," *IEEE Transactions on Magnetics*, Vol. 46, No. 7, 2010, pp. 2562–2565.

[27] Butta, M., et al., "Microwire Electroplated Under Torsion as Core for Coil-Less Fluxgate," *Sensor Letters*, Vol. 11, No. 1, January 2013, pp. 50–52.

[28] Butta, M., and P. Ripka, "Model for Coil-Less Fluxgate," *Sensors and Actuators A: Physical*, Vol. 156, No. 1, 2009, pp. 269–273.

[29] Sasada, I., "Orthogonal Fluxgate Mechanism Operated with Dc Biased Excitation," *Journal of Applied Physics*, Vol. 91, No. 10, May 2002, pp. 7789–7791.

[30] Butta, M., and I. Coroli, "Low Offset Drift-Low-Noise Orthogonal Fluxgate with Synchronized Polarity Flipping," *IEEE Transactions on Magnetics*, Vol. 53, No. 4, April 2017.

[31] Butta, M., and B. P. Schutte, "Low-Noise Orthogonal Fluxgate Using Flipped Current Joule Annealing," *IEEE Transactions on Magnetics*, Vol. 55, No. 7, July 2019.

[32] Janosek, M., et al., "1-pT Noise Fluxgate Magnetometer for Geomagnetic Measurements and Unshielded Magnetocardiography," *IEEE Transactions on Instrumentation and Measurement*, Vol. 69, No. 5, May 2020, pp. 2552–2560.

[33] Schonstedt, E. O., "Saturable Measuring Device and Magnetic Core Therefore," U.S. Patent 2916696, 1959.

[34] Butta, M., et al., "Fluxgate Effect in Twisted Magnetic Wire," *Journal of Magnetism and Magnetic Materials*, Vol. 320, No. 20, 2008.

[35] Sonoda, T., and R. Ueda, "Distinctive Features of Magnetic-Field Controlled Type Magnetic-Field Sensor," *IEEE Transactions on Magnetics*, Vol. 25, No. 5, September 1989, pp. 3393–3395.

[36] Blazek, J., et al., "New Generation of Magnetic Relaxation Sensors Based on the Melt-Spun FeCoBCu Alloys," *Acta Physica Polonica A*, Vol. 118, No. 5, November 2010, pp. 1010–1012.

[37] Takeuchi, S., and K. Harada, "A Resonant-Type Amorphous Ribbon Magnetometer Driven

by an Operational-Amplifier," *IEEE Transactions on Magnetics*, Vol. 20, No. 5, 1984, pp. 1723–1725.

[38] Moldovanu, A., et al., "Functional Study of Fluxgate Sensors with Amorphous Magnetic Materials Cores," *Sensors and Actuators A: Physical*, Vol. 59, No. 1-3, April 1997, pp. 105–108.

[39] Moldovanu, A., et al., "The Applicability of VITROVAC 6025 X Ribbons for Parallel-Gated Configuration Sensors," *Sensors and Actuators A: Physical*, Vol. 81, No. 1-3, April 2000, pp. 193–196.

[40] Saito, T. E. A., "Magnetometers for Geophysical Use, Part 1 Fluxgate Magnetometer with a 0.5 m Length Two-Core Sensor," *The Science Reports of the Tohoku University, Ser. 5*, Vol. 27, 1980, pp. 85–93.

[41] Ripka, P., F. Jireš, and M. Macháček, "Fluxgate Sensor with Increased Homogeneity," *IEEE Transactions on Magnetics*, Vol. 26, No. 5, 1990, pp. 2038–2040.

[42] Ripka, P., "Race-Track Fluxgate Sensors," *Sensors and Actuators A: Physical*, Vol. 37–38, No. C, 1993, pp. 417–421.

[43] Gordon, D. I., R. H. Lundsten, and R. A. Chiarodo, "Factors Affecting Sensitivity of Gamma-Level Ring-Core Magnetometers," *IEEE Transactions on Magnetics*, Vol. MAG1, No. 4, 1965.

[44] Clarke, D. B., "Demagnetization Factors of Ringcores," *IEEE Transactions on Magnetics*, Vol. 35, No. 6, November 1999, pp. 4440–4444.

[45] De Graef, M., and M. Beleggia, "The Fluxgate Ring-Core Demagnetization Field," *Journal of Magnetism and Magnetic Materials*, Vol. 305, No. 2, October 2006, pp. 403–409.

[46] Yaglidere, I., and E. O. Gunes, "A Novel Method for Calculating the Ring-Core Fluxgate Demagnetization Factor," *IEEE Transactions on Magnetics*, Vol. 54, No. 2, February 2018.

[47] Kubik, J., and P. Ripka, "Racetrack Fluxgate Sensor Core Demagnetization Factor," *Sensors and Actuators A: Physical*, Vol. 143, No. 2, May 2008, pp. 237–244.

[48] Hinnrichs, C., et al., "Dependence of Sensitivity and Noise of Fluxgate Sensors on Racetrack Geometry," *IEEE Transactions on Magnetics*, Vol. 37, No. 4, July 2001, pp. 1983–1985.

[49] Ripka, P., "Improved Fluxgate for Compasses and Position Sensors," *Journal of Magnetism and Magnetic Materials*, Vol. 83, No. 1-3, 1990, pp. 543–544.

[50] Ripka, P., "Contribution to the Ring-Core Fluxgate Theory," *Physica Scripta*, Vol. 40, No. 4, October 1989, pp. 544–547.

[51] Primdahl, F., et al., "Demagnetizing Factor and Noise in the Fluxgate Ring-Core Sensor," *Journal of Physics E-Scientific Instruments*, Vol. 22, No. 12, December 1989, pp. 1004–1008.

[52] How, H., L. Sun, and C. Vittoria, "Demagnetizing Field of a Ringcore Fluxgate Magnetometer," *IEEE Transactions on Magnetics*, Vol. 33, No. 5, September 1997, pp. 3397–3399.

[53] Nielsen, O. V., et al., "Analysis of a Fluxgate Magnetometer Based on Metallic-Glass Sensors," *Measurement Science and Technology*, Vol. 2, No. 5, May 1991, pp. 435–440.

[54] Perez, L., et al., "Analytical Model for the Sensitivity of a Toroidal Fluxgate Sensor," *Sensors and Actuators A: Physical*, Vol. 130, August 2006, pp. 142–146.

[55] Moldovanu, B. O., C. Moldovanu, and A. Moldovanu, "Computer Simulation of the Transient Behaviour of a Fluxgate Magnetometric Circuit," *Journal of Magnetism and Magnetic Materials*, Vol. 157, May 1996, pp. 565–566.

[56] Ripka, P., M. Butta, and M. Pribil, "Magnetostriction Offset of Fluxgate Sensors," *IEEE Transactions on Magnetics*, Vol. 51, No. 1, 2015.

[57] Gordon, D. I., et al., "A Fluxgate Sensor of High Stability for Low Field Magnetometry," *IEEE Transactions on Magnetics*, Vol. MAG4, No. 3, 1968.

[58] Miles, D. M., et al., "Low-Noise Permalloy Ring Cores for Fluxgate Magnetometers,"

Geoscientific Instrumentation Methods and Data Systems, Vol. 8, No. 2, September 2019, pp. 227–240.

[59] Butta, M., et al., "Electroplated FeNi Ring Cores for Fluxgates with Field Induced Radial Anisotropy," *Journal of Applied Physics*, Vol. 117, No. 17, 2015.

[60] Enpuku, K., et al., "Low-Noise Magnetometer Based on Inductance Modulation in High-Critical-Temperature Superconductor Coil," *Japanese Journal of Applied Physics*, Vol. 57, No. 6, June 2018.

[61] Shirae, K., "Noise in Amorphous Magnetic-Materials," *IEEE Transactions on Magnetics*, Vol. 20, No. 5, 1984, pp. 1299–1301.

[62] Narod, B. B., et al., "An Evaluation of the Noise Performance of Fe, Co, Si, And B Amorphous-Alloys on Ring-Core Fluxgate Magnetometers," *Canadian Journal of Physics*, Vol. 63, No. 11, 1985, pp. 1468–1472.

[63] Nielsen, O. V., et al., "A New Amorphous Ribbon Fluxgate Sensor Based on Torsional-Creep-Induced Anisotropy," *IEEE Transactions on Magnetics*, Vol. 26, No. 1, January 1990, pp. 276–280.

[64] Primdahl, F., et al., "The Sensitivity Parameters of the Short-Circuited Fluxgate," *Measurement Science and Technology*, Vol. 2, No. 11, November 1991, pp. 1039–1045.

[65] Vertesy, G., et al., "Influence of the Core Material Polishing on the Fluxset Sensor's Operation," *Journal of Magnetism and Magnetic Materials*, Vol. 215, June 2000, pp. 762–764.

[66] Murata, N., and R. Nomura, "Current Annealing of Glass-Coated Amorphous Wire for Noise Reduction of Low-Offset Fundamental Mode Orthogonal Fluxgate," *International Magnetics (INTERMAG) Conference*, 2018.

[67] Can, H., et al., "Systematic Optimization of the Sensing Properties of Ring-Core Fluxgate Sensors with Different Core Diameters and Materials," *Sensors and Actuators A: Physical*, Vol. 255, March 2017, pp. 94–103.

[68] Nielsen, O. V., et al., "Nanocrystalline Materials as the Magnetic Core in High-Performance Fluxgate Sensors," in A. Hernando, (ed.), *Nanomagnetism*, Boston, MA: Kluwer, 1993, pp. 27–31.

[69] Ruhmer, D., et al., "Vector Fluxgate Magnetometer for High Operation Temperatures Up to 250 Degrees C," *Sensors and Actuators A: Physical*, Vol. 228, June 2015, pp. 118–124.

[70] Primdahl, F., et al., "Digital Detection of the Flux-Gate Sensor Output Signal," *Measurement Science and Technology*, Vol. 5, No. 4, April 1994, pp. 359–362.

[71] Piil-Henriksen, J., et al., "Digital Detection and Feedback Fluxgate Magnetometer," *Measurement Science and Technology*, Vol. 7, No. 6, June 1996, pp. 897–903.

[72] Pedersen, E. B., et al., "Digital Fluxgate Magnetometer for the Astrid-2 Satellite," *Measurement Science and Technology*, Vol. 10, No. 11, November 1999, pp. N124–N129.

[73] Auster, H. U., et al., "Concept and First Results of a Digital Fluxgate Magnetometer," *Measurement Science and Technology*, Vol. 6, No. 5, May 1995, pp. 477–481.

[74] Auster, H. U., et al., "ROMAP: Rosetta Magnetometer and Plasma Monitor," *Space Science Reviews*, Vol. 128, No. 1-4, 2007, pp. 221–240.

[75] Auster, H. U., et al., "The THEMIS Fluxgate Magnetometer," *Space Science Reviews*, Vol. 141, No. 1-4, December 2008, pp. 235–264.

[76] Glassmeier, K. H., et al., "The Fluxgate Magnetometer of the BepiColombo Mercury Planetary Orbiter," *Planetary and Space Science*, Vol. 58, No. 1-2, January 2010, pp. 287–299.

[77] Kawahito, S., et al., "A 2-D CMOS Microfluxgate Sensor System for Digital Detection of Weak Magnetic Fields," *IEEE Journal of Solid-State Circuits*, Vol. 34, No. 12, December 1999, pp. 1843–1851.

[78] Magnes, W., et al., "Highly Integrated Front-End Electronics for Spaceborne Fluxgate Sensors," *Measurement Science and Technology*, Vol. 19, No. 11, November 2008.

[79] Russell, C. T., et al., "The Magnetospheric Multiscale Magnetometers," *Space Science Reviews*, Vol. 199, No. 1-4, March 2016, pp. 189–256.

[80] Magnes, W., et al., "Space Weather Magnetometer Aboard GEO-KOMPSAT-2A," *Space Science Reviews*, Vol. 216, Article 119, 2020.

[81] O'Brien, H., et al., "A Radiation Tolerant Digital Fluxgate Magnetometer," *Measurement Science and Technology*, Vol. 18, No. 11, November 2007, pp. 3645–3650.

[82] Russell, C. T., et al., "THEMIS Ground-Based Magnetometers," *Space Science Reviews*, Vol. 141, No. 1-4, December 2008, pp. 389–412.

[83] Iguchi, K., and A. Matsuoka, "A Digital-Type Fluxgate Magnetometer Using a Sigma-Delta Digital-to-Analog Converter for a Sounding Rocket Experiment," *Measurement Science and Technology*, Vol. 25, No. 7, July 2014.

[84] Cerman, A., et al., "Digitalization of Highly Precise Fluxgate Magnetometers," *Sensors and Actuators A: Physical*, Vol. 121, No. 2, June 2005, pp. 421–429.

[85] Forslund, A., et al., "Miniaturized Digital Fluxgate Magnetometer for Small Spacecraft Applications," *Measurement Science and Technology*, Vol. 19, No. 1, January 2008.

[86] Belyayev, S., and N. Ivchenko, "Effect of Second Harmonic in Pulse-Width-Modulation-Based DAC for Feedback of Digital Fluxgate Magnetometer," *Measurement Science and Technology*, Vol. 29, No. 4, April 2018.

[87] Miles, D. M., et al., "A Radiation Hardened Digital Fluxgate Magnetometer for Space Applications," *Geoscientific Instrumentation Methods and Data Systems*, Vol. 2, No. 2, 2013, pp. 213–224.

[88] Hercik, D., et al., "The MASCOT Magnetometer," *Space Science Reviews*, Vol. 208, No. 1-4, July 2017, pp. 433–449.

[89] Auer, M., et al., "Prototype Design of a Magnetometer Frontend-ASIC for Spaceborne Applications," *26th Austrian Workshop on Microelectronics*, Graz, Austria, 2018.

[90] Novotný, D., and V. Petrucha, "High Dynamic Range Digital Fluxgate Magnetometer," *IEEE Sensors Conference*, 2020.

[91] Marshall, S. V., "Gamma-Level Portable Ring-Core Magnetometer," *IEEE Transactions on Magnetics*, Vol. MAG7, No. 1, 1971.

[92] Heinecke, W., "Magnetic-Field Measurement with Fluxgate Magnetometers," *Technisches Messen*, Vol. 48, No. 1, 1981, pp. 3–9.

[93] Ando, B., et al., "Towards an Optimal Readout of a Residence Times Difference (RTD) Fluxgate Magnetometer," *Sensors and Actuators A: Physical*, Vol. 142, No. 1, March 2008, pp. 73–79.

[94] Son, D., "A New Type of Fluxgate Magnetometer Using Apparent Coercive Field-Strength Measurement," *IEEE Transactions on Magnetics*, Vol. 25, No. 5, September 1989, pp. 3420–3422.

[95] Ripka, P., and W. G. Hurley, "Excitation Tuning in Fluxgate Sensors," *IMTC 2002: Proceedings of the 19th IEEE Instrumentation and Measurement Technology Conference, Vols. 1 & 2*, 2002, pp. 677–680.

[96] Serson, P. H., and W. L. W. Hannaford, "A Portable Electrical Magnetometer," *Can. J. Tech.*, Vol. 34, 1956, pp. 232–243.

[97] Narod, B. B., and R. D. Russell, "Steady-State Characteristics of the Capacitively Loaded Flux Gate Sensor," *IEEE Transactions on Magnetics*, Vol. 20, No. 4, 1984, pp. 592–597.

[98] Primdahl, F., and P. A. Jensen, "Noise in the Tuned Fluxgate," *Journal of Physics E-Scientific Instruments*, Vol. 20, No. 6, June 1987, pp. 637–642.

[99] Ripka, P., and S. W. Billingsley, "Fluxgate: Tuned vs. Untuned Output," *IEEE Transactions on Magnetics*, Vol. 34, No. 4, July 1998, pp. 1303–1305.

[100] Primdahl, F., et al., "The Short-Circuited Fluxgate Output Current," *Journal of Physics E-Scientific Instruments*, Vol. 22, No. 6, June 1989, pp. 349–354.

[101] Primdahl, F., et al., "Sensitivity Parameters of the Short-Circuited Fluxgate," *Measurement Science and Technology*, Vol. 2, No. 11, 1991, pp. 1039–1045.

[102] Petersen, J. R., et al., "The Ring Core Fluxgate Sensor Null Feed-Through Signal," *Measurement Science and Technology*, Vol. 3, No. 12, December 1992, pp. 1149–1154.

[103] Ripka, P., and F. Primdahl, "Tuned Current-Output Fluxgate," *Sensors and Actuators A: Physical*, Vol. 82, No. 1, 2000, pp. 161–166.

[104] Scouten, D. C., "Sensor Noise in Low-Level Flux-Gate Magnetometers," *IEEE Transactions on Magnetics*, Vol. MAG8, No. 2, 1972.

[105] Burger, J. R., "Comments on Sensor Noise in Low-Level Flux-Gate Magnetometers," *IEEE Transactions on Magnetics*, Vol. MAG8, No. 4, 1972, pp. 797–798.

[106] Butta, M., et al., "Influence of Magnetostriction of NiFe Electroplated Film on the Noise of Fluxgate," *IEEE Transactions on Magnetics*, Vol. 50, No. 11, 2014.

[107] Ripka, P., M. Pribil, and M. Butta, "Fluxgate Offset Study," *IEEE Transactions on Magnetics*, Vol. 50, No. 11, 2014.

[108] Moldovanu, C., et al., "The Noise of the Vacquier Type Sensors Referred to Changes of the Sensor Geometrical Dimensions," *Sensors and Actuators A: Physical*, Vol. 81, No. 1-3, April 2000, pp. 197–199.

[109] Koch, R. H., and J. R. Rozen, "Low-Noise Flux-Gate Magnetic-Field Sensors Using Ring- and Rod-Core Geometries," *Applied Physics Letters*, Vol. 78, No. 13, March 2001, pp. 1897–1899.

[110] "Observatory Workshops at Geomagnetic Observatories, Surveys and Analyses," International Association of Geomagnetism and Aeronomy, International Union of Geodesy and Geophysics, https://www.bgs.ac.uk/iaga/vobs/.

[111] Cerman, A., et al., "Self-Compensating Excitation of Fluxgate Sensors for Space Magnetometers," *IEEE Instrumentation and Measurement Technology Conference*, 2008, pp. 2059–2064.

[112] Nishio, Y., F. Tohyama, and N. Onishi, "The Sensor Temperature Characteristics of a Fluxgate Magnetometer by a Wide-Range Temperature Test for a Mercury Exploration Satellite," *Measurement Science and Technology*, Vol. 18, No. 8, August 2007, pp. 2721–2730.

[113] Baumjohann, W., et al., "The BepiColombo–Mio Magnetometer En Route to Mercury," *Space Science Reviews*, Vol. 216, No. 8, 2020.

[114] Acuna, M. H., *The Design, Construction and Test of Magnetically Clean Spacecraft: A Practical Guide*, Technical Report, Goddard Space Flight Centre, 2000.

[115] Primdahl, F., *A Pedestrian Approach to Magnetic Cleanliness*, Danish Space Research Institute Research Report, 1990.

[116] Brauer, P., et al., "Transverse Field Effect in Fluxgate Sensors," *Sensors and Actuators A: Physical*, Vol. 59, No. 1-3, April 1997, pp. 70–74.

[117] Ripka, P., and S. W. Billingsley, "Crossfield Effect at Fluxgate," *Sensors and Actuators A: Physical*, Vol. 81, No. 1, 2000, pp. 176–179.

[118] Ripka, P., J. Vyhnanek, and A. Chirtsov, "Crossfield Response of Industrial Magnetic Sensors," *International Journal of Applied Electromagnetics and Mechanics*, Vol. 55, 2017, pp. S39-S47.

[119] Fornacon, K. H., et al., "The Magnetic Field Experiment Onboard Equator-S and Its Scientific Possibilities," *Annales Geophysicae-Atmospheres Hydrospheres and Space Sciences*, Vol. 17, No. 12, December 1999, pp. 1521–1527.

[120] Carr, C., et al., "The Double Star Magnetic Field Investigation: Instrument Design, Performance and Highlights of the First Year's Observations," *Annales Geophysicae*, Vol. 23, No. 8, 2005, pp. 2713–2732.

[121] Scarzello, J. F., and G. W. Usher, "Low-Power Magnetometer for Vehicle Detection," *IEEE Transactions on Magnetics*, Vol. 13, No. 5, 1977, pp. 1101–1103.

[122] Ripka, P., and P. Kaspar, "Portable Fluxgate Magnetometer," *Sensors and Actuators A: Physical*, Vol. 68, No. 1-3, 1998, pp. 286–289.

[123] Jankowski, J., and C. Sucksdorff, *IAGA Guide for Magnetic Measurements and Observatory Practice*, International Association of Geomagnetism and Aeronomy, 1996.

[124] Segawa, J., et al., "A New Model of Ocean Bottom Magnetometer," *Journal of Geomagnetism and Geoelectricity*, Vol. 35, No. 11-1, 1983, pp. 407–421.

[125] Ogawa, K., et al., "A New Miniaturized Magnetometer System for Long-Term Distributed Observation on the Seafloor," *Earth Planets and Space*, Vol. 70, July 2018.

[126] Lin, C. R., et al., "Evaluations of an Ocean Bottom Electro-Magnetometer and Preliminary Results Offshore NE Taiwan," *Geoscientific Instrumentation Methods and Data Systems*, Vol. 8, No. 2, September 2019, pp. 265–276.

[127] Nielsen, O. V., et al., "Miniaturization of Low-Cost Metallic-Glass Flux-Gate Sensors," *Journal of Magnetism and Magnetic Materials*, Vol. 83, No. 1-3, January 1990, pp. 405–406.

[128] Vincueria, I., et al., "Flux-Gate Sensor-Based on Planar Technology," *IEEE Transactions on Magnetics*, Vol. 30, No. 6, November 1994, pp. 5042–5045.

[129] Kawahito, S., et al., "A Weak Magnetic Field Measurement System Using Micro-Fluxgate Sensors and Delta-Sigma Interface," *IEEE Transactions on Instrumentation and Measurement*, Vol. 52, No. 1, February 2003, pp. 103–110.

[130] Kejik, P., "Contactless Measurement of Current by Using Fluxgate Method," Ph.D. Thesis, Department of Measurement, Czech Technical University, Prague, 1999. In Czech.

[131] Kejik, P., et al., "A New Compact 2D Planar Fluxgate Sensor with Amorphous Metal Core," *Sensors and Actuators A: Physical*, Vol. 81, No. 1-3, April 2000, pp. 180–183.

[132] Drljaca, P. M., et al., "Low-Power 2-D Fully Integrated CMOS Fluxgate Magnetometer," *IEEE Sensors Journal*, Vol. 5, No. 5, October 2005, pp. 909–915.

[133] Baschirotto, A., et al., "A Fluxgate Magnetic Sensor: From PCB to Micro-Integrated Technology," *IEEE Transactions on Instrumentation and Measurement*, Vol. 56, No. 1, February 2007, pp. 25–31.

[134] Baschirotto, A., et al., "A 2D Micro-Fluxgate Earth Magnetic Field Measurement Systems with Fully Automated Acquisition Setup," *Measurement*, Vol. 43, No. 1, January 2010, pp. 46–53.

[135] Hsieh, P. H., and S. J. Chen, "Multilayered Vectorial Fluxgate Magnetometer Based on PCB Technology and Dispensing Process," *Measurement Science and Technology*, Vol. 30, No. 12, December 2019.

[136] Ripka, P., et al., "Symmetrical Core Improves Micro-Fluxgate Sensors," *Sensors and Actuators A: Physical*, Vol. 92, No. 1-3, 2001, pp. 30–36.

[137] Dezuari, O., et al., "Printed Circuit Board Integrated Fluxgate Sensor," *Sensors and Actuators A: Physical*, Vol. 81, No. 1-3, April 2000, pp. 200–203.

[138] Kubik, J., L. Pavel, and P. Ripka, "PCB Racetrack Fluxgate Sensor with Improved Temperature Stability," *Sensors and Actuators A: Physical*, Vol. 130–131, Special Issue, 2006, pp. 184–188.

[139] Kubik, J., M. Janosek, and P. Ripka, "Low-Power Fluxgate Sensor Signal Processing Using Gated Differential Integrator," *Sensor Letters*, Vol. 5, No. 1, March 2007, pp. 149–152.

[140] Janosek, M., and P. Ripka, "Current-Output of Printed Circuit Board Fluxgates," *Sensor Letters*, Vol. 7, No. 3, 2009, pp. 299–302.

[141] Janosek, M., and P. Ripka, "PCB Sensors in Fluxgate Magnetometer with Controlled Excitation," *Sensors and Actuators A: Physical*, Vol. 151, No. 2, April 2009, pp. 141–144.

[142] Kawahito, S., et al., "High-Resolution Micro-Fluxgate Sensing Elements Using Closely

Coupled Coil Structures," *Sensors and Actuators A: Physical*, Vol. 54, No. 1-3, June 1996, pp. 612–617.

[143] Gruger, H., and R. Gottfried-Gottfried, "Performance and Applications of a Two Axes Fluxgate Magnetic Field Sensor Fabricated by a CMOS Process," *Sensors and Actuators A: Physical*, Vol. 91, No. 1-2, June 2001, pp. 61–64.

[144] Guo, L., et al., "Wide Linearity Range and Highly Sensitive MEMS-Based Micro-Fluxgate Sensor with Double-Layer Magnetic Core Made of Fe-Co-B Amorphous Alloy," *Micromachines*, Vol. 8, No. 12, December 2017.

[145] Snoeij, M. F., et al., "Integrated Fluxgate Magnetometer for Use in Isolated Current Sensing," *IEEE Journal of Solid-State Circuits*, Vol. 51, No. 7, July 2016, pp. 1684–1694.

[146] Primdahl, F., et al., "High-Frequency Fluxgate Sensor Noise," *Electronics Letters*, Vol. 30, No. 6, March 1994, pp. 481–482.

[147] Ripka, P., et al., "Ac Magnetic-Field Measurement Using the Fluxgate," *Sensors and Actuators A: Physical*, Vol. 46, No. 1-3, January-February 1995, pp. 307–311.

[148] Ioan, C., et al., "Extension of the Frequency Range of Fluxgate Magnetometers," *Journal of Magnetism and Magnetic Materials*, Vol. 157, May 1996, pp. 567–568.

[149] Le Contel, O., et al., "The Search-Coil Magnetometer for MMS," *Space Science Reviews*, Vol. 199, No. 1-4, March 2016, pp. 257–282.

[150] Fischer, D., et al., "Optimized Merging of Search Coil and Fluxgate Data for MMS," *Geoscientific Instrumentation Methods and Data Systems*, Vol. 5, No. 2, November 2016, pp. 521–530.

[151] Dallago, E., et al., "A CMOS 2D Micro-Fluxgate Earth Magnetic Field Detecting System with RS232 Digital Output," *2007 IEEE Sensors, Vols. 1–3*, New York: IEEE, 2007, pp. 240–243.

[152] Li, W., and J. L. Wang, "Magnetic Sensors for Navigation Applications: An Overview," *Journal of Navigation*, Vol. 67, No. 2, March 2014, pp. 263–275.

[153] Vcelak, J., and J. Kubik, "Influence of Sensor Imperfections to Electronic Compass Attitude Accuracy," *Sensors and Actuators A: Physical*, Vol. 155, No. 2, October 2009, pp. 233–240.

[154] Afanasiev, J. V., and L. J. Bushev, "Three Component Ferroprobe," *Pribori i sistemi upravlenia*, Vol. 1, 1978, pp. 29–31. In Russian.

[155] Primdahl, F., and P. A. Jensen, "Compact Spherical Coil for Fluxgate Magnetometer Vector Feedback," *Journal of Physics E-Scientific Instruments*, Vol. 15, No. 2, 1982, pp. 221–226.

[156] Nielsen, O. V., et al., "A High-Precision Triaxial Fluxgate Sensor for Space Applications: Layout and Choice of Materials," *Sensors and Actuators A: Physical*, Vol. 59, No. 1-3, April 1997, pp. 168–176.

[157] Langel, R., et al., "The Magsat Mission," *Geophysical Research Letters*, Vol. 9, No. 4, 1982, pp. 243–245.

[158] Brauer, P., et al., "Fluxgate Sensor for the Vector Magnetometer Onboard the 'Astrid-2' Satellite," *Sensors and Actuators A: Physical*, Vol. 81, No. 1-3, April 2000, pp. 184–188.

[159] Merayo, J. M. G., et al., "The Spinning Astrid-2 Satellite Used for Modeling the Earth's Main Magnetic Field," *IEEE Transactions on Geoscience and Remote Sensing*, Vol. 40, No. 4, April 2002, pp. 898–909.

[160] Cheng, B. J., et al., "High Precision Magnetometer for Geomagnetic Exploration Onboard of the China Seismo-Electromagnetic Satellite," *Science China-Technological Sciences*, Vol. 61, No. 5, May 2018, pp. 659–668.

[161] Ripka, P., and P. Navratil, "Fluxgate Sensor for Magnetopneumometry," *Sensors and Actuators A: Physical*, Vol. 60, No. 1-3, 1997, pp. 76–79.

[162] Janosek, M., et al., "Single-Core Fluxgate Gradiometer with Simultaneous Gradient and Homogeneous Feedback Operation," *Journal of Applied Physics*, Vol. 111, No. 7, 2012.

[163] Merayo, J. M. G., et al., "A Portable Single Axis Magnetic Gradiometer," *Sensors and Actuators A: Physical*, Vol. 93, No. 3, October 2001, pp. 185–196.

[164] Merayo, J. M. G., P. Brauer, and F. Primdahl, "Triaxial Fluxgate Gradiometer of High Stability and Linearity," *Sensors and Actuators A: Physical*, Vol. 120, No. 1, April 2005, pp. 71–77.

[165] Janosek, M., et al., "Dual-Core Fluxgate Gradiometer with Gradient Feedback," *2013 IEEE Sensors*, 2013, pp. 648–650.

[166] Sui, Y. Y., et al., "Compact Fluxgate Magnetic Full-Tensor Gradiometer with Spherical Feedback Coil," *Review of Scientific Instruments*, Vol. 85, No. 1, January 2014.

[167] Sui, Y. Y., et al., "Correction and Compensation of an Airborne Fluxgate Magnetic Tensor Gradiometer," *Exploration Geophysics*, Vol. 49, No. 5, October 2018, pp. 726–734.

[168] Janosek, M., et al., "Compact Full-Tensor Fluxgate Gradiometer," *Journal of Electrical Engineering-Elektrotechnicky Casopis*, Vol. 66, No. 7, December 2015, pp. 146–148.

CHAPTER 4

Ferromagnetic Magnetoresistive Sensors

Pavel Ripka, Mark Tondra, and Hans Hauser

This chapter covers the effects of electron scattering, depending on the spin direction with respect to the spontaneous magnetization in ferromagnetic materials. The anisotropic magnetoresistance (AMR) is utilized in thin films, and the giant magnetoresistance (GMR) and tunneling magnetoresistance (TMR) are phenomena based on exchange coupling in sandwiches and multilayers of ultrathin magnetic and nonmagnetic layers (superlattices).

Magnetoresistive sensors are well suited for use in medium field strengths (e.g., Earth field navigation or position measuring systems). They can be manufactured (also with on-chip electronics) by the technology of integrated circuits at small sizes and low costs, which are the main prerequisites for mass-market acceptance. Compared to Hall sensors, ferromagnetic magnetoresistors have higher sensitivity, lower noise, and higher operational temperature. They have better offset stability, as they do not not have a piezo effect.

This chapter is based on review books and articles [1–4] and the references cited there, all of which are well suited for further reading. A general description of the AMR phenomenology and materials characterization and fabrication aspects are followed by the discussion of linearization and stabilization techniques. The sensor layout is illustrated by selected examples of industrial products.

Three different physical effects in particular contribute to the influence of magnetic fields on the electrical resistivity of solid state materials:

- The first effect occurs in every conducting material and it is based on the magnetic part of the Lorentz force on the electric current carriers subjected to the magnetic field. An increase of the resistance is caused by deflection of the current paths and strongly depends on the device geometry: it is large in short structures, and in longer shapes the effect is reduced by Hall electrical field. The resistance is proportional to B^2. Semiconductor magnetoresistors are based on this effect. Once they were extensively used, but presently they are obsolete because of their small amount of magnetoresistance. These devices were made of high-mobility InSb and InAs. Feldplatte containing NiSb needles in InSb material belongs to the same historical category.
- Another contribution is found in paramagnetic and diamagnetic semiconductors and metals (e.g., bismuth). It is caused by band bending at the Fermi surface and it is also proportional to B^2. The bismuth resistivity is doubled

at the field of 2T at room temperature; the resistance change is 80 times at liquid nitrogen temperature. Bismuth was the material of first magnetoresistors in 1937 [1].

- The third effect appears distinctly in ferrimagnetic or ferromagnetic thin films with uniform orientation of the spontaneous magnetization, which is parallel to the easy axis of minimum uniaxial anisotropy energy in absence of an applied field. It is the AMR.

4.1 AMR Sensors

The anisotropic magnetoresistive effect has been discovered in 1857 by Sir W. Thomson and since that time it was studied mainly at low temperatures. Only the last five decades of research and development enabled its application first in read-heads for data storage devices and later as industrial sensors. This progress is based on modern microelectronics technology and the demands of miniaturization.

4.1.1 Magnetoresistance and Planar Hall Effect

The AMR effect is based on the anisotropic scattering of conduction electrons of the band with uncompensated spins (e.g., 3-D orbit for the first transition metals Fe, Co, and Ni) in this exchange split band: The energies of the two states of the magnetic spin moment ($\pm\mu_B$) differ by the quantum-mechanical exchange energy. These electrons are responsible for ferrimagnetism and ferromagnetism (Chapter 1).

Theoretical analyses of AMR are given in terms of the electron density of states diagram and the Fermi level. The difficulty is that the anisotropic part of the resistance depends on the exact 3-D shape of the Fermi surface (3-D envelope of the Fermi level) and this is not precisely known except for a very few magnetic materials. Theorists have therefore not succeeded in calculating the effect to better than one order of magnitude agreement. As a consequence, all materials data have to be found empirically [5]. Most of the materials have positive AMR coefficients, which means that the high resistivity state occurs when spontaneous magnetization M_s and current density J are parallel.

The description of the complex behavior of a general magnetoresistor can be simplified by dividing the problem into two parts. First, the relation between resistivity ρ and the direction of M_s and second, the relation between the applied field H and the magnetization direction.

4.1.1.1 Resistance and Magnetization

In soft magnetic thin films of the single-domain state, the AMR can be phenomenologically described very simply as a 2-D problem. Figure 4.1 shows the dimensions (length l, width b, and thickness d) of the rectangular thin ferromagnetic film (AMR element) and the coordinate system. An applied field H_y rotates M_s out of the

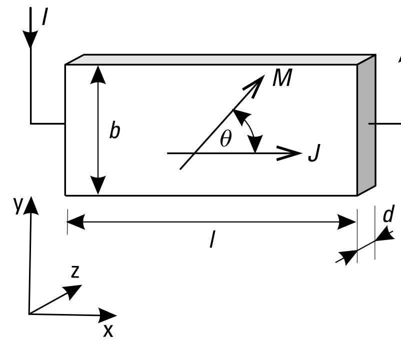

Figure 4.1 Current density and spontaneous magnetization in a single-domain thin-film strip carrying electric current.

easy axis towards the hard axis direction of the uniaxial anisotropy. The resistivity depends on the angle $\theta = \varphi - \psi$ between M_s and J. With

$$\rho(\theta) = \rho_o + \left(\rho_p - \rho_o\right)\cos^2\theta = \rho_o + \Delta\rho\cos^2\theta \tag{4.1}$$

and $\rho = \rho_p$ for M_s parallel with J, and $\rho = \rho_0$ for M_s orthogonal to J, the quotient $\Delta\rho/\rho_0$ is the magnetoresistive coefficient, which may amount to several percent. With the resistance

$$R(\theta) = \rho(\theta)\frac{l}{bd} = R + \Delta R\cos^2\theta \tag{4.2}$$

(see Figure 4.2) the voltage in the x direction is

$$U_x = I\frac{l}{bd}\left(\rho_o + \Delta\rho\cos^2\theta\right) \tag{4.3}$$

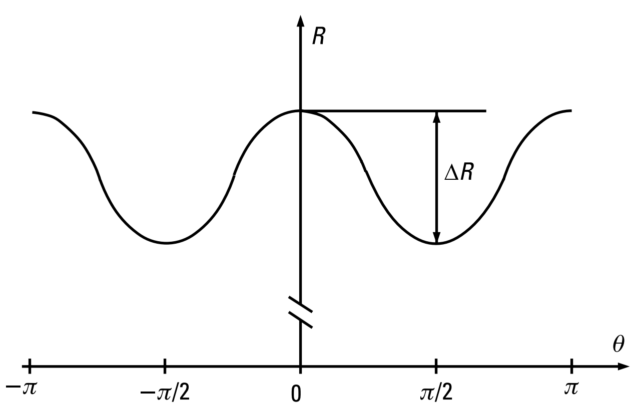

Figure 4.2 Dependence of the resistance R on the angle θ between M_s and J for a typical 20-nm-thick permalloy AMR sensor film.

Another effect related to AMR is determined by the tensor property of ρ. Perpendicular to the electrical field E_x causing the current density J_x is an electrical field

$$E_y = J_x \Delta\rho \sin\theta \cos\theta \tag{4.4}$$

Due to its direction, it is known as planar or extraordinary Hall effect. It must not be confused with the (ordinary) Hall effect because of different physical origin. Depending on sgn(θ), the planar Hall voltage

$$V_y = I\frac{\Delta\rho}{d}\sin\theta\cos\theta \tag{4.5}$$

resulting from (4.4) will be much lower than V_x because of $b << l$ in usual AMR sensor designs. The planar Hall effect can be considered for sensors measuring fields at very small dimensions with high spatial resolutions.

4.1.1.2 Magnetization and Applied Field

Let us briefly review the theory of coherent rotation of magnetization in thin films of the single-domain state. For the total energy density of a single domain of anisotropic material in the magnetic field H (Figure 4.3), we may write:

$$\mathrm{E} = E_A + E_H = \frac{1}{2}\mu_0 M_S H_0 \sin^2\phi - \mu_0 M_S H \cos\alpha \tag{4.6}$$

where M_s is the saturation magnetization, α is an angle between the magnetization M_s and external field $H = (H_x, H_y)$, and φ is an angle between the magnetization M_s and the easy direction x. The characteristic field H_0 is the sum of the demagnetizing field H_d and the anisotropy field H_k (see Chapter 1).

In order to find the energy minimum with respect to φ, we solve the equation $dE/d\varphi = 0$ and find

$$\sin\varphi = \frac{H\sin\psi\cos\varphi}{H_0\cos\varphi + H\cos\psi} \tag{4.7}$$

and if the external field H is much smaller than the anisotropy field $|H_x|, |H_y| << |H_0|$, we will find [1]:

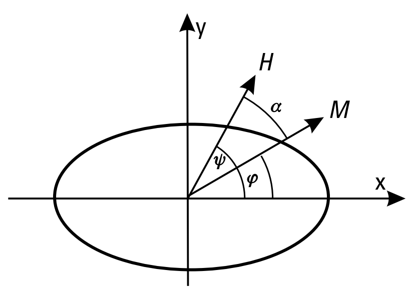

Figure 4.3 *M* in a thin-film ellipsoid, single-domain region subjected to external *H*.

$$\sin\phi = \frac{H_y}{H_x + H_0} \tag{4.8}$$

If H is acting in the y direction, the angle

$$\theta = \arcsin\frac{H_y}{H_0} \tag{4.9}$$

between M_s and J (for $-1 < H_y/H_0 < 1$) leads to the field dependence of the resistance

$$R\left(H_y\right) = R_0 + \Delta R\left[1 - \left(\frac{H_y}{H_0}\right)^2\right] \tag{4.10}$$

for $|H_y| \leq H_0$ and $R(H_y) = R_0$ for $|H_y| > H_o$, shown in Figure 4.4.

The magnetic field H, flux density B, and magnetization M are only homogeneous in ellipsoids. Therefore, H_d causes a variation of θ with respect to the y coordinate in general. If H_k is negligible compared with H_d and H_y is not strong enough to rotate M_s completely into the y direction, an analytical solution for θ in rectangular samples is

$$\theta(y) = \arctan\left(\frac{2H_y}{dM_s}\sqrt{\left(\frac{b}{2}\right)^2 - y^2}\right) \tag{4.11}$$

This effect is also shown in Figure 4.4. Even if $\theta = 60°$ in the middle of the sample ($y = 0$), there is still almost no deflection at the edges ($y = -b/2$ and $y + b/2$).

4.1.2 Magnetoresistive Films

The most important properties of AMR materials are large coefficients $\Delta\rho/\rho_0$ at a large ρ (high signal at low power with a small sensor area), low temperature

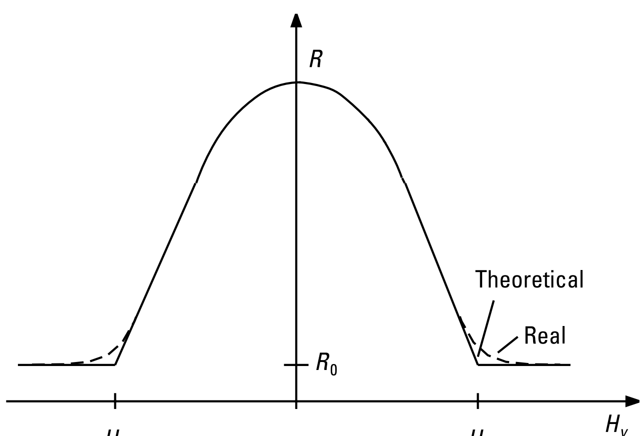

Figure 4.4 Dependence of the resistance R on the applied field H_y of a 20-nm thin permalloy film having $H_C \approx 0$; theoretical (solid line) and real (dashed line).

dependence of ρ and l (low offset drift), low anisotropy field H_k (high sensitivity), low coercivity H_c in the hard axis direction (high reproducibility), near-zero magnetostriction λ_s (magnetic properties independent of mechanical stress), and long term stability of these properties (no thermally activated effects, e.g. diffusion, recrystallization).

4.1.2.1 Materials

Besides amorphous ferromagnets, which are characterized by ideally zero H_k and high ρ but only $\Delta\rho/\rho_0 \approx 0.07\%$, the most established materials are crystalline binary and ternary alloys of Ni, Fe, and Co, in particular, permalloy 81Ni/19Fe. This material is characterized by $\mu_0 M_s = 1.1$T at 300K, $\rho = 2.2 \cdot 10^{-7}$ Ωm, AMR coefficient $\Delta\rho/\rho_0 = 2 \ldots 4\%$, thermal resistivity coefficient 0.3%/K, $H_k \approx 100 \ldots 1{,}000$ A/m, $H_c < 10$ A/m, and $\lambda_s \approx 0$. To achieve a material with simultaneously vanishing anisotropy and magnetostriction, it is necessary to add about 4% Mo (Supermalloy), but $\Delta\rho/\rho_0$ is also reduced in this case. Therefore, most AMR films are made of permalloy because of both very low H_k and λ_s at considerable $\Delta\rho/\rho_0$.

Materials with higher AMR coefficients are 90Ni/10Co (4.9%), 80Ni/20Co (6.5%), 70Ni/30Co (6.6%), and 92Ni/8Fe (5.0%), but they are not suitable for sensor applications due to either high H_k or high λ_s. Other low anisotropy materials are 50Ni/50Co (2.2%) and Sendust, which is used for magnetoresistive heads due to mechanical hardness requirements.

4.1.2.2 Film Processing

The two established methods for deposition of permalloy layers are vacuum evaporation and cathode sputtering at very low oxygen partial pressure. The main advantage of the latter procedure is the good correspondence of the composition of the film and the target alloy, which can be prepared by vacuum melting or sintering. Both elevated target and substrate temperatures have been proven to yield an AMR coefficient of $\Delta\rho/\rho_0 = 3.93\%$ in a 50-nm thin film [6], which is almost the bulk value of about 4%.

The thermally activated crystallite growth or the incorporation of residual gas atoms at grain boundaries, which reduces ρ, can also be done by an annealing process in vacuum or hydrogen, but that can increase coercivity. As the resistance increases with decreasing film thickness, the AMR coefficient decreases at constant $\Delta\rho$ to 3.5% at 20 nm (which is thought to be the optimum thickness for AMR films [5]). This leads to a trade-off between sensor resistance and AMR effect.

To establish the easy axis orientation, the deposition and/or annealing has to be done in a homogeneous magnetic bias field of some kA/m, providing a spatial aligning of Ni and Fe atom pairs. This leads to an additional induced anisotropy, which can be used to either decrease or increase the intrinsic anisotropy (effective anisotropy resulting from magnetocrystalline and shape anisotropy; see Chapter 1), depending on the bias field direction. In order to avoid unwanted anisotropy and texture, the amorphous substrates (glass or oxidized silicon) have to be very smooth.

The further processing of the film with contact and passivation layers are well-known microelectronic packaging technologies. As the dimensional tolerances for

AMR sensors are smaller than for other devices to reduce the bridge unbalance, the masks are made by high-precission electron beam lithography.

4.1.2.3 Measurements

The magnetic properties of the film can be determined by measuring the hysteresis loops (component M_H of M_s in H direction versus the intensity of H) in different directions of the homogeneous applied field, which can be provided by Helmholtz or cylindrical coils. Suitable methods are vibrating coil magnetometry (VCM) or reflected light modulation by the magneto-optical Kerr effect. Figure 4.5 shows such a hysteresis loop [8] parallel and perpendicular to the easy axis, which corresponds well to the theory of coherent rotation.

Furthermore, ρ and $\Delta\rho(H)$ are determined by a 4-point probe, arranged in a square or rectangle, under an applied field of variable direction and strength. Figure 4.4 shows the resistance dependence on H_y for the same sample.

4.1.3 Linearization and Stabilization

The simple magnetoresistive element of Figure 4.1 has several drawbacks without additional measures: the resistance change at low fields is about zero; the characteristics are nonlinear even in the vicinity of the inflection point, and the film would exhibit a multidomain state that could cancel out the AMR effect or at least give rise to magnetic Barkhausen noise. Therefore, linearization and stabilization have to be done by several biasing techniques. Perpendicular bias serves for linearization and longitudinal bias serves for stabilization. The best solution finally is the barber-pole structure, which serves both for linearization and stabilization.

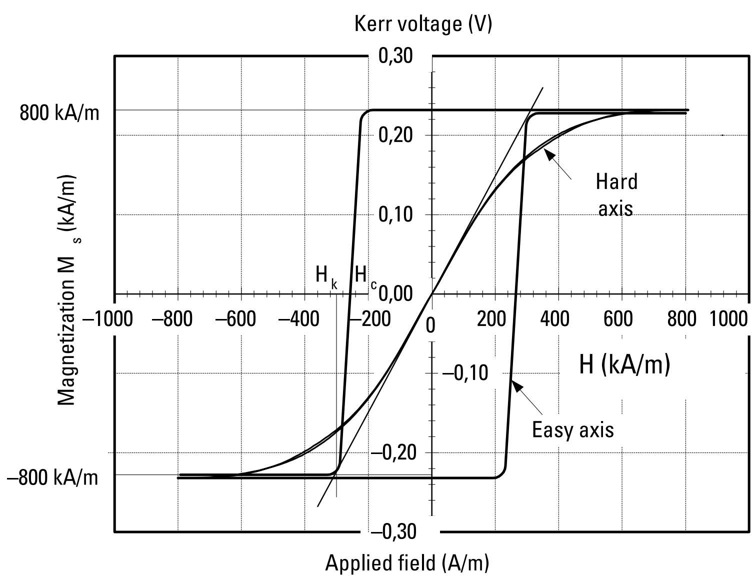

Figure 4.5 Hysteresis loops $M_H(H)$ of a 20-nm thin permalloy film ($\Delta\rho/\rho_0 = 3.4\%$). The field H is applied parallel to hard and easy axes.

Generated either by permanent magnets or currents in simple coils, an external magnetic field can be used for both purposes, but it is only advantageous if this field is also needed for the given application (e.g., position sensing via field distortion). In this section, only internal, integrated solutions will be discussed.

4.1.3.1 Perpendicular Bias for Linearization

Perpendicular bias is used to establish an angle $\theta > 0$ between M_s and J in the absence of H. This can be done either by applying a constant magnetic bias field H_B in the y direction or by rotating the current path out of the easy axis (which will be discussed separately as geometrical bias, mainly for the barber-pole structure, because of its practical importance). Replacing H_y in (4.10) by $H_y + H_B$ yields

$$R(H) = R_0 + \Delta R\left(\frac{2H_y H_B}{H_0^2} + \frac{H_y^2 + H_B^2}{H_0^2}\right) \tag{4.12}$$

which gives linear dependence $R(H_y)$ for for $H_y << H_B$.

Besides using an external magnet, a sandwich structure with a hard magnetic film can provide a bias field by simple magnetostatic coupling. The disadvantages are the magnetic stray field of the sensor itself and the fact that postfabrication adjustment of the bias field is impossible. Biasing can be also made by exchange coupling of the AMR film with an antiferromagnetic or a ferromagnetic layer or multilayer. These techniques are used for GMR and TMR sensors; in AMR technology, they have been replaced by barber-pole technology.

Another technique of biasing is using the magnetic field of the current line; again, this technique is more used for spin-dependent tunneling (SDT) (TMR) sensors than for AMR sensors.

4.1.3.2 Longitudinal Bias for Domain Stabilization

The theoretical dependence of resistivity change on the applied field as described in Section 4.1.1 is valid under the condition of a single-domain state of the film. Experimental investigations [6] had shown that the magnetization may divide into several domains. This is caused by the large stray field at the ends of a single domain and by the favored location of domain walls at imperfections of the film. The main effects are a smaller $\Delta\rho/\rho_0$ due to antiparallel domain magnetization and hysteresis with Barkhausen noise due to irreversible domain wall displacements.

Longitudinal bias is necessary to stabilize the single-domain state against perturbation by external fields and both thermal and mechanical stresses. This is achieved by pinning the end-zone domain walls (with similar techniques as in the previous sections) or by avoiding these domains by special geometric designs (e.g., triangular endings).

4.1.3.3 Geometrical Bias by Herring-Bone and Barber-Pole Structures

A much more efficient way to achieve linearity is to rotate the current direction by an angle ψ with respect to the easy axis. The two possible solutions for this kind

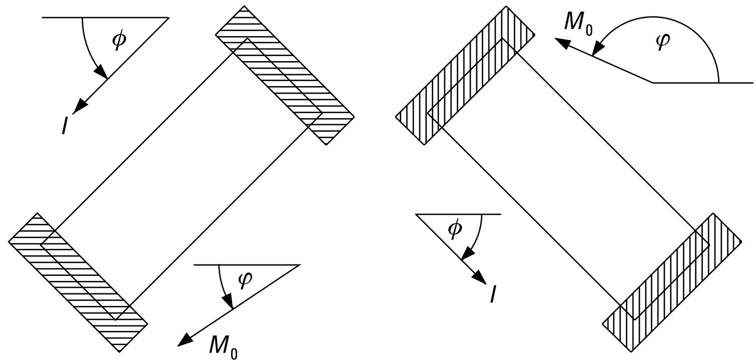

Figure 4.6 AMR elements with inclined easy axis by 45° with respect to the longitudinal direction.

of geometrical bias have been known since the beginning of the industrial AMR sensor production.

Herring Bones

The rectangular resistive element is inclined by an angle ψ (two possibilities) to the easy axis and the current is still flowing in the longitudinal direction, as shown in Figure 4.6. The spontaneous magnetization is in the direction of the minimum of the total anisotropy energy. The initial direction of M_s (two possibilities) has to be defined by an additional stabilizing field.

Using (4.2), and (4.7), the ideal case of resistance dependence on the applied field H_y is for $\psi = 45°$:

$$R\left(H_y\right) = R_0 \pm \Delta R \frac{H_y}{H_0} \sqrt{1 - \left(\frac{H_y}{H_0}\right)^2} \tag{4.13}$$

This characteristics is shown in Figure 4.7; the linearity is better than 5% for $H_y < H_0/2$.

A Wheatstone bridge can be realized by using AMR elements of different inclination signs (see Figure 4.5). The problem with this kind of geometrical bias is some uncertainty of the angles due to misalignment, lithographic limits, and strain-gauge effects.

Barber Poles

Entirely different to the methods described above, the barber-pole[1] biasing scheme is used successfully to establish the correct angle ψ between M_s and J. The AMR film is covered with stripes made of materials of high electrical conductivity (Al, Au, Ag, Cu), slanted by an angle of about 45° with respect to the easy axis of the film. If the resistance of the strips is much lower than that of the AMR film and if the contact resistance between barber-pole and AMR film is negligible, the current is inclined by 45° with respect to M_s, as shown in Figure 4.8. Therefore, the resistance characteristic can be described also by (4.13).

[1]The name originates from the rotating signs of barber shops.

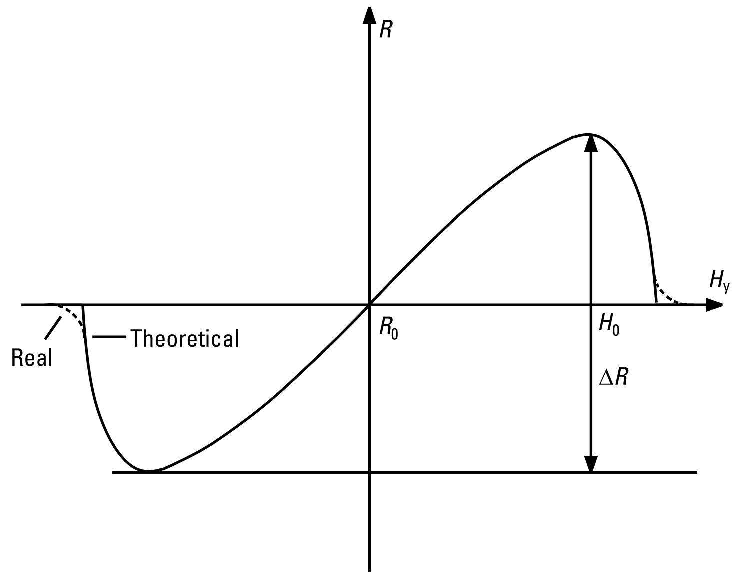

Figure 4.7 Characteristics of AMR elements with ψ = 45° due to geometrical bias; theoretical and for a 20-nm thin permalloy film with $H_C \approx 0$.

Imperfections of this linearization are caused by edge effects, where the current is still flowing parallel to the longitudinal direction of the film, and by a voltage drop along the barber-pole strips due to their finite conductivity. Therefore, the average current angle is less than 45°, which can be considered by correction terms. The sensor resistance is decreased by 2 to 4 times compared to other AMR sensor types of the same area due to partially shunting the film by the barber poles. The geometric design optimization is a trade-off between high sensitivity and linearity.

The current flowing in the barber poles generates a magnetic field with an x component

$$H_x = \frac{I}{2b}\frac{a}{a+s} \tag{4.14}$$

which can be used for stabilization by longitudinal bias [7].

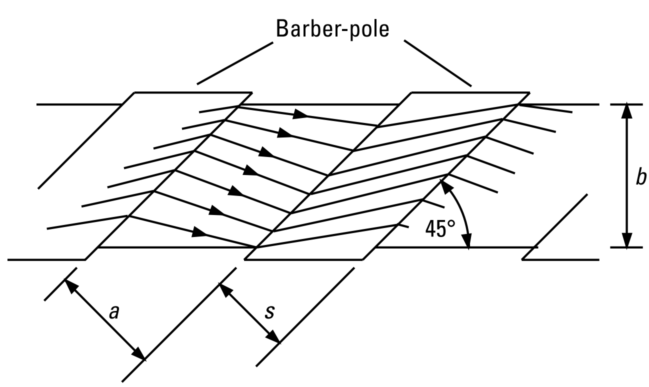

Figure 4.8 Barber-pole structure and directions of J in the AMR layer.

The resistance of a bridge consisting of AMR elements with different barber-pole slopes (±45°) depends slightly on the applied field. The main disadvantage of the barber-pole scheme is that only about 60% of the AMR film width contributes to the active sensor area. Nevertheless, this technique is successfully used for sensor fabrication because of its main advantage: The angle of M_s and J is set directly by geometry only.

4.1.4 Sensor Layout

Beside sensitivity and resistance, the type of linearization (longitudinal bias by magnetic fields or geometrical bias by slanted stripes or barber poles) mainly determines the layout. General restrictions exist for the lower limit of the film thickness (≈5 nm) due to decreasing $\Delta\rho/\rho_0$ and for the upper limit of the current density ($J_{\mathrm{rnax}} \approx 10^{10}$ A/m^2 for permalloy).

A simple stripe arrangement (see Figure 4.1) is used for very small sensor volumes (e.g., reading heads for data storage) or if only fields above a certain range have to be detected. In order to reduce thermal effects, increase the signal voltage, and further increase the linearity, full bridges or half-bridges are used for general-purpose sensors. Furthermore, both power and temperature limit gradients require low power dissipation $I^2 R$.

4.1.4.1 Sensitivity and Measuring Range

Due to the large demagnetizing field in the z direction, the sensitivity[2]

$$S = \frac{dU}{dH_y}\frac{V_{\max}}{\mu_0 V} \tag{4.15}$$

can be defined as the variation dV of the bridge voltage V with respect to the applied field H ($V_{\max}$ is the maximum permitted operating voltage), which yields the convenient unit V/T. Considering a full bridge barber-pole circuit and using (4.15) and (4.13), the maximum sensitivity is

$$S_{\max} = \frac{V_{\max}}{\mu_0}\frac{\Delta\rho}{\rho}\frac{\dfrac{1-2H_y^2}{\left(H_0+H_y\right)^2}}{\left(H_0+H_x\right)\sqrt{1-\dfrac{H_y^2}{\left(H_0+H_y\right)^2}}} \tag{4.16}$$

and for $H_y << H_0$, $H_x \approx 0$, it is

$$S_{\max} = \frac{\Delta\rho}{\rho}\frac{V_{\max}}{\mu_0 H_0} \tag{4.17}$$

[2]A different definition is $S_0 = S/\mu_0 V_{\max}$, which is measured in (mV/V)(kA/A) Other definitions also relate the sensitivity to the AMR film current.

The measuring range is also determined by the characteristic field H_0 and the linearity limit. Following (4.13) and Figure 4.4, the maximum field is

$$H_{max} \approx \frac{H_0 + H_x}{2} \tag{4.18}$$

and the sensitivity and the maximum field are inversely proportional. The demagnetizing field can be reduced by arranging parallel AMR strips (spacing in the range of the film thickness) connected electrically in series thus providing magnetically $l \approx b$. The bridge output signal is proportional to the operating voltage V_{max}, considering the maximum power dissipation P_{max} for the tolerable temperature rise.

The lower detection limit H_{min} is determined by the noise level of the bridge output voltage. The main contributions are the thermal noise ($4kTR\Delta f$ in bandwidth Δf) of resistors and the Barkhausen noise.

Offset drift (e.g., due to thermal gradients or thermal mismatch of the bridge circuit) can be minimized by operating the sensor at constant temperature and low power or by special layout as shown in the following section. The frequency bandwidth of magnetization reversal in thin films is theoretically from DC to the gigahertz range, but some 100 MHz have been already achieved.

4.1.4.2 Examples

Various designs of AMR read heads have been developed for magnetic recording, but only some characteristic layout possibilities for industrial AMR sensors are discussed in the following section. The principal schemes of spatial arrangements of full-bridge circuits are illustrated in Figure 4.9. The + and – signs in the rectangles (schematical resistors, distanced by Δx and Δy) denote the relative change of the resistance (increase or decrease) with respect to the applied field

$$H(x,y) = H_m + \frac{dH}{dx}\Delta x + \frac{dH}{dy}\Delta y \tag{4.19}$$

which is linearized around the medium field H_m, assuming a small spatial variance.

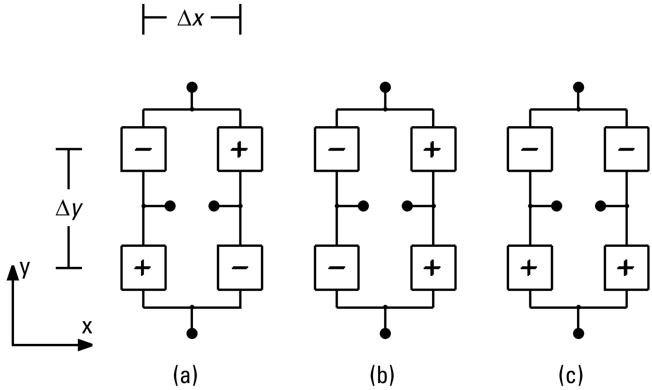

Figure 4.9 (a) Bridge circuits, (b) magnetometer, and (c) gradiometers.

Figure 4.9(a) is a magnetometer, the bridge output voltage is proportional to the field H_m in the center. Figures 4.9(b, c) are gradiometers, measuring dH/dx and dH/dy, respectively. The field at each resistor should not exceed the limit H_{max}.

Full-Bridge AMR Sensor with High Sensitivity

A full bridge with meandered resistors using the barber-pole scheme is shown in Figure 4.10. Depending on the stabilizing field H_m, the sensitivity S has been varied between 100 mV/mT and 10 mV/mT at maximum fields between ±0.6 mT and ±9 mT, respectively. A typical operation voltage is 10V. The bridge offset can be adjusted by laser trimming of integrated resistor networks.

Sensors for Weak Fields

If an AMR sensor is used as a magnetometer (e.g., to measure deviations of the Earth magnetic field), a method of switching the spontaneous magnetization between the two stable states in the AMR film is advantageous. This flipping procedure can be done by applying field pulses with an amplitude larger than H_0. The typical characteristics of different slope but equal bridge offset are shown in Figure 4.11. Using a PSD or similar electronic circuits, both sensor offset can be significantly reduced.

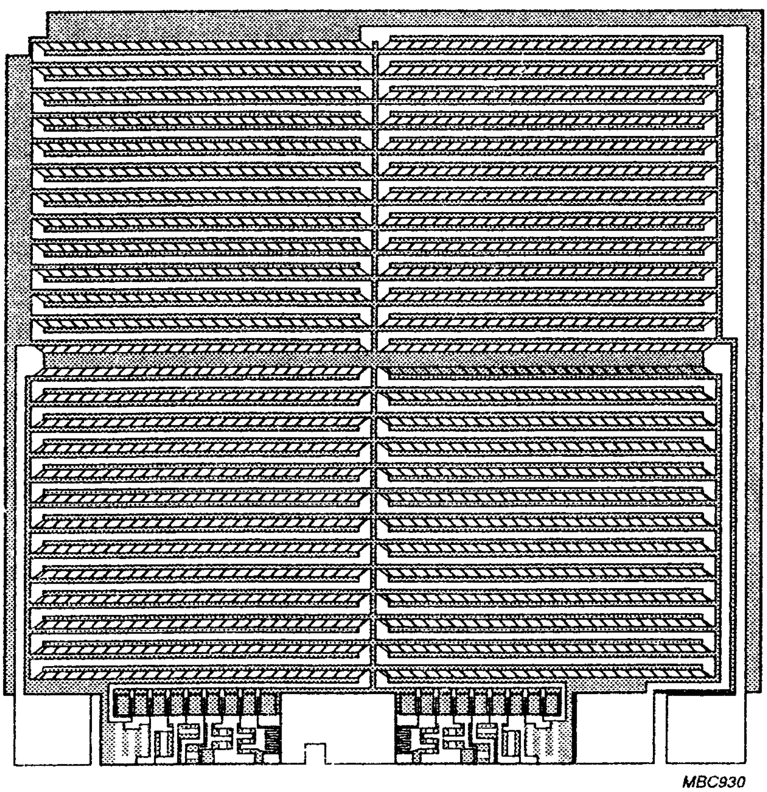

Figure 4.10 Full-bridge, highly sensitive AMR sensor with a barber-pole bias (former Philips KMZ10).

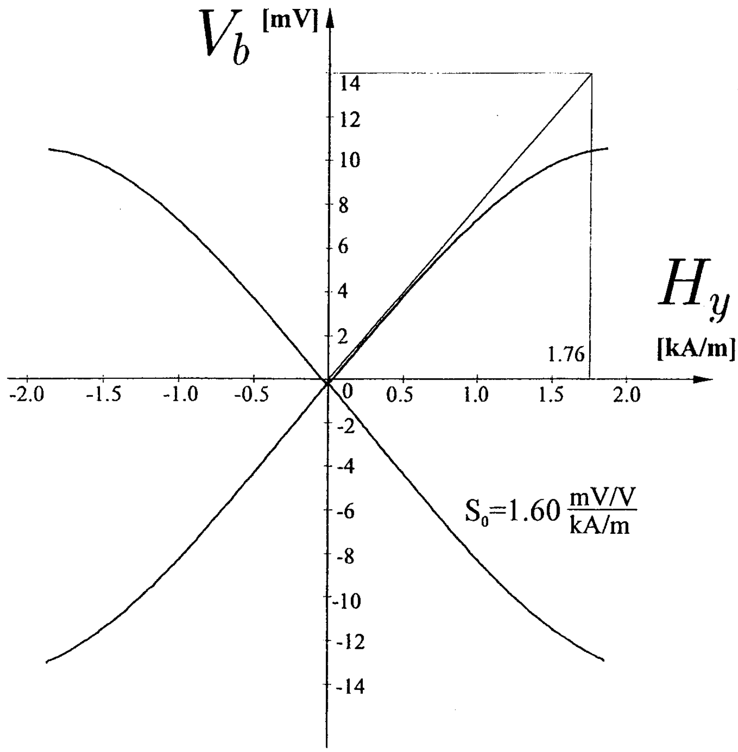

Figure 4.11 Mirror characteristics of an AMR sensor bridge: normal and flipped.

Figure 4.12 shows schematically an AMR sensor layout with flipping and compensation in-plane current straps. The current of the compensation conductor is the output signal, which is controlled to keep the bridge output at zero. A maximum sensitivity of 400 mV/mT and a resolution of 1 nT has been achieved for industrial sensors such as Honeywell HMC1001.

4.1.5 Crossfield Sensitivity of the AMR Sensor

Sensitivity to crossfield H_x perpendicular to the main measured field H_y is inherent to AMR devices.

Let us return back to formula (4.8). The resistance of the AMR strip as a function of field in arbitrary direction is calculated, for example, in [8]:

$$R(H_Y) = R_0 + \Delta R\left[1 - \left(\frac{H_Y}{H_x + H_0}\right)^2\right] = R_0 + \Delta R\cos^2\varphi \tag{4.20}$$

Using barber poles, the resistance equation becomes:

$$R = R_0 + \Delta R\cos^2(\varphi + 45°) \tag{4.21}$$

from which we will derive the following formula for the strip resistance:

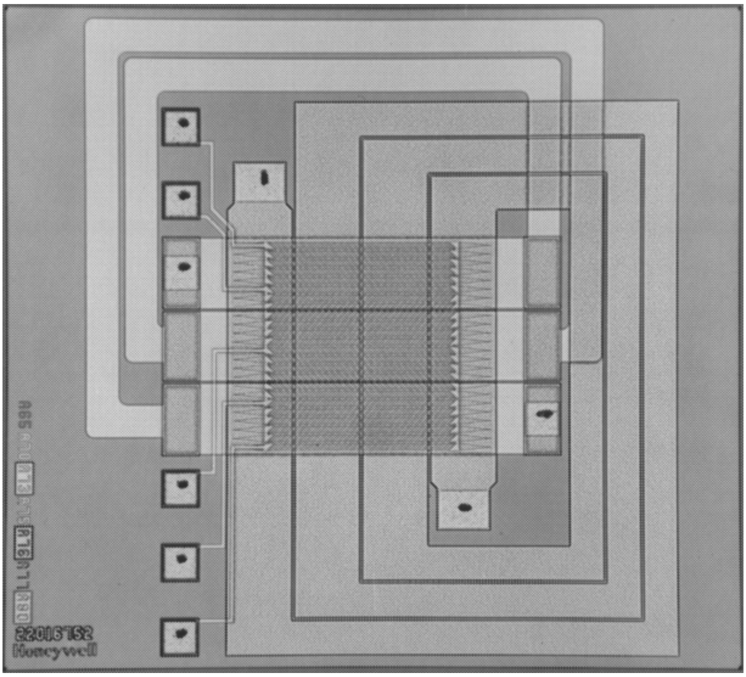

Figure 4.12 Industrial full-bridge layout with conductor strips for control of offset, field compensation, and flipping (set/reset) for weak field measurements. The on-chip straps for set/reset and offset fields are patented by Honeywell. (Courtesy of Honeywell.)

$$R = R_0' + \Delta R \frac{H_Y}{H_x + H_0} \sqrt{1 - \left(\frac{H_y}{H_x + H_0} \right)^2} \tag{4.22}$$

where

$$R_0' = R_0 + \frac{\Delta R}{2}$$

For $|H_x|, |H_y| << |H_0|$, we finally arrive at the simplified formula that appears in the application notes of the AMR sensor producers

$$R = R_0' + \Delta R \frac{H_Y}{H_0} \qquad V_1 \approx \frac{H_y}{H_x + H_0} \tag{4.23}$$

The anisotropy field for Honeywell HMC1001 is $H_0 = 0.8$ mT. Increasing H_0 leads to the suppression of the crossfield effect, but also to the decrease of sensitivity, which is accompanied by the increase of the magnetic field sensor noise [9].

Better method to suppress crossfield response is to compensate the measured field H_x by feedback. This is very efficient, but limited to small H_y values for which (4.22) is valid.

Many AMR sensors are stabilized by flipping (i.e., reversing the remanent magnetization of the magnetic layer by applying SET/RESET pulses into the flipping coil). Flipping pulses should have a large amplitude to restore the single-domain state of the sensor core [10]. The flipping field has the same direction as the crossfield. Flipping reduces sensitivity to crossfield. However, this is limited to small fields, as flipping cannot erase larger crossfields.

Another possibility is to measure H_x and perform numerical correction of crossfield sensitivity. For this, the simplified formula (4.23) cannot be used. Mohamadabadi et al. [11] used more precise approximation of the AMR equations

$$V_1 = \frac{aH_y}{\sqrt{\left(H_x + H_0\right)^2 + H_y^2}} \tag{4.24}$$

and they developed and experimentally verified correction method, which reduces the crossfield error without flipping by the factor of 8 and with flipping by the factor of 9. The problem of the mentioned correction methods is that they also work only at small fields and they also require two or three sensors.

AMR sensors are very sensitive to crossfield larger than the critical value, which is about 350 μT for the Honeywell HMC1001. It should be noted that this critical value is one order of magnitude lower than the anisotropy field H_0. This value is decreasing with increased value of the measured field H_y.

For larger values of the crossfield, the sensor characteristics are heavily distorted due to the fact that the single-domain state is broken. However, some reading is still possible for sensor with no flipping. Once the flipping is on, the sensor output is useless [9].

The crossfield effect in a triaxial AMR magnetometer with a vector and individual compensation of a measured magnetic field was examined in [12] for individually compensated axes (either by integrated compensation coils or by external solenoid) and vectorial compensation using the triaxial Helmholtz coil system. Vectorial compensation leaving all sensors in magnetic vacuum exhibited the best results: the crossfield error was below 4 nT up to 150-μT crossfield amplitude.

4.1.6 AMR Magnetometers

To keep offsets and offset drifts low, the AMR sensors are periodically flipped with a frequency of typically between 10 Hz and 10 kHz. Flipping frequency depends on required power consumption and bandwidth. Flipping pulse of 1-A range is usually generated by discharging a capacitor into the low-impedance coil, which is often integrated on the AMR chip. Flipping also suppresses the low-frequency noise of the preamplifier through modulation and demodulation and reduces crossfield error [10, 13].

Digitally compensated 3-axial magnetometer using the Honeywell HMC1021 sensor is described in [14]. The parameters were measured with 420-Hz flipping. The nonlinearity is 60 ppm for the 150-μT range (20 ppm for the 100-μT range), and noise is 150 pT/√Hz at 1 Hz in the closed loop (55 pT/√Hz for the open loop, 150-μT range). The systematic offset is 0.1 nT (Figure 4.13), gain drift is 200 ppm/K. The parameters are comparable to a state-of-the-art analog AMR magnetometers [15, 16].

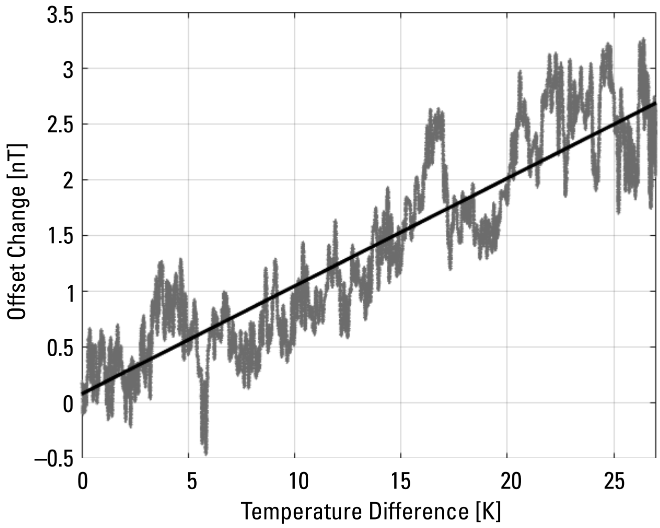

Figure 4.13 Offset change with temperature for AMR magnetometer based on flipped HMC1021 sensor.

Hybrid 3-axial AMR magnetometers are used for cheap compass modules for mobile phones. They are produced by TDK, NXP, MEMSIC, Honeywell, ST Microelectronics, and other companies. They usually contain 2-axial AMR chip for xy directions and separate 1-axial sensor for z direction. Sometimes the z-axis field is deflected into xy plane by soft magnetic flux guides so that only single AMR chip is used. The module contains also digital chip and often accelerometers. Comprehensive calibration study on these devices was made in [17]. The best performing sensors were HMC5983 by Honeywell, and the LSM303DLHC and LIS3MDL by ST Microelectronics. Their parameters are summarized in Table 4.1.

4.2 GMR and TMR (SDT) Sensors

Many applications in magnetic sensing and detection require high-sensitivity, high-speed, low-power transducers that can be integrated with silicon circuitry. GMR and TMR (also SDT) structures constitute a versatile foundation for these uses. They

Table 4.1 Parameters of Digital 3-Axial Hybrid AMR Magnetometers (Median-Worst Case)

Model	*HMC5983*	*LSM303DLHC*	*LIS3MDL*
Resolution (nT/LSB)	78–94	66–73	15
Angular alignment (deg)	0.4–2	1–7	1–3
Noise nT/√Hz at 1 Hz	21–23	12	87–124
Offset (μT)	0–20	0–25	0–50
Offset temperature drift (nT/K)	15–30	13–57	188–598

Source: [17].

can be made to have a wide range of saturation fields, resistance values, shapes, and sizes and can be formed directly on the surface of an integrated circuit. Because of their high sensitivity, they generally result in the smallest sensor size for a given magnetic sensing application. Because these sensors can be fabricated using the techniques and equipment developed for semiconductor manufacturing, they can be made small and cheap. An excellent example of this is the ubiquitous integrated read-head for hard disk drives.

GMR was first reported in 1988 independently by several research groups [18–20]. Albert Fert and Peter Grünberg were later awarded the Nobel Prize in 2007 for this discovery. The GMR is based on the interaction of ferromagnetic layers separated by a nonmagnetic layer and on spin-dependent scattering (Section 4.2.1.2). The simplest case is a sandwich (trilayer) (e.g., Fe/Cu/Fe which may be repeated in a multilayer Fe/Cu/Fe/Cu/Fe … .). The interaction is mediated by the conduction electrons in the nonmagnetic layer and is of the RKKY (Ruderman-Kittel-Kasuya-Yosida) type (i.e., the electrons passing through the nonmagnetic layer carry the information about the orientation of the moments from one to the other magnetic layer). This interaction depends on the thickness of the separating layer and it oscillates with the decreasing amplitude when the thickness is increased acquiring both positive and negative values [21]. For a sandwich with the antiferromagnetic interaction between the ferromagnetic layers, we obtain a structure where the application of external magnetic field changes the antiparallel arrangement of the magnetic moments of the magnetic layers to a parallel one that is accompanied by a dramatic change of the resistance both in the CPP (current perpendicular to the plane) and in a smaller extent also in the CIP (current in plane) geometries. This change was named GMR. CIP is used for all practical GMR devices, as the overall resistance for CPP is too small. The strongest AF interaction corresponds in the case of a Fe/Cu/Fe sandwich to the thickness of the Cu layer of about 1 nm; more often the second maximum of 2 nm is used. These distances correspond to just a small number of atomic planes. It is thus clear that the monitoring of the thickness of the layers is of the highest importance for the production of GMR elements.

The fast development of this technology was accelerated by the need of small sensing elements for reading heads for magnetic hard disks [22]. Later, a great deal of effort was put into developing GMR sensors for the full spectrum of magnetic sensing applications [23, 24]. Important sensor applications of GMR are angular sensors; TMR sensors dominate in biosensing. The first GMR structures were manufactured by Molecular Beam Epitaxy, which allows precise control of the thickness of the layers, in particular, the nonmagnetic one, but is a complicated production method suitable for laboratory use. The applications of GMR were enabled after Parkin succeeded in preparation of GMR stacks by sputtering [25].

Because the output of GMR/TMR sensors is directly related to the magnetic state of thin films of ferromagnetic metals, they have much in common with AMR sensors and fluxgate sensors. In particular, the design constraints revolve around the need for smooth and reproducible magnetization behavior. This section looks at the physical origins of the sensing capability, the technical aspects of design and construction of the GMR and TMR sensors, and some selected applications in which GMR/TMR sensors dominate.

GMR and TMR fundamentals and applications are covered in more detail in the books by Reig et al. [26] and Tumanski [1] and in reviews by Weiss et al. [27] and Freitas et al. [28, 29]. The trends are reviewed by the magnetoresistive roadmap [3].

4.2.1 GMR Effect Basics

4.2.1.1 Simple Spin Valves

A straightforward way of understanding GMR is to look at the resistive properties of the simplest GMR structure: the spin valve. It consists of two ferromagnetic metallic layers separated by a nonferromagnetic layer. To further simplify the magnetics, one of the ferromagnetic layers is pinned with an adjacent antiferromagnetic layer so that only one of the two magnetic layers is free to respond to an externally applied field. These layers are typically just a few nanometers thick, and the total stack thickness comes to 10 to 20 nm.

The resistance is lowest when the layers' magnetizations are parallel and highest when their magnetizations are antiparallel. This is true for all GMR and TMR structures.

The cross-section of common GMR structures (spin valve, sandwich, and multilayer) is shown in Figure 4.14. The vertical dimension is overstated so that the layered structure is visible. The typical dimensions of a GMR resistor in the film plane are 2 μm wide by hundreds of micrometers long, depending on the desired resistance value.

This structure has resistance versus field characteristics that look very much like the *B* versus *H* loops of the unpinned FM layer (Figure 4.15).

If the soft layer's magnetization is rotated in the film plane rather than irreversibly switched, the resistance varies smoothly as a function of the angle between

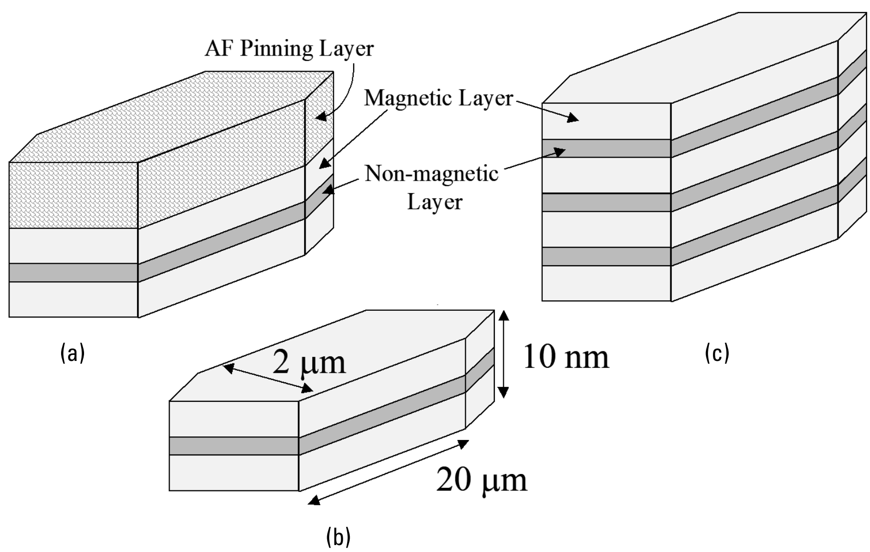

Figure 4.14 Cross-sections of common GMR structures: (a) spin valve, (b) sandwich, and (c) multilayer.

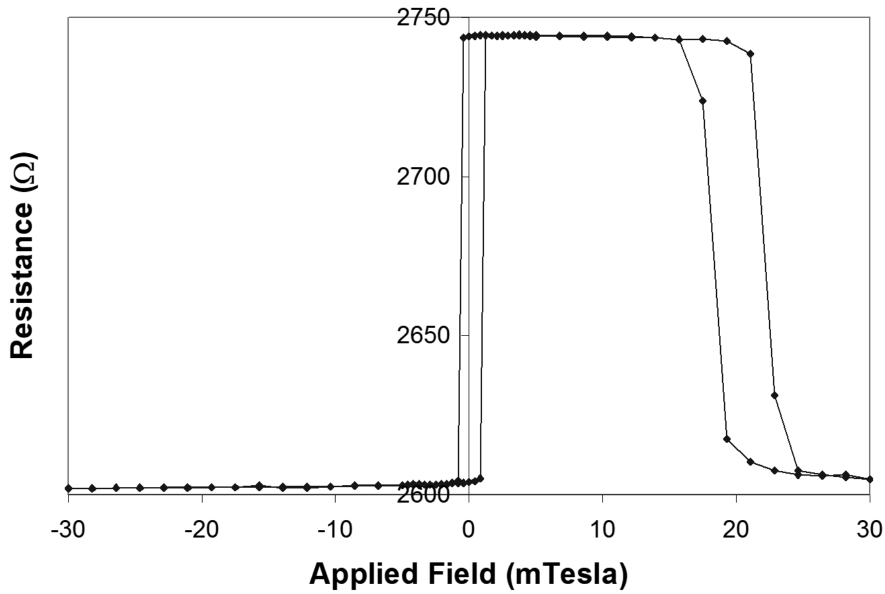

Figure 4.15 The high field (major loop) response of a spin valve when the applied field is parallel to the easy axis of the soft layer and pinning directions. The soft layer switches at about 1 mT while the pinning of the hard layer is overcome at about 20 mT.

magnetizations of adjacent layers. Assuming that the magnetization within each magnetic layer can be made uniform, this dependence of the resistance on the angle between magnetizations is:

$$R(\theta) = R_{\text{par}} + \left(\frac{\Delta R}{2}\right)\left[1 - \cos(\theta)\right] \tag{4.25}$$

Here, ΔR is the magnitude of the maximum change of resistance as the angle θ between the two ferromagnetic (FM) layers goes from parallel to antiparallel, and R_{par} and R_{anti} are the resistances when the magnetizations of the layers are parallel and antiparallel, respectively. Also,

$$\Delta R = R_{\text{anti}} - R_{\text{par}} = R_{\max} - R_{\min} \tag{4.26}$$

One can see, by differentiating, that the maximum slope for $R(\theta)$ is at $\theta = 90°$ (Figure 4.16). Consequently, when the soft layer of a spin valve element is magnetically biased orthogonally to the hard layer, the element's $R(\theta)$ is at its most sensitive point for very small external fields. The total GMR is usually calculated as a percentage:

$$\text{GMR} = \frac{\Delta R}{R_{\min}} = \frac{\left(R_{\text{anti}} - R_{\text{par}}\right)}{R_{\text{par}}} \tag{4.27}$$

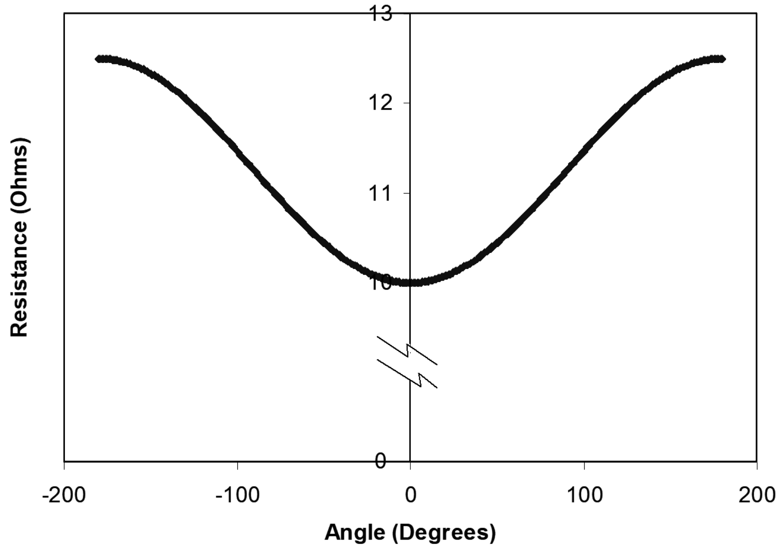

Figure 4.16 The resistance of a GMR spin valve as a function of angle between the pinned and free layers.

4.2.1.2 Origin of Spin-Dependent Scattering

A common term to describe the physical mechanism of GMR is spin-dependent scattering. As with AMR, the GMR effect is due to differences in the conduction properties of spin-up and spin-down conduction electrons. These differences arise because certain metals (primarily the transition metals Ni, Fe, Co) have a sizable mismatch in the density of states for up and down electrons at the Fermi energy. Simply speaking, electrons traveling through the uniformly magnetized ferromagnetic layer scatter more often when their spin directions are opposite to the magnetization of the material than when they are parallel to it. When two magnetic thin films are separated by a nonmagnetic metal film thin enough to allow electrons to pass from one magnetic layer to another, those electrons probe the density of states of the other magnetic layer. This is illustrated in Figure 4.17. When the two magnetic

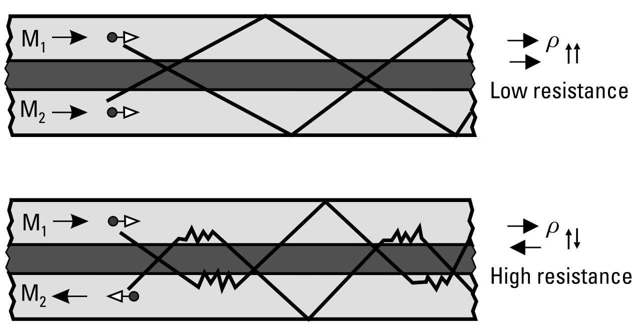

Figure 4.17 Explanation of spin-dependent scattering for current-in-plane. Only electrons that migrate into the second layer and thus contribute to GMR are shown. If the magnetizations of the two layers are parallel (upper case), no strong scattering occurs. When the magnetic moments are antiparallel, every time a spin-up electron enters the other ferromagnetic layer, it is scattered near the Cu interface. This extra scattering is the reason for GMR.

layers' magnetizations are parallel, their density of states are spatially matched and no unusual scattering occurs. But when the two magnetizations are antiparallel, the electrons traversing the nonmagnetic layer experience an inversion of the 3-D density of states upon reaching the other magnetic layer. In other words, electrons that were spin up become spin down, and vice versa. The mismatched densities of states of the two antiparallel magnetic layers result in increased scattering and thus increased resistance.

The same electrons that carry the current in these metals are also responsible for their ferromagnetic characteristics. They exhibit the AMR for similar reasons. In a well-constructed GMR structure, AMR is a smaller effect, but does contribute to the overall resistance versus field signal of a GMR sensor. The GMR and AMR can be deconvolved by making measurements with the current passing in different directions. The GMR is isotropic with current direction while the AMR will vary (as described in Section 4.1).

In order to observe the spin-dependent transport effect, several conditions must be met.

1. It is necessary for a significant fraction of conduction electrons to be able to transverse the nonmagnetic layer before significant scattering. This requires very thin nonmagnetic metal spacers (<50A).
2. There must be a way to rotate the relative magnetizations of the ferromagnetic layers from antiparallel to parallel.
3. Some fraction of electrons going from one ferromagnetic layer to the other must be spin-polarized and maintain that polarization as they go over. The magnitude of the GMR effect is qualitatively proportional to the polarization of the ferromagnetic material at the interfaces of the system.

Good lattice matching between the ferromagnetic and nonmagnetic layers in the GMR system seems to be important for maximizing GMR. The most common base systems are Co/Cu/Co and Fe/Cr/Fe. In practice, the structures are more complicated. For instance, a pinned sandwich might have the following structure:

[substrate] NiFeCo 3/CoFe 1.5/Cu 3/CoFe 4.5/IrMn 100 (in nanometers)

The NiFeCo and CoFe alloys are chosen for their high polarization with low magnetostriction. The bottom NiFeCo layer behaves better as a sensing layer (lower coercivity, higher anisotropy), while the CoFe has higher polarization.

A very large challenge in the construction of GMR films is to make the nonmagnetic layer thin enough without allowing magnetic pinholes to ferromagnetically connect the two magnetic layers. These pinholes do not necessarily change the nature of spin-dependent scattering, but they do make it very difficult to align the two magnetic layers antiparallel.

It is important to repeat that the net flow of electrons is parallel to the plane of the films (CIP) in the standard GMR sensor construction. Only a fraction of the conduction electrons have enough out-of-plane velocity to cross the nonmagnetic layer, regardless of their spin states. The measured GMR effect is much larger for a given structure when current is passed perpendicular to the film plane. In such a case, all electrons experience both films. Unfortunately, the vertical resistance of a thin-film material is so small that superconducting contacts are required to measure it unless submicron diameter pillars are made. However, we will see soon that the idea of current direction perpendicular to the film plane was realized in TMR sensors.

In practical commercial films, the GMR can routinely be made to be 8% in simple sandwich structures and 15% in multilayer structures. The GMR can be increased to over 100% by reducing the thickness of the nonmagnetic layer to the first maximum of the oscillatory dependence of GMR on thickness (at about 1 nm). However, these structures exhibit extremely large antiferromagnetic coupling, and the resulting high saturation fields (>1T). A useful figure of merit for GMR materials is sensitivity expressed in %/mT, which is calculated by taking the GMR and dividing by the saturation field. This parameter is on the order of 1%/mT in commercial GMR films.

Having described the magnetoresistive response of a simple spin valve and examined the physical origin of this effect, a few varieties of GMR structures are discussed:

4.2.1.3 GMR Unpinned Sandwich

A structure similar to the spin valve is the GMR sandwich, basically a spin valve without the pinning layer (see Figure 4.14(b)). While this historically first GMR structure has a simpler layer composition, its magnetoresistive response is harder to control. This is because both magnetic layers are free to rotate, adding an additional degree of freedom. Sensors using unpinned sandwich material must be carefully designed to achieve a useful response [23, 27, 30]. This response is typically unipolar, has some hysteresis, and is linear in a narrow range (Figure 4.18).

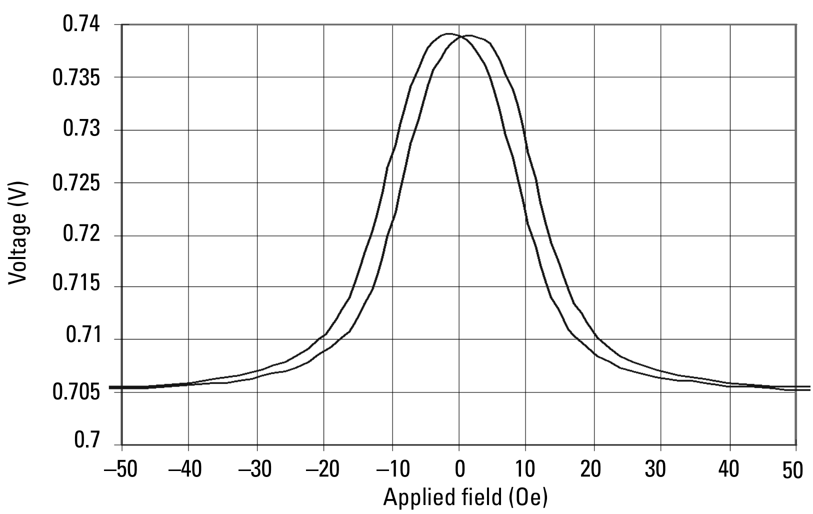

Figure 4.18 GMR sandwich structure output, resistance versus field.

4.2.1.4 GMR Multilayer

If the basic ferromagnet/nonferromagnet/ferromagnet structure is repeated several times, a GMR multilayer is constructed. Multilayer structures typically have higher GMR and higher saturation fields. One significant advantage is that they can be made to have linear output versus field (Figure 4.19) [23].

4.2.2 Tunnel Magnetoresistance (Spin-Dependent Tunneling)

Tunnel magnetoresistance (TMR) was reported in 1991 by Terunobu Miyazaki. The main difference between GMR and TMR is that the nonmagnetic layer is very thin insulator and the current direction is perpendicular to the layer plane. The electrons tunnel through an insulator that is several nanometers thick between the two ferromagnetic layers, which is a quantum mechanical phenomenon [31]. The two main principal advantages of TMR compared to GMR are:

1. In TMR all electrons experience both layers, unlike GMR, in which it is only a small fraction of electrons. As a result, TMR sensitivity is much higher, reaching over 100% in production and 1,000% in the laboratory.
2. TMR devices have a very large range of resistance values possible because the resistance increases strongly with insulator layer thickness. So, low power consumption sensors have relatively thick insulator layers and high-frequency uses such as memory and read heads have thinner insulator layers.

While the details of the conduction mechanisms are quite different, the resistance versus field response of TMR devices can be made to look exactly like that

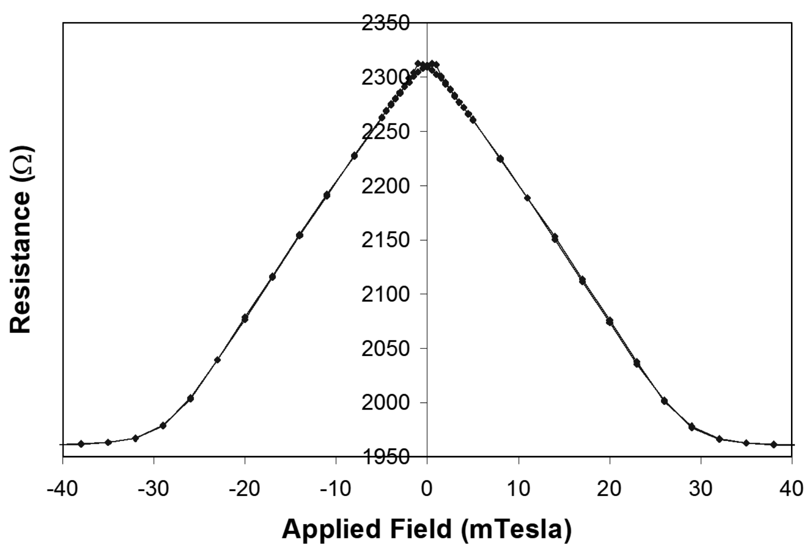

Figure 4.19 GMR multilayer structure output, resistance versus field.

of a GMR spin valve, by pinning the top magnetic layer while having the bottom be magnetically free.

4.2.3 GMR/TMR Sensor Design

4.2.3.1 Micromagnetic Design

Making a useful sensor out of a GMR material requires careful micromagnetic design. Several types of magnetic interactions influence the overall magnetic properties of the GMR sensor:

- Magnetostatic interlayer edge coupling;
- Magnetostatic interlayer coupling (Neel or "orange peel" coupling);
- Sense current field;
- Interlayer exchange coupling;
- Intralayer demagnetizing fields;
- Intralayer anisotropy energies.

All of these fields must be managed to give the resulting magnetoresistive structure high sensitivity to external fields while still having low hysteresis. The design parameters include GMR stripe width, current density, deposition conditions, and material composition.

Of all the interactions listed, interlayer exchange coupling is most unique to GMR systems. The GMR effect was first discovered by researchers looking for evidence of antiparallel interlayer coupling [18]. This coupling causes nearest ferromagnetic layers in an alternating nonmagnetic/ferromagnetic metallic stack to be antiparallelly aligned.

4.2.3.2 GMR/TMR Material Processing Techniques

There are two critical steps in the GMR/TMR material fabrication process: material deposition and resistor patterning.

Film Deposition

For commercial applications, GMR materials are deposited in vacuum systems. The most common arrangements are RF diode sputtering and ion beam sputtering. Many other types of depositions are done in research laboratory environments including evaporation, electrodeposition, molecular beam epitaxy (MBE), and DC magnetron sputtering. Making metallic layers whose thicknesses must be controlled to within fractions of an Angstrom is challenging for any deposition method.

Patterning Techniques

Standard photolithography techniques are used to pattern the wafers full of blank GMR/TMR material into resistors of various values. The material itself can be etched using dilute solutions of acid or ion milling/etching [32]. Because the magnetic behavior of thin ferromagnetic films is sensitive to the shape and texture of the edges, the detailed profile of the etching process is critical. Tapers, "mouse-bites,"

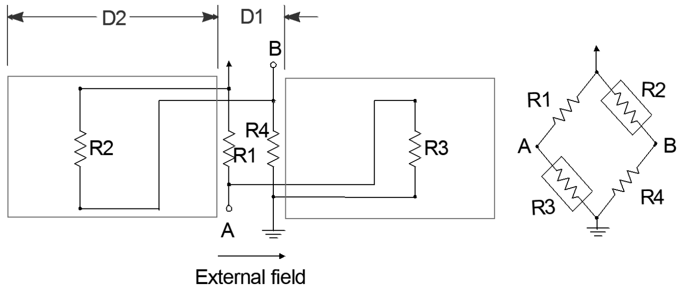

Figure 4.20 A schematic top view of a GMR sensor with D_2 long flux concentrators and D_1 wide gap, GMR resistors both under and between the concentrators, and external interconnects.

oxidation, and corrosion of the magnetic thin film edges all change the magnetization dynamics of the sensor material and potentially ruin the sensor.

4.2.3.3 Sensor Construction

Having good magnetoresistive material is a start towards a good magnetic field sensor, but it is only the beginning. Typically, a finished sensor is made of several GMR resistors in a Wheatstone bridge configuration. In order for the bridge to have a nonzero response, something must be done to make two of the resistors behave differently than the other two in an external field.

In GMR sensors, this is often accomplished with flux concentrators (Figure 4.20). These are two relatively thick (15-μm) formations of permalloy plated directly on the GMR sensor chip. The flux concentrators are positioned so that two of the resistors are in the gap between the two concentrators while the other two resistors are underneath the concentrators. The gap resistors experience a multiplication of the external field by a factor of about the length to gap ratio. The resistors underneath the flux concentrators are effectively shielded from the external field, so their resistance does not change for moderate fields (Figure 4.21).

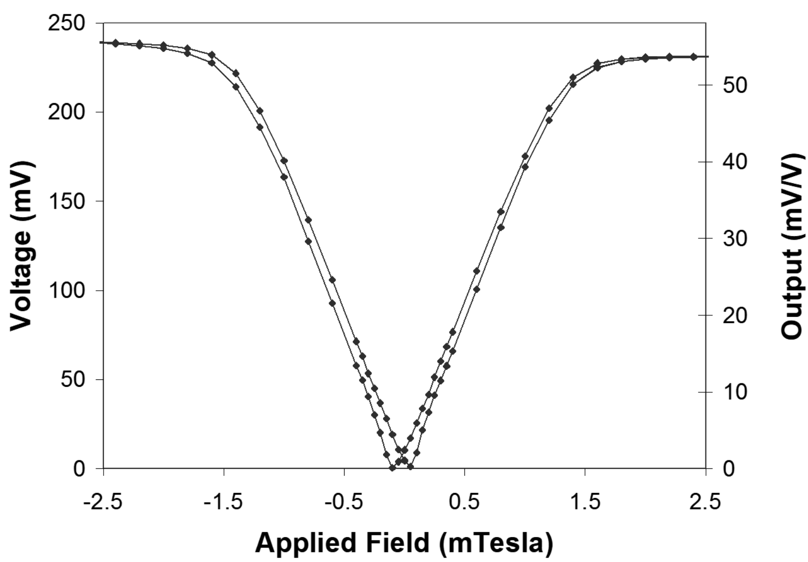

Figure 4.21 Data from an NVE AA00-02 GMR multilayer bridge sensor.

Bipolar Response Using Biasing Coils or Field Lines

Another technique for generating a nonzero output from a bridge is with on-chip planar biasing coils or straight conductor (field line or current strips or stripes). These coils can be used to create a localized field in different directions for different GMR resistors on the chip. This technique can be used to make a sensor with a bipolar response out of material with a unipolar magnetoresistive characteristic (Figures 4.22 and 4.23).

- *Bipolar structures:* GMR or TMR elements can be made to have a bipolar magnetoresistive response, as is typical with the spin valve structure. A bipolar spin valve must be perpendicularly biased to achieve a linear nonhysteretic output rather than a square open-loop-type response [33].

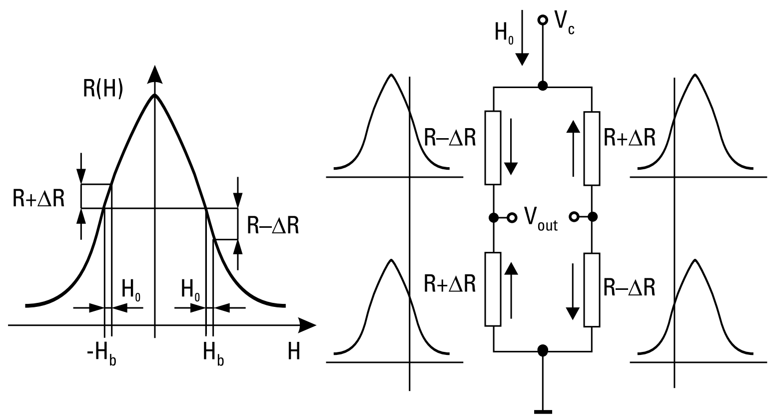

Figure 4.22 A GMR bridge with localized bias.

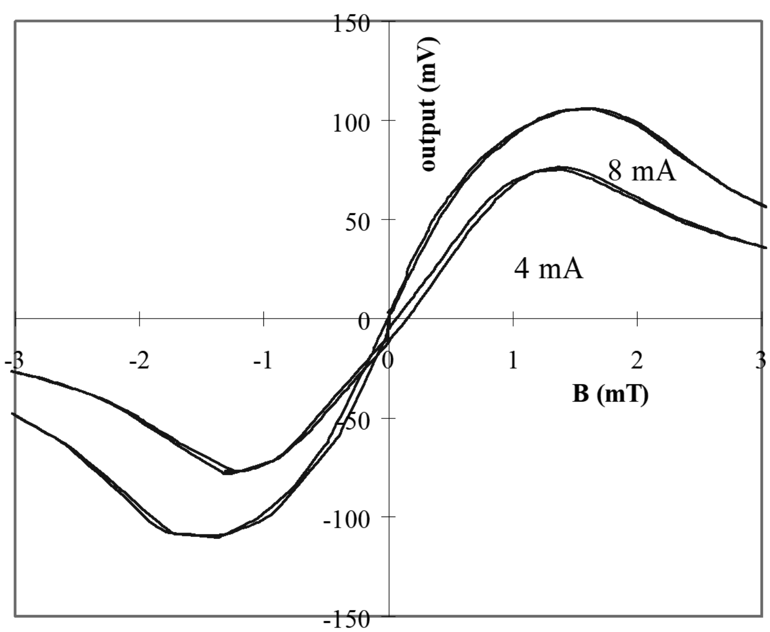

Figure 4.23 The output from a field-biased sandwich material bridge sensor. There are no flux concentrators on this sensor.

A characteristic of a biased TMR resistor is shown in Figure 4.24. Because the basic magnetoresistive response is the same, a similar technique can be used with a GMR spin valve. However, the TMR elements can be any shape and size while the spin valve material must be patterned into long, narrow stripes to get a measurable resistance. Consequently, it is easier to avoid undesirable demagnetizing fields in the TMR structure. The dashed line, included as a guide to the eye, has a slope of about 800 mV/mT.

Some manufacturers of TMR sensors such as Crocus Technology use field lines to magnetize locally the pinned layer into the required direction at elevated temperature. This process is called Differential Thermal Assisted Programming and allows one to set different magnetization directions to different magnetoresistors on the same chip.

A common magnetic tool for getting a linear response from almost any material is to incorporate a feedback coil and measure the current in this coil that is required to keep the sensor's output at a certain value. Flat coils or field lines generate this compensation field.

Using materials with perpendicular anisotropy may allow to build triaxial TMR sensor in the future. Magnetic tunnel junctions based on these materials were developed for spin transfer torque magnetic random access memory (STT-MRAM). Attention is on CoFeB system, which is promising for achieving linear response [34].

- *Gradiometer:* It is also useful to create a bridge whose opposite resistor legs are identical, but separated in space by a relatively large distance. Then the bridge output is nonzero only in the case where the field varies from one end of the sensor to the other. This type of sensor measures the field gradient rather than the absolute field and is very useful for detecting small nearby objects with relatively low magnetizations.
- *Temperature characteristics:* GMR/TMR materials have been shown to be able to operate in environments above 225°C [35]. This is particularly important

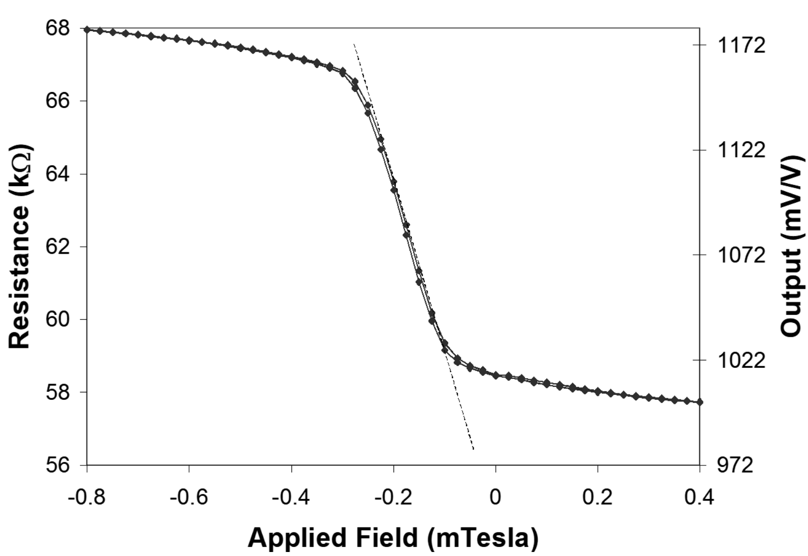

Figure 4.24 A biased TMR resistor.

for applications in the automotive industry. The output of every magnetoresistive sensor has some sensitivity to temperature. These effects come from two sources: (1) the usual increase in R with increasing T for metals, and (2) the decrease in magnetic moment (which ultimately leads to a decrease in GMR signal) with temperature. The resistance decrease with temperature is about 10%/100°C. The GMR decrease with temperature is not consistent from one type of structure to the other, but is on the order of 0.1%/°C at room temperature.

- *Cross-axis sensitivity:* Another operating parameter to consider is the cross-axis sensitivity. In other words, how much does an X-axis sensor react to fields in the Y and Z directions? This parameter can be specified by dividing the off-axis sensitivity by the X-axis sensitivity. GMR sensors have very little off-axis sensitivity to Z-axis fields due to their thin-film (X-Y plane) nature (demagnetizing fields are very strong in the Z direction). However, some designs of magnetoresistive sensors have significant off-axis sensitivity to Y-axis fields (10%). Flux concentrators keep off axis sensitivity to under 1%.
- *Trim sites:* Automated wafer test equipment dramatically improves the productability of GMR/TMR sensors. Sensors are designed with trim sites, which are specially designed links of GMR/TMR material connected in parallel with the other bridge resistors. These links are burned out with a short burst of a laser beam resulting in an increase in the total resistance of a bridge leg. The trimming process takes place with the sensor powered up and exposed to a known field.
- *Packaging:* GMR/TMR material has sufficiently good thermal stability to survive most standard integrated circuit packaging processes, but it is very important to choose a package with minimal magnetic material. This involves careful selection of the lead frame material to which the sensor is bonded and which becomes the pins for the finished package. GMR/TMR sensors can be made to fit inside the smallest available package type. The 8-pin dual in-line (DIP), 8-pin small outline integrated circuit (SOIC), and 4-pin thin small outline package (TSOP) are common GMR/TMR sensor packages.

4.2.4 Magnetoresistance Sensor Applications

Applications of magnetic field sensors are described in Chapter 9 and magnetic sensors for nonmagnetic variables are discussed in Chapter 11. Magnetoresistance sensors are often applied to these practical problems. GMR and TMR sensors have been used for eddy-current nondestructive testing [24, 36–38], electric current sensing [39–42], position sensing [43, 44], 3-D magnetic imaging [45, 46], detection of vehicles [47], and security [48]. Next we briefly discuss some of the specific uses of magnetoresistive sensors:

- *Magnetic particle detection:* GMR, and especially TMR, sensors can be easily designed to have dimensions on the order of ~1 μm. Magnetic particles such as those that are used in biochemical and chemical analysis, concentration, and separation are of that order or even smaller (10-nm diameter). When magnetic beads may be in close distance from the sensor of this size, the signal-to noise ratio is significantly better compared to larger sensors [49, 50].

- *Magnetic reading heads for currency detection:* Magnetic ink is used in most currencies, checks, and other financial instruments. Magnetic sensors can detect these inks and help sort currency and detect bogus currency. The main advantage of magnetoresistance here is the signal size in a small area. Because the sensor must be separated from the currency by 1 mm or more and the amount of magnetic ink is very small, the magnetic signal is at a premium. The ability to put an array of magnetoresistance sensors in a small area is an advantage for currency sensing.
- *Signal isolator:* To this point, the only purposes mentioned for on-chip planar coils have been for generating biasing and feedback fields, but a very important use of these coils is in a digital signal isolator.
- *Memory:* A digital memory circuit can be made by fabricating an array of bits, each of which is a tiny GMR or TMR sensor. This type of memory, magnetoresistive random access memory (MRAM), is nonvolatile. This means that it does not lose its information when the power is removed from the memory [51]. Despite long and massive efforts, these memories never found a way to the market.
- *Hard disk drive read-heads:* While read-heads are far and away the highest-volume TMR sensor application, a detailed discussion of that specific product is left to other writers.

4.3 Operating Parameters of Magnetoresistive Sensors

4.3.1 Noise

The noise of magnetoresistive sensors is extremely difficult to measure, as the corresponding voltage noise is very low. The magnetic noise of several types of commercial magnetoresistive sensors was compared in [52]. For the measured AMR and GMR sensors, both electric and magnetic components contribute to the overall sensor noise. This paper is also a reference for methodology and instrumentation of magnetic sensor noise. Maximum noise occurs at the bias field which gives maximum sensitivity. The noise of TMR-based sensors is primarily due to resistance fluctuations in the tunnel barrier, having little to no field dependence. The best low-field detectivity of the MR sensors that have been measured is on the order of 100 pT/√Hz at 1 Hz (Figure 4.25).

The noise of Honeywell HMC1021 AMR sensor with 400 Hz flipping was 100 pT/√Hz at 1 Hz [14]. The noise power density spectrum is shown in Figure 4.26: it has 1/*f* character up to frequency of about 5 Hz.

The temperature dependence of noise was measured for AMR and GMR sensors in [53]. Room-temperature noise of the AMR sensor AFF755 by Sensitec was 1 nT/Hz at 1 Hz and dropped to 700 pT/√Hz at 142°C. The noise of Sensitec GF 708 GMR sensor was 40 nT/√Hz at 1 Hz and it was temperature-independent.

Noise in TMR sensors is analyzed in [54]. Field noise reduction and strong reduction of 1/*f* corner frequency in TMR sensors can be achieved by introducing perpendicular anisotropy and subsequent reduction of sensitivity [55]. Figure 4.27 shows the noise spectra for AMR, GMR, and TMR sensors as well as fluxgates and Hall sensor. The minimum noise of commercially available TMR sensor TMR 9001

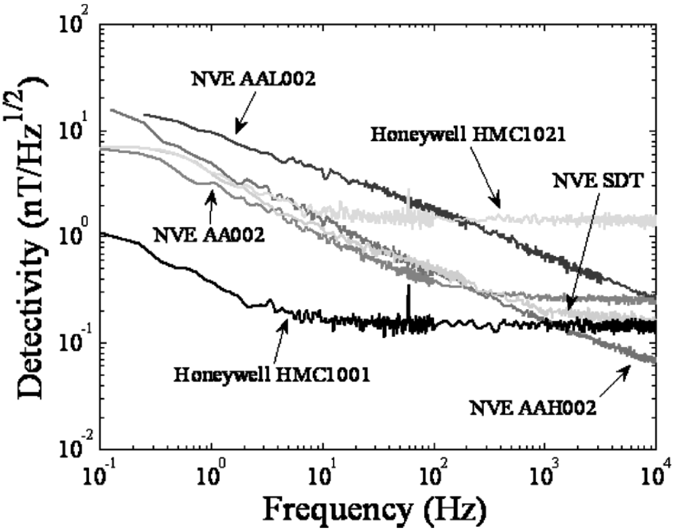

Figure 4.25 Detectivity of various commercial magnetoresistive sensors. (Reprinted from [52], with the permission of AIP Publishing.)

was 120 pT/√Hz at 1 Hz. TMR sensor prototype TMR-J1 with 9 × 9-mm chip size with flux concentrators reached 60 pT/√Hz at 1 Hz [56] which is comparable to 55 pT/√Hz at 1 Hz reported for AMR magnetometer [14]. TMR sensors without field concentrators have noise larger than 1 nT/√Hz at 1 Hz [33].

4.3.2 Field Range and Linearity

Magnetoresistive sensors cover a broad range of fields from 1 nT up to 1 T. AMR sensors usually have a maximum 1-mT range, and the range limit of GMR sensors

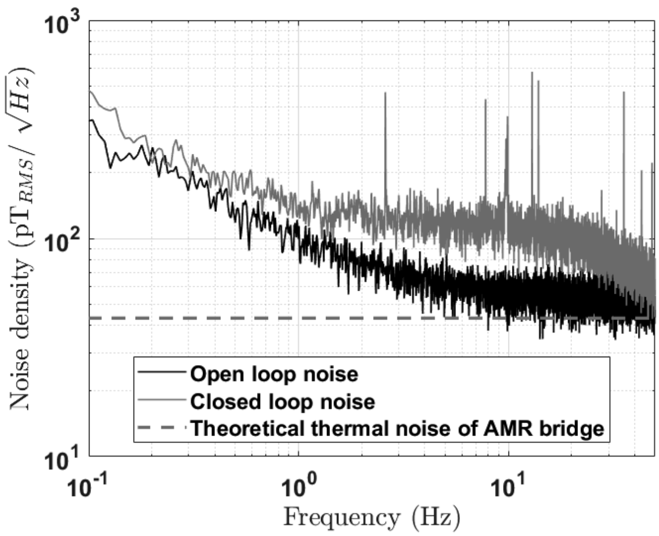

Figure 4.26 Noise spectrum of Honeywell HMC1021 AMR sensor with 400-Hz flipping. Courtesy of D. Novotný.

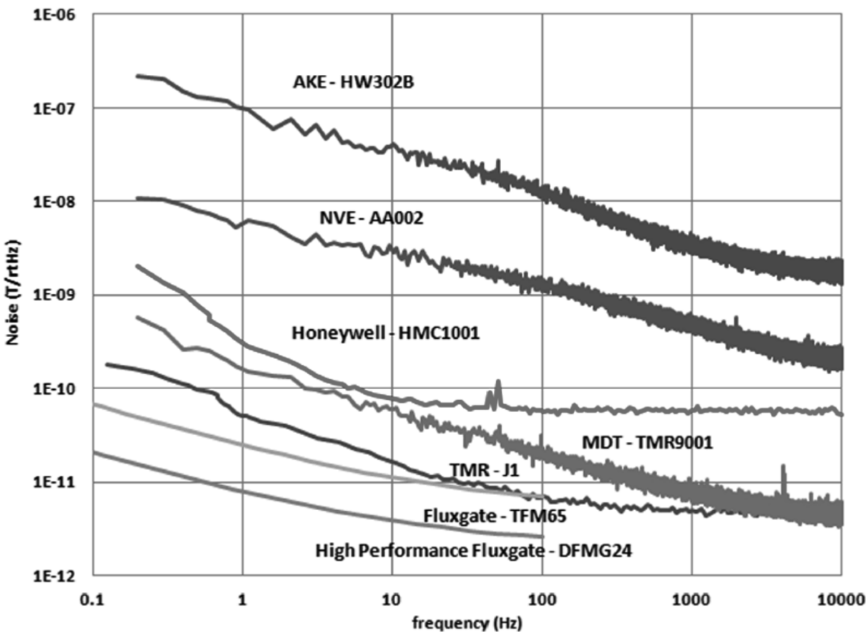

Figure 4.27 Noise of InSb Hall (AKE), AMR (Honeywell), GMR (NVE), TMR (MDT) and fluxgate (Billingsley) sensors. (*From:* [56] (CC BY).) AMR sensor without flipping, which reduces noise.

is usually 10 mT. The maximum range limit for TMR sensors is 1 T (TMR sensor AAKT001 with unipolar characteristics). The very large field range is probably due to internal shielding, but no details are available from the manufacturer. The linearity of magnetoresistive sensors in the open loop is usually 1% to 5%, and feedback-compensated magnetoresistors have a linearity error from 0.1% to 100 ppm.

4.3.3 Offset, Offset Drift, and Hysteresis

A weak point of GMR and TMR sensors is high offset and poor offset temperature stability. This may be partially caused by internal flux concentrators, which cannot be easily demagnetized. All magnetoresistive sensors display significant hysteresis. These parameters are often missing in the datasheets or they are masked by using misleading units. The disadvantage of precise AMR sensors is their large power consumption, especially if they are in feedback and flipping mode (S/R on). Some GMR and TMR sensors have locally oriented bias layers that can be remagnetized by a strong external field. If this happens, some sensors are permanently shifted or even destroyed (such as CT 100 by Crocus), while the others (such as TMR9002 by MDT) can be restored by applying a short pulse of a large current to the internal current strap. The pulse parameters are similar to the flipping current of the AMR sensor (2.5A/several μs).

Table 4.2 compares key properties of precise AMR, GMR, and TMR sensors and magnetometers based on AMR magnetoresistors.

Table 4.2 Commercially Available Precise Magnetoresistors

	HMC1021 Honeywell	*HMC1001 Honeywell*	*AA002 NVE*	*CT100 Crocus*	*TMR9002 MDT*
Technology	AMR		GMR	GMR	TMR
	Precise magnometer [14], feedback compensated	Module open loop, S/R on	Unipolar sensor	Bipolar sensor	Linear low-field sensor
Noise pT/√Hz at 1 Hz	100	500	6,000		150
Offset		20 nT < 60 nT		1 mT	15 µT
Offset drift (nT/K)	0.1	20		600	
Gain drift (ppm/K)	200	–600	+/–3,000	–350	–287
Hysteresis		0.1% < 0.2 µT (200-µT sweep)	40 µT, 4%	0.05%	0.2%
Linearity	50 ppm	0.1% (<2%)	2%	0.5%	0.5%
Range	0.15 mT	0.2 mT	1 mT	20 mT	0.1 mT
Max. field	∞	∞		0.2T	0.4T
Supply power/ current	0.3 W/axis	35 mA	1–5 mA	0.3 mW	20 µA

References

[1] Tumanski, S., *Thin Film Magnetoresistive Sensors*, Boca Raton, FL: CRC Press, 2001.

[2] Mapps, D. J., "Magnetoresistive Sensors," *Sensors and Actuators A: Physical*, Vol. 59, No. 1-3, April 1997, pp. 9–19.

[3] Zheng, C., et al., "Magnetoresistive Sensor Development Roadmap (Non-Recording Applications)," *IEEE Transactions on Magnetics*, Vol. 55, No. 4, April 2019.

[4] Mallinson, J. C., *Magneto-Resistive Heads*, San Diego, CA: Academic Press, 1996.

[5] McGuire, T. R., and R. I. Potter, "Anisotropic Magnetoresistance in Ferromagnetic 3D Alloys," *IEEE Transactions on Magnetics*, Vol. 11, No. 4, 1975, pp. 1018–1038.

[6] McCord, J., et al., "Domain Observation on Magnetoresistive Sensor Elements," *IEEE Transactions on Magnetics*, Vol. 32, No. 5, September 1996, pp. 4806–4808.

[7] Feng, J. S. Y., L. T. Romankiw, and D. A. Thompson, "Magnetic Self-Bias in the Barber Pole MR Structure," *IEEE Transactions on Magnetics*, Vol. 13, No. 5, 1977, pp. 1466–1468.

[8] Ripka, P., and M. Butta, "Origin of the Crossfield Effect in AMR Sensors," *Sensor Letters*, Vol. 7, No. 3, 2009, pp. 259–262.

[9] Ripka, P., J. Vyhnanek, and A. Chirtsov, "Crossfield Response of Industrial Magnetic Sensors," *International Journal of Applied Electromagnetics and Mechanics*, Vol. 55, 2017, pp. S39–S47.

[10] Hauser, H., et al., "Flipping Field and Stability in Anisotropic Magnetoresistive Sensors," *Sensors and Actuators A: Physical*, Vol. 106, No. 1-3, 2003, pp. 121–125.

[11] Mohamadabadi, K., C. Coillot, and M. Hillion, "New Compensation Method for Cross-Axis Effect for Three-Axis AMR Sensors," *IEEE Sensors Journal*, Vol. 13, No. 4, April 2013, pp. 1355–1362.

[12] Petrucha, V., V. Fura, and A. Platil, "Cross-Field Effect in a Triaxial AMR Magnetometer with Vector and Individual Compensation of a Measured Magnetic Field," *IEEE Transactions on Magnetics*, Vol. 53, No. 4, April 2017.

[13] Mlejnek, P., M. Vopálenský, and P. Ripka, "AMR Current Measurement Device," *Sensors and Actuators A: Physical*, Vol. 141, No. 2, 2008, pp. 649–653.

[14] Novotny, D., V. Petrucha, and M. Janosek, "A Digitally Compensated AMR Magnetometer," *IEEE Transactions on Magnetics*, Vol. 55, No. 1, January 2019.

[15] Brown, P., et al., "Space Magnetometer Based on an Anisotropic Magnetoresistive Hybrid Sensor," *Review of Scientific Instruments*, Vol. 85, No. 12, December 2014.

[16] Leitner, S., et al., "Design of the Magnetoresistive Magnetometer for ESA's SOSMAG Project," *IEEE Transactions on Magnetics*, Vol. 51, No. 1, January 2015.

[17] Schulz, L., P. Heinisch, and I. Richter, "Calibration of Off-the-Shelf Anisotropic Magnetoresistance Magnetometers," *Sensors*, Vol. 19, No. 8, April 2019.

[18] Grunberg, P., et al., "Layered Magnetic Structures: Evidence for Antiferromagnetic Coupling of Fe Layers Across Cr Interlayers," *Physical Review Letters*, Vol. 57, No. 19, November 1986, pp. 2442–2445.

[19] Baibich, M. N., et al., "Giant Magnetoresistance of (001)Fe/(001)Cr Magnetic Superlattices," *Physical Review Letters*, Vol. 61, No. 21, November 1988, pp. 2472–2475.

[20] Binasch, G., et al., "Enhanced Magnetoresistance in Layered Magnetic Structures with Antiferromagnetic Interlayer Exchange," *Physical Review B*, Vol. 39, No. 7, March 1989, pp. 4828–4830.

[21] Parkin, S. S. P., R. Bhadra, and K. P. Roche, "Oscillatory Magnetic Exchange Coupling Through Thin Copper Layers," *Physical Review Letters*, Vol. 66, No. 16, April 1991, pp. 2152–2155.

[22] Tsang, C., et al., "Design, Fabrication and Testing of Spin-Valve Read Heads for High Density Recording," *IEEE Transactions on Magnetics*, Vol. 30, No. 6, November 1994, pp. 3801–3806.

[23] Daughton, J., et al., "Magnetic Field Sensors Using GMR Multilayer," *IEEE Transactions on Magnetics*, Vol. 30, No. 6, November 1994, pp. 4608–4610.

[24] Romero-Arismendi, N. O., et al., "Design Method for a GMR-Based Eddy Current Sensor with Optimal Sensitivity," *Sensors and Actuators A: Physical*, Vol. 314, October 2020.

[25] Parkin, S. S. P., N. More, and K. P. Roche, "Oscillations in Exchange Coupling and Magnetoresistance in Metallic Superlattice Structures: Co/Ru, Co/Cr, and Fe/Cr R," *Physical Review Letters*, Vol. 64, No. 19, May 1990, pp. 2304–2307.

[26] Reig, C., S. Cardoso de Freitas, and S. Mukhopadhyay, *Giant Magnetoresistance (GMR) Sensors*, New York: Springer, 2013.

[27] Weiss, R., R. Mattheis, and G. Reiss, "Advanced Giant Magnetoresistance Technology for Measurement Applications," *Measurement Science and Technology*, Vol. 24, No. 8, August 2013.

[28] Freitas, P. P., et al., "Magnetoresistive Sensors," *Journal of Physics-Condensed Matter*, Vol. 19, No. 16, April 2007.

[29] Freitas, P. P., R. Ferreira, and S. Cardoso, "Spintronic Sensors," *Proceedings of the IEEE*, Vol. 104, No. 10, October 2016, pp. 1894–1918.

[30] Liu, S., et al., "Experimental Research on Hysteresis Effects in GMR Sensors for Analog Measurement Applications," *Sensors and Actuators A: Physical*, Vol. 182, August 2012, pp. 72–81.

[31] Moodera, J. S., and L. R. Kinder, "Ferromagnetic-Insulator-Ferromagnetic Tunneling: Spin-Dependent Tunneling and Large Magnetoresistance in Trilayer Junctions," *Journal of Applied Physics*, Vol. 79, No. 8, April 1996, pp. 4724–4729.

[32] Wongpanit, N., P. O. A. Persson, and S. Tungasmita, "Etching Behaviors of Tunneling Magnetoresistive (TMR) Materials by Ion Beam Etching System," *Materials Today-Proceedings*, Vol. 5, No. 7, 2018, pp. 15186–15191.

[33] Rasly, M., et al., "Magnetic, Magnetoresistive and Low-Frequency Noise Properties of Tunnel Magnetoresistance Sensor Devices with Amorphous CoFeBTa Soft Magnetic Layers," *Journal of Physics D-Applied Physics*, Vol. 54, No. 9, March 2021.

[34] Lei, Z. C., et al., "High TMR for Both In-Plane and Perpendicular Magnetic Field Justified by CoFeB Free Layer Thickness for 3-D MTJ Sensors," *AIP Advances*, Vol. 9, No. 8, August 2019.

[35] Wang, D., J. Anderson, and J. M. Daughton, "Thermally Stable, Low Saturation Field, Low Hysteresis, High GMR CoFe/Cu Multilayers," *IEEE Transactions on Magnetics*, Vol. 33, No. 5, September 1997, pp. 3520–3522.

[36] Bernieri, A., et al., "Eddy Current Testing Probe Based on Double-Coil Excitation and GMR Sensor," *IEEE Transactions on Instrumentation and Measurement*, Vol. 68, No. 5, May 2019, pp. 1533–1542.

[37] Park, J. W., et al., "Enhanced Detection of Defects Using GMR Sensor Based Remote Field Eddy Current Technique," *Journal of Magnetics*, Vol. 22, No. 4, December 2017, pp. 531–538.

[38] Ye, C. F., et al., "Frequency Domain Analysis of Magnetic Field Images Obtained Using TMR Array Sensors for Subsurface Defect Detection and Quantification," *NDT & E International*, Vol. 116, December 2020.

[39] Musuroi, C., et al., "High Sensitivity Differential Giant Magnetoresistance (GMR) Based Sensor for Non-Contacting DC/AC Current Measurement," *Sensors*, Vol. 20, No. 1, January 2020.

[40] Mattheis, R., M. Diegel, and R. Weiss, "Giant Magnetoresistance-Stack Optimization for Current Sensor Application with Low Hysteresis and a Temperature-Independent Sensitivity at Low Current," *IEEE Transactions on Magnetics*, Vol. 52, No. 10, October 2016.

[41] De Marcellis, A., et al., "Monolithic Integration of GMR Sensors for Standard CMOS-IC Current Sensing," *Solid-State Electronics*, Vol. 135, September 2017, pp. 100–104.

[42] Zhang, H. Q., et al., "Current Measurement with 3-D Coreless TMR Sensor Array for Inclined Conductor," *IEEE Sensors Journal*, Vol. 19, No. 16, August 2019, pp. 6684–6690.

[43] Muna, Y. B., and C. C. Kuo, "Magnetic Field Distribution of Magnetic Encoder with TMR Sensor Using Finite Element Analysis," *Microsystem Technologies-Micro-and Nanosystems-Information Storage and Processing Systems*, Vol. 26, No. 8, August 2020, pp. 2683–2701.

[44] Bhaskarrao, N. K., C. S. Anoop, and P. K. Dutta, "Oscillator-Less Direct-Digital Front-End Realizing Ratiometric Linearization Schemes for TMR-Based Angle Sensor," *IEEE Transactions on Instrumentation and Measurement*, Vol. 69, No. 6, June 2020, pp. 3005–3014.

[45] Hadadeh, F., et al., "3D Magnetic Imaging with GMR Sensors," *IEEE Sensors Journal*, Vol. 19, No. 22, November 2019, pp. 10403–10408.

[46] Ye, C. F., Y. Wang, and Y. Tao, "High-Density Large-Scale TMR Sensor Array for Magnetic Field Imaging," *IEEE Transactions on Instrumentation and Measurement*, Vol. 68, No. 7, July 2019, pp. 2594–2601.

[47] Huang, C. C., et al., "Vehicle Parking Guidance for Wireless Charge Using GMR Sensors," *IEEE Transactions on Vehicular Technology*, Vol. 67, No. 8, August 2018, pp. 6882–6894.

[48] Gao, J. Q., et al., "Magnetic Signature Analysis for Smart Security System Based on TMR Magnetic Sensor Array," *IEEE Sensors Journal*, Vol. 19, No. 8, April 2019, pp. 3149–3155.

[49] Crespo, R. D., et al., "Optimizing the Sensitivity of a GMR Sensor for Superparamagnetic

Nanoparticles Detection: Micromagnetic Simulation," *Journal of Magnetism and Magnetic Materials*, Vol. 446, January 2018, pp. 37–43.

[50] Wang, M. L., et al., "Imaging of Magnetic Nanoparticles Using Small TMR Sensor with an Excitation-Compensation Scheme," *IEEE Sensors Journal*, Vol. 20, No. 19, October 2020, pp. 11082–11089.

[51] Atasoyu, M., M. Altun, and S. Ozoguz, "Sensing Schemes for STT-MRAMs Structured with High TMR in Low RA MTJs," *Microelectronics Journal*, Vol. 89, July 2019, pp. 30–36.

[52] Stutzke, N. A., et al., "Low-Frequency Noise Measurements on Commercial Magnetoresistive Magnetic Field Sensors," *Journal of Applied Physics*, Vol. 97, No. 10, May 2005.

[53] Nording, F., et al., "Measurement System for Temperature Dependent Noise Characterization of Magnetoresistive Sensors," *Review of Scientific Instruments*, Vol. 88, No. 3, March 2017.

[54] Stearrett, R., et al., "Influence of Exchange Bias on Magnetic Losses in CoFeB/MgO/CoFeB Tunnel Junctions," *Physical Review B*, Vol. 86, No. 1, July 2012.

[55] Wisniowski, P., M. Dabek, and J. Wrona, "Field Noise in Tunneling Magnetoresistance Sensors with Variable Sensitivity," *Applied Physics Letters*, Vol. 106, No. 5, February 2015.

[56] Deak, J. G., Z. M. Zhou, and W. F. Shen, "Tunneling Magnetoresistance Sensor with pT Level 1/f Magnetic Noise," *AIP Advances*, Vol. 7, No. 5, May 2017.

CHAPTER 5

Hall-Effect Magnetic Sensors

Radivoje S. Popovic, Christian Schott, Ichiro Shibasaki, James R. Biard, Ronald B. Foster, and Pavel Ripka

Magnetic field sensors based on the Hall effect are probably the most widely used magnetic sensors. Interestingly, Hall magnetic sensors are relatively rarely used to measure just a magnetic field. Much more frequently, they are used as a key component in contactless sensors for linear position, angular position, velocity, rotation, and current. We estimate that the annual production of Hall magnetic sensors is more than 2 billion pieces. There is hardly any new car in the world without a dozen of Hall magnetic sensors inside, used mostly as position sensors; millions of ventilators and millions of disk drives in personal computers use brushless motors with Hall magnetic sensors inside; and millions of current sensors in various products depend also on Hall magnetic sensors. Moreover, the world production of Hall magnetic sensors is still increasing, and the application area is becoming ever broader. Although most of the Hall sensors are switches that have binary output, this chapter only deals with linear sensors.

Apart from their simplicity and good characteristics, such a big importance of Hall magnetic sensors is also due to their almost perfect compatibility with microelectronics technology. The optimal material characteristics, device structures and dimensions, and fabrication processes are similar to those readily available in semiconductor industry. Therefore, the development in Hall mˆagnetic sensors does not require much of specific investments in fabrication processes, in contrary to the case with all other magnetic sensors.

In terms of physical parameters, Hall magnetic sensors usually perform well in the following areas: at magn¶7etic flux densities higher than 1 mT, temperatures between −100°C and +100°C, and frequencies from DC to 30 kHz. The exact values of these parameters depend on material and design of a Hall device and may be considerably different in particular cases. Silicon-based CMOS sensors work only in the industrial temperature range −50°C/+125°C as they suffer of electron freeze-out at lower temperatures. The III-V semiconductor-based sensors work well even at cryogenic temperatures, while gallium nitride AlGaN/GaN sensors work at very high temperatures up to 500°C. High-end devices can measure with micro-tesla resolution.

At present, most of currently applied Hall magnetic sensors are low-cost, discrete devices. However, an ever-increasing proportion of them comes in the form of integrated circuits (ICs). The integration offers an opportunity to apply the system approach to improve the performance in spite of the mediocre characteristics of the basic Hall cells. Moreover, the integrated Hall magnetic sensors are smart:

they usually incorporate means for biasing, offset reduction, temperature compensation, signal amplification, signal level discrimination, and so on. They also have an ability to communicate digitally in both directions and perform autocalibration and diagnostics.

A note on the terminology: A basic device exploiting the Hall effect in the form similar to that in which it was discovered is usually called a Hall device, Hall element, or a Hall cell. In the magnetic field measurement community, a Hall magnetic field sensor, packaged in a suitable case, is normally referred to as a Hall probe. An IC, incorporating a combination of a Hall device with electronic circuitry, is often called an integrated Hall-effect sensor or just a Hall IC.

In this chapter, we first briefly discuss some basics of the Hall effect and Hall magnetic sensors (Section 5.2). Then, in the 3 subsequent sections, we present the three areas of, in our opinion, the highest practical importance in the field: high-mobility discrete Hall plates (Section 5.3), integrated Hall sensors (Section 5.4), and the technology of nonplate-like Hall sensors (Section 5.5).

5.1 Basics of the Hall Effect and Hall Devices

In this section, we present a summary of the physics of Hall magnetic sensors and discuss their basic characteristics. We limit the depth of the explanations to a level providing the basis for the following sections. The interested reader can find a more detailed treatment of the subject in monographs on Hall-effect devices by Popovic and Ramsden [1, 2]. While Popovic made an analysis of the Hall effect as a function of material properties, and he described the art of Hall sensors design, the book by Ramsden is more oriented on applications. In this book, we concentrate on the ordinary Hall effect, which is the only Hall effect having real sensor applications. The overview of all other Hall effects was made in the comprehensive review by Karsenty [3]. The most important of them is the quantum Hall effect, which is used in metrology. Much information on the modern Hall theory can be found in works of Ausserlechner et al. [4, 5].

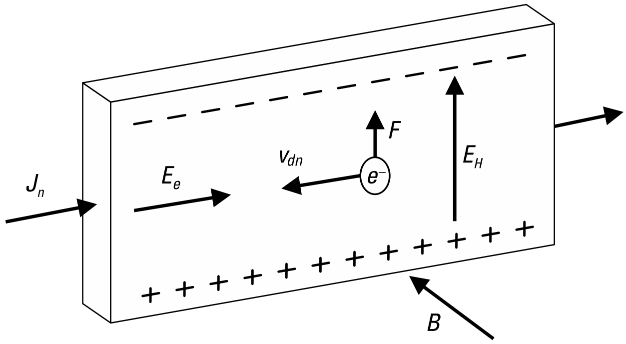

Figure 5.1 The Hall effect in long samples of n-material. The magnetic forces press the electrons towards the upper boundary of the strip so that a Hall voltage appears between the charged edges of the strips.

5.1.1 The Hall Effect

The Hall effect is the best known among the physical effects arising in a condensed matter carrying electrical current in the presence of a magnetic field. The effect is named after E. H. Hall, who discovered it in 1879.

The Hall effect shows up in its classical and simplest form when a long current-carrying strip is exposed to a DC magnetic field (Figure 5.1). All charge carriers in the strip are then affected by the Lorentz force:

$$\mathbf{F} = q \cdot \mathbf{E} + q[\mathbf{v} \times \mathbf{B}] \tag{5.1}$$

Here q denotes the electrical charge of a carrier, $\mathbf{E}$ is the local electrical field, $\mathbf{v}$ is the velocity of a charge carrier, and $\mathbf{B}$ is the magnetic flux density, which we take to be perpendicular to the strip plane.

Let us assume that the strip material is a strongly extrinsic n-type semiconductor. So we neglect the presence of holes. Along the length of the strip, in the x-direction, an external electrical field $\mathbf{E}_E$ is applied. Most of the electrical field $\mathbf{E}$ in (5.1) is due to this external field. The electrons respond to the external electrical field by moving along the strip with the average drift velocity

$$\mathbf{v}_{dn} = \mu_n \cdot \mathbf{E}_E \tag{5.2}$$

where μ_n is the drift mobility of electrons. The associated current density is given by

$$J_n = q \cdot n \cdot \mu_n \cdot \mathbf{E}_E \tag{5.3}$$

where n is the density of free electrons and q is the elementary charge.

The carrier velocity $\mathbf{v}$ in (5.1) is due to thermal agitation and drift. Let us neglect for a moment the thermal motion. Then the magnetic part of the Lorentz force (5.1) is given by

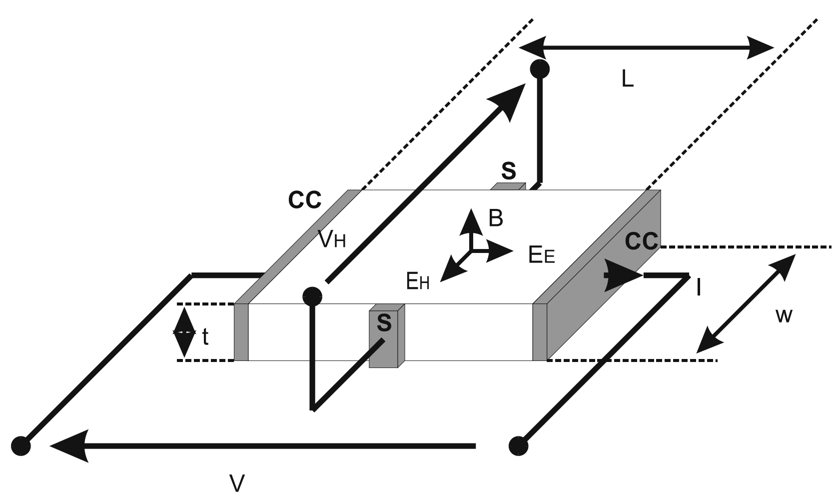

Figure 5.2 Conventional Hall sensor in the shape of a plate.

$$\mathbf{F}_{mn} = q \cdot \mu_n \left[\mathbf{E}_E \times \mathbf{B}\right] \tag{5.4}$$

This force pushes the electrons towards the upper edge of the strip. Consequently, the electron concentration at the upper edge of the strip increases and that at the lower edge decreases. Due to these space charges, an electrical field appears between the strip edges. This electrical field, denoted by $\mathbf{E}_H$ in Figure 5.1, acts on the electrons by a force

$$\mathbf{F}_{en} = -q \cdot \mathbf{E}_H \tag{5.5}$$

This force tends to decrease the excess charges at the edges of the strip. At steady state, the two transverse forces $\mathbf{F}_{mn}$ and $\mathbf{F}_{en}$ balance. By equating (5.4) and (5.5), we find

$$\mathbf{E}_H = -\mu_{Hn} \left[\mathbf{E}_E \times \mathbf{B}\right] \tag{5.6}$$

The transverse electric field $\mathbf{E}_H$ is called the Hall electric field. We use here the approximate sign since we neglected above the thermal agitation of the charge carriers. Nevertheless, (5.6) is a surprisingly close approximation of the accurate result. Without neglecting the thermal agitation of electrons, one obtains, instead of (5.6),

$$\mathbf{E}_H = -\mu_{Hn} \left[\mathbf{E}_E \times \mathbf{B}\right] \tag{5.7}$$

Here μ_{Hn} denotes the Hall mobility of electrons. The Hall mobility differs a little from the drift mobility: it is given by

$$\mu_{Hn} = r_H \cdot \mu_n \tag{5.8}$$

where r_H is the Hall scattering factor. In most cases, r_H differs less than 20% from unity.

According to (5.6) and (5.7), the Hall electrical field is proportional to the externally applied electrical and magnetic fields. The proportionality coefficient is the carrier mobility. This gives us the first idea about suitable materials to make a magnetic sensor based on the Hall effect: this should be a high mobility material. Since the mobility of electrons is always higher than the mobility of holes, it is better to use an n-type rather than a p-type semiconductor.

Another useful expression for the Hall electrical field is obtained when the external electrical field in (5.6) is expressed by the current density (5.3):

$$\mathbf{E}_H = -R_H \left[\mathbf{J} \times \mathbf{B}\right] \tag{5.9}$$

Here R_H denotes the Hall coefficient, in our case given by

$$R_H \approx \frac{1}{q \cdot n} \tag{5.10}$$

Here again we use the approximate sign since we neglected the thermal agitation of charge carriers. Without neglecting their thermal agitation, one obtains, instead of (5.10),

$$R_H = \frac{r_{\mathrm{H}}}{q \cdot n} \tag{5.11}$$

This gives us another criterion for the choice of the material for a Hall magnetic sensor: this should be a relatively low-doped semiconductor material.

When more than one type of charge carriers is present and/or the material is anisotropic, the Hall coefficient takes a more complicated form. However, if one type of carrier is predominant in terms of the product concentration times mobility, then the equation of the type (5.11) gives a good approximation for the Hall coefficient.

The most tangible thing associated with the Hall effect is the appearance of a measurable voltage between the edges of the strip. This voltage is known as the Hall voltage. With reference to Figure 5.1, let us chose two points M and N at the opposite edges of the strip so that the potential difference between them is zero when $\mathbf{B} = 0$. Then the Hall voltage is given by

$$V_H = \int_{S_1}^{S_2} E_H \, ds \tag{5.12}$$

In our particular case, we find

$$V_H = \mu_{Hn} \cdot \mathbf{E}_E \cdot \mathbf{B} \cdot w \tag{5.13}$$

where w denotes the width of the strip. Note that we assume here that the magnetic flux density vector **B** is perpendicular to the strip plane; otherwise, we have to replace **B** in (5.13) by the perpendicular component of **B**, which we denote by $\mathbf{B}_\perp$.

We may obtain another useful expression for the Hall voltage when we combine (5.3) and (5.13) and take into account that the current density in the strip is given by

$$J = \frac{I}{t \cdot w} \tag{5.14}$$

Here I denotes the current in the strip and t is the thickness of the strip. So the Hall voltage is also given by

$$V_H = \frac{R_H}{t} \cdot I \cdot B \tag{5.15}$$

This equation gives us an idea about another characteristics of a Hall magnetic sensor: a Hall magnetic sensor has usually the form of a thin plate with a low sheet electron density. Some Hall devices are truly 2-D: in such a case, we use sheet current density J_s instead of J.

Let us estimate the value of the Hall voltage in a typical Hall sensor application: take $n = 5 \cdot 10^{15}$ cm^{-3}, $t = 4$ μm, $I = 1$ mA, and $B_| = 100$ mT; then $V_H \sim 30$ mV.

5.1.2 Structure and Geometry of a Hall Device

In accordance with the conclusions that we drew in the previous section, we could imagine a practical Hall magnetic sensor as shown in Figure 5.2: a piece of a strip of n-type semiconductor material, fitted with four ohmic contacts at its periphery. The electrical energy is supplied to the device via two of the contacts, called the current contacts (CC) or the input terminals. The other two contacts are placed at two equipotential points at the plate boundary. These two contacts are used to retrieve the Hall voltage. They are called the voltage contacts or the sense contacts (S) or the output terminals. Some early Hall devices really had such a form, with the dimensions (L and W) of several millimeters. Most of modern Hall magnetic sensors are much smaller, but still have a general structure reminiscent of that in Figure 5.2. This is why a Hall device is often called a Hall plate.

Apart from the simple rectangular shape shown in Figure 5.2, many other shapes are possible, such as a square, an octagon, or a cross. All these shapes could be transformed into each other by conformal mapping [1]. Therefore, in the ideal case, the basic characteristics of a Hall device are not dependent on its general shape. However, the sensitivity of a Hall device to the parasitic effects, such as fabrication tolerances, may depend a lot on the basic shape of the device. The most commonly used shapes of Hall devices will be presented in the next sections in the examples of technological realizations of Hall magnetic sensors.

A particularly important issue in the geometry of a Hall device is the relative size of the contacts. If a contact is very small, then the contribution of the semiconductor material resistance adjacent to the contact to the total device resistance may be too high. If a sense contact covers an essential portion of the device periphery, it will short-circuit part of the bias current, and the Hall voltage will be lower than expected; similarly, if a current contact is large, it will short-circuit a part of the Hall voltage.

The influence of the geometry of a Hall plate, including the geometry of the contacts, can be represented by the geometrical correction factor G. This factor describes the diminution of the Hall voltage in a Hall device due to the above short-circuiting effects. Let us denote the actually measured Hall voltage by V_H and that of a hypothetical corresponding point-contact Hall device by $V_{H\sim}$. Then the geometrical correction factor is defined as

$$G = \frac{V_H}{V_{H\sim}} \tag{5.16}$$

Theoretically, $0 < G < 1$. In practical Hall devices, we usually find the values of G between 0.7 and 0.9.

Using the notion of G, we may now correct (5.15), which was developed for the case of an infinitely long strip. In a real Hall device, the Hall voltage is given by

$$V_H = G \cdot \frac{R_H}{t} \cdot I \cdot B \tag{5.17}$$

This is probably the most often used equation in the field of Hall magnetic sensors.

5.1.3 Main Characteristics of Hall Magnetic Field Sensors

To be useful as a magnetic sensor, a Hall device must feature a set of characteristics adequate for the intended application. We shall now discuss a few characteristics decisive for the applicability of Hall magnetic sensors.

5.1.3.1 Sensitivity

The responsivity of the output voltage of a Hall device to a magnetic field can be characterized by three figures of merit (i.e., absolute sensitivity S_A, supply-current-related sensitivity S_I, and supply-voltage-related sensitivity S_V).

The absolute sensitivity S_A is defined by

$$S_A = \frac{V_H}{B_\perp},\ V_H = S_A \cdot B_\perp \tag{5.18}$$

Here V_H is the Hall voltage and $B_\perp$ is the normal (to the Hall plate) component of the magnetic induction.

Supply-current related sensitivity (in short, sensitivity S_I) is defined by :

$$S_I = \frac{S_A}{I},\ V_H = S_I \cdot I \cdot B_\perp \tag{5.19}$$

where I is the supply (or bias) current of the Hall device. For a strongly extrinsic Hall plate (see (5.17)),

$$S_I = G \cdot \frac{R_H}{t} \tag{5.20}$$

where G denotes the geometrical correction factor ($G \le 1$), R_H is the Hall coefficient, and t is the thickness of the plate.

In most currently used Hall magnetic sensors, one finds the values of the sensitivity S_I of the order of 100 V/AT. It was estimated that a maximal value of the current-related sensitivity of about 3,000 V/AT could be reached in an integrated Hall device [1].

In low-voltage applications, the absolute sensitivity of a Hall magnetic sensor is often limited by the available supply voltage V. The relevant parameter is then the supply-voltage-related sensitivity (in short, sensitivity S_V), defined by

$$S_V = \frac{S_A}{V},\ V_H = S_V \cdot V \cdot B_\perp \tag{5.21}$$

For a strongly extrinsic Hall plate,

$$S_V = \mu_H \cdot \frac{w}{l} \cdot G \tag{5.22}$$

where μ_H is the Hall mobility of the majority carriers, w/l is the width-to-length ratio of the equivalent rectangle of the Hall plate, and G is the geometry correction factor.

The measured Hall voltage is then given as:

$$V_H = \mu_H \cdot \frac{w}{l} \cdot G \cdot V \cdot B_\perp \tag{5.23}$$

The value of the term $(w/l) \cdot G$ attains a maximum value for $w/l \approx 0.7$ and $G = 0.667$ (i.e., in large-contact Hall devices), the limit being

$$S_{V\max} = 0.471\mu_H \tag{5.24}$$

Sensitivity S_V depends strongly on the material used to fabricate a Hall device. While silicon, with its modest mobility, allows, at room temperature, $S_{V\max} \approx 0.066$ V/VT, GaAs gives 0.28 V/VT, InGaAs (QW) gives 0.33 V/VT, and InSb(n+) gives 0.71 V/VT [6]. Therefore, one clear and important trend in the development of Hall devices is the search for and the application of high-mobility materials.

5.1.3.2 Offset

The offset voltage of a Hall device is a quasi-static output voltage that exists in the absence of a magnetic field. With reference to Figure 5.3, in virtue of the symmetry, we would expect the output voltage of the Hall device V_H to be zero in the absence of the magnetic field. However, the symmetry of a Hall device is never perfect: there are always small errors in geometry and variations in doping density, surface conditions, and contact resistance. Also, a mechanical stress in the Hall device, in combination with the piezo-resistance effect, can produce an effective electrical nonsymmetry. The result is a parasitic component in the Hall voltage, which cannot be distinguished from the real quasi-static part of the Hall voltage. Therefore, the offset severely limits the applicability of Hall devices when nonperiodic or low-frequency magnetic signals have to be detected.

The offset of a Hall device is best characterized by the offset-equivalent magnetic induction B_{off}. Using (5.21) and (5.22), we find

$$B_{\text{off}} = \frac{1}{S_V} \cdot \frac{V_{\text{off}}}{V} \approx \frac{1}{\mu_H} \cdot \frac{V_{\text{off}}}{V} \tag{5.25}$$

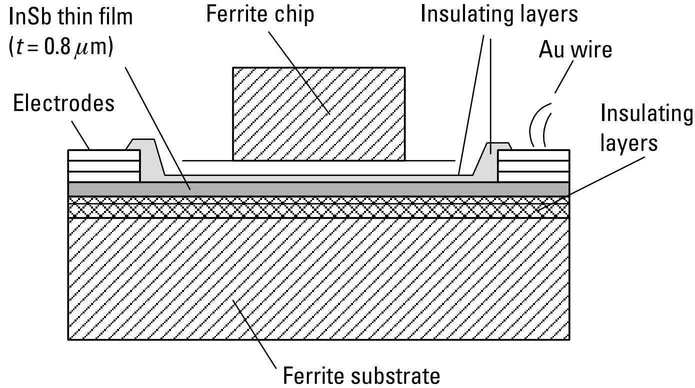

Figure 5.3 The highly sensitive InSb Hall element with ferrite flux concentrators (cross-section).

where we take $(w/l)\ G \approx 1$. This equation demonstrates once again the importance of a high Hall mobility of the material used for Hall devices.

When a microelectronics technology is used to fabricate a Hall device, the offset voltage amounts to usually less than 0.1% of the voltage applied between the input (current) contacts. Inserting this value in (5.25), we find $B_{\text{off}} \approx 10$ mT, 1 mT, 0.1 mT for Si, InGaAs, and InSb Hall devices, respectively.

It is important to note that the offset voltage is not stable. It varies with temperature and time. Even if all other influences are somehow eliminated, there remain long-term (over a period of more than an hour) fluctuations of the output voltage due to $1/f$ noise. In high-quality silicon Hall devices, these fluctuations correspond to a $B_{\text{off}} \approx 10\ \mu$T.

5.1.4 Other Problems

The applicability of Hall magnetic sensors depends also on the following nonideal characteristics: long-term stability of all characteristics, in particular, sensitivity and offset. Long-term instability due to the surface effects and piezo-resistive and piezo-Hall effects are rather well understood. We think that some bulk effects may also play a role, but practically nothing is published in the open literature on the subject. The best published long-term stability of the sensitivity S_I [7]:

$$\frac{\Delta S_I}{S_I} = 10^{-4}/\text{year} \tag{5.26}$$

Noise is a limiting factor in low level magnetic measurements, such as in current sensing. Usually, $1/f$ noise is the most disturbing. The $1/f$ noise may be decreased by several orders of magnitude if perfect materials and buried structures are used. In a good silicon Hall sensor, the noise-equivalent magnetic induction in the frequency range from 0.1 Hz to 10 Hz is about 1 μT [7]. The commercially available InSb Hall sensor AKE HW302 has $1/f$ noise with power spectrum density of 100 nT/√Hz at 1 Hz [8]. The GaAs quantum-well Hall sensor using the spinning-current modulation technique achieved 5 nT/√Hz white noise to the subhertz range [9].

The temperature cross-sensitivity of a Hall device is the undesirable sensitivity of its characteristics, such as magnetic sensitivity, to temperature. The temperature cross-sensitivity S_I is about 500 ppm/°C for silicon. For n+-InSb, S_I <100 ppm/°C and for GaAs QW S_I = 140 ppm/°C. These values can be easily improved by compensation. To extend the operating range to higher temperatures, wide bandgap semiconductors are used (i.e., GaAs and InSb up to 200°C and AlGaN/GaN up to 500°C).

5.2 High Electron Mobility Thin-Film Hall Elements

In this section, the fabrication and characteristics of thin-film InSb, InAs, and GaAs Hall elements will be described. Referring to (5.23), the Hall output voltage is proportional to the electron mobility, and so a high-electron-mobility material is suitable for fabricating Hall elements.

According to (5.17), in order to obtain a Hall element that is highly sensitive to a magnetic field, the active layer must be very thin and have a low carrier density.

Therefore, III-V thin-film semiconductors such as InSb, InAs, and GaAs and similar materials have been used for practical Hall elements because they have high electron mobility and their carrier (electron) densities can be easily controlled.

The physical properties of InSb, such as its extremely high electron mobility, were first reported by W. Welker in 1952. In 1975, Asahi Chemical Company developed a sensitive InSb thin-film Hall element using a novel vacuum deposition method. This Hall element has been mass-produced and used as a magnetic sensor in consumer electronics. Molecular beam epitaxy (MBE) technology was found to be a key technology for growing thin-film of III-V compound semiconductors having high electron mobility [10–12]. By using this technology, it is easy to epitaxially grow high electron mobility single crystal InAs thin films, or more complex structures such as an InAs quantum well on GaAs single crystal substrates, which are also used for making Hall elements.

5.2.1 InSb Hall Elements

In the early days, InSb Hall elements (Hall plates) were mainly fabricated from thin bulk single crystal InSb, making them expensive and not suitable for mass production. Under the pressure of a strong demand for low-cost, highly sensitive Hall elements for use in electronic equipment, such as small-size DC brushless motors, where Hall elements are mainly used as magnetic sensors for fine angular velocity control, highly sensitive InSb thin-film Hall elements were developed.

The production of InSb polycrystalline thin films having a high electron mobility of 20,000 to 30,000 cm^2/Vs and a thickness of 0.8 μm grown on thin mica substrates was established by the multisource vacuum deposition method.

The InSb thin-film Hall element with flux concentrators was also developed. The InSb thin film was removed from the thin mica substrate and sandwiched between a ferrite substrate and a small ferrite chip. This structure amplified the magnetic field in the gap between the ferrite substrate and chip by a factor of about 3 to 6 compared to the original magnetic field applied to the Hall element. This special structure is shown in Figures 5.3 and 5.4.

The basic V_H-B characteristics of the InSb Hall element is shown in Figure 5.5.

The temperature dependence of V_H at constant voltage drive and constant current drive are shown in Figure 5.6(a, b), respectively; the temperature dependence of these InSb Hall elements is 2.0%/°C.

To understand these important temperature characteristics, a brief discussion on the temperature dependence of Hall output voltage near room temperature is important. The temperature coefficient of the Hall output voltage V_H at constant voltage driving is easily derived from (5.1)

$$\frac{1}{V_H} \cdot \frac{dV_H}{dT} = \frac{1}{\mu_H} \cdot \frac{d\mu_H}{dT} \tag{5.27}$$

For constant current driving, it is also derived from (5.1) and expressed as

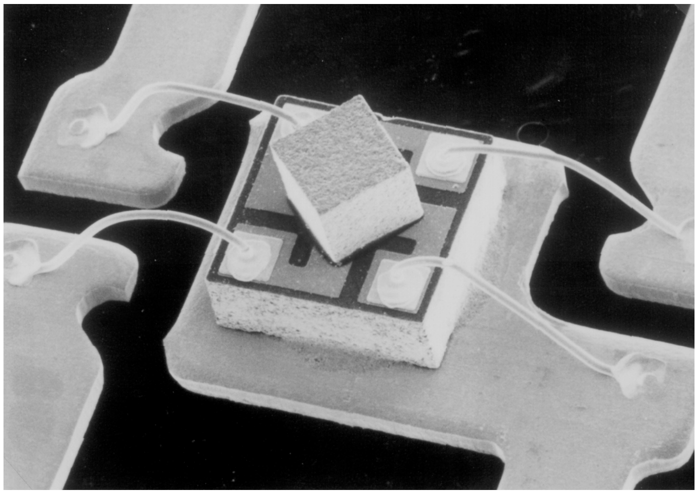

Figure 5.4 Photograph of InSb Hall element chip with ferrite flux concentrators (Asahi Kasei Electronics: InSb Hall elements HW series).

$$\frac{1}{V_H} \cdot \frac{dV_H}{dT} = \frac{1}{n} \cdot \frac{dn}{dT} \tag{5.28}$$

Early Hall elements made of single crystal InSb plates were driven at a constant current to avoid breakdown due to excess current because they had a very low input resistance of only a few ohms. Therefore, temperature dependence of V_H is approximately −2%/° as described by (5.28) because of the large temperature dependence of carrier density n due to the narrow bandgap energy of InSb. However, the thin-film InSb Hall elements have a high input resistance of around 350 Ω. Therefore, these Hall elements are stable under an input voltage of 1–2V, and they are driven at a constant voltage. Because the temperature dependence of V_H is the same as electron mobility as shown in (5.27), then this new driving technique reduces the temperature coefficient of the Hall output voltage from −2.0%/° to ±0.1–0.2%/° near room temperature as shown in Figure 5.6(a). The typical offset temperature drift is 3 μT/K, which is sufficient for many low-end applications.

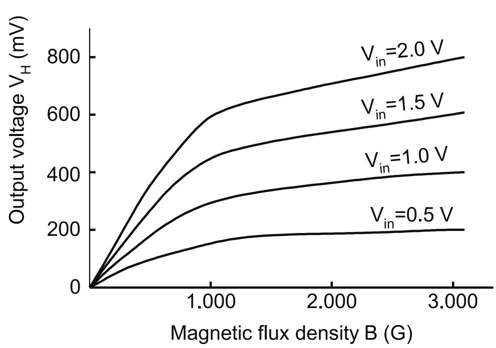

Figure 5.5 Magnetic field characteristics of thin-film InSb Hall element at constant voltage driving (V_H-B characteristics, Asahi Kasei Electronics HW-300A).

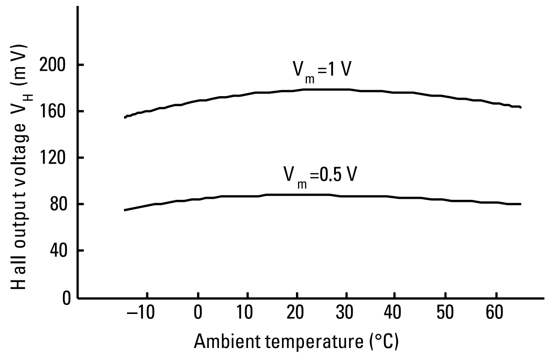

(a)

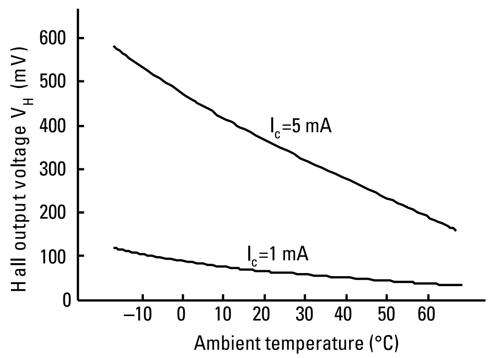

(b)

Figure 5.6 Temperature dependence of Hall output voltage (Asahi Kasei Electronics HW-300A): (a) at constant voltage driving, and (b) at constant current driving.

This InSb Hall element was a commercial success and opened up a new area for brushless DC motor technology and later resulted in the large-scale application of Hall elements as magnetic sensors in small DC brushless motors.

5.2.2 InAs Thin-Film Hall Elements by MBE

The only problem with the InSb Hall elements was their narrow operating temperature range, which is effectively restricted to be near room temperature and originates from the large temperature coefficient for the input resistance of 2.0%/°. To obtain a Hall element suitable for operation in industrial temperature range, InAs thin-film Hall elements were developed using MBE [10].

MBE is a technology for growing thin films on single crystal substrates in an ultrahigh vacuum chamber. Using this method, it is possible to fabricate thin films of InAs or III-V compound semiconductor on GaAs substrates [12].

Bulk single crystal InAs has a high electron mobility of more than 30,000 cm^2/Vsec. The InAs thin films grown by MBE also have a high electron mobility and a bandgap energy of 0.36 eV that is larger than for InSb with 0.17 eV.

To reduce the temperature dependence of the Hall output voltage for InAs Hall elements at higher temperatures, n-type impurity doping (i.e., Si doping of InAs) was

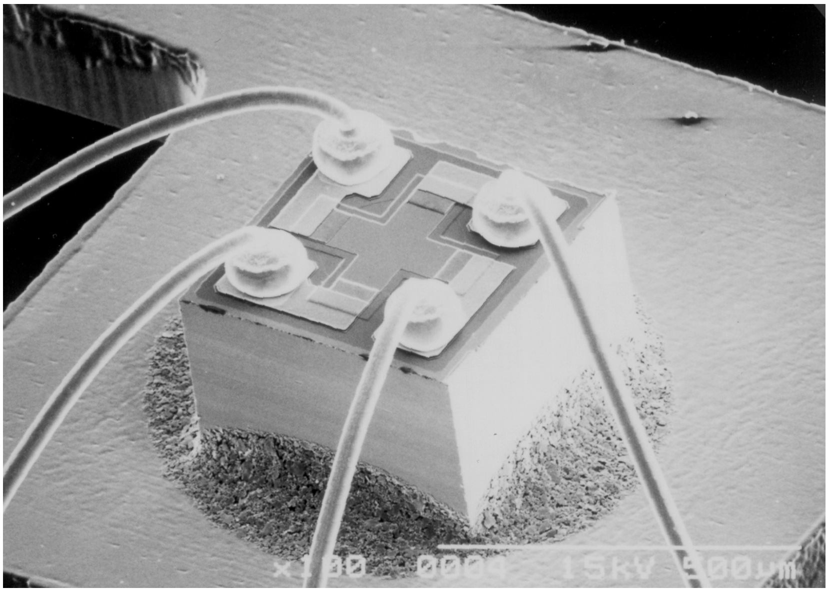

Figure 5.7 Photograph of the InAs Hall element chip.

found to be practically effective [13]. Highly doped InSb Hall sensor can work from 77 K up to 200°C. By proper high doping, the temperature coefficient of the magnetic sensitivity can be as low as 50 to 100 ppm/°C in the wide temperature range.

InAs thin films doped with Si were used for designing practical InAs Hall elements with 0.36-mm^2 chip size. A photograph of an InAs Hall element chip bonded on a lead island is shown in Figure 5.7.

Good linearity of the Hall output voltage for sensing a magnetic field is illustrated in Figure 5.8. The temperature dependence of the Hall output voltage is shown in Figure 5.9 and that of input resistance is shown in Figure 5.10.

High stability, low offset drift, and low 1/*f* noise properties are special features of the InAs Hall elements. Moreover, the temperature dependence of the

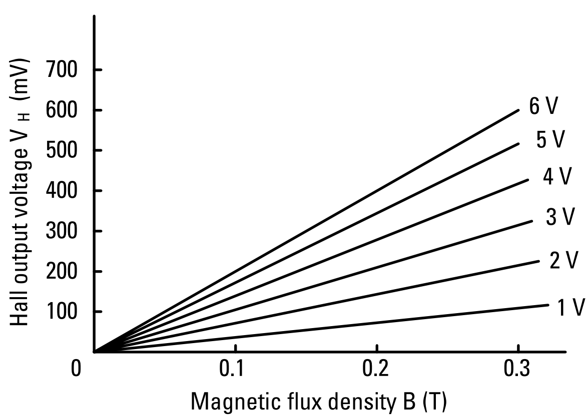

Figure 5.8 The magnetic field characteristics of Si-doped InAs Hall element (Asahi Kasei Electronics HZ-302C).

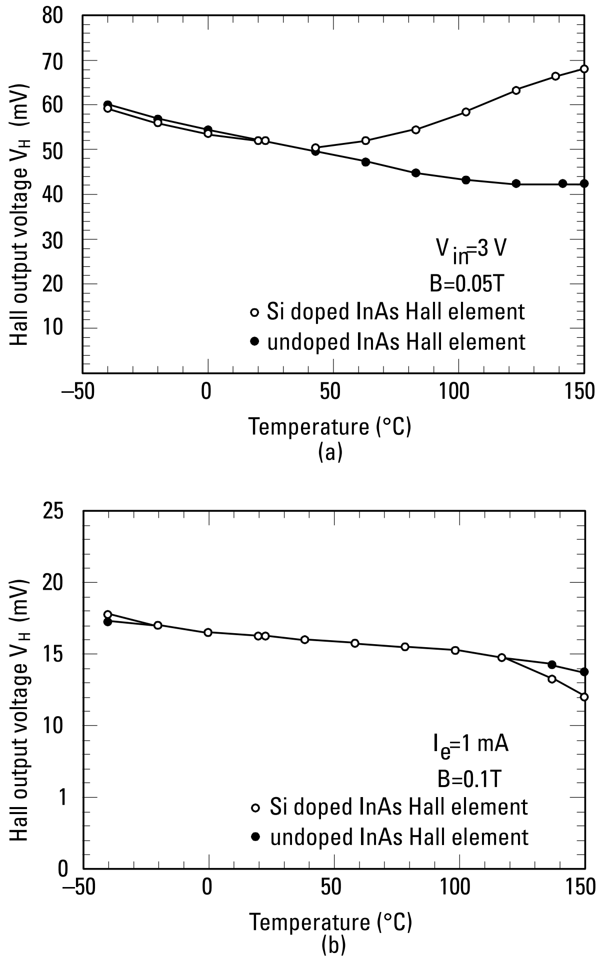

Figure 5.9 Temperature dependence of sensitivity for InAs Hall elements (Asahi Kasei Electronics HZ-302C): (a) constant voltage driving, and (b) constant current driving.

Hall output voltage and input resistance of heavily doped InAs Hall elements are very small over a wide temperature range (from –40°C to 160°C).

5.2.3 Deep Quantum Wells (DQW) and Application to Hall Elements

To achieve even higher sensitivity for Hall elements, a higher electron mobility and higher sheet resistance are required for the active layer. It is possible to use natural 2-D materials such as graphene; however, graphene-based devices show very high offset changes at higher temperatures [14]. An industrially proven method of achieving 2-D material is the quantum well. For InAs, this structure may contain an insulating layer from a quaternary material incorporating Sb having the same lattice constant as InAs and with a large bandgap energy of about 1.0 eV. This composition works well as a high potential barrier to form the InAs quantum well. For example, $Al_xGa_{1-x}As_ySb_{1-y}$ ($0 < x < 1$, $0 < y < 1$) is a suitable composition range. This

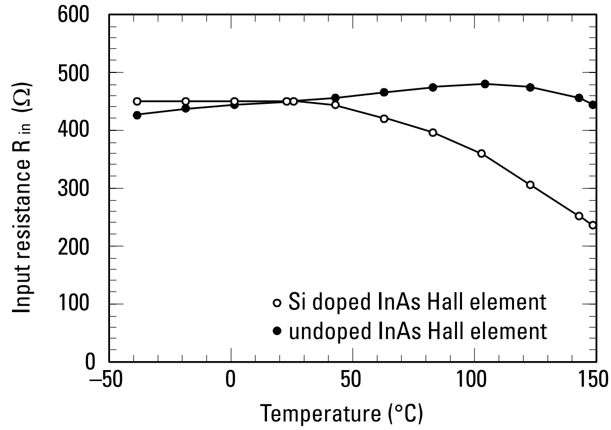

Figure 5.10 Temperature dependence of input resistance for InAs Hall elements (Asahi Kasei Electronics HZ-302C).

layer absorbs many kinds of defects produced by the large lattice mismatch (7.4%) between the GaAs substrate and the InAs. Moreover, these defects are electrically inactive and the layer acts as an insulating layer, pinning electrically active defects.

This insulating layer was used to form a deep quantum well with a conductive InAs channel layer (i.e., InAs DQW) and applied to a Hall element [11, 15–17]. A typical InAs DQW Hall element structure is shown in Figure 5.11.

A 15-nm-thick InAs well was used as an active layer and a structure comprising AlGaAsSb (35 nm)/InAs (15 nm)/AlGaAsSb (600 nm)/GaAs (at $x = 0.65$ and $y = 0.02$) was grown by MBE. The InAs DQW had a high electron mobility of 20,000–32,000 cm^2/Vsec.

The output voltage and temperature dependence of InAs DQW Hall elements is compared with various kinds of Hall elements in Figure 5.12. This figure shows that InAs DQW Hall elements have a high sensitivity comparable to an InSb thin-film Hall elements with a magnetically amplified structure and reasonably good stability over a wide temperature range [18, 19]. The InAs DQW Hall elements with a 50-nm-thick quantum well are now produced commercially by MBE.

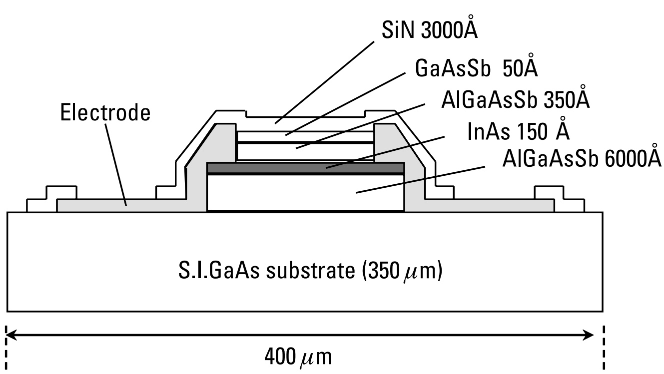

Figure 5.11 InAs DQW Hall element structure (cross-section)

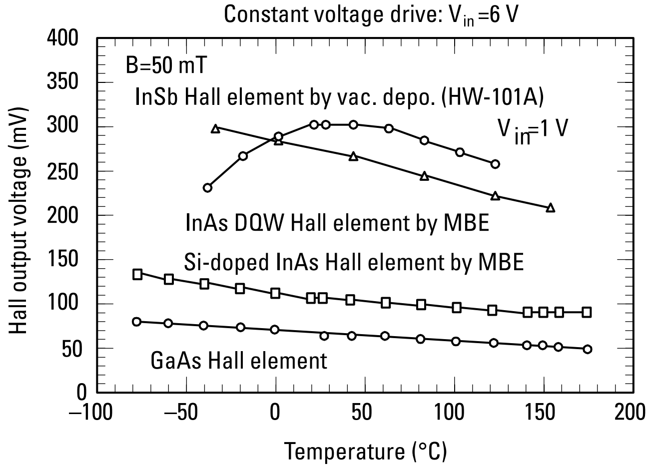

Figure 5.12 Temperature dependence of the Hall output voltage for various kinds of Hall elements.

5.2.4 GaAs Hall Elements

The practical or commercial GaAs Hall elements are fabricated by using a Si-implanted thin n-type layer. The process to make Hall elements is very simple and low-cost. The GaAs Hall elements have low magnetic field sensitivity, but good linearity, due to the small electron mobility of active layer. They have a very small temperature dependence at constant current driving and can be used for a wide range of temperature.

GaAs-based quantum well Hall sensors often use AlGaAs/InGaAs/GaAs or similar heterostructures to create 2-D electron gas with high mobility and very stable electron density [20, 21]. Low power (10.4 mW) and ultrasensitive linear Hall-effect IC using GaAs–InGaAs–AlGaAs 2-D electron gas technology achieved 1-μT resolution without modulation [22]. Using spinning-current modulation technique, 15 nT/√Hz white noise to subhertz range was achieved [9].

GaAs Hall sensors have better temperature stability if they are driven at a constant current. The offset temperature dependence is shown in Figure 5.13. The offset temperature coefficient is 5 μT/K, which is acceptable for many applications, but still very high compared to 20 nT/K for AMR sensors and 5 nT/K for micro-fluxgate sensors.

5.3 Integrated Hall Sensors

The Hall ICs are of the two main groups:

1. Monolithic microsystems integrating Hall plates and all electronics (including the digital one) and eventually also flux concentrators or guides on the same silicon chip [23–28];
2. Hybrid Hall IC composed of III-V Hall plate(s) and separate silicon chip in one package [18, 29–31].

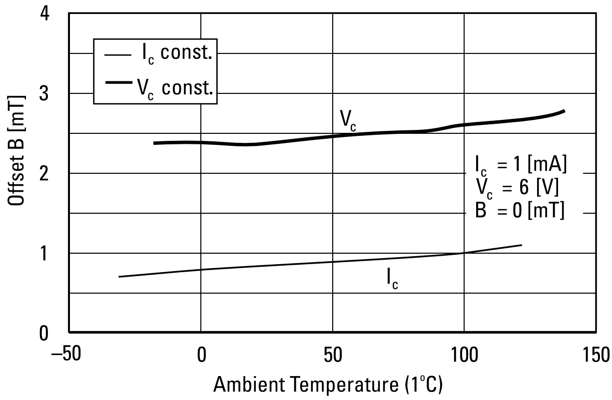

Figure 5.13 Temperature dependence of offset for GaAs Hall sensor HG-372 A (Asahi Kasei Microdevices).

In this section, we concentrate on the first group, which is far more produced and utilized. Devices of the second group were mentioned in the previous section.

Silicon as a material for Hall sensors has many disadvantages, such as:

- Low electron mobility: typically 1,200 $cm^2/(V{\cdot}s)$, leading to low sensitivity;
- Strong piezoresistive effect, leading to high offset and poor temperature offset stability due to stress;
- Low-temperature operation limited to about −50°C;
- Strong nonlinearity.

However, it also has three important advantages:

- Low cost;
- Compatibility with a standard CMOS process;
- Possibility to realize vertical Hall sensor and thus integrated 2-axis or 3-axis magnetic sensors.

5.3.1 Historical Perspective

The history of fully integrated Hall effect sensors started with the development of linear analog bipolar IC technology. At present, all developments concern compatibility with CMOS technology. The Hall element can be fabricated in microtechnology with no additional process steps, resulting in simplicity and low cost. In addition, both high-quality amplification and temperature compensation are readily provided. Complexity and parasitics associated with interconnect are easily managed by full integration, resulting in low cost and high reliability. For many applications, a requirement for built-in protection from voltage transients can be added, again with little or no added process complexity.

Figure 5.14 is an example of a magnetic sensor, which features a quad of cross-connected Hall elements. In this design, the Hall elements are placed along thermal and mechanical stress centerlines on the bipolar silicon IC. Although there is some trade-off with current draw from the power supply each time that an element is

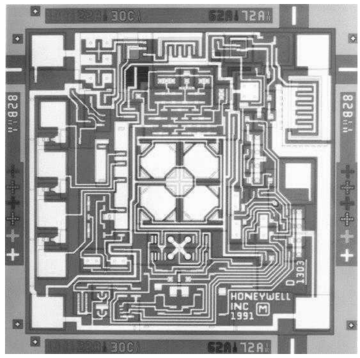

Figure 5.14 Magnetic sensor using four cross-connected Hall elements.

added, the resultant improvement in Hall sensitivity has made this approach worthwhile in many applications.

MOS IC technology has been rather slow to make inroads as the technology of choice for Hall effect ICs. In addition to the potential for added process complexity, MOS-based linear amplifiers are fundamentally more difficult to apply, due to higher amplifier offset voltages due to variations in threshold voltages. However, MOS-based Hall effect circuits become dominant due to their low cost. By applying circuit techniques such as auto-zeroing and chopper stabilization many of the circuit disadvantages of MOS can be overcome. In addition, the near perfect analog switch available with CMOS has been applied as part of a commutation strategy to reduce Hall offset voltages and thereby improve magnetic sensitivity and accuracy [32].

An N-type epitaxial layer on a high-resistivity P-type substrate is typically used in linear bipolar silicon technology to achieve high-performance vertical NPN transistors. This N-type layer is ideally suited to the fabrication of Hall elements with no adjustments. How such a device can be realized in integrated technology is shown in Figure 5.15.

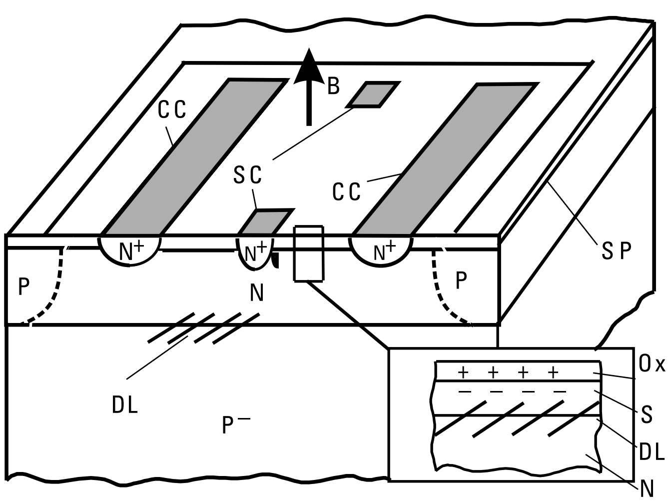

Figure 5.15 Cross-section view of a Hall device realized in integrated technology.

All current contacts (CC) and sensing contacts (SC) are realized as n+ implants at the surface of the epitaxial layer (N). The lateral isolation of the active volume is implemented using deep p-diffusion (P). The surface is covered by a shallow p-layer (SP) in order to keep the active zone away from the surface and so to achieve higher stability. The final layer on top is a protecting oxide layer (OX). In between each pn-diode, a depletion-layer (DL) appears, isolating the two parts.

The final sheet resistance of this layer is roughly 1,000–5,000 Ω/square. This corresponds to an impurity concentration of about 8.0×10^{14} to 5.0×10^{15} atoms/cm^3. At these levels of impurity concentration, the mobility is high being limited primarily by lattice scattering. This results in good Hall responsivity. Hall elements made from P-type silicon with the same impurity concentration have about one-third as much sensitivity because of the inherent mobility ratio of silicon. For low supply current requirements, it is desirable to have a higher sheet resistance. However, noise considerations limit the sheet resistance of the Hall element at the upper end. Process reproducibility is also more challenging as impurity concentrations are reduced. The standard N-type epitaxial layer concentration for a typical high-voltage linear bipolar silicon process is nearly ideal in every respect for fabrication of Hall elements.

A key requirement for Hall elements is low drift. A preponderant cause of drift in silicon-based Hall sensors are the piezo effects mentioned later. A nonrepeatable error in the form of drift cannot be compensated and therefore reduces overall accuracy. In order to fabricate a stable element, some form of protection from spurious surface charges must be incorporated into the design of the Hall element. Essentially, two techniques, both implementing what is generally described as a Faraday shield, have been applied successfully. The first is a metal field plate, which covers the oxide over the Hall element, and is connected to a stable voltage. Any surface charges that may appear on the surface of the metal are prevented from creating an image charge in the underlying silicon. The second approach is to add a P-type region over the N-type Hall element. Such a P-Cap will be tied to a known, stable circuit potential. Both approaches have seen broad usage.

The resolution of a magnetic sensor describes the minimum magnetic signal change that can be reliably detected. Resolution depends on signal-to-noise ratio. The signal, in this case, is determined by the magnetic responsivity of the Hall element. In a direct-coupled sensor, the noise is usually dominated by offset in the Hall element and input amplifier. Direct coupled integrated Hall sensors have been produced in high volume using standard linear bipolar silicon technology, which has a magnetic resolution of 5.0 mT over a temperature range from −40°C to 200°C. These same integrated sensors withstand repeated direct application of positive and negative voltage transients in excess of 100V on the supply and output pins.

5.3.2 CMOS Hall Elements

In the implementation of Hall elements in a CMOS circuit, there are two fundamental approaches that can be applied. Most standardized CMOS processes begin with a heavily doped P-type substrate covered with a more lightly doped P-type epitaxial layer. In order to maintain high mobility and thus high Hall responsivity, an N-type layer must be used for the Hall element. The Hall element can be accomplished as a simple N-type layer ion implanted into the P-type substrate (or P-type epitaxial layer). This could either be common with an implanted, diffused N-well that is used for fabrication of PMOS transistors, or it could be a separate, custom N-type implant. Most typically, there will not be common requirements for the CMOS N-well and the Hall element. The CMOS N-well is usually doped somewhat heavily in order to minimize circuit latch-up effects, to optimize the temperature coefficient of the threshold voltage, or to maximize field inversion thresholds. At the higher level of doping, the electron mobility is reduced, with resultant reduction in Hall responsivity. Assuming that a custom N-well is applied, then production costs may be increased relative to using the standard PMOS N-well. However, use of a custom N-well allows more freedom in the optimization of the Hall element.

The second solution may be to include an N-type ion-implanted region over a previously implanted and diffused P-well region. In this case, the resulting Hall element impurity levels may be higher than in the former case, making this approach less desirable due to a further reduction in mobility that results from greater impurity scattering. The lower electron mobility will reduce the Hall responsivity. In addition, due to process control considerations, it is difficult to actually fabricate a Hall element by first implanting and diffusing a P-well, then implanting an N-type layer. Nonuniformity in the two implants tends to be additive. As a result, this approach has given little service.

In the case of a Hall element integrated with a CMOS process, a P+ source-drain ion implant can be included over the Hall element to provide a Faraday shield. This shallow P-cap eliminates surface accumulation; there are no compensating effects on overall responsivity to magnetic field. The Hall responsivity of an implanted/diffused layer is generally degraded by the relativity lower mobility of the N-type ion implanted profile near the surface. Using a shallow P-cap as a Faraday shield converts the more heavily doped N-type surface region, and the Hall element begins below the surface. This reduces the peak concentration of donor impurities and electrons in the Hall element and results in higher mobility. However, the introduction of the implanted/diffused acceptor concentration in the P-cap results in some compensation in the active N-type layer. For a well-designed process, there is little change in the responsivity of the Hall element as the P-cap is included.

5.3.3 Hall Offsets

Relative to many other sensing technologies, such as piezoresistive pressure sensors or magnetoresistive sensors, for many magnetic sensor applications, which include the Hall sensor, the Hall voltage is quite small. Therefore, rather high amplification is required in Hall effect sensors. For example, a maximum Hall output voltage of 1.0 mV is somewhat typical. Any DC offset in the Hall element will also be amplified, and this DC offset will fundamentally limit the usefulness of the amplified output. If the application allows for AC coupling, then the DC offset can be eliminated, and other circuit limitations will set the overall achievable accuracy.

The usage of dual or quad Hall elements resulted in perhaps a 10-fold reduction in the net Hall offset. The most effective technique to offset suppression is use of a spinning current or commutation technique. Full rotation of the current and commutation of Hall voltage requires the integration of 16 CMOS switches. There are altogether eight permutations of current and voltage, but it is sufficient to use only four of them in a sequence illustrated in Figure 5.16. The outputs from the Hall element must be then properly demodulated to achieve the desired analog output. This procedure also cancels the offset and low-frequency noise of the input amplifier (before the demodulator). The demodulator requires four more switches and it is usually followed by a lowpass filter. A similar technique is used in silicon Hall ICs such as SS39ET by Honeywell, A1234 by Allegro, and MLX90242 by Melexis.

Munter [33] summarized the various components of the Hall offset. It is instructive to consider each of these components separately and to discuss the ability of the different cancellation techniques to deal with each component of offset voltage. First, the origin of various components of offset voltage can be considered to be either systematic or statistical in nature. Systematic variables are correlated, such that by knowing the gradients in one Hall element, then the gradients in the adjacent element can be predicted with high accuracy. For example, a gradient in the resistivity across a wafer could be considered to be systematic. Two Hall elements that are placed side by side tend to have the same local gradients in resistivity. Alternatively, a statistical variable is considered to be purely random in nature. The fabrication-related defects that might be found in the two adjacent Hall elements are typically uncorrelated.

Fabrication variables such as photomask misalignment, gradients in epitaxial sheet resistance or ion implant resistivity, and misalignment to the crystal plane are generally systematic. By careful design of a dual Hall element, offsets due to these variables can be nearly canceled.

Variables such as absolute Hall contact position or size, impurity concentration or crystal defect related variations in depletion layers, and point defects due to localized penetration of impurities are random in nature. While the dual Hall element provides some reduction in the effect of these variables, they are by no means canceled. Assuming that true randomness is at work, then the standard deviation of the Hall offset voltage due to statistical variables will be divided by the square root of 2 for a dual element and the square root of 4 for a quad element.

There are multiple thermal effects that influence the offset voltage. For a good thermal design in an integrated Hall sensor the temperature gradients across the Hall elements due to power dissipation in other circuit elements are well behaved

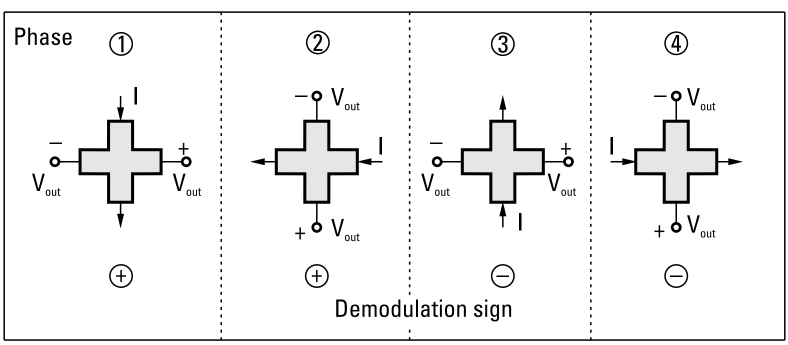

Figure 5.16 Optimum spinning current sequence to cancel the Hall sensor offset and low-frequency noise. (*After:* [7].)

and do not contribute to offset voltage. However, there may be inhomogeneity in the thermal resistance path that is randomly distributed. For a dual or quad Hall element, inhomogeneity will produce a randomly distributed offset.

Systematic thermal variables are the interrelated Seebeck and Peltier effects. The two side contacts of the Hall element will be at slightly different temperatures, giving rise to a potential difference due to the Seebeck effect. In an integrated Hall sensor, this temperature difference may be due to power dissipation in circuit elements other than the Hall element. The sense contact current is normally quite low; however, any current drawn from these side contacts will result in heat being absorbed or released due to Peltier effect. It is generally assumed that these variables are small in a well-designed Hall sensor.

Finally, stress effects must be considered. Since silicon has a significant piezoresistance effect, a Hall element can be an effective strain transducer. Thus, any inhomogeneity in the stress distribution in the Hall element will result in a component of offset voltage that cannot be distinguished from a magnetic signal. Mechanical stress may be an intrinsic part of the silicon crystal growth process and may also result from impurity diffusions, which generate localized lattice strains. However, the largest stresses are thought to arise from differences in thermal expansion coefficients between silicon and packaging materials. Since the piezoresistive coefficients of silicon are very orientation sensitive, the mechanical stress effects can be dramatically reduced by properly orienting the silicon. Use of a dual or quad Hall element will result in cancellation of the offset due to the symmetrical component of mechanical stress. However, unsymmetrical components of mechanical stress will produce offsets of a random nature.

Most typically, lead frame technology results in the silicon die being attached via an adhesion layer to a copper alloy. Attachment is completed at an elevated temperature. Once the temperature is reduced, a stress arises due to the mismatch in material properties. While the overall stress effects can be minimized by symmetrical design, the remaining effects are still important enough to generate significant offset voltages. It is worth noting that the component of Hall offset voltage due to piezoresistive stress effects is the only component that is fundamentally a function of temperature. Any approach to compensate for the offset voltage by trim techniques will be limited by the fact that the offset voltage will reappear as the temperature is moved away from the trim temperature.

In the continuation of the lead frame assembly, plastic material may be molded directly over the silicon die surface. The temperature-dependent stress associated with this material mismatch is also an important variable. Various approaches to buffer this stress have been attempted with varying success. Simplistically, by coating the silicon die surface with a material that will not transfer shear stress, the effect of expansion or contraction of the plastic will be minimized.

As has been mentioned, systematic variables can normally be canceled with a simple dual-element approach. Multiple elements will act to reduce, but not eliminate, the effects of statistical variables. In the case of the spinning current approach, cancellation occurs for any component of Hall offset that is symmetrical with respect to the bias switching terminals. In the simple, practical case of using only two bias orientations that are 90° apart, the performance of a commutated Hall element can be judged by comparison to a dual Hall element configuration. With commutation, the Hall element is being compared to itself; in the dual configuration, the cancellation is between two nearby but statistically different Hall elements. This means that compensation for many random variables can be accomplished with 90° commutation. For instance, offset due to a diffused point defect of any kind will be opposite and equal for the two bias orientations and will be averaged to zero. For the case of two current orientations, most components of Hall offset are averaged to zero. This includes the important temperature-dependent stress effects. However, there is an important statistical offset voltage that is not canceled by the spinning current approach. As the applied bias voltage is rotated, new depletion regions are created. Offset voltages due to the nominal depletion effects are canceled by averaging. However, inhomogeneity in the depletion region is random in nature and will therefore produce a statistical net offset voltage. For at least this reason, the two-current orientation approach to commutation of offset voltages is less than perfect.

Munter [33] reduced offset by spinning current from 2 mT to 200 μT by using 16 contacts. The spinning electronics can be integrated on the same CMOS chip with the silicon Hall sensor [34]. If using nonsilicon Hall sensors, the spinning electronics should be separate. Using GaAs quantum-well Hall sensor and spinning-current modulation, Mosser et al. demonstrated offset reduction from 630 μT to 100 nT and also significant noise reduction [9]. Single-chip devices have low parasitic capacitance and allow one to use a spinning frequency up to 1 MHz.

5.3.4 Excitation

Proper biasing of a silicon Hall element is important in achieving an optimum performance from an integrated Hall sensor over the operating temperature range. From (5.11) and (5.17), the Hall element responsivity is given by

$$\frac{V_H}{B} = \frac{r_H}{qnt} IG \tag{5.29}$$

For lightly doped N-type silicon Hall elements, the electron concentration, n, thickness, t, and geometrical correction factor, G, are constant over temperature. Thus, constant current bias in a Hall element gives a magnetic responsivity that has the temperature coefficient of the Hall factor, r_H. For a particular uniformly doped epitaxial Hall element with a donor concentration of ~$3.0 \times 10^{15}\text{cm}^{-3}$, the measured temperature coefficient of the Hall factor is 6.75×10^{-4}/°C. The temperature coefficient of r_H causes the magnetic responsivity to increase with increasing temperature. It follows that for this Hall element a constant magnetic responsivity over temperature can be achieved by biasing with a current source having a temperature coefficient of -6.75×10^{-4}/°C. For the temperature range from −40°C to 200°C, this represents a 16.2% decrease in bias current.

The resistance of the Hall element is given by

$$R = \frac{\rho}{t}\left(\frac{L}{W}\right)_e = \frac{1}{q\mu_c nt}\left(\frac{L}{W}\right)_e \tag{5.30}$$

where ρ/t is the sheet resistance of the Hall element, $(L/W)_e$ is the effective length-to-width ratio of the Hall element, μ_c is the conductivity mobility (drift mobility) of electrons, n is the electron concentration in the Hall element, and t is the thickness of the Hall element.

For the Hall element described above, the conductivity mobility changes rather dramatically with temperature. The measurements of this same particular N-type epitaxial Hall element have shown:

$$\mu_c = \mu_{co}\left(\frac{T_o}{T}\right)^{2.268} \tag{5.31}$$

where μ_{co} is the value of electron mobility at T_o, T_o is the reference temperature in K, and T is temperature of measurement in K.

Between −40°C and 200°C, the resistance of the Hall element changes by a ratio of ~5/1. With the negative temperature coefficient on the bias current required for constant magnetic responsivity, the voltage across the Hall element changes by a ratio of ~1/4.3 for this same temperature range.

Kanda and Yasukawa [35] showed that a slightly unbalanced Wheatstone bridge can represent the passive portion of the Hall element. Thus, the nominal offset voltage at the sense terminals is proportional to the bias voltage across the Hall element. Statistical inhomogeneity in the Hall element depletion layers introduces nonratiometric variations in the offset as the voltage bias changes with temperature. Package-induced stresses also cause variation of offset voltage with temperature. Biasing the Hall element with a constant current makes it difficult to trim the offset. Overall, the constant current bias has been found to have a poorer signal-to-offset ratio than the constant voltage bias.

When the Hall element is biased at constant voltage, the nominal offset voltage is independent of temperature. In this case, the temperature coefficient of the offset voltage is the result of packaging stress and laser trimming can remove the nominal offset. For constant voltage bias, the offset changes due to statistical depletion effects are eliminated. With constant voltage bias, the magnetic responsivity is given by

$$\frac{V_b}{B} = V_b \mu_H G\left(\frac{W}{L}\right)_e \tag{5.32}$$

where μ_H is the Hall mobility given by $\mu_H = r_H \mu_c$ and V_b is the bias voltage.

For constant voltage bias over the temperature range from −40°C to 200°C, the Hall mobility and magnetic sensitivity change by a ratio of ~4.3/1.

The elimination of statistical depletion effects with a constant voltage bias results in a higher signal-to-offset ratio for that biasing scheme as compared to the constant current bias. As a result, constant voltage bias has been used most widely in commercial integrated Hall sensors.

Constant voltage bias has also been widely used in linear Hall sensors. In this application, the power supply is applied directly to the Hall element to provide a means of calibrating the magnetic responsivity. From (5.9), the magnetic responsivity is directly proportional to V_b.

For epitaxial Hall elements with low donor concentration, the Hall and drift mobility is determined almost entirely by lattice scattering for the temperature range of interest. Normal run-to-run variations in donor concentration encountered in a silicon bipolar process are small enough that there is little effect on the magnetic responsivity. In integrated Hall sensors, N-type epitaxial resistors and zero temperature coefficient thin-film resistors can be used together to compensate for the variation of drift mobility over temperature. Such compensation schemes do not correct for the temperature coefficient of the Hall factor, r_H. Compensation for the temperature variation of r_H must be provided by other circuit means to obtain constant magnetic responsivity over temperature.

The possible system methods of compensation the temperature dependence of the sensitivity include on-chip calibration coils [36] and on-chip stress monitoring: either analog [37] or digital [38].

5.3.5 Amplification

The Hall element generates a differential signal at the sense terminals at a common-mode DC voltage of approximately $0.5V_b$. As a result, most integrated Hall sensors use a linear differential amplifier as the first stage in the on-chip signal conditioning circuitry. The first-stage amplifier is a critical part of the design of an integrated Hall sensor because its input offset voltage and noise add directly to the offset voltage and noise of the Hall element to determine the magnetic sensitivity of the sensor. Linear differential amplifiers can be constructed from both bipolar and CMOS transistors. However, the characteristics of the two types of amplifiers are considerably different.

A well-designed integrated NMOS amplifier using closely spaced transistors has a typical input offset voltage of 2 to 3 mV. The use of chopper stabilization tends to increase the area and complexity of the integrated Hall sensor but provides an input offset voltage of 10 to 20 μV.

The best input amplifier performance is obtained from a BiCMOS process. This combination allows the CMOS switches to be used to chopper-stabilize a bipolar input amplifier. Chopper stabilization can be used to reduce the input offset voltage by about a factor of 100.

The dynamic cancellation of the amplifier offset is achieved also by spinning current technology [9].

5.3.6 Geometry Considerations

The conformal mapping theory shows that all Hall elements with the same effective (L/W) will have the same magnetic responsivity. This means that the specific geometry of the Hall element can be selected to minimize the piezoresistance effects and to comply with layout requirements of integrated Hall sensors.

Two popular geometries that have been used in integrated Hall sensors are depicted schematically in Figure 5.17. It is evident that neither of these designs has the simple rectangular geometry often used to describe the Hall effect. The (L/W) of these Hall elements cannot be determined by inspection. However, the effective (L/W) can be determined from

$$\left(\frac{L}{W}\right)_e = \frac{R}{\rho_s} \tag{5.33}$$

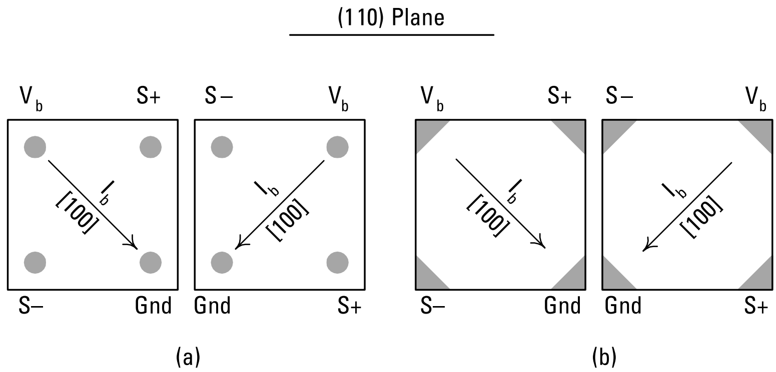

Figure 5.17 Hall element geometry.

where R is the measured resistance between the bias or sense contacts and ρ_s is the sheet resistance of the Hall element material, $\rho_s = \rho/t$.

Both of these geometries as depicted use contacts of significant size for both bias and sense. This means that there are two significant $(L/W)_e$ values that must be used to describe their operation. In general, the bias and sense contacts do not have to be the same size. The bias (L/W) is given by

$$\left(\frac{L}{W}\right)_b = \frac{R_b}{\rho_s} \tag{5.34}$$

and the sense (L/W) is given by

$$\left(\frac{L}{W}\right)_s = \frac{R_s}{\rho_s} \tag{5.35}$$

where R_b and R_s are the resistance values measured between the bias contacts and sense contacts, respectively.

The expression for magnetic responsivity in (5.34) must be rewritten as

$$\frac{V_b}{B} = V_b \mu_H G_T \left(\frac{W}{L}\right)_b \tag{5.36}$$

where G_T is the total geometry factor that includes the shorting effect of both the bias and sense contacts.

For (100) silicon wafers the mask patterns are typically oriented parallel to the (110) plane provided on the wafer. Both geometries shown in Figure 5.17 provide bias current flow in the [100] direction. This is the optimum bias current direction to minimize the piezoresistive response to mechanical stress. Both geometries have major feature edges aligned to the [110] directions for ease of layout and both are simple to arrange in dual or quad configurations. Offset voltage cancellation with no loss of magnetic responsivity is accomplished when the bias currents in the dual elements are orthogonal and when similarly named terminals connected with metal leads. The (100) plane in silicon has 4-fold symmetry. Thus, the diagonally located contacts allow orthogonal bias currents with both currents in the optimum (100) direction required to minimize piezoresistive effects.

To achieve accurate dimensional control, the circular contact geometry shown in Figure 5.17(a) normally uses shallow N+ implant/diffusion regions to form the contacts to the Hall element layer. In a bipolar process, this can be the emitter diffusion used in the NPN transistors. In a CMOS process, it can be the source/drain diffusion used in NMOS transistors. As a result, this design has a component of vertical current flow under the contacts. The diagonal contacts shown in Figure 5.17(b) could use either a shallow or deep N+ contact region. The deep N+ region acts as an equipotential contact and minimizes the vertical component of current in the Hall element. When used in dual or quad configurations, both of these geometries provide offset voltage cancellation for uniform sheet resistance gradients, small mask misalignments, and uniform mechanical stress.

Hall elements that are commutated using CMOS switches must have symmetrical contacts (i.e., the bias and sense contacts must be identical to achieve maximum offset reduction). Commutation with the diagonal contact arrangement shown in Figure 5.17 switches the bias current between orthogonal (100) directions. Both single and dual Hall elements may be commutated.

In sensors that do not use commutation, the bias and sense contacts may be made asymmetrical to achieve other performance advantages. A Hall effect simulator developed by Nathan [39] has been used to determine the total geometry factor for a variety of bias and sense contact geometries.

When point contacts are used for sense electrodes, G_b approaches 1 for $(L/W)_b > 4$; for $(L/W)_b < 0.25$, G_b approaches $0.742(L/W)_b$ [1]. However, in integrated Hall sensors, it is not desirable to use point contacts and the effects of both the bias and sense contacts must be taken into account. For symmetrical Hall elements like those shown in Figure 5.17, the term $G(W/L)$ has a maximum value of ~0.47 for $(L/W) = \sim 1.40$. As (L/W) increases above 1.4, the term (W/L) decreases more rapidly than G increases. As (L/W) decreases below 1.4, the term G decreases more rapidly than (W/L) increases. Symmetrical Hall elements are being used in many commercial integrated Hall sensors.

The output resistance set by $(L/W)_s$ is also important in determining the thermal and $1/f$ noise voltage contributed by the Hall element.

Integrated Hall sensors typically use junction-isolated Hall elements. The N-type Hall element is surrounded by P-type material. If a P-cap is used, the Hall element is surrounded by P-type material on all sides except in the contact areas. When bias is applied, most of the body of the Hall element is reverse-biased with respect to the surrounding P-type material. This geometry has a beneficial effect because the surrounding depletion region is continuously sweeping the thermally generated minority carrier holes out of the Hall element. As a result, the integrated Hall element is a true one-carrier device and no loss of magnetic responsivity due to thermally generated holes occurs at high temperature. The sweep-out of the minority carrier holes results in a leakage current distributed over the area of the Hall element. Inhomogeneity in this leakage current can cause increased offset voltage at high temperature.

5.3.7 Vertical Hall Elements

All of the Hall elements discussed up to this point have been in the plane of the surface of the integrated sensor die. In this configuration, the Hall element is responsive only to the vertical component of magnetic field. The vertical Hall element responds to magnetic field in the plane of the surface of the die. This device is called a vertical Hall element. Two vertical Hall elements oriented at 90° allow the magnetic field in the plane of the die surface to be split into orthogonal components. This makes it possible to sense an arbitrary magnetic field as three orthogonal components using a single integrated die. Vertical Hall sensors are discussed in Section 5.4.

5.3.8 Packaging for Integrated Hall Sensors

The earliest Hall effect ICs were packaged using a robust although costly approach of flip-chip bonding onto the ceramic substrate. The flip-chip approach still enjoys broad application today. In this configuration, both the electrical and mechanical connections to the substrate are created by first placing solder bumps onto the silicon die. The ceramic is prepared with a pattern of solderable material. When the die is inverted into position over the ceramic and both units are heated, the solder bump on the chip will wick into the surface of the solderable material on the prepared ceramic. This wicking results in self-alignment of the silicon chip. Any shear stresses that may arise due to differential thermal expansion of the silicon and ceramic are transmitted only through the bump connection. Therefore, it is relatively easy to manage these stresses, and the piezoresistive packaging effect on the Hall element and input amplifier offset voltage is small.

Low-cost packaging of semiconductor die utilizes the steps of the die attaching to a lead frame, wire-bonding, and encapsulation. The lead frame material typically has a temperature coefficient of expansion (TCE), which differs from that of silicon. The die attachment normally occurs at an elevated temperature. Therefore, when the die attach is completed, and the sandwich is cooled to room temperature, a net stress appears in the silicon. This packaging stress contributes to a change in the offset of the Hall element and/or input amplifier, due to piezoresistive effects. A similar effect may occur during plastic encapsulation [40]. Since this piezoresistive effect is the result of mismatched TCE in the sensor package, the resulting offset voltage will be temperature-sensitive. Creep or slip between elements of the package can cause hysteresis in offset voltage as a result of temperature cycling.

Various approaches have been applied successfully to reduce the degree of change in the Hall offset during packaging. In the die attaching operation, the properties of the glue layer may be considered. Obviously, the glue layer will also have a TCE that is different from that of silicon. However, this layer is usually fairly thin and therefore applies little stress to the silicon as it expands and contracts. More important are the mechanical properties of the glue layer. A relatively stiff glue layer will transmit shear stress from the underlying lead frame to the silicon, while a flexible glue layer will not support the transfer of shear stresses.

Some success has been achieved in reducing the effect of encapsulation layers on the offset voltage by applying thin buffer layers to the surface of the silicon die. Such buffer layers can either be applied as a thin-film overcoat during IC fabrication or, alternatively, may be dispensed onto the surface of the silicon die immediately prior to encapsulation. Examples of thin-film buffer layer materials are polyamide or photoresist. Each of these materials has seen some applicability in the semiconductor industry as protection layers to reduce mechanical damage and stress during packaging. In the case of dispensed materials, elastomers such as room-temperature vulcanizing (RTV) or other silicone compounds have been used.

With regard to the design of the Hall element itself in order to minimize the packaging effects on offset voltage, both experience and finite element modeling (FEM) have shown that placement of the Hall element symmetrically with respect to the die edges can result in lower offset voltages. In addition, a general trend exists that a larger die (in proportion to the Hall element) will have a somewhat lower package-induced offset voltage.

5.3.9 Applications and Trends

The first large application of the Hall element was as a switch used in computer terminal keyboards (1961). An integrated Hall element switch was the basis for an automotive solid state ignition system and antilock brake systems to detect wheel speed. These Hall sensors must also operate correctly over a wide ambient temperature range [41]. Another large application that requires tens of millions of sensors per year is the brushless DC motor. The integrated Hall sensor has found favor due to its inherent low-cost, wide temperature range of operation, insensitivity to dirty environments, and the ruggedness associated with noncontact measurement.

Linear sensors have found a main application in electric current sensing. For AC applications such as in the current sensing in electricity meters, precise Hall sensor achieved high linearity in a wide field range.

Hall sensors have been replaced by magnetoresistors in precise DC applications. AMR sensors have lower noise and better temperature stability. However, they have a much lower field range and they are more expensive.

5.4 Nonplate-Like Hall Magnetic Sensors

This section gives a survey of Hall devices that are not plate-like but do have 3-D structures. The survey covers the vertical Hall device, sensitive to a magnetic field parallel with the chip surface; the cylindrical Hall device, which behaves as a vertical Hall device combined with magnetic flux concentrators; the 2-axis vertical Hall device, for the two in-chip-plane components of a magnetic field; and the 3-axis Hall device, to measure all three components of a magnetic field. All these Hall magnetic sensors are fabricated using the vertical Hall silicon process [42].

While leaving the solid ground of conventional Hall plates, it is useful to formulate a set of general criteria that a good Hall device must fulfill. In the present context, the essential three criteria (in the usual notation) are:

1. The orthogonality of the vectors of the current density and of the magnetic field over the active region of the device, since the Hall electric field is given by

$$\mathbf{E}_H = -R_H[\mathbf{J} \times \mathbf{B}] \tag{5.37}$$

2. The accessibility of this active region in order to retrieve the Hall voltage, which is given by

$$V_H = \int_{S_1}^{S_2} E_H \, ds \tag{5.38}$$

(S_1 and S_2 indicate the positions of the sense contacts);

3. Moreover, in the absence of a magnetic field, the voltage difference between the points S_1 and S_2 should be zero. This means that along a suitable integration path S_1, S_2 (2), the biasing electrical field **E** and the Hall electric field $\mathbf{E}_H$ should be mutually orthogonal, that is,

$$\mathbf{E} \cdot \mathbf{E}_H = 0 \tag{5.39}$$

5.4.1 The Vertical Hall Device

Figure 5.18 illustrates the technological structure of the vertical Hall device. Its n-type active zone is confined into an approximately plate-like structure by a deep

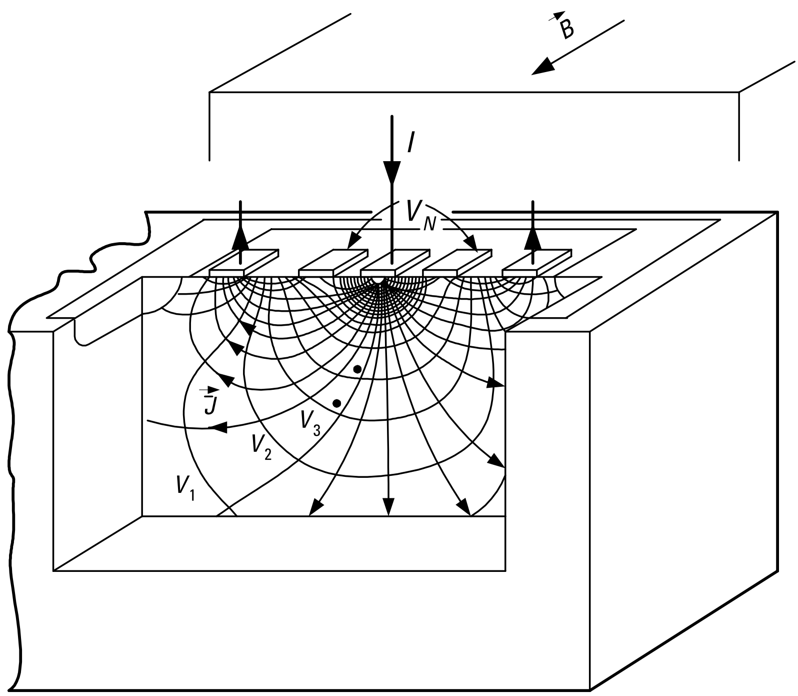

Figure 5.18 A cut through a vertical Hall device, showing the current and equipotential lines. (*Adapted from:* [1].) The vertical cut-plane is a symmetry plane of the sensitive volume (therefore vertical), but the whole sensitive volume is a 3-D structure. All three criteria are well fulfilled. Notably, the output signal is the Hall voltage V_H, given by the integral (5.39) of the Hall field over a line following an equipotential line (at $B = 0$) connecting the two sense contacts.

p-type ring and the depletion layer between the active zone and the ring. The active region of the device is embedded into the bulk of a silicon chip. This fact explains in part the long-term stability and robustness of this Hall device: its active zone is buried into a single crystal, far away from the chip surface.

Thanks to the quasi-radial form of the current density lines in a vertical Hall sensor, the planar Hall effect in it is much lower than in a Hall sensor of a conventional geometry.

All other Hall devices presented in this section are fabricated using the vertical Hall silicon process and share with the vertical Hall device the basic features of low supply current, low noise, and high long-term stability.

5.4.1.1 Linearity

Due to the opposite sign, mutual compensation between material and geometry-related nonlinearity can be achieved. For an appropriate design for the vertical Hall device the overall nonlinearity can be as small as 0.1% in magnetic flux density up to 2T.

5.4.1.2 Temperature Sensitivity

For strongly extrinsic n-type silicon at room temperature, all impurities have given their electron to the conduction band, so that for small variations of temperature, the density of charge-carries in the material remains constant. The thermal behavior of the sensitivity only depends upon the Hall scattering factor and has been found to be about +0.08%/K for silicon for constant current biasing [43]. Temperature cross-sensitivity can easily be compensated by modulating the current through the device, with the help of an appropriate resistor in parallel to the input contacts. The remaining variation of sensitivity is then usually less than 0.25% over the temperature range from −10°C to 60°C.

5.4.1.3 Planar Hall Effect

It is well known that Hall sensors with conventional plate-shape geometry are not only sensitive to a magnetic field perpendicular to the plate but also to a field in the plane of the plate. This planar Hall effect [44] adds an error voltage to the output Hall voltage. This planar voltage depends on the angle between current and field in the plane and is the strongest at odd multiples of $\pi/4$. It was shown that the particular crystal orientation and the unique shape of the vertical Hall device reduce the influence of such a planar Hall voltage by about one order of magnitude compared to conventional plate-shape devices. In such a way, vertical Hall sensors are very appropriate for the use of precision magnetic measurement instruments for mapping or control applications.

5.4.1.4 Accurate Magnetic Field Measurement Using Vertical Hall Devices

Silicon vertical Hall devices are commercially available products, used as key components in a meter for electrical energy and in high-accuracy magnetic field transducers. Their essential features are high current-related sensitivity (400 V/AT), moderate noise (<10 μT from 10^{-4} Hz to 10 Hz), and high long-term stability: magnetic sensitivity does not change more than 0.01% over a year.

Two matched vertical Hall sensors in the probe head can mutually compensate for offset, junction-field-effect, and planar Hall effect. Temperature cross-sensitivity and nonlinear behavior in the magnetic field can be effectively reduced using external compensation. Efficient temperature compensation is achieved by using the Hall sensor itself as a temperature sensor. Operating the Hall devices in the constant current mode allows for the implementation of all external compensation through bias-current modulation.

Based on these concepts, single-axis transducers with 0.01% accuracy for a flux density range up to 2T and a temperature range from 15°C to 35°C are available. Adding a temperature stabilization in the probe head and using computer calibration towards a precision NMR-meter, an absolute accuracy of 0.004% for the field range from −6 to 6T was achieved [45]. Thanks to the very small volume of the active zones of the vertical Hall device, even fields with nonlinear gradients of up to 30 T/m were measured with similar precision. The weak point of all types of Hall sensors, especially those based on silicon, is offset and its drift with temperature. Even with spinning current compensation, the offset of precise vertical Hall sensor is in the order of 10 μT [46] and its temperature stability is not better than ±1 μT/°C.

5.4.2 Two-Axis Vertical Hall Device

A merged combination of two vertical Hall devices gives a magnetic sensor for the simultaneous sensing of the two in-plane components of a magnetic field [47]. By sharing the center current contact, the active zone can be made very compact and the two orthogonal field components *X* and *Y* are measured in the same spot (Figure 5.19). Although the active regions of the two merged VHS are not electrically insulated, the orthogonal design decorrelates the magneto-galvanic effects and so efficiently reduces undesired cross-coupling.

A combination of such a magnetic sensor with a permanent magnet becomes a contactless angular position sensor (Figure 5.20).

The unique feature of such a combination is its great robustness. Relatively big variations in the position of the magnet have little influence on the result of the angle measurement. The information on the angle of the magnetic field vector with

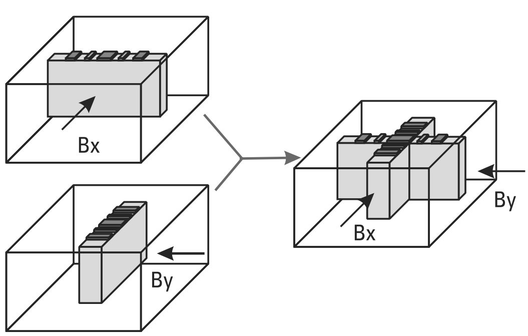

Figure 5.19 A merged combination of two orthogonally placed vertical Hall devices measures simultaneously the two in-plane components of a magnetic field.

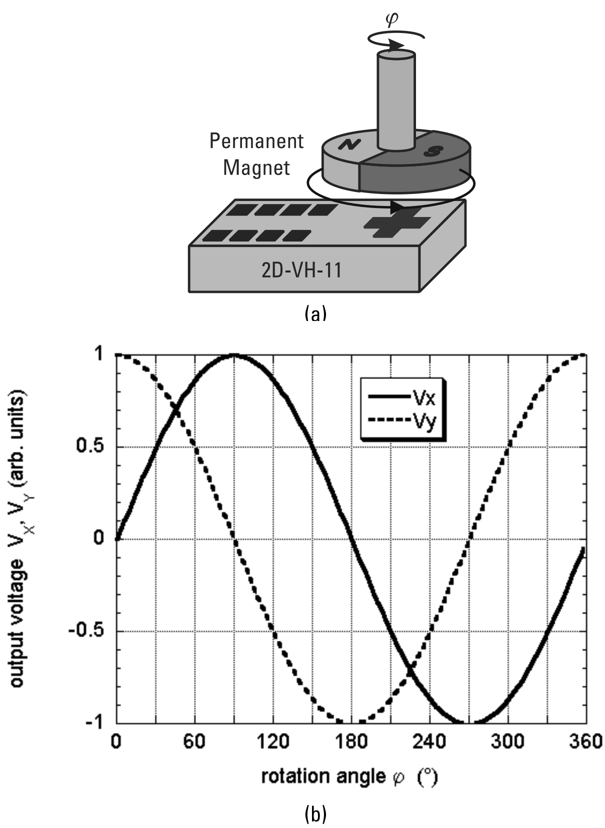

Figure 5.20 In a combination with a permanent magnet, a 2-D vertical Hall sensor becomes an accurate angular position sensor. The measured angle depends on the ratio of the two output voltages and not on their absolute values [48].

respect to the sensitive axes of the sensor can be retrieved from the ratio of the two output signals rather than from their absolute values. This renders the sensor virtually immune to the manufacturing tolerances and temperature fluctuations. An accuracy of ± 0.1° can be easily achieved with such a sensor.

5.4.3 Three-Axis Hall Devices

Even more challenging than a 2-D single-chip Hall sensor is the realization of a 3-D single-chip Hall sensor. Such a device in vertical Hall technology [49] has an active zone in the shape of a square with eight ohmic contacts at its surface (Figure 5.21). Here again, the lateral confinements are realized by a p-ring (not visible).

Four contacts in the corners are used alternatively as current input and current output contacts; the four midside contacts are Hall sense contacts. The total current flows in such a way through the device that three different Hall voltages corresponding to the three magnetic field components B_x, B_y, and B_z can be measured (Figure 5.22) [50].

The total active volume can be as small as $0.1 \times 0.1 \times 0.1$ mm^3, allowing for measurements with a high spatial resolution. Using four elements for each direction, the geometrical center can be adjusted to one point [51]. The sensor axes are

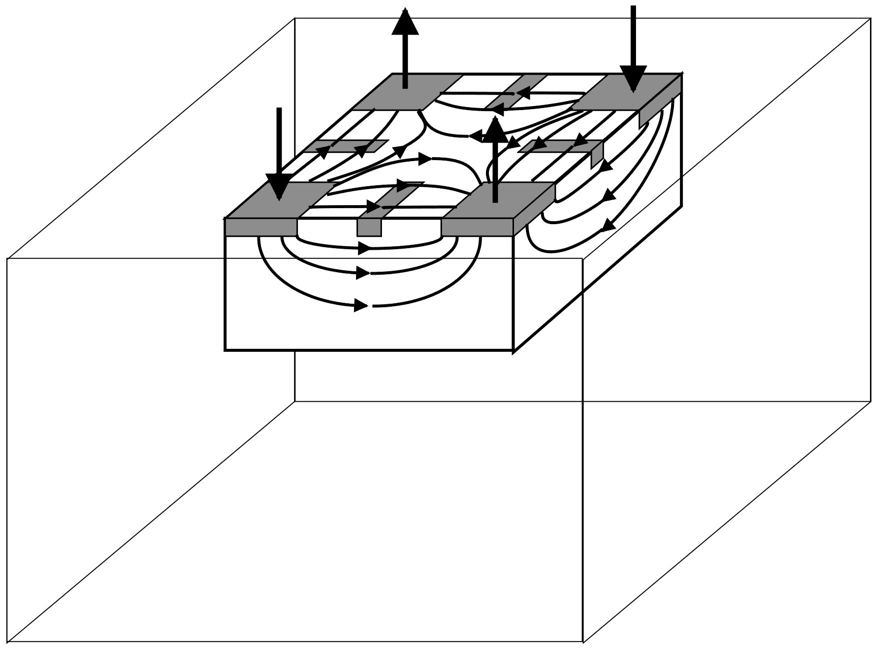

Figure 5.21 The 3-axis Hall magnetic sensor. The eight dark regions at the chip surface represent the contacts, the vertical arrows are the bias currents, and the curved arrows are the current density lines.

geometrically orthogonal due to the photolithographic manufacturing process and the three voltages are generated simultaneously, without any switching of currents or voltages. In reality, the cross-sensitivity of up to 10% is observed, caused mainly by the mask misalignment [51].

5.5 Hall Devices with Integrated Magnetic Concentrators (IMCs)

An alternative for achieving multi-axis magnetic field sensing capability with conventional horizontal plate-like Hall devices consists of combining them with a thin

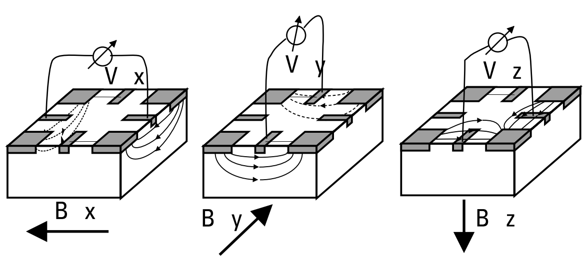

Figure 5.22 The voltmeter symbols indicate how the Hall voltages proportional to various magnetic field components are retrieved. The two in-plane magnetic field components B_x and B_y are measured between opposite Hall contacts. The sensitive regions are reminiscent of that of a vertical Hall device. The perpendicular component B_z is measured between adjacent Hall contacts, the sensitive region is similar to that of a Hall plate with the open bottom [50].

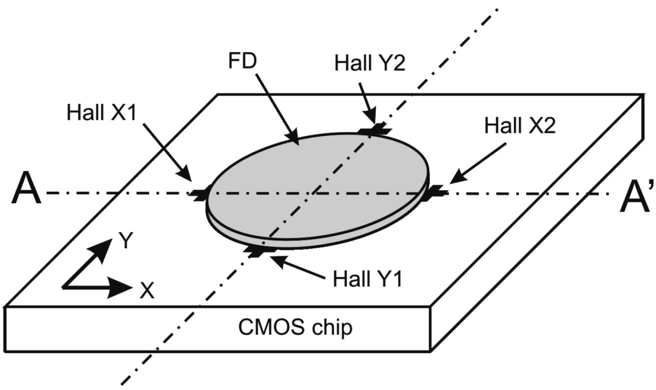

Figure 5.23 CMOS chip with four conventional Hall plates and a ferromagnetic flux concentrator.

layer of ferromagnetic material acting as an IMC [52]. Figure 5.23 shows a CMOS chip with 4 integrated Hall plates and a ferromagnetic disk (FD) structured on top of it in such a way that the Hall plates are just under its edge.

The cross-section view along the line A-A′ shows the structure exposed to a horizontal magnetic field, as shown in Figure 5.24. The flux lines enter the ferromagnetic disk ($\mu_r >> 1$) under right angles, a direct consequence of Maxwell's second equation stating the nonexistence of magnetic monopoles:

$$\nabla B = 0$$

Some flux lines enter the picture horizontally on the left, are locally rotated, pass through the Hall element X1 from the bottom, transit the IMC, pass through

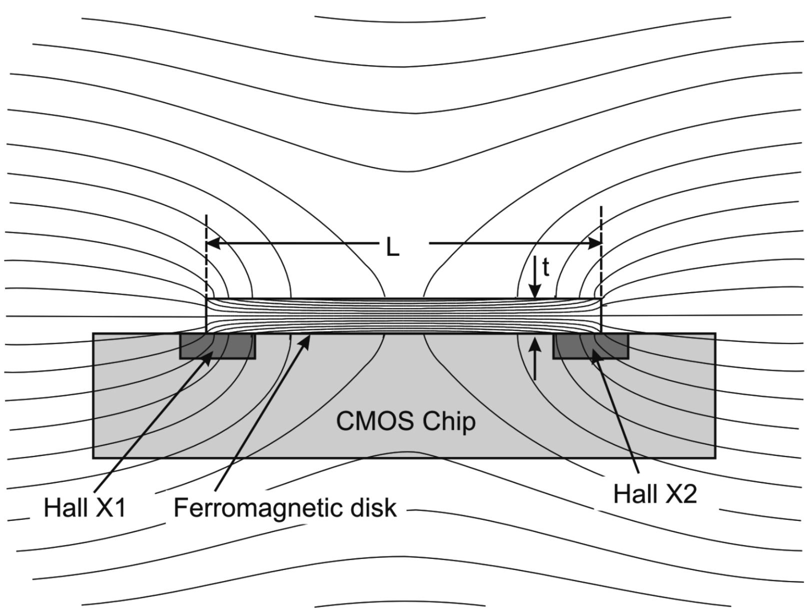

Figure 5.24 Cross-section view of the CMOS chip with Hall plates and IMC. (© 2005 IEEE. Reprinted, with permission, from [54].)

the Hall element X2 from the top, are rotated back to horizontal, and leave the picture on the right. With this effect, the externally applied field is first rotated to be measurable by conventional Hall plates and second it is amplified, resulting in an increased signal-to-noise ratio. Due to the opposite field direction on Hall elements X1 and X2, their outputs are subtracted to generate the combined output. Placing two sets of opposite Hall plates (Hall X1, X2 and Hall Y1, Y2) as in Figure 5.23, allows for the measurement of two orthogonal magnetic field components B_x and B_y in the sensor plane. If a dipole magnet is now rotating above this chip, the two sensitive axes generate a sin and cos signal, which can then be combined to determine the absolute rotary position of the magnet.

5.5.1 Rotary Sensor with IMC

This magnetic front end can now be embedded into an integrated CMOS electronic circuit together with an analog signal amplification chain, ADC, memory blocks,

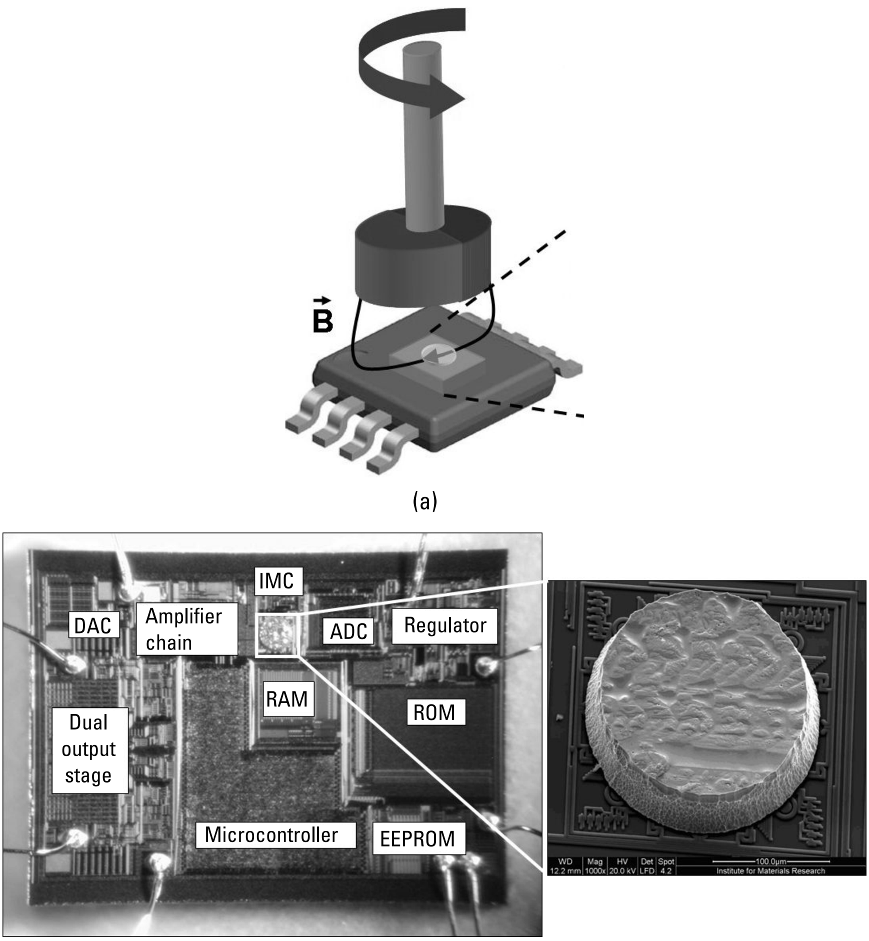

(b)

Figure 5.25 Smart CMOS rotary magnetic sensor with IMC. (© 2005 IEEE. Reprinted, with permission, from [53].)

and a microcontroller [53] as shown in Figure 5.25. On the SEM photograph inset, the IMC disk with 200-μm diameter and about 20-μm thickness is shown.

Over 1 billion such devices are used today inside hundreds of millions of cars worldwide and perform reliably all kinds of absolute rotary position measurement in windshield wipers, motors for ventilation and air-conditioning. They are also used as fuel-level sensors, chassis position sensors, steering sensors, pedal sensors, and transmission sensors.

5.5.2 3-Axis Sensor with IMC

Naturally, the four Hall elements from the previous device are also sensitive to the perpendicular magnetic field component B_z. However, instead of subtracting two Hall outputs, the signal representing B_z is generated by adding the outputs of two opposite Hall elements, using, for example, the ones aligned with the x-axis (Figure 5.26). In such a way, the four Hall elements can generate all three magnetic field components B_x, B_y, and B_z separately to the IC, merely depending on the combination of their output voltages.

The concept of 3-axis measurement is fundamental to complex position sensing tasks as they appear for example inside a joystick. Figure 5.27 shows how the

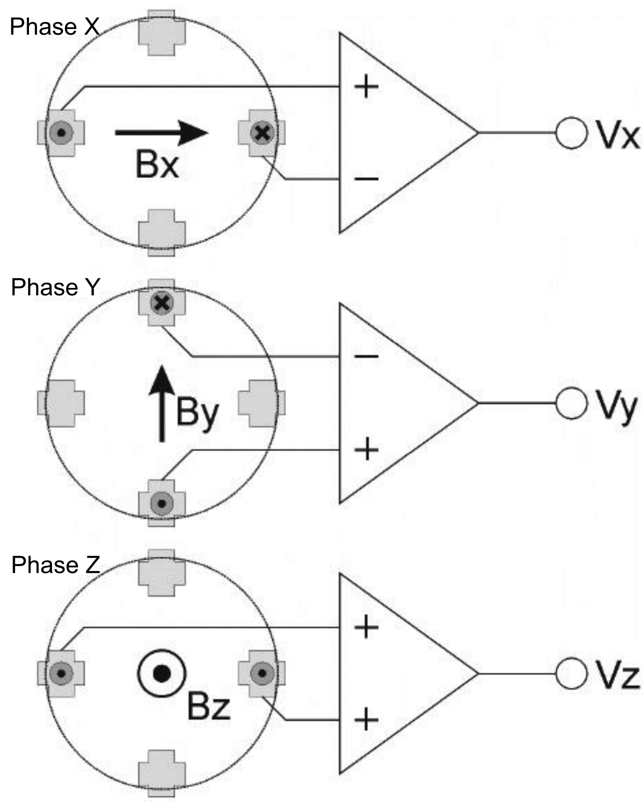

Figure 5.26 Concept of 3-axis magnetic field measurement. (© 2005 IEEE. Reprinted, with permission, from [54].)

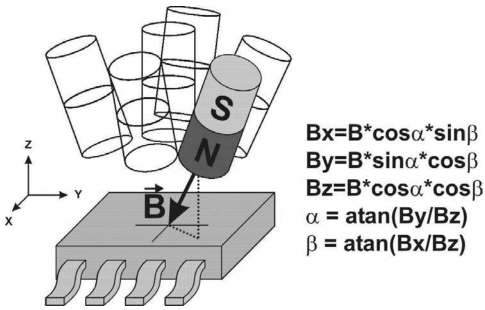

Figure 5.27 Joystick application of the 3-axis sensor measuring the two spherical angles α and β [54].

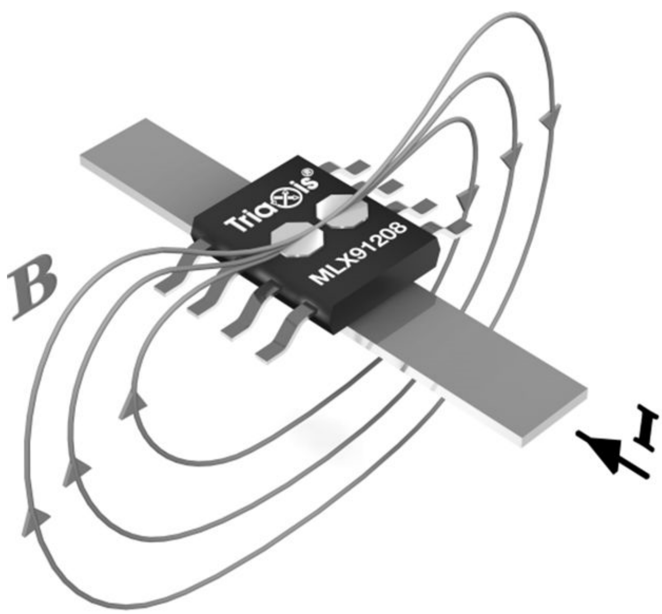

Figure 5.28 Electrical current sensor with IMCs.

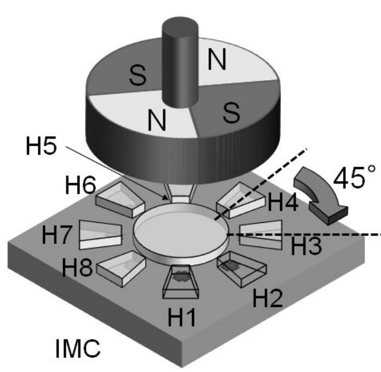

Figure 5.29 Concept of a gradiometric rotary sensor. (*From:* [56] (CC BY).)

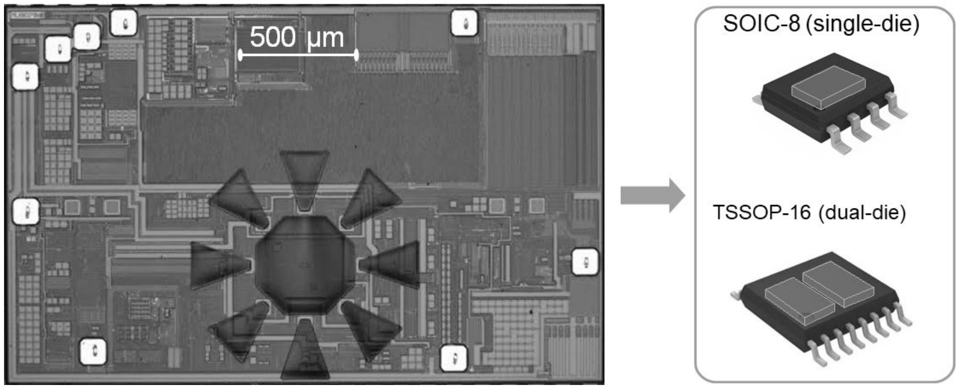

Figure 5.30 Gradiometric rotary sensor in 0.18-µm standard CMOS technology. (*From:* [56] (CC BY).)

cylinder magnet inside the joystick handle rotates by the two spherical angles α and β around the sensitive spot in the package center.

5.5.3 Integrated Current Sensor [55]

The IMC can also enhance the contactless measurement of the circular magnetic field around a current conductor. Figure 5.28 shows an integrated current sensor mounted onto a current-carrying bus bar. Two IMCs concentrate the magnetic flux onto two Hall elements that are positioned right under the inner edges close to the gap. Depending on the shape and size of the integrated concentrator parts, a magnetic gain of 2 to 5 is obtained.

The passive signal amplification of the IMC makes it possible to measure electrical current to the few milliampere range. Hall-based current sensors are today largely dominating in all markets due to their compactness and versatility. Electric current sensors are treated in Chapter 11.

5.5.4 Stray-Field Robust Gradiometric Sensors [56]

The increased electrification of the industry and the arrival of hybrid and electrical cars lead to the presence of electrical wires near the magnetic position sensor, carrying high currents. The sensor, in turn, must not be disturbed by the parasitic magnetic fields generated around those wires. A solution consists of not measuring field components anymore, but field gradients. This is a change of paradigm, as it affects not only the sensor, but also the magnetic source. The concept of such a device is shown in Figure 5.29. It is, again, based on a combination of Hall elements with IMC.

The magnetic source is a 4-pole magnet generating in-plane radial flux gradients between its pair of North poles and orthogonal to that between the South poles. These gradients, amplified by the concentrator gain g_C, give rise to eight Hall signals H1 … H8, which are combined as follows:

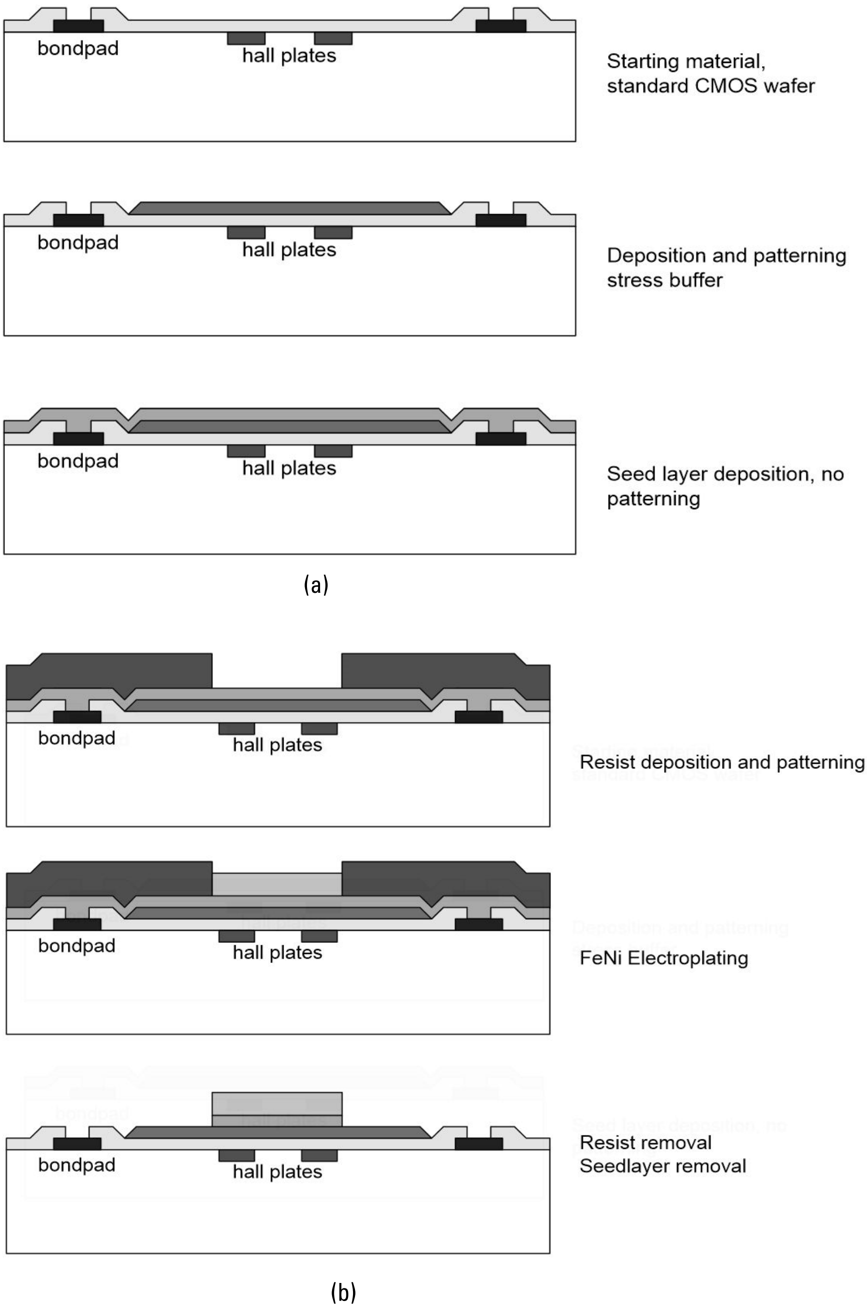

Figure 5.31 IMC deposition by electroplating onto the CMOS wafer.

$$\cos(2\alpha) = H2 - H4 + H6 - H8 = 2g_c\left(\frac{\partial B_x}{\partial x} - \frac{\partial B_y}{\partial y}\right)$$

$$\sin(2\alpha) = H1 - H3 + H5 - H7 = 2g_c\left(\frac{\partial B_x}{\partial y} - \frac{\partial B_y}{\partial x}\right)$$

So here again, a pair of quadrature sin and cos signals is generated, from which the magnet angle α can be easily retrieved via the arctan function.

The microphotograph of Figure 5.30 shows the implementation of the sensor structure with the Sun-like magnetic concentrator on top of the Hall elements. Those are positioned right underneath the inner tips of the Sun rays. Today this device is produced in volumes of several millions per year and is available as a single-die or dual-die version in various standard packages.

The inherent stray-field robustness is experimentally demonstrated in [57] on about 600 devices, showing that the maximum induced angle error generated by a worst-case 5-mT disturbing stray field is smaller than 0.25°.

5.5.5 IMC Technology

The IMC deposition on the CMOS wafer is a low-cost electroplating process following the steps illustrated in Figure 5.31. The material used is permalloy, which is a nickel–iron magnetic alloy with about 80% nickel and 20% iron content.

Due to full wafer post-processing, thousands of IMCs are structured in parallel with very tight tolerances.

References

[1] Popovic, R. S., *Hall Effect Devices*, Boca Raton, FL: CRC Press, 2003.

[2] Ramsden, E., *Hall-Effect Sensors: Theory and Application*, 2nd ed., Amsterdam: Newnes, 2006.

[3] Karsenty, A., "A Comprehensive Review of Integrated Hall Effects in Macro-, Micro-, Nanoscales, and Quantum Devices," *Sensors*, Vol. 20, No. 15, August 2020.

[4] Ausserlechner, U., M. L. Glasser, and Y. J. Zhou, "Symmetries of Certain Double Integrals Related to Hall Effect Devices," *Ramanujan Journal*, Vol. 53, No. 1, October 2020, pp. 39–48.

[5] Ausserlechner, U., "The Signal-to-Noise Ratio and a Hidden Symmetry of Hall Plates," *Solid-State Electronics*, Vol. 135, September 2017, pp. 14–23.

[6] Berus, T., M. Oszwaldowski, and J. Grabowski, "High Quality Hall Sensors Made of Heavily Doped n-InSb Epitaxial Films," *Sensors and Actuators A: Physical*, Vol. 116, No. 1, October 2004, pp. 75–78.

[7] Schott, C., et al., "High-Accuracy Analog Hall Probe," *IEEE Transactions on Instrumentation and Measurement*, Vol. 46, No. 2, April 1997, pp. 613–616.

[8] Deak, J. G., Z. M. Zhou, and W. F. Shen, "Tunneling Magnetoresistance Sensor with pT Level 1/f Magnetic Noise," *AIP Advances*, Vol. 7, No. 5, May 2017.

[9] Mosser, V., N. Matringe, and Y. Haddab, "A Spinning Current Circuit for Hall Measurements Down to the Nanotesla Range," *IEEE Transactions on Instrumentation and Measurement*, Vol. 66, No. 4, April 2017, pp. 637–650.

[10] Shibasaki, I., *Growth of InSb and InAs Thin Films and Their Application as Practical Magnetic Sensors*, Tokyo: Inst Pure Applied Physics, 2001.

[11] Kuze, N., et al., "Molecular Beam Epitaxial Growth of High Electron Mobility InAs/AlGaAsSb Deep Quantum Well Structures," *Journal of Crystal Growth*, Vol. 175, May 1997, pp. 868–872.

[12] Shibasaki, I., "Mass Production of InAs Hall Elements by MBE," *Journal of Crystal Growth*, Vol. 175, May 1997, pp. 13–21.

[13] Iwabuchi, T., et al., "High-Sensitivity Hall Elements Made from Si-Doped InAs on GaAs Substrates by Molecular-Beam Epitaxy," *Journal of Crystal Growth*, Vol. 150, No. 1-4, May 1995, pp. 1302–1306.

[14] Kachniarz, M., et al., "Quasi-Free-Standing Bilayer Graphene Hall-Effect Sensor," *IEEE Transactions on Magnetics*, Vol. 55, No. 1, January 2019.

[15] Kuze, N., et al., "InAs Deep Quantum-Well Structures and Their Application to Hall Elements," *Journal of Crystal Growth*, Vol. 150, No. 1-4, May 1995, pp. 1307–1312.

[16] Kuze, N., et al., "Interface Roughness of InAs/AlGaAsSb Deep Quantum Well Investigated by X-Ray Reflectivity," *Microelectronic Engineering*, Vol. 43-4, August 1998, pp. 185–190.

[17] Kuze, N., et al., "Molecular Beam Epitaxial Growth of InAs/AlGaAsSb Deep Quantum Well Structures on GaAs Substrates," *Journal of Vacuum Science & Technology B*, Vol. 16, No. 5, September-October 1998, pp. 2644–2649.

[18] Shibasaki, I., et al., "High Sensitivity InAs DQW Linear Hybrid Hall ICs with InAs Deep Quantum Well Hall Elements," *Electronics and Communications in Japan*, Vol. 98, No. 8, August 2015, pp. 1–8.

[19] Shibasaki, I., et al., "Low Temperature Transport Property of the InSb and InAsSb Quantum Wells with Al0.1In0.9Sb Barrier Layers Grown by MBE," *Journal of Crystal Growth*, Vol. 425, September 2015, pp. 76–79.

[20] Mosser, V., et al., "High-Sensitivity Hall Sensors with Low Thermal Drift Using AlGaAs/InGaAs/GaAs Heterostructures," *Sensors and Actuators A: Physical*, Vol. 43, No. 1-3, May 1994, pp. 135–140.

[21] Mosser, V., et al., "Low-Frequency Noise in AlGaAs/InGaAs/GaAs Hall Micromagnetometers, Noise and Information in Nanoelectronics, Sensors and Standards," *Proceedings of SPIE*, 2003, pp. 183–195.

[22] Sadeghi, M., et al., "Highly Sensitive Nanotesla Quantum-Well Hall-Effect Integrated Circuit Using GaAs-InGaAs-AlGaAs 2DEG," *IEEE Sensors Journal*, Vol. 15, No. 3, March 2015.

[23] Frick, V., et al., "CMOS Microsystem Front-End for MicroTesla Resolution Magnetic Field Measurement," *Analog Integrated Circuits and Signal Processing*, Vol. 36, No. 1-2, July-August 2003, pp. 165–174.

[24] Satav, S. A., and V. Agarwal, "Design and Development of a Low-Cost Digital Magnetic Field Meter with Wide Dynamic Range for EMC Precompliance Measurements and Other Applications," *IEEE Transactions on Instrumentation and Measurement*, Vol. 58, No. 8, August 2009, pp. 2837–2846.

[25] Kejik, P., et al., *First Fully CMOS-Integrated 3D Hall Probe*, New York: IEEE Press, 2005.

[26] Popovic, D. R., et al., "Three-Axis Teslameter with Integrated Hall Probe," *IEEE Transactions on Instrumentation and Measurement*, Vol. 56, No. 4, August 2007, pp. 1396–1402.

[27] Kejik, P., et al., "An Integrated Micro-Hall Probe for Scanning Magnetic Microscopy," *Sensors and Actuators A: Physical*, Vol. 129, No. 1-2, May 2006, pp. 212–215.

[28] Manyala, J. O., T. Fritz, and M. Z. Atashbar, "Integration of Triaxial Hall-Effect Sensor Technology for Gear Position Sensing in Commercial Vehicle Transmissions," *IEEE Transactions on Instrumentation and Measurement*, Vol. 61, No. 3, March 2012, pp. 664–672.

[29] Huang, L., et al., "Graphene/Si CMOS Hybrid Hall Integrated Circuits," *Scientific Reports*, Vol. 4, July 2014.

[30] Ishibashi, K., I. Okada, and I. Shibasaki, "High-Sensitivity Hybrid Hall Effect ICs with Thin Film Hall Elements," *Sensors and Materials*, Vol. 14, No. 5, 2002, pp. 253–261.

[31] Kerlain, A., and V. Mosser, "Low Frequency Noise Suppression in III-V Hall Magnetic Microsystems with Integrated Switches," *Sensor Letters*, Vol. 5, No. 1, March 2007, pp. 192–195.

[32] Bilotti, A., G. Monreal, and R. Vig, "Monolithic Magnetic Hall Sensor Using Dynamic Quadrature Offset Cancellation," *IEEE Journal of Solid-State Circuits*, Vol. 32, No. 6, June 1997, pp. 829–836.

[33] Munter, P. J. A., "A Low-Offset Spinning-Current Hall Plate," *Sensors and Actuators A: Physical*, Vol. 22, No. 1-3, March 1990, pp. 743–746.

[34] Schott, C., et al., "CMOS Single-Chip Electronic Compass with Microcontroller," *IEEE Journal of Solid-State Circuits*, Vol. 42, No. 12, December 2007, pp. 2923–2933.

[35] Kanda, Y., and A. Yasukawa, "Hall-Effect Devices as Strain and Pressure Sensors," *Sensors and Actuators*, Vol. 2, No. 3, 1982, pp. 283–296.

[36] Ajbl, A., M. Pastre, and M. Kayal, "A Fully Integrated Hall Sensor Microsystem for Contactless Current Measurement," *IEEE Sensors Journal*, Vol. 13, No. 6, June 2013, pp. 2271–2278.

[37] Huber, S., et al., "A Fully Integrated Analog Compensation for the Piezo-Hall Effect in a CMOS Single-Chip Hall Sensor Microsystem," *IEEE Sensors Journal*, Vol. 15, No. 5, May 2015, pp. 2924–2933.

[38] Ausserlechner, U., M. Motz, and M. Holliber, "Compensation of the Piezo-Hall Effect in Integrated Hall Sensors on (100)-Si," *IEEE Sensors Journal*, Vol. 7, No. 11-12, November-December 2007, pp. 1475–1482.

[39] Nathan, A., H. Baltes, and W. Allegretto, "Review of Physical Models for Numerical-Simulation of Semiconductor Microsensors," *IEEE Transactions on Computer-Aided Design of Integrated Circuits and Systems*, Vol. 9, No. 11, November 1990, pp. 1198–1208.

[40] Steiner, R., et al., "Influence of Mechanical Stress on the Offset Voltage of Hall Devices Operated with Spinning Current Method," *Journal of Microelectromechanical Systems*, Vol. 8, No. 4, December 1999, pp. 466–472.

[41] Schott, C., and M. Blyzniuk, "High Volume Production of Magnetic Sensors for the Automotive Market," *2012 IEEE Sensors Proceedings*, 2012, pp. 2086–2089.

[42] Popovic, R. S., "Not-Plate-Like Hall Magnetic Sensors and Their Applications," *Sensors and Actuators A: Physical*, Vol. 85, No. 1-3, August 2000, pp. 9–17.

[43] Long, D., "Scattering of Conduction Electrons by Lattice Vibrations in Silicon," *Physical Review*, Vol. 120, No. 6, 1960, pp. 2024–2032.

[44] Schott, C., P. A. Besse, and R. S. Popovic, "Planar Hall Effect in the Vertical Hall Sensor," *Sensors and Actuators A: Physical*, Vol. 85, No. 1-3, August 2000, pp. 111–115.

[45] Schott, C., et al., "High Accuracy Magnetic Field Measurements with a Hall Probe," *Review of Scientific Instruments*, Vol. 70, No. 6, June 1999, pp. 2703–2707.

[46] Sander, C., et al., "Ultra-Low Offset Vertical Hall Sensor in CMOS Technology," *28th European Conference on Solid-State Transducers (Eurosensors 2014)*, Vol. 87, 2014, pp. 732–735.

[47] Burger, F., P. A. Besse, and R. S. Popovic, "New Fully Integrated 3-D Silicon Hall Sensor for Precise Angular-Position Measurements," *Sensors and Actuators A: Physical*, Vol. 67, No. 1-3, May 1998, pp. 72–76.

[48] Burger, F., P. A. Besse, and R. S. Popovic, "New Single Chip Hall Sensor for Three Phases Brushless Motor Control," *Sensors and Actuators A: Physical*, Vol. 81, No. 1-3, April 2000, pp. 320–323.

[49] Schott, C., J. M. Waser, and R. S. Popovic, "Single-Chip 3-D Silicon Hall Sensor," *Sensors and Actuators A: Physical*, Vol. 82, No. 1-3, May 2000, pp. 167–173.

[50] Randjelovic, Z., et al., "A Non-Plate Like Hall Sensor," *Sensors and Actuators A: Physical*, Vol. 76, No. 1-3, August 1999, pp. 293–297.

[51] Beran, P., et al., "Impact of Contact Misalignment on Magnetic Cross Sensitivity of Integrated Vertical Hall Sensors," *IEEE Transactions on Magnetics*, Vol. 55, No. 1, January 2019.

[52] Popović, R. S., et al., "Integrated Hall Sensor/Flux Concentrator Microsystems," *Informacije Midem Ljubljana*, Vol. 31, No. 4, December 2001, pp. 215–219.

[53] Schott, C., R. Racz, and S. Huber, "Smart CMOS Sensors with Integrated Magnetic Concentrators," *IEEE Sensor Conference*, Irvine, CA, November 2005, pp. 959–962.

[54] Schott, C., R. Racz, and S. Huber, "CMOS Three Axis Hall Sensor and Joystick Application," *IEEE Sensors Conference*, Vienna, Austria, October 2004, pp. 977–980.

[55] Ackermann, M., and L. Coulot, "New Generation of Hall-Effect Based Current Sensor: Evolution from Core-Based to Integrated," *13th MR Symposium*, Wetzlar, Germany, 2015.

[56] Huber, S., et al., "A Gradiometric Magnetic Sensor System for Stray-Field-Immune Rotary Position Sensing in Harsh Environment," *Proc. Eurosensors*, Vol. 2, No. 13, 2018, p. 809.

[57] Dupré, N., et al., "Experimental Demonstration of Stray-Field Immunity Beyond 5 mT for an Automotive-Grade Rotary Position Sensor," *Proc. Eurosensors*, Vol. 2, 2018, p. 763.

CHAPTER 6

Resonance Magnetometers

Roland Lammegger

6.1 Introduction to Magnetic Resonance

Nuclear magnetic resonance (NMR) is a common term for a wide range of phenomena used for imaging diagnostics in medicine, for spectroscopic investigations of materials and compounds in chemistry, and for absolute measurement of weak magnetic fields.

As explained next, a coherent AC-magnetic NMR signal can be picked up by a coil surrounding a sample of atomic nuclei after suitable excitation. The various signal decay times in a constant large magnetic field are used for imaging diagnostics of different types of biological tissue, and the enhancements of specific AC frequencies, while the sample is exposed to a changing magnetic field, are used for chemical spectroscopy.

For the precise measurement of the magnitude of a weak magnetic field, the AC frequency emitted by a suitably excited and well-defined sample of atomic nuclei is determined in the nuclear resonance magnetometers. The resonance frequency is proportional to the magnetic field and, of all the stable nuclei, the proton has the largest proportionality constant or gyromagnetic ratio. The magnetic resonance of protons (in an aqueous sample of a spherical shape) constitutes an atomic reference for the Système International d'Unités (SI) units of current (ampere (A)) and magnetic field (tesla (T)).

Electron spin resonance (ESR) is the analogous phenomenon for electrons. This also finds wide application in medicine, material sciences, and chemistry, and the much higher spin frequency (about 600 times that of protons) offers the possibility of constructing highly sensitive and fast-responding scalar magnetometers. Where the classical proton magnetometer is excited by a DC magnetic field followed by the measurement of the frequency of the decaying nuclear spin signal, then the optically pumped electron spin magnetometers use light in resonance with an optical spectral line of the sample, and they produce a continuous ESR signal.

The Overhauser effect proton magnetometer combines the two phenomena. It uses an RF magnetic signal for ESR excitation of the electrons, which then, through collisions, transfer their excitation to the protons. Continuous excitation of the protons is thereby established, and this allows for a continuous proton resonance signal.

6.1.1 Historical Overview

The use of NMR was initiated by the publication of the classic article by Bloch [1]. Between 1948 and 1954, the proton-free precession principle was developed by the Varian Associates Research Laboratory [2] into an instrument offering up to one measurement per second of the scalar value of a weak magnetic field [3]. Soon thereafter, the proton magnetometer was introduced at Geomagnetic Observatories for precise measurement [2, 4–7].

Very early, proton magnetometers were carried to about 33-km altitude by a balloon and later launched into the Earth's ionosphere onboard a "Rockoon," a small-sounding rocket fired from a high-altitude balloon [8]. Other sounding rocket experiments carrying proton magnetometers abounded spanning from Burrows [9] to Olesen et al. [10]. The popularity of the proton magnetometer for space experiments was, in large part, due to the fact that no altitude information was needed to interpret the data, because only the scalar value (the magnitude) of the field was measured.

Soon after the first Soviet *Sputnik* in 1957, *Sputnik-3* launched on May 15, 1958, placed the first (fluxgate) magnetometer into space, and the *U.S. Vanguard III* satellite in 1961 carried a proton scalar magnetometer. Later, many U.S. and Russian satellites used proton magnetometers and cesium magnetometers for Earth's field monitoring (Cosmos-26/49/321 and OGO-2/4/6) [11].

In 1953, A. W. Overhauser published his discovery of the proton spin alignment effect by coupled RF ESR polarization [12]. For geophysical prospecting and at Magnetic Observatories, the continuously oscillating and less power-consuming Overhauser proton magnetometer was extensively used and the development of a field instrument [13] for prospectors made this scalar magnetometer even more popular.

An Overhauser magnetometer made by LETI, France [14] was launched on the Danish Geomagnetic Mapping Satellite *Ørsted* in 1999, and a second laboratoire d'électronique et de technologie de l'information (LETI) Overhauser instrument was launched in 2000 on the German challenging minisatellite payload (CHAMP) fields and potentials satellite.

Following Kastler's description of using optical techniques to produce magnetic polarization of the electrons in a vaporous sample [15], the development of optically pumped scalar magnetometers progressed from 1957. Where protons have the largest nuclear gyromagnetic ratio converting the field to the signal frequency of about 42.5 MHz/T, the optical magnetometers using ESR have even larger conversion constants of between 3.5 and 7.0 GHz/T for the alkali metals and up to 28 GHz/T for the metastable He^4 optical magnetometer.

Besides being continuously oscillating, the optical magnetometers thus have the advantages of a higher-frequency response and less sensitivity to platform rotation compared to the proton magnetometers [16].

Optically pumped scalar magnetometers are used for land, sea, and airborne surveys for prospecting and, to some extent, at geomagnetic observatories for measuring the field magnitude. They have also flown on many satellites. The absolute magnetic field standard onboard the NASA *Magsat* Earth's field mapping satellite (1979–1980) was a Cs^{133} optically pumped scalar magnetometer from Varian Associates [17].

Vector measurements using scalar magnetometers have been developed for Geomagnetic Observatories by sequentially adding stable bias fields to the background field in two or three orthogonal directions. Proton magnetometers have been used, but as the field-biasing sequence must be completed in a short time (in order to confidently follow the changes of the Earth's field), then the faster responding optical magnetometers seem to be preferred [3, 18].

6.1.2 Absolute Reproducibility of Magnetic Field Measurements

Until 2018, the SI was the internationally adopted unit system for measurements based on the equations of physics and on adopted exact values of specific constants of nature (such as the velocity of light). As a consequence, the 7 base units of measurement are defined, each having its own specific definition (realization). With the advances in technology and progress of measurement accuracies in all branches of physics, these definitions were changed several times.

Since 2019, the definition of the seven fundamental physical constants with fixed numerical values replaces the role of the 7 base units from the past [19]. From this basis set of fundamental physical constants, all other known physical quantities can be derived. Consequently, the (former) base units have (in principle) lost their exceptional position. However, the concept of the 7 base units is still kept to have the possibility of a coherent representation of the units of all physical quantities.

A consequence worth noticing, since important in the field of magnetometry, is the fact that the magnetic permeability μ_0 has changed its value from the former (exact) $4\pi \cdot 10^{-7}$ kg·m/(s^2·A^2) to $1.25663706212(19) \cdot 10^{-6}$ kg·m/(s^2·A^2) with a relative uncertainty of $1.5 \cdot 10^{-10}$ [20].

On basis of this approach, the inconstancies in the different precision measurements of the 7 fundamental constants (highly important in the field of atomic physics) are removed. Precision experiments for the measurement of other important constants (e.g., the electron mass) can be traced, at least theoretically, to the basis set of these 7 fundamental constants.[1]

The reference values for establishing the proper SI measure of magnetic field (tesla) are the proton gyromagnetic ratio[2] γ_p, the electron gyromagnetic ratio[3] γ_e, and the Landé g-factors[4] for the electron spin g_e, the nucleus g_I, and the electron orbital angular momentum g_L. With these atomic quantities, a measurement of the magnitude of a magnetic field can be realized with the much easier and very precise determination of a frequency.

As an example, the 2018 CODATA recommended values [21] for γ_p, γ_e, and g_e are:

$$\gamma_p = 2.675\,221\,8744(11) \cdot 10^8 \mathrm{s}^{-1}\mathrm{T}^{-1} \quad \text{or} \quad \frac{\gamma_p}{(2\pi)} = 42.577\,478\,518(18)\ \mathrm{MHz/T} \tag{6.1}$$

$$\gamma_e = 1.760\,859\,630\,23(53) \cdot 10^{11} \mathrm{s}^{-1}\mathrm{T}^{-1} \quad \text{or} \quad \frac{\gamma_e}{(2\pi)} = 28.024\,951\,4242(85)\ \mathrm{GHz/T} \tag{6.2}$$

[1] See also the discussion in [22].
[2] Related to the spin of the proton.
[3] Related to the spin of the electron.
[4] A lucid and useful collection of important atomic quantities with their numerical values and the corresponding references can be found in D. Steck's Alkali D Line Data [50].

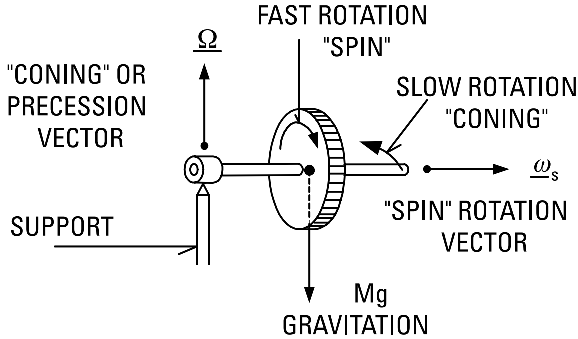

Figure 6.1 The mechanical gyroscope. The force of gravitation and the reaction from the support (not shown) constitute a mechanical torque, which makes the spinning wheel revolve slowly about the support.

$$g_e = -2.002\ 319\ 304\ 362\ 56(35) \tag{6.3}$$

These values are related to a virtually free particle. It is obvious that different couplings (e.g., a chemical shift [22]) can alter these values.[5]

For example, the proton gyromagnetic ratio in pure water and in a spherical container is given by[6]

$$\gamma'_p = 2.675\ 152\ 55 \times 10^8\ \mathrm{s}^{-1} \cdot \mathrm{T}^{-1} \tag{6.4}$$

because the chemical liquid and the shape of the vessel have a slight influence on the frequency [22–24]. This is why γ'_p is different from the single-proton γ_p.

6.2 Proton Precession Magnetometers

6.2.1 The Mechanical Gyroscope

In order to understand the basic principle of the nuclear resonance magnetometers (and of the ESR magnetometers), let us briefly consider the mechanical gyroscope, which many of us have played with and wondered about. Figure 6.1 shows a toy gyroscope consisting of a fast-spinning wheel with the axle supported at one end by a bearing, free to rotate about the support. When the spinning wheel (spin rate ω_s) is let loose, it starts to revolve about the vertical support in a slow counterclockwise precession with the rate Ω.

The key to understanding this motion is the inertial force acting on all parts of the spinning wheel. A differential volume at the edge of the wheel is kept in a circular orbit about the axis by the stress in the material, which delivers the centripetal force, just as the gravity of the Sun keeps a planet in orbit. The volume will

[5]See the discussion in [22], Chap. 7.1.2, page 270.
[6]The value was taken from [22], Chap. 7.1.2, page 270f.

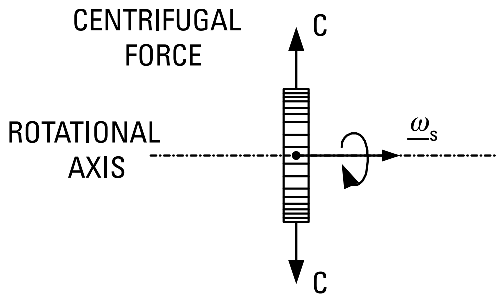

Figure 6.2 A spinning wheel in perfect balance while rotating about the body symmetry axis. The centrifugal forces C pass through the body center of gravity, and the parts of the wheel are forced to revolve about the axis by the stress forces in the material.

continue revolving as long as the breakdown limit of the material is not exceeded. If this happens, a catastrophic explosion of the wheel may result, demonstrating that we are dealing with real and very strong forces.

From the point of view of the wheel (i.e., in a coordinate system rotating with the wheel), it feels the inertial force called the centrifugal force tending to pull the wheel apart in all directions perpendicular to the axis of rotation. (Throw a stone, and your hand will feel an inertial force: the stone's reaction against being accelerated.) Figure 6.2 shows the situation when the wheel rotates about the body axis, and perfect balance exists. The centrifugal forces are directed symmetrically outward at right angles to the axis, and all the parts of the wheel are kept in place by internal stresses in the material.

A quite different situation exists if the wheel rotates about a skew axis not aligned with the body symmetry axis. Then the centrifugal forces no longer pass through the center of gravity and the balance of forces is upset. Figure 6.3 shows this situation, and clearly the centrifugal forces tend to rotate the wheel into a position symmetrical about the axis of rotation. The inertial centrifugal forces result in a mechanical torque on the wheel trying to twist the body axis parallel to the rotation axis.

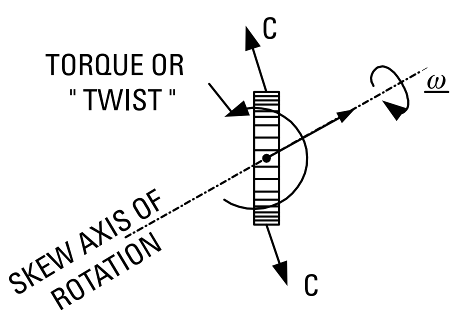

Figure 6.3 Rotation about a skew axis. The centrifugal forces miss the center of gravity and combine to form a mechanical torque on the wheel.

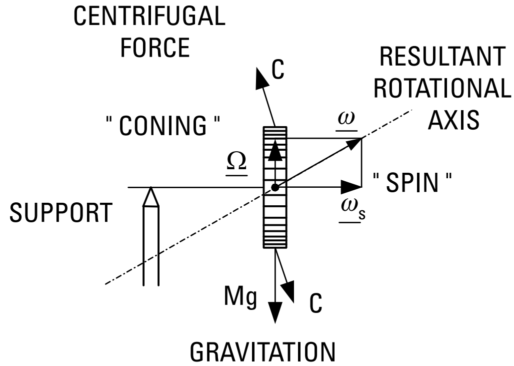

Figure 6.4 The spinning (ω_s) and coning (Ω) gyroscope supported at one end of the axle (free to spin and rotate in all directions) and acted upon by the mechanical torque from gravity ($M \cdot \mathbf{g}$) and the reaction of the support. The resulting rotation vector ω deviates from the symmetry axis and creates a balancing torque by the centrifugal forces **C**.

If the spinning wheel is rigidly mounted on a skew axle, then this will result in severe vibrations, which ultimately may destroy the system. This underlines the importance of balancing a high-speed revolving machine element in order to prevent destruction. However, a symmetrically mounted spinning wheel can be made to perform a stable rotation about an axis slightly different from the body axis. This follows from the fact that rotation vectors may be added vectorially to form a resultant instantaneous rotation vector. Figure 6.4 shows how this is acting on the toy gyroscope introduced earlier.

The wheel is spinning at the rate ω_s, and at the same time it is slowly revolving about the vertical axis of the support with the coning rate Ω (here shown displaced to the center of gravity). The combination of these two rotations is a resulting instantaneous rotation vector $\boldsymbol{\omega}$, which is twisted upwards a small angle relative to the symmetry axis of the wheel. The tangent to this small angle is Ω/ω_s.

The coning rate Ω adjusts to a magnitude so that the centrifugal forces exactly balance the torque from the gravitation.

A formal description uses the moment of inertia, I, about the axis:

$$I = \int_M r^2\, dm \tag{6.5}$$

Here dm is the mass of a differential volume of the wheel, r is the perpendicular distance of the volume from the axis of rotation, and the summing is extended over the total mass of the wheel. The angular momentum, **L**, is then given by:

$$\mathbf{L} = I \cdot \boldsymbol{\omega}_s \tag{6.6}$$

The mechanical torque, **T**, acting on the wheel from the force of gravity is:

$$\mathbf{T} = \mathbf{l} \times M \cdot \mathbf{g} \tag{6.7}$$

where $\mathbf{l}$ is the vector from the supporting point to the center of gravity and $M \cdot \mathbf{g}$ is the gravitational force on the wheel (M is the total mass and $\mathbf{g}$ is the acceleration of gravity). From Newton II follows the equation of the motion:

$$\dot{\mathbf{L}} = \mathbf{T} \tag{6.8}$$

stating that the time change of the angular momentum equals the mechanical torque vector. Thus, as an example, if we know the angular momentum (or spin), $\mathbf{L}$, of the wheel and observe the rate of precession (or coning), Ω, then (knowing the total mass, M, and the length, l, of the axle) the acceleration of gravity, $\mathbf{g}$, can be calculated.

6.2.2 The Classic Proton-Free Precession Magnetometer

The simplest and first of the nuclear precession magnetometers exploits the facts that protons possess a magnetic moment as well as an angular momentum (spin). Quantum mechanics tells us that the spin, $\mathbf{L}$, and the magnetic dipole moment, $\boldsymbol{\mu}_\mathbf{p}$, of the proton are atomic constants, and they are parallel and related by a fixed scalar constant called the proton gyromagnetic ratio, γ_p:

$$\boldsymbol{\mu}_\mathbf{p} = \gamma_p \cdot \mathbf{L} \tag{6.9}$$

Apart from that, nothing has been said about the internal structure of the spinning proton, but a mental picture illustrating the collective behavior in the classical limit of a large sample of protons may be the one shown in Figure 6.5. The proton behaves like a small mechanical gyroscope with the axle made of a bar magnet having North and South poles of magnitude $\pm m$ separated by the vector $\mathbf{l}$. If the proton is placed in an external field, $\mathbf{B}$, then the poles feel the forces $\mathbf{F} = \pm m \cdot \mathbf{B}$ constituting a mechanical torque $\mathbf{T} = m \cdot \mathbf{l} \times \mathbf{B} = \boldsymbol{\mu}_\mathbf{p} \times \mathbf{B}$.

The proton magnetic moment is $m \cdot \mathbf{l} = \boldsymbol{\mu}_\mathbf{p}$, and from a table of quantum mechanical constants, we have $\mu_p \cong 1.41 \times 10^{-26}$ Am^2 [21]. Using the value of $\gamma_p \cong 2.675 \times 10^8$ rad/s·T (Section 6.1.2) the proton angular momentum (or spin) is calculated to be:

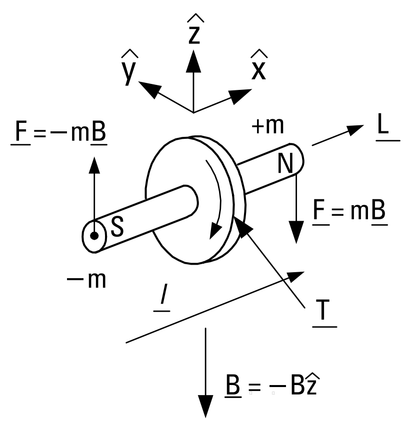

Figure 6.5 Protons have angular momentum or spin, L, and magnetic moment, $\boldsymbol{\mu}_\mathbf{p} = m \cdot \mathbf{l}$, much like a gyroscope with a bar magnet as an axle. An external field, $\mathbf{B}$, gives a torque, $\mathbf{T}$, on the moment.

$$L \cong 5.27 \times 10^{-35}\ \text{kg·m}^2/\text{s} \tag{6.10}$$

which is equal to $1/2\hbar$, as the proton spin should be (Planck's constant $\hbar \cong 1.0546 \times 10^{-34}$ J·s [21]).

In the coordinate system of Figure 6.5, the angular momentum, **L**, is precessing about the $\hat{z}$-axis:

$$\mathbf{L} = L\left(\cos(\omega t)\hat{\mathbf{x}} + \sin(\omega t)\hat{\mathbf{y}}\right) \tag{6.11}$$

$$\boldsymbol{\mu}_\mathrm{p} = \gamma_p L\left(\cos(\omega t)\hat{\mathbf{x}} + \sin(\omega t)\hat{\mathbf{y}}\right) \tag{6.12}$$

$$\dot{\mathbf{L}} = \omega L\left(-\sin(\omega t)\hat{\mathbf{x}} + \cos(\omega t)\hat{\mathbf{y}}\right) \tag{6.13}$$

$$\mathbf{T} = \boldsymbol{\mu}_\mathrm{p} \times \mathbf{B} = \begin{vmatrix} \hat{\mathbf{x}} & \hat{\mathbf{y}} & \hat{\mathbf{z}} \\ \cos(\omega t) & \sin(\omega t) & 0 \\ 0 & 0 & -B \end{vmatrix} = \gamma_p LB\left(-\sin(\omega t)\hat{\mathbf{x}} + \cos(\omega t)\hat{\mathbf{y}}\right) \tag{6.14}$$

Using $\dot{\mathbf{L}} = \mathbf{T}$, we get

$$\omega \cdot L = \gamma_p \cdot L \cdot B, \text{ and } \omega = \gamma_p \cdot B \tag{6.15}$$

The proton magnetic moment rotates clockwise about the magnetic field B with the frequency:

$$f = \left(\frac{\gamma_p'}{2\pi}\right)B \tag{6.16}$$

In a spherical sample of water, the value $\gamma_p' = 2.67515255 \times 10^8$ ($\gamma_p'/2\pi = 42.576375$ MHz/T) should be used (see Section 6.1.2). The modification of the proportionality constant is not caused by any real change of the proton gyromagnetic ratio, but it is because the external magnetic field $\boldsymbol{B}$ is slightly modified by the diamagnetism of water combined with the demagnetizing factor of the spherical shape of the sample. However, rather than computing the internal field B_i in the water sample and then correcting for shape and diamagnetism, the external field is obtained directly by using the modified gyromagnetic ratio γ_p'.

When a volume of a proton-rich liquid is exposed to a strong DC-polarizing magnetic field $\mathbf{B}_\mathrm{p}$, then the proton magnetic moments tend to be aligned along $\mathbf{B}_\mathrm{p}$ (Figure 6.6). However, this is counteracted by thermal agitation, resulting in the net alignment of only a small fraction of the protons. The fraction of aligned (or polarized) protons equals the ratio of magnetic energy to the average thermal energy:

$$\text{Fraction of aligned protons} \approx \frac{\text{Magnetic Energy}}{\text{Thermal Energy}} \approx \frac{\mu_p B_p}{kT}\ \left(\text{valid for } \mu_p B_p << kT\right) \tag{6.17}$$

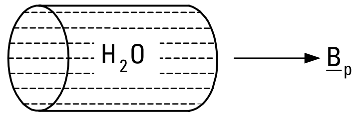

Figure 6.6 A sample of water is exposed to a strong polarizing DC magnetic field $\mathbf{B}_p$. The field tends to align the magnetic moments of the protons.

In a polarizing field, $B_p = 14.4$ mT, the magnetic energy of a proton is $\mu_p \cdot B_p \cong 2.03 \times 10^{-28}$ J. The average thermal energy is $kT = 4.14 \times 10^{-21}$ J, where $k \cong 1.381 \times 10^{-23}$ J/K is Boltzmann's constant, and $T = 300$K is the absolute temperature. The magnetic energy is much smaller than the thermal energy, and so the fraction of aligned protons is:

$$\frac{\delta n}{n} \approx \frac{\mu_p B_p}{kT} \cong 4.83 \times 10^{-8} \tag{6.18}$$

We may now calculate the magnetization of water exposed to a polarization field of 14.4 mT.

One cubic meter of water weighs 1,000 kg, and one H_2O molecule weighs 18 amu (atomic mass units) or $18 \times 1.67 \times 10^{-27}$ kg $= 3.01 \times 10^{-26}$ kg. Each water molecule has two protons, and so the density of protons in water is:

$$n \cong \frac{2 \times 10^3}{3.01 \times 10^{-26}} \cong 6.64 \times 10^{28} \text{ protons/m}^3 \tag{6.19}$$

The resulting magnetization (or the magnetic moment per unit volume) for a polarization field of $B_p = 14.4$ mT is then:

$$\begin{aligned} M_0 &= n \times \left(\frac{\delta n}{n}\right) \times \mu_p = 6.64 \times 10^{28} \times 4.83 \times 10^{-8} \times 1.41 \times 10^{-26} \text{ A/m} \\ &= 4.52 \times 10^{-5} \text{ A/m} \end{aligned} \tag{6.20}$$

M_0 is the saturation magnetization approached exponentially with a time constant of a few seconds in pure water after the application of the polarization field $\mathbf{B_p}$. Suddenly removing the polarization leaves the magnetization of the water $\mathbf{M}$ (approximately) in the direction of $\mathbf{B_p}$, and $\mathbf{M}$ then starts to rotate clockwise about the external field $\mathbf{B}$ with the frequency $f = (\gamma_p'/2\pi) \cdot B$. The changing magnetic field from the rotating magnetization will then induce an AC signal in a pickup coil wound around the water sample. The magnetization of the water decreases exponentially with time, and so the decaying signal can only be picked up for a couple of seconds (Figure 6.7).

The largest signal is obtained if the pickup coil axis is oriented at right angles to the external $\mathbf{B}$-field because $\mathbf{M}$ rotates about $\mathbf{B}$. The polarization field should also be applied at right angles to the external field $\mathbf{B}$, because this leaves the largest component of $\mathbf{M}$ perpendicular to $\mathbf{B}$. The same coil may be used for polarization and for signal pickup, but if the coil is a cylindrical solenoid, then a dead zone for $\mathbf{B}$ will

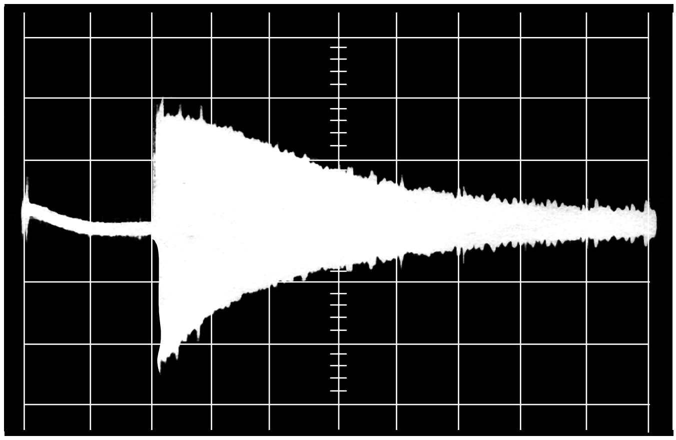

Figure 6.7 A decaying proton precession signal of about 2 kHz in the Earth's field. Vertical scale: 1 μV/div, horizontal scale: 1 s/div.

exist close to the coil axis. First, because **M** will be left mostly along **B** with a very small component rotating about **B**, and second, as **M** is rotating about an axis close to the coil axis, then the induced signal will still be smaller and disappear in noise.

Serson [6] introduced the omnidirectional Toroid sensor, and the author used this shape (see Figure 6.8) for sounding rocket experiments in the 1970s [10].

Regardless of the orientation, some parts of the coil will always be perpendicular to the external **B**-field. The largest signal is obtained when the field is along the symmetry axis, with a factor-of-2 decrease in signal amplitude, when the field is in the plane of the ring. The signal strength goes as $(2 - \sin^2\alpha)$, where α is the angle between the Toroid axis and the external **B**-field [25].

Because of its symmetry, the Toroid sensor will attenuate homogeneous AC noise fields from the environment, but still very strong noise signals may impair the proper functioning of the sensor. Sensors made of two antiparallel solenoids are

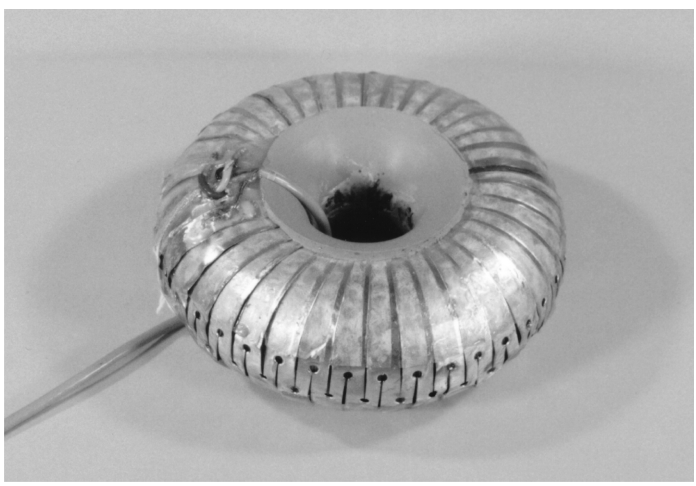

Figure 6.8 Omnidirectional Toroid proton magnetometer sensor. A hollow acrylic ring with kerosene and 1,000 turns of 1-mm-diameter Al wire. An external electrostatic screen improves the noise immunity of the Toroid; 16-cm overall dimension.

also relatively noise immune, but in contrast to the Toroid sensor, they still exhibit a null-zone close to the common axis.

Immediately after the polarization field, $\mathbf{B_P}$, is removed from the Toroid proton-rich liquid sample by rapidly switching off the polarization current I_P, and then the sample magnetization $\mathbf{M}_0$ starts to precess about the Earth's field $\mathbf{B_P}$ (see Figure 6.9). The magnetization along the center circle of the ring is:

$$M_{\text{axis}} = M_0 \cos(\omega t) \tag{6.21}$$

The magnetic field from this magnetization follows concentric circles along the ring, and the magnitude is given by:

$$B_M = \mu_0 (1 - D) M_{\text{axis}} \tag{6.22}$$

where the demagnetizing factor is $D \cong 0$ along the ring. We then have:

$$B_M \cong \mu_0 M_0 \cos(\omega t) \tag{6.23}$$

The induced voltage in the Toroid coil immediately after polarization is:

$$A = \pi \cdot r^2 = 2.0 \times 10^{-3} \text{ m}^2 \tag{6.24}$$

$$n = 1{,}000 \tag{6.25}$$

$$e(t) = nA\mu_0 \omega M \sin(\omega t) = 1.3\ \mu\text{V} \tag{6.26}$$

The signal-to-noise ratio depends on the Toroid coil and on the amplifier input circuit.

Koehler [26] gave a realistic estimate of the signal-to-noise ratio:

$$\frac{S}{N} = \frac{e}{e_{\text{noise}}} \cong 40 - 50 \tag{6.27}$$

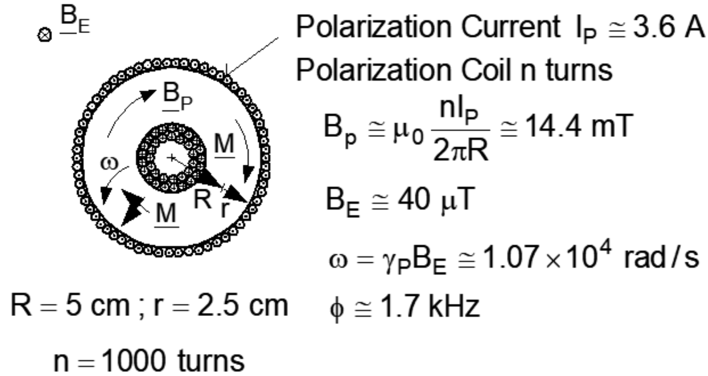

Figure 6.9 Cross-sectional view of a Toroid sensor after polarization by the field $\mathbf{B_P}$. The magnetization M rotates about the direction of the Earth's field $\mathbf{B_E}$ with the angular velocity ω.

During polarization, the sample is exposed to $\mathbf{B}_{\text{res}}$, the combination of the polarization field $\mathbf{B_P}$ and the Earth's field $\mathbf{B_E}$ at right angles to each other (see Figure 6.10).

From $\mathbf{B_P}(t) = \mathbf{B}_{\mathbf{P}\text{max}}$ to $\mathbf{B_P}(t) = 0$, the change of the direction φ of the resultant field $\mathbf{B}_{\text{res}}$ occurs with rapidly increasing speed. At first, the magnetization $\mathbf{M}$ follows $\mathbf{B}_{\text{res}}$, but at some point $\mathbf{B}_{\text{res}}$ starts to run away from the magnetization. This happens when the rate of change of the angle φ becomes larger than the natural angular velocity ω of the protons, if precessing in the instantaneous field $\mathbf{B}_{\text{res}}$.

$$\frac{d\varphi}{dt} \geq \omega_p = \gamma_p \cdot B_{\text{res}}; \quad B_{\text{res}} = \sqrt{B_P^2 + B_E^2} \tag{6.28}$$

$$\cot\varphi = \frac{B_P}{B_E}; \quad \frac{d\cot\varphi}{dt} = -\frac{1}{\sin^2\varphi}\frac{d\varphi}{dt} = \frac{1}{B_E}\frac{dB_P}{dt} \tag{6.29}$$

If $B_P(t)$ decreases linearly with time toward zero during the switching time T_S, then $dB_P/dt = -B_{P\text{max}}/T_S$ is constant. Counting time t from the beginning of the switch-off operation we have:

$$B_P(t) = B_{P\max} \cdot \left(1 - \frac{t}{T_S}\right) \tag{6.30}$$

Further, we may write (using $d\varphi/dt = \omega_P$):

$$\sin^2\varphi = \frac{B_E^2}{B_{\text{res}}^2}; \quad \frac{B_E^2}{B_{\text{res}}^2} \cdot \frac{B_{P\max}}{B_E \cdot T_S} = \gamma_p B_{\text{res}} \tag{6.31}$$

The time for switching off the polarizing field follows from the switch circuit parameters, and a reasonable value is $T_S \cong 1$ ms. This means that at the point where B_{res} runs away from $\mathbf{M}$, we have (see Figure 6.10 for the remaining numerical values):

$$B_{\text{res}} = \sqrt[3]{\frac{B_E \cdot B_{P\max}}{T_S \cdot \gamma_P}} = 129\ \mu\text{T} \tag{6.32}$$

The magnitude of the polarizing field is reduced from $B_{P\text{max}}$ to:

$$B_{P0} = \sqrt{B_{\text{res}}^2 - B_E^2} = 123\ \mu\text{T} \tag{6.33}$$

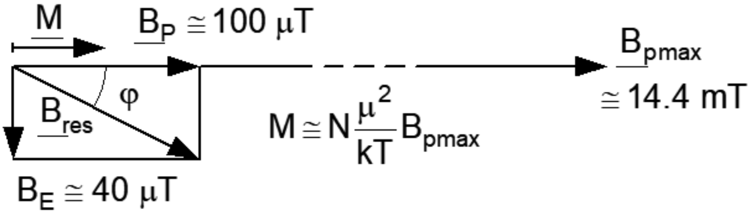

Figure 6.10 The polarizing field B_p decreases rapidly, and at some point in time the resultant field B_{res} starts to rotate the angle φ away from the polarizing direction and toward the direction of the Earth's field B_E.

The time t_0 from the beginning of the switching sequence until the runaway starts is:

$$t_0 = T_S \cdot \left(1 - \frac{B_{P0}}{B_{P\max}}\right) = 0.991 \text{ ms} \tag{6.34}$$

and at runaway the rotation angle φ_0 of **M** away from being perpendicular to the Earth's field $\boldsymbol{B}_E$ is:

$$\varphi_0 = \tan^{-1}\left(\frac{B_E}{B_{P0}}\right) = 18° \tag{6.35}$$

Because of the cubic root in the expression for B_{res}, then B_{P0} and φ_0 are relatively insensitive to changes in T_S. A doubling of T_S only means a factor of about 1.28 increase in the start runaway angle to 23°.

The growth of the magnetization of the proton-rich liquid sample follows an exponential curve towards the saturation value after application of the constant polarization field. Similarly, an exponential decay of the magnetization towards the equilibrium value in the Earth's field follows after the removal of the polarization. $M(t)$ grows as:

$$M(t) = M_0 \cdot \left(1 - e^{-\frac{t}{T_1}}\right) \tag{6.36}$$

where T_1 is the spin-lattice relaxation time constant. Figure 6.11 shows the growth of magnetization in oxygen-free water [27]. Because of its paramagnetism, dissolved oxygen in the water will lead to a rapid decay of the proton signal. Different proton-rich chemical liquids will, as to be expected, have different relaxation time constants.

$$\text{Distilled water } T_1 \cong 2 \text{ to } 3 \text{ seconds} \tag{6.37}$$

$$\text{Kerosene } T_1 \cong 0.5 \text{ second} \tag{6.38}$$

$$\text{Oxygen-free water } T_1 \cong 3.1 \text{ seconds} \tag{6.39}$$

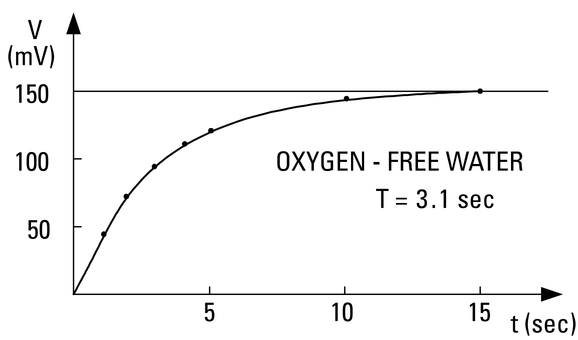

Figure 6.11 Amplified precession signal strength dependence of the polarization time. Growth of the magnetization with polarization time follows the same curve. (*After:* [27].)

The decay of the magnetization after switch-off of the polarization goes exponentially toward the very small Earth's field equilibrium value as:

$$M(t) = M_1 \cdot \left(e^{-\frac{t}{T_2}} \right) \tag{6.40}$$

where M_1 is the start magnetization and T_2 is the spin-spin relaxation time. In general, $T_2 \leq T_1$, and the time constants are selected according to the application of the proton magnetometer. For ground-based use, the time constants are often chosen to be as long as possible in order to get as long a time to measure the precession frequency as possible, whereas for the sounding rocket use, a short time constant is needed to increase the sampling rate to once per second or more.

A magnetic field gradient over the sensor will decrease the time constant of the precession signal decay (Figure 6.12) because the proton precession frequency will vary over the sample, and the resulting interference will lead to a faster signal decay.

After the polarization, all the protons start rotating from the same direction, but because of the gradient, the fields at the ends of the sample are different, and the precession frequencies are also different:

$$\omega_1 = \gamma'_P \cdot B_E^{(1)} \qquad \omega_2 = \gamma'_P \cdot B_E^{(2)} \tag{6.41}$$

After the time t, a phase difference between the protons at the two positions will evolve (they will have rotated trough slightly different angles):

$$\Delta\varphi = \left(\omega_1 - \omega_2\right) \cdot t = \gamma'_P \cdot \left(B_E^{(1)} - B_E^{(2)}\right) \cdot t = \gamma'_P \cdot \frac{\partial B}{\partial r} \cdot \ell \cdot t \tag{6.42}$$

When $\Delta\varphi = \pi$, then the magnetizations at the two ends of the sensor are antiparallel, and the signal is very much reduced. For $\ell = 10$ cm and the gradient $\partial B/\partial r$ = 400 nT/m, the time t_0 for signal disappearance is:

$$t_0 = \frac{\pi}{\left(\gamma'_P \cdot \left(\frac{\partial B}{\partial r}\right) \cdot \ell\right)} \cong 0.3\text{s} \tag{6.43}$$

which is much shorter than the relaxation time for oxygen-free water. This effect may be used to measure weak field gradients.

Magnetic material close to the sensor will expose it to a large field-gradient and destroy the signal. This may be used to verify that a precession signal is seen: the signal should disappear, when a magnet is brought near to the sensor.

Previously, the proton precession frequency measurement was done by counting the number of pulses from an absolute reference frequency generator during a predetermined number of precession periods, or by multiplying the precession frequency (using a phase-locked loop) by a suitably high number N, and then determining the number of pulses of the N-times-precession frequency for 1 second or 0.1-second periods derived from an absolute frequency standard. Both methods are sensitive to time jitter in the start and stop edges of the counting period determination, and to the ±1 count truncation error in the number of received impulses. The system can be optimized rendering these error sources negligible, and, in particular, the filtering properties of the phase-locked loop should be fully exploited.

However, with the availability of powerful digital signal processors (DSP), more efficient and better noise suppressing digital algorithms offer superior signal analysis methods compared to the classic frequency determination. Controlled by a stable and accurate time base crystal, the decaying precession signal is digitized after suitable amplification to match the analog-to-digital converter (ADC) input voltage range. The digital time series representing the precession signal is then analyzed in the DSP, most simply by fitting to the signal the initial amplitude a_0, the angular frequency ω, and the time decay constant δ in the following expression:

$$a(t) = a_0 \cdot e^{-\delta t} \cdot \sin(\omega t) \tag{6.44}$$

That immediately provides the precession frequency and the measurement quality parameters a_0 and the decay constant, as the result of an averaging process using all signal data.

More advanced NMR spectral analysis routines are based on fast Fourier transform (FFT) very well suited for DSPs. A predetermined number of spectral peaks come out as eigenvalues of an analysis matrix, and the algorithm may resolve double peaks caused by field gradients with pico-tesla resolution [28].

The classic proton magnetometer can be turned into a continuously oscillating instrument. Reimann [29] and Sigurgeirsson [30] described a system whose basic principle is shown in Figure 6.13.

Finally, it should be briefly mentioned that the principles of NMR are widely applied in NMR imaging in medicine [74].

6.2.3 Overhauser Effect Proton Magnetometers

In 1953, Alfred W. Overhauser (see Overhauser [12]) suggested that the large polarization of the electron magnetic moments would be transferred to the protons of the same sample by the various couplings between the electrons and the protons.

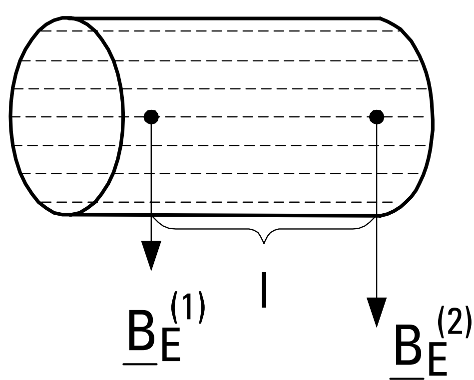

Figure 6.12 The effect of a field gradient: different fields will lead to different precession frequencies, and signal interference will shorten the signal decay time.

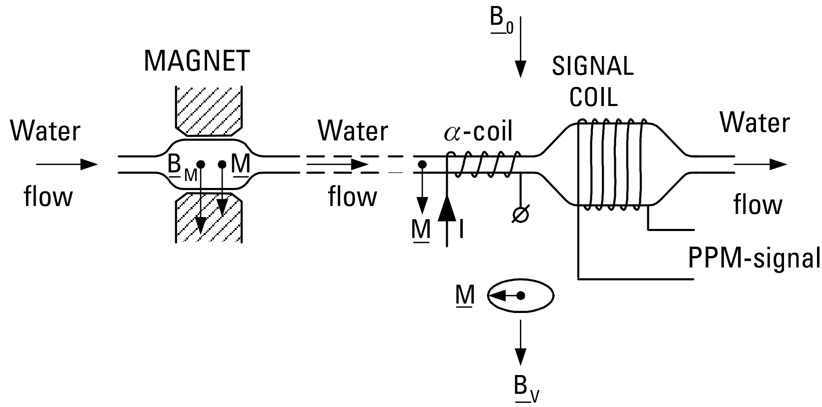

Figure 6.13 Continuously oscillating classical proton precession magnetometer. The polarization is done by a permanent magnet, and the water is pumped to a signal pickup coil at a safe distance. The α-coil field rotates the magnetization perpendicular to the Earth's field.

This offers an alternative method for proton spin alignment [32] requiring far less power than the classic Bloch method [1] using large DC polarization fields. The upper energy level of the free electrons in an external DC magnetic field can be continuously saturated using an RF signal in resonance with the corresponding ESR spectral line, which is determined by the environmental magnetic field. In some cases, the ESR peak is narrow, meaning that the RF power needed for polarization saturation of the electrons is modest, even if continuous RF pumping of the electrons is maintained. This is the dynamic nuclear polarization (DNP), and the theoretical enhancement of the proton polarization by DNP is about 330 times their natural polarization in the same magnetic field [13].

The trick is to have a proton-rich liquid sample, and at the same time to have some free electrons available for RF ESR. In most stable chemical compounds, the electrons are paired and unavailable for ESR, but in the free radicals a single unpaired electron exists. This, in passing, also makes the free radical somewhat aggressive and with a tendency to be chemically unstable.

The ESR line for nitroxide is fairly broad, up to about 100 μT in the Earth's field. By using Perdeuterated Tempone (i.e., substituting deuterium for the hydrogen atoms), the ESR line width is reduced to 20 to 30 μT with a resulting substantial reduction of the RF power needed to saturate the electron polarization (see Figure 6.14) [33]. In contrast to this, the proton NMR spectral line can be less than 2 nT in solvents of reasonably long relaxation time constants, and the inaccuracies can be limited to a small fraction of a nano-Tesla [13].

The Overhauser scalar magnetometer sensor has the liquid proton sample (with an optimized amount of Tempone dissolved) inside a 60-MHz cavity resonator, and with the cavity connected to a continuously operating 60-MHz RF oscillator via a coaxial cable. A sustained forced-precession oscillation of the protons at the precession frequency $f = \gamma_p' \cdot |\mathbf{B}_{\text{Earth}}|$ may then be obtained by letting the proton sample be the frequency determining part of a feedback circuit. Intermittent proton-free precession can also be established by first RF-polarizing the electrons of the sample for a (short) time long enough to establish the proton polarization. After switching off the RF, a short DC impulse in the pickup coil turns the proton moments

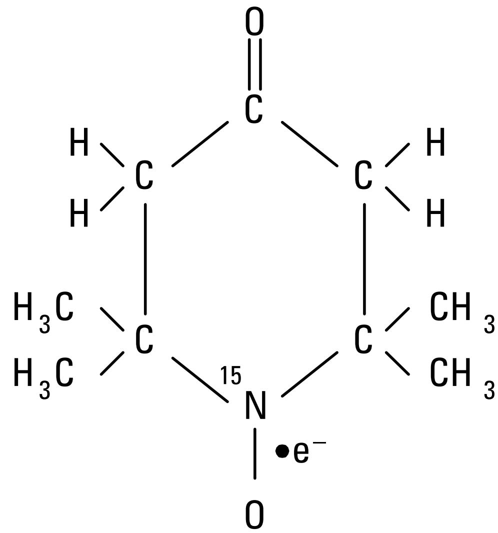

Figure 6.14 Tempone nitroxide free radical. The unpaired electron indicated by the dot near the nitrogen atom is available for ESR polarization. (*After:* [33].)

perpendicular to the Earth's field, and the decaying proton precession signal can be observed just as in the classical proton magnetometer.

As for the DC-polarized free-precession magnetometer, a null line exists for **B**-vector directions along the pickup coil axis, close to which the proton signal disappears into the noise. Due to the large dynamic proton polarization by the Overhauser effect, the half opening angle of this theoretical null cone is quite small. For the commercial GEM-19 magnetometer [13], the null cone is barely noticeable as a slight increase in the measurement noise from typically 0.1 nT for **B** perpendicular to the null line to about 1.0 nT for **B** closer than about 5°. It is of little concern for most applications because the instrument still produces valid, albeit slightly noisier, measurements. The LETI Overhauser magnetometer sensor [14] for the *Oersted* and *CHAMP* satellite missions was constructed to be omnidirectional by using highly inhomogeneous AC excitation fields from the proton precession forcing coils. Regardless of the direction of the external field, some parts of the liquid always have the precession forcing field perpendicular to the external field and to the sensor coil axis.

For low fields below about 15,000 nT, the proton-free precession rate becomes proportionally smaller and the amplitude of the induced signal correspondingly lower. However, the signal-to-noise ratio can be maintained by narrowing the frequency bandpass of the analog signal-handling circuits at the expense of a longer sampling time. At low fields, the Overhauser effect based on Tempone presents a slight disadvantage because of a double-positive/negative response of the DNP factor as a function of the ESR RF-signal frequency. The double peak response is particular to Tempone and caused by a complicated ESR spectral line structure.

Figure 6.15 shows the Tempone double structure in two different solvents [34]. This has been very elegantly used by LETI in their magnetometer in order to obtain proton polarization along the environmental field in one cell and antiparallel to the field in a second cell using the same RF signal. However, the ESR frequency

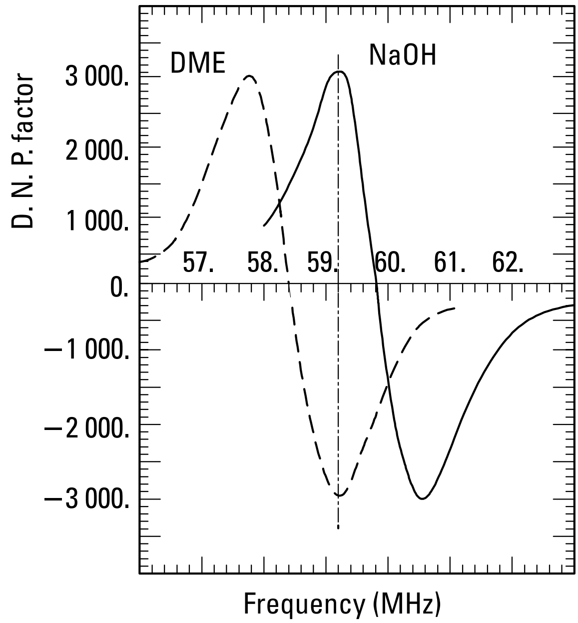

Figure 6.15 The double-positive/negative proton polarization structure of the Tempone Nitroxide free radical. (*After:* [34].) The DNP factor is shown against the ESR RF-pumping frequency for Tempone in two solvents: methanol (MeOH) full line and dimethoxyethane (DME) dashed line. The chemical shift in the two solvents is demonstrated by the frequency displacement of the two curves.

separation between the positive and the negative peaks depends on the external field, and at low fields (below about 16,000 nT) the peaks are so close together that a substantial reduction in the DNP-factor results. The consequence is that the signal-to-noise ratio approaches zero more rapidly than does the proton precession

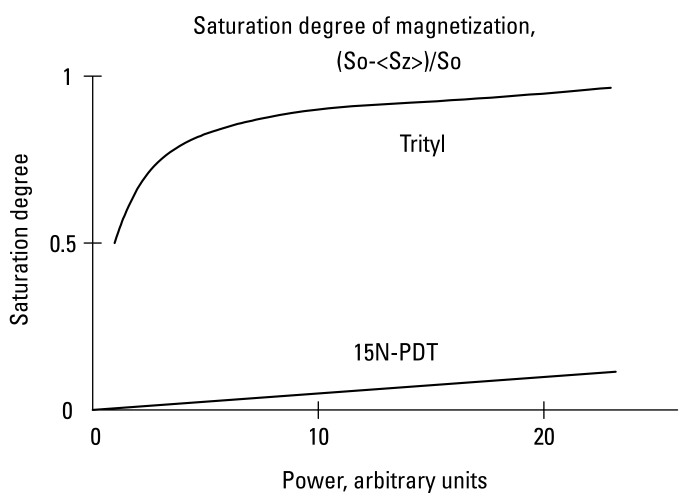

Figure 6.16 Polarization saturation degree versus ESP RF power for Trityl and Tempone. Trityl reaches saturation polarization for much less power than does perdeuterated Tempone Nitroxide.

frequency, when the B-field goes to zero. This effect is of little concern for Earth's field measurements. However, for interplanetary applications, the deep-space low-fields performance of a scalar instrument is of importance.

The ESR RF-power decreases dramatically with a narrowing ESR line width, and a free radical not having the double-positive/negative peak structure of Tempone will present a superior low-field performance. An alternative free radical of the Trityl group has a single ESR line of only 2.5-μT width (see [35]) compared to 20 μT or more for the nitroxide. The RF saturation power of the ESR is proportional to (at least) the square of the line width, and so the power is milliwatts compared to watts for the nitroxide free radical. Figure 6.16 shows a comparison between the nuclear polarization degree against RF power for the nitroxide and for Trityl.

Trityl does not have the zero-field splitting and so the free electron only sees the external field; no effective additional nuclear field exists as in the case of the nitroxide. Full ESR saturation is obtained at a modest RF-power level, and the free radical concentration can be optimized for maximum polarization coupling between the electrons and the protons, because there is room for the consequential slight broadening of the line and associated increase in saturation power. DNP can either take place in the Earth's field requiring the RF to track the field, or a homogeneous DC field of about 10 mT may be applied, thereby further enhancing the proton polarization and reducing the need for RF tracking.

6.3 Optically Pumped Magnetometers

6.3.1 Alkali Metal Vapor Magnetometers

All magnetometers based on the principle of magnetic resonance can be divided into two classes. The distinction here is made in the method of detection of the signals, which ultimately comes from two different projections of the magnetic moment [36].[7]

However, both types of magnetometers have in common that magnetic transitions in the fine or hyperfine structure are excited in various ways. To achieve this, the alkali metals with an unpaired outer electron and, consequently, a magnetic moment have proven to be very favorable in many respects.

In this case, small amounts of the solid metal are contained in a glass vessel with a buffer gas, and the cell is heated and maintained at a suitable temperature for obtaining the optimum alkali vapor partial pressure in a buffer gas minimizing the effects of inter-atomic collisions. Coating the cell walls with a material having an argon electron structure reduces the wall collision effects. The temperature for a vapor pressure of 10^{-6} Torr is 126°C for Na^{23}, 63°C for K^{39}, 34°C for both Rb isotopes, and 23°C for Cs^{133}, and of all the alkali atoms, cesium needs the least heating power [37, 38].

Typical to all natural isotopes of alkali atoms are a nuclear spin $\mathbf{I} > 0$ (e.g., $\mathbf{I} = 3/2$ for Na^{23}, K^{39}, K^{41}, and Rb^{87}). As a result, in the weak magnetic field range (approximately $B < 0.1\text{T}$), the total angular momentum of the electron shell $\mathbf{J} = \mathbf{L} + \mathbf{S}$

[7]See Chapter 4.2, page 63f.

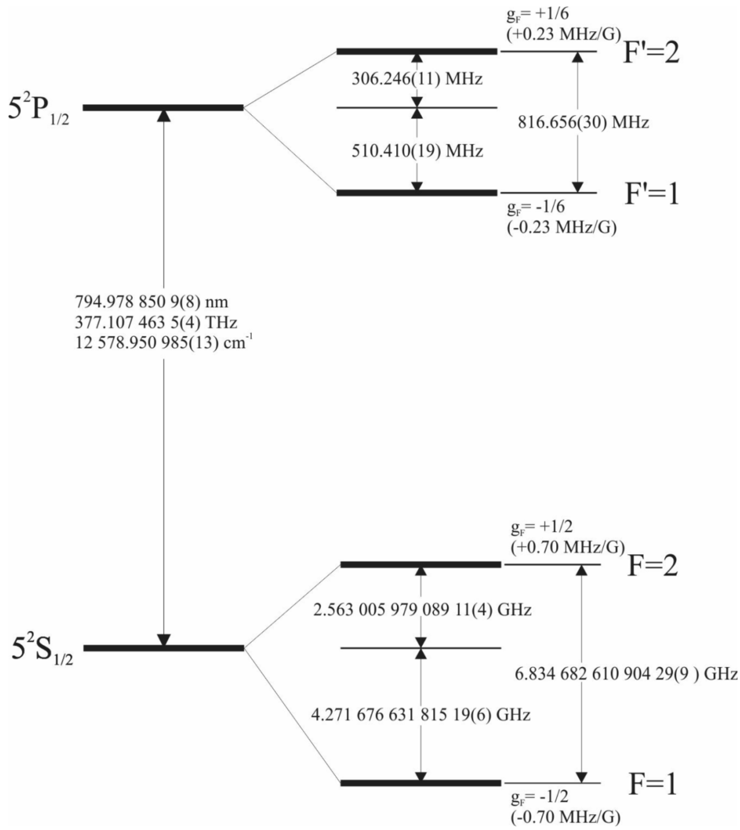

Figure 6.17 Energy-level diagram of Rb^{87} as an example of an alkali hyperfine structure (not to scale). (*After:* [38].)

couples with the nuclear spin **I** giving the total angular momentum **F**. The consequence is the occurrence of a hyperfine structure splitting of the energy levels (see Figure 6.17).

The spectral line structure of the alkali atoms is therefore somewhat more complex than that of the (metastable) triplet system of the He^4 atom (see Figure 6.19). The Zeeman substructure levels denoted by m_F cannot be resolved in the Earth's magnetic field[8] by ordinary laboratory techniques [36, 39].[9] In the alkali metal vapor magnetometer, the coupling of spin-, orbit-, and nuclear-angular momentum (appearance of the hyperfine structure) leads to effective gyromagnetic ratios of about 7.00 Hz/nT for Na^{23}, K^{39}, and Rb^{87}, 4.66 Hz/nT for Rb^{85}, and about 3.50 Hz/nT for Cs^{133} [37, 38]. They are smaller than that of He^4 (28.0 Hz/nT). The gyromagnetic ratio is still about a factor of 100 larger than that of the proton magnetometer, and the optically pumped magnetometers are thus proportionally less sensitive to a potential instrument rotation [16].

[8]The two K isotopes are an exception.
[9]See [36, Chapter 4.3.2, page 75f].

6.3.1.1 M_z Magnetometers

The basic idea behind this type of magnetometer is the fact that a resonant RF field applied to an atomic transition (e.g., the Zeeman structure of an alkali metal hyperfine structure) reduces the population difference created by optical pumping [39].

The detected signal is related to the longitudinal component M_z of the magnetic moment **M** of the used medium. In this configuration, both magnetic field and laser light propagation are oriented along the z-axis. From the time evolution of the magnetic moments, given by the Bloch equations, it follows that M_z is constant in time. The M_z magnetometers are characterized by their high accuracy, because the detected signal is derived from the constant M_z component. Phase errors that occur during detection therefore do not play a significant role [36].[10] Opposite to that is the limited bandwidth.

An optically pumped/swept RF-oscillator M_z mode magnetometer like the He^4 light absorption instrument or alkali M_z magnetometer can be correspondingly constructed according to Figure 6.20 (Section 6.3.2). The typical M_z signal detected in this configuration has a Lorentzian-like contour with the extremum at the resonance point and is, as mentioned above, constant in time. Therefore, phase-sensitive modulation techniques are necessary to stabilize an oscillator driving the B_{RF} coil at a frequency $\omega_{RF} = \omega_0 = \gamma \cdot B_0$ identical to the resonance point (gyromagnetic ratio γ, main magnetic field component B_0). The modulation frequency ω_{mod} in this configuration is often limited by the line width of the M_z signal, which is, in turn, limited by T_1 or T_2 ($\omega_{mod} < 1/T_1$, $1/T_2$).[11] This limitation means that the time constant of the lock-in detection unit must be set accordingly high ($1/T_{LockIn} < \omega_{mod}$) The consequence is, as already mentioned, the limited (low) bandwidth of the M_z magnetometer.

The Lorentzian-like contour brings the advantage of this configuration not being as sensitive to line center shifts if more than one resonance line is (unresolved) present. The resultant is, in this case, a convolution of many Lorentzian line shapes[12] of different amplitudes.[13] In typical magnetometer designs and in Earth's field applications (20,000–60,000 nT), the absolute level may change because of the spectral line averaging: up to 182 nT for Rb^{85}, 82 nT for Rb^{87}, and 6 nT for Cs^{133} [40, 41]. This absolute error is dependent on many parameters like light and RF-field intensity, the orientation of the magnetic field B_0 relative to the optical axis [39].[14]

The cesium magnetometer seems to be often the preferred type of the common optical magnetometers because of the medium to high accuracy and the low heating demands. Moreover, the setup can be simple as laser diodes especially at 850 nm (Cs-D_2-Line) are easily available. The fact that Cs^{133} is the only natural isotope reduces the price for the alkali metal cells since no isotope separation is needed.

---

[10]See [36, Chapter 4.2, pages 66–67].

[11]Generally, applies the relationship ($T_1 > 2 \cdot T_2$).

[12]This happens, especially in Earth field applications ($B_0 \approx 50$ µT) if Cs, Rb, or Na is used as working substance. This effect is almost negligible for fields $B_0 < 5$ µT. The Zeeman levels in K^{39} and K^{41} are completely resolved in the 50-µT regime.

[13]See [36, Chapter 4.2.1, page 66] for an extended discussion.

[14]Further influencing parameters are listed in [36, page 76].

Besides the common Cs-magnetometer, an alkali-helium magnetometer is in use in some applications. Here, the working substance is helium in the metastable 2^3S_1 state polarized by optically oriented alkali atoms [42].

Another interesting approach is the hyperfine structure magnetometer. It is based on the resonance between different Zeeman levels (magnetic sublevels) of different hyperfine structure levels (different F quantum number) of the ground states of the alkali atoms. This approach solves some of the weaknesses of the other types of magnetometers mentioned (see [36, page 73f] and [43]).

6.3.1.2 M_x Magnetometers

The detected signal is related to the transverse component M_x of the magnetic moment **M** [39]. This component is a quantity that varies over time expressed in the laboratory frame.

The optical pumping polarizes the electrons, and the RF-coil B-field (oscillating at the Larmor frequency) cause the electrons to precess in-phase about the external B_0 field. Whenever the coherently rotating electron magnetic moments are closest to the propagation direction of the optical path, then the cell transmission increases, and half a Larmor period later when the electrons are most antiparallel to the optical path, then the transmission drops and the photo cell output decreases. A simple explanation is that when all the electron magnetic moments (and spins) are (most) parallel to the optical path, then very few electrons with spins in other directions are available for light absorption. Similarly, when the electron spins are rotated away from the direction of the optical path, then a large number of electrons are available for absorption of the light. This is an M_x-mode operation because light absorption with the optical path (having some component) across the B_0 field is observed. The time evolution of the magnetic moment **M** and its components are vividly described by Bloch's equations. The vector hodograph of **M** lays on the Bloch sphere. The typical evolution is a spiral on a sphere surface under certain circumstances.[15]

The detection of M_x components[16] is often somewhat easier because they oscillate in time. This circumstance allows, for example, the realization of a self-oscillating [39] or a phase lock loop (PLL)-type M_x magnetometer [44, 45]. In this case, a synchronous phase detection method allows the selective use of the in phase- (u) and the quadrature- (v) components. Most convenient here is the use of the dispersive-shaped u component as a frequency discriminator. However, residual phase delay in the electronics causes systematic shifts of the u-component's zero crossing. This leads to frequency errors and thus to an error in the B-field measurement [36, 39].

M_x magnetometers are characterized by their high bandwidth, which is not limited by either the longitudinal T_1 or the transverse T_2 relaxation time.

The upper (theoretical) bandwidth limit is given by the Larmor frequency $\omega_0 = \gamma \cdot B_0$. For typical designs, the bandwidth of M_x configurations is higher than that of the M_z configurations.

[15] A discussion can be found in [36, Chapter 4.1].

[16] The amplitude and the relative phase components are important in this context.

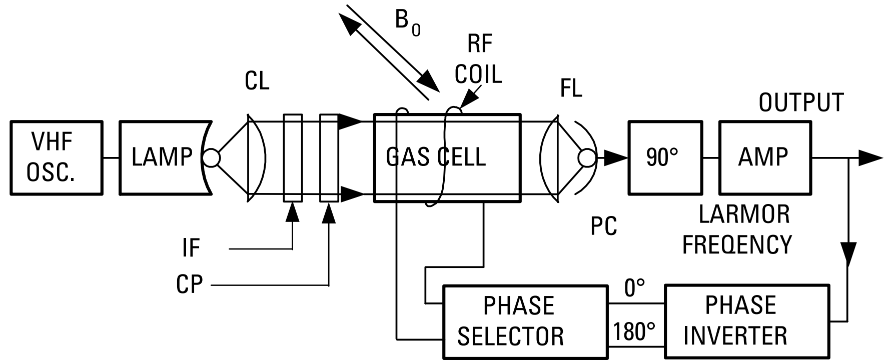

Figure 6.18 The principle of the Varian Associates' self-oscillating optically pumped alkali metal vapor magnetometer. (*After:* [40].)

The Varian Associates developed the Larmor frequency self-oscillating optical M_x magnetometer in great detail [39]. Figure 6.18 shows the principle of the simplest type [37, 40].

The VHF oscillator excites the alkali metal vapor in the lamp, and the light is collected by the collimating lens (CL) and sent through the absorption gas cell containing the same alkali vapor as the lamp. The interference filter attenuates the unwanted D_2 line and permits the D_1 line after circular polarization (CP) to pass through the absorption cell and to be focused by the field lens (FL) on the photo cell (PC) [40, 46]. The electrical photo cell output depends on the gas cell transmission coefficient.

When the system is running, the photo cell output is modulated at the Larmor frequency, and after a 90° phase shift this signal is used to drive the RF B-coil in a self-oscillating system. This only operates when the external B_0 field is directed toward +135°/–45° relative to the optical path. The angle can be changed to +45°/–135° if the feedback signal phase is inverted 180°. Depending on the feedback phase, a practical system will operate when the external field is inside an angular range close to one of these two directions. The magnetometer does not operate when B_0 is closer than 15° to the optical axis or closer than 10° to being perpendicular to the optical path. Within the operating angular ranges, the magnetometer output shifts slightly in frequency when the B_0 aspect angle changes because of a shift in the weights of the multiple line average.

A symmetrical dual-cell system was developed by Varian Associates [47, 48] that operates in both ±45°/±135° sectors and that has much reduced angular dependence of the photo cell output frequency. Misalignment of the RF-feedback coil with the optical axis will cause large frequency shifts, particularly when the field is close to the null zones and the winding of the coil and the positioning of the optics must be tightly controlled [46, 49]. In the group of A. Weis laser based Cs magnetometers in M_x configuration with a noise density of < 100 fT/ Hz1/2 [44, 45] and even of 15 fT / $Hz^{1/2}$ [50] are developed in a laboratory environment.

Potassium has a fully resolved optical spectrum throughout the entire range of the Earth's magnetic field, and a very high-resolution absolute accuracy has been developed based on a mixture of K^{41} and K^{39}. Sensitivities of 1 pT/√Hz and no systematic errors exceeding 10 pT have been reported [41]. The instrument development is ongoing in collaboration with GEM Systems Inc., Toronto, Canada.

6.3.1.3 Special Excitation Principles

Due to the large number of possible excitation schemes within the fine or hyperfine structures, many other magnetometer types have been proposed.[17]

However, many of these magnetometers have not yet found any application outside the laboratory environment, or initial attempts are under way to use them in a broader field. As an example, the spin exchange relaxation-free magnetometer is sometimes called a zero-field magnetometer (see Chap. 5 of [36]). This configuration has advantages in low B-field application and in applications where low noise ($fT/Hz^{1/2}$ region in a band of 10 … 100 Hz) is demanded. In this configuration, a bias field to zero the external B-field is necessary. It is also extendable to a vector mode operation. The second example is the coherent population trapping resonance magnetometer. Here, the coherent pumping into a quantum mechanical superposition of the energy eigenstates creates a resonance phenomenon (the dark states) with similar properties as in a conventional optical pumping scheme. A balanced version called a coupled dark state magnetometer was developed for space applications. This kind of magnetometer has the advantage of being omnidirectional (without dead zones) and has a fully optical excitation [51, 52]. The achieved noise is below 50 $pT/Hz^{1/2}$ at 1 Hz and no $1/f$ characteristic is observable down to 100 μHz [53].

6.3.2 The Metastable He^4 Magnetometer

The most common He^4 isotope has two protons and two neutrons in the nucleus with no net nuclear magnetic moment; furthermore, the two electrons fill up the first shell, also without any uncompensated electron spin or magnetic moment. For observing the electron Zeeman splitting in a gaseous sample of He^4, the atom is lifted from the 1^1S_0 ground state and into the 2^3S_1 metastable level by a sustained high-frequency glow discharge excitation. The He^4 atom in this condition may then be regarded as the ground state of a new atom with both electrons available for ESR.

In passing, the He^3 isotope (a decay product of Tritium) has a net nuclear magnetic moment with a gyromagnetic ratio of about 60% of that of a proton. The He^3 nuclear magnetic moment can be polarized by interactions with optically pumped electrons in the RF-excited metastable state as for He^4, and then a nuclear resonance magnetometer similar to the Overhauser effect proton magnetometer can be constructed.

A sealed glass vessel with He^4 gas of suitable partial pressure is exposed to an electrodeless high-frequency glow discharge producing the metastable 2^3S_1 ground state of the He^4-triplet system by electron collisions. The transition from 2^3S_1 to the energetically lowest-laying singlet ground state 1^1S_0 is dipole-forbidden ($\Delta L = 0$ and $\Delta S \neq 0$). Thus, the lifetime of this metastable triplet ground state is in the order of milliseconds and about 10^6 times longer than the lifetimes of the dipole transitions

[17] See [36] for a more extensive overview.

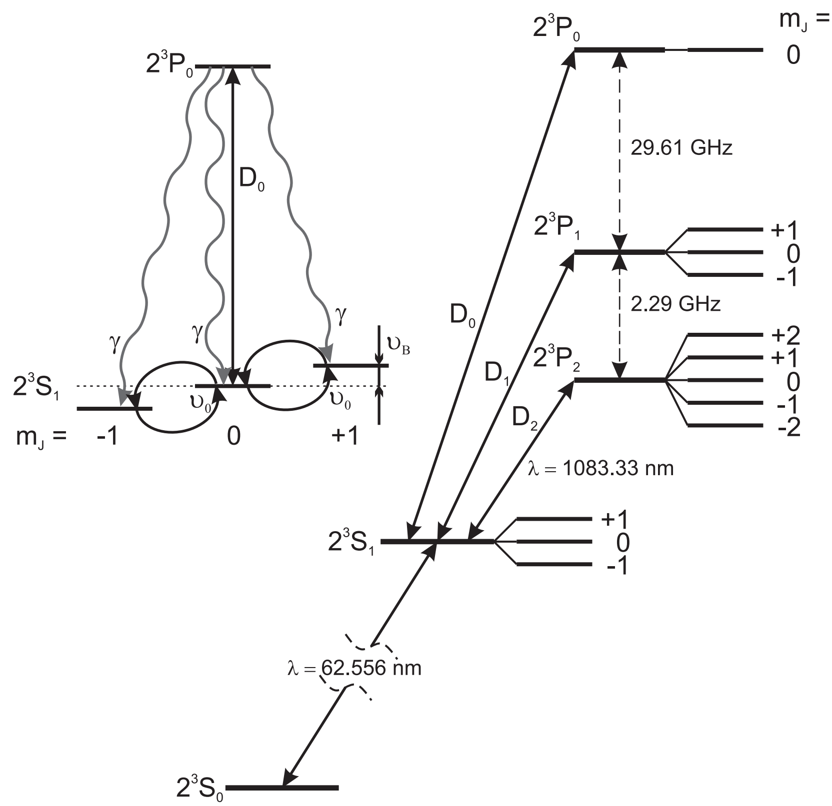

Figure 6.19 Relevant energy levels of a He^4 atom in an external magnetic field (not to scale). The first excited state (2^3S_1) of the triplet system is metastable. (*After:* [56].) The excitation of the (well-separated) D_0 line by linear polarized light is illustrated in the inset. The decay rates γ into the 2^3S_1, $m_j = -1$, 0, and +1 states are all equal, leading to a population transfer into the $m_j = -1$ and +1 Zeeman substates. An applied AC magnetic field B_{RF} with frequency $v_0 = v_B = g_j \cdot m_j \cdot \gamma_e/(2\pi) \cdot B_0$ leads to a redistribution accompanied by an increase in the absorption. In this way, the energy splitting of the Zeeman substates can be detected.

(e.g., that of the D_0, D_1, and D_2 lines) (Figure 6.19). This circumstance allows to sufficiently populate the 2^3S_1 state by the high-frequency discharge and to establish an efficient optical pumping scheme with the 2^3P_0 state.

The external magnetic field B_0 lifts the threefold degeneracy of the 2^3S_1 state and splits it into three Zeeman sublevels, designated as $m_J = +1$, $m_J = 0$, and $m_J = -1$. From a macroscopic point of view, the +1 level has the magnetic moment of the electrons antiparallel to the external magnetic field and the −1 level has the moment parallel to the field.[18] The Zeeman transition from $m_J = \pm 1$ to 0 can be induced by a resonance AC magnetic field $B(t) = B_1 \cdot \cos(2\pi v_0 t)$, where v_0 is the electron Larmor frequency or the precession frequency of the electrons about the external field $\mathbf{B}_0$.

A quantum mechanical treatment to the levels 2^3S_1 and 2^3P_0 enables the determination of the (Larmor) resonance frequency v_0 and yields the scalar magnitude of the external field according to:

[18]The 2^3S_1 $m_j = +1, 0, -1$ (eigen-)energies are therefore arranged to be $E_{+1} > E_0 > E_{-1}$.

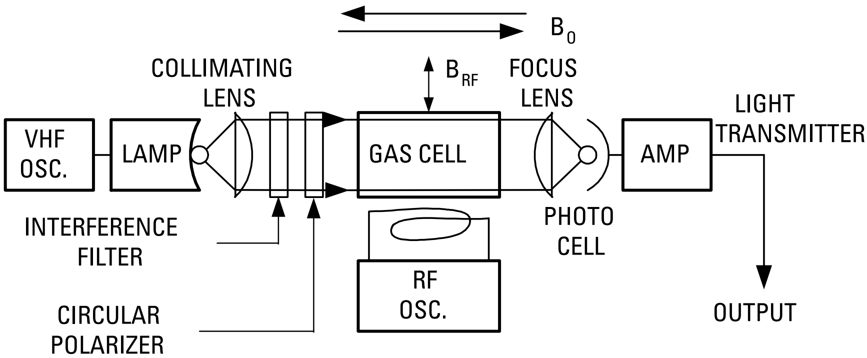

Figure 6.20 M_z mode optically pumped He^4 magnetometer. The optical absorption is measured for a light transmission path along the external magnetic field B_0, the z-axis. The high-frequency discharge lamp can also be replaced by a suitable laser source locked to the D_0 transition. The cell becomes less transparent when the frequency of the AC magnetic field B_{RF} (or B_1) perpendicular to B_0 approaches the Larmor frequency $\nu_0 = 2 \cdot \gamma_e/(2\pi) \cdot B_0$. (*After:* [40].)

$$\Delta E = h\nu_0 = g_j \cdot m_J \cdot \gamma_e \cdot \hbar \cdot B_0 = 2 \cdot \mu_e \cdot B_0$$
or
$$\nu_o = \frac{g_j \cdot m_J \cdot g_e}{(2\pi) \cdot B_0} \approx \frac{2 \cdot \gamma_e}{(2\pi) \cdot B_0} \tag{6.45}$$

where the free electron gyromagnetic ratio $\gamma_e/(2\pi) = (2 \cdot \mu_e/h) = 28.02495 \ldots$ GHz/T (see Section 6.1.2), which is the largest conversion factor of any optically pumped magnetometer, larger than those of the alkali metal vapor instruments [37, 54]. The magnetic Zeeman quantum number m_J in the equation can be seen from Figure 6.19. The g_j – Landé factor related to the 2^3S_1 state can be calculated[19] to be $g_j = g_e = 2.002319 \ldots \approx 2$ as the orbital angular momentum in the S-state is $\mathbf{L} = 0$ and both spins are coupled to be $\mathbf{S} = 1$.

The determination of the frequency ν_o is established in the following way. The electrons in the triplet metastable 2^3S_1 state can be optically excited into the higher 2^3P_0 energy level by infrared light of about 1,083-nm wavelength. From the energy-level diagram (Figure 6.19), it can be seen that this transition, corresponding to the D_0 spectral line, is well separated from the D_1 line by 0.9879 cm^{-1} (about 29.61 GHz) and from the D_2 line by 1.0643 cm^{-1} (31.907 GHz) [55]. It can be therefore picked out separately by a suitable narrow light source.

The D_0 transition can be excited by unpolarized as well as circularly or linearly polarized light [56, 57] with the light propagating along (a component of) the external magnetic field $\mathbf{B}_0$, and this is termed the M_z mode, because the z-axis (longitudinal component) of the magnetic moment of the detection medium is along $\mathbf{B}_0$. For the sake of simplicity, we assume that light driving the 2^3S_1 to 2^3P_0 transition is linearly polarized ($\Delta m_J = 0$; see the D_0 transition in Figure 6.19).[20] Originally,

[19]The calculation is based on first-order perturbation of the He^4 energy eigenvalue spectrum [63].
[20]In case of circularly polarized light, a transition with $\Delta m_J = +1$ or -1 is induced.

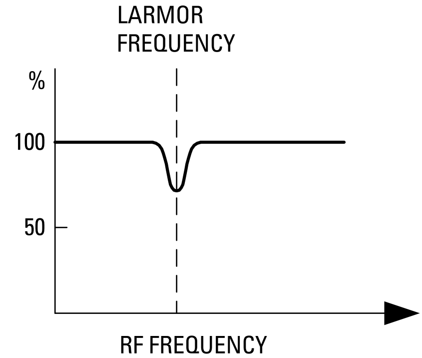

Figure 6.21 Absorption of the transmitted light through the cell against the RF of the transverse AC magnetic field. Sweeping the frequency periodically $\pm\Delta f$ about the center frequency results in a pure sweep second-harmonic output of the photo cell when the center frequency equals the Larmor frequency ν_0. (*After:* [40].)

the three states 2^3S_1 with $m_J = 0, \pm1$ are equally populated at normal temperatures, and light is absorbed as long as 2^3S_1, $m_J = 0$ electrons are available for transition into the single 2^3P_0 $m_J = 0$ state. Relaxation will occur with equal probabilities into the three $m_J = 0, \pm1$ states, so after some time the $m_J = 0$ will have a much reduced population, and absorption of the light cannot any longer take place. This is line saturation when (almost) all the $m_J = 0$ electrons are removed, and the cell then recovers the full transparency. However, by applying the AC magnetic resonance field $B_1 \cdot \cos(2\pi\nu_o t)$ at right angles to the external field, electrons are induced to go from the 2^3S_1 $m_J = \pm1$ states back into the $m_J = 0$ state, and $m_J = 0$ electrons again become available for light absorption [54].

The general principle of the He^4 M_z-mode magnetometer is shown in Figure 6.20. For the He^4 magnetometer the circular polarizer shown may be replaced by a linear polarizing filter, and the need for an interference filter depends on the actual light source used. A laser can be locked to the single D_0 line [58], whereas a He-lamp will transmit the D_1 and D_2 lines as well, and requires some filtering in order to minimize absorption transitions at these lines [59–62].

Figure 6.21 shows the light absorption versus the AC magnetic resonance field frequency. By frequency-modulating the resonance field RF oscillator with a suitable low-frequency Ω and an RF swing $\pm\Delta f$, then, close to the Larmor frequency, the amplitude and phase of the first-harmonic 1Ω output signal from the photo cell is a direct measure of the deviation of the RF-oscillator center frequency from the Larmor frequency ν_0. This deviation signal can be used in a feedback loop to control and maintain the center frequency at ν_0. In lock, the 1Ω signal goes to zero and the second-harmonic 2Ω signal is maximum. The presence of a large 2Ω signal is a safe indication of proper RF-oscillator lock to the Larmor frequency ν_0 [64]. The RF-oscillator center frequency is subsequently determined and transmitted as the measure of the external magnetic field B_0.

In a typical design, the sweep frequency is 200–300 Hz, modulation sweep range is ±1,400 Hz corresponding to ±50 nT and the Larmor precession line width is larger than 1 kHz, so the system is relatively fast-responding [60, 64]. He^4 as a noble gas is in the gaseous state in the relevant temperature range, so the He^4 cell

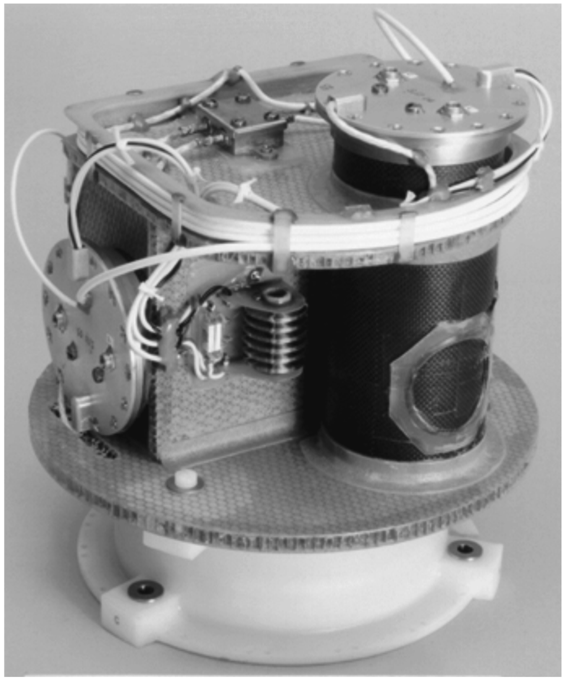

Figure 6.22 The Jet Propulsion Laboratory two-cell He^4 scalar sensors with the optical paths orthogonal to each other. The combined sensor only has one null line, along which the field cannot be measured [65].

needs no further heating[21] or any tight temperature control, and the magnetometer starts immediately after switch-on. The instrument operates for $\mathbf{B}_0$ field directions out to about 60° from the optical path [65], and combining two sensors at right angles reduces the null zone to a single narrow cone, which is acceptable for most magnetic mapping missions (see Figure 6.22). The overall sensitivity is relatively low, so a fairly intense light source is needed, and this introduces a small shift of the order of ±0.5 nT depending on the light intensity (light shift).[22] In order to obtain and maintain this low shift, a very precise and stable alignment of the RF coil and the optical system has to be established. An absolute comparison between the Jet Propulsion Laboratory (JPL) Scalar Helium Magnetometer and a proton magnetometer showed a scatter of ±0.5 nT, including the errors from both instruments [64].

A highly stable and very low-noise vector-field-measuring version of the JPL Helium Magnetometer with added bias coils was onboard the *Ulysses* solar polar mission [66] which was operational between 1990 and 2009. On the *Cassini* mission (1997–2017), the Jet Propulsion Laboratory had a single cell vector/scalar helium magnetometer [67].

[21]Eddy-current heating occurs in the high-frequency discharge of the helium cell.

[22]It can be distinguished between the virtual and the real light shift Chap. 10.2.3, page 195f of [36] and [70, 71]. The virtual light shift is caused by off-resonant (e.g., it happens if the transition is not perfectly matched) circularly polarized light. The real light shift occurs in the case of coherence transfer between the excited $2^3P_{0,1,2}$ states (level-mixing) in case of higher He^4 pressures [72, 73].

An omnidirectional scalar He^4 magnetometer has been developed by LETI, CEA Advanced Technologies, Grenoble, France [54, 68, 69], for the three-satellite *Swarm* mission. As for the JPL Scalar Helium Magnetometer, the He^4 atoms are brought into the 2^3S_1 metastable state. The RF-ESR coil and an optical linear polarizer are mechanically coupled and can be rotated simultaneously by a piezoelectric motor controlled by the 1Ω modulation signal output from the photosensitive detector. For any orientation of the external $\mathbf{B}_0$ field, both the $\mathbf{E}_0$ light polarization direction and the resonance AC magnetic field $\mathbf{B}_1$ are maintained at right angles to the external $\mathbf{B}_0$ field, as required for isotropic operation. Rotation of the sensor in two planes proved the isotropy to be better than 20 pT. The instrument noise floor is 1 pT/√Hz in a bandwidth of (DC-) 300 Hz and the band noise is 17 pT_{rms}. The linewidth of the RF resonance corresponds to about 70 nT and this combined with the modest cell dimensions (4 by 6 cm) makes it tolerant to gradients up to 1 μT/m.

References

[1] Bloch, F., "Nuclear Induction," *Physical Review*, Vol. 70, 1946, pp. 460–485.

[2] Varian, R. H., "Methods and Means for Correlating Nuclear Properties of Atoms and Magnetic Fields," U.S. Patent Office, Re. 23,767; Original No. 2,561,490, dated July 24, 1951, Serial No. 55,667, October 21, 1948 (Reissued January 12, 1954).

[3] Alldredge, L. R., and I. Saldukas, "The Automatic Standard Magnetic Observatory," Technical Bulletin No. 31, U.S. Department of Commerce, Environmental Science Services Administration, Coast and Geodetic Survey, Washington, D.C.: U.S. Government Printing Office, 1966.

[4] Packard, M. E., and R. H. Varian, "Free Nuclear Induction in the Earth's Magnetic Field," Abstract only, *Physical Review*, Vol. 93, 1954, p. 941.

[5] Waters, G. S., and G. Phillips, "A New Method for Measuring the Earth's Magnetic Field," *Geophysical Prospecting*, Vol. 4, 1956, pp. 1–9.

[6] Serson, P. H., *A Simple Proton Precession Magnetometer*, Dominion Observatory, Report, Ottawa, Ontario, Canada, May 1962.

[7] Serson, P. H., "Proton Precession Magnetometer," U.S. Patent No. 3,070,745, 1962.

[8] Cahill, L. J., Jr., "Investigation of the Equatorial Electrojet by Rocket Magnetometer," *Journal of Geophysical Research*, Vol. 64, 1959, pp. 489–503.

[9] Burrows, K., "A Rocket Borne Magnetometer," *Journ. Brit. IRE*, Vol. 19, 1959, pp. 767–776.

[10] Olesen, J. K., et al., "Rocket-Borne Wave, Field and Plasma Observations in Unstable Polar Cap E-Region," *Geophysical Research Letters*, Vol. 3, 1976, p. 711.

[11] Dolginov, Sh., "The First Magnetometer in Space," Haerendel, Grzedzielski, Cavallo, and Battrick, 40 Years of COSPAR,ESA Publications Division, ESTEC, 1998, pp. 55–63.

[12] Overhauser, A. W., "Dynamic Nuclear Polarisation," in D. M. Grant and R. K. Harris, (eds.), *Encyclopaedia of Nuclear Magnetic Resonance, Vol. 1*, 1966, pp. 513–516.

[13] Hrvoic, I., "Proton Magnetometers for Measurement of the Earth's Magnetic Field," GEM Systems Inc., *Toronto, Canada, Proc. Int. Workshop on Geomagn. Observatory Data Acquisition and Processing, Nurmijärvi Geophysical Observatory*, Finland, May 1989, Section 5.8, Finnish Meteorological Institute, Helsinki, Finland, 1990, pp. 103–109.

[14] Duret, D. N., et al., "Overhauser Magnetometer for the Danish Oersted Satellite," *IEEE Transactions on Magnetics*, Vol. 31, 1995, pp. 3197–3199.

[15] Kastler, A., “Quelques suggestions concernant la production optique et la détection optique d’une inégalité de population des niveaux de quantifications spatiale des atomes. Application de l’experiénce de Stern et Gerlach et la résonance magnetique,” *Journ. de Phys. et le Radium*, Vol. 11, 1950, p. 255.

[16] Alexandrov, E. B., and F. Primdahl, “On Gyro-Errors of the Proton Magnetometer,” *Measurement Science and Technology*, Vol. 4, 1993, pp. 737–739.

[17] Langel, R. A., et al., “The Magsat Mission,” *Geophysical Research Letters*, Vol. 9, 1982, pp. 243–245.

[18] De Vuyst, A. P., *Magnétomètre Theodolite a Protons*, Institut Royal Météorolique de Belgique, Miscellanea, SERIE C, No/r 2, Report to the International Association of Geomagnetism and Aeronomy, General Assembly, Moscow, 1971.

[19] Proceedings of the 26th meeting of the General Conference on Weights and Measures, ISBN 978-92-822-2276-8, Versailles, November 13-16, 2018.

[20] See CODATA 2018.

[21] “2018 CODATA Recommended Values,” https://pml.nist.gov/cgi-bin/cuu/Category?view=html&Atomic+and+nuclear.x=118&Atomic+and+nuclear.y=11.

[22] Ripka, P., (ed.), *Magnetic Sensors and Magnetometers*, Norwood, MA: Artech House, Section 7.1.2, **2001**, p. 270.

[23] Belorisky, E. W., et al., “Sample-Shape Dependence of the Inhomogeneous NMR Line Broadening and Line Shift in Diamagnetic Liquids,” *Chemical Physics Letters*, Vol. 175, No. 6, December 28, 1990, pp. 579–584.

[24] Belorisky, E., et al., “Demagnetizing Field Effect on High Resolution NMR Spectra in Solutions with Paramagnetic Impurities,” *Journal of Physics B Atomic and Molecular Physics*, Vol. 1, No. 5, May 1991, pp. 527–541.

[25] Acker, F. E., “Calculation of the Signal Voltage Induced in a Toroid Proton Precession Magnetometer Sensor,” *IEEE Transactions on Geoscience Electronics*, Vol. 9, 1971, pp. 98–103.

[26] Koehler, J. A., “Proton Precession Magnetometer,” November 2004, Manuscript, about 55 pages plus figures, http://perso.infonie.be/j.g.delannoy/BAT/KoehlerMag.pdf.

[27] Faini, G., A. Fuortes, and O. Svelto, “A Nuclear Magnetometer,” *Energia Nucleare*, Vol. 7, 1960, pp. 705–716.

[28] Pijnappel, W. F., et al., “SVD-Based Quantification of Magnetic Resonance Signals,” *Journal of Magnetic Resonance*, Vol. 97, 1992, pp. 122–134.

[29] Reimann, R., “Messung von Schwachen Magnetfeldern Mittels Kernresonanz,” *Nuclear Instruments and Methods*, Vol. 45, 1968, pp. 328–330.

[30] Sigurgeirsson, T., “A Continuously Operating Proton Precession Magnetometer for Geomagnetic Measurements,” *Scientia Islandica*, Science in Iceland, Vol. 2, 1970, pp. 67–77.

[31] Schott, C., and M. Blyzniuk, “High Volume Production of Magnetic Sensors for the Automotive Market,” *2012 IEEE Sensors Proceedings*, 2012, pp. 2086–2089.

[32] Hartmann, F., “Resonance Magnetometers,” *IEEE Transactions on Magnetics*, Vol. 8, 1972, pp. 66–75.

[33] Kernevez, N., et al., “Weak Field NMR and ESR Spectrometers and Magnetometers,” *IEEE Transactions on Magnetics*, Vol. 28, 1992, pp. 3054–3059.

[34] Kernevez, N., and H. Glenat, “Description of a High-Sensitivity CW Scalar DNP-NMR Magnetometer,” *IEEE Transactions on Magnetics*, Vol. 27, 1991, pp. 5402–5404.

[35] Primdahl, F., “Scalar Magnetometers for Space Applications,” in R. F. Pfaff, J. E. Borovsky, and D. T. Young, (eds.), *Measurement Techniques in Space Plasmas: Fields*, Geophys. Monograph 103, Washington, D.C.: American Geophysical Union, 1998, pp. 85–99.

[36] Budker, D., and D. F. J. Kimball, *Optical Magnetometry*, Cambridge, U.K.: Cambridge University Press, 2013.

[37] Lokken, J. E., "Instrumentation for Receiving Electromagnetic Noise Below 3,000 CPS," in D. F. Bleil, (ed.), *Natural Electromagnetic Phenomena Below 30 kc/s*, New York: Plenum Press, 1964.

[38] https://steck.us/alkalidata/.

[39] Bloom, A. L., "Principles of Operation of the Rubidium Vapor Magnetometer," *Applied Optics*, Vol. 1, 1962, p. 61.

[40] Ness, N. F., "Magnetometers for Space Research," *Space Science Reviews*, Vol. 11, 1970, pp. 459–554.

[41] Alexandrov, E. B., and V. A. Bonch-Bruevich, "Optically Pumped Magnetometers After Three Decades," *Optical Engineering*, Vol. 31, 1992, pp. 711–717.

[42] Keiser, G. M., H. G. Robinson, and C. E. Johnson, "Polarization of $^4He(2^3S_1)$ by Optically Pumped Rb," *Phys. Lett. A*, Vol. 51, 1975, p. 5.

[43] Vershovskii, A. K., A. S. Pazgalev, and E. B. Aleksandrov, "The Design of a Λ-HFS Magnetometer," *Technical Physics*, Vol. 45, No. 1, 2000, pp. 88–93.

[44] Bison, G., R. Wynands, and A. Weis, "A Laser-Pumped Magnetometer for the Mapping of Human Cardiomagnetic Fields," *Appl. Phys. B*, Vol. 76, 2003, p. 325.

[45] Bison, G., R. Wynands, and A. Weis, "Optimization and Performance of an Optical Cardiomagnetometer," *J. Opt. Soc. Am. B*, Vol. 22, 2005, p. 77.

[46] Fathing, W. H., and W. C. Folz, "Rubidium Vapour Magnetometer for Near Earth Orbiting Spacecraft," *Review of Scientific Instruments*, Vol. 38, 1967, pp. 1023–1030.

[47] Morris, R. and L. Langan, "Varian Associates' Space Magnetometers 1956–1961," *Geophysical Technical Memorandum*, No. 8, Quantum Electronics Division, Varian Associates, Palo Alto, CA, 1961.

[48] Ruddock, K. A., "Optically Pumped Rubidium Vapour Magnetometer for Space Experiments," *Space Research*, Vol. II, 1961, pp. 692–700.

[49] Mobley, F. F., et al., "MAGSAT—A New Satellite to Survey the Earth's Magnetic Field," *IEEE Transactions on Magnetics*, Vol. 16, 1980, pp. 758–760.

[50] Groeger, S., et al., "A High-Sensitivity Laser-Pumped Mx Magnetometer," *Eur. Phys. J. D*, Vol. 38, 2006, p. 239.

[51] Lammegger, R., "Method and Device for Measuring Magnetic Fields," PCT Patent WO/2008/151 344, June 12, 2008.

[52] Cheng, B. J., et al., "High Precision Magnetometer for Geomagnetic Exploration Onboard of the China Seismo-Electromagnetic Satellite," *Sci. China Tech. Sci.*, Vol. 61, 2018, pp. 659–668.

[53] Pollinger, A., et al., "Coupled Dark State Magnetometer for the China Seismo-Electromagnetic Satellite," *Measurement Science and Technology*, Vol. 29, No. 9, 2018, p. 095103.

[54] Alcouffe, F., et al., "An Isotropic Helium 4 Scalar Magnetometer with Extended Frequency Capabilities," *Proceedings of the EMMS Conference*, Brest, France, July 5–9, 1999.

[55] NIST Online Database, last update October 2020, https://physics.nist.gov/PhysRefData/Handbook/Tables/heliumtable5.htm.

[56] Colegrove, F. D., and P. A. Franken, "Optical Pumping of Helium in the $^3S_1$ Metastable State," *Physical Review*, Vol. 119, No. 2, 1960, p. 680.

[57] Franken, P. A., U.S. Patent 3,122,702, February 25, 1964.

[58] Slocum, R. E., U.S. Patent 5,036,278, July 30, 1991.

[59] McGregor, D. D., "High-Sensitivity Helium Resonance Magnetometers," *Review of Scientific Instruments*, Vol. 58, 1987, pp. 1067–1076.

[60] Slocum, R. E., and D. D. McGregor, "Measurement of the Geomagnetic Field Using Parametric Resonance in Optically Pumped He^4," *IEEE Transactions on Magnetics*, Vol. 10, 1974, pp. 532–535.

[61] Schearer, L. D., in J. R. Singer, (ed.), *Advances in Quantum Electronics*, New York: Columbia University Press, 1961, p. 239.

[62] Slocum, R. E., "Orientation Dependent Resonance and Non-Resonance Effects in Optically Pumped Triplet Helium," PhD. Dissertation, University of Texas at Austin, 1969.

[63] Yang, F., and J. H. Hamilton, *Modern Atomic and Nuclear Physics*, Rev. ed., New York: World Scientific, 2010, p. 132.

[64] Slavin, J. A., "JPL Scalar Helium Magnetometer, Report," Technical Note, Jet Propulsion Laboratory, Pasadena CA, 1984.

[65] Smith, E. J., et al., "ARISTOTELES Magnetometer System," *Proceedings of the Workshop on Solid-Earth Mission ARISTOTELES*, Anacapri, Italy, September 23–24, 1991, ESA SP-329, December 1991, pp. 83–89.

[66] Balogh, A., et al., "The Magnetic Field Investigation on the Ulysses Mission: Instrumentation and Scientific Results," *Astronomy & Astrophysics*, Suppl. Series, Vol. 92, 1992, pp. 221–236.

[67] Dunlop, M. W., et al., "Operation of the Dual Magnetometer on Cassini: Science Performance," *Planetary and Space Science*, Vol. 47, 1999, pp. 1389–1405.

[68] Fratter, I., et al., "Swarm Absolute Scalar Magnetometers First In-Orbit Results," *Acta Astronautica*, Vol. 121, 2016, pp. 76–87.

[69] Jager, T., "SWARM Absolute Scalar Magnetometer Accuracy: Analyses and Measurement Results," *2010 IEEE Sensors*, 2010, pp. 2392–2395.

[70] Barrat, J. P., and C. Cohen-Tannoudji, "Enlargement and Displacement of Magnetic Resonance Radiation Caused by an Optical Excitation," *J. Phys. Radium*, Vol. 22, 1961, p. 443.

[71] Cohen-Tannoudji, C., "Observation d'un deplacement de raie de resonance magnetique causee par l'excitation optique," *Compt. Rend. Acad. Sci. Paris*, Vol. 252, 1961, p. 394.

[72] Schearer, L. D., "Energy Shifts of the Magnetic Sublevels of 3S1 Helium Caused by Optical Pumping," *Phys. Rev.*, Vol. 127, 1962, p. 512.

[73] Slocum, R. E., "Advances in Optically Pumped He4 Magnetometers: Resonance and Nonresonance Techniques," *Rev. Phys. Appl. (Paris)*, Vol. 5, 1970, p. 109.

[74] Jianming, J., *Electromagnetic Analysis and Design in Magnetic Resonance Imaging*, Boca Raton, FL: CRC Press, 1999, p. 282.

CHAPTER 7

SQUID

Robert L. Fagaly

7.1 Introduction

Superconducting quantum interference devices (SQUIDs) have been a key factor in the development and commercialization of ultrasensitive electric and magnetic measurement systems. In many cases, SQUID instrumentation offers the ability to make measurements where no other methodology is possible. In addition to measuring magnetic fields, SQUID sensors can be configured to measure a wide variety of electromagnetic properties. The ability of a SQUID sensor to measure changes in magnetic fields and currents are based on four effects:

- Superconductivity;
- Meissner effect;
- Flux quantization;
- The Josephson effect.

7.1.1 Superconductivity

At temperatures approaching absolute zero, certain materials undergo a transition to what is known as the superconducting state. In 1911, Kamerlingh-Onnes [1] discovered that the resistance of mercury, when cooled below 4.2K, dropped to an immeasurably small value (Figure 7.1(a)).

This transition from normal resistance to resistanceless behavior takes place over a narrow temperature range—about 0.001K for pure, strain-free metals and a degree or more for alloys and ceramics. Below this temperature, known as the transition temperature (T_c), the material is characterized by a complete lack of electrical resistance. Subsequent investigations indicated that a large number of materials undergo a similar superconducting transition. According to the Bardeen-Cooper-Schriefer (BCS) theory [2], the mechanism that permits superconductivity is the phonon exchange between paired electrons (Cooper pairs). The average distance between the electron pairs is the coherence length ξ_o; the mechanism that permits superconductivity is depaired by thermal (critical temperature), kinetic (critical current density) or magnetic (critical field) interactions. The temperature, current density, and magnetic field under which the particular material is superconducting form the phase space. In 1986, Bednorz and Müller [3] discovered a new class of ceramic oxides that became superconducting near 30K, significantly warmer than any previously known superconductor. Since then, newer materials have been developed with the superconducting transition temperatures above 130K, well above the boiling point of liquid nitrogen. $YBa_2Cu_3O_{7-\delta}$ (Figure 7.1(b)) with $T_c > 90K$ (often

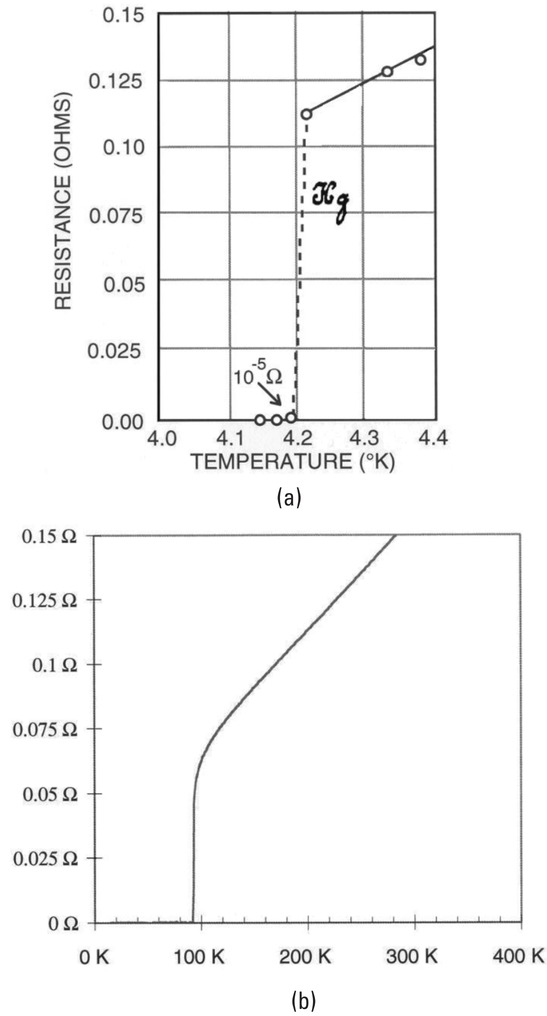

Figure 7.1 (a) Resistance of mercury [1] and (b) $YBa_2Cu_3O_{7-\delta}$ vs. temperature

referred to as YBCO) is the most commonly used superconducting ceramic oxide. To distinguish between the types of materials used in making SQUID sensors and other superconducting devices and materials, we denote the traditional metallic superconductors that typically operate at liquid helium temperatures (4.2K) as low-temperature superconductors (LTS) and the newer materials that can operate above 30K (typically at liquid nitrogen temperatures—77K) as high-temperature superconductors (HTS).

7.1.2 Meissner Effect

An interesting property of the superconducting state is observed if a superconductor is put in a magnetic field and then cooled below its transition temperature [4]. In the normal state, magnetic flux lines can penetrate through the material (Figure 7.2(a)). As the material becomes superconducting, the magnetic flux is expelled (Figure 7.2(b)), unlike a perfect conductor where flux is not expelled. This is a

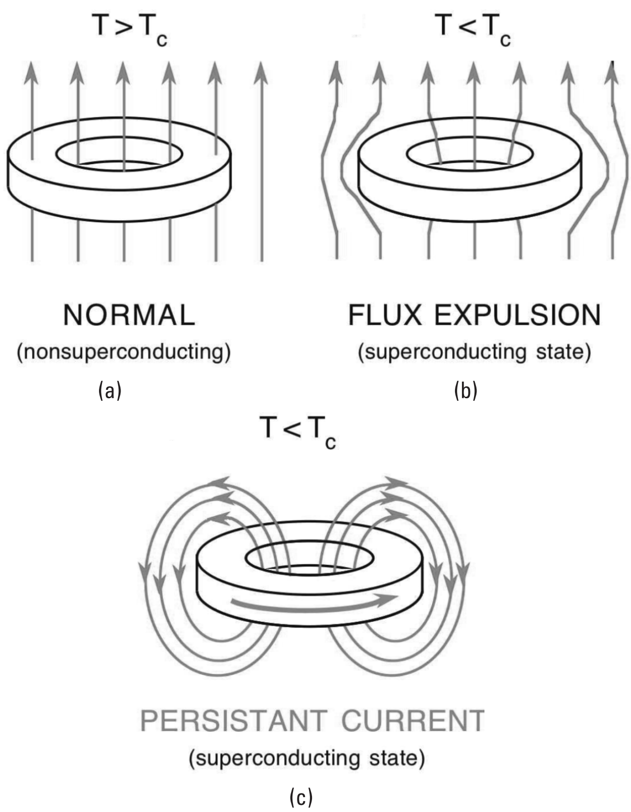

Figure 7.2 The Meissner effect in a superconducting loop cooled in an externally applied magnetic field. The transition from state b to state c occurs when the external field is removed.

consequence of Maxwell's equations where an electric field gradient cannot exist inside a superconductor. If the superconducting material forms a loop, the flux interior to the loop is trapped when the loop becomes superconducting (Figure 7.2(c)).

If the magnetic field is turned off, a current is induced that circulates around the loop keeping the magnetic flux ($\Phi = \int BdA$) inside constant (Figure 7.2(c)). Because of the electrical resistance, the current in a loop made of a normal (nonsuperconducting) metal will quickly decay. The current decay is exponential with a time constant that is related to the resistance (R) and inductance (L) of the loop, $I(t) = I_o\ e^{-tR/L}$. For a superconducting loop, $R = 0$ and a persistent current is established. The current continues to circulate as long as the loop is kept cold (below T_c). It should be noted that superconducting loops of tin have been made to carry circulating DC for a period much greater than a year, disconnected from any power source, without any measurable decrease in current [5]. This is equivalent to saying that the resistivity of superconducting tin is at least 17 orders of magnitude less than that of room-temperature copper.

7.1.3 Flux Quantization

As long as the current persists, the magnetic flux remains trapped. This trapped flux has some very unusual properties. First, one cannot vary magnetic flux within

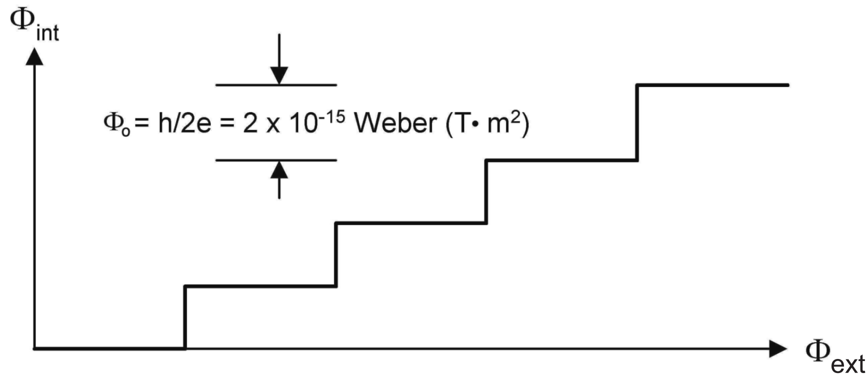

Figure 7.3 Flux quantization within a superconducting loop ($\Phi_{int} = n\Phi_o$; $n = 0, \pm1, \pm2, \pm3, \ldots$).

a superconducting loop in a continuous manner. One can only trap discrete levels of the magnetic flux (Figure 7.3). In other words, the magnetic flux is quantized and exists only in multiples of a very small fundamental quantity called a flux quantum ($\Phi_o = h/2e$) whose magnitude is 2.068×10^{-15} Webers (1 Wb/m^2 = 1T). Equivalently, for a superconducting loop with an area of 1 cm^2, the field inside the loop can only exist in discrete multiples of 2.068×10^{-11} T. It should be noted that flux outside superconductor ring is not quantized.

7.1.4 The Josephson Effect

For a loop of superconducting wire interrupted by a normal (resistive) region, one would expect it to behave the same as a continuous loop of normal metal. That is, a current flowing in the loop would quickly decay. In 1964, Josephson [6] predicted the possibility of electrons tunneling from one superconducting region to another that had been separated by a resistive (insulating) barrier (usually referred to as a weak link). For distances less than the coherence length, ξ_o, and currents less than a critical current, I_c, that is characteristic of the weak link, a current can penetrate the resistive barrier with no voltage drop (Figure 7.4(c)). In an ideal Josephson junction, the transition from resistive to superconducting behavior would be a sharp vertical transition, at I_c, rather than the real-world curved transition (due to noise rounding and self-heating) shown.

The critical current (I_c) of a Josephson junction is defined to be point midway between superconducting and resistive behavior. A bias current (I_{bias}) is applied (2 I_c in the case of a DC SQUID) defining the operational point on the *I-V* curve (Figure 7.4(c)). Inductively coupling magnetic flux into the SQUID loop creates screening currents ($I_{loop} = \Phi_{loop}/L_{loop}$) that will effectively increase or decrease the net current through the junction(s), depending on the direction of the induced flux. Shunt resistors are used to prevent hysteretic behavior [7] in the *I-V* curve (Figure 7.4(d)).

7.1.4.1 Weak Links

There are many ways to make a weak link. The junction can be an insulating (superconducting-insulator-superconducting (SIS)) barrier such as a point contact

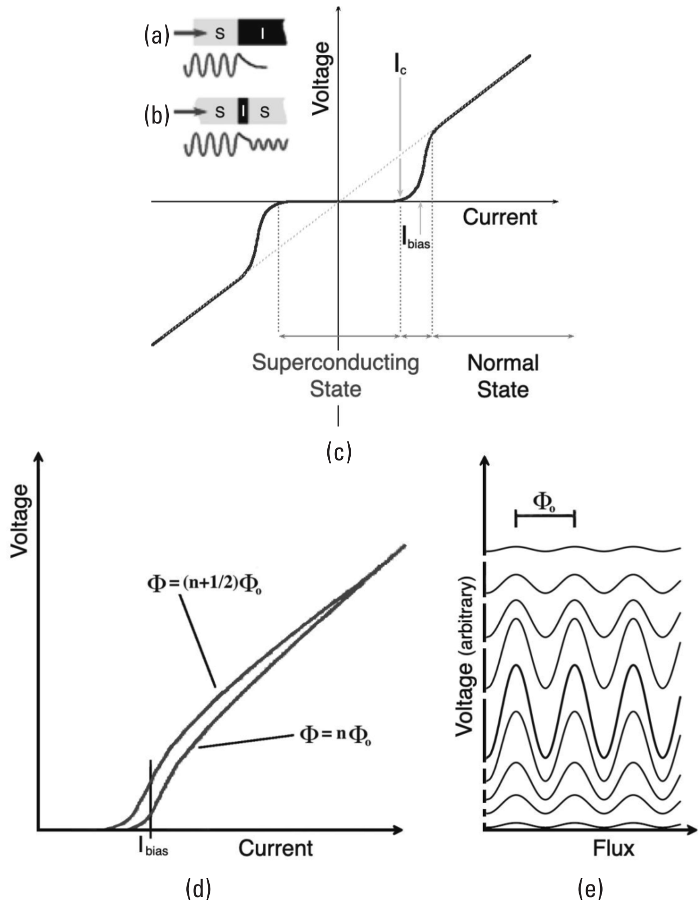

Figure 7.4 (a) Quantum mechanical wave function of a superconducting current penetrating a normal region, showing the attenuation of the wave function as it penetrates an insulating (i.e., resistive) layer. (b) Quantum mechanical wave function penetrating a thin insulating region separating two superconducting regions. (c) Current versus voltage curve of a shunted Josephson tunnel junction measured across the junction; note that here $I_{bias} > I_c$. (d) *I-V* characteristics for integer and half integer values of applied flux. (e) V-Φ at increasing bias currents for a DC SQUID.

(Figure 7.5(a)), a normal metal (superconducting-normal-superconducting (SNS)) barrier, or a microbridge (Figure 7.5(b)). Present-day LTS devices use tunnel junction weak links (Figure 7.5(c)). HTS devices use either intrinsic (bicrystal—Figure 7.5(d) or step edge grain boundary—Figure 7.5(e)) junctions or extrinsic (step edge SNS—Figure 7.5(f) or ramp edge—Figure 7.5(g)) structures.

The weak link can be a region in which the current flowing is higher than the current needed to drive the superconductor normal (I_c). A typical weak link might have a critical current ~10 μA. If the loop has a diameter of 2 mm, this is equivalent to several flux quanta. For a loop of superconductor interrupted by a weak link Josephson junction, magnetic flux threading through a superconducting loop sets up a current in the loop. As long as the current is below the critical current, the complete loop behaves as if it were superconducting. Any changes in the magnetic flux threading through the loop induce a shielding current that generates a small magnetic field to oppose the change in magnetic flux.

7.1.5 SQUIDs

SQUIDs use the Josephson effect phenomena to measure extremely small variations in magnetic flux. The theory of different types of SQUIDs has been described in detail in the literature [8–10]. SQUIDs are operated as either RF or DC SQUIDs. The prefix RF or DC refers to whether the Josephson junction(s) is biased with an AC (RF) or a DC. While the simplest SQUID would use a bare loop, flux is normally (inductively) coupled into the SQUID loop via an input coil that connects the SQUID to the experiment (Figure 7.6). Because the input coil is superconducting, its impedance is purely inductive.

By fixing I_{bias} at a slightly higher value than I_c, when an external magnetic flux ($\Phi_{\text{ext}} = B_{\text{ext}} A$) is coupled into the SQUID loop, the voltage drop across the Josephson junction will change. As the external flux increases (or decreases), the voltage will change in a periodic manner with the period being that of the flux quantum, Φ_o (Figure 7.4(e))—which shows the effect of increasing I_{bias} from zero to well above I_c, with a maximum amplitude in the V-Φ relationship when $I = I_{\text{bias}}$ (see the bias point indicated in Figure 7.4(d)). Monitoring the change in voltage allows determination of the magnetic flux that has been coupled into the SQUID loop. By using external feedback, it is possible to lock the SQUID at a unique point on the V-Φ curve; the feedback current (usually coupled into the SQUID loop—Figure 7.6) is then a measure of the externally applied flux. SQUIDs are normally operated at the steepest part of the V-Φ curve where $dV/d\Phi$ is a maximum. This allows the SQUID to act as a flux-to-voltage transducer. Because of periodic behavior of the voltage (or current) transfer function (Figure 7.4(d)), a single SQUID is not suitable for measuring absolute values of magnetic field (in contrast to superconducting quantum interference filter (SQIF) devices, which are discussed in Section 7.3.3).

There is also the need for the feedback electronics to be able to track large changes in applied fields. For signal changes larger than ¼ Φ_o, the electronics need to be able to apply negative feedback fast enough to keep the voltage at the operating or lock point. If the electronics cannot change the feedback current (slew) fast

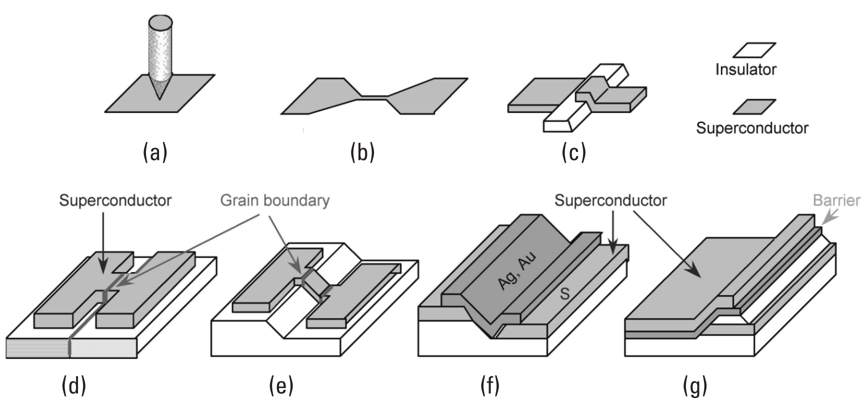

Figure 7.5 Different types of Josephson junctions: (a) point contact; (b) microbridge, also known as a Dayem bridge; (c) thin-film tunnel junction; (d) bicrystal; (e) step edge grain boundary; (f) step edge superconductor-normal-superconductor; and (g) ramp edge superconductor-normal-superconductor with an insulating $PrBa_2Cu_3O_{7-\delta}$ barrier.

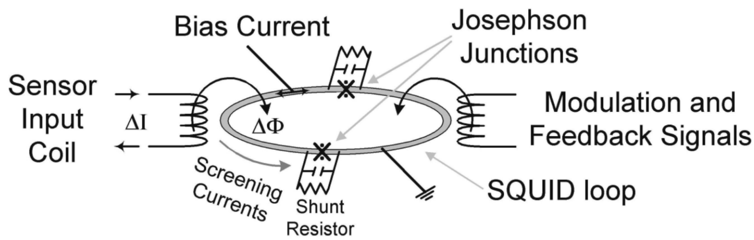

Figure 7.6 Dual junction (DC) SQUID loop. The capacitor represents the self-capacitance of the junction.

enough, it is possible that they could end up at a different point on the V–Φ curve (same V, different Φ). If flux jumping occurs, it may be necessary to go to faster electronics or limit the dynamic range (or bandwidth) of the input signal (source). SQUIDs can also be voltage-biased [11]; a number of SQUID systems for biomagnetism (e.g., magnetoencephalography—Section 7.10.5) use such feedback systems as they can simplify the readout electronics for high channel count systems.

7.2 SQUID Sensors

There are fundamental differences between LTS and HTS. LTS materials are metallic (although some nonmetallic and organic compounds have been found to be superconducting) and isotropic and have coherence lengths, ξ_o, that are tens to hundreds of interatomic distances. HTS materials are ceramics, brittle, and anisotropic (essentially planar) and have coherence lengths in the c direction (perpendicular to the a-b plane) that are significantly smaller (Table 7.1). Not only is there a temperature limitation to superconductivity, but there is also a field dependence. The material remains in the superconducting state below a critical field $H_c(T) = H_{c0}\,[1 - (T/T_c)^2]$ where H_{c0} is the critical field at $T = 0$ (Figure 7.7). T_c can be increased by pressure [2]; however, it is not feasible to fabricate usable SQUID devices when the material(s) must be maintained at GPa pressures [12].

Another parameter of interest is the London penetration depth (λ_L) [13], which is determined by the superfluid density and characterizes the depth (z) into which a magnetic field penetrates into a superconductor, that is, $B(z) = B_{\text{ext}}e^{-z/\lambda_L}$. Typical values of λ_L range from 50 to 500 nm. Precise measurements of λ_L at $T = 0$K are important to understand the mechanisms of HTS. Penetration depth is important when fabricating thin-film devices and superconducting shields.

7.2.1 Materials

Materials (typically pure metallic elements such as Hg or Pb) that totally exclude flux inside a superconductor (up to a well-defined transition temperature T_c) are referred to as type-I superconductors (Figure 7.7(a)). Materials that exhibit a partial Meissner effect are referred to as type-II superconductors (Figure 7.7(b)).

Below a lower critical field H_{c1}, they act as type-I superconductors. Above H_{c1}, the material is (incompletely) threaded by flux lines and the material can be

Table 7.1 Properties of Superconducting Materials

LTS	*Type*	T_c *(K)*	H_{c0} *(T)*	H_{c2} *(T)*		x_o *(nm)*
Aluminum	I	1.18	0.01			1,600
Mercury	I	4.15	0.04			
Lead	I	7.19	0.08			83
Niobium	II	9.23	0.18 ($H_{c1}\downarrow$)	0.28		38
NbTi	II	9.5	0.015	15		4
NbN	II	17.3	0.03	15		4
Nb_3Sn	II	18	0.44	29		3
HTS	Type	T_c (K)	H_{c1} (T)	H_{c2} (T)	$\xi_{a,b}$ (nm)	ξ_c (nm)
MgB_2 (thin film)	II	39	~0.2	38	6.5	4
$Ba_{0.6}K_{0.4}Fe_2As_2$	II	38	~0.04	>100	~3	~1.5
$YBa_2Cu_3O_{7-\delta}$	II	95	~0.005	~130	4	0.7
$Bi_2Sr_2Ca_2Cu_2O_{10}$	II	110	~0.006	>100	4.5	0.2
$Tl_2Bi_2Ca_2Cu_3O_{10}$	II	125				
$HgBa_2Ca_2Cu_3O_{8+\delta}$	II	135				
LaH_{10}	II	~250 (at 150 GPa)				
$CS_{17}H_{54}$	II	288 (at 267 GPa)	~63			

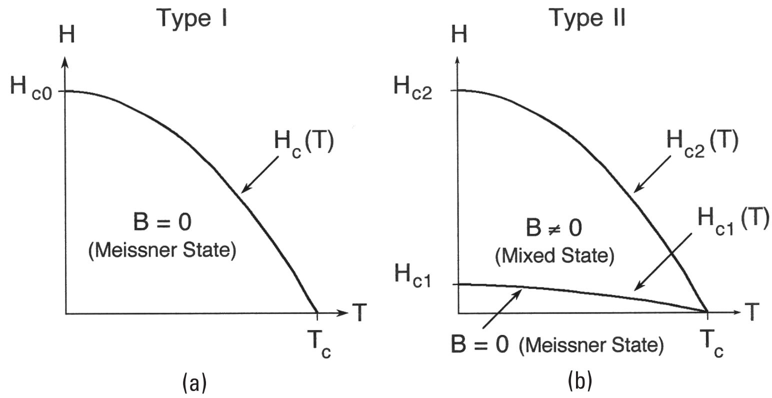

Figure 7.7 The H-T phase space for (a) type-I and (b) type-II superconductors.

considered to be in a vortex state [9]. The higher the applied field, the greater number of allowed flux lines until the upper critical field H_{c2} is reached, where the entire material transitions to the normal state. Type-II superconductors (e.g., NbTi and Nb_3Sn) tend to be alloys or transition metals with high electrical resistivity in the normal state. All HTS materials are type-II superconductors. Superconducting magnets are fabricated from type-II materials that allow multitesla fields to be attained.

LTS devices have significant advantages and one disadvantage (operating temperature) over HTS devices. Because LTS materials are isotropic and have long coherence lengths (Table 7.1) relative to their interatomic distances, it is possible to fabricate devices with 3-D structures. This allows crossovers and multilayer structures that permit higher sensitivity than single-turn devices. HTS crossovers (needed for multiturn coils) require larger dimensions than the coherence length of YBCO (Table 7.1) in the *c*-direction. The effect is that an HTS crossover acts as a Josephson or insulating junction with the addition of significant $1/f$ noise (see Section 7.3.5). The associated flux creep that can occur (particularly in HTS materials) by operating in the mixed (vortex) state can lead to nonlinearity or hysteretic effects. While their pinning energies are somewhat lower than YBCO, bismuth and thallium compounds (Table 7.1) seem to have much lower densities of pinning sites [14]. As a result, the flux creep (and its associated resistivity) is considerably higher. By operating at lower temperatures (20–30K), it is possible to freeze out the hysteretic effects seen in bismuth and thallium devices at 77K. Because of this, most HTS SQUIDs are fabricated from YBCO because of its sufficiently strong (and intrinsic) flux pinning at 77K.

Another difference is that LTS materials (e.g., NbTi) are ductile and, in wire form, can be made into complex 3-D structures such as axial gradiometers (see Section 7.7.4). Additionally, using NbTi (or Nb_3Sn) allows detection coils to be in high field regions, while the actual LTS SQUID sensor can be placed in a low field environment. Because of the inability to make a truly superconducting flexible 3-D structure, axial HTS gradiometers are not possible, although thin-film planar gradiometers are. Even if it was possible to make a separate HTS coil, the inability to make superconducting joints (or joints with contact resistances at the sub-pΩ level) due to the shorter coherence length of HTS materials (Table 7.1) prevents a true DC response in discrete-element HTS circuits [14].

Another advantage of LTS materials is that they are stable in air, whereas moisture can degrade the HTS structure. Thus, passivation layers or overcoatings are required and add to the complexity of manufacture. Although LTS materials have superior properties, the ability to operate a device at liquid nitrogen rather than liquid helium temperatures gives HTS devices significant operational advantages and cannot be discounted.

The barrier used for fabricating the weak link is critical. Early point contact devices used an oxide layer (NbO). The first commercial DC SQUID [16] used an amorphous SiO_2 barrier that allowed junctions with critical currents within a few percentages to be easily fabricated. An unfortunate side effect was that the amorphous barrier had significant temperature-dependent resistivity that caused frequency-dependent noise (see Section 7.4.4). Present-day LTS SQUIDs utilize thin-film AlO_x barriers with temperature-independent critical currents. Bicrystal (Figure 7.5(d)) and ramp edge (Figure 7.5(g)) junctions have become popular in commercial HTS devices. Koelle et al. [15] gave an excellent overview on HTS SQUIDs. While SQUIDs have been fabricated from Nb, NbN, YBCO, MgB_2, bismuth, and thallium compounds, commercially available SQUIDs are based on either Nb or YBCO.

7.3 SQUID Operation

Typically, a SQUID is a loop of superconductor interrupted by one or more Josephson junctions (Figure 7.6). A bias current (I_{bias}) is applied (2 I_{bias} in the case of a DC SQUID) putting the operational point on the *I-V* curve (Figure 7.4) midway between superconducting and resistive behavior. Shunt resistors are used to prevent hysteretic behaviors in the *I-V* curve [17]. Inductively coupling magnetic flux into the SQUID loop creates screening currents ($I_{loop} = \Phi_{loop}/L_{loop}$) that will effectively increase or decrease I_c, depending on the direction of the induced flux. HTS SQUIDs often use direct coupling (current injection) for the feedback and/or modulation signals.

The major difference between RF and DC SQUIDs is that the DC SQUID may offer lower noise when compared to an RF SQUID. The cost of this increase in sensitivity can be the complexity of the electronics needed to operate a DC SQUID and the difficulty in fabricating two nearly identical Josephson junctions in a single device. From a historical viewpoint, although the LTS DC SQUID was the first type of SQUID magnetometer made, early LTS development was with RF SQUIDs. With modern thin-film fabrication techniques and improvements in control electronics design, the DC SQUID offers clear advantages over the RF SQUID for many applications.

One way to measure the change in external flux (or inductively coupled current from the sensor input coil) is to simply count the number of periods that it produces in the detected output. The commonly used mode of operation is a negative feedback scheme, which locks in on either a peak or valley (Figure 7.8(b)) or the maximum $dV/d\Phi$ in the V-Φ curve (Figure 7.9(b)). A feedback flux is applied to the SQUID that just cancels the change in flux from the input coil, allowing flux resolution to $\mu\Phi_o$ levels. This manner of operation is called a flux-locked loop.

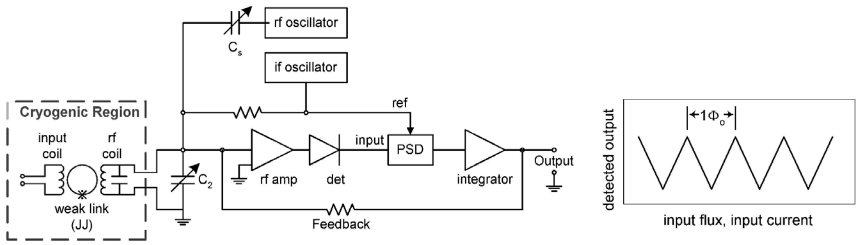

Figure 7.8 (a) Block diagram of SQUID input and electronics for locked-loop operation; and (b) triangle pattern showing detected output voltage as a function of flux in the SQUID (V-Φ relationship).

7.3.1 The RF SQUID

The first commercial SQUID was the RF SQUID. It utilizes a single Josephson junction and flux is normally (inductively) coupled into the SQUID loop via an input coil that connects the SQUID to the experiment and an RF coil that is part of a high-Q resonant circuit to read out the current changes in the SQUID loop (Figure 7.8(a)).

This tuned circuit (e.g., operated at 19 MHz) is driven by a constant current RF oscillator that is weakly coupled to the SQUID loop. As the oscillator drive amplitude is increased, the (peak) detected output of the RF amplifier increases until a critical level is reached. That is, an increase in drive amplitude produces a very small increase in output. The RF drive is set so that the SQUID operates on this plateau, where the detected output depends on the current flowing in the input coil. Any changes in the input coil current will induce a change in the current flowing in the SQUID loop. This shielding current causes the total flux linking the SQUID loop to remain constant as long as the loop remains superconducting. Another contribution to the total flux in the SQUID (and to the shielding current) comes from the RF current in the 19-MHz tuned circuit. Thus, we can consider the shielding current to consist of an AC component and a DC component, which biases the junction. When the amplitude of the AC component increases, the critical current of the weak link will be reached and a transition occurs changing the flux state of the SQUID by a single flux quantum. This transition temporarily reduces the level of oscillation in the RF coil, which then builds up again to its maximum value and the process repeats itself. Just after the transition, the weak link again becomes a superconductor and the shielding bias current due to the current in the input coil reestablishes itself to quantize the flux in the SQUID. When the RF oscillations have

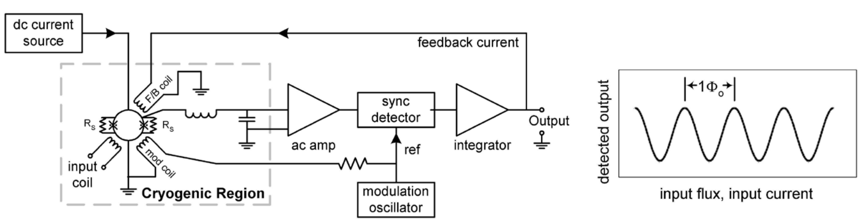

Figure 7.9 (a) Block diagram of a typical DC SQUID. The detection coil (connected to the input coil) is omitted for clarity; and (b) V-Φ relationship showing detected output voltage as a function of flux in the SQUID.

been reduced sufficiently, the Josephson junction will again be superconducting and the amplitude of the RF oscillations will begin to increase again.

If the DC in the input coil is changed, the DC bias of the shielding current in the SQUID is changed so that the RF-induced transition occurs at a different level of oscillation in the RF coil. The detected RF output is found to be the periodic function shown in Figure 7.8(b). It should be noted that the RF and input coils (Figure 7.8(a)) are not wound around the SQUID loop, but are inductively coupled to the SQUID loop. A minor advantage of the RF SQUID is that its cryogenic connections are simple; only a single coax or a single twisted pair of leads from room temperature is needed. Additional details on the operation of RF SQUIDs can be found in [8].

7.3.2 The DC SQUID

The DC SQUID differs from the RF SQUID in the manner of biasing the Josephson junction and the number of junctions. Since there are two junctions (Figure 7.6), they need to be matched as do the shunt resistors. The ideal shunt resistor should have a temperature-independent resistivity. The use of noble metal resistors such as Pd is preferred over amorphous materials or materials with superconducting transitions, which would prevent operation below their T_c.

Figure 7.9 shows a schematic of a typical DC SQUID. Like the RF SQUID (Figure 7.8(a)), the input, feedback, and modulation coils are not wound around the SQUID loop, but inductively coupled to it. It is biased with a DC approximately equal to twice I_c and develops a DC voltage across the junctions (and shunt resistors). A change in the magnetic flux applied through the SQUID loop induces a wave function phase change that enhances the current through one Josephson junction and reduces the current through the other. This asymmetry, which is periodic in Φ_o, is used to provide a feedback current (via the modulation coil) that nulls the flux penetrating the SQUID loop. Like the RF SQUID, this feedback current (presented as a voltage at the output) is a direct measure of changes in flux applied to the SQUID.

The DC SQUID typically requires at least four pair of leads (bias, modulation, signal, feedback) between the SQUID and its electronics. Additional details on the operation of DC SQUIDs may be found in [17].

7.3.3 SQIFs

An array of different superconducting loop sizes, in series or in parallel configuration or in a 2-D combination of both, acting as grating structures, can be used to form a SQIF, also known as SQUID array (SQA) [18]. This type of interferometer is based on the phase-dependent superposition of currents flowing through a nonperiodic multiloop network (series, parallel, or series-parallel as in Figure 7.10(a) of Josephson junctions), where the loop areas (A_{ij}) are designed to be nonidentical. The effect of such an arrangement is that the contributions of the loops to the output signal mutually cancel each other for any finite value of the ambient magnetic field. For zero magnetic fields, a mutual enhancement occurs by means of the coherent superposition yielding a unique dip at zero-field (Figure 7.10(b)). In contrast to conventional SQUIDs, the characteristic flux dependence of the voltage output (V-Φ) of a SQIF is nonperiodic.

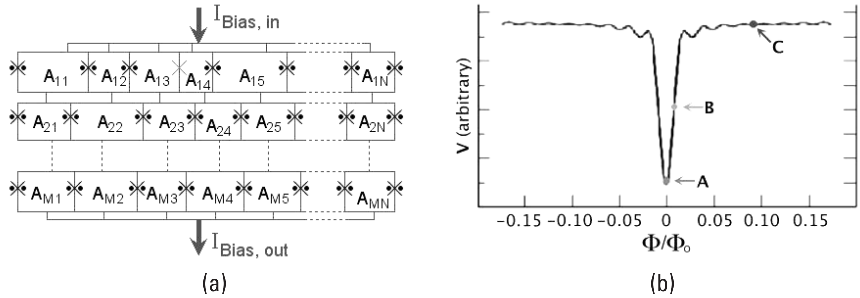

Figure 7.10 (a) Schematic of a 2-D (*N* series by *M* parallel elements) SQIF array (A_{ij} is the area of the *ij*th Josephson loop); and (b) SQIF transfer function [A: mixing mode (V-Φ very nonlinear), B: detection mode (V-Φ is linear), C: not useful ($dV/d\Phi$ very small)].

The unique dip in the V-Φ curve allows for the absolute field magnetometry [19] and high-precision RF-applications like amplifiers and mixers [20]. The sensitivity [21] and dynamic range of a SQIF scales proportionally to the square root of the number of loops ($N \times M$) in the array (Table 7.2). With even a moderate number of loops, this should allow absolute field measurements to be made at sensitivities at or below the fT/√Hz level. Another advantage of SQIFs is that the Josephson junction parameters (e.g., I_c) need not be well matched (i.e., less than a few percentages), which is much more serious in HTS where parameter spreads can be much larger. This makes fabrication of SQIF devices from HTS materials significantly easier. SQIFs also have the ability to operate at frequencies above 20 GHz.

7.3.4 Fractional-Turn SQUIDs

Another way to increase the sensitivity of a bare SQUID loop is to connect not just a single detection coil, but a number of coils, not in series (as is done in traditional multiturn coils; e.g., Figure 7.15), but in parallel (Figure 7.11(a)). The critical concept is keeping the inductance of the SQUID loop itself very small, while having a large area for coupling to an external coil. This is because thermal noise puts an upper bound on the inductance of the loop itself. Referred to as a fractional turn, rather than a multiturn SQUID [22], this improves sensitivity by reducing the input inductance by roughly $L_{poly}/N^2 + L_{spoke}/N + L_{jp}$, where L_{poly} is the total inductance of a polygonal pickup coil without spokes, L_{spoke} is the inductance of the spoke, L_{jp} is the small parasitic inductance of the Josephson junction connection lines, and N is the number of turns in the SQUID loop [23]. By directly coupling a fractional-turn input coil, this allows a small diameter input coil that can match the input

Table 7.2 Theoretical Scaling Properties of SQIFs (*N* Parallel, *M* Series Loops)

Output voltage	*M*	*Maximize*
Power gain	$M \times N$	Maximize
Signal-to-noise dynamic range	$M \times N$	Maximize
Spur-free dynamic range	$(M \times N)^{2/3}$	Maximize
Output resistance	M/N	Target (e.g., 50Ω)

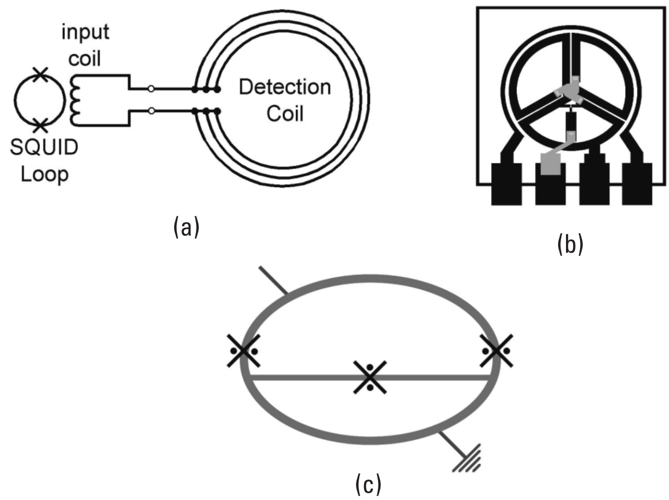

Figure 7.11 (a) Schematic of fractional turn SQUID sensor with detection coils in parallel; (b) fabricated device (the pads are for coupling in the bias and feedback currents); and (c) schematic of bi-SQUID (shunt resistors not shown).

impedance of the SQUID loop to be fabricated. Devices with $N = 3$ (Figure 7.11(b)) to $N = 16$ have been fabricated with significantly reduced field noise.

While fractional-turn SQUIDs have better sensitivity, it should be noted that their spatial resolution (for nearby objects) may be significantly poorer. A qualitative explanation is that when an object that is quite close moves from one loop to another, there is little or no change in the total detected flux. This is due to the individual loops being in parallel and that the total detected flux is the arithmetic sum of the individual loops. Depending on the geometry of the fractional-turn SQUID, the spatial resolution can be as poor as half the device diameter, while conventional coils have demonstrated spatial resolutions better than one-tenth of the coil diameter. Because of this, fractional-turn SQUIDs may not be the best choice for use in magnetic microscopy of magnetic dipoles.

7.3.5 The Bi-SQUID

The standard DC SQUID (Figure 7.6) can be modified by adding a nonlinear inductance, in the form of a third Josephson junction (Figure 7.11(c)) [24]. This third junction, when combined with the main inductance in the loop, acts as a single-junction SQUID yielding a device (known as a bi-SQUID) that has a triangular V-Φ transfer function (similar to the RF SQUID—Figure 7.9(b)) with significantly improved linearity.

7.4 Noise and Sensitivity

SQUID noise is often presented as the spectral density of the equivalent flux noise $S_\Phi(f)$ as a function of frequency or noise energy per unit bandwidth

$$E_N(f) = \frac{S_\Phi(f)}{2L} \tag{7.1}$$

where L is the inductance of the input coil. To allow devices with differing input inductances to be directly compared, the sensitivity of SQUID devices is best discussed in terms of the energy sensitivity:

$$E_N = \frac{1}{2} L_{\text{input}} I_N^2 = \frac{\Phi_N^2}{2L_{\text{input}}} \tag{7.2}$$

where (when configured as a current sensor—Figure 7.6), L_{input} is the input inductance of the SQUID sensor, I_N is the current noise, and Φ_N is the flux sensitivity. E_N is often expressed in units of the Planck's constant h (= 6.6 × 10^{-34} J/Hz).

Figure 7.12 shows typical energy sensitivities for LTS and HTS SQUIDs. As can be seen, the noise can be described as the sum of frequency-independent (white) and frequency-dependent ($1/f$) terms.

Magnetometers are often discussed in terms of field sensitivity. However, because the field sensitivity is as much dependent on the geometry of the detection coil geometry (area, number of turns) as the SQUID itself, energy sensitivity allows comparison of SQUID sensors independent of coil geometry or input impedance. Calculation of magnetic field sensitivity is discussed in Section 7.7.

7.4.1 White Noise

7.4.1.1 RF SQUID

The typical white noise for a LTS RF SQUID operating at 19 MHz is 10^{-28} J/Hz (Figure 7.12(a)). The major limiting factor in the white noise of an RF SQUID is

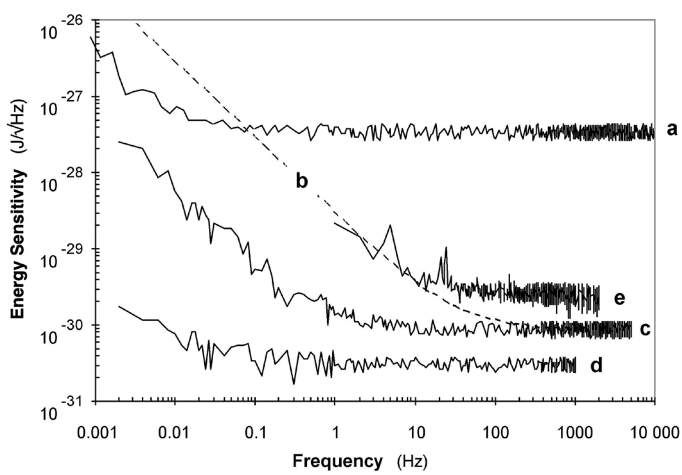

Figure 7.12 Energy sensitivity versus frequency for a number of different SQUID devices: (a) a LTS RF SQUID operated at a bias frequency of 19 MHz (SHE model HSQ); (b) a DC biased LTS DC SQUID with amorphous silicon barriers (SHE model DSQ); (c) (b) using AC biasing; (d) a DC-biased LTS DC SQUID with AlO_x barriers (Quantum Design model 50); and (e) an AC-biased HTS DC SQUID utilizing a ramp edge junction (Tristan model HTM-8; see Figure 7.5(g)).

the bias frequency (f_{bias}) used to excite the tank circuit. Noise in RF SQUIDs is proportional to $1/\sqrt{f_{\text{bias}}}$ [25]. Increasing the bias frequency from 19 MHz [26] to 180 MHz [27] has been shown to reduce noise by a factor of 3. As f_{bias} increases, the complexity of the electronics also tends to increase. With the discovery of HTS, the first HTS SQUIDs were single-junction RF SQUIDs. HTS RF SQUIDs have used bias frequencies as high as 1 MHz in an attempt to approach the sensitivity levels of DC SQUIDs. As it is not known (at least theoretically) if there is a fundamental limit to the white noise of RF SQUIDs, at 1 GHz, an RF HTS SQUID may be quieter than a DC HTS SQUID.

7.4.1.2 DC SQUIDs

The minimum noise energy for a DC SQUID is given by [7]:

$$E_N \approx 16 k_B T \sqrt{\frac{L_{\text{loop}}}{\omega_J R_s}} \Rightarrow 16 k_B T \sqrt{\frac{L_{\text{loop}} C}{\beta_c}} \tag{7.3}$$

where k_B is Boltzmann's constant, L_{loop} is the inductance of the SQUID loop, $\omega_J/2\pi$ is the Josephson frequency, R_s is the shunt resistance, and C the capacitance of the junction. To remove ω and R_s from (7.3), we define the Stewart-McCumber hysteresis parameter [28] as $\beta_c = \omega_J R_s C$. To prevent hysteretic behavior, we require that $\beta_c \lesssim 1$.

Substituting appropriate numbers indicates that the minimum noise energy (E_N) for a DC SQUID is on the order of $h/2$ and devices with sensitivities of $\sim h$ have been constructed. These extremely low noise levels are achieved by limiting dynamic range and avoiding feedback. The need for practical (useful) devices require that feedback be used and that the SQUID electronics has a reasonable dynamic range. Commercially available DC SQUIDs typically have sensitivities at the 10^{-31} J/Hz level.

7.4.2 Temperature Dependence

Due to the strong temperature dependence of superconducting properties, for example, energy gap $\Delta(T)$, the energy needed to decouple the paired electrons, critical current (I_c), surface resistivity (R_s), and basic SQUID parameters such as bias and modulation drive, especially near T_c, will experience variations as a function of temperature.

The best noise performance is obtained when the SQUID is operated at or below $\frac{1}{2}T_c$, when $\Delta(T) \approx \Delta(0)$. A niobium LTS SQUID operating at 4.2K has $T/T_c = 0.44$ while a YBCO SQUID at 77K has $T/T_c = 0.83$. Independent of the type of SQUID, it still needs to be operated at a temperature such that the energy gap is significantly greater than zero, for example, below $\frac{5}{6}$ T_c where $\Delta(T)/\Delta(0) > 0.67$. It should be noted that above $\frac{1}{2}T_c$, $\Delta(T)$ is highly nonlinear and the majority of improvement from reducing operating temperature comes from the increased energy gap, rather than the improvement implied in (7.3).

With the discovery of room-temperature superconductivity [12], albeit at GPa pressures (Table 7.1), refrigeration requirements (Section 7.8) may be significantly reduced or even eliminated. However, for a SQUID device to be usable at room temperature, it would need to be based on a superconducting material whose T_c is greater than 360K.

Operating at lower temperatures also means potentially lower noise; see (7.3). A significant temperature variation may require retuning for optimum performance. A typical LTS SQUID (e.g., Figures 7.12(c, d)) will have a temperature variation of ~0.1 Φ_o/K, an HTS device (Figure 7.5(f)) has $d\Phi/dT \approx 0.015\ \Phi_o$/K. Because liquid cryogens are normally used to cool SQUID devices, ambient pressure and pressure variations can change the cryogen temperature with a commensurate change in SQUID operating parameters. For example, geophysical applications may require operation in deep mines or underwater. A 1-torr pressure variation at 760 torr is equivalent to a 1.5-mK change in the temperature of a liquid helium bath and a 11-mK change in the temperature of a liquid nitrogen bath, equivalent to 150 $\mu\Phi_o$ and 165 $\mu\Phi_o$ for LTS and HTS devices, respectively. Because of this, it may be advisable to thermally isolate SQUID sensors from liquid cryogen baths, especially if measurements are being taken during significant changes in depth or altitude (e.g., airborne operation of SQUIDs—see Section 7.10.3). The use of a closed-cycle refrigerator (Section 7.8.2) can cause significant temperature variations (±0.1K at 1 Hz for a 4K Gifford-McMahon cycle cryocooler). A temperature controller and/or a large thermal mass (e.g., Figure 7.19) may be needed to smooth out these variations.

7.4.3 Field Dependence

In normal operation, LTS SQUIDs are operated in the Earth's magnetic field or lower (<60 μT) environments. LTS experiments requiring operation in high fields usually employ coils that transport the measured flux or currents to the LTS SQUID sensor located in a low field region of the cryostat. Because HTS coils are located on the same substrate as SQUID itself, the HTS SQUIDs are subjected to the environment being measured. Some HTS devices simply will not function in fields exceeding tens of micro-tesla. In addition, the decreased flux pinning in HTS devices at high fields results in reduced slew rates. The development of ramp edge junctions (Figure 7.5(g)) has allowed HTS devices to operate in fields >0.1T with white noise scaling as $\sqrt{H}$ [29].

7.4.4 1/*f* Noise

Along with white noise, there exists a frequency-dependent contribution that increases as the frequency decreases (Figure 7.12). The onset of this 1/*f* noise can be dependent on the ambient magnetic field when the SQUID sensor is cooled. Cooling the SQUID sensor in low ambient magnetic fields (less than 1 μT may significantly improve 1/*f* performance, particularly with HTS SQUIDs using grain boundary junctions (Figure 7.5(d, e)). It should be noted that measurements of 1/*f* noise, usually taken at frequencies well below 1 Hz, are difficult. The SQUID sensor should be placed in a superconducting can, which is itself inside mu-metal shielding. Care should be taken to eliminate any potential mechanical motion. As vibration often appears as a $1/f^2$ contribution, excessive low-frequency noise may be identified by its spectral content.

7.4.4.1 Sources of 1/*f* Noise

Thermally activated critical current fluctuations due to trapping and release of electrons in the barrier produce fluctuations in the (Josephson) barrier height (thermally activated critical current I_c). A large contribution to this noise in some DC SQUIDs can arise from the presence of the DC bias. Flux noise probably arises from motions of flux lines trapped in body of SQUID and is thought to be thermally activated. Flux motion between pinning sites (flux hopping) can be reduced by reducing the width of the superconductor. Slotted structures (moats), holes, or vortex pinning centers (e.g., ion-implanted impurities or nanoparticles) have also been shown to reduce 1/*f* noise [29]. Flux noise fluctuations have not been able to be reduced by any known modulation scheme.

7.5 Control Electronics

SQUIDs are commonly operated in a flux-locked loop (e.g., Figures 7.8 and 7.9). This amplifies the small signals generated by the SQUID and linearizes the transfer function of the SQUID providing sufficient output voltage and dynamic range.

The system output voltage of a flux-locked loop is the voltage drop across the feedback resistor in a negative feedback loop controlled by the SQUID electronics. The feedback signal is generated in response to changes in the output signal of the SQUID sensor. The output of the SQUID sensor is periodic in the field coupled into the SQUID loop. Negative feedback (similar to a phase-locked loop technique) is used to maintain the system operating point at a particular (and arbitrary) flux quantum (e.g., the midpoint of the V-Φ curve in Figure 7.9). An open-loop operation can allow tracking of small ($<\frac{1}{4}\ \Phi_o$) signals much greater than the bandwidth of a flux-locked loop. Systems requiring gigahertz bandwidths (e.g., SQIFs) are operated in this manner. Details of flux-locked loop operation can be found in [17, 31].

One important factor of SQUID design is such that the feedback electronics be able to follow changes in the shielding currents. If the shielding current changes so fast that the flux in the SQUID loop changes by more than $\frac{1}{2}\ \Phi_o$, it is possible that the feedback electronics will lag behind the rapidly changing flux. When the electronics finally catch up, they can lock on an operating point (Figure 7.4(d)) different from the original. In this case, the SQUID has lost the lock because the SQUID has exceeded the maximum slew rate of the electronics. This places an upper limit on the bandwidth of the system. The typical bandwidth of most commercially available analog (i.e., flux-locked loop) SQUID electronics is DC to 50+ kHz. However, bandwidths of 5 MHz or more are available. Typical slew rates for SQUIDs are in the range of 10^5–$10^6\ \Phi_o$/s with some custom systems approaching $10^7\ \Phi_o$/s.

Even though one may not need or want to observe rapidly changing signals, situations may arise when ambient noise (e.g., 60 Hz) may determine the slew rate requirements of the system. To recover a signal from such interference, it is necessary that the system be able to track all signals present at the input, including the noise. When system response is sped up to handle very fast signals, sensitivity to RF interference and spurious transients is also increased. Since the ability to remain locked while subjected to strong electrical transients is greatest when the maximum slew rate is limited (slow), while the ability to track rapidly varying signals is greatest when the maximum slew rate is greatest (fast), it is desirable to be able to match the maximum slew-rate capability to the measuring situation. As a matter of convenience, many commercial SQUID systems offer user selectable slew rates along with highpass and lowpass filters for noise reduction.

Alternative readout concepts include additional positive feedback (APF), two-stage SQUIDs, SQUID series arrays, relaxation oscillation SQUIDs, and digital SQUIDs. Methods for increasing the dynamic range of SQUID systems (e.g., flux-quanta counting and dynamic field compensation (DFC)) were described in [32]. With DFC, the residual magnetic field at the SQUID can be kept close to zero even if the device is moved in the Earth's field.

A large contribution to $1/f$ noise in some DC SQUIDs can arise from the presence of the DC bias. By chopping the DC bias in combination with the conventional flux modulation techniques, it is possible to reduce this added $1/f$ noise. This AC bias reversal approach [33] separates the original signal waveform from the noise associated with the DC bias and can reduce $1/f$ noise at very low frequencies. Bias reversal limits the maximum bandwidth to less than half the bias reversal frequency.

7.6 Limitations on SQUID Technology

When utilizing SQUID-based measurement systems and data reduction algorithms, it is important to bear in mind several fundamental limitations on their ability to measure magnetic field changes:

1. *Differential measurements:* A fundamental limitation of conventional SQUIDs is that they are sensitive to relative flux changes. This is a consequence of the fact that the output voltage of a SQUID is a periodic function (Figure 7.4(d)) of the flux penetrating the SQUID loop. The SQUID is flux locked on an arbitrary maximum (or minimum) on the V-Φ curve, (actually at the point of the largest $dV/d\Phi$) and the SQUID output is sensitive to flux changes relative to this lock point. If the SQUID electronics are reset, the lock point may be at a different portion of the V-Φ curve with the potential to lose knowledge of ΔB during the reset.

   It is possible to make a SQUID magnetometer into an absolute magnetometer by rotating a coil 180° such that the field change (maximum to minimum) is twice the maximum field normal to the axis of rotation. To determine the total field, this needs to be done in all three axes. One such flip-coil magnetometer used a centimeter diameter coil that was rotated using plastic bevel gears actuated from room temperature to achieve field resolution at the pT level. In the case of large fields (i.e., μT total fields if pT resolution is desired), caution must be taken not to exceed the dynamic range of the electronics. If the speed of rotation is slow enough to allow for flux counting (adding the number of resets of the electronics), the dynamic range of the measurement can be extended by orders of magnitude.

   Unlike conventional RF or DC SQUIDs, SQIFs can be used for absolute field measurements. In the absence of an external magnetic field, the anti-peak (Figure 7.10(b)) of a SQIF's V-Φ response is located at $H = 0$. An external field will bias the location of the anti-peak by the amount of the applied field. Measuring H_{offset} in all three axes can allow the absolute determination of H_{total}. The precision in determining H_{offset} will be dependent on the sharpness of the anti-peak.

2. *Slew-rate limitations:* If the signal changes faster than the feedback electronics can follow (i.e., the slew rate is exceeded) and the total signal change exceeds ½ Φ_o, it is possible for the operating point to shift by one or more flux quanta (Figures 7.8(b) or 7.9(b)). If high bandwidths are needed, it is possible to operate the electronics in a limited range mode where the raw output is amplified without use of a feedback signal. Although the SQUID has an intrinsic bandwidth > 10 GHz, when operated with standard flux-locked loop electronics using AC flux modulation, the maximum usable bandwidth of most commercially available electronics is typically 50–100 kHz with some systems exceeding 1 MHz.
3. *1/f noise:* As mentioned, another limitation is the presence of $1/f$ noise. HTS SQUIDs, typically operating at liquid nitrogen temperatures (and early commercial LTS DC SQUIDs), typically operating at liquid helium temperature exhibit excess $1/f$ noise due to critical current fluctuations of the Josephson junctions. This noise can be reduced by chopping the DC bias voltage (Figure 7.13). This limits the maximum bandwidths less than half the bias reversal frequency. If the bias reversal frequency is too high, noise can be induced due to voltage spikes in the transformer coupled preamplifier input circuit. Because of this, the maximum bandwidth of present-day HTS SQUIDs is typically ~50 kHz. If megahertz bandwidths are required, AC bias is not used; however, there will be excess noise below 1 kHz.
4. *The vector nature of SQUID magnetometers:* Finally, SQUID magnetometers are vector magnetometers. For a pure magnetometer operating in the Earth's magnetic field, a 180° rotation will sweep out a total field change of ~100 μT. If the magnetometer has a sensitivity of 10 fT/√Hz, tracking the total field change requires a dynamic range of 100 μT/10 fT = 200 dB, well beyond the capabilities of current analog electronics. In addition, the rotational speed must not cause the current flowing through the SQUID sensor to exceed its slew rate limitations. An ideal gradiometer is insensitive to a uniform field and would not suffer this dynamic range limitation. In reality,

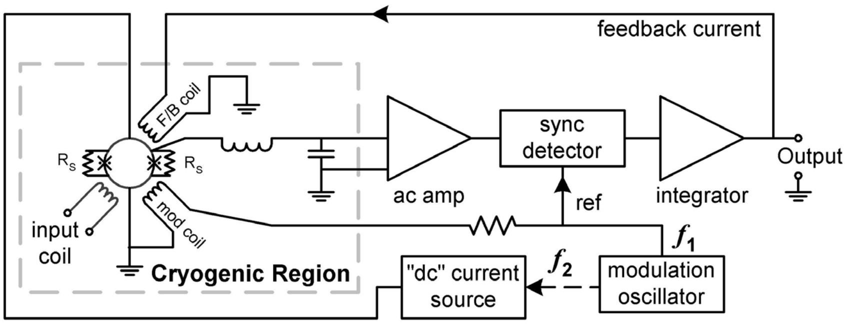

Figure 7.13 AC biasing. The modulation oscillator is used to chop the DC bias current at a frequency at least twice that of the modulation frequency (here $f_2 = 2\ f_1$).

gradiometers are not perfect and have some magnetometer component (see (7.8)) that can place motion restrictions even on well-balanced gradiometers.

7.7 Input Circuits

7.7.1 Packaging

Although it is possible to couple magnetic flux directly into the SQUID loop, environmental noise considerations (see Figure 7.20) make this difficult, if not impossible in an unshielded environment. In addition, the area (A) of a typical SQUID loop is small (<0.1 mm^2) and its resulting sensitivity to external flux changes ($\Delta\Phi = A \cdot \Delta B$) small. Although a larger loop diameter would increase the SQUIDs sensitivity to external flux, it would also make it much more susceptible to environmental noise. For this reason, external flux is normally inductively coupled to LTS SQUID loops by a flux transformer. Because HTS devices have the detection coil grown on the same substrate or inductively coupled via a flip-chip, the Josephson loop is exposed to the environment being measured. This limits the ability of HTS devices to operate in high fields (see Section 7.3.3).

The packaging of the sensor should be sufficiently rugged to allow use under adverse conditions. A niobium can will shield LTS devices from external fields up to 150 mT. If an experiment requires high fields, it is desirable to use a magnet with a compensation coil that generates a null field region. The SQUID sensor is placed within the null-field region and connected to the experiment by twisted pairs of NbTi leads for fields < 10 T. Nb_3Sn leads may permit superconducting connections and detection coils in fields above 20T. HTS devices require isolation from humid environments to prevent degradation of the YBCO film. Normally a surface passivation layer over the YBCO is combined with encapsulating the HTS SQUID in a gas-filled sealed G-10 or plastic enclosure. For HTS SQUIDs configured as a magnetometer or gradiometer, it defeats its purpose to enclose the SQUID within a superconducting shield. If frequencies significantly higher than the measurement frequencies are a source of noise, then enclosing the HTS SQUID within an eddy current (RF) shield may improve performance relative to an unshielded device.

Today, SQUIDs are fabricated as planar devices. In this configuration, the superconducting loop, Josephson junctions, and coils (input, feedback, and modulation) are patterned on the same device. Multilayer deposition techniques are used (primarily in LTS devices) and coils are normally in the form of a square washer. The planar configuration leads to quite small devices, occupying only a few mm^3 compared to 5+ cm^3 (1.2-cm diameter × 5 cm) for older toroidal RF SQUIDs [34]. Another advantage of the planar device is that it is possible to have the detection coils as part of the SQUID sensor, eliminating the need for separate 3-D detection coils. Such an integrated sensor has the potential to significantly reduce the complexity of multichannel systems.

7.7.2 The SQUID as a Black Box

Whether an RF or DC SQUID, a SQUID system can be considered as a black box that acts like a current (or flux)-to-voltage amplifier with extremely high gain. In

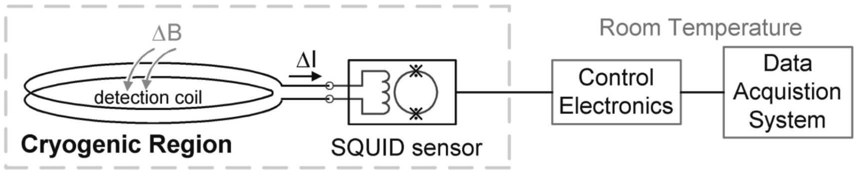

Figure 7.14 Schematic diagram of typical SQUID input circuit.

addition, it offers extremely low noise, high dynamic range (>140 dB), flat phase response, excellent linearity (>1:10^7) and a wide bandwidth that can extend from DC to >10 GHz. Conceptually, the easiest input circuit to consider for detecting changes in magnetic fields is that of a SQUID sensor connected to a simple superconducting coil (Figure 7.14).

Since the total flux in a superconducting loop is conserved, any change in external field through the detection coil will induce a current in the flux transformer which must satisfy:

$$\Delta\Phi = NA\Delta B = \left(L_{\text{coil}} + L_{\text{input}}\right)\Delta I \tag{7.4}$$

where ΔB is the change in applied field; N, A, and L_{coil} are the number of turns, area, and inductance of the detection coil, respectively, L_{input} is the inductance of the SQUID input coil, and ΔI is the change in current in the superconducting circuit. If the lead inductance is not negligible, it must be added to L_{coil} and L_{input}. Typically, twisted pair 0.005″ NbTi wire has $L_{\text{lead}} \approx 0.3$ μH/meter.

7.7.3 Sensitivity

Maximum sensitivity is almost never the optimum sensitivity. Nevertheless, an understanding of the techniques used to maximize sensitivity is essential to any discussion of optimum sensitivity. Since the SQUID system has an output that is proportional to the input current, maximum sensitivity is obtained by using the input circuit that provides the maximum current into the SQUID and satisfies all other constraints of the experimental apparatus.

A common constraint is the physical size of the detection coil. As is seen in (7.3) and (7.4), it is clear that maximum sensitivity to uniform fields is obtained with an infinitely large coil. Infinitely large coils fit quite nicely into dewars with infinitely large necks, but they have the serious disadvantage of boiling off liquid cryogens at an infinitely fast rate. It is therefore common practice to build the largest diameter detection coil that will fit in a physically realistic dewar neck.

Another constraint on coil design is spatial resolution, which is dependent on the nature of the source, the geometry of the detection coil, and the distance between the coil and the source. If nearby objects are to be measured (e.g., biomagnetism or magnetic microscopy), then spatial resolution may be more important than absolute sensitivity. One rule of thumb is not to have the coil diameter significantly less than the distance between the coil and the source. This distance includes the tail spacing (gap) of the dewar (Figure 7.18) used to provide the cryogenic environment.

The object(s) being measured will determine the trade-off between sensitivity and spatial resolution. For example, from the $1/z^3$ field dependence of a single magnetic dipole source less than 1 coil diameter from the detection coil, it is easily shown that spatial resolution can be better than one-tenth of the coil diameter. Multiple or higher-order (e.g., quadrupole) sources may have spatial resolution on the order of the coil diameter. For sources many diameters distant from the coil, resolution may be multiples of the coil diameter. In that situation, larger coils are recommended. However, it makes no sense to design coils for significantly higher sensitivity than environmental constraints (noise) permit.

To calculate the sensitivity and noise level of a simple detection coil system, the inductance of the detection coil must be known. The inductance of a flat, tightly wound, circular multiturn loop of superconducting wire is given by [35]:

$$L_{\text{coil}} = \mu_o N^2 r_{\text{coil}} \left[\log_e \left(\frac{8 r_{\text{coil}}}{r_{\text{wire}}} \right) - 2 \right] \tag{7.5}$$

where $\mu_o = 4\ \text{p} \times 10^{-7}$ henry/meter is the magnetic permeability of free space, r_{coil} is the radius of the detection coil, N is the number of turns, and r_{wire} is the radius of the superconducting wire. Knowing the coil inductance L_{coil}, we can rewrite (7.4) as

$$\Delta B = \frac{\left(L_{\text{coil}} + L_{\text{input}}\right)\Delta I}{NA} \tag{7.6}$$

Since the SQUID system has an output proportional to the input current, maximum sensitivity is obtained by using the input circuit that provides the maximum current into the SQUID and satisfies all other constraints of the experimental apparatus. For a pure magnetometer of a given diameter, the maximum sensitivity will occur when the impedance of the detection coil matches that of the SQUID sensor ($L_{\text{coil}} = L_{\text{input}}$).

7.7.4 Detection Coils

Several factors affect the design of the detection coils [36]. These include the desired sensitivity of the system, size, and location of the magnetic field source and the need to match the inductance of the detection coil to that of the SQUID. The ability to separate field patterns caused by sources at different locations and strengths requires a good signal-to-noise ratio. At the same time, one has to find the coil configuration that gives the best spatial resolution. Unfortunately, these two tasks are not independent. For example, increasing the signal coil diameter improves field sensitivity, but sacrifices spatial resolution. In practice, system design is restricted by several constraints: the impedance and noise of the SQUID sensors, the size of the dewar, the number of channels, and the distribution and strength of noise sources.

It is extremely important for the DC response that the detection coil(s) be superconducting. Resistance in the detection circuit has two effects: (1) attenuating the signal, and (2) adding Nyquist noise. Resistive attenuation is important only below a frequency f_o, such that the resistive impedance is equal to the sum of the inductive impedances in the loop (e.g., $f_o \approx R/L_{\text{tot}}$, where L_{tot} is the total inductive impedance of the loop). Resistive noise is only important if it becomes comparable to other noise sources or the signal ($<10^{-30}$ J/Hz for biomagnetism, $<10^{-29}$ J/Hz for geophysics). For a SQUID with $E_N \approx 10^{-30}$ J/Hz, the total resistance of the circuit, including any joints, must be less than $10^{-13}\Omega$ [14]. Thus, it is very important that all solder joints, press-fits, or connections have as low a joint resistance as possible. If flux trapping in the detection coil(s) is problematic, the addition of a heat switch (along the lines of those used in persistent mode superconducting magnets) may be advisable. Such heat switches were used in the first commercial SQUID susceptometers (Section 7.10.1.4).

Figure 7.15 displays a variety of detection coils. The magnetometer (Figure 7.15(a)) responds to the changes in the field penetrating the coil. More complicated coil configurations provide the advantage of discriminating against unwanted background fields from distant sources while retaining sensitivity to nearby sources.

Because of the present inability to make flexible wire or make true superconducting joints in HTS materials, 3-D HTS coil structures (e.g., Figures 7.15(b, d, e)) are not possible. Present-day HTS magnetometers are fabricated as planar devices and are available only as pure magnetometers (Figure 7.15(a)) and planar gradiometers (Figure 7.15(c)). As a result, commercially available HTS devices are currently in the form of magnetic sensing rather than current sensing devices.

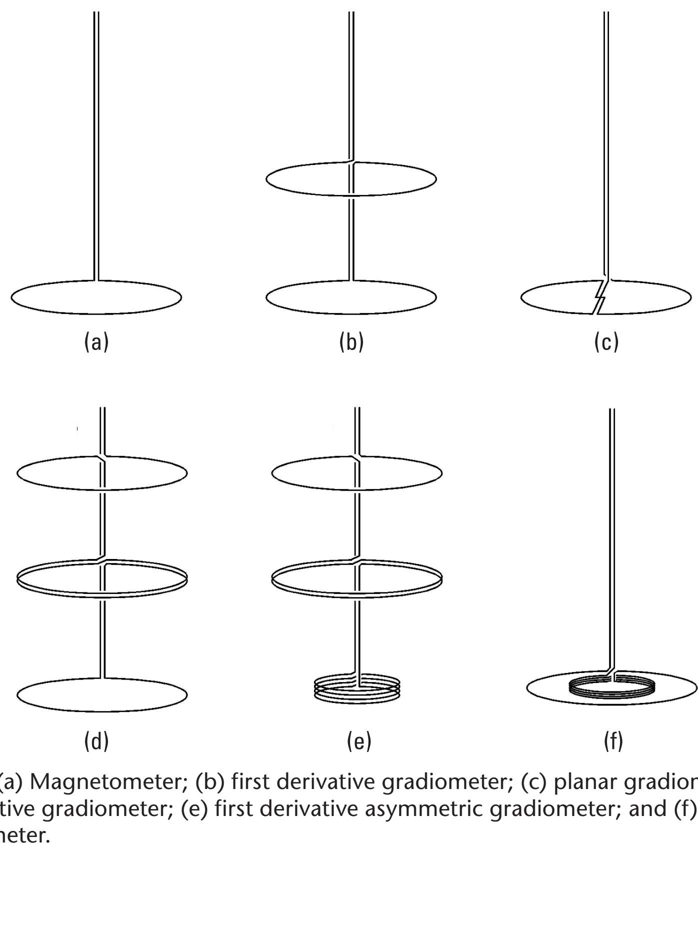

Figure 7.15 (a) Magnetometer; (b) first derivative gradiometer; (c) planar gradiometer; (d) second derivative gradiometer; (e) first derivative asymmetric gradiometer; and (f) first derivative radial gradiometer.

7.7.5 Gradiometers

Magnetometers are extremely sensitive to the outside environment. This may be acceptable if one is measuring ambient fields. If what is to be measured is close to the detection coil and weak, outside interference may prevent measurements at SQUID sensitivities. If the measurement is of a magnetic source close to the detection coil, a gradiometer coil may be preferred. The field of a magnetic dipole is inversely proportional to the cube of the distance between the dipole and the sensor. It follows that the field from a distant source is relatively uniform in direction and magnitude at the sensor. If we connect in series two identical and exactly parallel loops wound in opposite senses, separated by a distance b (the baseline), we obtain a coil (Figure 7.15(b)) that will reject uniform fields.

Since the response of a single coil to a magnetic dipole goes as $1/z^3$, an object that is much closer to one coil than the other will couple better to the closer coil than the more distant. Sources that are relatively distant will couple equally into both coils. For objects that are closer than $0.3b$, the gradiometer acts as a pure magnetometer, while rejecting more than 99% of the influence of objects more than $300b$ distant (Figure 7.16). In essence, the gradiometer acts as a compensated magnetometer. It is possible to use two gradiometers connected in series opposition (Figure 7.15(d)) to further minimize the response of the system to distant sources. This can be extended to higher orders by connecting in series opposition two second-order gradiometers. However, doing so reduces the sensitivity of the instrument to the signal of interest and may not significantly improve the signal-to-noise ratio.

Rejection of distant noise sources depends on having a precise match (or balance as it is sometimes referred to) between the number of area turns in the coils. A symmetric gradiometer (Figure 7.15(b)) requires that $N_{\text{signal}}\, A_{\text{signal}} = N_{\text{comp}}\, A_{\text{comp}}$ where N is the number of turns and A the area of the signal and compensation coils, respectively. An asymmetric design (Figure 7.15(e)) has the advantage that the inductance (L_{signal}) of the signal coil(s) is much greater than the compensation coils (L_{comp}); greater sensitivity is achieved than with a symmetric design. Another advantage is that the signal coil diameter is reduced, leading to potentially higher spatial resolution. The optimum conditions for the number of turns in an asymmetric signal coil is given by [37]:

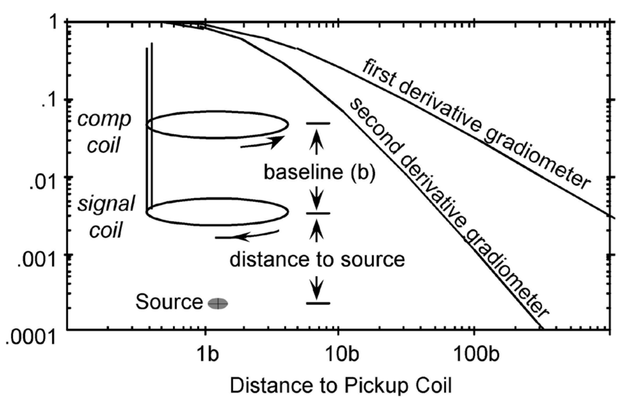

Figure 7.16 Response of gradient coils relative to magnetometer response ($1/z^3$ suppressed).

$$\left(L_{\text{signal}} + L_{\text{comp}} + L_{\text{input}} + L_{\text{leads}}\right) - N_{\text{signal}} \frac{\partial}{\partial N_{\text{signal}}}\left(L_{\text{signal}} + L_{\text{comp}} + L_{\text{input}} + L_{\text{leads}}\right) = 0 \tag{7.7}$$

If the gradiometer is perfectly made (balanced), it will reject uniform fields. However, if one coil has a larger effective diameter than the other, the response will not be that of a perfect gradiometer, but that of a gradiometer in series with a magnetometer. Mathematically, the balance, b, can be defined as

$$V_t \propto \boldsymbol{G} + \boldsymbol{\beta} \cdot \vec{B} \tag{7.8}$$

where V_t is the system response, $\boldsymbol{G}$ is the coil's response to a gradient field (e.g., dB_z/dz), and $\vec{B} = B_x\hat{x} + B_y\hat{y} + B_z\hat{z}$ is the applied uniform field.

If the coils are coplanar, there should not be any x or y field components detected. However, the reality of fabrication (e.g., tilt due to coil forms constructed from multiple pieces) is such that there may be b with x and y components. Typically, coil forms used to wind gradiometers can be machined (grooved) to achieve balances that range from $\beta = 0.01 \sim 0.001$. Planar devices, through photolithography, can achieve factors of 10^{-4} or better. Superconducting trim tabs [38] placed within the detection coils can improve β to the ppm level. High degrees of balance can allow a SQUID gradiometer to operate in relatively large (even tesla) ambient fields while maintaining sensitivities in the tens of fT.

For multichannel systems (such as used in biomagnetism), it is not possible to use externally adjustable trim tabs—each tab tends to interfere with each other when the detection coils are in proximity. The use of electronic balancing [39] can provide balance ratios at the ppm level.

7.7.6 Electronic Noise Cancellation

In this situation, portions of (additional) magnetometer reference channel response(s) are summed electronically with the gradiometers' input to balance out its effective magnetometer response. The simplest scheme is to use a second B_z magnetometer coil and subtract its output, $V(B_z)$, from the output of the gradiometer, V_t. The actual output is attenuated as to exactly cancel the imbalance (β) of the gradiometer. By adjusting the field components—$b_i\ V(B_j)$ to equal $-\beta \cdot \vec{B}$ (see (7.8)), the net result goes to $\boldsymbol{G}$. Since there can be imbalance in the x and y components, a 3-axis set of coils (Figure 7.17) allow compensation of the B_x, B_y, and B_z components.

In addition to field noise, gradient fields generated by distant sources can be large enough to mask the signals being measured. Additional improvement can be achieved by the addition of a second gradiometer compensation channel (typically first-order). Thus, the system output can be described as:

$$V_{\text{out}} \propto \boldsymbol{G} + \boldsymbol{\beta} \cdot \vec{B} + b_1 V\left(B_x\right) + b_2 V\left(B_y\right) + b_3 V\left(B_z\right) + g_4 V\left(G_z\right) \tag{7.9}$$

where b_1 is the weighting for the B_x component, b_2 is the weighting for the B_y component, B_y is the weighting for the B_z component, and g_4 is the weighting for the gradient reference $g_4\ V(G_z)$ component.

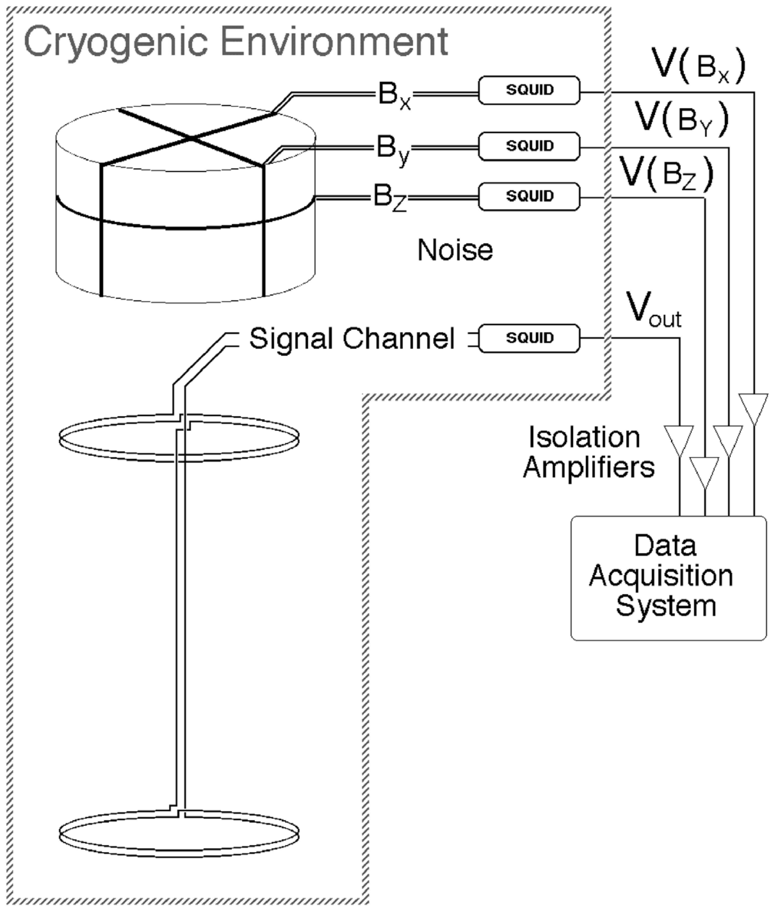

Figure 7.17 First-order gradiometer with three noise cancellation channels.

For a single axial gradiometer, the use of 3 magnetometers (B_y, B_y, B_z) will give an attenuation of externally generated noise of 12 dB [40]. The addition of an external gradient reference channel improved noise rejection to better than 40 dB. Moving the reference gradiometer 1m away from the signal coil reduced noise rejection by a factor of 4 (12 dB). This gradient channel should be located sufficiently far from the sources being measured as not to detect a significant signal, but close enough so that it sees the same gradient noise.

Since the detection coil is not perfectly balanced, ideally, one should subtract all field and gradient components (expanding (7.8)). To do this would require eight noise channels, for example, B_y, B_y, B_z, dB_x/dx, dB_y/dy, dB_x/dy, dB_x/dz and dB_y/dz. From these components, all nine elements of the gradient tensor can be created (see (7.13)) and used to compensate for any imbalance of the detection coil(s). The use of 8-element tensor arrays as reference channels can further improve external noise rejection, with rejection values exceeding 60 dB [39]. A major advantage of electronic balancing is significant improvement in immunity to low-frequency environmental noise.

The simplest way to perform the noise cancellation is to simultaneously take data from the detection coil(s) and the noise channels. Then, in post-processing, digitize the data and determine the weighting factors for each noise channel to minimize any common-mode noise. One can also include time derivatives of the field and gradient components into the cancellation algorithm to minimize effects of the eddy-current noise. If there is sufficient processing power, it may be possible to do real-time processing of the noise contribution.

7.8 Refrigeration

The superconducting nature of SQUIDs requires them to operate well below their superconducting transition temperature (9.3K for niobium and 93K for $YBa_2Cu_3O_{7-\delta}$). Ideally, the cryogenic environment should provide stable cooling (mK or μK depending on the $d\Phi/dT$ of the sensor; see Section 7.4.2), no time-varying magnetic signature, be reasonably compact and reliable, and, if mechanical in nature, introduce neither mechanical vibration nor a magnetic signature into the detection system. The thermal environment for the SQUID sensor and detection coil has typically been liquid helium or liquid nitrogen contained in a vacuum insulated vessel known as a dewar (Figure 7.18). The cryogen hold time depends on the boil-off rate (heat load) and the inner vessel volume.

7.8.1 Dewars

The major heat load on dewars is due to thermal conduction down the neck tube and magnetometer probe along with black-body radiation. The space between the inner and outer walls is evacuated to prevent thermal conduction between room temperature and the cryogen chamber. Within the vacuum space, a thermal shield (anchored to the neck tube) acts to reduce heat transfer by thermal (black-body) radiation. The thermal shield can be either vapor cooled (Figure 7.18(a)), using the enthalpy of the evaporating helium or nitrogen gas, or having the shield thermally connected to a liquid nitrogen reservoir (Figure 7.18(b)). Dewars with removable sections (e.g., tails) use liquid nitrogen cooled shields. Often, the bottom section diameter is reduced to the neck diameter (or smaller) to minimize the liquid cryogen volume in the experimental region.

If the experiment involves measurements interior to the dewar (see Figures 7.22(a, c–e)), then a metallic dewar is preferable. Metallic dewars offer significant shielding from environmental noise at frequencies above 10~100 Hz. If the system is to measure magnetic fields exterior to the dewar, the dewar must be magnetically transparent and metallic construction is not appropriate. Dewars for external field measurements (Figure 7.18(c)) are normally constructed of nonmetallic, low-susceptibility materials to minimize their magnetic interactions with the SQUID sensors and detection coils. Materials used are typically glass-fiber epoxy composites such as G-10. To get the detection coil(s) as close as possible to the object being measured, a tailed design is often used. This decreases the forces on the bottom of the dewar and allows the use of thinner end pieces (closer tail spacing). Dewars for

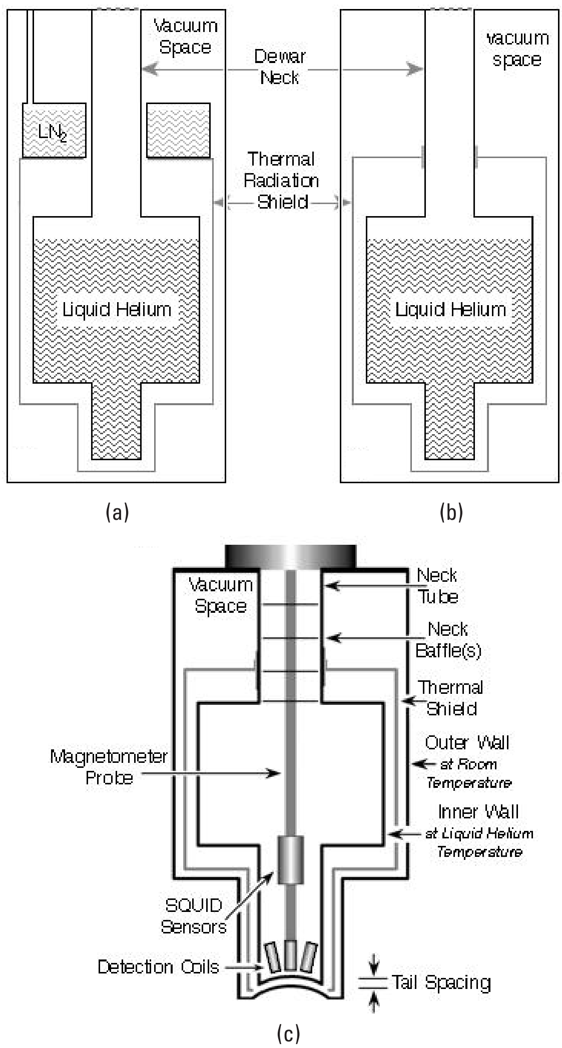

Figure 7.18 (a) LN_2 shielded dewar; (b) vapor shielded dewar; and (c) fiberglass dewar used for biomagnetic measurements.

biomagnetic measurements often have curved tails to get closer to the head, chest, or abdomen (Figure 7.18(c)).

Since the dewar is cold, thermal contraction will decrease the length of the inner vessel by nearly 1%. Thus, for a 100-cm-tall dewar, the spacing between the bottom of the inner vessel and the bottom of the outer (warm) vessel (also known as a tail gap) will increase by nearly 1 cm. Adjustable tail dewars use an annular screw mechanism (and O-rings or bellows to prevent vacuum loss between the inner and outer vessels) to allow tail gaps less than 2 mm from liquid helium or nitrogen to room temperature. This is useful for SQUID microscopy (Section 7.10.4.1) and other measurements where sensor-to-sample distance is critical.

The major advantage of HTS is the simplified cryogenics and reduced spacing between cryogenic regions and room temperature. The thermal load (due to conduction and black-body radiation) is less and the heat capacity of what needs to be cooled is larger (implying smaller temperature variations for a given heat load). Since the latent heat/unit volume of liquid nitrogen is 60 times larger than liquid helium, hold times can become months rather than days for an equivalently sized dewar.

7.8.2 Closed Cycle Refrigeration

As an alternative to the use of liquid cryogens, closed cycle refrigeration [41] is desirable for several reasons. These include reduction of operating costs (especially in respect to liquid helium), use in remote locations, operation in nonvertical orientations, avoiding interruptions in cryogen deliveries, safety, and the convenience of not having to transfer every few days. Parameters governing suitability include physical size, absence of periodic replacement of cryogenic fluid, and, most importantly, vibration and magnetic signature. If low-frequency, vibrationally induced noise is out of the frequency band of interest, and $d\Phi/dT$ due to the thermal oscillations of the cryocooler is insignificant, the SQUID sensor can be mounted directly to the cold tip of the cryocooler (e.g., using a single-stage Stirling cycle cryocooler in conjunction with a HTS SQUID). While cryocoolers [42] can have large cooling capacities (watts), unless hundreds of channels are involved (e.g., MEG—Section 7.10.5), only milliwatts of cooling capacity are needed to maintain SQUID sensors at their operating temperatures as the main heat leak is thermal conduction down the electrical leads and to a lesser degree from the support structure(s) holding the SQUID sensor(s).

The first practical cryocooled SQUID system was the BTi CryoSQUID [43]. Based on a two-stage Gifford-McMahon (GM) refrigerator, the use of a vibrationally decoupled Joule-Thompson (JT) stage allowed 4K operation with reduced vibration. An electronic comb filter was required to filter the ~1-Hz compressor vibration from the output of the DC SQUID electronics to achieve the system performance of 20 fT/√Hz. However, the acoustic (audible) noise from the nearby compressor prevented its use in auditory evoked brain measurements (Section 7.10.5).

Initially, multichannel cryocooled systems for neuromagnetic measurements [44] utilized GM refrigeration directly coupled to the SQUID sensors. These systems suffered from vibration and the magnetic signature of the cryocooler. The development of pulse tube refrigeration [45] allows operation with a significantly reduced vibration. Another method utilizing closed-cycle refrigeration is the use of a mechanically isolated cryocooler to cool a small liquid helium volume (Figure 7.19). This liquid ballast technique isolates the experimental volume (e.g., the SQUID sensors and detection coils) and reduces the ±0.1K (or greater) thermal variations of the cryocooler to mK levels. It can also allow short interruptions of electrical power without having the system warm up. Liquid helium ballasted systems have been implemented on commercial SQUID neuromagnetometers, rock magnetometers, and magnetic microscopes. Present-day cryocooled systems use a pulse tube rather than GM cryocoolers due to their significantly reduced vibration.

7.9 Environmental Noise (Noise Reduction)

The greatest obstacle to SQUID measurements is external noise sources. If the object being measured is within the cryostat (such as is typical in most laboratory

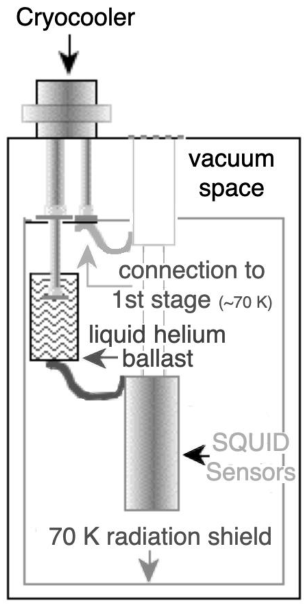

Figure 7.19 Liquid helium ballasted dewar.

experiments), metallic shielding can minimize external noise (e.g., act as a lowpass eddy-current shield). The use of gradiometer detection coils (Section 7.7.5) can significantly attenuate the effect of distant noise sources. Superconducting shields essentially eliminate all external field variations. This assumes that any electrical inputs to the experimental region have been appropriately filtered. Powerline or microprocessor clock frequencies can severely degrade performance. Unfortunately, if external objects are to be measured, superconducting shields are not appropriate.

When measuring external fields, the SQUID magnetometer must operate in an environment, the magnetic field of the Earth, that can be 10 orders of magnitude greater than its sensitivity (Figure 7.20). The magnetic field at the surface of the Earth is generated by a number of sources. There exists a background field of ~50 μT with a daily variation of ±0.1 μT. In addition, there is a $\sim 1/f^{3/2}$ contribution (below 1 Hz) from the interaction of the solar wind with the magnetosphere. The remaining contributions to external magnetic fields are primarily man-made. These can be caused by structural steel and other localized magnetic materials such as furniture and instruments that distort the Earth's field and result in field gradients, moving vehicles that generate transient fields, electric motors, elevators, radio, television, microwave transmitters, and the ever-present powerline electromagnetic field and its harmonics. As Figure 7.20 shows, measurement location can have a significant influence on external noise sources.

7.9.1 Gradiometers for Noise Reduction

If the purpose of the measurement is to detect the magnetic field of a relatively close object, the detection coil(s) can be configured as a gradiometer (see Section 7.7.5)

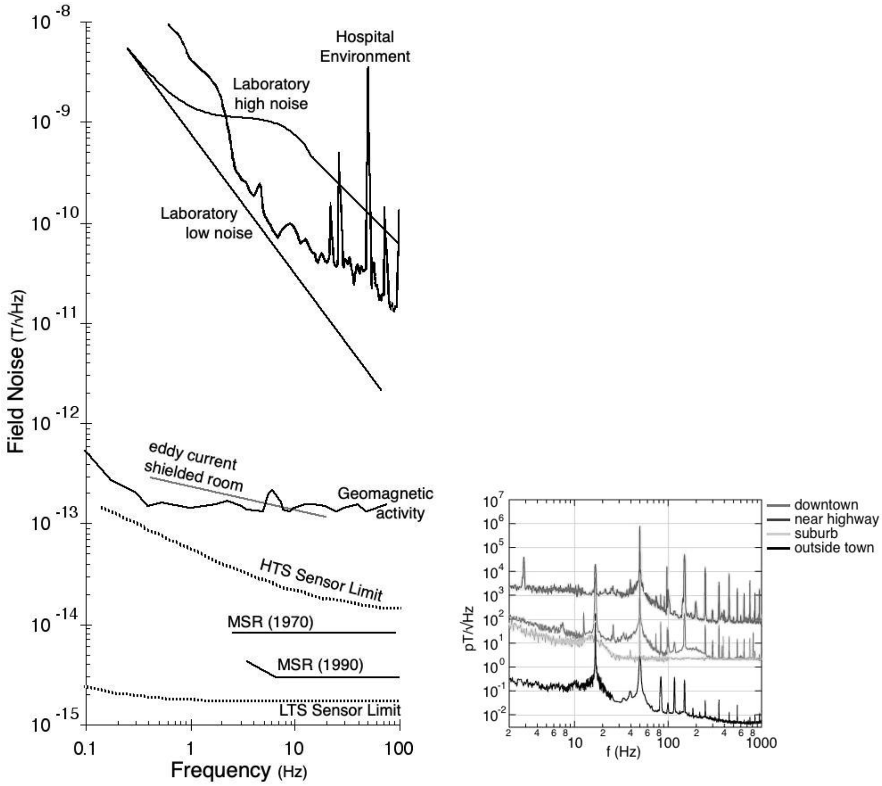

Figure 7.20 (a) The rms field noise spectra in various environments as a function of frequency. (*After:* [46].) (b) The rms field noise in and around Hamburg, Germany.

whose baseline is larger than the distance from the coil(s) to the object. This can allow the rejection of external noise by more than 120 dB with less than a decibel loss of signal for objects and signal sources within a few diameters of the detection coil(s). Thus, it is standard practice to configure SQUID measurement systems for biomedical and nondestructive evaluation measurements as gradiometers.

7.9.2 Magnetic Shielding

One method to attenuate external noise sources is with an eddy-current shield that generates fields that act to cancel the externally applied fields within the conducting material. The shielding effect is determined by the skin depth, *d*, the distance where the field is attenuated by a factor 1/*e*. For a sinusoidal varying wave:

$$\delta = \sqrt{\frac{\rho}{\pi \mu f}} \tag{7.10}$$

where *r* is the electrical resistivity and μ is the magnetic permeability of the shield material, with *f* being the frequency of the applied field. In situations where the wall thickness $t << \delta$, external fields are attenuated by:

$$\frac{B_{\text{internal}}}{B_{\text{external}}} = \frac{1}{1 + (2\pi f L/R)^2} \tag{7.11}$$

where L is the inductance of the enclosure and R is the resistance along the path of current flow. Unfortunately, induced currents in the shield generate noise. For a cylindrical shape at a temperature T, the induced noise is given by:

$$B_{\text{rms}} = \sqrt{\frac{64\pi k_B T t}{h d \rho}} \tag{7.12}$$

where h is the length and d the diameter of the can. The cutoff frequency (above which shielding starts to become effective) is given by $f_{-3\text{dB}} \approx \rho/\pi\mu_o td$. Because of noise considerations (see (7.12)), eddy-current shields that are to be placed near the detection coils should be made from relatively poor conductors such as BeCu.

7.9.2.1 Shielded Rooms

One eddy-current room was constructed with 2-cm high purity aluminum walls, achieving shielding factors >40 dB at 60 Hz with improved performance at higher frequencies [47]. The equivalent field noise is less than 200 fT/√Hz at frequencies above 1 Hz. In the situation where $t >> \lambda$, the attenuation goes as $(r/\lambda)e^{t/\lambda}$, where, in the case of a spherical MSR, r is the radius of the MSR.

The need for shielding at lower frequencies has led to the use of magnetically shielded rooms (MSR). If pure eddy-current shielding is used, this would require wall thicknesses that could exceed 1m or more (below 1 Hz). For a ferromagnetic material, the permeability of the material [$\mu = \mu_o(1 + \chi)$] replaces μ_o in (7.9). The shielding is due to the fact that flux prefers the path with the highest permeability. Since magnetically soft materials (e.g., mu-metal) can have permeabilities that exceed 10^4, the external magnetic flux is routed around the walls, avoiding the interior. The use of multiple shields can act to further shield the interior of a MSR. For the 8-layer Berlin MSR (Figure 7.20(a)), shielding factors exceeded 80 dB at frequencies above 0.01 Hz with noise levels at or below the 3 fT/√Hz. All commercial MSRs combine multiple mu-metal and aluminum walls, albeit with noise levels 10 or more dB higher.

7.10 Applications

Since the introduction of the SQUID as a commercial product [16], SQUID systems have generated well over a half-billion dollars in product revenues. A large number of applications [48] configure the SQUID as a magnetometer (Figure 7.21). The state of the art in materials processing and properties limits the variety of superconducting input circuits that can be used with HTS SQUIDs. As mentioned, there is no existing method for making superconducting connections to SQUIDs

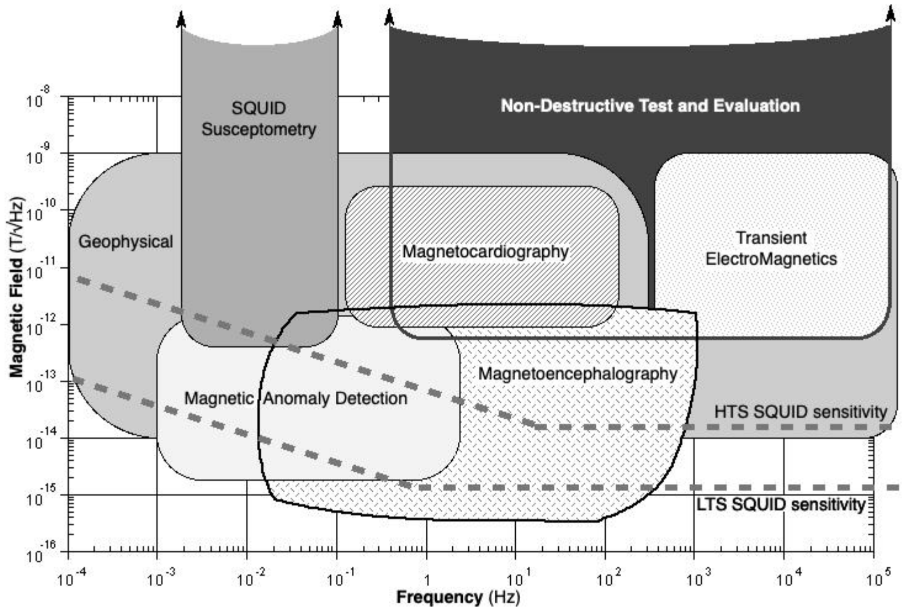

Figure 7.21 Field sensitivities and bandwidths typical of various applications. The lines indicate the sensitivity of commercially available SQUIDs (LTS (Figure 7.12(d)), HTS (Figure 7.12(e))).

with HTS wire. As a result, commercially available HTS devices are currently in the form of magnetic sensing (Figure 7.22(b)) rather than current sensing devices (Figures 7.22(a, c–f)).

SQUIDs can be configured to measure a wide variety of electromagnetic properties (Figure 7.22).

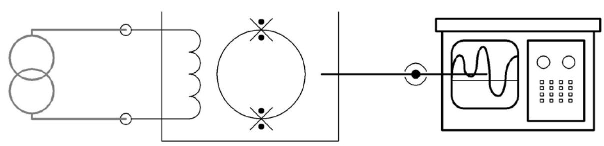

(a)

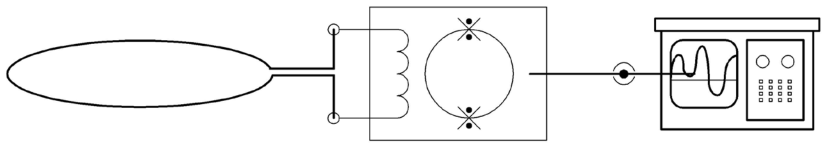

(b)

Figure 7.22 (a) AC and DC; (b) magnetic field; (c) DC voltage; (d) DC resistance; (e) AC resistance/inductance bridge; and (f) AC mutual inductance (susceptibility bridge), sample in lower coil.

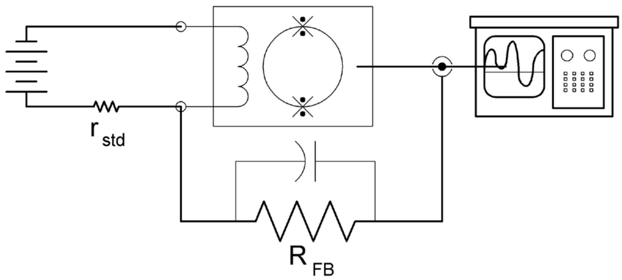

(c)

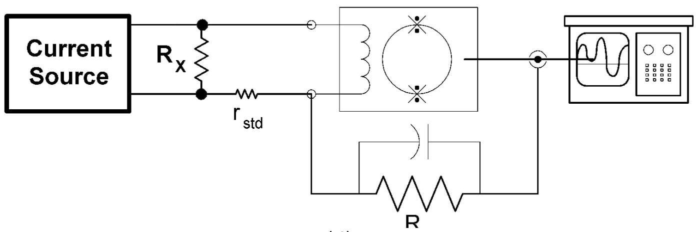

(d)

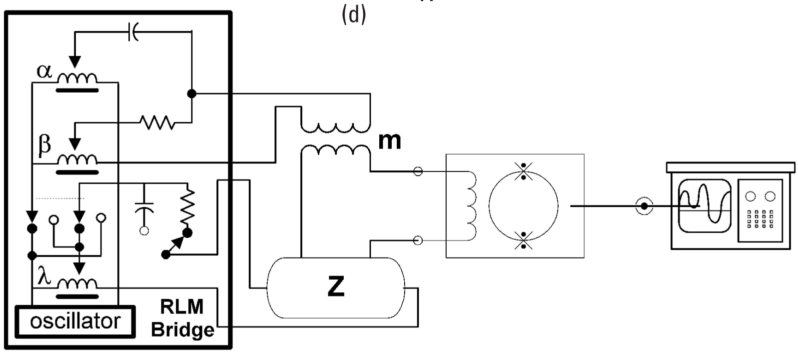

(e)

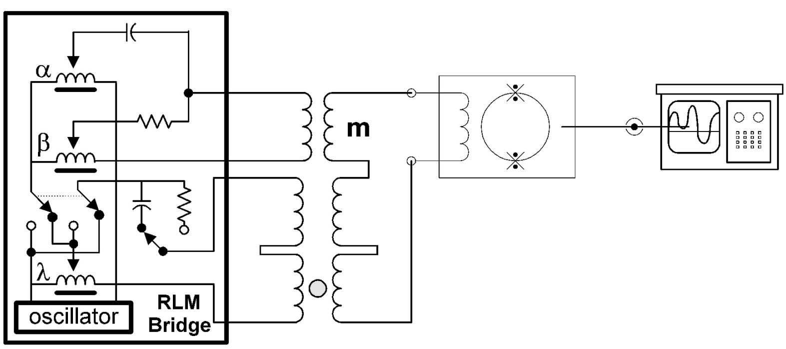

(f)

Figure 7.22 (Continued)

Table 7.3 Typical Sensitivities of SQUID Instrumentation

Measurement	*Sensitivity (DC or 1-Hz Bandwidth)*
Current (Figure 7.22(a))	10^{-12} ampere
Magnetic fields (Figure 7.22(b))	10^{-15} tesla
DC voltage (Figure 7.22(c))	10^{-14} volt
DC resistance (Figure 7.22(d))	10^{-12} Ω
Mutual/self-inductance (Figure 7.22(e))	10^{-12} Henry
Magnetic moment (Figure 7.22(f))	10^{-10} emu

7.10.1 Laboratory Applications

Table 7.3 shows typical capabilities of SQUID-based instruments. The number in the parenthesis refers to the corresponding Figure 7.22. Additional information on laboratory applications of SQUID systems can be found in [48, 49].

7.10.1.1 Current

One common use of a SQUID is as an ammeter (Figure 7.22(a)). The input can be connected to an experiment at liquid helium temperatures or to room temperature. If the signal is to be inductively coupled to a detection coil that is connected to the SQUID input, then the circuit must be superconducting if the DC response is desired. If the measurement is of a current that passes through the detection coil, a toroidal geometry for the detection coil has the advantage of extremely good coupling to the source while rejecting contributions due to external sources. Because the measurement is inductive, there is no loading of the current-generating elements. Toroidal geometries have been used for noncontact measurements of beam strengths in particle accelerators [50] and biological current flows in neurons [51].

7.10.1.2 Voltage

Typically, most applications use superconducting circuits. However, there are several applications where resistive circuits are used. One example is the detection of extremely small voltages or resistances (Figure 7.22(c, d)). When a voltage V_{in} is applied across the input terminals, a current is generated in the SQUID input coil. In this situation, the feedback current (I_{FB}) that would normally be applied to the SQUID loop is fed back via R_{FB} through r_{std} until the voltage drop across r_{std} is equal to V_{in} and there is no net current through the SQUID. V_o measures the voltage drop across R_{FB} and r_{std} with $V_{in} = V_o\, r_{std}/(R_{FB} + r_{std})$. The voltage gain of the system is determined by the ratio of R_{FB}/r_{std}. Typical values for R_{FB} and r_{std} are 3 and 30 μΩ, respectively, giving a voltage gain of 10^8. The standard resistor r_{std} is typically at 4.2K. However, the voltage source may be at a completely different temperature.

The input noise of a SQUID picovoltmeter (~10^{-14} V) is a function of the source resistance (R), temperature, the inherent voltage noise (due to r_{std}), and the inherent current noise of the SQUID. The measurement of the Johnson noise in a resistor ($\langle V^2 \rangle = 4\, k_B\, TR\Delta f$, where Δf is the bandwidth of the measurement) can determine absolute temperature. Commercially available LTS SQUIDs have equivalent device temperatures <1 μK and are suitable for noise thermometry [8].

With the addition of an appropriate current source (Figure 7.22(d)), it is possible to measure resistance. Resolutions of $10^{-11}\,\Omega$ can be achieved for $R_x < 10^{-2}\Omega$. Other applications of picovoltmeters include measurements of thermopower, thermal electromotive forces (EMFs) (thermocouples), and infrared bolometers.

7.10.1.3 AC Measurements

The SQUID can also be used as the null detector in an AC bridge circuit (Figure 7.22(f)) to measure both resistive and reactive components of a complex impedance. The unknown impedance **Z** is excited by a current generated by an oscillator voltage which is attenuated by a precision ratio transformer ($\boldsymbol{\lambda}$). The difference between the voltage developed across the unknown impedance **Z** and that developed in the secondary of a nulling mutual inductor **m** is applied to the input of the SQUID circuit. The primary current in **m** is proportional to the oscillator voltage and defined by the setting of the ratio transformer ($\boldsymbol{\alpha}$). An additional reactive current is supplied by a second ratio transformer ($\boldsymbol{\beta}$), which causes the primary current to be passed through a capacitor rather than a resistor, thus generating a 90° phase shift in the voltage applied to **m**. The amplified off-balance signal which appears at the output of the SQUID control electronics can be displayed by means of a lock-in amplifier tuned to the oscillator frequency. Assuming $IN \approx 1$ pA/√Hz, such a system is capable of measuring self-inductances and mutual inductances between 10^{-12} H and 10^{-3} H with 1:10^6 part resolution [8, 49].

Figure 7.23(a) shows a typical experimental setup for measurement of AC susceptibility. Such a configuration can be used for thermometry by measuring

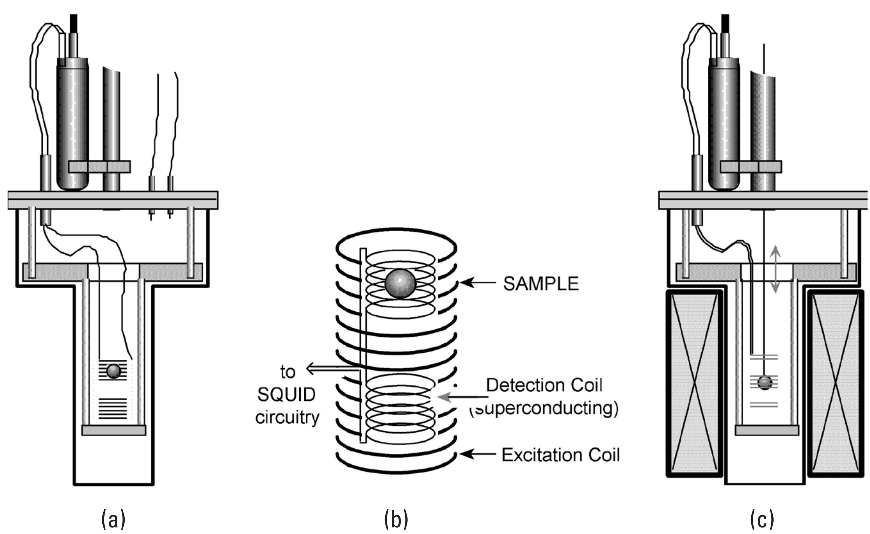

Figure 7.23 Magnetic susceptibility measurement apparatus (liquid helium dewar not shown): (a) AC susceptibility; (b) signal and excitation coil details; and (c) second derivative oscillating magnetometer for DC measurements with external DC field coils.

the susceptibility of paramagnetic salts such as $Ce_2Mg_3(NO_3)_{12} \cdot 24H_2O$, usually referred to as CMN [52] down to mK temperatures.

7.10.1.4 SQUID Magnetometer/Susceptometers

Instead of using a secondary AC excitation coil (Figures 7.22(f) and 7.23(b)), a DC field can be used to magnetize samples. Typically, the field is fixed and the sample moved into the detection coil's region of sensitivity (Figure 7.23(c)). The change in detected flux is directly proportional to the magnetic moment of the sample. Because of the superconducting nature of SQUID input circuits, true DC response is possible.

Commonly referred to as SQUID magnetometers, these systems are properly SQUID susceptometers. They have a homogeneous superconducting magnet to create a very uniform field over the entire sample measuring region and the superconducting pickup loops. The magnet induces a moment allowing a measurement of magnetic susceptibility ($\chi = \boldsymbol{M}/\boldsymbol{H}$). The superconducting detection loop array is rigidly mounted in the center of the magnet. This array is configured as a gradient coil to reject external noise sources. The detection coil geometry determines what mathematical algorithm is used to calculate the net magnet moment. Oppositely paired axial (B_z) and transverse (B_x, B_y) Helmholtz coils, first and second derivative gradiometers have all been successfully used. Coupling two axial channels of differing gradient order can significantly improve noise rejection.

Sensitivities better than 10^{-8} emu have been achieved, even at applied fields of 9T (Figure 7.23(c)). Placement of secondary excitation coils can allow AC susceptibility measurements approaching 10^{-8} emu to be made in the presence of a significant DC bias field. Variable temperature capability (1.7 to 800K) is achieved by placing a reentrant cryostat within the detection coils.

7.10.1.5 NMR

NMR signals [53] can be measured by placing a sample (e.g., protons or ^{19}F) in the center of SQUID detection coils and either sweeping the external field or applying an RF excitation to the sample. The same experimental concept can be used to measure electron paramagnetic resonance (EPR) signals. Although limited to 100-ppm field uniformities, SQUID susceptometers (Section 7.10.1.4) are excellent platforms for basic demonstrations of NMR measurements. The relationship between the resonant frequency and applied magnetic field is given by the gyromagnetic ratio γ (for protons, $\gamma = 42.58$ MHz/T). For some materials, γ is so small (e.g., ^{39}K where $\gamma = 1.99$ MHz/T) that a detection frequency of 383 MHz (equivalent to 9T for protons) would require an applied field of 193T. Similar to NMR, SQUIDs offer an improved signal-to-noise ratio for measurements of nuclear quadruple moments [54].

The use of SQUID detection coils can offer significant improvements over conventional coils at a given field strength or allow an equivalent signal-to-noise ratio at lower applied fields (reducing magnet cost or even eliminating it when the bias field is the Earth's magnetic field). T_1 (relaxation time of proton spin lattice) contrast imaging is widely used in conventional MRI to distinguish different types of tissue. Since T_1 contrast can be much higher in low fields, SQUID-based MRI

[55] offers diagnostic capabilities in screening cancer and other disease conditions. Chapter 6 discusses the methodology of NMR in more detail.

7.10.1.6 Other Measurement Techniques

SQUID sensors can be used to detect gravitational field changes and gravity gradients [56]. They have been used for more esoteric applications including temperature measurements with resolution near 10^{-12} K [57] and to measure position for gravity wave detectors with subnanometer resolution [58]. SQUIDs are also used as ultrahigh resolution (nano-radian) angular position detectors in the Gravity Probe B program, which tested several predictions of Einstein's general theory of relativity [59]. SQUIDs have been used in cosmological searches for cold dark matter such as weak interacting massive particles (WIMPs) and axions along with measurements of the polarization of the cosmic microwave background.

7.10.2 Cryogenic Current Comparators (CCC)

The CCC [60] is used in electrical metrology for highly precise comparative measurements of electric resistances (e.g., Josephson voltage standards, quantum Hall effect) or for the amplification and measurement of extremely small electric currents (e.g., particle accelerator beam diagnostics). The simplest CCC (Figure 7.24) consists of two wires, carrying currents I_1 and I_2, respectively, both passing through a long superconducting tube with thick walls.

The fields due to these currents will induce a supercurrent I in the walls of the tube whose result, due to the Meissner effect, is to null the net flux in the tube and is thus of magnitude $I = -(I_1 + I_2)$. The current I flowing in the outside wall of the tube will produce a field that can be detected with a SQUID, whose output can be fed back in the usual nulling way to adjust the current I_2 to make $I_1 = 0$, at which point I_2 will exactly equal I_1. By extension, if the wires carrying I_1 and I_2 pass through the tube N_1 and N_2 times, respectively, the net current is $I = (N_1 I_1 - N_2 I_2)$, so that at null $I_2 = (N_1/N_2)I_1$.

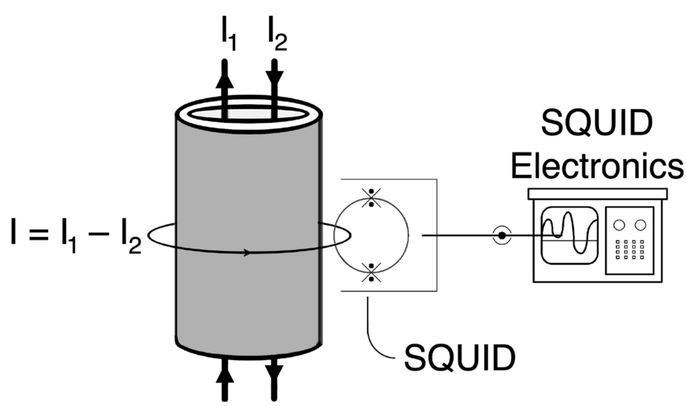

Figure 7.24 Schematic of a CCC.

LTS CCCs have been used in association with Josephson voltage standards in resistance bridges, allowing the precise determination of voltages ranging from mVs to 10+ V CCCs can allow standard wire-wound resistors to be calibrated against quantum Hall resistance standards. In addition, they have also been used as ultralow current amplifiers with sensitivities down to 0.08 fA/√Hz have been achieved. This has allowed direct sensing of charged particle beams [61].

7.10.3 Geophysical Applications

Stolz et al. [62] presented a comprehensive review of the development and application of superconducting technology in geophysics with a particular emphasis on mineral exploration.

7.10.3.1 Passive Methods

Passive methods such as magnetotellurics (MT) and audio MT (AMT) use the interaction of the solar wind in the ionosphere as an electric and magnetic field generator. In general, they cover the frequency range of megahertz to 10 Hz and 10 Hz to 1 kHz, respectively. SQUID magnetometers are used to measure the Earth's magnetic field (Figure 7.20) at frequencies ranging between 10^{-4} Hz and 1 kHz. A technique known as magnetotellurics [63] can be used to determine the electrical conductivity distribution of the Earth's crust by measuring the Earth's electric and magnetic field. Because the Earth is a good electrical conductor compared to the air, the electrical field generated in the ionosphere (due to the solar wind) is reflected at the Earth's surface, with components of both the electric and magnetic field decaying as they penetrate into the Earth. The decay length or skin depth is $\delta \approx 500\sqrt{\rho\tau}$, where ρ is the electrical resistivity of the Earth and τ is the period of the electromagnetic wave. Magnetotellurics (the first industrial application of SQUIDs [16]) has been used in oil exploration and typically requires sub-pT/√Hz sensitivities. The first SQUID magnetometer systems initially used LTS sensors, but now HTS technology is adequate, as is existing room-temperature technology (meter length copper coils). However, the significantly more compact SQUID magnetometers (along with their much wider frequency range and true DC response) make them much more attractive for geophysical measurements.

In magnetotellurics, the electric field as a function of frequency is related to the magnetic field via an impedance tensor where $\boldsymbol{E}(\omega) = Z\boldsymbol{H}(\omega)$. The impedance tensor ($Z$) contains four complex elements Z_{xx}, Z_{xy}, Z_{yx}, and Z_{yy} and is related to the resistivity by $\rho_{ij} \approx 200\ |Z_{ij}(\omega)|^2 t$ where Z has units of V/m-T.

Magnetic anomaly detection (MAD) utilizes spatial components of $\nabla\boldsymbol{B}$ to uniquely locate a magnetic dipole [64]. This has applications in mineralogical surveys and detection of unexploded ordinance. MAD requires knowledge of the first-order gradient of the magnetic field, which reduces to only five independent components (see (7.13)) according to Maxwell's equations for quasi-stationary conditions ($B_{ij} = -B_{ji}$ and, due to $\nabla\boldsymbol{B} = 0$, $B_{xx} = -B_{xx} - B_{yy}$) and in the absence of flowing currents in the gradiometer's vicinity:

$$\begin{pmatrix} \frac{\partial B_x}{\partial x} & \frac{\partial B_x}{\partial y} & \frac{\partial B_x}{\partial z} \\ \frac{\partial B_y}{\partial x} & \frac{\partial B_y}{\partial y} & \frac{\partial B_y}{\partial z} \\ \frac{\partial B_z}{\partial x} & \frac{\partial B_z}{\partial y} & \frac{\partial B_z}{\partial z} \end{pmatrix} \Rightarrow \begin{pmatrix} \frac{\partial B_x}{\partial x} & \\ \frac{\partial B_y}{\partial x} & \frac{\partial B_y}{\partial y} \\ \frac{\partial B_z}{\partial x} & \frac{\partial B_z}{\partial y} \end{pmatrix} \tag{7.13}$$

with the location of the anomaly (in two dimensions) given by [64]:

$$X = \frac{-3B_x \frac{\partial B_z}{\partial x}}{\frac{\partial B_z}{\partial x} + \frac{\partial B_z}{\partial y}} \qquad Y = \frac{-3B_y \frac{\partial B_z}{\partial y}}{\frac{\partial B_z}{\partial x} + \frac{\partial B_z}{\partial y}} \tag{7.14}$$

Typically, the three field vector components (B_x, B_y, B_z) are also measured to correct for any contribution to the gradiometer's response to a uniform field (7.7.5).

It should be noted that superconducting magnetometers are vector devices and motion in the Earth's magnetic field produces an output that can mask the desired signal. For airborne gradiometer systems [65], noise cancellation (compensation of motion-induced artifacts) via electronic balancing is the critical technology, not SQUID sensitivity. The detection (distance) limit for such a gradiometer system is proportional to the fourth root of magnetic moment of the object being detected.

7.10.3.2 Active Methods

Rather than using the electromagnetic field generated by the solar wind, active methods create a time-dependent magnetic field generated by a loop driven by an electric current, with the magnetometer detecting the induced field. Measurements can either be in the time domain (e.g., transient electromagnetics (TEM)) or the frequency domain (e.g., controlled source audio magnetotelluric (CSAMT)).

7.10.3.3 Rock Magnetometers

Knowledge of the magnetic field orientation of a rock or core sample can give information as to how the rock was formed. By changing the thermal history of the sample, it may be possible to determine the Curie and/or Néel temperature of the rock's constituents. By raising the applied field above the saturation field of any ferromagnetic components, it may be possible to study paramagnetic components. Normally, a 3-axis rock magnetometer is used for paleomagnetic measurements. By using orthogonal field coils (B_x, B_y, B_z) or rotating the sample in a single coil, the anisotropy of the sample can be determined. Time-dependent behavior can also be studied after rapid changes in either temperature or applied field.

There are multiple ways to measure the remanent magnetic moment of rock samples. The most convenient way is to place the sample inside orthogonal field

Table 7.4 SQUID-Based NDE Techniques

Imaging
Intrinsic currents
Remanent magnetization
Embedded magnetic sensors
Flaw-induced perturbations in applied currents
Johnson noise in metals
Eddy currents in an applied AC field (flaws)
Printed circuit board flaws
Pipeline inspection
Hysteretic magnetization due to
Cyclic stress (strain)
Simultaneous DC and AC magnetic fields
Magnetization of paramagnetic, diamagnetic, and ferromagnetic materials in DC magnetic fields

coils. The use of LTS SQUID sensors allows sensitivities of 10^{-10} emu (10^{-13} Am^2) to be reached, equivalent to 10^{-8} A/m for a 10-cc rock sample. SQUID rock magnetometers are quite similar to SQUID susceptometers (Section 7.10.1.4), but without the need for a superconducting magnet.

7.10.4 Nondestructive Test and Evaluation

Magnetic sensing techniques such as eddy-current testing have been used for many years to detect flaws in structures (Table 7.4 and Figure 7.25). A major limitation on their sensitivity is the skin depth (see (7.10)) of metallic materials. Because SQUID sensors have a true DC response and superior sensitivity, they can see deeper into metallic structures. DC response also means that they can detect remanent magnetization. Their flat frequency response and zero phase distortion allow for a wide range of applications. One potential application of SQUIDs is in detection of stress or corrosion in reinforcing rods used in bridges, aircraft runways, or buildings.

SQUIDs can also be used to magnetically evaluate integrity and reliability of the infrastructure of gas pipelines from the surface [66]. A SQUID telescope uses a superconducting source coil encircling a superconductive pickup loop that inductively couples magnetic flux to a SQUID. The magnetic field oscillating at several hertz in the source penetrates the overburden to illuminate defects in a pipe wall. Magnetic flux concentrates in the wall and leaks out at defects. A defect then appears as a magnetic dipole. The use of millimeter and smaller detection coils can allow for magnetic microscopy with micrometer spatial resolutions.

7.10.4.1 SQUID Microscopes

For maximum sensitivity, the gap of between the detection coil of a SQUID microscope and the sample should be less than a few detection coil diameters. Commercial

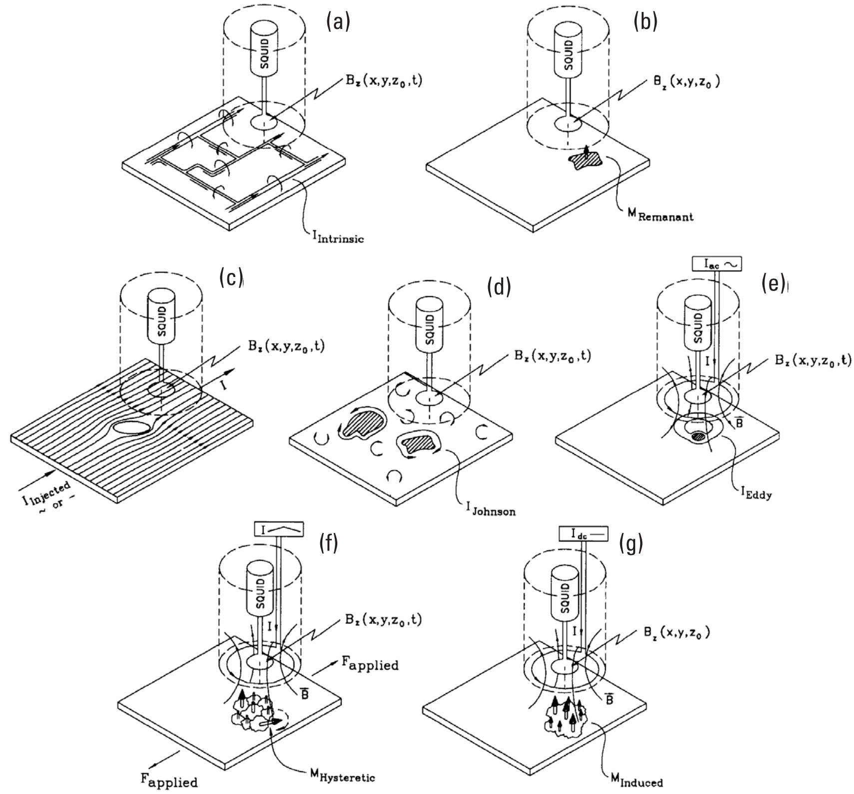

Figure 7.25 Measurement configurations for SQUID NDE: (a) intrinsic currents; (b) remanent magnetization; (c) flaw-induced perturbations in applied currents; (d) Johnson noise or corrosion activity in conductors; (e) eddy currents induced by an applied ac magnetic field; (f) hysteretic magnetization by application of stress or an applied field); and (g) diamagnetic and/or paramagnetic materials in an applied field. (Courtesy J. P. Wikswo, Jr.)

HTS SQUIDs often use bare SQUIDs to maximize spatial resolution with sensitivity proportional to the square of loop diameter [48] (Figure 9.8). Because LTS SQUID microscopes can use multilayer detection coils, higher sensitivities can be achieved for a given coil diameter (and equivalent spatial resolution). Some SQUID microscopes use adjustable tail dewars to achieve submillimeter standoff distances.

SQUID microscopes have been used to make noncontact measurements of electronic circuits [67]; one instrument has better than 10-μm resolution [68]. Such instruments with megahertz to gigahertz bandwidths could be used for circuit board and IC mapping. Jenks et al. [69] gave an excellent overview of SQUID NDE research.

7.10.5 Medical Applications of SQUIDs

The use of bioelectric signals as a diagnostic tool is well known in medicine, for example, the electrocardiogram (EKG) for the heart and the electroencephalogram (EEG) for the brain [47]. The electrical activity that produces the surface electrical activity that is measured by EEG and EKG also produce magnetic fields. The

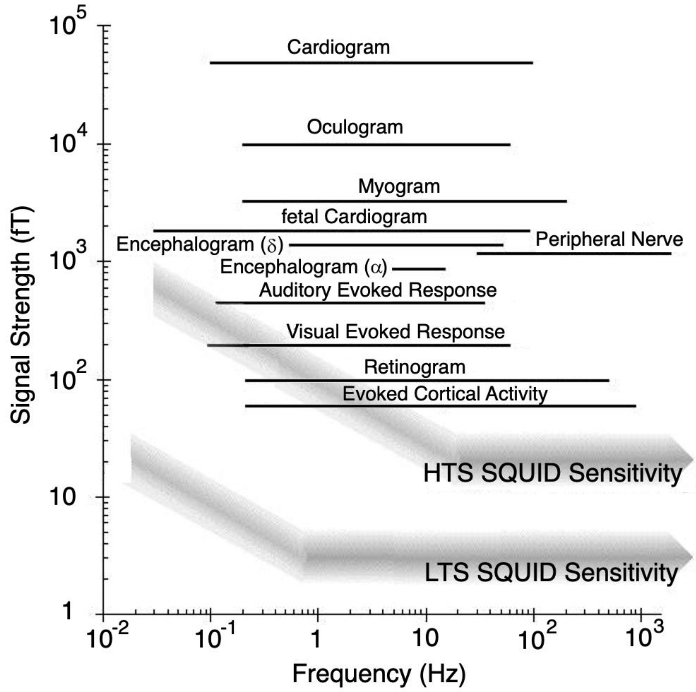

Figure 7.26 Typical amplitudes and frequency ranges for various biomagnetic signals (based on a ~1-cm tail gap).

analogous magnetic measurements are known as the magnetocardiogram (MCG) and the magnetoencephalogram (MEG). Other physiological processes also generate electrical activity with analogous magnetic fields (Figure 7.26).

Magnetic fields from active electrical sources in the body can be measured passively and external to the body by placing the magnetometer in proximity to the body's surface. It has been shown that a population of neurons in the brain can be modeled as a current dipole that generates a well-defined magnetic field profile. The response of a simple magnetometer to a current dipole in free space [70] can be expressed by:

$$Q_{\min} = \frac{\pi \Phi_{\min} \sqrt{m}}{\mu_o \sqrt{\dfrac{r}{\rho\left[(1 - m/2)K(m) - E(m)\right]}}} \tag{7.15}$$

where $m = 4r\rho/\sqrt{[(r+\rho)^2 + z^2)]}$ and $Q_{\min}$ is the smallest current dipole that can be detected, $\Phi_{\min}$ is the minimum detectable magnetic flux in the detection coil (e.g., (7.4)), r is the radius of the pickup coil, ρ is the off-axis distance (in cylindrical coordinates), z is the axial distance of the current dipole below the bottom of the pickup coil, and K and E are elliptical integrals of the first and second kinds, respectively (the elliptic integrals are a result of integrating the Biot-Savart law over a circular coil area).

Unlike the response of a magnetic dipole, which goes as $1/z^3$, the response of a current dipole goes as $1/z^2$. Also, the maximum sensitivity is not located directly beneath the detection coils, but offset (Figure 7.27) with the response directly beneath the detection coil being zero [71].

Mapping of these field profiles can be used to infer the location of the equivalent active dipole site region to within millimeters. Using evoked response techniques, the location of signal pathways and information processing centers in the brain can be mapped at different delay times (latencies) following the stimulus.

In some circumstances, it is much more difficult to record an electric than a magnetic signal. This is the case for fetal cardiograms. Studies [73] have demonstrated the critical advantages of fetal magnetocardiography for evaluation of life-threatening fetal arrhythmias.

There are also magnetic measurements for which there are no electrical analogs [74]. These are measurements of static magnetic fields produced by ferromagnetic materials ingested in the lungs [75] and measurements of the magnetic susceptibility of materials in the body. In particular, information on the quantity and depth of diamagnetic or paramagnetic materials (such as iron stored in the liver) can be obtained by using magnetizing and detection coils of differing sizes in the same instrument and measuring the induced field as a function of distance. This technique [76] has been used for more than three decades to clinically monitor patients suffering from iron overload diseases such as sickle-cell disease, thalassemia, and hemochromatosis.

The development of the SQUID has allowed the development of noninvasive clinical measurements of biomagnetic fields. Although somewhat dated, Körber et al. [77] discuss potential improvements in SQUID methodologies applicable to healthcare. The use of gradiometers can allow measurements to be made in unshielded environments at sensitivities below 20 fT/√Hz. Typically, however, neuromagnetic measurements are made in room-sized MSRs [71] that will allow measurements of the magnetic field of the brain over the entire surface of the head (>200 positions simultaneously). Table 7.5 gives some of the areas in which SQUID magnetometers are currently being used in medical research.

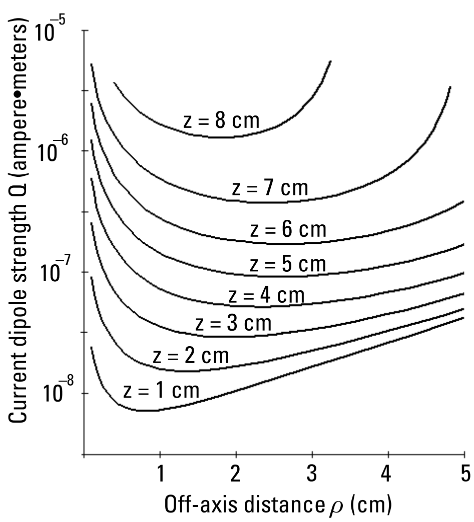

Figure 7.27 Minimum detectable current dipole for a first derivative (Figure 7.15(b)), six turn, 5 fT/√Hz gradiometer with a coil diameter of 2 cm [72] as a function of off-axis position (*r*) and depth (*z*).

Table 7.5 Areas in Which SQUID Magnetometers are Being Used in Medical Research

Studies of the brain—neuromagnetism
Epilepsy
Presurgical cortical function mapping
Drug development and testing
Cognitive impairment (traumatic brain injury, stroke, Alzheimer disease)
Neuromuscular disorders
Prenatal brain disorders
Performance evaluation
Studies of the heart—magnetocardiography
Arrhythmia
Heart muscle damage
Fetal cardiography
Other medical applications
Noninvasive in vivo magnetic liver biopsies (ferritometry)
Studies of the stomach—gastroenterology
Intestinal ischemia
Spinal cord and peripheral and single nerve studies
Lung function and clearance studies (magnetopneumography)
Nerve damage assessment
Low-field MRI
Magnetoimmunoassay

References

[1] Kamerlingh-Onnes, H., "The Resistance of Pure Mercury at Helium Temperatures," *Akad. van Wetenschappen, Amsterdam*, Vol. 120b, 1911.

[2] Bardeen, J., L. Cooper, and R. Schriefer, "Theory of Superconductivity," *Phys. Rev.*, Vol. 108, 1957, pp. 1175–1204.

[3] Bednorz, J. G., and K. A. Müller, "Possible High T_c Superconductivity in the Ba-La-Cu-O System," *Z. Phys.*, Vol. B64, 1986, pp. 189–193.

[4] Meissner, W., and R. Oschsenfeld, "Ein Neuer Effekt bei Eintritt der Supraleitfahigkeit," *Naturwissenschaften*, Vol. 21, 1933, pp. 787–788.

[5] Quin, D. J., and W. B. Ittner, "Resistance in a Superconductor," *J. Appl. Phys.*, Vol. 33, 1962, pp. 748–749.

[6] Josephson, B. D., "Possible New Effect in Superconductive Tunneling," *Phys. Lett.*, Vol. 1, 1962, pp. 251–253.

[7] Tesche, C. D., and J. Clarke, "DC SQUID: Noise and Optimization," *J. Low Temp. Phys.*, Vol. 29, 1982, pp. 301–331.

[8] Giffard, R. P., R. A. Webb, and J. C. Wheatley, "Principles and Methods of Low-Frequency Electric and Magnetic Measurements Using an rf-Biased Point-Contact Superconducting Device," *J. Low Temp. Phys.*, Vol. 6, 1972, pp. 533–610.

[9] Van Duzer, T., and C. W. Turner, *Principles of Superconductive Devices and Circuits*, New York: Elsevier, 1981.

[10] Orlando, T. P., and K. A. Delin, *Foundations of Applied Superconductivity*, Reading, MA: Addison-Wesley, 1991.

[11] Liu, C., et al., "An Insight into Voltage-Biased Superconducting Quantum Interference Devices," *Appl. Phys. Lett.*, Vol. 101, 2012, p. 222602.

[12] Snider, E., et al., "Room-Temperature Superconductivity in a Carbonaceous Sulfur Hydride," *Nature*, Vol. 586, 2020, pp. 373–377.

[13] Kittel, C., *Introduction to Solid State Physics*, New York: John Wiley & Sons, 2004, pp. 273–278.

[14] Stephens, R. B., and R. L. Fagaly, "High Temperature Superconductors for SQUID Detection Coils," *Cryogenics*, Vol. 31, 1991, pp. 988–992.

[15] Koelle, D., et al., "High-Transition-Temperature Superconducting Quantum Interference Devices," *Rev. Mod. Physics*, Vol. 71, 1999, pp. 631–686.

[16] Fagaly, R. L., "The Commercialization of SQUIDs," *IEEE Transactions on Applied Superconductivity*, Vol. 25, No. 3, June 2015.

[17] Drung, D., and Mück, M., "SQUID Electronics," Chapter 4 in J. Clarke and A. Braginski, (eds.), *The SQUID Handbook: Volume I: Fundamentals and Technology of SQUIDs and SQUID Systems*, New York: John Wiley & Sons, 2004.

[18] Oppenländer, J., et al., "Highly Sensitive Magnetometers for Absolute Magnetic Field Measurements Based on Quantum Interference Filters," *Physica C*, Vol. 368, 2002, pp. 119–124.

[19] Caputo, P., et al., "Superconducting Quantum Interference Filters as Absolute Magnetic Field Sensors," *IEEE Transactions on Applied Superconductivity*, Vol. 15, 2005, pp. 1044–1047.

[20] Caputo, P., et al., "Quadratic Mixing of Radio Frequency Signals Using Superconducting Quantum Interference Filter," *Applied Physics Letters*, Vol. 89, No. 6, March 2006.

[21] Schopohl, N., "Superconducting Quantum Interference Filters Operated in Commercial Miniature Cryocoolers," *IEEE Transactions on Applied Superconductivity*, Vol. 15, 2005, pp. 936–939.

[22] Zimmerman, J. E., "Sensitivity Enhancement of Superconducting Quantum Interference Devices Through the Use of Fractional-Turn Loops," *J. Appl. Phys.*, Vol. 42, 1971, pp. 4483–4487.

[23] Drung, D., S. Knappe, and H. Koch, "Theory for the Multiloop Dc Superconducting Quantum Interference Device Magnetometer and Experimental Verification," *J. Appl. Phys.*, Vol. 77, 1995, pp. 4088–4098.

[24] Soloviev, I. I., et al., "Superconducting Josephson Structures with High Linearity of Transformation of Magnetic Signal into Voltage," *Physics of the Solid State*, Vol. 52, 2010, pp. 2252–2258.

[25] Prance, R. J., et al., "Fully Engineered High Performance UHF SQUID Magnetometer," *Cryogenics*, Vol. 21, 1981, pp. 501–506.

[26] SHE model 330X RF SQUID electronics.

[27] Quantum Design Model 2000 RF SQUID electronics.

[28] Clarke, J., "SQUID Fundamentals," in Harold Weinstock, (ed.), *SQUID Sensors: Fundamentals, Fabrication and Applications*, Boston, MA: Kluwer Academic Publishers, 1996, pp. 1–62.

[29] Faley, M. I., et al., "Operation of HTS dc-SQUID Sensors in High Magnetic Fields," *IEEE Transactions on Applied Superconductivity*, Vol. 9, 1999, pp. 3386–3391.

[30] Dantsker, E., S. Tanaka, and J. Clarke, "High-Tc SQUIDs with Slots or Holes: Low $1/f$ Noise in Ambient Magnetic Fields," *Appl. Phys. Lett.*, Vol. 70, 1997, pp. 2037–2039.

[31] Drung, D., "Readout of Superconducting Detectors," in E. Wolf et al., (eds.), *Josephson Junctions History, Devices, and Applications*, Pan Stanford, 2017.

[32] Drung, D., "High-T_c and Low-T_c dc SQUID Electronics," *Supercond. Sci. Technol.*, Vol. 16, 2003, pp. 1320–1336.

[33] Simmonds, M. B., and R. P. Giffard, "Apparatus for Reducing Low Frequency Noise in dc Biased SQUIDs," U.S. Patent No. 4,389,612, 1983.

[34] Fagaly, R. L., "Superconducting Magnetometers and Instrumentation," *Sci. Prog., Oxford*, Vol. 71, 1987, pp. 181–201.

[35] Grover, F. W., *Inductance Calculations, Working Formulas and* Tables, New York: Dover, 1962.

[36] Wikswo, Jr., J. P., "Optimization of SQUID Differential Magnetometers," *AIP Conference Proceedings*, Vol. 44, 1978, pp. 145–149.

[37] Ilmoniemi, R., et al., "Multi-SQUID Devices and Their Applications," in D. F. Brewer, (ed.), *Progress in Low Temperature Physics, Vol. XII*, New York: Elsevier, 1989, pp. 1–63.

[38] Jaworski, F. B., and D. B. Crum, "Sources of Gradiometer Imbalance and Useful Balancing Techniques," in H. Weinstock and W. C. Overton, (eds.), *SQUID Applications to Geophysics*, Tulsa, OK: Society of Exploration Geophysicists, 1981, pp. 19–25.

[39] Vrba, J., "SQUID Gradiometers in Real Environments," in H. Weinstock, (ed.), *SQUID Sensors: Fundamentals, Fabrications and Applications*, Boston, MA: Kluwer Academic Publishers, 1996, pp. 117–178.

[40] Robinson, S. E., "Environmental Noise Cancellation for Biomagnetic Measurements," in S. J. Williamson et al., (eds.), *Advances in Biomagnetism*, New York: Plenum Press, 1989, pp. 721–724.

[41] Walker, G., *Miniature Refrigerators for Cryogenic Sensors and Cold Electronics*, Oxford, U.K.: Clarendon Press, 1989.

[42] Radebaugh, R, "Cryocoolers: The State of the Art and Recent Developments," *J. Phys.: Condens. Matter*, Vol. 21, 2009, 164219.

[43] Buchanan, D. S., D. N. Paulson, and S. J. Williamson, "Instrumentation for Clinical Applications of Neuromagnetism," in R. W. Fast, (ed.), *Advances in Cryogenic Engineering*, Vol. 33, New York: Plenum, 1988, pp. 97–106.

[44] Sata, K., "A Helmet-Shaped MEG Measurement System Cooled by a GM/JT Cryocooler," in T. Yoshimoto et al., (eds.), *Recent Advances in Biomagnetism*, Sendai: Tohoku University Press, 1999, pp. 63–66.

[45] Heiden, C., "Pulse Tube Refrigerators: A Cooling Option," in H. Weinstock, (ed.), *SQUID Sensors: Fundamentals, Fabrications and Applications*, Boston, MA: Kluwer Academic Publishers, 1996, pp. 289–306.

[46] Romani, G. L., S. J. Williamson, and L. Kaufman, "Biomagnetic Instrumentation," *Review of Scientific Instruments*, Vol. 53, 1982, pp. 1815–1845.

[47] Stroink, G., et al., "Aluminum Shielded Room for Biomagnetic Measurements," *Review of Scientific Instruments*, Vol. 52, 1981, pp. 463–468.

[48] Fagaly, R. L., "Superconducting Quantum Interference Device Instruments and Applications," *Review of Scientific Instruments*, Vol. 77, 2006, 101101.

[49] Sarwinski, R. E., "Superconducting Instrumentation," *Cryogenics*, Vol. 17, 1977, pp. 671–679.

[50] Kuchnir, M., J. D. McCarthy, and P. A. Rapidis, "SQUID Based Beam Current Monitor," *IEEE Transactions on Magnetics*, Vol. MAG-21, 1985, pp. 997–999.

[51] Wikswo, J. P., "Improved Instrumentation for Measuring the Magnetic Fields of Cellular Action Currents," *Review of Scientific Instruments*, Vol. 53, 1982, pp. 1846–1850.

[52] Lounasmaa, O., *Experimental Principles and Methods Below 1K*, London, U.K.: Academic Press, 1974.

[53] Webb, R. A., "New Technique of Improved Low-Temperature SQUID NMR Measurements," *Review of Scientific Instruments*, Vol. 48, 1977, pp. 1585–1594.

[54] Hilbert, C., et al., "Nuclear Quadrupole Resonance Detected at 30 MHz with a dc Superconducting Quantum Interference Device," *Appl. Phys. Lett.*, Vol. 47, 1985, pp. 637–639.

[55] Clarke, J., M. Hatridge, and M. Mößle, "SQUID-Detected Magnetic Resonance Imaging in Microtesla Fields," *Annu. Rev. Biomed. Eng.*, Vol. 9, 2007, pp. 389–413.

[56] Paik, H. J., "Superconducting Tensor Gravity Gradiometer with SQUID Readout," in H. Weinstock and W. C. Overton (eds.), *SQUID Applications to Geophysics*, Tulsa, OK: Society of Exploration Geophysicists, 1981, pp. 145–152.

[57] Klemme, B. J., et al., "PdMn and PdFe: New Materials for Temperature Measurement Near 2 K," *J. Low Temp. Phys.*, Vol. 116, 1999, pp. 133–146.

[58] Solomonson, N., et al., "Construction and Performance of a Low Noise Inductive Transducer for the Louisiana State University Gravitational Wave Detector," *Review of Scientific Instruments*, Vol. 65, 1977, pp. 174–181.

[59] Lockhart, J. M., et al., "Magnetic Susceptibility of Instrument Materials Below 10 K," *IEEE Transactions on Applied Superconductivity*, Vol. 7, 1997, pp. 2354–2357.

[60] Harvey, I. K., "A Precise Low Temperature Dc Ratio Transformer," *Review of Scientific Instruments*, Vol. 43, 1972, pp. 1626–1639.

[61] Hao, L., et al., "HTS Cryogenic Current Comparator for Non-Invasive Sensing of Charged Particle Beams," *IEEE Transactions on Instrumentation and Measurement*, Vol. 52, 2003, pp. 617–620.

[62] Stolz, R., et al., "Superconducting Sensors and Methods in Geophysical Applications," *Supercond. Sci. Technol.*, Vol. 34, 2021, 033001.

[63] Vozoff, K., "The Magnetotelluric Method in the Exploration of Sedimentary Basins," *Geophysics*, Vol. 37, 1972, pp. 98–114.

[64] Wynn, W., et al., "Advanced Superconducting Gradiometer/Magnetometer Arrays and a Novel Signal Processing Technique," *IEEE Transactions on Magnetics*, Vol. 11, 1975, pp. 701–707.

[65] Meyer, U., et al., "New Airborne Methods and Procedures for the Exploration of Mineral Resources—An Overview of BGR Activities." *22nd European Meeting of Environmental and Engineering Geophysics*, 2016.

[66] Podney, W., "Magnetic Telescope for Surveys of Gas Pipelines from the Surface," in D. O. Thompson and D. E. Chimenti, (eds.), *Review of Progress in Quantitative Nondestructive Evaluation, Vol. 20*, New York: American Institute of Physics, 2001.

[67] Fagaly, R. L., "SQUID Detection of Electronic Circuits," *IEEE Transactions on Magnetics*, Vol. MAG-25, 1989, pp. 1216–1218.

[68] Kirtley, J., "Imaging Magnetic Fields," *IEEE Spectrum*, Vol. 33, 1996, pp. 40–48.

[69] Jenks, W. G., S. S. H. Sadeghi, and J. P. Wikswo, "SQUIDs for Nondestructive Evaluation," *J. Phys. D: Appl. Phys.*, Vol. 30, 1997, pp. 293–323.

[70] Wikswo, J. P., "Optimization of SQUID Differential Magnetometers," *AIP Conf. Proc.*, Vol. 44, 1978, pp. 145–149.

[71] Fagaly, R. L., "Neuromagnetic Instrumentation," Chapter 2, in Susumu Sato, (ed.), *Advances in Neurology, Vol. 54: Magnetoencephalography*, New York: Raven Press, 1990, pp. 11–32.

[72] Knuutila, J., et al., "Large-Area Low-Noise Seven-Channel dc SQUID Magnetometer for Brain Research," *Review of Scientific Instruments*, Vol. 58, 1987, pp. 2145–2156.

[73] Cuneo, B. F., et al., "In Utero Diagnosis of Long QT Syndrome by Magnetocardiography," *Circulation*, Vol. 128, 2013, pp. 2183–2191.

[74] Fagaly, R. L., and S. E. Robinson, "Biomagnetic Instrumentation: Current Capabilities & Future Trends," *Proceedings of the ASME*, Vol. AES-9, 1989, pp. 7–12.

[75] Paulson, D. N., R. M. Toussint, and R. L. Fagaly, "Superconducting Magnetometer System for Detecting Lung Contaminants," *IEEE Transactions on Magnetics*, Vol. MAG–23, 1987, pp. 1315–1318.

[76] Paulson, D. N., et al., "Biomagnetic Susceptometer with SQUID Instrumentation," *IEEE Transactions on Applied Superconductivity*, Vol. MAG–27, 1991, pp. 3249–3252.

[77] Körber, R., et al., "SQUIDs in Biomagnetism: A Roadmap Towards Improved Healthcare," *Supercond. Sci. Technol.*, Vol. 29, 2016, 113001.

CHAPTER 8

Magneto-Optical Sensors and Other Principles

Pavel Ripka and Ludek Kraus

In this chapter, we cover magneto-optical sensors and also the unusual types of magnetic field sensors that do not fall into the categories covered by Chapters 2 to 7. *Unusual* here means that these sensors are not widely available on the market in 2020. Unusual does not mean that these sensors are rare: magnetic sensors inside animal bodies are made in enormous quantities, but the manufacturer provides no datasheets. People have used scientific methods to prove that the animal navigation is based on these sensors, but in some cases, they have significant problems in finding out how they function or even where are they located. We will mention these biological sensors in Section 8.4.

Unusual also does not mean that these sensors are unknown. Sometimes they are a subject of numerous scientific papers, later they are forgotten, and sometimes they reappear, in most cases, soon to be forgotten again, but sometimes the development in technology, instrumentation, and data processing may cause a revival of an almost-forgotten principle. One example is the sensor based on the Lorentz force on a current conductor [1]. The micromachined silicon resonating structure with a high Q is activated by an AC and the movement is detected by a capacitive method. The advantage of such a sensor is potentially a very high dynamic range up to 1T with a theoretical nano-tesla resolution (if operated with low damping, that is, in vacuum).

The sensor market is very dynamic and varied; if some sensor type described in the literature is not commercially available, it usually means that it has some serious drawbacks. A typical problem for many types of sensors such as giant magnetoinductance (GMI), which is often ignored in journal articles, is temperature dependence and perming. Nevertheless, there are application areas for unusual sensors. If we want to measure the field profile along the optical cable or average the field value over a long line, magnetostrictive sensors may be a good solution.

Here we have to briefly mention semiconductor sensors other than the most popular Hall sensors, which are covered in Chapter 5. The most important of them are semiconductor magnetoresistors [2, 3]. They have nonlinear characteristics and their main application is for position switching and revolution counters (Section 9.4 and Chapter 11). Other types of semiconductor magnetic sensors such as magnetodiodes, magnetotransistors, and carrier-domain devices are not very practical. Information about their principles can be found in [4].

8.1 Magneto-Optical Sensors

8.1.1 Faraday Effect and Optical Sensors of the Magnetic Field

In 1845, Michael Faraday discovered the following phenomenon: If linearly polarized light passes through a medium placed in the magnetic field and the direction of the magnetic field is parallel to that of light propagation, the plane of polarization of light rotates. Figure 8.1 shows a scheme of the classical Faraday setup: A linearly polarized light passes through magneto-optical material 3 and analyzer 4 and is collected by photoreceiver 5. The rotation of the polarization plane (Faraday rotation) is detected by means of the photoreceiver's signal: According to the Malus law, the intensity of light transmitted by the analyzer is proportional to the cosine squared of the angle between the polarization of the incident light and the main plane of the analyzer. Thus, by measuring the intensity of light for given orientation of the analyzer, we can determine the direction of polarization of light emerging from magneto-optical material 3. Faraday found that the angle of rotation is proportional to the magnetic field H and to the length, l of the magneto-optical material

$$\theta_F = VlH \tag{8.1}$$

The proportionality constant V is called the Verdet constant with units of angular degrees/ampere. The Faraday effect represents an odd effect with respect to the H direction. A change in the sign of H causes a change in the sense of Faraday rotation. Therefore, when light passes through the magneto-optical material forth and back, the angle of rotation doubles. This nonreciprocity of the Faraday effect provides an opportunity (successfully being used since experiments conducted by Faraday himself) to substantially increase the angle of the polarization rotation by passing the light many times forth and back through the magneto-optical material.

Equation (8.1) is valid for paramagnets and diamagnets; the Verdet constant of diamagnets is rather low (5×10^{-4} °/A for silica), but exhibits low temperature dependence. Despite the generally accepted definition in (8.1), Faraday rotation is not proportional to the external magnetic field, but rather is a function of the magnetization. The Faraday effect in transparent ferromagnetic is thus very strong, achieving a Verdet constant of 1°/A.

The Faraday effect is related to the fact that the magnetized state cannot be described by a single refraction index. The magnetic field in the medium makes a

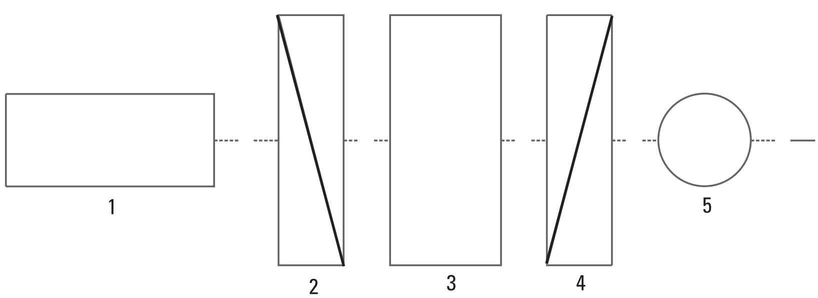

Figure 8.1 Faraday effect scheme.

difference between refraction indices for circularly polarized light with opposite senses of polarization rotation.

Often the circular birefringence is combined with linear birefringence. Linear birefringence is associated with spatial nonuniformity and means that the refraction indices of the medium depend on the polarization orientation. Linear birefringence originates from the crystallographic structure, from the strains that occurred during the manufacturing process of the sensor material (remanent birefringence), from mechanical stresses taking place during operation, and from temperature changes. Linear birefringence substantially affects the state of polarization of light and distorts the results of measurements.

8.1.1.1 Detection of the Polarization Angle

When the conventional Faraday scheme shown in Figure 8.1 is used for measurement of the Faraday rotation, the intensity of light incident on the photoreceiver (usually a photodiode) reads as

$$I = I_0 \cos^2\left(\gamma - \theta_F\right) \tag{8.2}$$

where I_0 is the intensity of light incident on the magneto-optical material and γ is the angle between the main planes of the polarizer and the analyzer. The sensitivity of the detection with respect to the Faraday rotation is maximum for $\gamma = 45°$.

The results of the measurement are very sensitive to the fluctuations of the output power of the light source. There are several schemes to substantially reduce that drawback. In the dual-quadrature polarimetric configuration, shown in Figure 8.2, a polarization beam splitter is used instead of the analyzer 4 in Figure 8.1. Light beams polarized in the main plane of the splitter and in the orthogonal plane emerge from the splitter in two different directions. Intensities of the light beams $I_\perp$ and $I_{||}$ are measured by two separate photoreceivers.

If the main planes of the splitter and the polarizer are parallel, then the ratio of the intensities gives the Faraday rotation on the sensing element:

$$\tan^2 \theta_F = \frac{I_\perp}{I_{||}} \tag{8.3}$$

The results of the measurement are still very sensitive to linear birefringence. Better results are obtained by using the ratiometric formula:

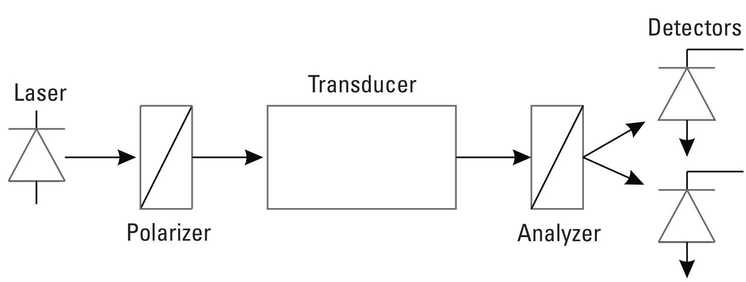

Figure 8.2 Dual-quadrature configuration.

$$2\theta_F f \doteq \sin 2\theta_F = \frac{\left(I_\perp - I_\parallel\right)}{\left(I_\perp + I_\parallel\right)} \tag{8.4}$$

The most important sensing application of Faraday effect is electric current sensor based on optical fiber. These magneto-optical current transformers are based on Ampere's law and they are used mainly to measure currents at high-voltage lines, as the sensor has perfect galvanic insulation. More details on current sensors are given in Chapter 11.

Fiber-optic magnetometer using Faraday effect in nanocomposite polymer was described in [5]. The achieved Verdet constant was 32×10^7°/T · m ≈ 402°/A and the authors claim 20 fT/√Hz noise at 0.01 Hz, but this figure was not confirmed by an independent laboratory. Thus, the measurement of large AC is the only known application of the Faraday effect in the measurement of magnetic fields.

8.1.2 Magneto-Optical Kerr Effect and Observation of Domains

The magneto-optical Kerr effect manifests in the change of parameters of light reflected from a magnetic sample. This action of the sample on the light strongly depends on the mutual orientations of the plane of incidence of light and of the direction of the sample's magnetization. There are three basic types of the Kerr effect:

1. *Polar Kerr effect:* The magnetization is perpendicular to the reflective surface and parallel to the plane of incidence, as shown in Figure 8.3(a).
2. *Longitudinal (meridional) Kerr effect:* The magnetization is parallel both to the reflective surface and to the plane of incidence, as shown in Figure 8.3(b).
3. *Transverse (equatorial) Kerr effect:* The magnetization is parallel to the reflective surface and perpendicular to the plane of incidence, as shown in Figure 8.3(c).

In the polar Kerr effect, the linearly polarized light becomes elliptically polarized after reflection, with the large axis of the polarization ellipse rotated with respect to the initial polarization direction. Similar changes are observed also in the longitudinal Kerr effect. A common feature of these two effects is that there exists a component of the wave vector of light on the direction of the magnetization vector.

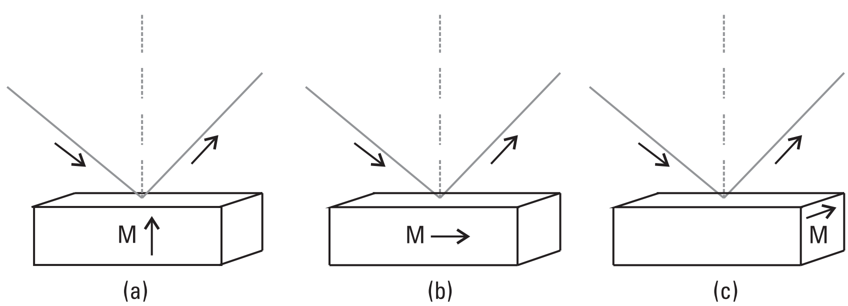

Figure 8.3 Magneto-optical Kerr effect: (a) polar Kerr effect; (b) longitudinal Kerr effect; and (c) transverse Kerr effect.

This fact is responsible for the analogy of these effects with the Faraday effect and allows us to consider all these effects as longitudinal effects. The transverse Kerr effect results in the change of the intensity and in the phase shift of the reflected light. The phase shift takes place if the polarization plane of the incident light is not parallel or perpendicular to the plane of incidence.

The main application of the Kerr effect is observation of magnetic domains. This topic is covered by an excellent book of Hubert and Schäfer [6].

8.2 Magnetoimpedance and Magnetoinductance

8.2.1 Principle

Magnetoinductive effects in ferromagnetic conductors may be used for various sensors. Magnetoinductive effects are related to magnetization of a magnetic conductor (wire, strip, thin film) by a magnetic field, which is produced by an electric current passing through the conductor itself. If the current is varying with time, the magnetic flux in the conductor also varies and induces the electromotive force, which is superimposed to the ohmic voltage between its ends. For instance, in a wire with a circular cross-section, the circumferential magnetic field H induced by a constant current with the density j is $H = jr/2$, where r is the distance from the wire axis. For a wire of diameter 1 mm and the current density of 10^6 A/m, which is low enough not to greatly increase the temperature by the Joule heating, the maximum magnitude of a magnetic field on the wire surface is 250 A/m. To get a sufficiently high magnetoinductive voltage, which can be easily detected on the ohmic background signal, the circumferential reversal of conductor magnetization must take place in magnetic fields of this order or lower. Therefore, good soft magnetic metals with a high circumferential permeability are required for these applications.

A large magnetoinductive effect has been found in the zero-magnetostrictive amorphous CoFeSiB wire with the circumferential, bamboo-like domain structure in the outer shell. When an AC of 1 kHz was applied to the wire, sharp peaks (about 0.2V) were induced on the background ohmic signal by the circumferential magnetization reversal in the outer shell. The amplitude of peaks is decreasing with an increasing external DC magnetic field. Utilizing this effect, a simple magnetic head (see Figure 8.4) was constructed and was used for a noncontact rotary encoder and a cordless data tablet [7].

Another magnetoinductive effect observed in soft ferromagnetic metals is the GMI, which is characterized by a strong dependence of AC impedance on an applied

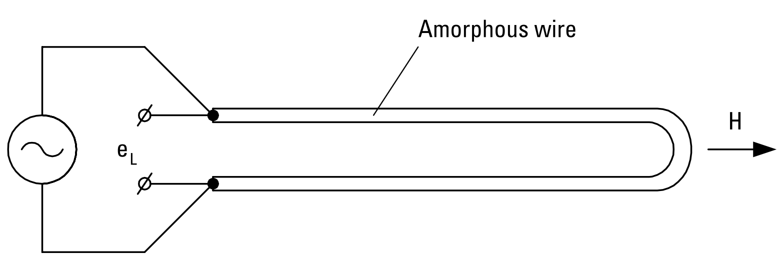

Figure 8.4 Simple magnetoinductive head using an amorphous wire. (*After:* [7].)

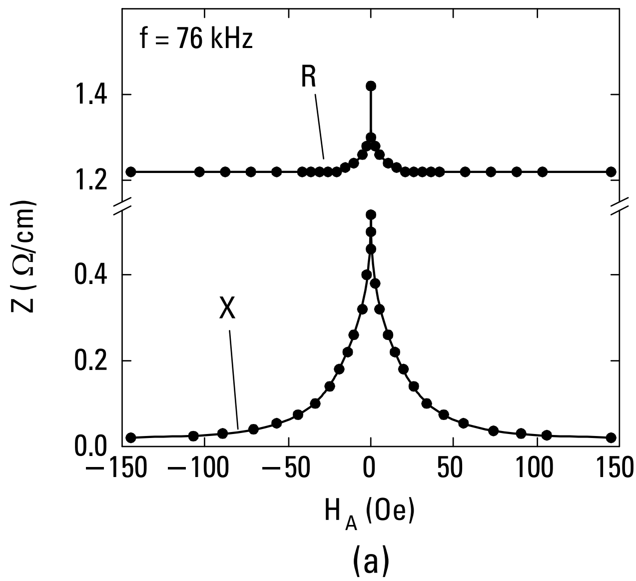

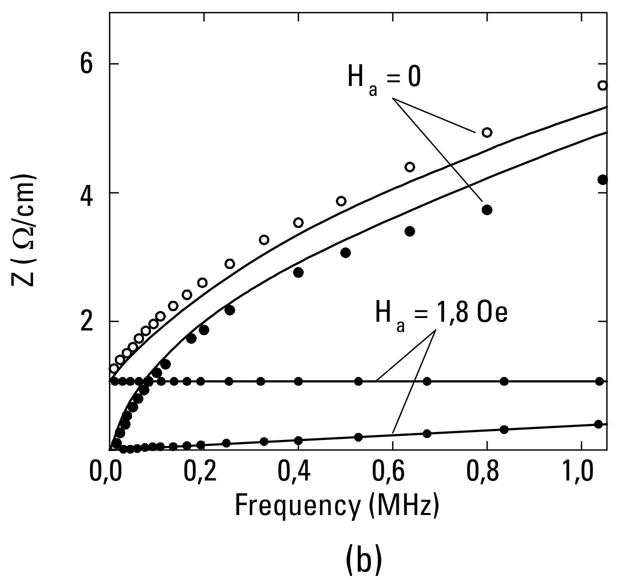

Figure 8.5 GMI of amorphous CoFeSiB wire. (*After:* [8].) (a) *R* resistance and *X* reactance as functions of applied field. (b) Resistance (open symbols) and reactance (filled symbols) as functions of frequency.

magnetic field (see Figure 8.5). This effect is observed only at sufficiently high frequencies and can be explained by means of classical electrodynamics [8]. It is known that the RF current is not homogeneous over the cross-section of conductor, but tends to be concentrated near the surface (skin effect). The exponential decay of current density from the surface into the interior is described by the skin depth

$$\delta = \sqrt{\frac{2\rho}{\omega\mu}} \tag{8.5}$$

which depends on the circular frequency of the RF current ω, the resistivity ρ, and the permeability μ. In ferromagnetic materials, the permeability depends on the frequency, the amplitude of the AC magnetic field, and also on other parameters, such as the magnitude and the orientation of the DC bias magnetic field, mechanical strain, and temperature. The large permeability of soft magnetic metals, and its strong dependence on the bias magnetic field is the origin of GMI effect. The theory of the GMI effect is described in [9].

By definition, the complex impedance $Z(\omega) = R + iX$ of a uniform conductor (see Figure 8.6) is given by the ratio of voltage amplitude U to the amplitude of a sinusoidal current $I \sin\omega t$, passing through it. The real part of impedance is called the resistance, and the imaginary part the reactance. For a conductor of length L and cross-section area q, the impedance is given by the formula

$$Z = \frac{U}{I} = \frac{LE_z(S)}{A\langle j_z\rangle_A} = R_{\mathrm{dc}}\frac{j_z(S)}{\langle j_z\rangle_A} \tag{8.6}$$

where E_z and j_z are the longitudinal components of an electric field and current density, respectively, and R_{dc} is the DC resistance. The symbol S refers to the value at the surface and $\langle\ \rangle_q$ to the average value over the cross-section q. As can be seen, for a uniform current density, the impedance is equal to the DC resistance. The definition (8.6) is valid only for linear elements, that is, when the voltage U is proportional to the current I. However, it should be noted that a ferromagnetic conductor is generally a nonlinear element. This means that the voltage is not exactly proportional to the current and moreover, it also contains higher-order harmonics of the basic frequency. Therefore the term "impedance" should be taken with some precaution.

8.2.2 Materials

In real soft magnetic metals, the maximum GMI effect experimentally observed to date is much lower than the theoretically predicted values. Research in this field is focused on special heat treatments of already known soft magnetic metals or the development of new materials with properties appropriate for practical GMI applications. The GMI curve $\eta(H)$ is defined as

$$\eta(H) = 100\% \times \left(\frac{|Z(H)|}{|Z_0|} - 1\right) \tag{8.7}$$

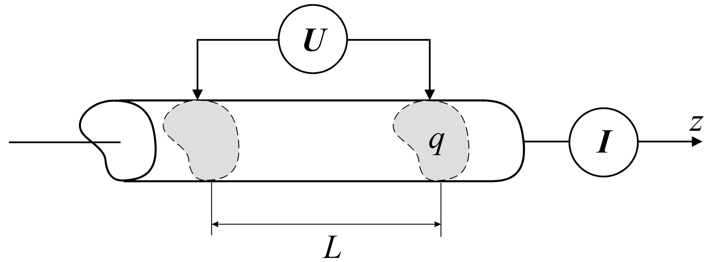

Figure 8.6 The impedance definition.

where $Z(H)$ is the impedance for bias field H, measured at a given frequency and constant driving current. Z_0 is the impedance for $H \to \infty$, which should be equal to the impedance of a nonmagnetic conductor with the same cross-section q and the same resistivity ρ. Practically, for Z_0, the value of impedance measured with maximum field H_{max}, available for the given experimental equipment, is used. Some authors use $Z_0 = Z(0)$, but this value depends on the remanent magnetic state, which may not be well defined. The parameters that well characterize the GMI efficiency are the maximum GMI, η_{max}, and the maximum field sensitivity, $(d\eta/dH)_{max}$.

Although GMI was first reported for amorphous metals with η_{max} of 400%, some crystalline materials also exhibit large GMI. Sometimes, the crystalline metals are even better than the amorphous ones. According to one theory, the largest GMI should be obtained in materials with low resistivity ρ, high saturation magnetization M_s, and low damping parameter α. The crystalline metals have the advantage of lower resistivity, but in amorphous metals, better soft magnetic behavior can be obtained due to the lack of magnetocrystalline anisotropy. Because the magnetoelastic contribution to magnetic anisotropy substantially deteriorates the soft magnetic behavior, the nonmagnetostrictive materials also show the best GMI performance.

Amorphous Co-rich ribbons, wires, and glass-covered microwires are good candidates for GMI applications. The low magnetostriction and the easy control of magnetic anisotropy by appropriate heat treatment are the advantages of these materials; high resistivity is the disadvantage. Soft magnetic nanocrystalline metals exhibit GMI behavior similar to that of amorphous metals. Their somewhat higher M_s and lower ρ can lead to a small improvement. The low resistivity and bulk dimensions of crystalline soft magnetic alloys lead to better performance, especially at low driving frequencies (<1 MHz). Excellent GMI behavior was found in combined conductors consisting of a highly conductive nonmagnetic metal core (such as Cu or CuBe) with a thin layer of soft magnetic metal on the surface [10]. An insulating interlayer between the core and the magnetic shell of the wire results in further improvement of GMI behavior. Instead of a wire, GMI sensor can be made as a sandwich of thin-film structures.

Not only are η_{max} and $(d\eta/dH)_{max}$ important for sensor applications, but also the particular shape of the $\eta(H)$ curve. The shape of a GMI curve can be controlled by induced magnetic anisotropy and/or bias DC. For wires and ribbons with transversal magnetic anisotropy, the double-peak GMI curve with the maxima close to $\pm H_K$ is observed. If the easy direction is parallel to the conductor axis, the single peak at $H = 0$ is present (as in Figure 8.5). In this case, however, the η_{max} sharply decreases with increasing anisotropy field. Helical anisotropy, induced in amorphous wires by torque stress or torque annealing, combined with a bias DC results in an asymmetric GMI curve [11]. Such a curve may be exploited by a linear field sensor.

8.2.3 Sensors

The high sensitivity of magnetoimpedance to external DC and low-frequency AC bias field (here the low frequency means the frequency that is at least one order lower than the driving frequency) can be used for magnetic field sensors and other sensors based on the change of a local magnetic field (such as displacement and electric current). The high driving frequency, which must be used to get sufficient sensitivity, involves many problems such as parasitic displacement currents in the circuits connecting the magnetoimpedance (MI) element with the signal source and the measuring unit, impedance mismatching, and the presence of reflected signals. To avoid these problems oscillation circuits are used, such as the Colpitts oscillator or the resonance multivibrator, with the MI element as the circuit inductance.

Because the MI elements may be as small as 1 mm, very localized weak magnetic fields can be detected. These types of sensors can be used, for example, for the detection of stray fields due to the cracks in steel sheets or for magnetic rotary encoders of high resolution.

The miniature magnetic field sensors based on the GMI effect have been used for various applications. They are especially appropriate for medical applications as small permanent magnet movement sensors for the control of physiological functions of the human body.

The temperature dependence of the GMI effect is analyzed in [12, 13]. Significant part of the temperature offset drift is caused by the temperature dependence of DC resistivity. Using optimized alloy composition, this effect was reduced and the remaining offset temperature coefficient of 30 nT/K is mainly caused by a temperature dependence of circular permeability. Further improvement down to 1.8 nT/K was achieved by using double-frequency bias-current modulation. The trade-off of this technique is an increase of the noise level [14].

8.2.3.1 Off-Diagonal GMI

These sensors are called magnetoimpedance, but they are of induction type, similar to transverse fluxgates (Chapter 3). While the sensor is still excited by the current flowing through the magnetic wire, the output is voltage induced into the solenoid coil wound around the wire. The origin of this induced voltage is the AC longitudinal magnetization of the wire, which depends on the external field applied in the direction of the wire. In amorphous wires with circumferential anisotropy, this sensitivity can be obtained by superimposing a DC component onto the AC excitation current. The main advantage of off-diagonal GMI sensors is their better offset temperature stability [15].

Small, off-diagonal GMI sensors are fabricated by Aichi Steel for use in compass modules for some mobile phones and wristwatches. They use a 0.5-mm-long amorphous wire, which is set on the lower part of the patterned coil and after that an upper part is plated forming the solenoid coil. Two electrodes of the amorphous wire ends are formed with plating. A coil pitch of the plated patterned coil can be as low as 2 μm. The sensor core is magnetized by short current pulses and the voltage induced into the solenoid pickup coil is processed [16].

8.2.3.2 Noise and Offset Stability of GMI Sensors

The sources of GMI sensor noise were analyzed in [17]. Probably the lowest achieved noise level for GMI sensors is 30 pT/√Hz for a 24-mm-long off-diagonal device presented in [15]. Due to the small diameter of the wire core, the sensors may have high spatial resolution and thus serve for detecting microbeads [18].

The disadvantage of GMI and similar sensors compared to a fluxgate is the perming effect, because the ferromagnetic core is usually not demagnetized during sensor operation.

8.3 Magnetoelastic Field Sensors

A number of mechanical variables such as force and torque are measured using magnetostriction: these are briefly covered in Chapter 11. In this chapter, we strictly discuss the sensors of the magnetic field.

In order to reach high sensitivity, magnetostrictive field sensors are often excited at longitudinal mechanical resonance. The response of the magnetostrictive sensors is, in general, not dependent on the field direction so the characteristic is odd and the sensitivity for low fields is very small. To obtain a linear response, either the DC bias field or AC modulation should be applied. In the former case, the sensor stability critically depends on the stability of this bias field. AC modulation technique requires an extra coil and a phase-sensitive detector, which increases the sensor complexity. Another disadvantage of magnetostrictive sensors is the sensitivity to temperature changes and mechanical vibrations.

8.3.1 Fiber-Optic Magnetostriction Field Sensors

The new wave of fiber-optical technology also brought new magnetic field sensors. Some of them, which are based on the Faraday effect, were described in Section 8.1. Here we mention the application of the optical fibers coupled to magnetostrictive material. The sensing element is either tape or wire, glued to the fiber [19], or a layer deposited on the fiber surface. The strain of the magnetostrictive transducer caused by an applied magnetic field causes a length change of the optical fiber, which is sensed by the interferometer. The block diagram of the sensor based on an all-fiber Mach-Zehnder interferometer is shown in Figure 8.7. Such a magnetometer is complicated and it has limited stability: 1-nT/hour drift at constant temperature is typical for these devices [20]. An array of fiber optic magnetostriction magnetometers for underwater detection of vessels was described in [21]. The sensors are powered with copper cable, but all the signals are transmitted optically. The sensors with 5-cm-long magnetostrictive amorphous strips exhibit 30 pT/$\sqrt{\text{Hz}}$ at 1-Hz noise, which is higher than that of the fluxgate sensor of the same length (Chapter 3).

Experiments were also carried out using magnetic fluids coupled to an optical fiber, but the performance of these sensors is poor [22]. Fiber Bragg grating is another technology that can be used to measure fiber elongation; it was also used for magnetic sensing [23].

8.3.2 Magnetostrictive-Piezoelectric (Magnetoelectric) Sensors

Magnetostrictive sensors may have piezo excitation or detection. The sensor geometry is shown in Figure 8.8.

The former piezo-driven type is excited by AC voltage applied to the electrodes of the piezo element, which is coupled usually through a viscous fluid to the high

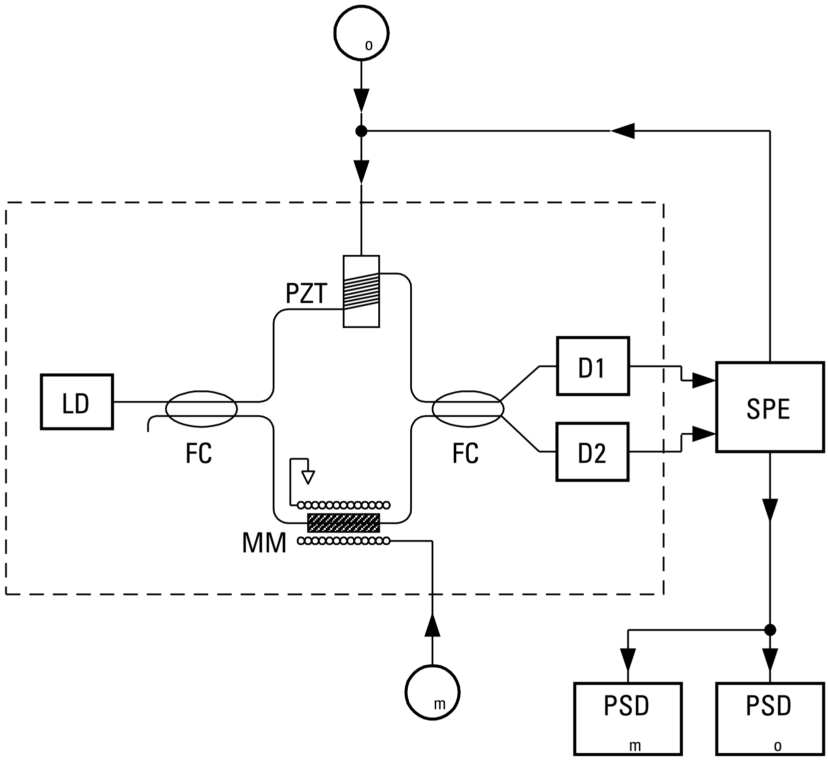

Figure 8.7 A fiber-optic magnetostriction magnetic field sensor based on a Mach-Zehnder interferometer consists of a laser diode (LD), fused couplers (FC), optical detectors (D1, D2), magnetostrictive material coupled to the fiber signal arm (MM), and a piezoceramic element for active compensation of the reference arm (PZT). (*After:* [20].)

magnetostriction ferromagnetic core. The sample vibration causes a change of the core properties, which are detected by the solenoid coil [24]. The hysteresis can be removed by magnetic shaking [25]. Such sensors may have a 1-nT resolution and a linear range of 1 to 100 μT, but poor temperature stability.

The latter type uses magnetic excitation of the core by an AC-supplied solenoid coil. The piezoelectric element is again interfaced to the core, but here it serves as a detector. Another possibility is to excite the core by an electric current flowing through it, so no coil is necessary [26]. If the current flowing through the core has frequency f, the size changes, and thus the output signal has frequency of $2f$; this is an advantage over other types of piezo-magnetostrictive sensors, because the excitation signal can be easily filtered out of the output. The common disadvantage of all the sensors excited by the current through the core is that the high amplitude of the excitation field is only close to the surface; the field in the middle is zero, which may cause hysteresis and perming. Serious problems are also associated with the current contacts.

Bulk magnetoelectric materials exhibit electric polarization when exposed to an external magnetic field. However, most magnetoelectric elements are artificial multilayer structures consisting of magnetostrictive and piezoelectric layers, which give larger magnetoelectric coefficients (dE/dH) than bulk magnetoelectric materials. Sensitivity of magnetoelectric structures can be increased by operating in the

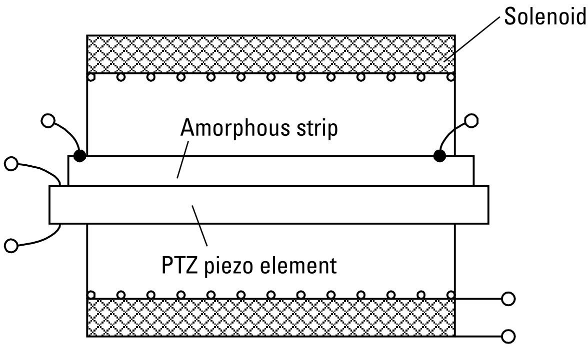

Figure 8.8 Magnetostrictive-piezoelectric magnetic field sensor.

mechanical resonance [27]. The achieved noise was 60 pT/√Hz at 10 Hz, which is more than one order of magnitude larger than that of fluxgate sensors.

Magnetoelectric sensors utilizing arrays of magnetoelectric nanowires composed of barium titanate and cobalt ferrite are presented in [28]. By utilizing magnetoelectric nanowires suspended across electrodes above the substrate, substrate clamping is reduced when compared to layered thin-film architectures; this results in enhanced magnetoelectric coupling. However, all similar devices are far from practical applicability as they are sensitive to mechanical vibrations and temperature changes.

8.3.3 Shear-Wave Magnetometers

The last type of the magnetoelastic magnetic field sensors is based on the magnetic field dependence of the elastic modulus E (ΔE effect), which causes a change of acoustic wave velocity. The basic sensor is shown in Figure 8.9. The piezo transmitter is driven by an RF source (1.8 MHz) and creates an acoustic wave that propagates with

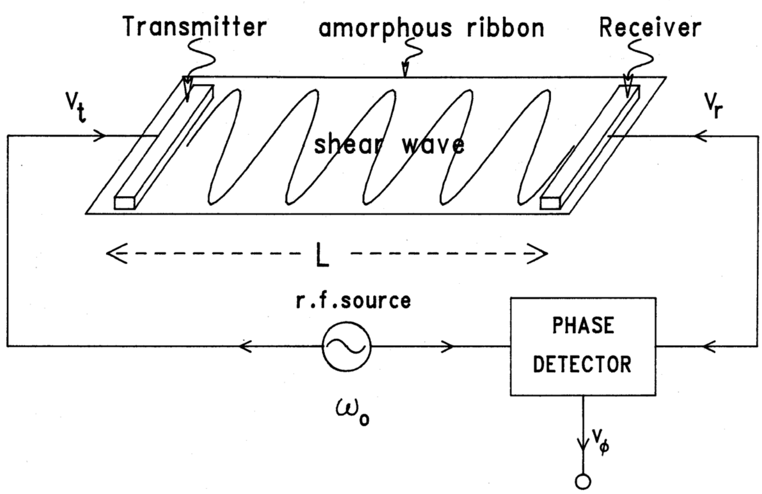

Figure 8.9 The principle of the shear-wave magnetometer.

2.6 km/s speed along the ribbon towards the piezo receiver. The device works in the continuous mode; the transmitted and received signals are processed in the phase comparator, which has a voltage output proportional to their phase difference and thus to the field-dependent velocity. The basic characteristic is odd (Figure 8.10(a)) and the phase noise caused by mechanical and temperature disturbances is high.

Thus, the modulation technique is used: the measured DC field is superposed by a low-frequency AC field produced by the solenoid. The low-frequency AC signal is phase-modulated as shown in Figure 8.10. With changing slope of the first odd curve, the phase of the response is reversed. If the receiver output is demodulated by another phase-sensitive detector, the resulting response is even; see Figure 8.10(b). The sensor was completed by field feedback (Figure 8.11), which improves the linearity [29]. The resulting sensor has a noise of 100 pT/√Hz at 1 Hz, but still with a large offset temperature coefficient of 8.4 nT/K.

8.4 Lorentz Force Magnetometers

A micromachined Lorentz force magnetic sensor achieved a field resolution of 10 nT for a 100-μA measuring current [30]. The Lorentz force, which is proportional to the measured field and the measuring current, deflects the free-standing MEMS structure. The motion is made periodic by applying an AC measuring current, usually at the mechanical resonance frequency. The advantage of Lorentz force magnetometers is their high linearity and the possibility to change their range widely by selecting the measuring current. The sensor can work up to 50T [31].

A remotely interrogated 3-axis fiber laser magnetometer based on the Lorentz force was described in [32]. Each sensor comprises a current carrying nonmagnetic bridge, which experiences the Lorentz force generated in a magnetic field. A metalized fiber laser attached to the bridge measures the induced strain. The 2-nT/√Hz noise is achieved with only 75 mA-rms of current. The sensor node is separated from the interrogation electronics with a 1-km fiber optic cable and qualified to an operating depth of 100m.

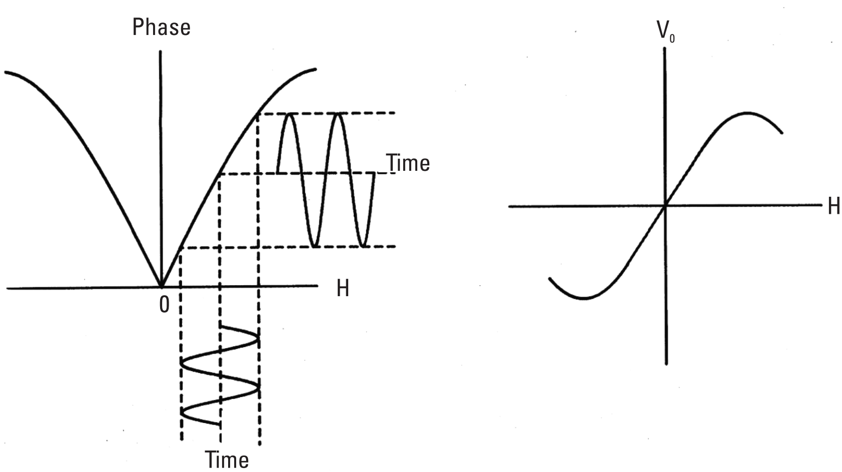

Figure 8.10 Principle of the AC phase modulation.

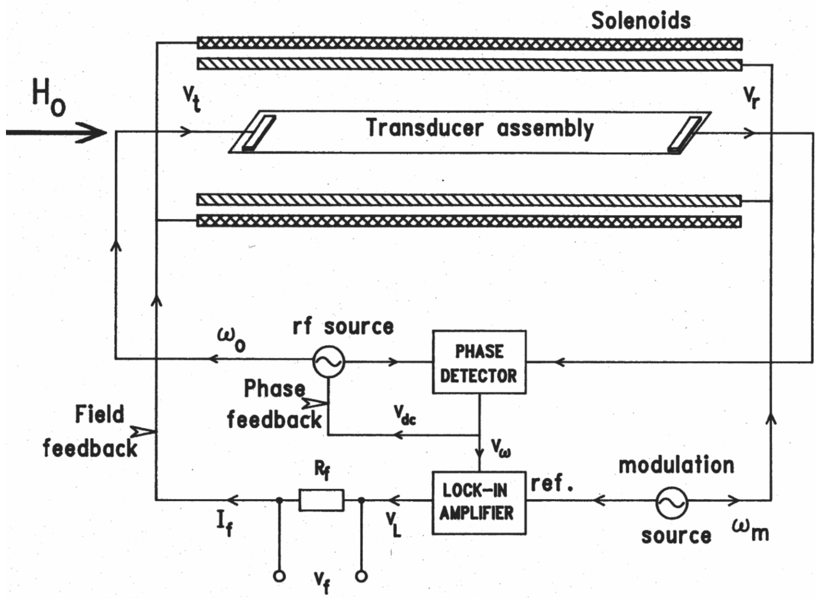

Figure 8.11 Complete shear-wave feedback magnetometer.

A dual-resonator MEMS magnetic field gradiometer based on the Lorentz force with a noise level of 3.07 μT/√ Hz was reported in [33].

8.5 Biological Sensors

Magnetic orientation was first proven in birds and later in some kinds of fish, sea turtles, and honeybees. A lot of information can be found in the book written by R. Wiltschko and W. Wiltschko [34].

8.5.1 Magnetotactic Bacteria

Magnetotactic bacteria are found in salt and fresh water sediments. In most cases, they use the Earth's magnetic field to find the vertical direction, as their density is too low to use gravitation. They are anaerobic, so if they are stirred up into the surface oxygen-rich water, they move downwards into their favorable environment. Magnetotactic bacteria in the Southern hemisphere are reversely polarized than those from the Northern hemisphere. They can be reversed by a strong magnetic field. Although the bacteria actively move, the magnetic alignment along the field lines is a passive process. The magnetic response is caused by chains of magnetite (Fe_3O_4) or greigite (Fe_3S_4). Some bacteria actually produce magnetic minerals for themselves from nonmagnetic FeS_2 [35].

8.5.2 Magnetic Orientation in Birds

Migrating birds and homing carrier pigeons use the Earth's field for navigation besides the Sun and stars. The magnetic sensor in birds is very different from man-made compasses. The bird can perceive the field direction, but not the polarity. Reversing the field direction causes no response. This behavior is called inclination compass: according to the inclination, the bird can distinguish between the poleward direction (i.e., when field lines point to the ground) and equatorward direction (field lines point to the sky). The birds are magnetically disoriented if the field has a horizontal direction. The bird can use its compass only if the magnetic field is constant within about ±5% to 10% of the steady level, but they can slowly adopt to another constant level.

Sea turtles also have an inclination compass, while salmon have a polarity compass, which works well in a horizontal field. The magnetic compass orientation can be innate (first migration of young birds) or acquired (local orientation and homing). Magnetic orientation is normally only one component in the animal integrated navigation system, besides the Sun, and star compass, inclination sensors, internal clock, memory for visual landmarks, and other factors such as odors.

There are indications that some animals (e.g., carrier pigeons) may even use the information about local magnetic gradients and anomalies such as man-made sophisticated autonomous missiles.

The knowledge of how the animals sense the magnetic field is very weak. Three realistic principles were suggested: induction sensors, chemical sensors, and force sensors (based on magnetized particles).

Induction sensors are very likely used by fish: movement in the Earth's field induces voltages inside the body, which are strong enough to be detected by the fish electroreceptors.

Chemical sensors, mainly photopigments, are another hypothesis. Although their mechanism is unclear, there are behavioral and physiological indications that, in some cases, the magnetic field information comes from the eye and depends on visible light. Magnetic particles are present mainly as single-domain, but they may form chains. They may interact with membranes and neurons; however, the complete evidence of such a mechanism has not been given yet.

References

[1] Herrera-May, A. L., et al., "Mechanical Design and Characterization of a Resonant Magnetic Field Microsensor with Linear Response and High Resolution," *Sensors and Actuators A: Physical*, Vol. 165, No. 2, February 2011, pp. 399–409.

[2] Heremans, J., "Solid-State Magnetic-Field Sensors and Applications," *Journal of Physics D-Applied Physics*, Vol. 26, No. 8, August 1993, pp. 1149–1168.

[3] Roumenin, C., *Solid-State Magnetic Sensors*, New York: Elsevier, 1994.

[4] Hinz, G., and H. Voigt, "Magnetoelastic Sensors," Chapter 4 in Boll, R., and K. J. Overshott (editors), *Magnetic Sensors*, Veiden: VCH, 1989, pp. 153–205.

[5] Amirsolaimani, B., et al., "High Sensitivity Magnetometer Using Nanocomposite Polymers with Large Magneto-Optic Response," *Optics Letters*, Vol. 43, No. 19, October 2018, pp. 4615–4618.

[6] Hubert, A., and R. Schäfer, *Magnetic Domains: The Analysis of Magnetic Microstructures*, New York: Springer, 2014.

[7] Mohri, K., et al., "Magnetoinductive Effect (MI Effect) in Amorphous Wires," *IEEE Transactions on Magnetics*, Vol. 28, No. 5, September 1992, pp. 3150–3152.

[8] Beach, R. S., and A. E. Berkowitz, "Giant Magnetic-Field Dependent Impedance of Amorphous FECOSIB Wire," *Applied Physics Letters*, Vol. 64, No. 26, June 1994, pp. 3652–3654.

[9] Knobel, M., M. Vazquez, and L. Kraus, "Giant Magnetoimpedance," in K. Buschow, (ed.), *Handbook of Magnetic Materials*, New York: Elsevier, 2003.

[10] Kurlyandskaya, G. V., et al., "Magnetoimpedance of Sandwiched Films: Experimental Results and Numerical Calculations," *Journal of Magnetism and Magnetic Materials*, Vol. 242, April 2002, pp. 291–293.

[11] Martinez-Garcia, J. C., et al., "Asymmetrical Magnetoimpedance Effect in Partially Devitrified Co66Fe4Si16B12Mo2 Ribbons," *Sensor Letters*, Vol. 7, No. 3, June 2009, pp. 507–511.

[12] Malatek, M., P. Ripka, and L. Kraus, "Temperature Offset Drift of GMI Sensors," *Sensors and Actuators A: Physical*, Vol. 147, No. 2, October 2008, pp. 415–418.

[13] Hernando, B., et al., "Temperature Dependence of Magnetoimpedance and Anisotropy in Nanocrystalline Finemet Wire," *IEEE Transactions on Magnetics*, Vol. 44, No. 11, November 2008, pp. 3965–3968.

[14] Esper, A., et al., "Offset Reduction in GMI-Based Device by Using Double-Frequency Bias-Current Modulation," *IEEE Transactions on Magnetics*, Vol. 55, No. 1, 2019, pp. 1–4.

[15] Nabias, J., A. Asfour, and J. P. Yonnet, "Effect of the Temperature on the Off-Diagonal Giant Magneto-Impedance (GMI) Sensors," *International Journal of Applied Electromagnetics and Mechanics*, Vol. 59, No. 2, 2019, pp. 465–472.

[16] Mohri, K., et al., "Recent Advances of Amorphous Wire CMOS IC Magneto-Impedance Sensors: Innovative High-Performance Micromagnetic Sensor Chip," *Journal of Sensors*, 2015.

[17] Traore, P. S., et al., "Noise Performance of SDR-Based Off-Diagonal GMI Sensors," *IEEE Sensors Journal*, Vol. 17, No. 19, October 2017, pp. 6175–6184.

[18] Kim, D., et al., "Operating Field Optimization of Giant Magneto Impedance (GMI) Devices in Micro Scale for Magnetic Bead Detection," *IEEE Transactions on Magnetics*, Vol. 44, No. 11, November 2008, pp. 3985–3988.

[19] Zhang, N. H., et al., "Temperature-Insensitive Magnetic Field Sensor Based on an Optoelectronic Oscillator Merging a Mach-Zehnder Interferometer," *IEEE Sensors Journal*, Vol. 20, No. 13, July 2020, pp. 7053–7059.

[20] Koo, K. P., et al., "A Compact Fiberoptic Magnetometer Employing an Amorphous Metal Wire Transducer," *IEEE Photonics Technology Letters*, Vol. 1, No. 12, December 1989, pp. 464–466.

[21] Bucholtz, F., et al., "Demonstration of a Fiber Optic Array of 3-Axis Magnetometers for Undersea Application," *IEEE Transactions on Magnetics*, Vol. 31, No. 6, November 1995, pp. 3194–3196.

[22] Luo, Y., et al., "A Novel Optical Fiber Magnetic Field Sensor Based on Mach-Zehnder Interferometer Integrated with Magnetic Fluid," *Optik*, Vol. 174, 2018, pp. 252–258.

[23] Shao, Z. H., et al., "Fiber-Optic Magnetic Field Sensor Using a Phase-Shifted Fiber Bragg Grating Assisted by a TbDyFe Bar," *Sensors and Actuators A: Physical*, Vol. 261, July 2017, pp. 49–55.

[24] Mermelstein, M. D., "A Magnetoelastic Metallic-Glass Low-Frequency Magnetometer," *IEEE Transactions on Magnetics*, Vol. 28, No. 1, January 1992, pp. 36–56.

[25] Prieto, J. L., et al., "Reducing Hysteresis in Magnetostrictive-Piezoelectric Magnetic Sensors," *IEEE Transactions on Magnetics*, Vol. 34, No. 6, November 1998, pp. 3913–3915.

[26] Prieto, J. L., et al., "Magnetostrictive-Piezoelectric Magnetic Sensor with Current Excitation," *Journal of Magnetism and Magnetic Materials*, Vol. 215, June 2000, pp. 756–758.

[27] Tu, C., et al., "Mechanical-Resonance-Enhanced Thin-Film Magnetoelectric Heterostructures for Magnetometers, Mechanical Antennas, Tunable RF Inductors, and Filters," *Materials*, Vol. 12, No. 14, July 2019.

[28] Bauer, M. J., et al., "Magnetic Field Sensors Using Arrays of Electrospun Magnetoelectric Janus Nanowires," *Microsystems & Nanoengineering*, Vol. 4, December 2018.

[29] Kilby, C. F., P. T. Squire, and S. N. M. Willcock, "Analysis and Performance of a Shear-Wave Magnetometer," *Sensors and Actuators A: Physical*, Vol. 37-8, June-August 1993, pp. 453–457.

[30] Kyynarainen, J., et al., "A 3D Micromechanical Compass," *Sensors and Actuators A: Physical*, Vol. 142, No. 2, April 2008, pp. 561–568.

[31] Park, B., et al., "Lorentz Force Based Resonant MEMS Magnetic-Field Sensor with Optical Readout," *Sensors and Actuators A: Physical*, Vol. 241, April 2016, pp. 12–18.

[32] Cranch, G. A., et al., "Remotely-Interrogated Three-Axis Fiber Laser Magnetometer," *IEEE Sensors Journal*, Vol. 13, No. 3, March 2013, pp. 890–899.

[33] Kahr, M., et al., "Dual Resonator MEMS Magnetic Field Gradiometer," *Sensors*, Vol. 19, No. 3, February 2019.

[34] Wiltschko, R., and W. Wiltschko, *Magnetic Orientation in Animals*, New York: Springer, 2012.

[35] Lin, W., et al., "On the Origin of Microbial Magnetoreception," *National Science Review*, Vol. 7, No. 2, February 2020, pp. 472–479.

CHAPTER 9

Applications of Magnetic Field Sensors and Magnetometers

Pavel Ripka, Mario H. Acuña, and Werner Magnes

In this chapter, we describe applications of precise magnetic field sensors and magnetometers such as the detection of small magnetic objects, navigation, and geophysics. We cover applications for space and security most extensively, as those sectors are traditional accelerators for the magnetometer development. Applications of magnetic principles for the measurement of nonmagnetic variables such as distance, force, torque, and electric current are described in Chapter 11.

9.1 Biomagnetic Measurements

Magnetic trackers (Chapter 11) are used to determine the position of tools inside the body (endoscope, colonoscope, biopsy needle) and to observe biomechanical motions (eyelid movement, articulatory movement). Trackers are also used in biomechanical feedback systems for handicapped individuals. A simple device to detect the vicinity of magnetic markers was developed for laparoscopic surgery [1]. Magnetic distance sensors were used for monitoring the gastric motility [2]. The relative joint angle was measured in [3] by using a pair of triaxial AMR magnetometers fused with accelerometers and angular rate sensors. Thanks to the use of magnetic sensors, the system is resistant to all translatory and angular body movements and drifts of inertial sensors. A bilayer thin-film curvature (bending) sensor attached to the neck was used to measure cardio-respiratory activity [4]. Glass-covered magnetic wires were used as targets to monitor the movement of the heart valve [5].

The radiation-free magnetic method to measure gastric emptying was developed by Forsman [6]. The magnetic particles of maghemite (γ-Fe_2O_3) were ingested in the form of pancakes. Before each measurement, the intragastric powder was magnetized by a 40-mT field generated by an air coil pair. The first-order gradient in the direction perpendicular to the skin surface was measured by a 140-mm base length fluxgate gradiometer. The field gradient was scanned by moving the tested person on a pneumatically driven bench. Measuring the particle remanence has advantages over the susceptibility method: the required amount of the magnetic tracer is smaller (0.4 g for remanence method instead of 15 g for susceptibility), and position error is smaller (signal ~$1/r^3$ instead of $1/r^6$). The drawback is the tendency of magnetized particles to form clusters along with a high required field (40 mT was not sufficient). The magnetic method was proved to be sufficiently sensitive to replace radio-labeled tests in case of repeated measurements or pregnancy. An AC system with an array of AMR sensors was developed by Paixao et al. for monitoring movements of the magnetic tablet or food marked with magnetite [7].

Magnetic particles are used for the magnetic labeling of drugs, analytes, antibodies, and other substances [8]. They are also used for targeted drug delivery, for enhancing the contrast of MRI, and for hyperthermia. Another application is for manipulation and detection in microfluidic devices [9, 10]. TMR sensors are well suited for the detection of individual magnetic particles because of their small size [11, 12].

Magnetic particle imaging uses the nonlinearity of their magnetization characteristics. Magnetic particle imaging uses a magnetic gradient field (typically 2–6 T/m), known as a selection field, to saturate all superparamagnetic particles outside the selected region. Particles in this region are detected and their number is estimated. The excitation field for the particles is typically a very pure sinewave with 20–45-kHz frequency and 20-mT amplitude. The selected region is shifted over an imaging volume via a rapidly varying excitation/drive field to produce an image. The field of view can be increased by mechanical translation [13].

Magnetopneumography is a magnetic method that can detect ferromagnetic dust deposited in human lungs by using its magnetic moment after DC magnetization [14, 15]. It may be used for the examination of welders, grinders, and other metal workers. Ferromagnetic dust was found also in the lungs of miners and other professions, but the scaling and interpretation of the field values are much more difficult as the magnetic properties of the dust are quite variable. A study of the magnetic properties of the tissue and extracted dust samples from the lungs of exposed workers had shown that even the dust and aerosols originating from nonmagnetic stainless steel can be detected, as they become ferromagnetic during the welding or grinding process. The DC field necessary to sufficiently magnetize the dust in lungs is 100–200 mT (i.e., the magnetization device should be either a superconducting coil or an electromagnet with a yoke); lower field values from air coils give irreproducible results.

Magnetic dust has also been used as a tracer for measuring lung dust clearance. An inhaled dosage of 1 mg is sufficient to follow clearance over 1 year and longer [16, 17].

SQUID magnetometers are traditionally used for biomagnetic measurements (Table 7.5). It has been shown that fluxgate gradiometers (Chapter 3) can be made sufficiently sensitive for magnetopneumography [18, 19]. Fluxgates are much cheaper, can be made portable, and require no cryogenic refrigeration. Although atomic magnetometers (Chapter 6) also do not require cooling, a problem with the current technology is that the sensitivity is inversely dependent on the ambient magnetic field, which makes them unsuitable for magnetopneumography.

A magnetopneumographic system consists of three parts [20]:

1. A magnetization device, which generates a magnetic field of a required magnitude in the whole volume of human lungs;
2. A gradiometer, which maps the remanent magnetic field of the lungs;
3. Software that solves the inverse problem (i.e., estimates the size, location, and density of the dust deposit).

Figure 9.1 shows the magnetic field distribution of a local dust deposit modeled by 250 mg of magnetite distributed in 250-cm^3 volume in the central part of the lung model. The deposit position is shown and the coordinate system is defined in Figure 9.1(a). The sample was magnetized by a 100-mT DC field and the remanent field in the z direction (perpendicular to skin) was measured as a function of distance, as shown in Figure 9.1(b). The magnetic field distribution in the xy-plane is shown in Figure 9.1(c).

Figure 9.2 shows the situation in which the dust is homogeneously deposited in the whole lung volume; it is clear how fast the spatial resolution drops with distance from the measured object.

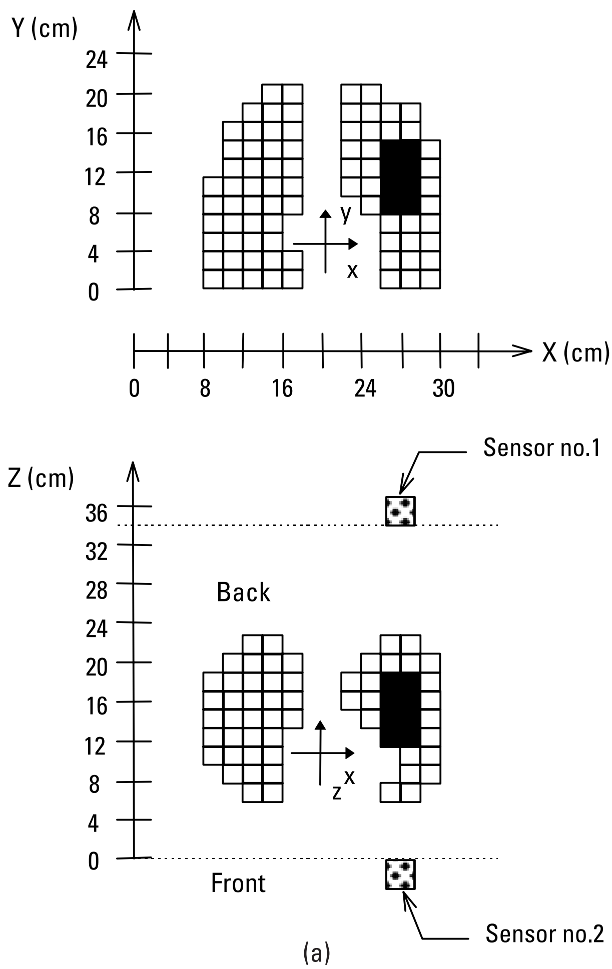

Figure 9.1 Magnetic fields of a local deposit of magnetite in the model of human lungs (250 mg of magnetite in 256 cm^3). (a) Size and location; (b) magnetic field in the z direction as a function of the sensor distance (shown are the measured and calculated values (dipole $1/r^3$ model)); and (c) magnetic field distribution in the xy-plane (measured values) in the distance $z = 0$ (skin surface).

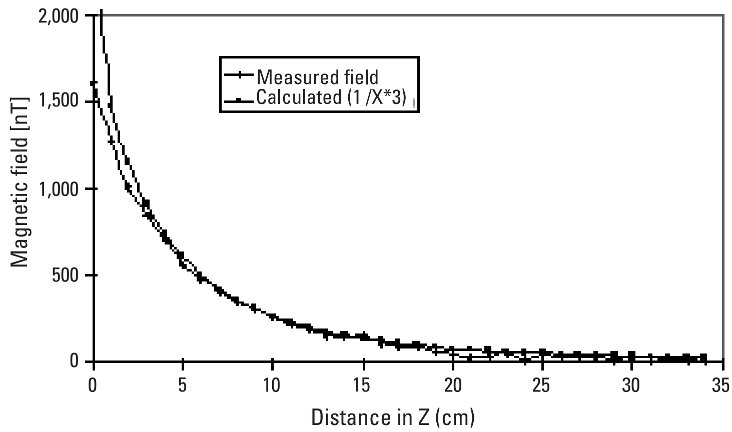

(b)

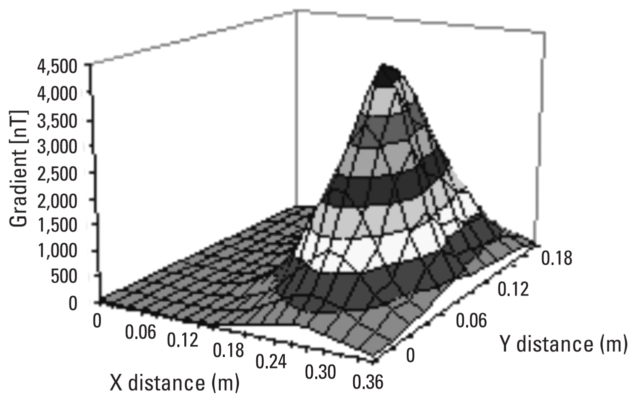

(c)

Figure 9.1 (continued)

Figure 9.3 shows the field gradient distribution of a professional welder. The concentration of the dust is decreasing towards the waist, which is caused by filtration mechanism of lungs.

Magnetocardiography is measurement of magnetic field of heart. This is mostly made by SQUID (Chapter 7), but can also be made by best fluxgates. Fetal magnetocardiography requires a much better resolution, so a shielded room and SQUID are standard. An atomic gradiometer with sufficient resolution was also reported [21].

Magnetoencephalography is measurement of the magnetic field of brain. This requires a shielded room and SQUID; details are described in Chapter 7.

9.2 Navigation

For centuries, the magnetic compass has been one of the main navigation devices [22]. The compass should be gimbaled (leveled) and its reading should be corrected by a declination angle, because the magnetic North is not on the Earth's rotational

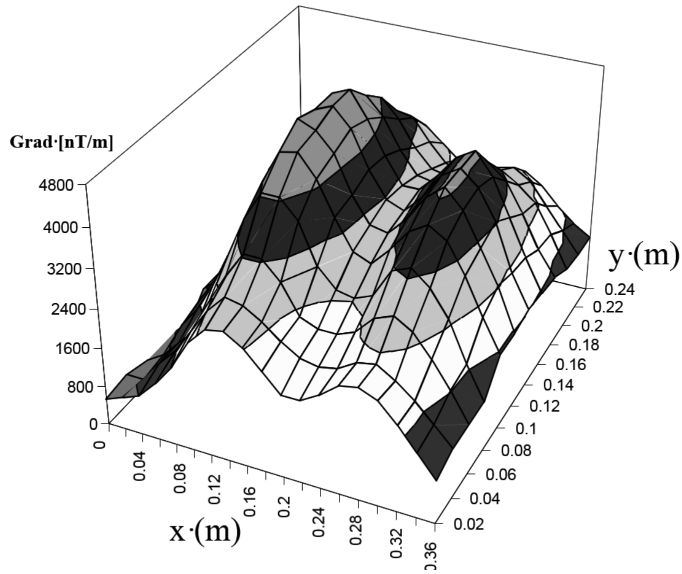

(a)

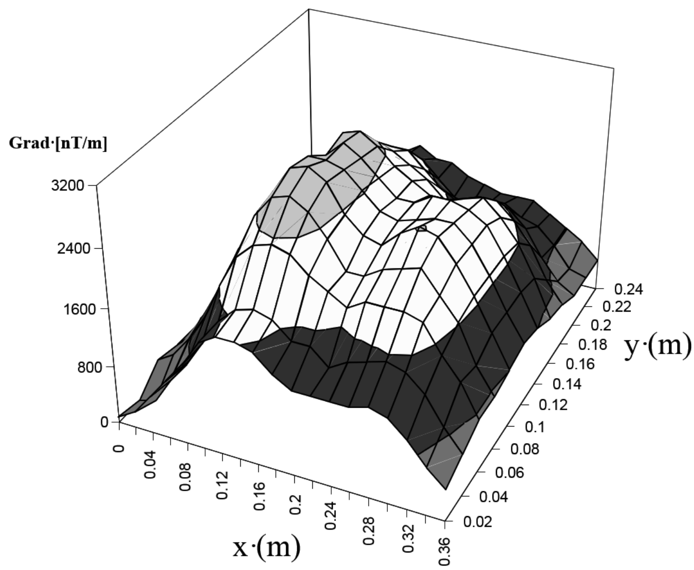

(b)

Figure 9.2 Gradient distribution in the *xy*-plane 6 cm from the lung model containing 4g of magnetite in the distance: (a) $z = 6$ cm and (b) $z = 8$ cm.

axis. Declination changes with position on Earth and slowly changes with time. The angle between the Earth's field vector and the horizontal plane is called dip or inclination (Figure 9.4). This angle is close to 90° in the polar regions, which causes well-known navigation problems. Local field anomalies may also cause fatal errors.

The limiting factor of the precision of magnetic navigation is often the magnetic field of the vehicle, which can be caused by magnetic materials and DC loops. DC loops can be minimized by design (twisted conductors instead of using chassis as one conductor), but they still are a serious problem in the case of solar cells. A lot

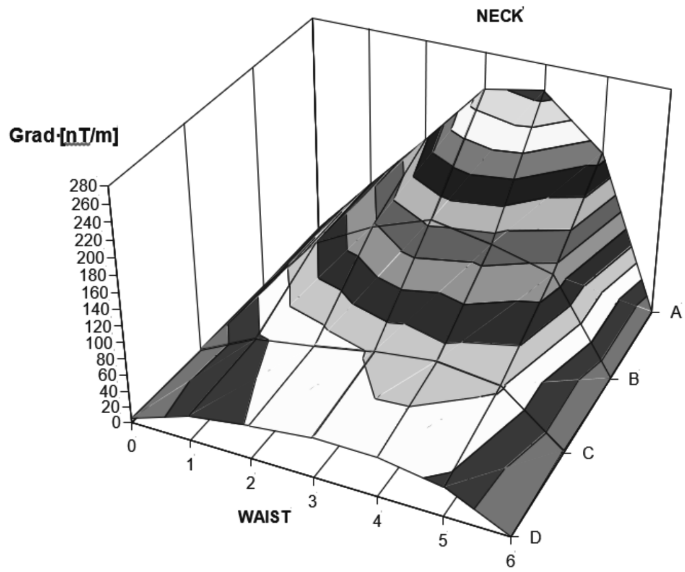

Figure 9.3 Magnetic field gradient measured in vivo on a welder. The grid was 5 cm.

of magnetic navigation systems allow compensation for field distortion caused by ferromagnetic parts, but they need periodical recalibration. The Earth's field is too weak to saturate the magnetic parts in the vehicle. Therefore, their magnetization characteristics is nearly linear with a constant (hard) component and a field proportional (soft) component. The hard component (remanent magnetization) is caused by permanent magnets and remanence of magnetized iron parts; its effect is equivalent to offsets of field sensors. The soft component (induced magnetization) is caused by the permeability of ferromagnetic parts; its effect is equivalent to a change of sensitivity of the field sensors [23]. The vehicle magnetometer readings as a function of direction are shown in Figure 9.5. If the host is magnetically clean, the polar plot is a circle, and individual sensor outputs are orthogonal sinewaves, as shown in Figure 9.5(a). The soft component causes that the polar circle becomes ellipsoid; the hard component causes the center of this ellipsoid to be displaced from the [0,0] point, as shown in Figure 9.5(b). After a simple compensation (four variables: two sensitivities and two offsets), some distortion of the polar plot still exists, as shown in Figure 9.5(c). This may be caused by field gradients, contributions to a vehicle horizontal field from the Earth's field vertical components due to the tensor character of the effective (apparent) permeability and other effects. Some systems allow more complex compensation, which uses more than the mentioned 4 correction coefficients.

The traditional pivoting needle has serious constraints: the sensor cannot be separated from the display, it does not allow to make automatic corrections of the reading, the instrument has a moving part, it is sensitive to vibrations; thus, for use in vehicles, it should be damped by liquid in order to slow the response to fast maneuvers.

The fluxgate compass is a popular device used in aircraft, ships, and cars. It is still a part of modern navigation systems together with GPS and inertial sensors.

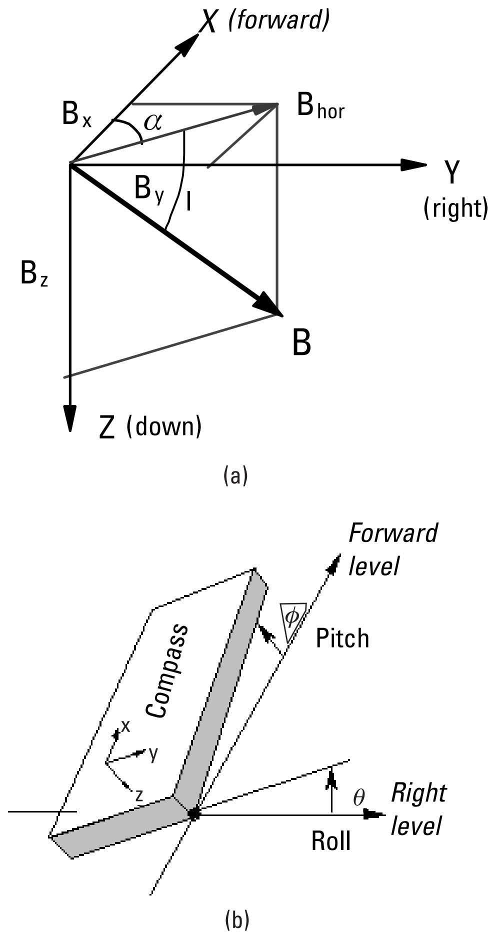

Figure 9.4 (a) Earth's field vector **B** components: vertical component $\mathbf{B}_z$ and horizontal component $\mathbf{B}_{hor}$, which is a vector sum of $\mathbf{B}_x$ and $\mathbf{B}_y$. α is the magnetic azimuth or heading, and *I* is the inclination or dip. (b) Pitch and roll are the inclinations of the magnetometer from a horizontal plane. True azimuth should be corrected for declination.

Nowadays, it is used mostly as a backup during the loss of the GPS signal. The traditional type of fluxgate compass consists of a leveled (gimbaled), double-axis, single ring-core sensor with a pair of orthogonal pickup coils (Section 3.14). The 0.1° precision is easily achievable in a wide temperature range, but a lot of cheap and low-power devices have an accuracy of 0.5° or 1°, which is still sufficient for consumer products such as compass watches [24].

The strapdown or electronically gimbaled compass has a 3-axial sensing head, which is fixed to the host. The sensing head inclination is measured by two inclinometers (usually measuring the roll (angle between trajectory and horizontal plane) and pitch (inclination orthogonal to trajectory). The horizontal field component and the heading information are then calculated from the magnetometer and inclinometer readings.

Magnetoresistors are standard sensors for compass applications if 1° accuracy is sufficient [25]. AMR compass sensors with electronics are integrated on multichip modules. The high-temperature dependence of their sensitivity (~600 ppm/°C) is

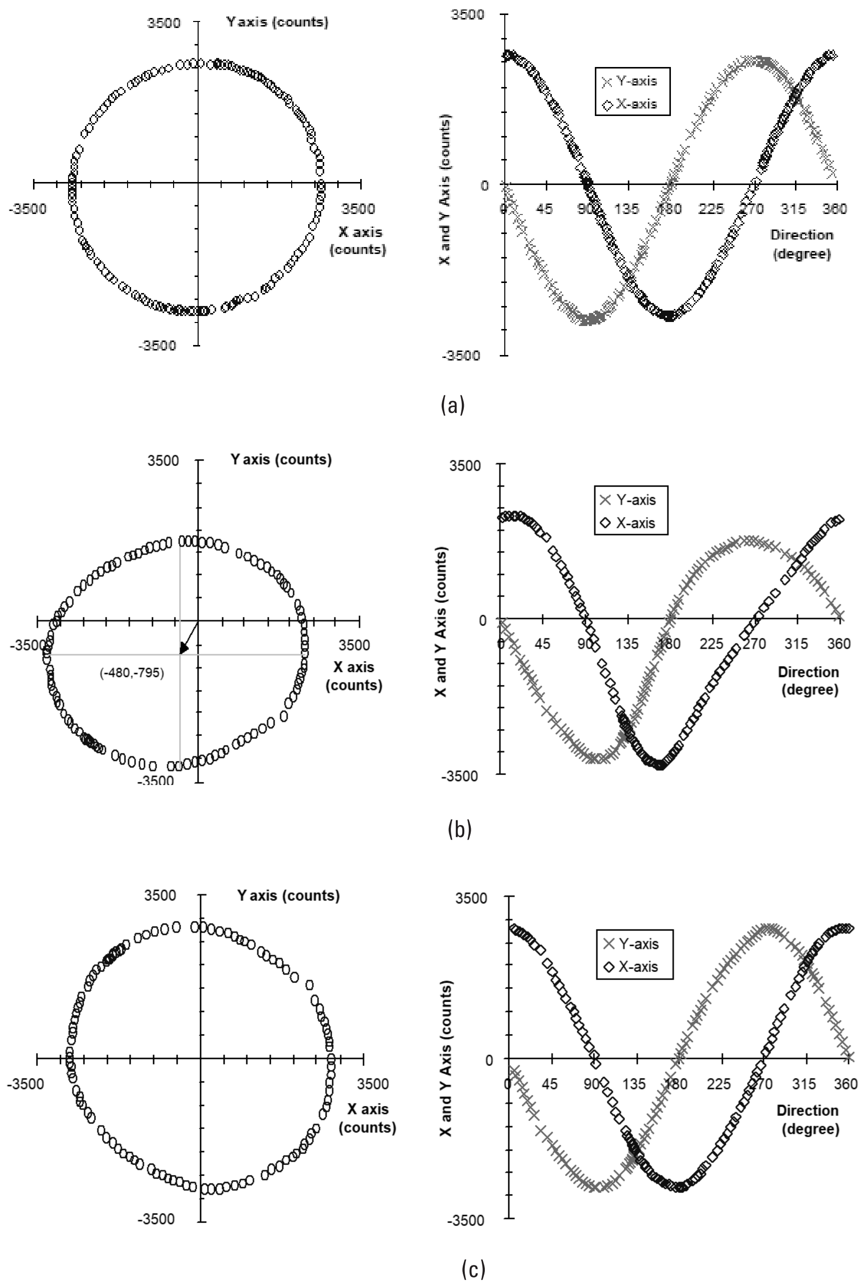

Figure 9.5 Vehicle magnetometer readings as a function of direction: (a) without disturbances, (b) disturbed by the vehicle magnetic field, and (c) corrected for soft (scale) and hard (offset) components [23].

suppressed by ratiometric output of two perpendicular sensors. Using the flipping mechanism (Chapter 4), offset temperature variations may be below 0.25 nT/°C, which corresponds to an angular error below 0.1° in the military temperature range from −55°C to 125°C. Honeywell manufactures a digital compass module HMR 3000, which has 0.1° resolution and 0.5° rms accuracy. Although the manufacturer specifies the typical offset drift as ±114 ppm/°C, which corresponds to 23 nT/°C, the measured average value of the offset temperature coefficient was 0.2 nT/°C (with set and reset flipping pulses continuously on). Other modules may have digital output and smaller size or power consumption, but they are less accurate.

Navigation of mobile robots is a specific discipline, which was covered in the classic book by Borenstein, Everett, and Feng [26]. The magnetic methods include a magnetic compass, artificial landmarks made by permanent magnets, magnetic guides made of AC-powered induction loops, RF beacons, and also tracking methods, which are described in Chapter 11.

Magnetic navigation is used also in the drilling industry, both for vertical drilling [27] and for horizontal drilling [28, 29].

9.3 Military and Security

Magnetic sensors are used for the detection of ferromagnetic and conduction objects at checkpoints and ports and the surveillance of large areas including maritime surveys. All these measurements should be made in the presence of noise and clutter. These tasks usually require using multisensory systems and complicated data processing [30]. All these technologies have also industrial applications such as the detection of ferromagnetic objects for protecting conveyor belts in surface coal mines [31].

9.3.1 Unexploded Ordnance (UXO)

UXO contains dangerous explosives, propellants, or chemical agents. It may be unexploded either through malfunction or intentionally by design. The size ranges from several millimeters (pistol munition) to several meters (missiles and bombs). UXO represents a serious hazard and it should be located and cleaned from former military areas and battlefields. Searches for unexploded bombs from World War II should still be made prior to starting construction work in many European and Asian cities.

The most effective method of location of buried ordnance is mapping the magnetic field. The magnetometers are man-portable or vehicle-towed or they can be carried under the drone. The instruments used are either scalar magnetometers (proton, Overhauser or Cesium vapor; see Chapter 6) or vector fluxgates (Chapter 3). SQUID magnetometers (Chapter 7) have also been used, but only on an experimental basis [32]. The remanent magnetization of ordnance is usually small; for example, airborne bombs can be demagnetized by ground impact. The magnetic signature does not depend much on the ferrous mass; objects with a thick iron shell and a nonmagnetic central part behave similarly as if they were solid. The signature is proportional to outer volume, shell thickness, relative permeability, length/diameter ratio, and orientation in the geomagnetic field [33, 34]. Prolate objects in vertical or North-South horizontal position are easily detectable; if they are positioned exactly North-West, their total field signature may be very low. Figure 9.6 shows calculated magnetic signature of a 155-mm projectile in middle latitudes (65° declination of the Earth's field). If a 150-cm-deep object is located horizontally in North-South direction, the signature has a typical local peak maximum and valley

(Figure 9.6(a)), while the total field signature of vertically located projectile has only one peak (Figure 9.6(b)).

The field work techniques for location of UXO are similar to those used for geophysical prospecting (Section 9.7). The realistic detectable field signature is 1 nT, although the instrument noise is sometimes declared to be much better. A large 2.4-m-long bomb can be easily located from more than a 6-m distance, while a 12.7-mm caliber projectile is hardly detectable from 20 cm. A database of real ordnance signatures at various geographical locations is available from the webpage of Geneva International Centre for Humanitarian Demining: https://www.gichd.org/.

One method of inversion of magnetic data measured by scalar gradiometer was described in [35]. Vectorial or tensor gradiometers are less stable and require calibration, but potentially give more information [36]. Using total magnetic field gradient, a dipole can be localized using a closed-form formula [37]. A detector for the magnetic anomaly of a moving ferromagnetic target in the signal of 3-axis

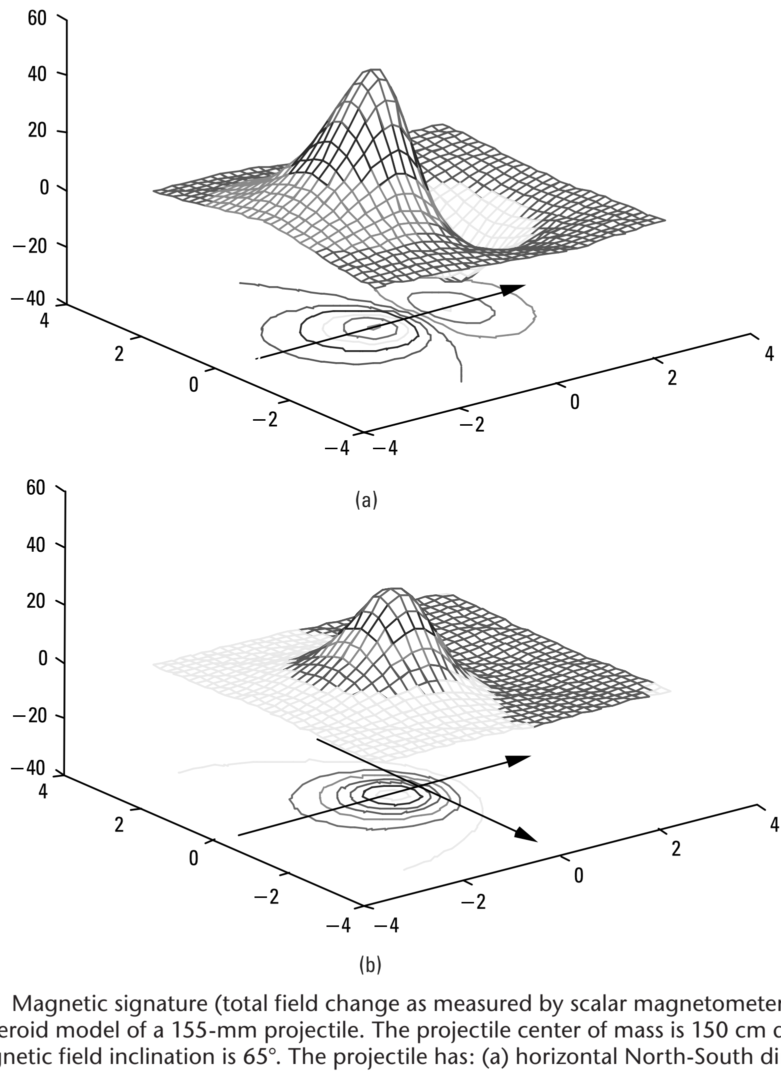

Figure 9.6 Magnetic signature (total field change as measured by scalar magnetometer) of a prolate spheroid model of a 155-mm projectile. The projectile center of mass is 150 cm deep. Earth's magnetic field inclination is 65°. The projectile has: (a) horizontal North-South direction and (b) vertical direction. (*From:* [34].)

magnetometer is described in [38]. The detector can be implemented as a digital filter that allows for real-time applications such as intruder detection. Applications of this class are used for perimeter protection to detect a person passing with a ferromagnetic item. Magnetic signature analysis using TMR sensor array for security checks allows detection and recognition of items such as knives, guns, and phone from a 50-cm distance [39].

Electromagnetic methods utilize eddy currents for measuring the difference between the conductivity of the soil and buried objects. The source coil is either supplied by a variable frequency sinewave (frequency-domain systems) or a pulsed source (time-domain systems). The field from an eddy current is usually detected by a coil (which may be identical with the transmitter coil in the time-domain systems). Mine locators with proper signal processing may work even in ferromagnetic soils [40]. Using an array of AMR or GMR sensors for this purpose may increase the system sensitivity and resolution [41]. Another electromagnetic method is a ground penetrating radar, which directs short electromagnetic pulses into the ground and monitors the reflections. These methods can detect nonferrous or even nonmetal objects such as plastic landmines. Similar magnetic and electromagnetic methods are used for weapon detection.

The methods of underwater UXO and cables detection and localization are reviewed in [42].

9.3.2 Target Detection and Tracking

Magnetic sensors are used to detect and locate vehicles and to track the autonomous missiles or intelligent ammunition during the flight. The fluxgate sensors used for projected grenades should be able to withstand accelerations of several thousands of gravitational force (g) when they are launched.

Submarine detection is a special topic. Underwater sensor fields can detect very small field gradients, because these sensors (usually fluxgate) are kept at a constant temperature and they can be made long. The countermeasures include demagnetization (degaussing) of the whole submarine and extensive use of nonmagnetic materials such as titanium instead of iron.

9.3.3 Antitheft Systems

Goods in shops or books in libraries contain small labels which could be detected at the exit. These labels should be invisible, give strong specific response, and if possible enable an easy deactivation. Various electromagnetic antenna resonators, magnetoelastic resonators (Section 9.6), and Wiegand wires (Chapter 11) are being used. Deactivation may be performed, for example, by burning of the flat coil resonator by a strong pulse of high-frequency electromagnetic energy or by demagnetization of the magnetically hard part of the Wiegand wire. Exhibited pieces of art may have an attached permanent magnet. Several magnetic sensors (fluxgates or magnetoresistors) then detect field change, which accompanies any movement.

Similar methods are used for identification and authorization, but here the label may be visible. Although magnetic credit cards and door keys are mostly replaced by smarter chip systems, which may contain more information and communicate wirelessly, magnetic strips will remain on disposable tickets. Magnetic ink patterns are found on some banknotes.

Reed contacts together with permanent magnets are still the most common sensors used for door switches. They need no power and can be made resistant against disabling (Chapter 11).

9.4 Automotive

The main automotive application of magnetic sensors is position sensing with permanent magnet and a moving magnetic circuit. The basic configurations are proximity sensors, tooth sensors, analog contactless potentiometers, and brushless motors with permanent magnet rotors [43]. The used sensor types are Hall sensors, InSb magnetoresistors, AMR, GMR, and SDT (TMR) magnetoresistors. The main selection criteria are temperature stability in the required temperature range of −20°C to +150°C and low price. Position sensors are described in Chapter 11.

Car navigation systems use magnetic compasses (Section 9.2): fluxgate and magnetoresistive [23]. Other magnetic navigation methods are also used in unmanned (driverless) vehicles or experimental cars [26].

Stationary magnetometers are used in traffic monitoring and control to detect passing vehicles and eventually recognize their type. The basic device is an induction loop placed under the road surface. The determination of the vehicle type (car-van-lorry-trailer) has an efficiency between 75% and 95%; it can fail at low speeds as in traffic jams [23]. The DC magnetic sensors give more information: Using a 3-axial fluxgate or magnetoresistive magnetometer buried under the road surface allows to recognize the vehicle type. Figure 9.7 shows the components of the magnetic field of a small car. A single sensor may be used to monitor the car's presence (for example, in garages), two separated sensors can measure the direction and driving speed; in a noisy environment, correlation techniques should be used [23].

9.5 Nondestructive Testing

Magnetic methods of nondestructive evaluation can be used either for monitoring the material state and properties (such as residual stresses), or to find defects. The overview can be found in a book written by Jiles [44] and also in Section 8.10.4. The material properties are tested by using Barkhausen effect, magneto-acoustic emission, monitoring of the hysteresis loop, and magnetoelastic methods. Material inhomogeneities, cracks, and other defects are monitored by DC methods: magnetic particle inspection and magnetic flux leakage method, or AC eddy currents. Magnetic flux leakage is usually measured by fluxgate sensors. One of the fathers of this method and author of classic papers was Foerster, who founded a company that is one of the leading producers of magnetic testing equipment. The magnetic leakage method is also often used in magnetic pigs, which are used for in-pipe inspections [45].

Eddy-current methods can be used for nonmagnetic metals. Eddy-current probe for detection of small defects in conducting media was proposed by Sasada and

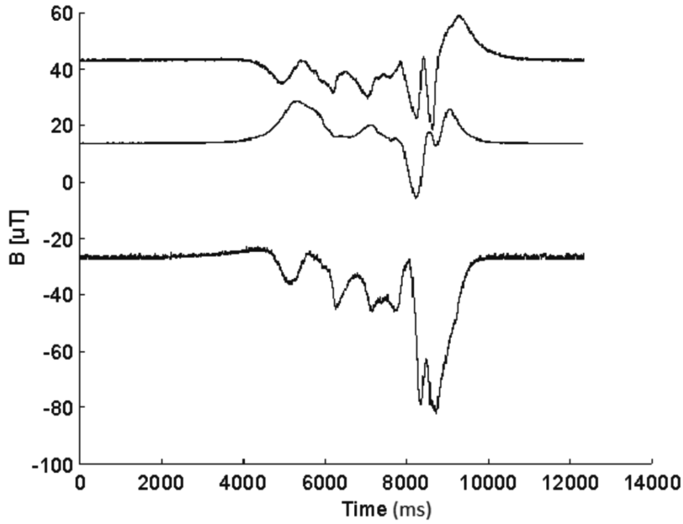

Figure 9.7 Magnetic field of the car: vertical component (upper trace), component in the movement direction (middle trace), and perpendicular horizontal component (lower trace). (From: Honeywell HMR 3000 Digital Compass Module, Datasheets and Application Notes.)

Watanbe [46]. The probe consists of excitation and figure-8 pickup coils wound on ferrite. The excitation frequency is 10 kHz or 60 kHz. The coils are cross-coupled, that is, if no defect is present, the voltage induced in the pickup coil is zero. An array of such sensors with a common excitation coil can be scanned to map the sample surface.

Another method used for evaluation of materials is magnetic imaging. Two methods are of great importance: magnetic force microscope (MFM), and scanning SQUID microscope (SSM); see Section 7.10.4.1. MFM measures the force between the magnetized tip and the specimen surface; it has 50-nm spatial resolution and 10-μT sensitivity. One particular SSM has 1-nT sensitivity, but spatial resolution is only 10 μm [47]. Higher spatial resolution can be obtained, a bit at the loss of sensitivity (Figure 9.8). The use of a ferromagnetic flux transporter [48] (indicated

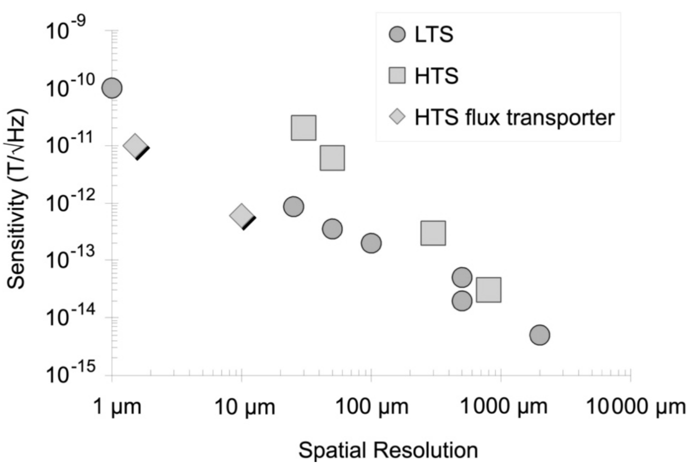

Figure 9.8 Sensitivity and spatial resolution of a number of SQUID microscopes [49].

by diamonds in Figure 9.8) can offer significant improvement in spatial resolution in HTS microscopes, but at a loss in the AC response.

Magneto-optic methods also allow noncontact evaluation of the materials [50].

LTS refers to systems operating at liquid helium temperatures, and HTS refers to systems operating at liquid nitrogen temperatures. With the exception of the (10^{-10} T/√Hz, 1 μm) data point, all sensitivities refer to room temperature samples.

9.6 Magnetic Marking and Labeling

Magnetoelastic labels use resonance of longitudinal vibrations in high-magnetostriction strips. Fe-rich amorphous materials (metallic glasses) are ideal for this application, as they have a high magnetoelastic coupling coefficient, so that they are able to transform most of the elastic energy into magnetic energy and vice versa [51]. Therefore, the vibrations can be excited and also detected by remote coils. A magnetostrictive strip has maximum absorption of an AC magnetic field at its mechanical resonance frequency. Some systems use a pulse mode: after the excitation frequency is switched off, the signal from the magnetostrictive label is detected. The label can be deactivated by demagnetization of the parallel strip of magnetically hard material [52]. These labels can be coded by combination of several strips with different lengths [53]. Some materials also exhibit a large ΔE effect (change of the Young's modulus with the bias DC field), so that the resonating frequency depends not only on the strip dimension, but also on the applied DC field. This property may be used for position sensing of a vibrating strip in a known DC field gradient.

Another type of label uses a nonlinear magnetic element that produces rich harmonic components of magnetization [54].

Magnetic marking of steel ropes, pipes, and rails is similar to magnetic storage technology. The sensors for reading should be more sensitive, because the medium-sensor distance is large and the marked object is made of construction steel, which is not optimized for magnetic performance. An example is the magnetic stripping of steel winding ropes in British and Swedish mines.

Magnetic barcodes can be used in dirty environments and they can be made invisible. A micro-head made of two perpendicular U-shaped amorphous wire cores is able to detect 1-mm pitch strips made of magnetic ink. Each core is wrapped by a coil: one coil is excited by a 100-kHz current and the other coil detects the sample field. If no strip is present, the output is zero due to the symmetry [55]. Miniature fluxgate sensors (Chapter 3) or magnetoresistors (Chapter 4) are also used for this purpose.

9.7 Geomagnetic Measurements: Mineral Prospecting, Object Location, and Variation Stations

The problems associated with the Earth's field magnetometry and the instrumentation used for geomagnetic research are reviewed by Campbell [56]. A book by Kearey et al. is devoted to geophysical exploration [57]. Breiner [58] wrote a practical handbook for using portable magnetometers for geological and archeological prospecting, magnetic mapping, and also the measurement of magnetic properties of rocks. Instrumentation, measurement, and calibration techniques for magnetic observatories are described in a book issued by International Association of Geomagnetism and Aeronomy (IAGA) [59].

The Earth has a crust, a mantle, and a metallic core. While most of the core is liquid, the inner part is solid. Complex processes are associated with the increase of the inner core (freezing) together with the Earth's rotation drive, the Earth's magnetic dynamo, which is believed to cause the Earth's magnetic field [56]. The Earth's field (Figure 9.9) has a dipole character; in Northern Canada, about 1,000 km from the geographical North Pole, there is the North magnetic pole. Paradoxically, it is a South pole of an equivalent bar magnet, because it attracts the North pole of the magnet needle. The Earth's field is changing in time. At present, the amplitude is decreasing by 0.1% each year, the North Pole is drifting westward by 0.1°/year. The tilt of the dipole axis, which was 9.6° in 2021, is decreasing by 0.02°/year [56].

The Earth's field at the magnetic poles has a vertical direction (90° inclination) with a magnitude of about 60 μT, while in the equatorial region the direction is horizontal (0° inclination) with a magnitude of about 30 μT. Local anomalies are associated with remanent or induced magnetization of rocks. A 400-km-long anomaly near Kursk in Russia has a top vertical field of 180 μT, the change in declination is as large as 180°. In Kiruna, Sweden, the magnetite ore causes the vertical field of 360 μT. Smaller-size anomalies of geological origin are numerous and they cause serious navigation problems. Similar or even larger fields are associated with man-made iron structures.

The daily (diurnal) variations are in the order of 10 to 100 nT, as shown in Figure 9.10(a). They are caused by a solar tide of ionized gas in the ionosphere, which creates electric currents. Micropulsations (Figure 9.10(b)) have periods of 10 ms to 1 hour, with amplitudes up to 10 nT. Magnetic storms, graphed in Figure 9.10(c), can occur up to several times per month with duration of up to several days

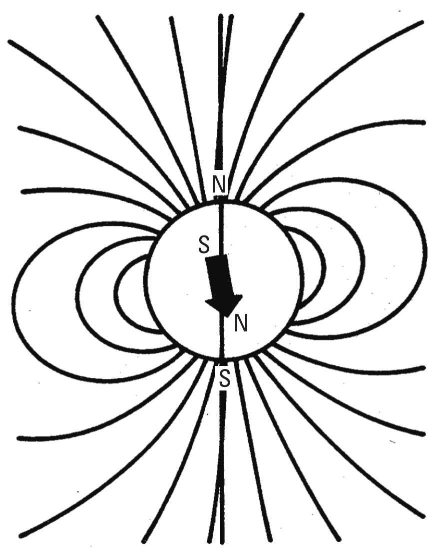

Figure 9.9 The Earth's magnetic field.

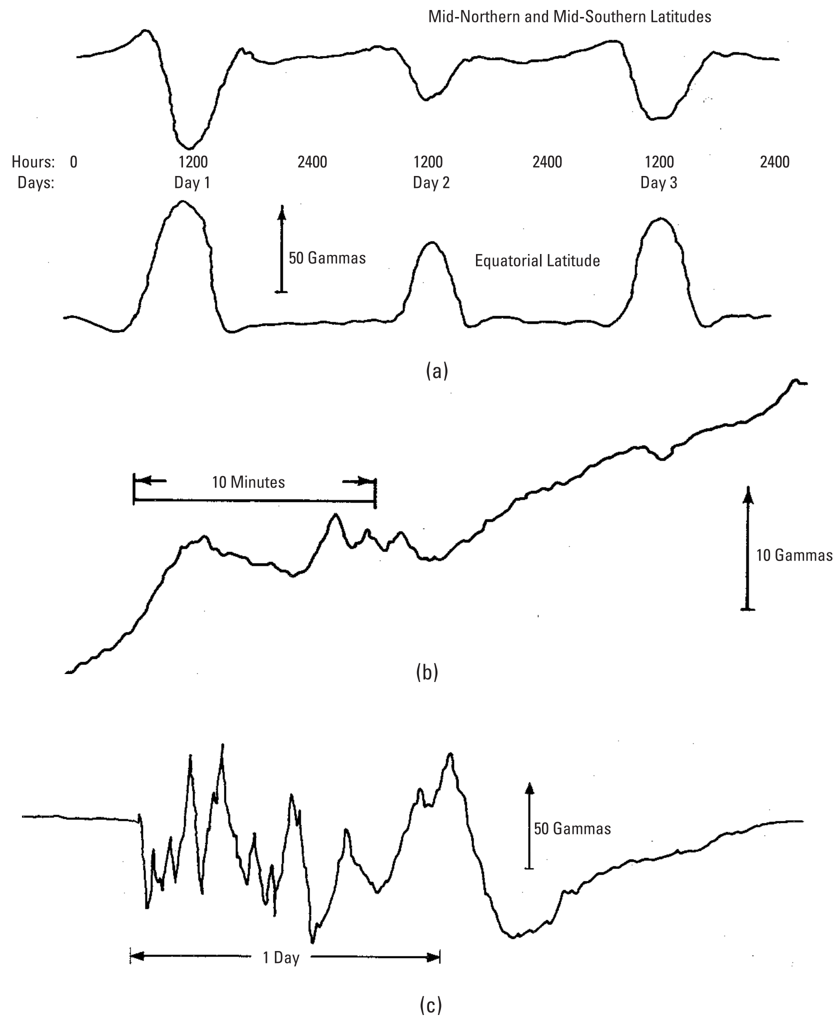

Figure 9.10 Variations of the Earth's magnetic field: (a) daily or diurnal, (b) micropulsations, and (c) magnetic storm. (*From:* [58].) 1 gamma = 1 nT (traditional unit).

and amplitudes of several hundreds of nanotesla. Storms are caused by interaction between the coronary plasma bubble in the solar wind and magnetosphere and secondary (mega-ampere) currents associated with a flow of charged particles in the magnetosphere. A typical storm begins with a sudden field jump followed by a long-term depression of the field caused by the secondary ring current.

Surface magnetic mapping is still mainly made by a walking operator (nonmagnetic vehicles and drones are rarely used). The operator should be free of magnetic materials, and the sensor is usually carried on a 2-m stick; sometimes a 4-m-long stick is used in order to remove the sensor from the locally disturbing fields of surface materials [58].

Airborne magnetic surveys for ore prospecting are performed in low heights (300 m or less, often using drones); geophysical mapping is made at higher attitudes (3,000–10,000 m) or from low-orbit satellites (~500 km). In order to reduce the influence of stray fields from the aircraft or drone, the sensor is often towed.

Magnetic sensors are also used down-hole. Applications for the oil industry are reviewed in [27]. Fluxgate magnetometers together with inclinometers serve for the navigation for directional drilling. Directional drilling is the intentional deviation of a well from a vertical path at a predetermined trajectory, which allows access to locations that cannot be reached efficiently with a vertical well drilled from the surface. NMR down-hole spectrometers measure the properties of the rock outside the drill.

Instruments most often used in geophysical measurements are scalar resonance magnetometers: classic proton magnetometers were often replaced by Overhauser magnetometers (Chapter 6). Optically pumped instruments are more expensive, but, in general, they offer a high bandwidth together with an excellent precision so that they are used for airborne surveys, where the field changes may be very fast. If a vector measurement is required, the most usual instrument is the fluxgate magnetometer (Chapter 3).

The Earth's field variations during the surveys should be monitored and corrections made. Another possibility is to use gradiometers. They compensate not only for natural field variations, but also for noise from distant sources. Gradiometers are advantageous for localization of small and close objects. Most often, vertical gradient of total field is estimated as a difference between the readings of two scalar resonant magnetometers (separated by 90 cm or larger distance). The advantage of a vertical gradient is that the vertical direction is easily defined, also at medium and higher latitudes, where the vertical Earth's field component is stronger; the vertical gradient is usually rich on information about buried objects. Some gradiometer systems (mainly for search applications) use fluxgate sensors: either two single-axis sensors mounted vertically, or multisensor systems.

Geophysical methods are also used to locate the buried man-made ferromagnetic structures such as pipelines, tanks, drums, and UXO (Section 9.3). Most pipelines have a strong remanent field, which changes at the pipe sections that had a different magnetic history. The pipelines are often magnetized after a DC magnetic defectoscopy. Sometimes the pipes should be demagnetized before welding, as the strong remanent field deflects the welding arc. Long horizontal pipes produce a field that decreases as $1/r^2$. Short objects have a dipole field character, the field decreases as $1/r^3$ (compare the field of straight DC conductor, which decreases with $1/r$). As a rule of thumb, 1 kg of iron makes 1-nT field in the distance of 3m, and a 1000 kg single piece of iron such as large bomb makes 1nT field at the distance of 30m. 15-cm diameter iron pipeline makes 1nT field in the distance of 30m [58]. Figure 9.11 shows the total field profiles of induced dipoles at various inclinations.

The permanent dipole has a constant field signature independently of the Earth's field magnitude and direction, but the total field measured by scalar magnetometer is the vectoral sum of the Earth's field and dipole field so that it changes with their angle. Figure 9.12 shows this problem: if the small dipole field **M** is perpendicular to the high Earth's field **F**, the resulting change in total field may be a very small at equatorial (horizontal) field. This is one of the reasons why vectoral fluxgate magnetometers are used for some search applications, although they have worse stability than resonant magnetometers. Three-axis vector magnetometers give more information such that the interpretation is much easier. Figure 9.13 illustrates how

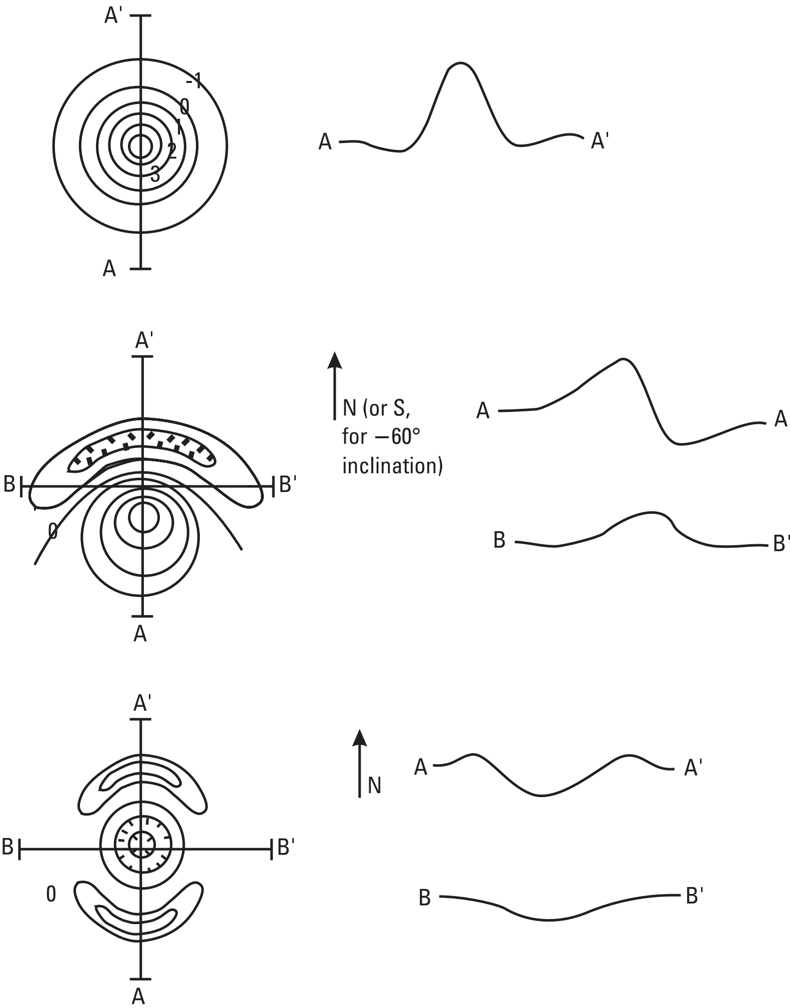

Figure 9.11 The total field profiles of induced dipoles at various inclinations: (a) in a polar region, where inclination is 90° (permanent dipole has a similar field signature); (b) at 60° inclination; and (c) 0° inclination (close to the equator, where the Earth's field has a horizontal direction). (*From:* [58].)

the total field anomaly width increases with object depth. A simple but very useful rule is that the total field anomaly width is approximately 1 to 3 times the depth.

The common instruments used for the location of reinforcing steel and small-diameter steel gas lines are based on eddy currents. They allow estimating the rod/pipe location and diameter independently [60]. A scanning device based on AC AMR gradiometers was described in [61].

Magnetic observatories for long-term measurement of the Earth's field variations form a world network called Intermagnet (https://www.intermagnet.org/). The observatories are on magnetically clean locations, far from gradients and interferences. The measured data, together with several handbooks, can be found on the Web. The standard instrumentation is a resonant magnetometer and stable thermostated triaxial fluxgate. Periodical absolute calibration is performed with the help of nonmagnetic theodolite with a mounted single-axis fluxgate sensor [59].

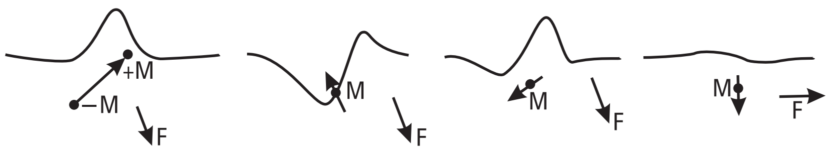

Figure 9.12 Total field profiles of permanent dipole **M** not parallel to Earth's field **F**. (*From:* [58].)

Figure 9.13 Depth/amplitude behavior of dipole anomalies. (*From:* [58].)

Magnetic susceptibility and remanent magnetization of rock samples can be measured by a magnetometer, if the sample is slowly rotated in the Earth's field. Susceptibility is also measured in AC bridges; the sample inserted into the air coil slightly changes its impedance. Remanent magnetization can be measured with a SQUID magnetometer such as in Model 755 Superconducting Rock Magnetometer manufactured by 2G company [62] (also Section 7.10.3.3) or by rotating sample magnetometers: the sample rotates inside the magnetic shielding, the AC field is measured by an induction coil (such as in AGICO JR-6 Spinner Magnetometer [63]) or by a fluxgate magnetometer (former Molspin system [64]). The resolution of SQUID rock magnetometer is 10^{-6} A/m, which is only 2.4 times better than spinner magnetometer, but the main advantage of the SQUID instrument is that it allows measurement of rock samples with arbitrary shape. High values of the sample remanent magnetization are caused by heating effects: during cooling through the Curie temperature, the sample is magnetized by the Earth's field. The heating may be natural such as in igneous rocks, or artificial such as in case of baked pottery, bricks, or other archeological objects subjected to fire: they remember the magnetization direction, which may be different from today's Earth's field, as the position of magnetic poles is changing in time [65]. Magnetic surveys and susceptibility mapping are often used in archeological prospection. They include mapping of magnetic field gradient and of susceptibility.

9.8 Space Research

The accurate measurement of the ambient magnetic field vector and its orientation in space is recognized as a basic requirement for space physics research. The range of field strengths to be measured in exploratory missions may cover up to 9 orders of magnitude from $5 \cdot 10^{-3}$ nT to $2 \cdot 10^{6}$ nT. The required accuracy can be as low as 0.01 nT in the outer heliosphere where the field strength is just a few nanotesla and it is typically 1 nT for measurements of the full Earth's field with a field strength of up to 50,000 nT in the low Earth orbit. While an angular determination accuracy of the measured field direction relative to an inertial coordinate system of the order of

0.5° is generally sufficient for most studies, in special cases, accuracies of the order of arcseconds are required for detailed mapping surveys of planetary magnetic fields.

The vast majority of magnetic field measuring instruments used to date has been of the vector type, which measures three orthogonal components of the local field with a frequency response that covers a range from theoretically 0 Hz (DC) up to about 100 Hz. The time resolution of the measurements ranges from several seconds to several hundred samples per second, depending on the scientific objectives [66, 67]. The most commonly used vector magnetometers for this frequency range are of the fluxgate type (Chapter 3). Search coil magnetometers (Chapter 2) are used for the measurement of the magnetic component of electromagnetic waves from about 1 Hz up to several kilohertz. Combined with electric field measurements, these AC magnetic sensors are of importance for the characterization of electromagnetic waves in orbits around planets as well as in the interplanetary space. Scalar-type instruments (Chapter 6) measure the magnitude of the ambient field without providing directional information. During the last decades, they have been used for specialized missions that require their intrinsic absolute accuracy (e.g., geomagnetic field surveys) as reference for the in-flight calibration of the vector sensors.

Common to all types of magnetometers is the fact that instruments onboard a spacecraft, especially the boom-mounted sensors (Figure 9.14), are exposed to harsh environments: for example, vacuum, extreme temperatures, radiation, and high mechanical loads during launch. Yet despite such difficult conditions, these instruments must also be exceptionally reliable and fully functional throughout the entire mission time, which could last for more than 10 years, as they cannot be repaired during the journey. In order to make the instruments so highly reliable, a number of prototype models are first developed and tested before the actual flight model is built.

9.8.1 Deep-Space and Planetary Magnetometry

In the early years of the space program, the measurements of the Earth's magnetic field were collected with rockets and balloons. The instruments measured the strength of the equatorial electrojet, the auroral current system, and other high-altitude magnetic phenomena. Using space flight measurement techniques adapted from instruments developed around World War II, early space probes established the comet-like morphology of the distant Earth's magnetic field and discovered many of the features and boundaries of the magnetosphere (the bow shock, magnetopause, and geomagnetic tail). Dolginov et al. [68, 69], Sonnett [70], Cahill [71], and Ness [72] were among the first investigators to equip the early probes with magnetic field measuring instruments and carry out measurements in the Earth's magnetosphere and interplanetary medium.

Space missions such as *Pioneer Venus*, *Mariners*, *Voyager*, *Helios*, *Ulysses*, *Giotto*, *Galileo*, *Phobos*, *Vega*, *NEAR*, *Magsat*, *Mars Global Surveyor*, *Cassini*, *CHAMP*, *Venus Express*, *MESSENGER*, *Rosetta*, *Swarm*, *Juno*, and *MAVEN* have carried out magnetic field measurements around most of the planets in our solar system, in the interplanetary medium, and near comets and asteroids [73–76]. Planetary magnetic fields like those of Earth, Jupiter, and Saturn are believed to be generated by currents driven by thermal convection in the interface between their

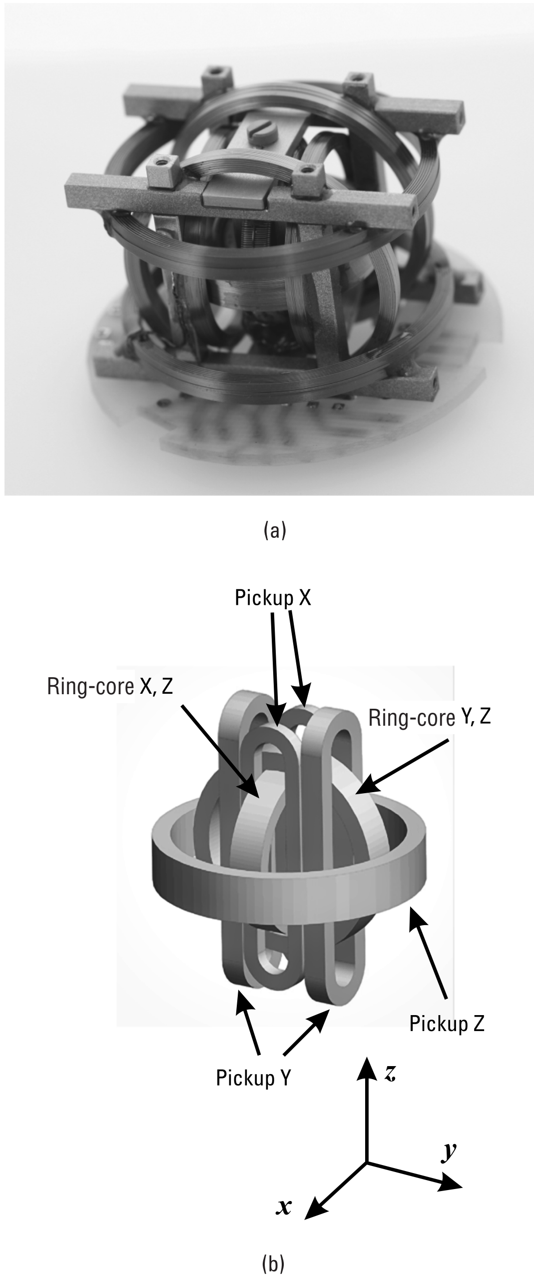

Figure 9.14 A compact fluxgate sensor that has been used for many scientific space missions by Technical University Braunschweig and commercial ground as well as space applications by Magson GmbH. (a) Picture of the sensor including triaxial Helmholtz feedback coils (courtesy of Magson GmbH). (b) Sketch of ring-cores and pickup coil system.

mantles and liquid metallic cores. Uranus and Neptune are assumed not to have formed metallic cores, and their magnetic fields are thought to be generated closer to the surface, where electrical currents can flow in the high-conductivity liquid crust [77–80]. In terrestrial planets, Venus does not possess an intrinsic magnetic field [81], while Mercury is magnetized by the remains of an ancient dynamo [82, 83]. Mars Global Surveyor established that Mars does not currently possess an intrinsic magnetic field but that it had one in its early history about 3.9 billion years ago. That field left a significant portion of Mars's crust strongly magnetized [84, 85]. Magnetic fields with a strength of up to 1,600 nT were measured at an altitude of approximately 100 km during the second aero-braking phase of this mission compared to the upper limit of a few nanotesla expected from a possible global field. The crustal magnetization is effectively restricted to the very old, heavily cratered terrain in the highlands in the southern hemisphere.

Only two types of measurements from an orbiting or flyby spacecraft provide clues about the interior of a planetary body, either its structure or thermal history: the effects of gravity on the spacecraft orbit or trajectory and the internal magnetic field strength and geometry. In addition, many missions utilize magnetic field measurements for engineering applications. For instance, Earth-orbiting spacecraft apply magnetic field information to attitude determination and control, spacecraft momentum management, and scientific instrument pointing. The Earth's magnetic field provides one of the basic natural forces that modern systems and spacecraft utilize to establish their orientation with respect to a reference frame when inertial systems are too complex or costly to implement. Measurement accuracies of about 10 nT and even above are needed for this purpose, which makes the magnetic field measurement a practical alternative.

Magnetic field measurements are also essential to complement onboard, energetic, charged particle measurements to aid in understanding of the behavior of plasmas in the solar system and energetic trapped particles around magnetized planets. Electrically charged particles move easily along the local magnetic field line but have great difficulty moving transverse to it. Hence, magnetic field lines are important tracers of particle motion geometry, trapping, and drift around magnetized bodies.

While numerous discoveries have been made in researching the sources and behavior of planetary magnetic fields [66], there is still much to be learned [86].

9.8.2 Space Magnetic Instrumentation

Both scalar and vector instruments have been used onboard spacecraft to measure magnetic fields in space, but vector magnetometers are far more common because of their ability to provide directional information. This section presents a brief discussion of their advantages and disadvantages and the general problem of performing sensitive magnetic field measurements onboard an orbiting spacecraft or planetary probe. Comprehensive reviews of early and more recent space research magnetometers have been published by Balogh [66], Ness [67], Snare [87], and Acuña [88].

9.8.2.1 Scalar Magnetometers

Scalar magnetometers have been used from the very beginning of spaceborne magnetic field measurements [89]. The first scalar magnetometer in space was of the proton precession type aboard the *Vanguard 3* spacecraft in 1959 [67]. The polarize/count cycle of the typical proton precession magnetometer requires 1 second or more in traditional designs, and the liquid sample volume is relatively large and massive, particularly when the polarizing coil mass is considered. Liquids that can operate over a wide temperature range are necessary, and the polarizing power required to generate the 10-mT (or more) polarizing field is significant; useful signals can be obtained only for ambient fields larger than approximately 20,000 nT. Those limitations have restricted the use of classic proton precession instruments onboard spacecraft, although substantial use has been made in sounding rocket applications, in which short flight durations in the Earth's field are typical. The advanced proton precession magnetometer based on the Overhauser effect, which uses an indirect technique to polarize the sample and generate a continuous Larmor precession signal, has superseded the classical proton precession magnetometer, especially for ground-based applications; but it was also used in space [90, 91].

Optically pumped magnetometers are another class of magnetic field measuring instruments that have found considerable application onboard spacecraft, both as scalar and as vector instruments. In the scalar configuration, they are capable of measuring magnetic fields over a wider range than the proton precession instruments and with much higher time resolution. Based on the Zeeman effect, these instruments use the energy required to transfer atomic electrons from one energy level to another as the mechanism for magnetic field detection. In the past, a cell containing a suitable gas was irradiated with light from a discharge lamp at the proper frequency to excite the atoms. Nowadays, laser diodes are used for this purpose. The most established chemical elements for optically pumped magnetometers are helium and alkali metals such as cesium and rubidium. Rather historic but still representative instruments have been described in [92, 93]. Helium and its isotopes in particular are still in use in high-accuracy, high time resolution scalar and vector measurements aboard spacecraft [94–98].

Traditional helium and alkali metal magnetometer require a rather complex sensor design with, for example, double-cell sensors in order to guarantee isotropic, dead-zone-free measurements. Moreover, artificial magnetic fields or radio frequencies are needed for the excitation of the medium used in the sensor cell. A recently developed rubidium vapor instrument that overcomes this complication by measuring the magnetic field all-optically is based on the coherent population trapping (CPT) effect [99, 100].

See Chapter 6 for more details about scalar magnetometers.

9.8.2.2 Vector Magnetometers

Vector magnetometers are, by a large margin, the most widely used type of instrument for magnetic field measurements onboard spacecraft, balloons and sounding rockets [101]. In addition to providing information about the field strength, they also indicate the direction of the ambient field. Triaxial orthogonal arrangements of single-axis sensors are used to measure the three components of the ambient field in a coordinate system aligned with the sensor magnetic axes. In contrast to scalar magnetometers, whose accuracy is determined by quantum mechanical constants, vector magnetometers must be calibrated against known magnetic fields, both in strength and direction. Their output for zero field (offset), scale factor, and stability with temperature and time depends on electrical component values and mechanical structure dimensions, with aging of the instruments as well as their exposure to the space environment. In spite of those shortcomings, vector instruments are capable of measuring magnetic fields over a large dynamic range ($5{\cdot}10^{-3}$ nT to more than

$2 \cdot 10^6$ nT), are lightweight, and consume little power. In addition, they are capable of operation over a wide temperature range and have proved to be extremely reliable and extremely resistant to the destructive effects of intense radiation from solar particle events and energetic trapped particles in planetary magnetospheres.

Representative fluxgate magnetometers with miniaturized sensor and electronics designs for space exploration are described in [102–104], and a compact fluxgate sensor with two crossed ring cores (diameters, 18 and 12 mm) is shown in Figure 9.14 [102]. It combines vector compensation for the nulling of the magnetic field within the sensor, low mass, and an implementation of the pickup and feedback coils without support bobbins, which enables a wide temperature range.

Specific sensor constellations with fluxgate and star sensors on an optical bench plus a scalar sensor on the same boom for absolute reference have been used to map the Earth's magnetic field from orbit with unprecedented accuracy, both in magnitude as well as direction [74, 105].

9.8.3 Measurement of Magnetic Fields Onboard Spacecraft

9.8.3.1 Magnetic Cleanliness

The instruments described so far are carried into space onboard spacecraft that include complex systems of mechanical, electrical, and electronic components. Those components, unless carefully controlled, have the potential to generate strong magnetic fields of their own. Batteries, solar arrays, motors, wiring, and other materials must be especially designed and selected to minimize the generation of stray magnetic fields that will affect measurements. The design and implementation of a magnetically clean spacecraft meeting the stringent requirements of planetary and interplanetary missions are a demanding task that has tested the fiber of many seasoned project managers and engineers. Because it is practically impossible to reduce the stray spacecraft magnetic field to the small levels required for sensitive measurements, the use of long booms to place the magnetic sensors away from the main body of the spacecraft is commonplace (Figure 9.15). This technique exploits the fact that magnetic fields from most sources decrease rapidly away from their source, proportionally to $1/r^3$ as a minimum, where r is the distance to the source.

The booms must be rigid and preserve the required alignment between the magnetic sensors and the attitude-determination sensors mostly mounted in the main spacecraft body, which limits their practical length. Dependent on the available resources and the importance of the magnetic field measurements, boom lengths have varied between 1 m (*Venus Express*) and 13 m (*Voyager 1 and 2*). For a given spacecraft design, the trade-off between boom length and level of magnetic cleanliness required in the main body is a major decision that must take into account many conflicting requirements, including whether the spacecraft is spin stabilized or 3-axis stabilized.

Details of magnetic interference, spacecraft testing, and magnetic cleanliness programs can be found in [66, 67]. In sensitive missions, a magnetics control program is usually carried out to ensure that the sources of stray magnetism onboard the spacecraft are eliminated or minimized to the required levels [103, 106]. Such

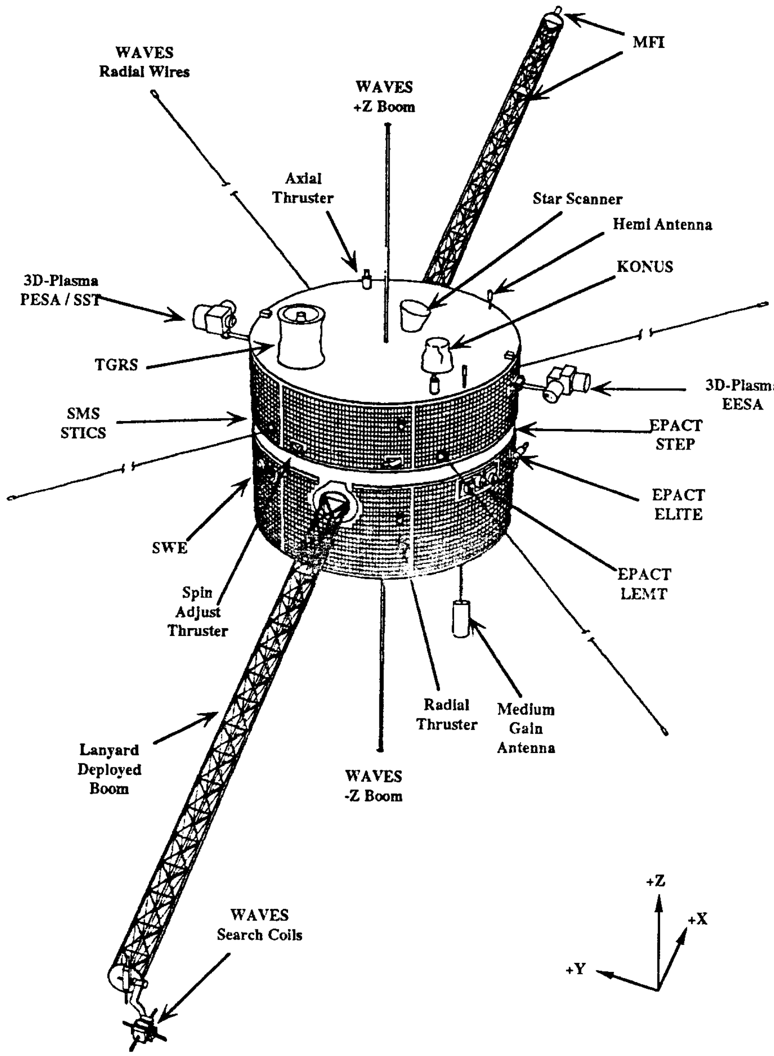

Figure 9.15 Satellite with booms for magnetic sensors.

programs originally emphasized the control of all spacecraft-generated fields, either static or dynamic. With the advent of wide dynamic range instruments and high-resolution digitization of the magnetic field, they now emphasize control of dynamic fields over static fields, because a constant but known DC offset or even a low-frequency dynamic stray field at the location of the sensor would be acceptable as long as a proper in-flight calibration allows for an attenuation of its contribution to the overall measurement error to below the mission requirement.

The dual-magnetometer technique was introduced in 1971 by Ness et al. to ease the problem of making sensitive magnetic field measurements in the presence of a significant spacecraft field [107]. The method, which is illustrated schematically in Figure 9.16, is based on the experimental observation that beyond a certain distance most spacecraft-generated magnetic fields decrease as expected for a simple dipole

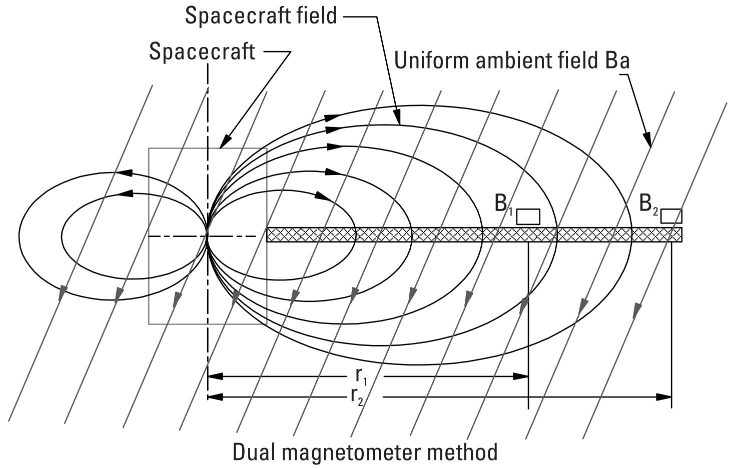

Figure 9.16 Dual magnetometer method.

source located at the center of the spacecraft ($1/r^3$). Thus, it can be shown that if two magnetometer sensors are used, mounted along a radial boom and located at distances r_1 and r_2, it is possible to uniquely separate the spacecraft generated magnetic field from the external field being measured. If we denote as $\mathbf{B}_1$ and $\mathbf{B}_2$ the vector fields measured at radial locations 1 and 2, with $r_2 > r_1$, the ambient field and the spacecraft field at location *1* are given by [108]:

$$\mathbf{B}_\mathrm{a} = \frac{(\mathbf{B}_2 - a \cdot \mathbf{B}_1)}{(1 - a)} \tag{9.1}$$

$$\mathbf{B}_{S/C1} = \frac{(\mathbf{B}_1 - \mathbf{B}_2)}{(1 - a)} \tag{9.2}$$

where

$$a = \left(\frac{r_1}{r_2}\right)^3 \tag{9.3}$$

$$\mathbf{B}_1 = \mathbf{B}_\mathrm{a} + \mathbf{B}_{S/C1} \tag{9.4}$$

$$\mathbf{B}_2 = \mathbf{B}_\mathrm{a} + \mathbf{B}_{S/C2} \tag{9.5}$$

$$\mathbf{B}_{S/C2} = a \cdot \mathbf{B}_{S/C1} \tag{9.6}$$

Note that these equations imply that the spacecraft field can be correctly represented by a single dipole centered on the main body and that the offsets of the magnetic field sensors are known with reasonable accuracy. A detailed error analysis of the dual-magnetometer method together with an ideal placement of several collinear sensors is provided in [108].

A particular advantage of the dual magnetometer method is that it allows the unambiguous real-time identification and monitoring of changes in the spacecraft field. Especially when no or only a reduced magnetic cleanliness program is put in place during the design and development phase of a spacecraft in combination with a rather short boom, the gradiometer method based on two or even more sensors is the only way forward for reasonably clean magnetic field measurements. A good example is the method developed for the *Venus Express* mission with one magnetic field sensor at the tip of a one meter long boom and the second sensor mounted to the side wall of the spacecraft at the boom root. It allowed for a removal of disturbances from several different sources based on additional information about the spacecraft operation and the implementation of fuzzy logic [109].

A multisensor approach has been developed for the magnetic field measurements aboard a meteorological satellite in geostationary orbit that was designed without magnetic cleanliness control. The magnetometer contains two science-grade fluxgate sensors on an approximately 1-m-long boom and two additional magnetoresistance sensors mounted within the spacecraft body [110]. The method has aimed for a correction technique that reduces the processing effort to a linear (or, at most, quadratic) combination of the magnetic field values measured by the four sensors without input from other sources, which can also be calculated onboard [111]. Maximum-variance processing is used to decouple multiple disturbance sources and to minimize the introduction of artefacts to the components free of the targeted disturbance. An adaptive canceling of magnetic interference using a pair of magnetometers that is especially effective for a time-varying interference with an unknown signature is discussed in [112].

In addition to the gradiometer-based cleaning of the magnetic field measurements from spacecraft-originated stray fields, the use of two (or more) sensors provides a measure of redundancy that has proved extremely useful not only for long-duration missions, like those to the outer planets.

9.8.3.2 In-Flight Calibration, Coordinate Systems, and Onboard Processing

In spite of the many advantages of fluxgate magnetometers, the stability of its calibration parameters (offsets, scale factors, orthogonality, and alignment) and the sensor noise have been and will continue to be the major challenges for sensitive measurements (Chapter 10.4, and [66]). It is therefore important to apply certain processing techniques, which are very much dependent on the mission scenario, to estimate the calibration parameters in flight [113, 114].

In the case of zero levels (offsets), several techniques have been developed for their determination in flight for both spinning and nonspinning spacecraft, techniques that also minimize the problems associated with drifts. The interplanetary magnetic field is characterized by frequent changes in direction rather than magnitude, which can be used to advantage to statistically estimate effective magnetometer zero levels [115]. Spinning spacecraft and spacecraft maneuvers help to resolve zero levels in the rotation plane by modulating the ambient signal.

For an interpretation of the measurements in a physical sense, the measurements must be expressed in a coordinate system that is different from that of the magnetic field sensors [116]. Therefore, coordinate transformations are required that must take into account not only the orientation of the spacecraft in inertial space but also the internal rotations associated with booms and other instruments and sensors onboard and possibly their time dependence. In general, it is difficult to simulate accurately the zero-g flight environment for booms and appendages on the ground; hence, sensor alignment must be verified in flight. Like for the offset calibration, spacecraft maneuvers and rotations about principal axes, but in addition onboard 1-D and 2-D coil systems are appropriate means to establish sensor alignment with respect to the spacecraft coordinate system. Furthermore, the measurement of a well-modeled field environment (e.g., measurement of the Earth's field during flyby maneuvers of interplanetary missions) can be used for a proper confirmation of the sensor alignment.

Spinning spacecraft is preferred for space plasma physics applications because the rotational motion helps the scanning of ambient particle distribution functions through a large solid angle. In the case of magnetometers, however, the spacecraft spin modulates the ambient magnetic field perpendicular to the spin axis, and additional bandwidth is required to transmit that information to the ground unless onboard despin data processing is used. This is a classic example of data processing and compression algorithms, which are frequently used to reduce the bandwidth required to transmit the information to ground [86]. On spinning spacecraft, the data need to be de-spun to an inertial coordinate system using spin-phase information generally provided by the spacecraft attitude control system. This is a nontrivial task if the spin tone and its harmonics contributions to the overall power spectrum are to be minimized. However, the de-spinning process allows for the almost continuous determination of 8 of a total of 12 calibration parameters [113].

The study of the frequency spectrum of dynamic perturbations of the magnetic field is a powerful tool used to identify the types and characteristics of waves and other time-variable phenomena detected by spacecraft instruments. The outputs from DC magnetic field sensors typically are digitized with high-resolution ADCs to resolve small amplitude fluctuations superimposed on larger background fields. Space instruments may include onboard FFT processors and other digital implementations of data compression techniques to reduce the bandwidth required to transmit the information to ground.

9.8.3.3 Multispacecraft Measurements

In many space missions, the motion of the medium and the spatial boundaries in response to the time variability of the solar inputs significantly affect the interpretation of single spacecraft magnetic field measurements. The instruments may detect a rapid change in the ambient conditions, but the observation cannot be interpreted unambiguously because the crossing of a spatial boundary or a simple temporal variation yields similar signatures in the data. Therefore, simultaneous multispacecraft measurements are required to remove those ambiguities from the observations. Simultaneous observations by two spacecraft provide ambiguity resolution only along a straight line (single dimension), while at least four spacecraft are required to provide full 3-D resolution [117–119].

References

[1] Ohdaira, T., H. Nagai, and M. Shoji, "Intraoperative Localization of Colorectal Tumors in the Early Stages Using a Magnetic Marking Clip Detector System (MMCDS)," *Surgical Endoscopy and Other Interventional Techniques*, Vol. 17, No. 5, May 2003, pp. 692–695.

[2] Tomek, J., et al., "The Precision of Gastric Motility and Volume Sensing by Implanted Magnetic Sensors," *Sensors and Actuators A: Physical*, Vol. 142, No. 1, 2008, pp. 34–39.

[3] O'Donovan, K. J., et al., "An Inertial and Magnetic Sensor Based Technique for Joint Angle Measurement," *Journal of Biomechanics*, Vol. 40, No. 12, 2007, pp. 2604–2611.

[4] Katranas, G. S., et al., "A Novel Bi-Layer Thin Film Sensor System for Registering Cardio-Respiratory Activity," *Sensor Letters*, Vol. 5, No. 1, March 2007, pp. 215–217.

[5] Rivero, G., et al., "Magnetic Sensor for Early Detection of Heart Valve Bioprostheses Failure," *Sensor Letters*, Vol. 5, No. 1, March 2007, pp. 263–266.

[6] Forsman, M., "Gastric Emptying of Solids Measured by Means of Magnetised Iron Oxide Powder," *Medical & Biological Engineering & Computing*, Vol. 36, No. 1, January 1998, pp. 2–6.

[7] Paixao, F. C., et al., "Development of an AMR-ACB Array for Gastrointestinal Motility Studies," *IEEE Transactions on Biomedical Engineering*, Vol. 59, No. 10, October 2012, pp. 2737–2743.

[8] Taton, K., et al., "Lateral Flow Immunoassay Using Magnetoresistive Sensors," *Journal of Magnetism and Magnetic Materials*, Vol. 321, No. 10, May 2009, pp. 1679–1682.

[9] Tondra, M., A. Popple, A. Jander, R. L. Millen, N. Pekas, and M. D. Porter, "Microfabricated Tools for Manipulation and Analysis of Magnetic Microcarriers," *Journal of Magnetism and Magnetic Materials*, Vol. 293, No. 1, pp. 725–730.

[10] Jamshaid, T., et al., "Magnetic Particles: From Preparation to Lab-on-a-Chip, Biosensors, Microsystems and Microfluidics Applications," *Trac-Trends in Analytical Chemistry*, Vol. 79, May 2016, pp. 344–362.

[11] Giouroudi, L., and E. Hristoforou, "Perspective: Magnetoresistive Sensors for Biomedicine," *Journal of Applied Physics*, Vol. 124, No. 3, July 2018.

[12] Llandro, J., et al., "Magnetic Biosensor Technologies for Medical Applications: A Review," *Medical & Biological Engineering & Computing*, Vol. 48, No. 10, October 2010, pp. 977–998.

[13] Wu, L. C., et al., "A Review of Magnetic Particle Imaging and Perspectives on Neuroimaging," *American Journal of Neuroradiology*, Vol. 40, No. 2, February 2019, pp. 206–212.

[14] Cohen, D., "Measurements of Magnetic-Fields Produced by Human Heart, Brain, and Lungs," *IEEE Transactions on Magnetics*, Vol. MA11, No. 2, 1975, pp. 694–700.

[15] Stroink, G., D. Dahn, and F. Brauer, "A Lung Model to Study the Magnetic-Field of Lungs of Miners," *IEEE Transactions on Magnetics*, Vol. 18, No. 6, 1982, pp. 1791–1793.

[16] Moller, W., et al., "Mucociliary and Long-Term Particle Clearance in Airways of Patients with Immotile Cilia," *Respiratory Research*, Vol. 7, January 2006.

[17] Cohen, D., S. F. Arai, and J. D. Brain, "Smoking Impairs Long-Term Dust Clearance from the Lung," *Science*, Vol. 204, No. 4392, 1979, pp. 514–517.

[18] Tomek, J., A. Platil, and P. Ripka, "Multiple Layer Scanning in Magnetopneumography," *IEEE Sensors Journal*, Vol. 9, No. 4, April 2009, pp. 383–389.

[19] Platil, A., et al., "Magnetopneumography Using Optical Position Reference," *Sensor Letters*, Vol. 11, No. 1, 2013, pp. 69–73.

[20] Paulson, D. N., et al., "Superconducting Magnetometer System for Detecting Lung Contaminants," *IEEE Transactions on Magnetics*, Vol. 23, No. 2, March 1987, pp. 1315–1318.

[21] Sulai, I. A., et al., "Characterizing Atomic Magnetic Gradiometers for Fetal Magnetocardiography," *Review of Scientific Instruments*, Vol. 90, No. 8, August 2019.

[22] Barber, G. W., and A. S. Arrott, "History and Magnetics of Compass Adjusting," *IEEE Transactions on Magnetics*, Vol. 24, No. 6, November 1988, pp. 2883–2885.

[23] Caruso, M. J., and L. C. Withanawasam, "Vehicle Detection and Compass Applications Using AMR Magnetic Sensors," 1999, https://aerospace.honeywell.com/.

[24] Včelák, J., P. Ripka, A. Zikmund, and M. Butta, "Precise Magnetic Sensors for Navigation and Prospection," *Journal of Superconductivity and Novel Magnetism*, Vol. 28, No. 3, 2015, pp. 1077–1080.

[25] Včelák, J., et al., "Errors of AMR Compass and Methods of Their Compensation," *Sensors and Actuators A: Physical*, Vol. 129, No. 1-2, Special Issue, 2006, pp. 53–57.

[26] Borenstein, J., H. R. Everett, and L. Feng, *Navigating Mobile Robots*, Wellesley, MA: A.K. Peters, 1995.

[27] Gooneratne, C. P., B. D. Li, and T. E. Moellendick, "Downhole Applications of Magnetic Sensors," *Sensors*, Vol. 17, No. 10, October 2017.

[28] Vcelak, J., P. Ripka, and A. Zikmund, "Precise Magnetic Sensors for Navigation and Prospection," *Journal of Superconductivity and Novel Magnetism*, Vol. 28, No. 3, March 2015, pp. 1077–1080.

[29] Park, B., and H. Myung, "Resilient Underground Localization Using Magnetic Field Anomalies for Drilling Environment," *IEEE Transactions on Industrial Electronics*, Vol. 65, No. 2, February 2018, pp. 1377–1387.

[30] Weiss, E., and R. Alimi, *Low-Power and High-Sensitivity Magnetic Sensors and Systems*, Norwood, MA: Artech House, 2019.

[31] Praslicka, D., et al., "Industrial Applications of Magnetometry," *Journal of Electrical Engineering-Elektrotechnicky Casopis*, Vol. 66, No. 7, December 2015, pp. 190–192.

[32] Gamey, T. J., "Development and Evaluation of an Airborne Superconducting Quantum Interference Device-Based Magnetic Gradiometer Tensor System for Detection, Characterization and Mapping of Unexploded Ordnance," SERDP Project MM-1316, August 2008, https://www.researchgate.net/publication/235203927.

[33] Butler, D. K., et al., "Review of Magnetic Modeling for UXO and Applications to Small Items and Close Distances," *Journal of Environmental and Engineering Geophysics*, Vol. 17, No. 2, June 2012, pp. 53–73.

[34] Altshuler, T. W., "Shape and Orientation Effects on Magnetic Signature Prediction for UXO," *Proc. UXO Forum*, 1996.

[35] Wigh, M. D., T. M. Hansen, and A. Dossing, "Inference of Unexploded Ordnance (UXO) by Probabilistic Inversion of Magnetic Data," *Geophysical Journal International*, Vol. 220, No. 1, January 2020, pp. 37–58.

[36] Ripka, P., et al., "DC Gradiometers for Bomb Detection: Scalar Versus Vectorial," *Sensor Letters*, Vol. 5, No. 1, 2007, pp. 271–275.

[37] Fan, L. M., et al., "A Fast Linear Algorithm for Magnetic Dipole Localization Using Total Magnetic Field Gradient," *IEEE Sensors Journal*, Vol. 18, No. 3, February 2018, pp. 1032–1038.

[38] Sheinker, A., et al., "Magnetic Anomaly Detection Using a Three-Axis Magnetometer," *IEEE Transactions on Magnetics*, Vol. 45, No. 1, pp. 160–167, January 2009.

[39] Gao, J. Q., et al., "Magnetic Signature Analysis for Smart Security System Based on TMR Magnetic Sensor Array," *IEEE Sensors Journal*, Vol. 19, No. 8, April 2019, pp. 3149–3155.

[40] Ripka, P., A. M. Lewis, and J. Kubik, "Mine Detection in Magnetic Soils," *Sensor Letters*, Vol. 5, No. 1, 2007, pp. 15–18.

[41] Vyhnanek, J., M. Janosek, and P. Ripka, "AMR Gradiometer for Mine Detection," *Sensors and Actuators A: Physical*, Vol. 186, October 2012, pp. 100–104.

[42] Szyrowski, T., et al., "Developments in Subsea Power and Telecommunication Cables Detection: Part 2—Electromagnetic Detection," *Underwater Technology*, Vol. 31, No. 3, 2013, pp. 133–143.

[43] Fleming, W. J., "New Automotive Sensors-A Review," *IEEE Sensors Journal*, Vol. 8, No. 11-12, November-December 2008, pp. 1900–1921.

[44] Jiles, D., *Introduction to Magnetism and Magnetic Materials*, Boca Raton, FL: CRC Press, 2015.

[45] Ab Rashid, M. Z., et al., "Modeling of the In-Pipe Inspection Robot: A Comprehensive Review," *Ocean Engineering*, Vol. 203, May 2020.

[46] Sasada, I., and N. Watanabe, "Eddy-Current Probe for Nondestructive Testing Using Cross-Coupled Figure-8 Coils," *IEEE Transactions on Magnetics*, Vol. 31, No. 6, November 1995, pp. 3149–3151.

[47] Anderberg, J., et al., "LTS SQUID Microscope with Micron Spatial Resolution," *IEEE Transactions on Applied Superconductivity*, Vol. 13, No. 2, June 2003, pp. 231–234.

[48] Poppe, U., et al., "High Temperature Superconductor dc-SQUID Microscope with a Soft Magnetic Flux Guide," *Superconductor Science & Technology*, Vol. 17, No. 5, May 2004, pp. S191–S195.

[49] Fagaly, R. L., "Superconducting Quantum Interference Device Instruments and Applications," *Review of Scientific Instruments*, Vol. 77, No. 10, October 2006.

[50] Joubert, P. Y., and J. Pinassaud, "Linear Magneto-Optic Imager for Non-Destructive Evaluation," *Sensors and Actuators A: Physical*, Vol. 129, No. 1-2, May 2006, pp. 126–130.

[51] Gutierrez, J., and J. M. Barandiaran, "High Magnetostriction Metallic Glasses Used as Magnetoelastic Labels," *IEEE Transactions on Magnetics*, Vol. 31, No. 6, November 1995, pp. 3146–3148.

[52] Herzer, G., "Magnetoelastic Sensors for Electronic Article Surveillance," *Sensor Letters*, Vol. 5, No. 1, March 2007, pp. 259–262.

[53] Arndt, M., and L. Kiesewetter, "Coded Labels with Amorphous Magnetoelastic Resonators," *IEEE Transactions on Magnetics*, Vol. 38, No. 5, September 2002, pp. 3374–3376.

[54] Hasegawa, R., "Applications of Amorphous Magnetic Alloys," *Materials Science and Engineering A-Structural Materials Properties Microstructure and Processing*, Vol. 375, July 2004, pp. 90–97.

[55] Watanabe, N., I. Sasada, and N. Asuke, "A New High Density Magnetic Bar Code System," *Journal of Applied Physics*, Vol. 85, No. 8, April 1999, pp. 5462–5464.

[56] Campbell, W. H., *Introduction to Geomagnetic Fields*, Cambridge, U.K.: Cambridge University Press, 2003.

[57] Kearey, P., M. Brooks, and I. Hill, *An Introduction to Geophysical Exploration*, New York: John Wiley & Sons, 2013.

[58] Breiner, S., *Applications Manual for Portable Magnetometers*, Sunnyvale, CA: GeoMetrics, 1973.

[59] Jankowski, J., and C. Sucksdorff, *IAGA Guide for Magnetic Measurements and Observatory Practice*, 1996, http://www.iaga-aiga.org/publications/guides/.

[60] Ha, T. H., et al., "Role of Sensors in Corrosion Monitoring and Durability Assessment in Concrete Structures: The State of the Art," *Sensors and Materials*, Vol. 16, No. 3, 2004, pp. 133–158.

[61] Janosek, M., J. Vyhnanek, and P. Ripka, "CW Metal Detector Based on AMR Sensor Array," IEEE Sensors conference 2011 DOI: 10.1109/ICSENS.2011.6127370, pp. 1515–1517.

[62] 2G Enterprises, http://www.2genterprises.com/srm.html.

[63] "Agico JR-6 Spinner Magnetometer," https://www.agico.com/text/products/jr6/jr6.php.

[64] Stephenson, A., and L. Molyneux, "A Versatile Instrument for the Production, Removal and Measurement of Magnetic Remanence at Different Temperatures," *Measurement Science and Technology*, Vol. 2, No. 4, 1991, pp. 280–286.

[65] Gallet, Y., et al., "On the Use of Archeology in Geomagnetism, and Vice-Versa: Recent

Developments in Archeomagnetism," *Comptes Rendus Physique*, Vol. 10, No. 7, September 2009, pp. 630–648.

[66] Balogh, A., "Planetary Magnetic Field Measurements: Missions and Instrumentation," *Space Science Reviews*, Vol. 152, 2010, pp. 23–97.

[67] Ness, N. F., "Magnetometers for Space Research," *Space Science Reviews*, Vol. 11, 1970, pp. 459–554.

[68] Dolginov, S. S., L. N. Zhuzgov, and N. V. Pushkov, "Preliminary Report on Geomagnetic Measurements Carried Out from the Third Soviet Artificial Earth Satellite," *Iskusstvennyye Sputniki Zemli*, Vol. 2, 1958, pp. 50–53 (*Artificial Earth Satellites*, Vol. 2, 1959, pp. 63–67; *Planet. Space Sci.*, Vol. 5, 1961, pp. 244–247).

[69] Dolginov, S. S., L. N. Zhuzgov, and V. A. Selyutin, "Magnetometers in the Third Soviet Earth Satellite," *Iskusstvennyye Sputniki Zemli*, Vol. 4, 1960, pp. 135-160 (Artificial Earth Satellites, Vol. 3-5, New York: Plenum Press, 1960, pp. 366–396).

[70] Sonnet, C. P., "The Distant Geomagnetic Field: 2. Modulation of a Spinning Coil EMF by Magnetic Signals," *Journal of Geophysical Research*, Vol. 68, 1963, pp. 1229–1232.

[71] Cahill, L. J., "The Geomagnetic Field," in D. P. LeGalley and A. Roser, (eds.), *Space Physics*, New York: John Wiley & Sons, 1964, pp. 301–349.

[72] Ness, N. F., "The Earth's Magnetic Tail," *Journal of Geophysical Research*, Vol. 70, 1965, pp. 2989–3005.

[73] Ness, N. F., "Space Exploration of Planetary Magnetism," *Space Science Reviews*, Vol. 152, No. 1–4, 2009, pp. 5–22.

[74] Olsen, N., et al., "Measuring the Earth's Magnetic Field from Space: Concepts of Past, Present and Future Missions," *Space Science Reviews*, Vol. 155, No. 1, 2010, pp. 65–93.

[75] Russell, C. T., and M. K. Dougherty, "Magnetic Fields of the Outer Planets," *Space Science Reviews*, Vol. 152, No. 1–4, 2010, pp. 251–269.

[76] Stevenson, D. J., "Planetary Magnetic Fields: Achievements and Prospects," *Space Science Reviews*, Vol. 152, No. 1–4, 2009, pp. 651–664.

[77] Ness, N. F., et al., "Magnetic Fields at Uranus," *Science*, Vol. 233, 1986, pp. 85–89.

[78] Ness, N. F., et al., "Magnetic Fields at Neptune," *Science*, Vol. 246, 1989, pp. 1473–1478.

[79] Connerney, J. E. P., M. H. Acuña, and N. F. Ness, '"The Magnetic Field of Uranus," *Journal of Geophysical Research*, Vol. 92, 1987, pp. 234–248.

[80] Connerney, J. E. P., M. H. Acuña, and N. F. Ness, "The Magnetic Field of Neptune," *Journal of Geophysical Research*, Vol. 96, 1991, pp. 19023–19042.

[81] Phillips, J. L., and, C. T. Russell, "Upper Limit on the Intrinsic Magnetic Field of Venus," *Journal of Geophysical Research*, Vol. 92, 1987, pp. 2253–2263.

[82] Ness, N. F., "The Magnetic Fields of Mercury, Mars, and Moon," *Annual Review of Earth and Planetary Sciences*, Vol. 7, 1979, pp. 249–288.

[83] Anderson, B. J., et al., "Low-Degree Structure in Mercury's Planetary Magnetic Field," *Journal of Geophysical Research*, Vol. 117, No. E12, 2012.

[84] Acuña, M. H., et al., "Magnetic Field and Plasma Observations at Mars: Initial Results of the Mars Global Surveyor Mission," *Science*, Vol. 279, 1998, pp. 1676–1680.

[85] Acuña, M. H., et al., "Magnetic Field of Mars: Summary of Results from the Aerobraking and Mapping Orbits," *Journal of Geophysical Research*, Vol. 106, No. E10, 2001, pp. 23403–23417.

[86] Baumjohann, W., et al., "The BepiColombo–Mio Magnetometer En Route to Mercury," *Space Science Reviews*, Vol. 216, No. 8, October 2020, p. 125.

[87] Snare, R. C., "A History of Vector Magnetometry in Space," in R. F. Pfaff et al., (eds.), *Measurement Techniques in Space Plasmas: Fields, Vol. 103*, Washington, D.C.: American Geophysical Union (AGU), 1998, pp. 101–114.

[88] Acuña, M. H., "Space-Based Magnetometers," *Review of Scientific Instruments*, Vol. 73, No. 11, 2002, pp. 3717–3736.

[89] Primdahl, F., "Scalar Magnetometers for Space Applications," in R. F. Pfaff et al., (eds.), *Measurement Techniques in Space Plasmas: Fields, Vol. 103*, Washington, D.C.: American Geophysical Union (AGU), 1998, pp. 85–99.

[90] Duret, D., et al., "Overhauser Magnetometer for the Danish Oersted Satellite," *IEEE Transactions on Magnetics*, Vol. 31, No. 6, 1995, pp. 3197–3199.

[91] Duret, D., et al., "Performances of the OVH Magnetometer for the Danish Oersted Satellite," *IEEE Transactions on Magnetics*, Vol. 32, No. 5, 1996, pp. 4935–4937.

[92] Slocum, R. E., and F. N. Reilly, "Low Field Helium Magnetometer for Space Applications," *IEEE Transactions on Nuclear Science*, Vol. NS-10, 1963, pp. 165–171.

[93] Farthing, W. H., and W. C. Folz, "Rubidium Vapor Magnetometer for Near Earth Orbiting Spacecraft," *Review of Scientific Instruments*, Vol. 38, 1967, pp. 1023–1030.

[94] Balogh, A., et al., "The Magnetic Field Investigation on the ULYSSES Mission: Instrumentation and Preliminary Scientific Results," *Astronomy and Astrophysics Supplement Series*, Vol. 92, 1992, pp. 221–236.

[95] Dunlop, M. W., et al., "Operation of the Dual Magnetometer on Cassini: Science Performance," *Planetary and Space Science*, Vol. 47, No. 10, 1999, pp. 1389–1405.

[96] Smith, E. J., et al., "Scalar Helium Magnetometer Observations at Cassini Earth Swing-By," *Journal of Geophysical Research*, Vol. 106, No. A12, 2001, pp. 30129–30139.

[97] Fratter, I., et al., "Swarm Absolute Scalar Magnetometers First In-Orbit Results," *Acta Astronautica*, Vol. 121, 2016, pp. 76–87.

[98] Jager, T., "SWARM Absolute Scalar Magnetometer Accuracy: Analyses and Measurement Results," *2010 IEEE Sensors*, 2010, pp. 2392–2395.

[99] Lammegger, R., "Method and Device for Measuring Magnetic Fields," German Patent WO/2008/151344 (WIPO), 2008, https://patentscope.wipo.int/search/en/detail.jsf?docId=WO2008151344.

[100] Pollinger, A., et al., "Coupled Dark State Magnetometer for the China Seismo-Electromagnetic Satellite," *Measurement Science and Technology*, Vol. 29, No. 9, 2018, p. 095103.

[101] Musmann, G., and Y. Afanassiev, *Fluxgate Magnetometers for Space Research*, Books on Demand, 2010.

[102] Auster, H. U., et al., "The THEMIS Fluxgate Magnetometer," *Space Science Reviews*, Vol. 141, No. 1–4, 2008, pp. 235–264.

[103] Russell, C. T., et al., "The Magnetospheric Multiscale Magnetometers," *Space Science Reviews*, Vol. 199, No. 1, 2016, pp. 189–256.

[104] Miles, D. M., et al., "A Radiation Hardened Digital Fluxgate Magnetometer for Space Applications," *Geoscientific Instrumentation, Methods and Data Systems*, Vol. 2, No. 2, 2013, pp. 213–224.

[105] Tøffner-Clausen, L., et al., "In-Flight Scalar Calibration and Characterisation of the Swarm Magnetometry Package," *Earth, Planets and Space*, Vol. 68, No. 1, 2016.

[106] Harten, R., and K. Clark, "The Design Features of the GGS WIND and POLAR Spacecraft," *Space Science Reviews*, Vol. 71, 1995, 4 vols., C. T. Russell, (ed.), pp. 23–40.

[107] Ness, N. F., et al., "Use of Two Magnetometers for Magnetic Field Measurements on a Spacecraft," *Journal of Geophysical Research*, Vol. 76, 1971, pp. 3564–3573.

[108] Neubauer, F. M., "Optimization of Multimagnetometer Systems on a Spacecraft," *Journal of Geophysical Research*, Vol. 80, No. 22, 1975, pp. 3235–3240.

[109] Pope, S. A., et al., "Exploring Planetary Magnetic Environments Using Magnetically Unclean Spacecraft: A Systems Approach to VEX MAG Data Analysis," *Annales Geophysicae*, Vol. 29, No. 4, 2011, pp. 639–647.

[110] Magnes, W., et al., "Space Weather Magnetometer Aboard GEO-KOMPSAT-2A," *Space Science Reviews*, Vol. 216, No. 8, 2020, p. 119.

[111] Constantinescu, O. D., et al., "Maximum-Variance Gradiometer Technique for Removal of Spacecraft-Generated Disturbances from Magnetic Field Data," *Geoscientific Instrumentation, Methods and Data Systems*, Vol. 9, 2020, pp. 451–469.

[112] Sheinker, A., and M. B. Moldwin, "Adaptive Interference Cancelation Using a Pair of Magnetometers," *IEEE Transactions on Aerospace and Electronic Systems*, Vol. 52, 2016, pp. 307–318.

[113] Plaschke, F., et al., "Advanced Calibration of Magnetometers on Spin-Stabilized Spacecraft Based on Parameter Decoupling," *Geoscientific Instrumentation, Methods and Data Systems*, Vol. 8, 2019, pp. 63–76.

[114] Anderson, B. J., et al., "In-Flight Calibration of the NEAR Magnetometer," *IEEE Transactions on Geoscience and Remote Sensing*, Vol. 39, 2001, pp. 907–917.

[115] Plaschke, F., "How Many Solar Wind Data Are Sufficient for Accurate Fluxgate Magnetometer Offset Determinations?" *Geoscientific Instrumentation, Methods and Data Systems*, Vol. 8, 2019, pp. 285–291.

[116] Russell, C. T., "Geophysical Coordinate Transformations," *Cosmic Electrodynamics*, Vol. 2, 1971, pp. 184–196.

[117] Escoubet, C. P., R. Schmidt, and M. L. Goldstein, "Cluster—Science and Mission Overview," *Space Science Reviews*, Vol. 79, 1997, pp. 11–32.

[118] Angelopoulos, V., "The THEMIS Mission," *Space Science Reviews*, Vol. 141, 2008, p. 5.

[119] Burch, J. L., et al., "Magnetospheric Multiscale Overview and Science Objectives," *Space Science Reviews*, 2016, pp. 5–21.

CHAPTER 10

Testing and Calibration Instruments

Ichiro Sasada, Eugene Paperno, and Pavel Ripka

Magnetic sensor specifications were discussed in Section 1.8. In this chapter, we describe equipment for sensor testing and calibration and also discuss some techniques in more detail.

A single-axis magnetometer has two basic calibration parameters: sensitivity and offset. Furthermore, the sensing direction should also be determined as two angles with respect to a reference axis, which is usually connected with the sensor body. Sensitivity is mostly calibrated using calibration coils (Section 10.1) and offset and its stability (drift or noise) is best calibrated within a magnetic shielding (Section 10.3). The calibration of angular deviations is discussed in Section 10.4, which is devoted to the calibration of 3-axial magnetometers. Coil systems for the compensation of external fields are described in Section 10.2

The sensor offset can be measured by rotating the sensor through 180°. While in the presence of the Earth's field, this method requires very precise positioning using a theodolite and complex compensation of the axis misalignment [1], it becomes very simple when used in the low residual field inside a shielding. The technique of flipping the sensor was used for in-flight calibration of the offset (e.g., aboard the active magnetospheric particle tracer explorer (AMPTE) subsatellite for in-flight calibration of the offset). Some satellites and rockets rotate with respect to their major principal axis to stabilize the trajectory. This rotation modulates the component of the field perpendicular to the axis, and so the rotation can be used for the same calibration purpose. The method of in-flight calibration of magnetometers on a spinning spacecraft is described in [2, 3].

10.1 Calibration Coils

The magnetic field in a distance x on the axis of a single current loop of diameter d can be calculated from the Biot-Savart law as

$$H = \frac{Id^2}{\sqrt{\left(d^2 + 4x^2\right)^3}} \tag{10.1}$$

The magnetic field of a long solenoid with N turns is $H = NI/l$. In the center of a solenoid with finite length, the field is equal to [4]:

$$H = \frac{NI}{\sqrt{4R^2 + l^2}} \tag{10.2}$$

where l is the coil length, R is its radius, N the number of turns, and I is the coil current.

If we cut the $2l$ long solenoid with $2N$ turns into halves, we easily obtain the formula for the field at the ends of the $2l$ long solenoid with N turns:

$$H = \frac{NI}{2\sqrt{R^2 + l^2}} \tag{10.3}$$

so that the field at the end of the solenoid is approximately one-half of the field in its center.

The field at any point on the axis can be calculated using (10.3) if we formally divide the solenoid at that point into two shorter solenoids and add their contributions.

Solenoids are used for compensation windings of many sensors. If the compensation solenoid is not long enough, the field inhomogeneity together with nonlinearity of the sensor may result such that even the feedback-compensated sensor has a nonlinear response.

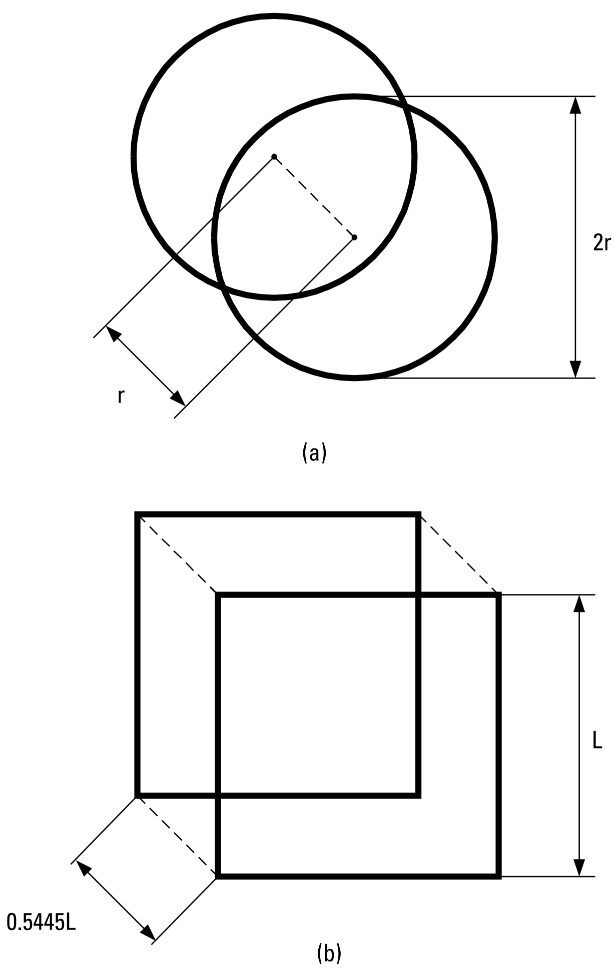

Figure 10.1 Helmholtz coils: (a) circular, and (b) rectangular.

Solenoids are not very practical calibration devices as the access to their center, where the sensor under test should be located, may be complicated. The most common calibration device is thus the Helmholtz coil pair, as shown in Figure 10.1(a), which consists of two identical thin circular coils separated by the distance of their radius *r*. The field distribution inside the Helmholtz coils is shown in Figure 10.2. The 100-ppm homogeneity is achieved inside a cylinder, which has 10% the radius of the coils.

The field in the middle of the circular Helmholtz coils is:

$$H = \frac{NI\left(\frac{1.6}{\sqrt{5}}\right)}{r} \cong \frac{0.7155NI}{r} \tag{10.4}$$

which corresponds to $B = 899.18\ NI/r$ (nT/A).

The field gradient in the midpoint of Helmholtz coils is zero. If we connect the two coils antiserially, the field in the middle is zero and we have there a region of a constant field gradient. However, to have a uniform gradient over the inner 10% separation, the coils must be separated by $\sqrt{3}r$ (Figure 10.3(b)). Otherwise, the gradient response is parabolic within the center region (Figure 10.3(a)).

Rectangular coils (Figure 10.1(b)) are easier to realize in large sizes and their field is only slightly less uniform [5] than that of circular coils; they give larger working volume for modest values of uniformity. The distance between the square coils for the best homogeneity should be 0.5445 *L*, where *L* is the length of the side of the square.

The field in the midpoint of such a rectangular Helmholtz coil pair is [5]

$$B = \frac{1{,}628.7NI}{L}(nT, A) \tag{10.5}$$

A simple 3-axial Helmholtz coil system is described in [6].

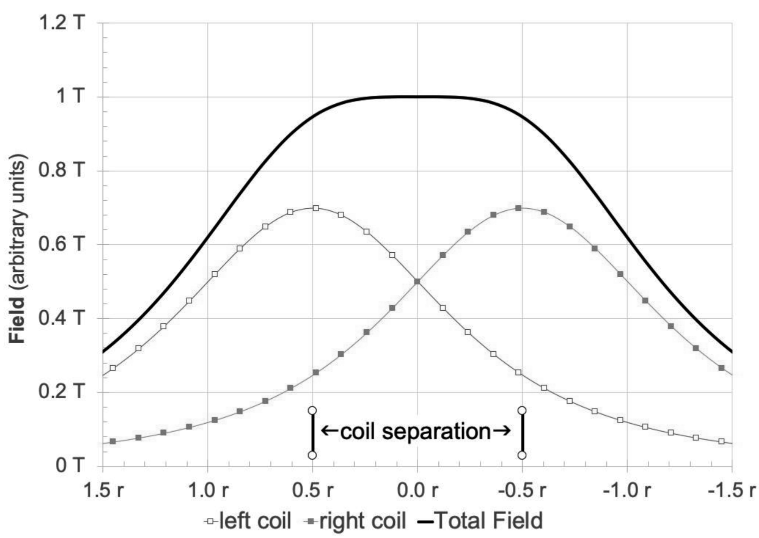

Figure 10.2 Helmholtz coils: field versus position.

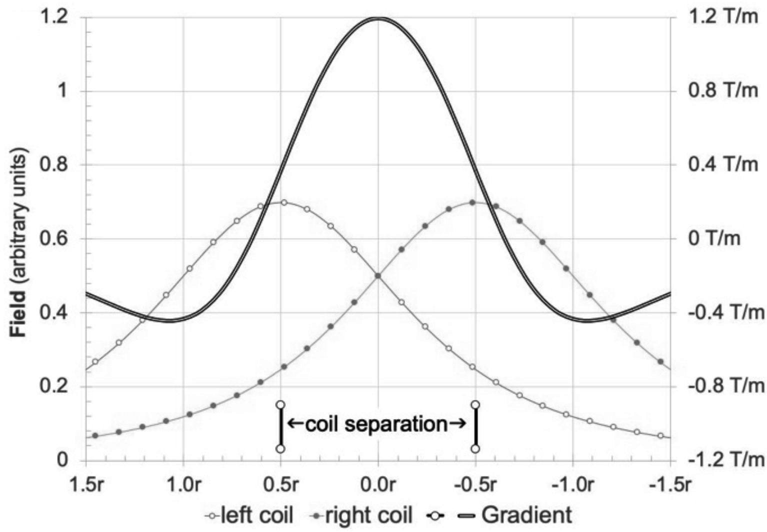

(a)

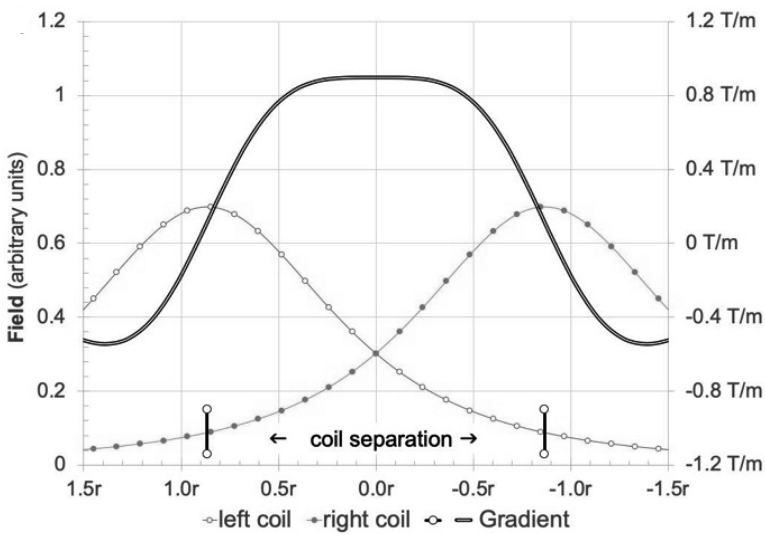

(b)

Figure 10.3 (a) Gradient fields (in arbitrary units on right vertical axis) for $r = 1$ (Helmholtz) and (b) $r = \sqrt{3}$ coil separations.

Alldred and Scollar calculated a system of four rectangular coils, which give more than 10 times better homogeneity than two coils [7]. The coil system is shown in Figure 10.4. The coil dimensions are calculated for rational current ratios, which can be obtained by a realistic number of turns. Such a system was built and calibrated in the Nurmijarvi Magnetic Observatory for $N_1/N_2 = 21{:}11$, $L_1 = 0.9552\ L_2$, $d_1 = 1.0507\ L_2$, and $d_2 = 0.28821\ L_2$ [8]. The whole system consists of three orthogonal sets of four square coils with side lengths ranging from 1.6m to 2.2m. It produces a uniform field with a 10-ppm theoretical accuracy in a spherical volume of 30-cm

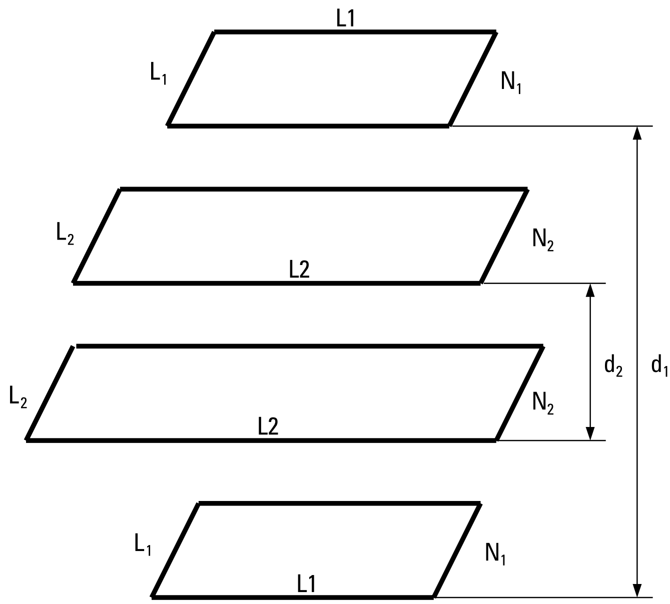

Figure 10.4 Rectangular coil system of Alldred and Scollar. Not in scale. (*After:* [7].)

diameter (100 ppm for 40-cm diameter). The coil directions were found by using a nonmagnetic theodolite with 0.5-arc minute precision and the individual coil constants were calibrated by a proton magnetometer with 10-ppm accuracy. Using these coils supplied by computer-controlled current sources and a distant reference magnetometer monitoring the variations of the Earth's field, a precise system for the calibration of magnetometers was built. Such a system should be located at a magnetically clean and quiet place in a nonmagnetic thermostated room. In order to ensure the geometrical stability, the coil system should be mounted on a concrete pillar. The ideal, but very expensive, material for large coils and their support system is quartz; a coil support made of glass was used for the compensation system in Pruhonice [9]. Wooden constructions are sensitive to humidity; aluminum has a large temperature dilatation, but it is most often used together with temperature stabilization [1].

Numerous other field coil systems are described in the literature such as a four-coil rectangular Merritt system (Figure 10.5) or a 5-coil Rubens system [10]. Some of them allow all the coils to have the same area, but they require exotic current ratios into the coil sections, which are difficult to keep stable. It should be noted that the only realistic design is that all the coils for the given direction are connected in series and a precise and stable relationship between the individual loop currents is maintained by the number of their turns.

Saddle coils are used to create a prolate volume of a uniform field, which is necessary for testing long objects such as submarines [11]. Similar coils are used for magnetic resonance experiments [12, 13].

Sometimes the magnetic field outside the coil system must be calculated, for example, to estimate the influence on sensors in their vicinity. A current loop has a magnetic moment of $m = NIA$ where A is the loop area and, from a large distance, it can be considered as a magnetic dipole. The field components at a distance r are

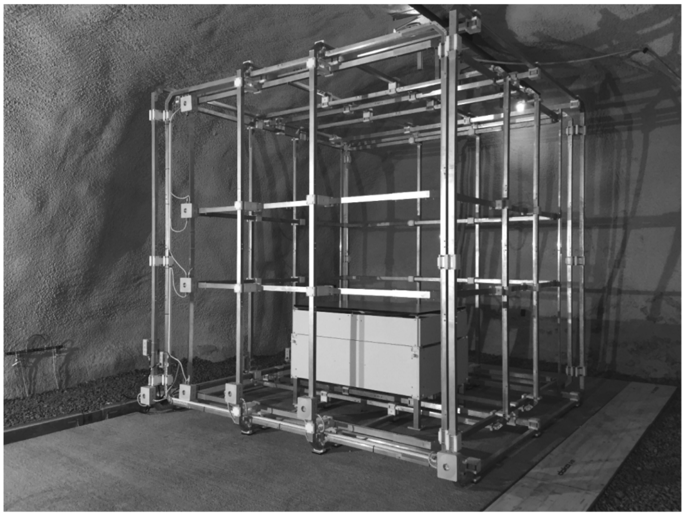

Figure 10.5 A 3-D Merritt coil in the calibration (side) tunnel of the Conrad Observatory in Austria. (Courtesy of the Austrian Academy of Sciences.)

$$
\begin{aligned}
B_r &= \frac{2\mu_0 m \cos\phi}{4\pi r^3} \text{ ... radial component} \\
B_\phi &= \frac{\mu_0 m \sin\phi}{4\pi r^3} \text{ ... tangential component}
\end{aligned} \tag{10.6}
$$

where ϕ is the angle between the coil axis and the direction to the measured point.

In case of a Helmholtz coil pair, the magnetic field is twice as large. If we want to create a magnetic moment (e.g., for a calibration of induction magnetometers), a compact one-layer solenoid with a length/diameter ratio of 0.86:1 is theoretically the most convenient coil shape [14].

Ideal spherical coils generate an ideal homogenous field in the whole inside volume. A real spherical shell coil consisting of 50 turns on each hemisphere has 100-ppm homogenous field in 67% of the volume (compared to 9% for the Helmholtz coils) and a 10-ppm homogeneous field in 50% of the volume (5% for the Helmholtz coils) [15]. Spherical coils are difficult to manufacture and access to the inside volume is complicated. They are often used in proton magnetometers (Chapter 7) and also as a triaxial CSC system for feedback compensation in a fluxgate magnetometer (Section 3.14.1).

Probably the largest magnetic field calibration facility was built at the NASA Goddard Space Flight Center. The coil system is of the Braunbek type, consisting of 12 circular coils (4 for each axis). The 10-ppm homogeneity volume has a 1.8-m diameter. The largest coil is 12.7m in diameter and the access window is 3m × 3m. The coils are wound from aluminum wire on an aluminum structure and they are temperature-compensated. The system is able to compensate the Earth's field using a magnetic observatory, which is located at a distance of about 100m in a direction with a low natural gradient. Independent of field cancellation, the system is able to generate an artificial field up to 60 μT with an arbitrary direction [16].

Several rules should be observed when making coil calibrations. At first, it is necessary to precisely adjust and determine the sensor position. In most cases, the directional response of a vector sensor is a cosine type, so 100-ppm precision requires 0.8° alignment; 10-ppm precision requires 0.25° alignment. The adjustment should be made magnetically, as the sensor geometrical axis may differ from its magnetic sensitivity axis. The best solution is to adjust the sensor position using perpendicular coils, for which the angular response is much sharper. The final correction is then made numerically, taking into account the estimated angles between the calibration coils.

Large calibration coils have large time constants. It is therefore important to wait after each field change until the current is constant. It is necessary to monitor field interferences during the measurement and repeat each calibration step several times. The environmental noise and other variations caused (e.g., by the noise of the calibration current or by mechanical vibrations) can be suppressed by using a long integration time of the voltmeters, simultaneous measurements of all the variables, and averaging. According to our experience, 2-ppm resolution in sensitivity measurement in a normal laboratory requires 2-second integration time for each voltage measurement and averaging from 100 readings. Simultaneously triggered 6½ digit voltmeters such as a HP 34401 are sufficient for this purpose. Such measurements are time-consuming, and it is difficult to keep all the parameters constant. An alternative is to use low-frequency AC calibration field and synchronous detection at the output. Modern digital lock-in amplifiers are fast enough even if the reference signal is very slow. The resolution and accuracy of AC calibration are limited; they can be increased by compensation methods.

Coils for AC calibration should satisfy additional requirements. First, the coil self-resonant frequency should be well above the required frequency range. The coil supporting structure should be nonconductive to prevent eddy currents. Also, all metal objects in the coil vicinity should be avoided. It is even important to check the ground resistivity; the reasonable minimum is 5,000 Ωm.

In general, the calibration coil should be 5 to 20 times larger than the sensor under the test. The only exceptions are the air-coil induction magnetometers, which are perfectly linear so that the error caused by the calibration field inhomogeneity can be corrected for. The correction factors were calculated by Nissen and Paulsson showing that the correction is only 1% if the radius of the induction coil under the test is one-half of the radius of the Helmholtz coils [17].

For precise measurements, the coil system must be calibrated. The traditional calibration method is based on the triaxial magnetometer and a theodolite. It utilizes the similar method to declination inclination flux measurement [1], but the method is very time-consuming and it depends on the quality of the triaxial magnetometer.

The scalar method for calibration of 3-D coil systems was described in [18]. The main idea is based on the directionally independent scalar measurement of the magnetic field. The scalar magnetometer is inside the homogeneous space of the calibrated coil system and the current sequence excites the coils. Then the parameters of the system are calculated from the total magnetic field measurement and current measurement by an analytical method (sensitivity) and a nonlinear optimization method (orthogonality), respectively. Calibration can be easily made with uncertainty of 0.004° for angles between the coils and 30 ppm for the sensitivity.

10.1.1 Coils as Sources of the Magnetic Moment

Solenoid coils are used as field sources for geomagnetic studies and for position tracking and distance measurement. Using a ferromagnetic core brings significant advantages over air-core transmitters in weight, power, and volume efficiency. As an example, at 100 Hz, the maximum weight efficiency for a 0.5-m-long rod antenna made from Metglas was found to be 310% larger than a 0.5-m air-core antenna. The power efficiencies associated with the maximum weight efficiencies for these two cases differ by 420%. The volume efficiency of the Metglas rod antenna was calculated as about 500% larger than the 0.5-m air-core antenna [19].

A small coil can be used to imitate a magnetic dipole for magnetometer calibration or distance measurement. In case a of single-layer coil, the optimum length-to-diameter ratio (L/D) is 0.86:1; the imitation error, computed for a 4-radii distance from the coil's center, is reduced by a factor of 12 (from 9.4 down to 0.73%) relative to a single-turn coil. An even more precise dipole source can be made by multilayer coils, with a further reduction of the imitation error to <0.28% [14].

10.2 Field Compensation Systems

Field compensations systems use coil systems to cancel the variations of external fields, mainly the Earth's natural field variations. Such systems work only when the field sources are distant. The requirements for the field gradient depend on the required quality of the field stabilization. One example may be a simple compensation system for a mass spectrometer, which suppresses the field variations below 100 nT; it can work in a normal laboratory environment with strong field sources located in approximately 20-m distance. The field sensor may be an AMR magnetoresistor mounted directly on the spectrometer instrument.

The system for thermal demagnetization of rock samples (Section 9.7) requires a magnetic vacuum below 0.5 nT; such a system should be located in a nonmagnetic building kilometers from the interference sources. If the field sensors were nonmagnetic such as rotating coil magnetometers [9], they could be positioned inside the coil system. If the sensors contain magnetic materials, which is the case of the most common fluxgate sensors, they should be located far from the coils.

Systems that are able not only to compensate the field changes or cancel the field completely but also to create independent artificial calibration field have usually the field sensors outside the coils. The compensation sensor distance is usually sufficiently large so that the field from the coil system and also from the device under test is negligible; the external field gradients between the coil system and the sensors should be very small. This is the way the NASA's magnetic calibration facility (described in Section 10.1) is operated. A similar magnetic field simulation facility is managed by the Industrieanlagen-Betriebsgesellschaft mbH (IABG) in Ottobrunn, Germany. It has been used for the magnetic characterization of many ESA missions (e.g., Cluster). The IABG facility has a 15-m diameter coil system with parameters given in Table 10.1 [20].

Table 10.1 Parameters of the IABG 15-m Coil System

Parameter	*Value*
Maximum level of artificial magnetic field	75,000 nT
Field resolution	0.1 nT
Field accuracy	1 nT
Field uniformity	0.5 nT within a diameter of 4m
Field stability	0.5 nT per hour

The Magnetsrode calibration facility of TU Braunschweig has also been used for many international space missions [21, 22].

If the calibration should be made in normal laboratory environment with large gradients and high noise level, it is better to position the compensation sensors closer to the coil system [23]. Another possibility is to use a coil system inside the ferromagnetic shielding. However, due to the shielding nonlinearity and nonhomogeneity, the accuracy is decreased [24].

Active noise compensation systems for magnetically shielded rooms use induction coils, SQUIDs, or fluxgates as noise-reference sensors. A shielding factor improvement of more than 40 dB in the frequency range 0.1 Hz to 10 Hz is achievable [25].

10.3 Magnetic Shielding

For the measurement of sensor noise and offset, a place with very low magnetic field is required. Shielding of the ambient field (the geomagnetic field of about 50,000 nT, its variations up to 500 nT and magnetic noise originating from human activities ranging from 10 nT at magnetically silent locations to 1 mT in industrial environment) may be performed by various means. Ferromagnetic shielding is usually made in the form of a multilayer cylinder from permalloy or an amorphous material. This type of shielding is available from several manufacturers in a large selection of sizes up to shielded rooms, which are used for biomagnetic measurements using SQUIDs (Chapter 7). Magnetic shieldings are often custom-made for specific requirements. A typical shielding for the calibration of offset and noise of magnetic sensors has cylindrical shape with internal diameter of 15 to 20 cm. The shielding has typically 60-cm to 1-m length, the access is from the top side and the bottom side is closed. The best location of the sensor under test is about 10 to 15 cm from the bottom lid. The calibration shielding has typically up to 6 layers of 1-mm-thick permalloy (mu-metal) and it should be once annealed and periodically demagnetized by an air coil supplied with 50/60-Hz current. The demagnetization coil is inserted inside and slowly pulled out. The demagnetization field should be sufficiently strong to saturate all the shielding layers. Such cylindrical shieldings have become standard equipment in geophysical laboratories. The field inside is typically at nanotesla levels and it is caused more by remanence of the shield material than by the uncompensated remainder of the external field.

Three-layer shielding described in [26] consists of vertical cylinders closed by lids. The residual horizontal field is less than 1 nT and the residual vertical field is about 2 nT. The nonhomogeneity is about 0.1 nT/cm.

The literature on magnetic shielding is very fragmented. We believe that following section gives both the basic theory and the practical rules for the design, maintenance, and application of ferromagnetic shieldings.

A superconducting shield based on the Meissner effect (Chapter 7) was described by Brown [27]. It has an attenuation factor in the order of 10^{-7} in transverse and 10^{-9} in radial direction. At present, superconducting shieldings are used only as a part of cryogenic instruments; much cheaper ferromagnetic shieldings are sufficient for testing and operation of room-temperature devices.

Another way to make a magnetic vacuum is to actively compensate the field by means of a 3-D system of coils. Such systems are described in Section 10.2. AC magnetic fields may be suppressed by eddy-current shields (see Section 7.9.2) made of thick conductive material. There were 45-mm-thick aluminum plates used for the Tampere shielded room [28].

10.3.1 Magnetic Shielding Theory

Magnetic shielding provides a low reluctance path guiding the magnetic flux around the region to be shielded (Figure 10.6). For the sake of simplicity, it is generally assumed that a magnetic shield is placed in a uniform external field, and the permeability does not depend on the magnetic induction. The frequency, f, of the ambient field is assumed to be low enough to satisfy quasi-static conditions: the skin depth $\delta = 1/\sqrt{(\pi f \mu_0 \mu_r \sigma)}$ is below the thickness, t, of a shield with the relative permeability μ_r and conductivity σ.

The shielding effectiveness is described by two main parameters: the shielding factor, defined as the ratio of the external field to the residual field (the field within the shielded region), and the uniformity of the residual field. It is quite obvious that the shielding effectiveness depends on the geometry, thickness, and permeability of the magnetic shell. Less obvious is that an introduction of air gaps between the shielding shells (see Figure 10.6(b) can greatly increase the shielding factor. Mathematical solutions for the transverse magnetic field penetration into ideal single-shell and multiple-shell shields illustrate the above statements quantitatively.

10.3.2 Transverse Magnetic Shielding

Shielding assemblies such as a set of concentric spheres or infinitely long cylinders are considered ideal because they provide a uniformly reduced residual field (see Figure 10.6).

For a single shell of the thickness t, diameter D, and a constant relative permeability μ, the transverse shielding factor is given as follows [29]:

$$S_T \approx 1 + G\frac{\mu t}{D} \tag{10.7}$$

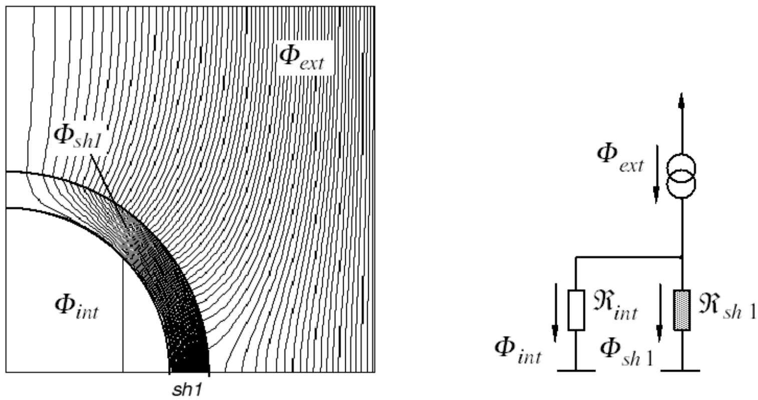

(a)

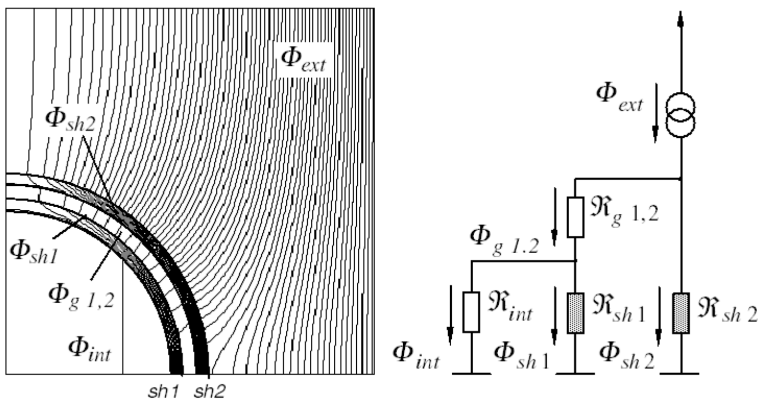

(b)

Figure 10.6 Transverse magnetic shielding: (a) single-shell and (b) double-shell cylindrical shields and their equivalent magnetic circuits. (Note that residual flux, Φ_{int}, is uniform.) The flux distributions are obtained numerically for $\mu = 100$.

In the case of high-permeability, $\mu >> 1$, and a relatively small thickness, $t/D << 1$, exact solutions can be reduced to simple forms. The transverse shielding factor for a double-shell shield becomes

$$S_{T\text{double}} \approx 1 + S_1 + S_2 + S_1 S_2 \left(1 - \frac{W_1}{W_2}\right) \tag{10.8}$$

where $S_i \approx (\mu_i t_i / D_i)$ is the transverse shielding factor for an individual shell, W_i is the volume of a sphere or cross-sectional area of a cylinder defined by the outer and inner surfaces of shells i and j, respectively. The total shielding factor for the n-fold-shell shield is calculated in a similar way.

The transverse shielding factor for a finite-length cylindrical shield with open ends is reduced by the fringing fields penetrating through the openings [30]. Roughly, fringing fields are attenuated by a factor 10^3 per diameter distance from the open end [31].

Equation (10.8) represents the main principle of magnetic shielding with multiple shells: decoupling the shells ($W_i/W_j >> 1$) allows a multiplicative rather than an additive increase in shielding. As a result, the shielding factor for a set of thin concentric shells can be much greater than that for a single thick shell built with the same amount of the material. A single shell is more effective concerning the weight only for a small μ, up to $\mu \approx 3D/4t$.

With thin multiple shells, the best minimum weight arrangement is when the diameters of the shells grow in geometric progression, $D_j = aD_i$, and the shielding material is distributed evenly among the shells [32]. However, for practical reasons, the thickness of shells is often uniform. Maximum shielding is obtained when the successive diameter ratio, α, is roughly 1.3 to 1.4 for spheres and 1.5 to 1.6 for cylinders. A simple estimation of shielding with multiple-shell shields is suggested in [32].

Cylinders with rectangular cross-sections are treated in [33]. The transverse shielding factor for square cylinders can be calculated according to (10.7) where the diameter, D, equals the side of the square, $G \approx 0.70$ for a square cylinder in a perpendicular external field, and $G \approx 0.91$ for a square cylinder in a diagonal external field.

10.3.3 Axial Magnetic Shielding

10.3.3.1 Axial Shielding with Single-Shell Shields

In many cases, cylindrical shields cannot easily be positioned with the axis of the shield perpendicular to the ambient magnetic field. Analytical calculation of the shielding factor is complicated and does not give accurate results; therefore, we present the results of finite element modeling (FEM).

The openings reduce the axial shielding factor dramatically only for relatively short cylinders. The flux distribution is shown in Figure 10.7. Fringing fields penetrating through the open ends decay approximately exponentially and are attenuated by a factor of about 10^2 per diameter distance from the open end.

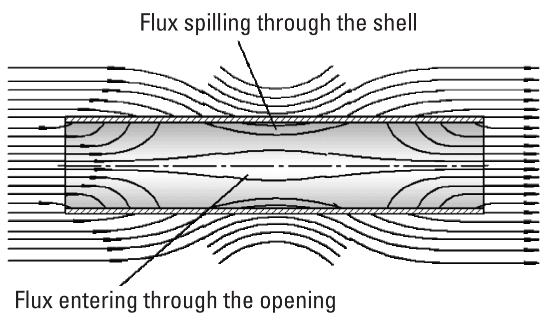

Figure 10.7 Simplified flux distribution around and within an open-ended cylinder in axial field.

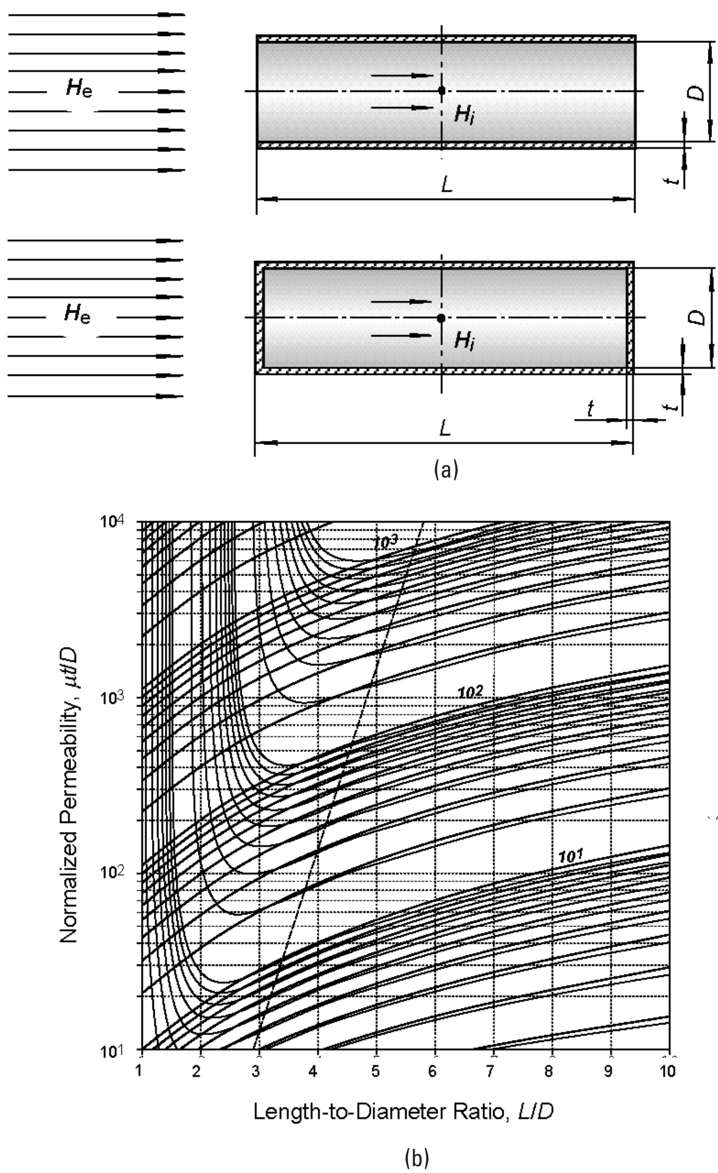

Figure 10.8 Axial shielding with single cylinders: (a) open-ended and closed cylinders; and (b) a numerically obtained chart (contour plot) describing the axial shielding factors (bold numbers) of closed cylinders (monotonic curves) and open-ended cylinders.

The axial shielding factors for both open and closed cylinders ($D/t = 100$) versus the length-to-diameter ratio, L/D, and normalized permeability, $\mu t/D$, are shown in Figure 10.8 as a chart (contour plot) that is obtained numerically by FEM analysis in ANSYS. This chart illustrates behavior of the shielding factor as being affected by the shields' geometry and permeability. The two following geometry-related effects cause decrease in the axial shielding factor: the effect of the openings for open-ended shields, and decreasing the axial shielding factor by increasing the length for both open-ended and closed shields.

Although open cylinders are generally considered to provide a less uniform residual field, numerical calculations show that this situation is abruptly changed when the shields' aspect ratios approach the values depicted by the dashed line in the chart of Figure 10.8(b). In the region right from the dashed line, the residual field inside open-ended cylindrical shielding becomes nearly uniform over a relatively wide shielded area and even outperforms the uniformity within corresponding closed cylinders.

10.3.3.2 Axial Shielding with Double-Shell Shields

Unfortunately, existing quasi-analytical estimations of axial shielding with multi-shell shields predict contradictory results. However, employing special charts [34] describing shielding performance for the most widely applicable, canonical shielding structures can be a relatively accurate and time-saving alternative for many scientists and shield designers.

It is important to note that shortening the inner shell is not always effective. For instance, it is worth choosing the same length for short shields with $L_2/D_2 \leq 3$, especially for high permeability materials. In such a case, it is more important to reduce the effect of the openings by increasing the L_1/D_1 ratio of the inner shell rather than to screen the ends of this shell.

As in the previous case of single-shell shields, a better uniformity of the residual field can be obtained within a properly constructed double-shell, open-ended shield.

10.3.4 Flux Distribution

Although a linear case is usually assumed in calculations, it is always important to remember that the permeability depends strongly on the magnetic induction. Assuming that $\mu >> 1$, the maximum flux density within the shielding material can be estimated according to [35], and corresponding permeability can be obtained from the normal magnetization curve given by manufacturers. Particular attention should be given to make the shielding shells—especially the outermost one—thick enough to avoid the dramatic decrease in the permeability when the material approaches saturation.

Considering $\mu >> 1$, the maximum flux density, $B_{m\text{transv}}$, within the material for a single-shell transverse cylindrical shield can be estimated as D/t times greater than the ambient field, B_0.

10.3.5 Annealing

Generally, once fabrication is completed, the shielding shell should be annealed. Annealing relieves mechanical stresses induced during fabrication. As a result, the shielding material reaches its optimum permeability. A standard annealing cycle for crystalline permalloy materials includes heating above 1,100°C in dry hydrogen for several hours and then cooling slowly. After the annealing is completed, the shield or its parts should be handled with care. Even little mechanical stress can seriously reduce the permeability and reannealing would be necessary.

Modern, commercially available shielding materials, such as cobalt-based thin amorphous ribbons are much less sensitive to mechanical stresses. Materials of this type make an excellent alternative to avoid the expensive annealing cycle in the manufacturing process. As these materials are very thin, they can be easily saturated. Therefore, they are suitable as inner layers of multilayer shieldings.

10.3.6 Demagnetizing

The lowest achievable DC field within a magnetic shield depends strictly on the magnetic history of the material after the annealing has been completed [32]. The remanent magnetization of the shielding material can be reduced and the shielding factor against DC magnetic fields can be greatly increased by demagnetizing (degaussing) the shield in situ. Although demagnetization generally can be done magnetically or thermally, the magnetic method is usually easier. The magnetic state of the material is cycled by a field decaying slowly from the amplitudes that saturate the material to zero. Typically, the minimum DC residual field obtainable is 1–10 nT and is limited by stray fields from imperfections of the material granular structure. After AC demagnetization, the field inside the shielding is changing; thus, it is advisable to wait 1 hour before using it for calibration. In general, after the application of an external magnetic field to permalloy cylinder, the magnetic flux density at the center of the shielded volume decreases by roughly 20% over periods of hours to days [36].

10.3.7 Enhancement of Magnetic Shielding by Magnetic Shaking

Magnetic shaking is an inexpensive and effective method to significantly increase the permeability and shielding performance against low-frequency magnetic fields. By applying a relatively strong, high-frequency magnetic field, magnetic shaking keeps the domain walls within the material in continuous vibrant motion and allows the material to be more responsive to a slowly varying, weak ambient field. In simple words, it is like sliding friction and static friction, the energy needed to move the domain walls is supplied by a fairly strong shaking field; therefore, the permeability seen for the slowly varying low-level magnetic field becomes high [37–41]. Magnetic shaking is not actual mechanical motion; the source of domain wall vibration is the AC magnetic field.

The most important key to effective magnetic shaking is the selection of the right shielding material. Soft amorphous ferromagnets, such as Metglas 2705M, with small magnetostriction and a highly rectangular hysteresis loop seem to be the best choice. With Metglas 2705M, shaking increases the effective incremental permeability 200-fold to 300-fold, resulting in μ from 4×10^5 to 6×10^5. Magnetic shaking is not effective if applied to permalloy, in which incremental permeability enhances only several times [42].

Shaking efficiency strongly depends on the orientation of the magnetic anisotropy of the shielding material, namely, the easy direction should be aligned along the corresponding shielding direction to achieve great shielding enhancement [43]. The direction of the shaking field is less important. Shaking enhancement is observed with fields that are both parallel and perpendicular to the easy direction. However in the latter case, the shaking amplitude should be about 10 times greater, ~30 A/m versus ~3 A/m, to obtain maximum shaking enhancement.

10.3.8 Magnetic Shielded Rooms

The magnetically shielded rooms are used for physical experiments, magnetometer calibration, and every magnetoencephalogram (MEG) detection system. They are generally made up of alternate layers of metal with high permeability, such as moly-permalloy, and metal with high conductivity, usually aluminum [44].

The 3-layer shielded room built in Helsinki in 1982 has a static shielding factor of 10,000 [45]. The 8-layered magnetically shielded room of the PTB Berlin was constructed in 2000 [46]. The magnetic shells consist of panels built up with strips of 0.5 mm finally annealed mu-metal similar to the commercially available shielded rooms made by Vacuumschmelze (VAC). For each of the magnetic shells, a set of 4 coils is installed for demagnetization [47]. The facility delivers a passive shielding factor at 0.01 Hz of 75,000 and values over 2×10^6 are achieved with active shielding. Active shielding is achieved by a 12-m size 3-axial coil system around the shielded room.

After suppressing the external variations by a high shielding factor, other noise sources remain. The inner wall, nearly always chosen to be the highest permeability metal, is a source of magnetic noise because of thermally generated electrical currents (Johnson noise) and magnetic domain motion (related to magnetic viscosity). The achievable noise level inside the shielding is 0.50 fT/√Hz at 100 Hz [44].

A transportable 2-layer magnetic shielding with a low residual field and gradient is described in [48]. A residual field of 700 pT within a central volume of 1m × 1m × 1m and a field gradient less than 300 pT/m was achieved despite the low shielding factor of 300.

10.4 Calibration of 3-Axial Magnetometers

The calibration of 3-axial magnetometers means the finding of nine unknown parameters: three sensitivities (S_x, S_y, and S_z), three offsets (O_x, O_y, O_z), and the angular deviations between the three individual sensors (θ, φ, and ψ). B_{xm}, B_{ym}, and B_{zm} are the uncalibrated magnetometer components of the measured field.

The true field components will be then

$$\begin{bmatrix} B_x \\ B_y \\ B_z \end{bmatrix} = \begin{bmatrix} S_x & & \\ & S_y & \\ & & S_z \end{bmatrix} \begin{bmatrix} \cos\theta\cos\varphi & -\sin\theta\cos\varphi & \sin\varphi \\ & \cos\psi & -\sin\psi \\ & & 1 \end{bmatrix} \begin{bmatrix} B_{xm} \\ B_{ym} \\ B_{zm} \end{bmatrix} + \begin{bmatrix} O_x \\ O_y \\ O_z \end{bmatrix} \tag{10.9}$$

There are two groups of methods for the calibration of the sensor sensitivity and angles between the sensor axes in 3-axial magnetometers: the first one is called the vectoral calibration and the second one is called the scalar calibration. Both methods can use either the Earth's field or a 3-axial calibration coil system.

10.4.1 Vectoral Calibration of 3-Axial Magnetometers

Using the Earth's field for vectoral calibration requires precise positioning of the sensor under test and it can be only used for low-field sensors such as fluxgate and AMR sensors. This technique is still in use at some magnetic observatories. The absolute accuracy achievable is about 10 nT (down to 1 nT at some quiet magnetic observatories). The procedure requires a precise reference proton precession (e.g., Overhauser) or cesium magnetometer (Chapter 6), a nonmagnetic theodolite, a magnetically clean and quiet place, and a lot of patience. The calibration procedures are described in geophysical literature such as [1] and also in [49, 50].

Vectoral calibration can also be made using precise coils supplied with accurate current sources [7]. A simple procedure for angular calibration based on sensor rotation in a 3-axial coil system is described in [51]. The achieved uncertainty is 27×10^{-5} rad, and the procedure allows one to calibrate coil system and magnetometer simultaneously. A similar procedure was used in [24] for triaxial coil system inside ferromagnetic shielding; due to the shielding, the accuracy was decreased to 10 nT, but the system can work in an environment with large gradients.

10.4.2 Scalar Calibration of 3-Axial Magnetometers

Scalar calibration is based on a statistical procedure that does not require precise positioning. The 3-axial magnetometer is placed in a homogeneous field (usually the Earth's field at a magnetically clean location, space without ferromagnetic objects that would distort the field homogeneity) and rotated in a way that all directions are evenly distributed. The 3-D magnetic field samples are collected, and, from this dataset, the nine unknown calibration parameters from (10.9) can be calculated by linear or nonlinear optimization method. It minimizes the variations of the total field $B = \sqrt{\left(B_x^2 + B_x^2 + B_x^2\right)}$ in the dataset, as ideally B is independent on heading [52]. By using this method, an Earth's field range magnetometer can be calibrated to an accuracy of 0.5 nT and a nonorthogonality of better than 2 arc-sec. The procedure can be automated by using a nonmagnetic positioning platform [53]. While a 2-axial positioning system is sufficient for the calibration of the magnetometer [54], the full calibration of a compass requires all 3 positioning axes.

Scalar calibration can be also made inside a 3-axial coil system; in this case, the magnetometer is stable and an artificial magnetic field created by the coil is rotated. To achieve this, the Earth's magnetic field including its variations must be canceled. This type of calibration is called a thin shell [55].

References

[1] Jankowski, J., and C. Sucksdorff, *IAGA Guide for Magnetic Measurements and Observatory Practice*, International Association of Geomagnetism and Aeronomy, 1996, http://www.iaga-aiga.org/publications/guides/.

[2] Farrell, W. M., et al., "A Method of Calibrating Magnetometers on a Spinning Spacecraft," *IEEE Transactions on Magnetics*, Vol. 31, No. 2, March 1995, pp. 966–972.

[3] Plaschke, F., et al., "Advanced Calibration of Magnetometers on Spin-Stabilized Spacecraft Based on Parameter Decoupling," *Geoscientific Instrumentation Methods and Data Systems*, Vol. 8, No. 1, February 2019, pp. 63–76.

[4] Jiles, D., *Introduction to Magnetism and Magnetic Materials*, Boca Raton, FL: CRC Press, 2015.

[5] Restrepo, A. F., et al., *A Comparative Study of the Magnetic Field Homogeneity for Circular, Square and Equilateral Triangular Helmholtz Coils*, New York: IEEE Press, 2017.

[6] Batista, D. S., et al., "Three-Axial Helmholtz Coil Design and Validation for Aerospace Applications," *IEEE Transactions on Aerospace and Electronic Systems*, Vol. 54, No. 1, February 2018, pp. 392–403.

[7] Alldred, J. C., and I. Scollar, "Square Cross Section Coils for Production of Uniform Magnetic Fields," *Journal of Scientific Instruments*, Vol. 44, No. 9, 1967.

[8] Pajunpää, K., et al., "Accredited Vector Magnetometer Calibration Facility," *Geophysica*, Vol. 43, No. 1-2, 2007, pp. 59–76.

[9] Prihoda, K., et al., "MAVACS—A New System for Creating a Non-Magnetic Environment for Paleomagnetic Studies," *Geologia Iberica*, No. 12, 1988.

[10] Merritt, R., C. Purcell, and G. Stroink, "Uniform Magnetic-Field Produced by 3-Square, 4-Square, and 5-Square Coils," *Review of Scientific Instruments*, Vol. 54, No. 7, 1983, pp. 879–882.

[11] Dinale, J., and J. Vrbancich, "Generation of Long Prolate Volumes of Uniform Magnetic Field in Cylindrical Saddle-Shaped Coils," *Measurement Science and Technology*, Vol. 25, No. 3, March 2014.

[12] Bonetto, F., E. Anoardo, and M. Polello, "Saddle Coils for Uniform Static Magnetic Field Generation in NMR Experiments," *Concepts in Magnetic Resonance Part B-Magnetic Resonance Engineering*, Vol. 29B, No. 1, February 2006, pp. 9–19.

[13] Nespor, D., K. Bartusek, and Z. Dokoupil, "Comparing Saddle, Slotted-Tube and Parallel-Plate Coils for Magnetic Resonance Imaging," *Measurement Science Review*, Vol. 14, No. 3, 2014, pp. 171–176.

[14] Paperno, E., and A. Plotkin, "Cylindrical Induction Coil to Accurately Imitate the Ideal Magnetic Dipole," *Sensors and Actuators A: Physical*, Vol. 112, No. 2-3, May 2004, pp. 248–252.

[15] Everett, J. E., and J. E. Osemeikhian, "Spherical Coils for Uniform Magnetic Fields," *Journal of Scientific Instruments*, Vol. 43, No. 7, 1966.

[16] Vernier, R., T. Bonalksy, and J. Slavin, *Spacecraft Magnetic Test Facility*, NASA report X-754-83-9, 1984.

[17] Nissen, J., and L. E. Paulsson, "Influence of Field Inhomogeneity in Magnetic Calibration Coils," *IEEE Transactions on Instrumentation and Measurement*, Vol. 45, No. 1, February 1996, pp. 304–306.

[18] Zikmund, A., et al., "Precise Scalar Calibration of a Tri-Axial Braunbek Coil System," *IEEE Transactions on Magnetics*, Vol. 51, No. 1, 2015.

[19] Jordan, J. W., B. Sternberg, and S. L. Dvorak, "Size, Weight and Power Efficiency for High-Power, Nonlinear, Geophysical-Transmitter, Rod-Core Antennas," *Journal of Environmental and Engineering Geophysics*, Vol. 16, No. 1, March 2011, pp. 1–12.

[20] Proceedings of the 5th International Symposium on Environmental Testing for Space Programmes Noordwijk, The Netherlands (ESA SP-558, June 2004). Compiled by: K. Fletcher., pp. 407–414.

[21] Glassmeier, K. H., et al., "RPC-MAG—The Fluxgate Magnetometer in the ROSETTA Plasma Consortium," *Space Science Reviews*, Vol. 128, No. 1-4, 2007, pp. 649–670.

[22] Hercik, D., et al., "The MASCOT Magnetometer," *Space Science Reviews*, Vol. 208, No. 1-4, July 2017, pp. 433–449.

[23] Janosek, M., et al., "Magnetic Calibration System with Interference Compensation," *IEEE Transactions on Magnetics*, Vol. 55, No. 1, January 2019.

[24] Pan, D. H., et al., "A New Calibration Method for Triaxial Fluxgate Magnetometer Based

on Magnetic Shielding Room," *IEEE Transactions on Industrial Electronics*, Vol. 67, No. 5, May 2020, pp. 4183–4192.

[25] Terbrake, H. J. M., R. Huonker, and H. Rogalla, "New Results in Active Noise Compensation for Magnetically Shielded Rooms," *Measurement Science and Technology*, Vol. 4, No. 12, December 1993, pp. 1370–1375.

[26] Magnes, W., et al., "A Spaceborne Magnetometer Tested Under Extended Temperature Conditions (Experiment MAREMF-OS/MARS-96)," *Measurement Science and Technology*, Vol. 9, No. 8, August 1998, pp. 1219–1228.

[27] Brown, R. E., "Device for Producing Very Low Magnetic Fields," *Review of Scientific Instruments*, Vol. 39, No. 4, 1968.

[28] Malmivuo, J., et al., "Improvement of the Properties of an Eddy-Current Magnetic-Shield with Active Compensation," *Journal of Physics E-Scientific Instruments*, Vol. 20, No. 2, February 1987, pp. 151–164.

[29] Thomas, A. K., "Magnetic Shielded Enclosure Design in DC and VLF Region," *IEEE Transactions on Electromagnetic Compatibility*, Vol. EM10, No. 1, 1968.

[30] Mager, A. J., "Magnetic Shields," *IEEE Transactions on Magnetics*, Vol. MAG6, No. 1, 1970.

[31] Freake, S. M., and T. L. Thorp, "Shielding of Low Magnetic Fields with Multiple Cylindrical Shells," *Review of Scientific Instruments*, Vol. 42, No. 10, 1971.

[32] Dubbers, D., "Simple Formula for Multiple Mu-Metal Shields," *Nuclear Instruments & Methods in Physics Research Section A-Accelerators Spectrometers Detectors and Associated Equipment*, Vol. 243, No. 2-3, March 1986, pp. 511–517.

[33] Mager, A., "Magnetostatic Shielding Factors of Cylinders with Rectangular Cross-Sections," *Physica B & C*, Vol. 80, No. 1-4, 1975, pp. 451–463.

[34] Paperno, E., H. Koide, and I. Sasada, "Charts for Estimating the Axial Shielding Factors for Triple-Shell Open-Ended Cylindrical Shields," *IEEE Transactions on Magnetics*, Vol. 37, No. 4, July 2001, pp. 2881–2883.

[35] Paperno, E., I. Sasada, and K. Tashiro, "Experimental Correction of the Axial Shielding Equation," *IEEE Transactions on Magnetics*, Vol. 38, No. 5, September 2002, pp. 3324–3326.

[36] Feinberg, B., and H. Gould, "Placed in a Steady Magnetic Field, the Flux Density Inside a Permalloy-Shielded Volume Decreases over Hours and Days," *AIP Advances*, Vol. 8, No. 3, March 2018.

[37] Sasada, I., S. Kubo, and K. Harada, "Effective Shielding for Low-Level Magnetic-Fields," *Journal of Applied Physics*, Vol. 64, No. 10, November 1988, pp. 5696–5698.

[38] Sasada, I., et al., "Low-Frequency Characteristic of the Enhanced Incremental Permeability by Magnetic Shaking," *Journal of Applied Physics*, Vol. 67, No. 9, May 1990, pp. 5583–5585.

[39] Sasada, I., E. Paperno, and H. Koide, "Design of a Large-Scale Vertical Open-Structure Cylindrical Shield Employing Magnetic Shaking," *Journal of Applied Physics*, Vol. 87, No. 9, May 2000, pp. 5962–5964.

[40] Sasada, I., and M. Shiokawa, "Noise Characteristics of Co-Based Amorphous Tapes to Be Applied as Magnetic Shielding Shell for Magnetic Shaking," *IEEE Transactions on Magnetics*, Vol. 39, No. 5, September 2003, pp. 3435–3437.

[41] Sasada, I., et al., "Cylindrical Magnetic Shield Made of a CFRP/Amorphous Magnetic Tape/CFRP Layered Composite with Built-In Shaking Coil," *Journal of Applied Physics*, Vol. 99, No. 8, April 2006.

[42] Kelha, V. O., R. Peltonen, and B. Rantala, "The Effect of Shaking on Magnetic-Shields," *IEEE Transactions on Magnetics*, Vol. 16, No. 4, 1980, pp. 575–578.

[43] Paperno, E., and I. Sasada, "Effect of Magnetic Anisotropy on Magnetic Shaking," *Journal of Applied Physics*, Vol. 85, No. 8, April 1999, pp. 4645–4647.

[44] Khan, S., and D. Cohen, "Note: Magnetic Noise from the Inner Wall of a Magnetically Shielded Room," *Review of Scientific Instruments*, Vol. 84, No. 5, May 2013.

[45] Kelha, V. O., et al., "Design, Construction, and Performance of a Large-Volume Magnetic-Shield," *IEEE Transactions on Magnetics*, Vol. 18, No. 1, 1982, pp. 260–270.

[46] Bork, J., et al., "The 8-Layered Magnetically Shielded Room of the PTB: Design and Construction," *Proc. 12th Intl. Conference on Biomagnetism (Biomag2000)*, 2000.

[47] Thiel, F., et al., "Demagnetization of Magnetically Shielded Rooms," *Review of Scientific Instruments*, Vol. 78, No. 3, March 2007.

[48] Altarev, I., et al., "A Magnetically Shielded Room with Ultra Low Residual Field and Gradient," *Review of Scientific Instruments*, Vol. 85, No. 7, July 2014.

[49] Ripka, P., and A. Zikmund, "Testing and Calibration of Magnetic Sensors," *Sensor Letters*, Vol. 11, No. 1, 2013, pp. 44–49.

[50] Včelák, J., et al., "AMR Navigation Systems and Methods of Their Calibration," *Sensors and Actuators A: Physical*, Vol. 123-124, 2005, pp. 122–128.

[51] Lassahn, M. P., and G. Trenkler, "Vectorial Calibration of 3D Magnetic-Field Sensor Arrays," *IEEE Transactions on Instrumentation and Measurement*, Vol. 44, No. 2, April 1995, pp. 360–362.

[52] Merayo, J. M. G., et al., "Scalar Calibration of Vector Magnetometers," *Measurement Science and Technology*, Vol. 11, No. 2, February 2000, pp. 120–132.

[53] Petrucha, V., et al., "Automated System for the Calibration of Magnetometers," *Journal of Applied Physics*, Vol. 105, No. 7, April 2009.

[54] Auster, H. U., et al., "Calibration of Flux-Gate Magnetometers Using Relative Motion," *Measurement Science and Technology*, Vol. 13, No. 7, July 2002, pp. 1124–1131.

[55] Risbo, T., et al., "Orsted Pre-Flight Magnetometer Calibration Mission," *Measurement Science and Technology*, Vol. 14, No. 5, May 2003, pp. 674–688.

CHAPTER 11

Magnetic Sensors for Nonmagnetic Variables

Pavel Ripka, Ichiro Sasada, Ivan J. Garshelis, and Ryan Kari

In this chapter, we briefly cover the large world of magnetic sensors, which measure variables other than the magnetic field. They are still called magnetic because they are based on magnetic principles. These sensors are not a primary topic of this book, so the main target of this chapter is to make an overview and refer to valuable information sources rather than to fully explain all the fine details and design rules. Some of these devices are using similar principles as magnetic field sensors (for example, position sensors with a permanent magnet target). The measured physical quantities may, in principle, affect the magnetic properties of sensing material or to change parameters of the magnetic circuit.

We will try to concentrate on principles that are already used in devices or that are likely to become widely used. Further reading on basic principles and interfacing can be found in [1–5]. A good introduction to magnetic design was given in [6].

11.1 Position Sensors

Magnetic position sensors are very widely used in industry. They are reliable, precise, rugged, and durable. They are inexpensive and are therefore very popular for industrial, automotive, aerospace, security, and defense applications. Unlike optical sensors, they are not sensitive to contamination (e.g., by grease or by dust). They sense either linear or angular position. Some of them have linear output, and the others have digital output: either bistable like proximity switches, or encoded like incremental and absolute position sensors. Another group combines digital (rough) and analog (fine) outputs.

The target, whose position is measured, may be a permanent magnet (induction sensors), soft magnetic material (linear variable differential transformer (LVDT), variable reluctance sensors), or just electrically conducting material (eddy-current sensors). Some of these devices work on DC, others work on AC principles, and another group needs both AC excitation and DC biasing. The requirements of industrial position sensors are very different from fine specifications of scientific magnetometers: instead of ppm accuracy, we discuss percentages, but the most important parameters are ruggedness, temperature stability, and electromagnetic compatibility (EMC). They have a much larger market than optoelectronic sensors, which are sensitive to contamination in the sensing path.

11.1.1 Sensors with a Permanent Magnet

The position sensors of this type consist of a magnetic field sensor, which measures the field of a permanent magnet. This magnet is either connected to the target, or the magnet is attached to the sensor and the target is made of ferromagnetic material; in both cases, moving the target changes the sensed field.

The sensor may be just a passive induction coil; in such a case, only the movement is sensed, not the static position. This type of sensor (called an induction sensor, speed sensor, or magnetic pickup) has output voltage proportional to the speed, so it fails as a position sensor at low speeds. However, moving coil sensors are used to measure linear or rotational speed.

All the other types use DC magnetic sensors: most often Hall, AMR, GMR, and semiconductor magnetoresistors. The specific details of these sensors can be found in their respective chapters of this book. Here, we only mention common problems and some design examples.

11.1.1.1 Nonlinearity of the Field Dependence

A small magnet far from the sensor behaves like a dipole, so that $B \sim 1/x^3$. Although this nonlinearity may be numerically corrected, it may still cause gross errors for large distances. The range (stroke) can be extended by using a linear array of sensors, which may detect zero crossing of the field (Figure 11.1). An overview of sensors of this type can be found in [2]. Another approach is to use a single triaxial sensor and an array of permanent magnets [7].

Rotational position sensors with radial permanent magnets are standard devices in the industry. Figure 11.2 shows the most popular configuration with a multipole ring.

Magnetic encoders can be made both incremental and absolute. Classic absolute encoders use multiple tracks coded in the Gray code to avoid gross error during logical hazards. Using the nonius (Vernier) principle [8], an absolute encoder can be constructed with only two magnetic tracks: 19-bit resolution (equivalent to 2.5

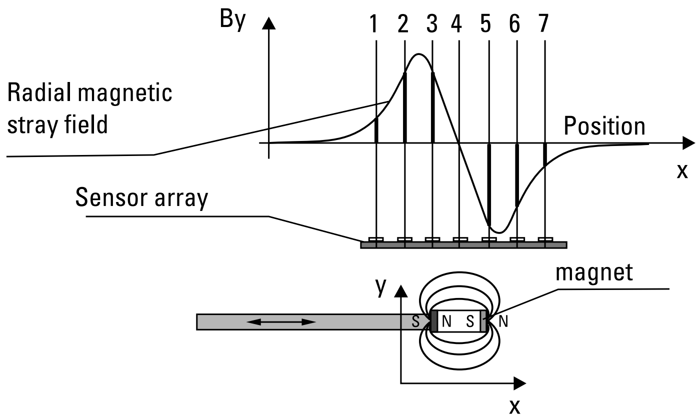

Figure 11.1 A linear sensor array for the position sensing of a permanent magnet.

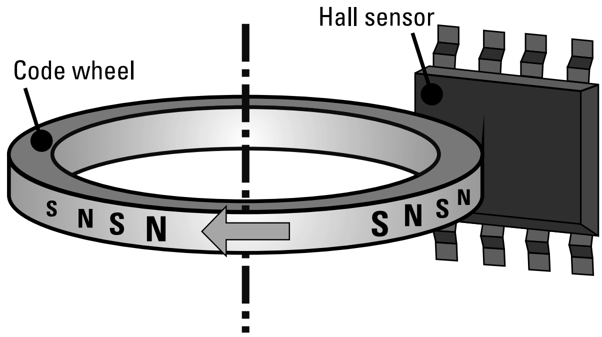

Figure 11.2 Rotational speed/incremental position sensor with an integrated Hall sensor. (*After:* Allegro.)

arcseconds) is obtained for rotation speeds up to 11,000 rpm. A combined magnetic rotational encoder, 67.11 mm in diameter (including the shaft) and 6.9 mm in thickness, has a precision of ±6′, comparable with a 15-bit photoelectric encoder and static resolution of ±0.6′ [9]. Another technique is using a track with a pseudorandom code sequence for the absolute position. Using this principle together with an interpolated incremental track, a 26-bit linear position sensor with 0.244-μm resolutions was constructed by Renishaw.

A permanent magnet can be also attached to the end of the shaft. In this case, GMR spin valves and also TMR sensors are ideal for angular sensing in the saturated mode (Figure 11.3). The free layer is rotated by the magnet. Once the layer is saturated, the output depends only on the angular position and not on the distance between the sensor and the magnet. Two perpendicular sensors are used to achieve 360° range without ambiguity. Similar AMR sensors are more precise, but have only 180° range. Some companies such as Infineon therefore integrate AMR and GMR angular sensors into one package achieving 0.03° error at room temperature and 0.3° error within the industrial temperature range. Hall sensors are also being used in this application. They are less precise, but may be more stable at elevated temperatures and they are also resistant to high fields.

11.1.2 Eddy-Current Sensors

The target of the eddy-current sensors should be electrically conducting, but not necessarily ferromagnetic. In this, they differ from variable gap sensors, which measure the displacement of the ferromagnetic part of an AC magnetic circuit. Eddy current-based instruments measure displacement, alignment, dimensions, vibrations, speed, and also identify and sort metal parts in industrial applications. Eddy-current sensors have no lower limit on target speed. The technologies behind eddy-current (inductive) proximity and linear displacement sensors are discussed in [10]. Eddy-current sensors are sometimes called inductive or inductance sensors, which can be rather misleading, confusing them with other types of sensors.

The AC magnetic field is created by the sensor coil fed by an oscillator. The coil is usually tuned by a parallel capacitor, and the LC circuit oscillates at the resonant frequency. If the conducting target is present, the eddy currents (mostly on the target surface) create a secondary magnetic field, decreasing the coil flux and thus the effective coil inductive reactance. The sensor sensitivity depends on the target conductivity. An excellent target is aluminum; the recommended thickness is >0.3 mm and the diameter is 2.5 to 3 times the diameter of the sensor coil [11]. In any case, the target thickness should be larger than the skin depth δ

$$\delta = \frac{1}{\sqrt{0.5\omega\mu\sigma}} \tag{11.1}$$

where σ is electrical conductivity, ω is angular frequency, $\mu = \mu_r\mu_0$ is permeability, μ_r is relative permeability, μ_0 is a permeability of the open space.

In the case of the ferromagnetic target, the situation is complicated, as the coil inductance is simultaneously increased by the target permeability $\mu_r > 1$. Figure 11.4 shows the relative eddy-current output for various target materials.

Because of the complex dependence on the target geometry and material, the position measuring system should usually be individually calibrated. For ferromagnetic targets, we may expect increased sensitivity to target axial displacement and to temperature changes and also worse repeatability and long-term stability. However, ferromagnetic targets increase the measuring range. The usual measuring range is up to 30% of the coil diameter. A lower range of 5% or 10% coil diameter is recommended for high-precision measurements, while in low-accuracy (for example, switching) applications, the range can be more than 50% of the coil diameter. In any case, the minimum coil-to-target distance is usually 10% of the range; this distance is often defined by the thickness of the sensor housing.

The sensing coils are often accompanied by a ferromagnetic circuit, which focuses their AC field into one direction so that the sensor is insensitive to conducting materials from the side or from the back. The working frequencies range from kilohertz to 1 MHz, the core material is usually ferrite, and the typical shape is pot core (Figure 11.5).

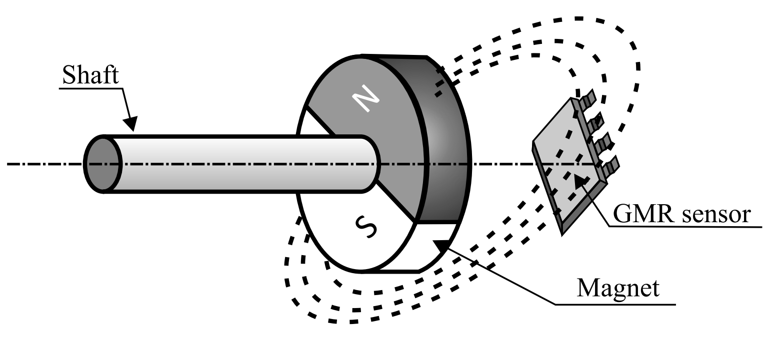

(a)

Figure 11.3 An angular rotation end-of-shaft sensor with GMR: (a) configuration of the permanent magnet and sensor, (b) internal sensor structure, and (c) sensor output. (*After:* Infineon.)

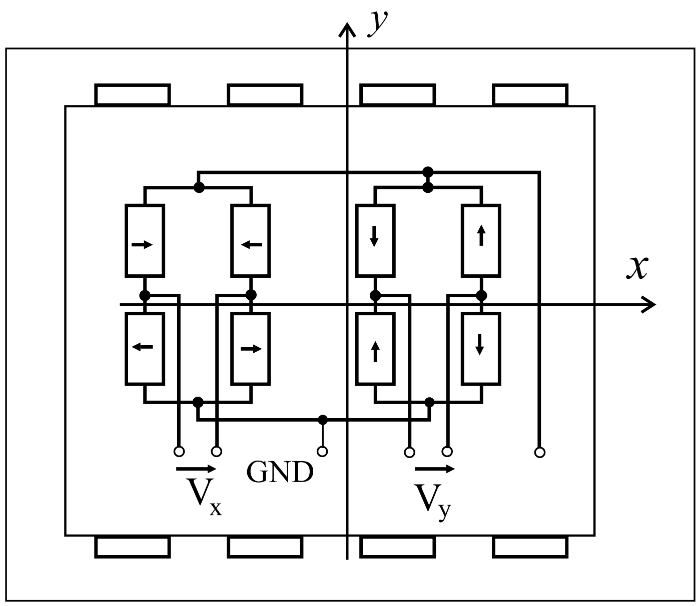

(b)

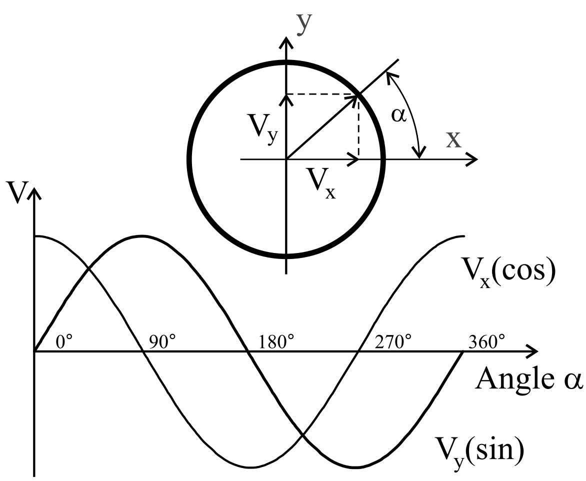

(c)

Figure 11.3 (continued)

The sensor diameter ranges from 8 mm to 150 mm, with sensing distances between about 2 mm and 100 mm. The analytical solution of eddy-current sensors is usually not possible. A number of software modeling tools based on the finite-element method is available. Improved core shapes are shown in Figure 11.6. Figure 11.7 shows the measured Q factors of the 47-turn coils wound on cores from Figures 11.5 and 11.6 at the 300-kHz frequency versus the target distance [12]. It

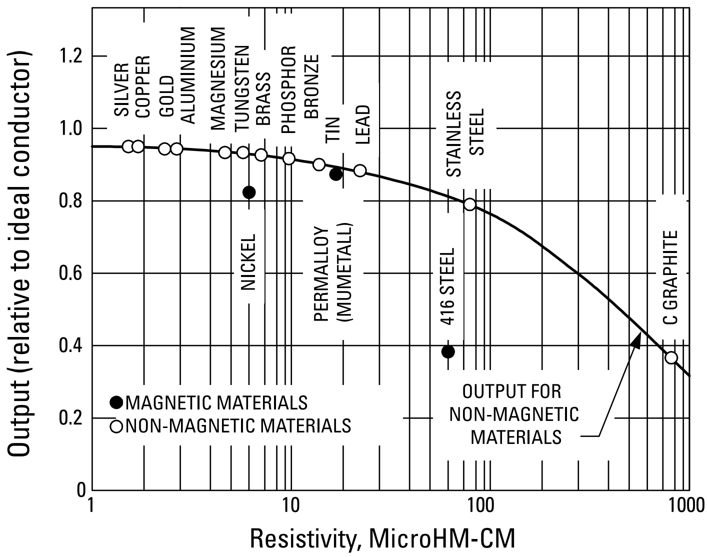

Figure 11.4 Influence of the target material on the relative sensitivity of the eddy-current sensor. (*After:* [11].)

was shown that the flat face of the transducer increases the value of B in the axial direction. The larger radiating surface increased the measuring range up to double the value of the pot core. Magnetic short circuits by the core itself or by ferromagnetic housing should be avoided. Eddy-current sensors working at higher frequencies should be wound from litz (stranded) wire.

The sensors work either in frequency modulated (FM) mode, when the oscillator frequency changes with target position (relaxation oscillator) or in amplitude modulated (AM) mode, when the variable is the oscillator amplitude.

This principle is also often used in bipolar-output proximity switches (Section 11.5); in this case, the electronics may be much simpler. The most popular type of the eddy-current proximity switch is the killed oscillator (also blocking oscillator): a metallic object moving close to the coil adds load to the oscillator, which stops the oscillation.

Miniature eddy-current sensors use flat air coils. The proximity sensor based on a differential relaxation oscillator (Figure 11.8) was described in [13]. The oscillator

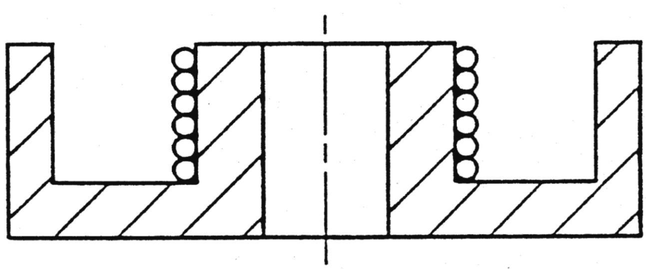

Figure 11.5 Standard pot core used for eddy-current sensors. The diameter of this core is 22 mm and the height is 6.7 mm. (*From:* [12]. © 1997 IEEE.)

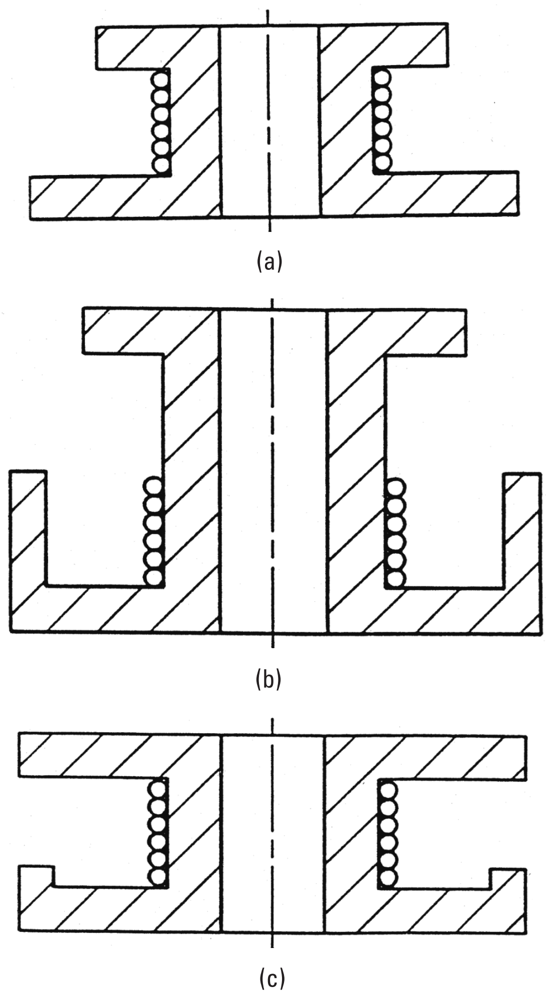

Figure 11.6 Alternative shapes of ferrite cores for eddy-current sensors. (*From:* [12]. © 1997 IEEE.)

frequency changes with the position of the target. The 1 × 1-mm coil on top of the integrated complementary metal-oxide-semiconductor (CMOS) readout circuit was developed for short-range applications with limited accuracy. The 3.8-mm side coil temperature-compensated sensor is working in the 3–4.5-MHz output frequency range. The dependence of the output frequency on distance of the aluminum target before and after temperature compensation is shown in Figure 11.9. The measured distance of the aluminum target changes with temperature by less than +/–1% (for an aluminum target 1 mm from the sensor) in the whole –20°C to 80°C industrial temperature range.

Eddy-current sensors can be used for measuring the speed of conducting objects that are moving perpendicularly to the sensor axis [14]. Eddy-current metal detectors are used for the detection of metal objects in detection frames, for the location of antipersonnel mines, and also by hobbyists to locate coins on beaches [15].

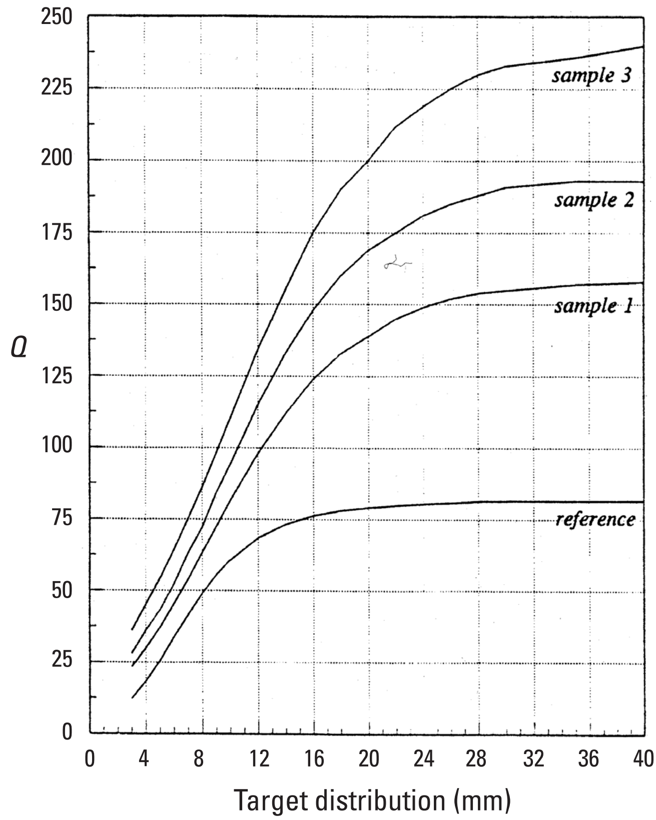

Figure 11.7 Measured Q for reference pot (Figure 11.5) and alternative cores (Figure 11.6). (*From:* [12]. © 1997 IEEE.)

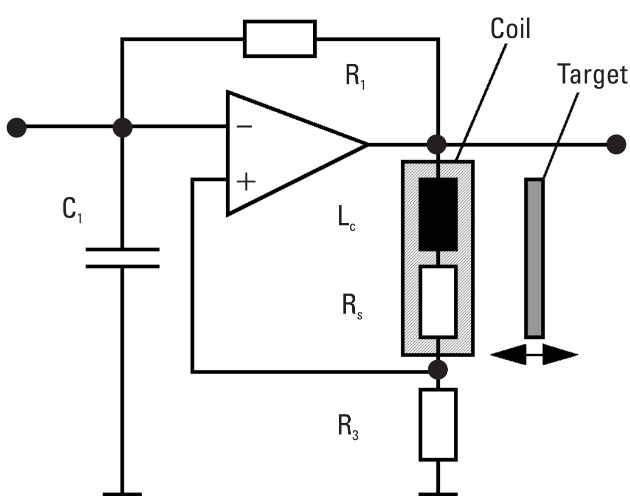

Figure 11.8 Inductive (eddy-current) proximity sensor based on a differential relaxation oscillator. The output frequency is a function of the conducting target position. (*From:* [13].)

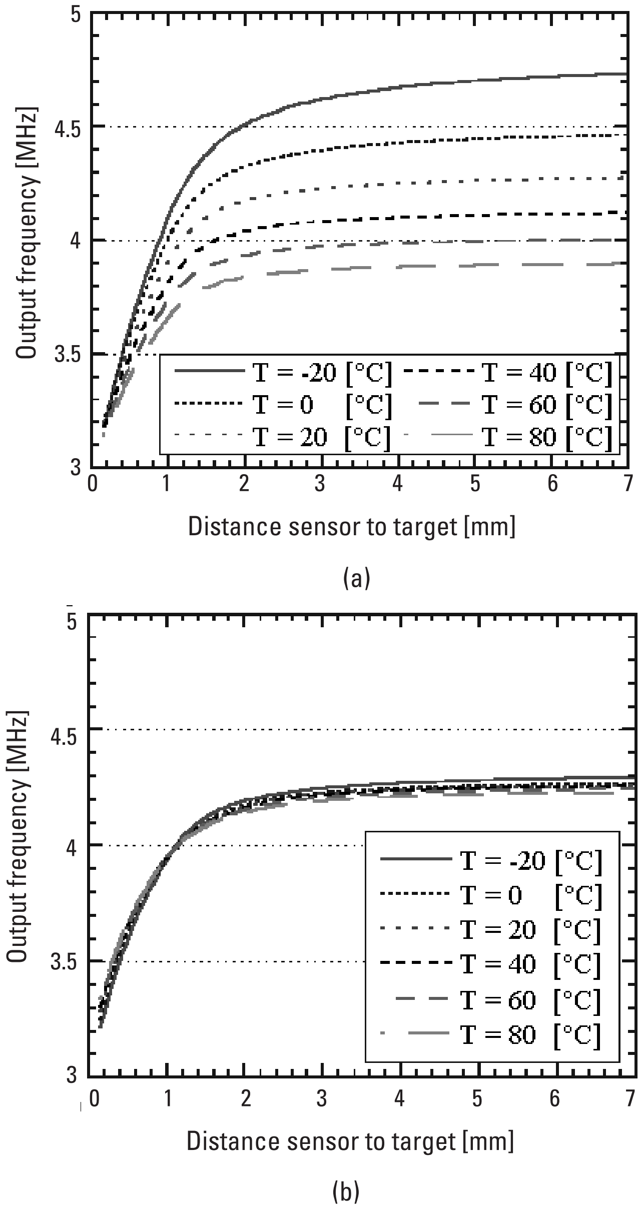

Figure 11.9 Output frequency of the integrated inductive (eddy-current) proximity sensor as a function of the distance of the aluminum target at various temperatures: (a) before and (b) after temperature compensation. (*From:* [13].)

11.1.3 Linear Transformer Sensors

11.1.3.1 LVDT

An LVDT is probably the most popular magnetic position sensor. Because of zero friction, the device is highly reliable. It is based on the variation of mutual inductance between the primary P and two secondary windings S_1 and S_2 caused by the movement of the ferromagnetic core (Figure 11.10).

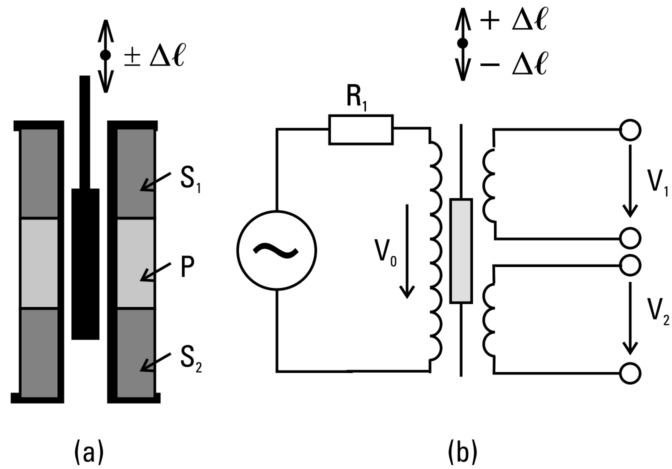

Figure 11.10 LVDT: primary winding P and two secondary windings S_1 and S_2 and their respective voltages V_0, V_1, and V_2.

The device has a high reproducibility, the practical resolution may be better than 0.1% or below 1 μm, with a linearity up to 0.05%, and the temperature coefficient of sensitivity is typically 100 ppm/°C. The linear range is 30% to 85% of the device length. Standard measurement ranges are from 200 μm to 50 cm. The excitation frequency is usually between 50 Hz and 20 kHz. The output signal (V_1–V_2) of antiserially connected secondary windings can be processed by PSD (synchronous rectifier, lock-in amplifier), but more often V_1 and V_2 are measured separately and ratiometric processing is made. It is possible to integrate the complete sensor electronics including the excitation generator into the sensor housing. Differential transformer design allows simple temperature compensation, which gives 0.15% accuracy in a wide temperature range. LVDT linearity can be significantly improved by signal processing [16, 17].

The differential variable inductance transducer (DVRT), a half-bridge LVDT, has only two windings; the core position is measured by differential inductance. DVRT sensors with a 1.5-mm outside diameter and a 60-nm resolution are available.

11.1.3.2 Variable Gap Sensors

Variable gap (also variable reluctance) sensors are based on change of the air gap in a magnetic circuit (between core and armature) of the inductor of a transformer. They are usually less precise than LVDTs but are still being used in conjunction with mechanical transducers to measure pressure, strain, force, torque, and other mechanical variables that can be converted into mechanical displacement.

11.1.3.3 The Permanent Magnetic Linear Contactless Displacement (PLCD) Sensor

The PLCD sensor is shown in Figure 11.11. The sensor consists of a long magnetic strip core with homogeneous secondary winding. The primary winding has two sections connected antiserially, which are supplied with ~4-kHz sinewave. A permanent magnet in the core vicinity causes localized core saturation, which effectively

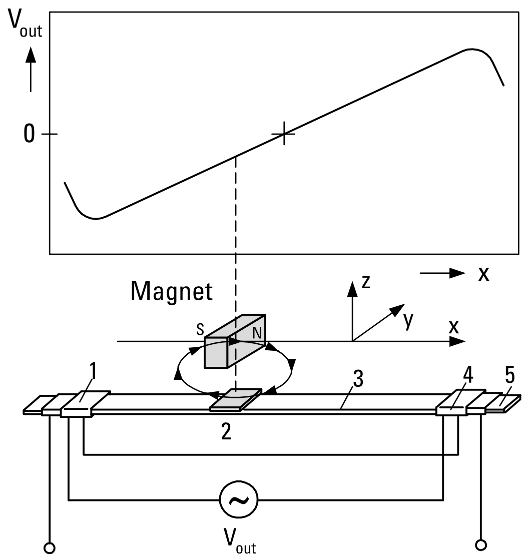

Figure 11.11 PLCD sensor. (Courtesy of Siemens.)

divides the core into two halves whose lengths determine the signal induced into the secondary winding. The induced voltage is synchronously rectified in order to obtain linear output. The typical resolution is 0.2%, and the linearity is 1% of the range (which is between 20 mm and 150 cm). The main advantage is that the device is tolerant to the changes of an air gap between the magnet and core.

11.1.3.4 Inductosyn

Inductosyn [18] consists of two parallel flat meander coils: scale and slider. The slider usually has two windings (sine and cosine) shifted by 1/4 of the mechanical period (pitch). Inductive coupling between scale and slider coils measures the displacement. Inductosyn combines the advantages of incremental sensors (increment is one pitch) and analog sensors (sinewave dependence of the output voltage allows to interpolate the fine position with a resolution of up to pitch/65,000). The scale winding is usually supplied by AC of typically 10-kHz frequency, and the voltages induced in the sine and cosine slider coils are processed; however, it is also possible to supply the slider sine and cosine coils by quadrature (sine and cosine) voltages and to process the voltage induced in the ruler (stator) coil. The standard pitch size is 2 mm, and the ruler length may range from 25 cm up to 36m or more. Inductosyn is also made rotary. Multiple patterns can be combined in one device in order to increase the incremental resolution by employing techniques known from optical encoders (such as the N/(N – 1) method).

11.1.4 Rotation Transformer Sensors

Although rotation transformers are sometimes considered to be archaic devices, they still find application in extreme conditions, as they are more rugged than optical encoders.

11.1.4.1 Synchros

Synchros are electromechanical devices that replicate the rotor position in a distant location. They have three stator windings displaced by 110°. They combine the properties of the sensor and the actuator; a typical application is the antenna rotator.

11.1.4.2 Resolvers

Resolvers have windings displaced by 90°. The outputs are sine and cosine voltages, which are often processed by specialized resolver-to-digital converters. Brushless resolvers use another rotational transformer to supply the rotor. Resolvers can be made to withstand temperatures from 20K to 200°C, radiation of 10^9 rads, acceleration of 200g (battleship cannons, punching devices), and vacuum or extreme pressures.

Some manufacturers (e.g., Pewatron) use the term “linear resolver” for linear position sensors that also have sin/cos outputs but are based on two AC-supplied magnetoresistive elements.

11.1.5 Magnetostrictive Position Sensors

Magnetostrictive position sensors measure time of flight of a strain pulse to sense a position of moving permanent magnet (Figure 11.12). The sensing element is a wire or pipe from magnetostrictive material (sonic waveguide). The devices are based on the Wiedeman effect: if the current passes through the waveguide and the perpendicular DC magnetic field is present, the torsional force is exerted on the waveguide.

The device works so that after the current pulse is applied, the torsional force is generated in the location of permanent magnet. This torsional strain pulse travels

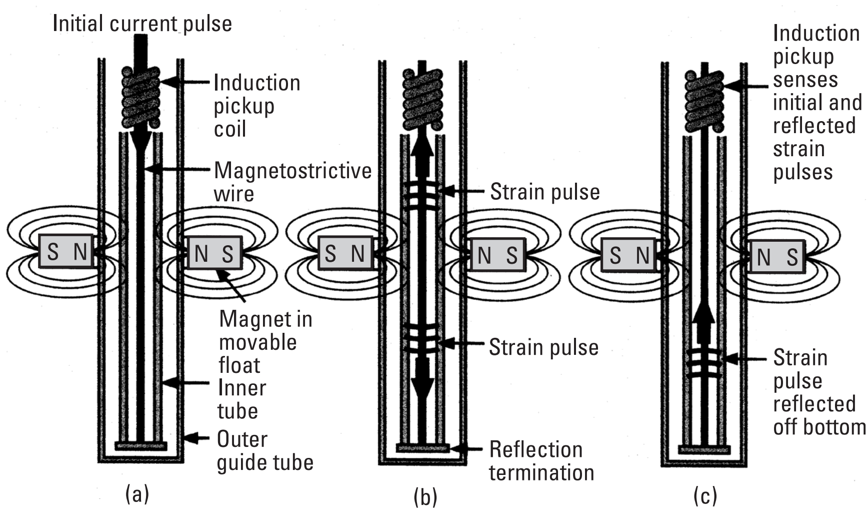

Figure 11.12 Magnetostrictive position transducer. The approach to magnetostricive detectors shown in this graphic is patented technology assigned to AMETEK Patriot Sensors, USA (U.S. Patent Number 5,017,867.)

with a ~3-km/s speed along the waveguide and it is detected by the small induction coil at the sensor head. The hysteresis may be as low as 0.4 μm, uncorrected linearity is 0.02% FS, and some devices have an internal linearization and temperature compensation. The maximum sensor length is about 4 m. Sensors based on similar principles are manufactured by Gemco-Patriot, MTS, and Balluff.

Other devices based on a delay line principle were suggested in [19]. The mechanical strain in the delay line is caused by the current pulse in the perpendicular movable conductor. The acoustic pulse is again detected in a small axial induction coil close to the end of the delay line due to inverse magnetostriction effect. The delay line position sensors have an accuracy of approximately 1 mm, so they may be suitable to measure distances of about 1 m to 5 m, with the upper limit being determined by attenuation.

11.1.6 Wiegand Sensors

In 1981, Wiegand patented a revolutionary sensor that generated a high-voltage pulse when the magnetic field reached some threshold value; the shape of the voltage pulse is highly independent of the rate of the field change and the device is passive, having just two terminals [20]. Wiegand made his sensors from 0.3-mm wire from Vicalloy ($Co_{52}Fe_{38}V_{11}$), which was twisted to cause plastic deformation resulting in higher coercivity in the outer shell and elastic stress in the central part. The central part forms a single domain. The pulse is caused by one large Barkhausen jump when this single domain reverses its magnetization. The pulse width is determined by eddy-current damping. A 30-mm-long wire with a 1,000-turn coil may generate 7-V pulses. The main disadvantage of Wiegand configuration is that the outer shell cannot be made really magnetically hard, so it can be unintentionally remagnetized by an external field higher than 25 mT. Therefore, the main application field of Wiegand wires is not magnetic sensing, but marking and security application. Wiegand wires have been also used for energy harvesting and energy transmission [21]. Similar properties have some amorphous glass-covered microwires.

11.1.7 Magnetic Trackers

Trackers are devices that measure the location and relative orientation of the target. A complete tracker has 6 degrees of freedom (linear position in 3 axis and 3 rotation angles). The applications include body tracking in virtual reality, motion capture in animation and biomechanical measurement, and indoor navigation [22]. Miniaturized sensors are used to locate the position of probes and instruments such as biopsy needles inside the body. The target may be a source of a signal (permanent magnet or transmitter coil) whose amplitude (and eventually phase) is sensed by receiving coils, or the sensor is attached to the target.

The simplest type of transmitting target is a small permanent magnet. Such systems have been used for observing biomechanical movements [23]. The LC resonant target is truly wireless, but has a limited accuracy of 2 mm in the 60-mm distance. Similar targets are used as security labels for shops and libraries.

Magnetic trackers with a sensing target consist of a transmitting coil (which may be flat) and miniature sensors (usually induction coils) attached to the target. The tracker accuracy may be 1 mm and 0.5° within a 1-m^3 volume [24]. The sensor signal may be wirelessly transmitted to the control unit. Some systems use a pulse DC magnetic field instead of an AC field, and sample the position after the decay of eddy currents; this technique reduces the errors caused by conducting objects. The accuracy in a large area can be increased by using multiple source coils [25].

Other systems are using triaxial magnetoresistive sensor attached to the target. Using DC magnetic sensors allows one to combine a compass with an AC source: such a system is using only a uniaxial transmitting coil. With a 16-mm-diameter transmitting coil, the tracking distance for 2-mm accuracy is 100 mm [26].

Advanced tracking systems for biomechanics fuse signals from inertial sensors, magnetometers, and optical sensors [27]. Another application of magnetic trackers is underground drilling. These systems utilize compass, active beacons, and inertial sensors [28]. Systems for petroleum extraction require drilling multiple parallel holes. For this type of work, local magnetic field anomalies are also employed to increase accuracy [29].

11.2 Proximity and Rotation Detectors

These sensors have bistable (digital) output. They may be either activated by a moving magnet, or biased by a fixed magnet and activated by magnetically soft target. A typical example of a naturally bipolar sensing element is a reed contact, but any other magnetic sensor followed by a comparator or Schmidt trigger may be used for this purpose. The most popular are Hall sensors, AMR, and, recently, also GMR magnetoresistors and some semiconductor magnetoresistors.

Reed contacts are very cheap and totally passive devices. They consist of two magnetic strips of soft or semi-hard magnetic material sealed in a glass pipe filled with inert gas. Normally, open contacts are connected at a certain field by an attractive magnetic force between the free ends. Other contact types are normally closed. The reed contacts have hysteresis and their switching zones have a complicated shape. However, they are still very popular because of their simplicity. Figure 11.13 shows that if the magnet is perpendicular to the contact and moves along it, there may be two switch-on zones. If the contact and magnet have the same direction and the magnet moves along it, there may be three switching zones or one switching zone. This behavior is easy to explain by the shape of the magnet field lines.

High-security balanced switches use two reed contacts in the vicinity of the magnet; one of them is normally open and the other is normally closed. Any movement of the magnet causes a transfer of one of the switches. The normally open contacts are usually crossed by a resistor, which allows one to monitor the continuity of the wires.

Eddy-current sensors (for any conducting targets) and AC-excited variable gap sensors (only for magnetic targets) are also used for linear or angular gear position sensing. An example of an integrated inductive gear tooth sensor is shown in Figure 11.14.

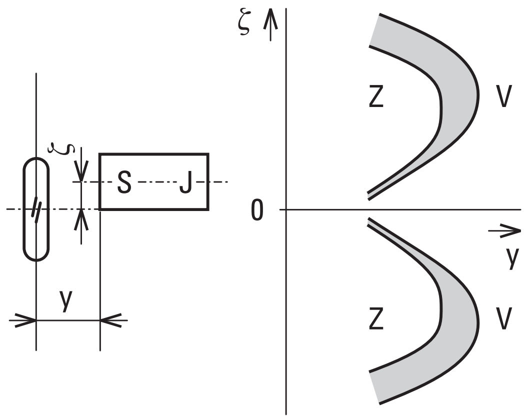

(a)

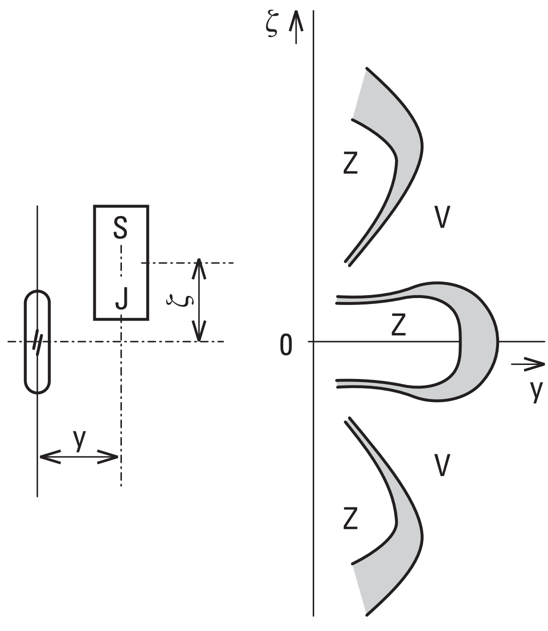

(b)

Figure 11.13 Switching zones of the reed contacts. The sensor state is uncertain in gray regions due to the sensor hysteresis.

11.3 Force and Pressure

We skip all the sensors that convert force, pressure, and torque into the displacement by using springs, diaphragms, columns, proving rings, and other mechanical converters [31].

Most of the force, pressure, torque, and accelerometric magnetic sensors are based on the inverse magnetostrictive (Villari) effect: the permeability of the sensing material changes due to applied strain [32]:

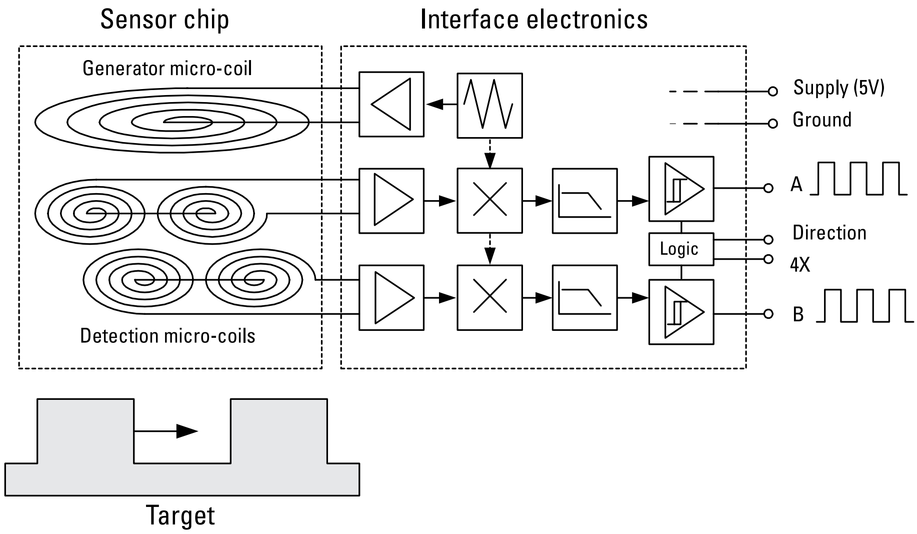

Figure 11.14 Block diagram of miniature inductive gear tooth sensor. (Courtesy of CSEM [30].)

$$\mu = \frac{M_s^2}{\left(2K + 3\lambda E_0 \varepsilon\right)} \tag{11.2}$$

where E_0 is the Young's modulus and ε is the strain (positive if the material is in compression).

The device sensitivity is high if λ is high and K is low. Magnetostrictive materials are also called piezomagnetic. The situation may be complicated by a change of E with an applied field (ΔE effect).

The stress $\sigma = E_0\varepsilon = F/A$ may be caused by the measured force F, or indirectly by other variables.

Amorphous alloys are suitable for magnetoelastic sensors; they have excellent elastic properties: almost ideally linear stress-strain curves, even superior to spring alloys, with no plastic flow. Elastic strains of more than 1% are feasible, which is 10 times more than with crystalline materials. The ΔE effect may cause nonlinearity at low stress levels. Negative magnetostriction materials are preferred, as they show linear increase of magnetoelastic anisotropy with mechanical stress. A lot of force sensors using amorphous tapes [33] and wires [34] were described in scientific articles, but these devices are not widely used in the industry. The advantage of magnetic microwires is that they can be embedded into smart materials and remotely interrogated [35].

The most popular industrial magnetic load cells are Pressductors or Torductors, which are based on variation of the flux distribution in the magnetic core (Figure 11.15). In an unloaded state, the mutual inductance between the perpendicular primary and secondary windings is zero. After loading, stress-induced anisotropy causes that part of the primary coil flux to be coupled to the secondary transformer.

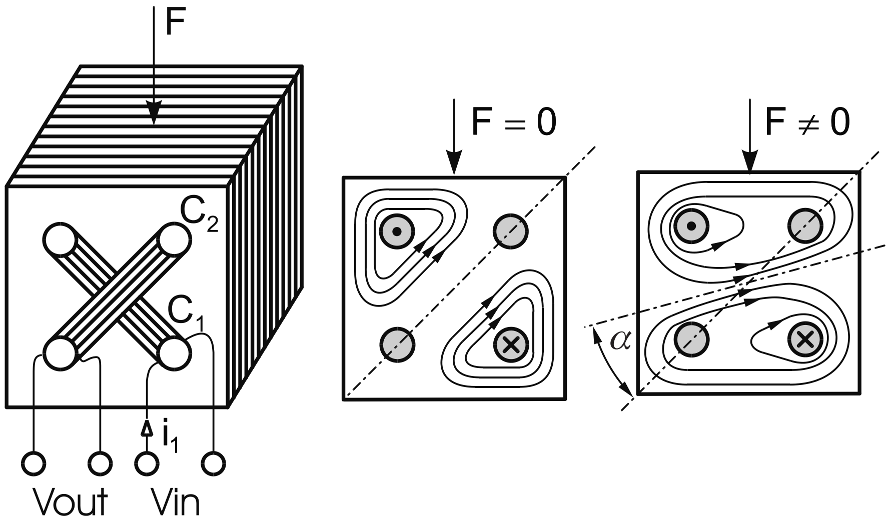

Figure 11.15 Magnetic load cell (Pressductor or Torductor).

These devices can measure forces up to 5 MN with a linearity of 0.1% and a hysteresis of 0.2%. They are well temperature compensated and withstand overloading.

Magnetoelastic resonance sensors vibrate in a response to an AC excitation field. The vibration amplitude can be monitored by magnetic, acoustic, capacitive, or optical techniques. The amplitude and resonant frequency of vibrations depend on the viscosity of the surrounding medium, temperature, and mechanical load on a vibrating element. Vibrating tape can be functionalized by a thin coating of polymers or oxide materials that selectively binds molecules of analyte. Mass load then shifts the mechanical resonant frequency; this is a principle of many chemical biosensors [36].

11.4 Torque Sensors

Applications for sensing torque fall into two general categories: those in which the torque is transmitted by a rotating shaft, and those in which the torque tends to twist a shaft having one end clamped. Devices for this latter category, often called reaction torque sensors, generally have simpler constructions, because there is no relative motion between the shaft and the electrical wiring associated with the actual torque detecting means. With rotating shafts, considerations of wear, friction, and reliability favor torque detection methods that require no physical contact with the shaft.

Three basic principles are available for measuring, without physical contact, the torque transmitted by a rotating shaft. The torque T can be determined from the measurement of the twist angle θ, of the surface strain ε, or of magnetic quantities related to the surface stress, s. The relationships between T and the relevant variables are shown schematically in Figure 11.16, and are given quantitatively by

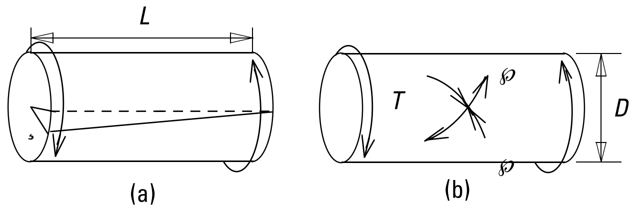

Figure 11.16 Twist angle: (a) principal stresses, and (b) induced by the applied torque.

(11.3)–(11.5), where G is the modulus of rigidity of the shaft material (8.3×10^{10} N/m^2 for most steels) [37]. It should be noted that, in round shafts, tensile and compressive principal stresses, and hence principal strains, occur at ±45° angles to the rotational axis.

$$\sigma = \frac{16T}{\pi D^2} \tag{11.3}$$

$$\varepsilon = \frac{\sigma}{2G} = \frac{8T}{\pi G D^3} \tag{11.4}$$

$$\theta = \frac{2L(2\varepsilon)}{D} = \frac{32LT}{\pi G D^4} \tag{11.5}$$

Changes in the surface strain and thus torque can be measured by strain gauges attached to the shaft. These strains are generally too small (at most, a few parts of 10^3) to be accurately measured directly. Therefore, the common practice is to use 4 gauges arranged in a Wheatstone bridge circuit. With rotating shafts, coupling means, such as rotary transformers, are required to feed the excitation current to the gauges and to acquire the signal from the bridge circuit in a noncontacting manner.

The twist angle or phase shift method of torque measurement generally requires a slender portion of the shaft to enhance the twist (2° to 3° at most for $L/D = 5$) in response to applied torque and a pair of identical toothed disks attached at opposite ends of the slender portion. The twist angle and thus torque can be determined from the phase difference between magnetically or optically detected tooth/space patterns on each of the disks. This method generally requires the shaft to be rotating.

The rest of this section is devoted to a more detailed explanation of the operation of torque sensors based on magnetoelastic methods that provide an inherently noncontacting basis for measuring torque. The magnetoelastic effect provides a mutual interaction path between mechanical energy (elastic energy) and magnetic energy. The influence of the elastic energy is brought into the magnetic system through the stress-induced magnetic anisotropy, K_σ, given by (11.6), where λ is the magnetostriction constant of the shaft material.

$$K_\sigma = 3\lambda\sigma = \frac{48\lambda T}{\pi D^3} \tag{11.6}$$

Magnetic anisotropy causes magnetic moments to incline toward the easy axis. When several sources of magnetic anisotropy are present at the same time, each having a different easy axis orientation, the magnetic moments will be inclined at that orientation where the anisotropies balance. Shafts are generally made of polycrystalline magnetic materials (steels) wherein, in the absence of torque, a magnetocrystalline anisotropy provides an easy axis orientation for the magnetic moments in each grain. The stress-induced magnetic anisotropy, K_σ, has its easy axis parallel to the line of tension if $\lambda > 0$, or parallel to the line of compression if $\lambda < 0$. Therefore, the greater the applied torque, the more nearly will the equilibrium orientation of the magnetic moments be inclined towards the K_σ easy axis. A reversal of the direction of the torque will interchange the lines of tension and compression, resulting in a 90° rotation of the K_σ easy axis orientation. Due to this interaction, the permeability of a magnetic shaft material is related to the torque, showing larger values along the stress-induced easy axis and smaller values along the hard axis, which is perpendicular to the former, if $\lambda > 0$.

There are two general ways of utilizing the stress-induced magnetic anisotropy as the sensing mechanism for torque sensors. In the permeability-based method, the stress-induced magnetic anisotropy causes the permeability to change in the shaft surface affecting the permeance of a magnetic flux path, which includes a magnetizing source and a pickup (sensing) coil. In the remanent magnetization-based method, the stress-induced magnetic anisotropy causes a remanently magnetized magnetoelastically active member to generate magnetic flux. It is desirable for sensors of both types to have axisymmetric structures to avoid rotation-dependent outputs that degrade the attainable accuracy. It is also desirable that torque sensors work in a differential mode of operation, because this makes them robust against common-mode types of disturbances, such as the ambient temperature.

Figure 11.17 shows an example of a permeability-type torque sensor constructed in accordance with fundamental principles and utilizing the magnetoelastic effect inherent in a shaft made principally of iron [38]. A pair of mutually orthogonal, U-shaped cores is combined, with their open ends facing toward the shaft but separated by small air gaps. The coils on the legs of the vertical core provide an AC excitation field to the shaft and the coils on the legs of the horizontal core are used to pick up imbalances in the cyclically varying magnetic flux. The operating principle resembles that of ordinary bridge circuits if we consider the magnetic flux as the electric current. The permeability of the shaft becomes anisotropic under the stresses shown in Figure 11.17: larger in directions parallel to the line connecting points P1 and S1 and smaller in directions parallel to the line connecting points P1 and S2. Hence, the magnetic path, P1 ⇒ S1 ⇒ horizontal core (to the right) ⇒ S2 ⇒ P2 ⇒ vertical core ⇒ P1, has a larger permeance than the magnetic path, P1 ⇒ S2 ⇒ horizontal core (to the left) ⇒ S1 ⇒ P2 ⇒ vertical core ⇒ P1, thus yielding a net

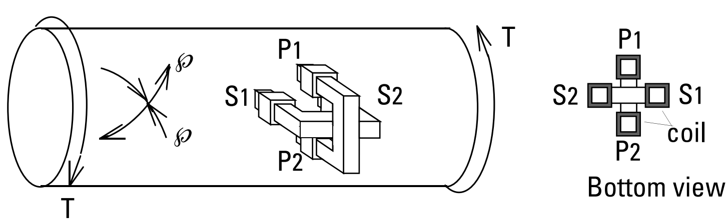

Figure 11.17 A torque sensor based on changes in permeability in response to applied torque.

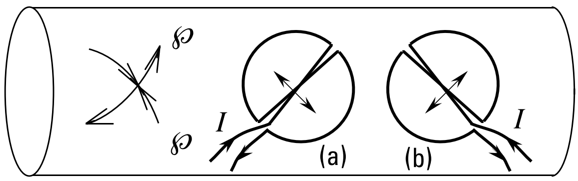

Figure 11.18 Operating principle of a pair of figure-of-8 coils to detect torque.

magnetic flux in the horizontal core. Since the excitation is AC, voltages reflecting this net flux will be induced in the pickup coils. It should be noted that the phase of the AC magnetic flux, hence the voltages induced in the pickup coils, corresponds to the direction of the applied torque. Another well-known excitation/pickup coil system, using a 5-leg magnetic core, was proposed by Beth and Meeks [39].

The advantages of this type of torque sensor stem from its obviously simple and mechanically robust construction. However, local variations in magnetic properties of typical shaft surfaces limit their accuracy. A common practice to improve the accuracy is to use several circumferentially distributed excitation/pickup coils and average their outputs.

In order to allow multiple installations of the excitation/pickup coils within a small radial space, low-profile structures have been developed based on using a pair of figure-of-8 coils [40]. The operating principle of this arrangement is readily understood with the help of Figure 11.18.

The center branches of the two figure-of-8 coils shown in Figure 11.18 are aligned at +45° and –45° angles to the shaft axis. With the torque-induced stresses shown, the self-inductance of the left (a) figure-of-8 coil decreases, whereas that of the right one (b) increases. The difference in self-inductance between the two coils provides

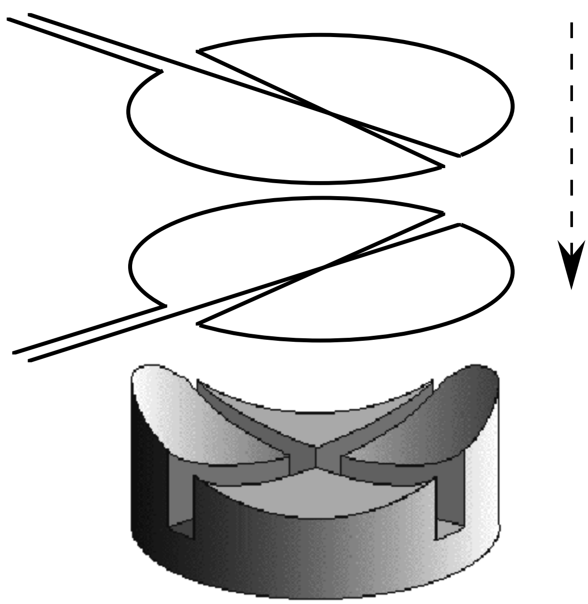

Figure 11.19 Structure of low-profile pickup coils.

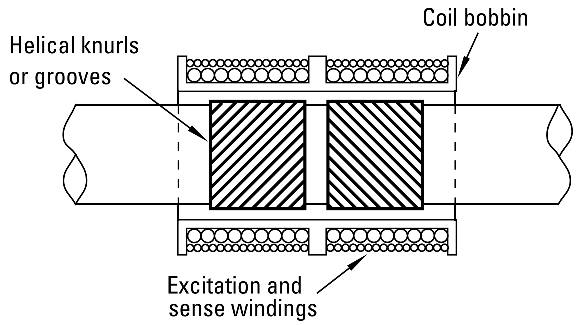

Figure 11.20 A torque sensor of axisymmetric structure.

a measure of the torque. A small, simple, and mechanically robust construction is achieved by stacking the two coils shown in Figure 11.18 and embedding them both into a single ferrite core as shown in Figure 11.19.

Another important group of permeability-type torque sensors utilizes an axisymmetric construction, an example of which is shown in Figure 11.20. In the construction shown, oppositely directed helical grooves are machined or formed (typically along ±45° angles to the axis) on adjacent circumferential regions of a steel shaft [41]. Solenoidal coils encircling these regions are used for excitation and sensing. The axial permeability of a grooved region increases when the easy axis of the stress-induced magnetic anisotropy occurs in parallel to the line of grooves, whereas it decreases otherwise. This results in different voltages being induced in the sense windings, and this difference provides the measure of the torque. The advantage of this design is that the axisymmetric structure of the windings hides local variation of the magnetic properties of the shaft. Steels containing a few percentage of nickel are especially suitable for this torque sensor construction; indeed, nickel as an alloying element tends to enhance the performance of all types of magnetoelastic torque sensors as its presence both increases the magnetostriction constant and decreases the magnetocrystalline anisotropy.

Magnetoelastic torque sensors based on remanent magnetization rely on torque to create a stress-induced magnetic anisotropy that acts to reorient the remanent magnetization resulting in the emergence of a measurable magnetic flux in the space around the shaft. Torque sensors based on this method are generally either constructed with a thin ring of magnetoelastically active material rigidly attached

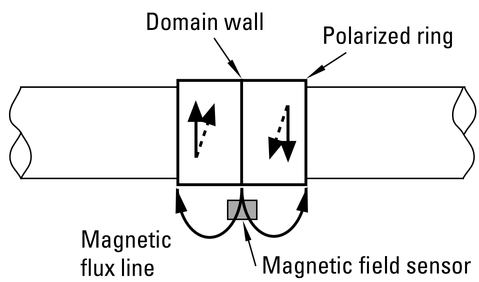

Figure 11.21 A torque sensor having a magnetoelastically active ring with double polarization.

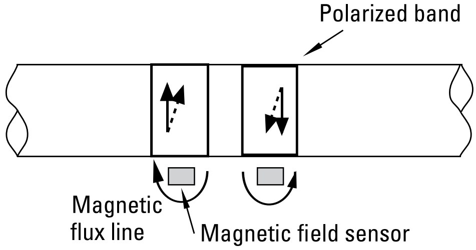

Figure 11.22 A torque sensor in which the shaft itself acts as the transducer with double polarization.

to the shaft [42] or use the material of the shaft itself as the transducer [37]. With respect to constructions that use a ring to serve as the transducer, the ring is expanded during installation on the shaft, thereby developing a magnetic anisotropy having the easy axis along the circumferential direction, while constructions without a ring rely on the material characteristics of the shaft itself to provide the necessary magnetic anisotropy and magnetostriction. The ring or transducer shaft is typically manufactured from steel that contains at least several percentages of nickel and is heat-treated after machining. A typical example of a ringed construction is shown in Figure 11.21, and construction without a ring is shown in Figure 11.22. As indicated by the solid arrows in the figures, the ring or transducer shaft is magnetized in a way that each axial half is polarized in an opposite circumferential direction [37, 42]. Two-region polarization can be accomplished by rotating the shaft while applying a radially oriented magnetization to the ring or region on the shaft intended to function as the torque transducer, alternating the polarity of the magnetization on each axial half. When torque is applied the associated magnetic anisotropy within the transducer causes the magnetizations to tilt toward helical directions (dashed arrows) creating a divergence in the magnetization which gives rise to a magnetic flux in the regions around the shaft. The polarity of the magnetic flux reverses when the applied torque changes its direction. Torque is determined by measuring magnetic flux with one or more magnetic field sensors, typically flux-gate magnetometers that are configured to reject common fields as well as the radial position of the shaft through the use of diametrically opposed pairs. Magnetic shielding is commonly used to further minimize the influence of external magnetic fields.

The advantage of a ringed construction is that the ring can be installed over a shaft that does not have suitable magnetoelastic properties for use as a torque transducer and the output of the transducer tends to be very linear and nonhysteretic. The ring and shaft geometry must be carefully controlled as variations in the stress and magnetic anisotropy within the ring may result in inconsistencies in the output versus circumferential position. Additionally, the peak allowable torsional stress applied to the shaft must remain below that at which slippage occurs at the ring/shaft interface, typically less than 50 MPa. The ability to use the shaft itself as the transducer results in a much less complicated assembly should the shaft be manufactured from a material with suitable magnetoelastic properties; however, comparatively, there is typically more nonlinearity and hysteresis in the transducer output. As the nonlinearity and hysteresis are dependent on many factors including the material characteristics and peak torsional stress ranges to be applied to the shaft, it is typical that the accuracy for a particular application can be optimized through material selection and choosing the shaft diameter to provide a suitable torsional stress for the material selected, which can range from 30 MPa to beyond 300 MPa. As magnetoelastic torque sensors respond to stress and not strain, the shaft can be sized to allow the transducer to measure torques as small as micro-newton-meters to more than hundreds of thousands of newton-meters. An example of a torque-transducer that uses the magnetoelastic properties of an existing engine output shaft without the addition of a ring was described in an article by Kari et al. [43]. Further improvement in accuracy can be made to all types of torque sensors through electronic compensation for inaccuracies including temperature-related issues, offset drift, and hysteresis.

11.5 Magnetic Flowmeters

If the conducting fluid flows in the magnetic field, the electric field **E** is generated. In an ideal case,

$$\mathbf{E} = \mathbf{v} \times \mathbf{B} \tag{11.7}$$

In case that **v** is perpendicular to **B**, voltage V is induced between two electrodes, which are at the distance of d perpendicularly to both **v** and **B**

$$V = k \cdot d \cdot \mathbf{v} \cdot \mathbf{B} \tag{11.8}$$

where k is a constant depending on fluid conductivity and the geometry. The magnetic field is either AC or pulse DC in order to avoid polarization effects. The coils are of the saddle shape. Induction flowmeters work for fluids with a conductivity higher than 1 μS/cm, which includes drinking water. The typical accuracy is 0.5%. Flowmeter for liquid metal coolant for nuclear reactor is excited by a Halbach array of permanent magnets with a DC field of 0.78T [44].

More complicated designs of contactless induction flowmeters use capacitive sensing instead of contact electrodes. Although these devices are less accurate than contact flowmeters, they find applications in the measurement of fluids, which would create sediments on electrodes.

11.6 Electric Current Sensors

The current measurement using a shunt resistor is, in some cases, impractical or impossible. Magnetic current sensors offer galvanic insulation; detailed information on these sensors can be found in some articles [5, 45, 46] and in a comprehensive book by Iwansson et al. [47]. This section is based on [45] with kind permission of the IOP.

Besides fulfilling the requirements common to magnetic field sensors, contactless current sensors should be geometrically selective (i.e., sensitive to measured currents and resistant against interferences from other currents and external fields). The easiest way to guarantee this is to use a closed magnetic circuit with a measured

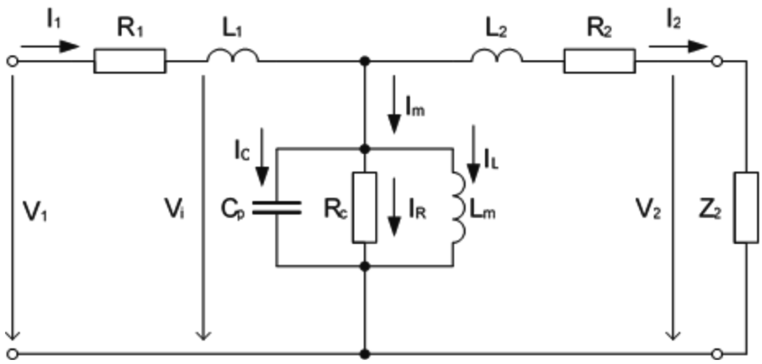

Figure 11.23 Equivalent circuit of the current transformer. R_1, R_2, L_1, and L_2 represent resistances and leakage inductances of primary and secondary windings, R_c is the resistance representing losses in the ferromagnetic core, L_m is the magnetizing inductance, C_p represents the parasitic capacitances of the winding, Z_2 is the burden, and I_m is the magnetization current. (*From:* [45] with permission of IOP.)

conductor inside. The best shape of the magnetic circuit is toroid with a high cross-sectional area and high permeability, as it has large demagnetization factor against external fields. If this is not possible, magnetic sensor arrays may be used, which approximate the line integral in the Ampère's circuital law.

$$\sum I = \oint_S \boldsymbol{H}\, d\boldsymbol{s} \tag{11.9}$$

where ΣI is the total current surrounded by closed curve S.

Circular arrays are made of Hall [48], AMR [49], and microfluxgate [50] sensors. Magneto-optical current sensors measure ideally the mentioned field integral around the conductor, so theoretically they are immune against the external field.

The magnetic field in the vicinity of large currents is high, so that precise magnetic sensors such as AMR or microfluxgate cannot be used. For a precise AMR sensor with 200-A/m range, the minimum distance from a 10-kA current would be 8 m. A solution of this problem is to use gradiometric sensor inside the hole in the conductor [51].

11.6.1 Magneto-Optical Current Sensors

Magneto-optical current sensors are based on the Kerr effect in optical fibers or in the bulk material: the polarization plane rotates by angle proportional to the magnetic field. These sensors are ideal for high-voltage applications, but their resolution is limited by noise and drift. The achievable accuracy is 0.1% for currents from 1 kA to 500 kA [52]. The real suppression of the external fields is limited by nonhomogeneity of the fiber. By proper design, the crosstalk of 0.3% from the external conductor at a distance of 30 cm can be reduced to 0.002% [53].

A magneto-optical current sensor based on bulk glass can be designed in the form of clamps. The maximum range is 65 kA, and 0.1% accuracy was achieved for a 1.2-kA current. For this range, the maximum error was 11 mA [54].

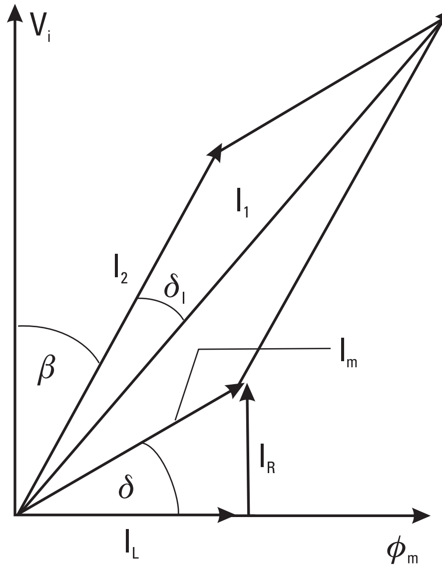

Figure 11.24 I_m is magnetizing current of current transformer, consisting of components I_R and I_L, Φ is the magnetic flux of the core, δ is the loss angle of the ferromagnetic core, δ_I is the current transformer phase displacement, and β is the phase displacement of the secondary burden (which is often negligible). (*From:* [45] with permission of IOP.)

11.6.2 Current Transformers

Instrument current transformers have a primary winding with few turns (or a single conductor through the core opening) and a secondary winding, which should be ideally short-circuited. The core material should have high permeability, high saturation induction, and low loss angle. While silicon steel has been used for low-cost units and permalloy for precise current transformers, nanocrystalline alloys presently dominate the market for high-performance current transformers [55].

Figure 11.23 shows the equivalent circuit of the current transformer for low and medium frequencies. A current transformer is a self-compensating sensor: the short-circuited secondary current compensates the effect of primary current, so that the core flux is small, ideally zero. Without this effect, the core would be saturated by the measured current.

This equivalent circuit is valid for a 1:1 current ratio. For other current ratios, the circuit parameters can be recalculated either to the primary side or to the secondary side. Currents and voltages are recalculated by the turn number ratio N, and impedances are recalculated by N^2.

At low and medium frequencies, the influence of parasitic capacitances and leakage inductances can be neglected, and a simplified phasor diagram according to Figure 11.24 can be used.

For a properly working current transformer, the phase error δ_I is small and, according to Figure 11.25, we can write for the amplitude and phase errors:

$$\varepsilon_I = \frac{|\mathbf{I}_2| - |\mathbf{I}_1|}{|\mathbf{I}_1|}100 \cong -\frac{I_m \sin(\delta + \beta)}{I_1}100 \ \ (\%) \tag{11.10}$$

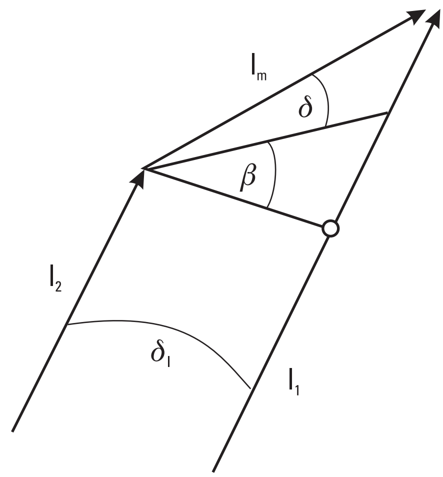

Figure 11.25 Derivation of amplitude and phase errors for small phase error δ_1. (*From:* [45] with permission of IOP.)

$$\delta_I \cong tg\delta_I \cong -\frac{I_m \cos(\delta + \beta)}{I_1} \quad \text{(rad)} \tag{11.11}$$

It is clear that, in order to keep the error low at low frequencies, it is important to keep R_c and L_m high and also to keep R_2 and Z_2 small. The magnetizing inductance L_m is given by

$$L_m = \frac{\mu_r \mu_0 N^2 A_C}{l_C} = \frac{\mu_r \mu_0 N^2 A_C}{2\pi r} \tag{11.12}$$

where r is the mean radius of the toroidal core and A_c is the cross-sectional area of the core.

L_m is kept high when using a high permeability core with a high number of turns. As the inductance depends on the square of the number of turns N^2 and the wire resistance depends only on N, a 1:5 turn ratio gives a larger error than 10:50. By increasing the number of turns, we can bring the core to saturation: this should be avoided by using a higher-diameter ring. The main inductance also depends linearly on the cross-sectional area of the core. For this reason, precise current transformers are large.

At low frequencies (such as 50/60 Hz), the dominant source of error is the magnetizing current I_m, which is inversely proportional to the frequency. The following methods can be used to reduce this current:

- Use a core material with high permeability;
- Increase the core cross-sectional area;
- Increase the number of turns;
- Virtually increase the core permeability by a feedback amplifier (used in self-balancing current comparators).

The magnetizing inductance L_m, the secondary resistance R_2, and the burden resistance R form a highpass filter circuit. Another approach to improve transformer accuracy at low frequencies is therefore to decrease the burden resistance R, which can be done by using a current-to-voltage converter [56].

Some current transformers have almost a constant ratio error for a wide range of measured currents. In this case, the error can be compensated for by adding extra turns to the secondary winding. This is called turn error compensation. Transformers with such compensation show anomalous behavior; their error increases when the burden decreases. Magnetization of the current transformer core (e.g., due to a lightning strike) may also lead to increased errors when the measured current is small so that the current transformer core is not demagnetized [57].

11.6.2.1 Electronically Enhanced Current Transformers

The first step is to connect the output of the current transformer to a current-to-voltage converter with a very small input resistance. This will minimize the burden, and it keeps the flux in the current transformer core at a low level, but not at zero; this is clear from the equivalent circuit of the current transformer in Figure 11.23. In order to achieve really zero flux, it is necessary to keep $V_i = 0$, and not only $V_2 = 0$. This can be achieved by a simple analog circuit [58]. The test was performed with a low-cost current transformer with a ferrite core: at 50 Hz and also for higher frequencies up to 450 Hz, the ratio error was reduced from 2% to 0.7%. The phase error was reduced from 45 mrad to 3 mrad at 50 Hz, but this error increased linearly with frequency due to the delay in electronic circuits. It should be noted that this type of enhancement does not work properly for a current transformer with a turn error compensation.

Electronically enhanced two-stage current transformers show accuracy improvement by two orders of magnitude: with a low burden, the resulting error is below 10 ppm [59]. These devices can also indicate the remanence of the transformer core or DC component in the primary current, which may degrade the performance of a classical current transformer; they may have a lower number of turns, which avoids problems with parasitic capacitances and enables the device to be used at higher frequencies; and finally, the volume of the core may be reduced.

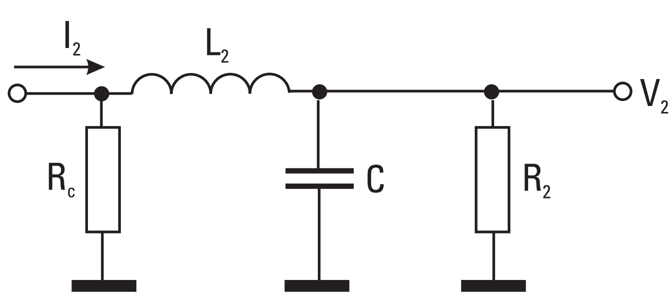

Figure 11.26 High-frequency equivalent circuit of the current transformer. (*After:* [56].)

At higher frequencies, parasitic capacitances between the turns and layers of the winding are the dominant source of error. Here, increasing the number of turns increases the error. For precise fast-current transformers, amorphous cobalt-based cores or ferrite cores are used, which give high permeability at megahertz frequencies. High-frequency current transformers work up to 50 MHz [60].

Similar transformers are used to observe short beam pulses in particle accelerators. Bergoz manufactures transformers with cutoff frequencies up to 2 GHz.

A high-frequency model of a current transformer is given in Figure 11.26 [56]. It is shown that the effect of L_m, R_1, and L_1 can be neglected. We also neglect the inductance of the sensing resistor. The frequency bandwidth is usually given by the first pole $f_{p1} = 1/2\pi R_2 C$. A second pole, defined by the stray inductance $f_{p2} = R_c/2\pi L_2$, is normally at a much higher frequency.

There have also been efforts to digitally compensate the frequency-dependent errors of current transformers. If the current transformer is considered to be a linear system (which is often true for low burdens), its frequency characteristics can be identified and corrected using a frequency filter with inverse characteristics. An efficient way to build this type of filter is with the use of a field-programmable gate array (FPGA). Both the amplitude and the phase error of a low-cost current transformer with an accuracy class of 0.5 was reduced by a factor of 20 [61]. Such a solution can be cost-effective, due to the very low cost of digital hardware. A disadvantage is that digital electronics introduces an inevitable time delay. If this cannot be eliminated by post-processing, it will lead to large, frequency-dependent phase error.

Current transformers are often used in electronic watt and energy meters. For this application, it is very important to make them resistant against saturation, either from a strong permanent magnet, or from a DC component in the measured current [62]. The possible methods for avoiding such saturation are:

1. Use a flat-loop magnetic material, which has a very high saturation field H.
2. Use composite cores, consisting of a high-permeability ring for precision and a low-permeability ring for saturation immunity.
3. Detect saturation by other means.
4. Use a Rogowski coil instead of a current transformer, which has no magnetic core.

The composite high-permeability core gives low angular and amplitude error for resistive load, but very high error may appear if the load is inductive or capacitive. Flat-loop materials such as Vacuumschmelze VAC do a better job, but these materials are expensive. It was recently shown that some cheap low-permeability rings can also be used for this application: they have a relatively large phase shift, but it is constant over the wide range of measured currents and can therefore be compensated [63, 64].

Fe-based nanocrystalline alloys are ideal materials for very precise small-size current transformers [55]. They may have the same permeability as permalloys or Co-based amorphous alloys, but they have much larger saturation induction, so that instrument current transformers are smaller. Field-annealed or stress-annealed Fe-based nanocrystalline ring cores may have almost constant permeability over

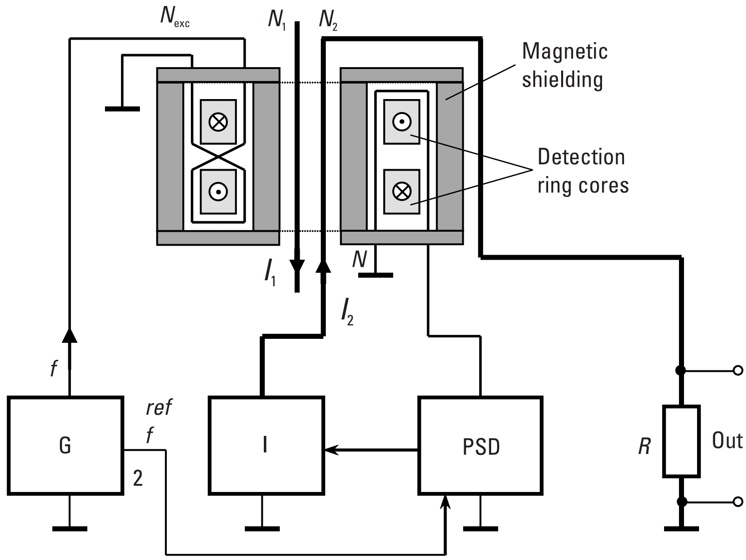

Figure 11.27 DC comparator. (Credit: P. Kejik.)

a wide range of induction. This gives a low amplitude error and a constant phase error in a wide range of the measured current. Such a constant phase error can easily be compensated. In large amounts, Fe-based nanocrystalline materials can be purchased at competitive prices.

Current transformers measure only AC, and they can be saturated by a DC component. After they have been magnetized, they lose precision, and they need to be demagnetized [65]. Demagnetization can also be achieved by increasing the burden [66].

Current comparators have been described in a book written by Moore and Miljanic [67]. The AC comparator is, in principle, a 3-winding device on the ring (toroidal) core. AC comparators have errors below 1 ppm in amplitude and 3×10^{-6}° in phase.

11.6.3 Fluxgate Current Sensors

Fluxgate-like DC sensor modules use the fluxgate principle described in Chapter 3. In this case, the measured value is electric in a conductor wound around the ring core, or a single conductor in the ring axis, which causes radial flux. These sensors are similar to DC comparators (Figure 11.27) but have simpler design. They are manufactured by LEM, VAC, and other manufacturers for measurement ranges between 40 A and 1,000 A. The accuracy of a typical low-cost 40-A module is 0.5%, linearity is 0.1%, and current temperature drift is <30 μA (–25°C to 70°C). High-end LEM ULTRASTAB devices have 0.01% accuracy.

A self-oscillating sensor of this type has been described by Ponjavic and Duric [68]. The fluxgate current sensor in PCB technology was described in [69]. Its sensor had a single winding of 36 turns over a toroidal core made of amorphous magnetic tape. It achieved 10-mV/A sensitivity and ranges up to 5A. A prototype of a fluxgate current sensor with an electroplated core in PCB technology was described in [70].

However, most of the fluxgate current sensors have a massive core. Because of their low offset drift, fluxgate-based DC transformers are superior to current transducers that have a Hall sensor in the air gap [71–74]. A disadvantage of these devices is their large power consumption.

11.6.3.1 DC Comparators

DC comparators are based on a fluxgate effect. These devices have also been described in the classic book written by Moore and Miljanic [67]. The core consists of two detection ring cores excited in opposite directions by the excitation winding N_{exc} supplied by current generator G (Figure 11.27). The second-harmonic component of the voltage induced into the detection winding N is measured by PSD. The output from PSD is filtered and amplified, and controls the DC compensation current I_2. In the ideal case, $N_1I_1 = N_2I_2$ and the device output is derived from I_2 using shunt resistor R. Only one layer of magnetic shielding under the secondary winding is shown in the figure. The role of this shielding is twofold: it reduces the leakage fluxes originating from the nonhomogeneity of the detection cores and the nonhomogeneity of the windings, and it also provides magnetic shielding against ambient fields.

DC comparators can have errors below 1 ppm. Even more precise are cryogenic current comparators, which use superconducting shielding and a SQUID as a null detector. They are used in resistance bridges with relative measurement uncertainties of about 10^{-9} [75].

11.6.3.2 Particle Beam Sensors

A large bandwidth electron beam sensor works from DC up to 50 MHz. Unser [76] described a high-resolution current sensor developed at CERN for particle accelerators. This parametric current transformer is a complicated device with 5 separate magnetic cores made of amorphous cobalt-based Vitrovac 6025, and several magnetic shields. The name is derived from a parametric amplification, which is used in the magnetic modulator. The magnetic modulator is excited by 7 kHz, 2.5 A_{pp} current, and its output is synchronously detected at 14 kHz. This channel measures the DC and low-frequency component of the current. The high-frequency component is measured by an active current transformer. The full-scale range of the instruments can be 10 mA to 100A. The achieved linearity error is 10 ppm of the full-scale range, the temperature offset drift is ±5 μA/°C, the resolution is ±0.3 ppm of the full-scale range ±0.4 μA, and the frequency band is DC up to 100 kHz. This device was later industrialized by Bergoz Instrumentation.

11.6.4 Rogowski Coils

The Rogowski coil for measuring current is an air coil wound around the measured current conductor. Detailed description of the principle and recent trends can be found in [77]. The basic operating principle is given by the mutual inductance M between the primary (single turn) and the secondary (many turns). The output voltage is proportional to the derivative of the current:

$$u = M\left(\frac{dI}{dt}\right) \tag{11.13}$$

The coil should be precisely manufactured with constant winding density and diameter. Ideally, a homogeneous coil has excellent geometrical selectivity (i.e., it is insensitive to external fields and to the position of the measured conductor), as it follows Ampere's law in the open air:

$$\oint_C \vec{B} \cdot d\dot{l} = \mu_0 i_C \tag{11.14}$$

where the integration path C is the central line of the coil (usually a circle).

In order to obtain the AC waveform, a Rogowski coil is used together with an integrator. Single-chip digital integrators have been developed to process the signal of Rogowski coils (also known as *dI/dt* sensors) for energy meters.

The Rogowski coil contains no ferromagnetic material, and thus it has excellent linearity and an extremely large dynamic range. Users often rely on their linearity and use them to measure currents that are much higher than the currents used for calibration. Care should be taken with the geometry of the connecting bus bars and the return conductor to reduce the effect of magnetic coupling. As the output voltage is small, the core should have a good electrostatic shielding. The grounded shielding should have proper distance from the coil in order to keep parasitic capacitance low. It is also possible to use magnetic shielding [78].

The Rogowski coil can be very simply temperature compensated. With increasing temperature the coil former expands, causing about 50-ppm/K temperature coefficient of the scale factor. However, the resistance of the copper coil increases with a 3,900-ppm/K temperature coefficient. By connecting a proper low-temperature coefficient resistor in parallel to the Rogowski coil, we create a voltage divider which compensates the thermal expansion. The resulting temperature coefficient can be as low as 2 ppm/K [79].

Stationary Rogowski coils are used to measure AC or transient currents or changes in DC. For long-term measurements, the limiting factor is the offset drift of the integrator. It is also possible to measure DC with an openable Rogowski coil: the output voltage is integrated while the coil is closed around the measured conductor.

Flexible Rogowski coils can be easily wound on top of a plastic cable with thick insulation, such as a coaxial cable with removed shielding. The inside conductor is used as a return loop, which compensates the perpendicular virtual loop created by the winding advance. An uncompensated loop would cause sensitivity to external magnetic fields in the axial direction. A detailed description of the production and testing of such coils and the following integrator and filter can be found in [80]. The error caused by the off-center position of the measured current was below 1.5%, and the suppression of the external currents was better than 100.

Rogowski coils are useful for measuring transient currents. The coil self-inductance and the parasitic capacitance form a resonant circuit. In order to increase the resonance frequency of this circuit, a lower number of turns should be used, which decreases the sensitivity. A 1–3-MHz resonance frequency is typical for flexible coils, while multiturn solid coils may have resonance as low as 50 kHz. At high

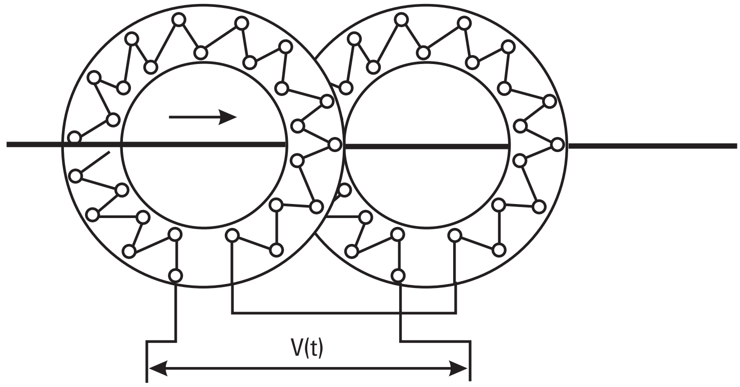

Figure 11.28 A Rogowski coil in PCB technology. Each layer is wound in the opposite direction to compensate for the loop created by turn advancement. (*From:* [45] with permission of IOP.)

frequencies, the active integrator can also cause errors due to the limited bandwidth and slew rate of the amplifier. An alternative technique for extending the frequency range is to use the current output instead of integrating the output voltage or to use parasitic capacitance for self-integration.

PCB technology was used to produce Rogowski coils with a more precise geometry and improved temperature stability. To compensate the virtual perpendicular loop, two PCB coils with opposite winding directions are connected in series. In order to achieve perfect compensation, it is important to design these two coils with the same diameter, as shown in Figure 11.28.

An improved twin-loop PCB Rogowski coil with a transfer ratio of 4V/400 kA was used to measure the plasma current in the Tokamak [81].

11.6.5 Sensors with a Gapped Core

Traditional current sensors are based on the Hall element in the air gap of a magnetic yoke (Figure 11.29). The yoke has three important effects: (1) increasing the sensitivity, (2) increasing the geometrical selectivity (i.e., shielding the external fields), and (3) decreasing the influence of the position of the measured current.

Even when using a magnetic yoke, Hall current sensors are sensitive to external magnetic fields and nearby currents, and also to the position of the measured conductor, due to the nonhomogeneity associated with the air gap.

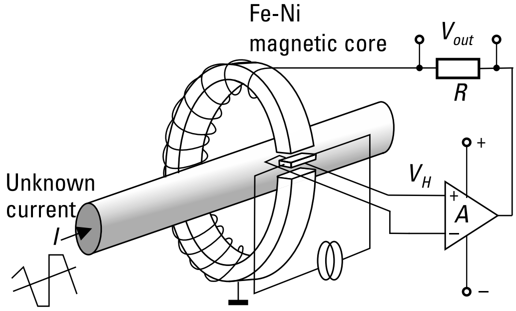

Figure 11.29 A Hall DC sensor in closed-loop configuration

A serious DC offset can be caused by the remanence of the magnetic core; only a few Hall current meters have an AC demagnetization circuit to erase perming after the sensor has been exposed to a large DC or external field.

In general, the yoke material should have large saturation induction B_s and low coercivity H_c. A widely used material is a cheap grain-oriented FeSi, and for precise applications 50% Ni–Fe alloy is used. By proper annealing, the coercivity of 50% Ni–Fe can be decreased below 2 A/m. It is also important to mount the core properly to avoid temperature-induced stresses. Widely used epoxy coatings degrade the performance at temperatures below 0°C. The nonhomogeneity of magnetic materials has an influence on the linearity of open-loop current sensors. By increasing the air gap, the influence of this nonlinearity is decreased, as is the influence of the remanence. The hysteresis error is approximately 0.2% to 0.5% for a 1-mm air gap and different grades of 50% Ni–Fe [82]. However, a larger air gap leads to unwanted sensitivity to the position of the measured conductor within the core and also reduces the suppression of external currents and fields.

The sensor linearity can be increased by using the feedback principle. Feedback-compensated devices cancel the field in the yoke by using multiturn compensation winding as shown in Figure 11.29. These sensors can achieve 0.02% error and a temperature coefficient of sensitivity of only 50 ppm/K. However, if the DC component is of concern, the main weak point is still the limited zero stability due to the Hall sensor offset: the typical offset drift of a 50-A sensor is 600 mA in the 0°C to 70°C range. This parameter is 20 times worse than that of fluxgate-type current sensor modules.

The sensing direction of microfluxgates and magnetoresistors is in the plane of the sensing layer, so they should be inserted into the slot in the core (Figure 11.30). The shown microfluxgate sensor has integrated excitation and signal processing electronics, including the feedback amplifier.

The field in the air gap is temperature-dependent due to the magnetostriction, the thermal expansion, and the temperature dependence of the core permeability.

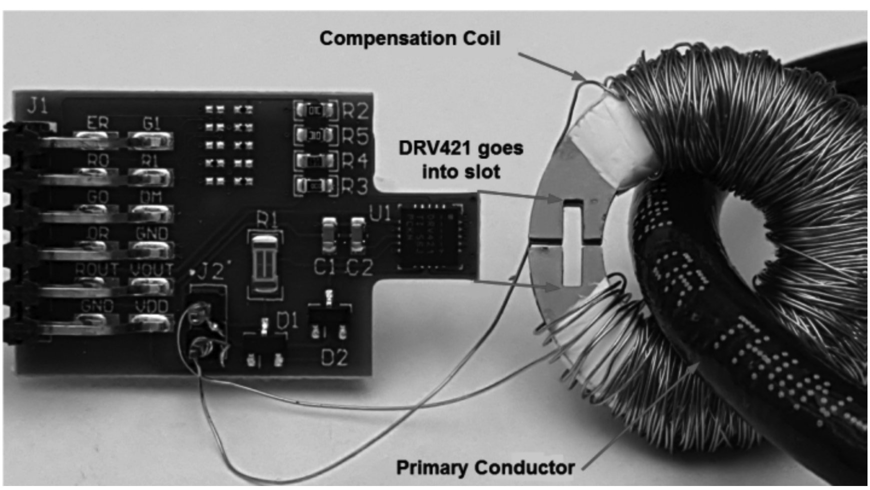

Figure 11.30 Prototype of the feedback compensated electric current sensor. The microfluxgate serves as a zero detector. In the final version, the compensation coil is wound around the whole core and the inserted sensor is not visible (Texas Instruments).

Methods for achieving self-compensation are discussed in [83]. Some sensors may have multiple gaps to achieve symmetry or to measure the currents in the power cord [84].

Some current sensors use a combination of a Hall sensor (for the DC and low-frequency component) and a current transformer (for the high-frequency component), using a gapped ferrite core. A frequency range of 30 MHz was achieved for 40-A range [85]. The matching between the two sensors can be made without an electronic stage. The idea is as follows: a high-frequency current transformer should have a low number of turns, which increases the lower corner frequency. The Hall sensors are therefore added to cover this frequency region.

11.6.6 Coreless Current Sensors

Current sensors without core are small, lightweight, and cheap. However, they are very sensitive to the position of the measured conductor and also to external magnetic fields, including those induced by electric currents in other conductors in their vicinity. The ideal solution is to use a circular sensor array around the conductor that approximates the line integral in the Ampère's circuital law. Such arrays are made of Hall [48], AMR [49], and microfluxgate [50] sensors. Less ideal solution is to use gradiometric sensor close to the conductor or inside the hole in the conductor, if the current to be measured is high [51]. For a typical configuration, the error from current in the 5-cm vicinity is 5% for a single sensor, 0.5% for two sensors connected as gradiometer, and well below 0.1% for circular arrays [5].

11.6.6.1 Hall Coreless Current Sensors

Some Hall current sensors use field concentrators, which increase the measured field but do not completely surround the measured current. In this case, the danger of saturation is much lower, but the position of the measured conductor should be fixed, and suppression of the external fields and currents should be achieved by other means. A low-cost current sensor based on a highly sensitive Hall sensor with simple integrated flux concentrators was described in [86]. The field concentrators transform a lateral field locally into the vertical direction as explained in Chapter 6. The sensor is manufactured by Melexis with 1% accuracy in the ±12-A range. It can be used to measure the currents in both PCB conductors and free-standing conductors.

The realization and the optimization of gradiometric current transducers based on Hall effect sensors were described in [87, 88]. The influence of the external current on the gradiometric busbar sensor was analyzed in [89]. Complete suppression of external fields and gradients requires more sensors [90]. For measurements of currents up to the 50-A range, gradiometric sensors with a short base are often positioned inside the folded conductor [88, 91].

The circular arrays of Hall sensors have received significant attention [48]. The main advantage of a circular array is that it provides much better suppression of external currents than a differential sensor configuration. Suppression well below 0.1% can be achieved if the sensors are calibrated for sensitivity and geometrical misalignment [92].

An integrated current sensor based on two Hall sensors placed on both sides of the current strip was developed by Frick et al. [93]. The differentially connected Hall sensors reject the common-mode inference from the external magnetic fields. Proper autobalancing is achieved using built-in calibration coils. The resulting accuracy was 0.5% in the 5-A range with 1.5-kHz bandwidth.

The background calibration using integrated coils together with the spinning current technique can reduce the temperature sensitivity drift of the Hall sensor to less than 50 ppm/°C, while the bandwidth can be as high as 500 kHz. Sensitivity variations due to mechanical stresses and aging are also compensated [94]. This technique can significantly improve the performance of current sensors if feedback compensation is not possible [95].

Magnetic shielding can be used to isolate the coreless current Hall sensors from the influence of the nonmeasured currents. The difference between yoke and field concentrators and shielding is that, in the case of shielding, the sensor is not in the air gap of the magnetic circuit. An example of such a system is a three-phase 400-A current sensor for a power converter. The thickness of the U-shaped shields should be 1.5 mm to avoid saturation and to suppress the neighboring currents by a factor of 100 [96].

11.6.6.2 Coreless Current Sensors Based on Magnetoresistors

Magnetoresistors have higher resolution than Hall sensors. The popular configuration is again a bridge measuring the magnetic gradient from the current, since it is resistant against homogeneous external magnetic fields (e.g., from distant currents). The bridge also suppresses the temperature variation of the electric resistivity of the magnetoresistive material (Figure 11.31). This type of sensor usually has the current conductor integrated with the sensors in a single device to ensure stable geometry. The bridge has all the barber poles in the same direction, which

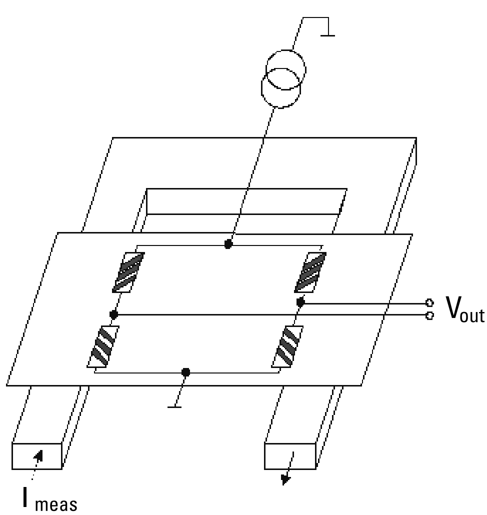

Figure 11.31 AMR current sensor. (*From:* [45] with permission of IOP.)

means that it is made insensitive to a homogeneous external field, but sensitive to measured current through the bus bar. The measured current can be compensated by a feedback current through a compensation conductor. A typical application is galvanically isolated current sensing in a pulse width modulation regulated brushless motor. These sensors are manufactured by Sensitec (also under the F.W. Bell label) with ranges from 5 A to 220 A. The achieved linearity is 0.1%, temperature coefficient of sensitivity is 100 ppm/K, and the offset drift in the −45°C to +85°C range is 1.4% of the full-scale range.

A similar sensor with a GMR detector was developed by Siemens [97] and was later improved by Pannetier-Lecouer et al. [98] and De Marcellis et al. [99].

GMR sensors may exhibit a large irreversible change of characteristic after a magnetic shock created by a large external field or overcurrent.

11.6.6.3 Coreless Current Sensors Based on Fluxgate

Low-cost, self-oscillating fluxgate transducers have also been used to measure high currents [100]. The first microfluxgate sensor on the market was developed by Texas Instruments for current sensing applications [101]. Microfluxgate sensors use pulse excitation to reduce power consumption [102]. Microfluxgates have been used for busbar current sensors with the sensors inside the busbar and with the sensors around the busbar.

As the integrated fluxgate sensor has a 2-mT range, the circular array around the conductor can measure DC and AC up to 500 A [50]. The rectangular array transducer is presented in [103]. Compared to industrial transducers with a yoke, the new transducer has 15 times lower noise, 7 times better temperature stability, and the same crosstalk.

An elegant solution to increase the current range is to insert a gradiometric sensor inside a hole drilled in the busbar [51]. The sensitivity and the range of the current transducer can be adjusted by changing the distance between sensors in the gradiometric pair. For this type of gradiometric sensor, there is also limited rejection of the signal from external currents: current at a distance of 14 cm is suppressed only by a factor of 66 [89]. This can be improved to 1,300 by using a larger number of sensors [90].

11.6.7 Current Clamps

AC clamps are based on current transformers made on openable ferrite core. The measured conductor forms a primary winding; secondary winding is terminated by a small resistor or is connected to current-to-voltage converter. Very accurate clamp current transformers use electronic compensation of the magnetization current and achieve errors of 0.05% from the measured value in 1% to 100% full-scale range. High-current AC and AC/DC openable current transformer clamps [104] and a low-current multistage clamp-on current transformer with ratio errors below 50 ppm [105] have been developed. Noninvasive current measurement can be also made using split core sensors [106]. Most of the available DC clamps are based on the Hall sensor.

These devices may have a 10-mA resolution, but the maximum achieved accuracy is typically 30 mA, even if they are of the compensated type. Their main disadvantage is unwanted sensitivity to external fields, due to the air gap in the magnetic circuit, which is necessary for the Hall sensor. Even the change of position with respect to the Earth's field causes a significant error, and the offset should be manually nulled.

Precise DC/AC clamps based on a shielded fluxgate current sensor are manufactured by Tektronix, Hioki, Yokogawa, and other companies.

Not only traditional clamps but also flexible sensors can form an openable magnetic circuit. The most popular are flexible Rogowski coils (Section 4.2).

11.6.8 Magnetometric Measurement of Hidden Currents

DC cables can be located and their current can be remotely monitored by measuring the magnetic field in several points. This technique was used for locating underwater optical cables that contain a metallic conductor delivering a DC of about 1A to supply the repeaters. The field distribution was measured by two 3-axial fluxgate magnetometers. The cables were detected from a distance of 40 m, and their position was determined with 0.1-m accuracy from a distance of 4 m [107, 108]. The method for localization and measurement of a hidden AC was described in [109].

The magnetometric current is also used to locate and measure the AC and DC fault currents in building structures, such as bridges. The natural variation of the Earth's field induces currents in long conductors, which may cause electrochemical corrosion: a 70-A current was measured in the Alaska Oil Pipeline [110].

References

[1] Tumanski, S., "Modern Magnetic Field Sensors—A Review," *PRZEGLAD ELEKTROTECHNICZNY*, Vol. 89, No. 10, 2013.

[2] Reininger, T., F. Welker, and M. von Zeppelin, "Sensors in Position Control Applications for Industrial Automation," *Sensors and Actuators A: Physical*, Vol. 129, No. 1-2, May 2006, pp. 270–274.

[3] George, B., Z. C. Tan, and S. Nihtianov, "Advances in Capacitive, Eddy Current, and Magnetic Displacement Sensors and Corresponding Interfaces," *IEEE Transactions on Industrial Electronics*, Vol. 64, No. 12, December 2017, pp. 9595–9607.

[4] Ripka, P., et al., "Inductive Position and Speed Sensors," *Sensors*, Vol. 20, No. 1, 2019.

[5] Ripka, P., "Contactless Measurement of Electric Current Using Magnetic Sensors," *Tm-Technisches Messen*, Vol. 86, No. 10, October 2019, pp. 586–598.

[6] Brauer, J. R., *Magnetic Actuators and Sensors*, New York: Wiley IEEE Press, 2014.

[7] Ortner, M., M. Ribeiro, and D. Spitzer, "Absolute Long-Range Linear Position System with a Single 3-D Magnetic Field Sensor," *IEEE Transactions on Magnetics*, Vol. 55, No. 1, January 2019.

[8] Quasdorf, J., "The Vernier Scale Goes Digital," *Sensors Magazine*, 2009.

[9] Feng, T., et al., "Development of a Combined Magnetic Encoder," *Sensor Review*, Vol. 36, No. 4, 2016, pp. 386–396.

[10] Fericean, S., and R. Droxler, "New Noncontacting Inductive Analog Proximity and Inductive Linear Displacement Sensors for Industrial Automation," *IEEE Sensors Journal*, Vol. 7, No. 11-12, November-December 2007, pp. 1538–1545.

[11] Welsby, S. D., and T. Hitz, "True Position Measurement with Eddy Current Technology," *Sensors*, No. 11, 1997, pp. 30–40.

[12] Anim-Appiah, K. D., and S. M. Riad, "Analysis and Design of Ferrite Cores for Eddy-Current-Killed Oscillator Inductive Proximity Sensors," *IEEE Transactions on Magnetics*, Vol. 33, No. 3, May 1997, pp. 2274–2281.

[13] Passeraub, P. A., P. A. Besse, and R. S. Popovic, "Temperature Compensation of an Integrated Low Power Inductive Proximity Microsensor," *Sensors and Actuators A: Physical*, Vol. 82, No. 1-3, May 2000, pp. 62–68.

[14] Mirzaei, M., P. Ripka, and V. Grim, "A Novel Eddy Current Speed Sensor with a Ferrite E-Core," *IEEE Magnetics Letters*, Vol. 11, 2020.

[15] Ripka, P., "Security Applications of Magnetic Sensors," *Journal of Physics: Conference Series*, Vol. 450, No. 1, 2013.

[16] Petchmaneelumka, W., et al., "Compensation of Temperature Effect for LVDT Transducer," *Journal of Circuits Systems and Computers*, Vol. 27, No. 12, November 2018.

[17] Petchmaneelumka, W., W. Koodtalang, and V. Riewruja, "Simple Technique for Linear-Range Extension of Linear Variable Differential Transformer," *IEEE Sensors Journal*, Vol. 19, No. 13, July 2019, pp. 5045–5052.

[18] http://www.inductosyn.com/products.htm.

[19] Hristoforou, E., "Magnetostrictive Delay Lines: Engineering Theory and Sensing Applications," *Measurement Science and Technology*, Vol. 14, No. 2, February 2003, pp. R15–R47.

[20] https://www.posital.com/en/products/wiegand-sensors/wiegand-sensors.php.

[21] Takahashi, K., T. Yamada, and Y. Takemura, "Circuit Parameters of a Receiver Coil Using a Wiegand Sensor for Wireless Power Transmission," *Sensors*, Vol. 19, No. 12, June 2019.

[22] Hehn, M., et al., "High-Accuracy Localization and Calibration for 5-DoF Indoor Magnetic Positioning Systems," *IEEE Transactions on Instrumentation and Measurement*, Vol. 68, No. 10, October 2019, pp. 4135–4145.

[23] Taylor, C. R., H. G. Abramson, and H. M. Herr, "Low-Latency Tracking of Multiple Permanent Magnets," *IEEE Sensors Journal*, Vol. 19, No. 23, December 2019, pp. 11458–11468.

[24] https://www.ndigital.com/.

[25] Attivissimo, F., et al., "A Novel Electromagnetic Tracking System for Surgery Navigation," *Computer Assisted Surgery*, Vol. 23, No. 1, 2018, pp. 42–52.

[26] Dai, H. D., et al., "6-D Electromagnetic Tracking Approach Using Uniaxial Transmitting Coil and Tri-Axial Magneto-Resistive Sensor," *IEEE Sensors Journal*, Vol. 18, No. 3, February 2018, pp. 1178–1186.

[27] Lapinski, M., et al., "A Wide-Range, Wireless Wearable Inertial Motion Sensing System for Capturing Fast Athletic Biomechanics in Overhead Pitching," *Sensors*, Vol. 19, No. 17, September 2019.

[28] Vcelak, J., P. Ripka, and A. Zikmund, "Long-Range Magnetic Tracking System," *IEEE Sensors Journal*, Vol. 15, No. 1, January 2015, pp. 491–496.

[29] Park, B., and H. Myung, "Resilient Underground Localization Using Magnetic Field Anomalies for Drilling Environment," *IEEE Transactions on Industrial Electronics*, Vol. 65, No. 2, February 2018, pp. 1377–1387.

[30] MS 1100 Inductive position, speed and direction sensor, www.csem.ch.

[31] Fraden, J., *Handbook of Modern Sensors*, New York: Springer International Publishing, 2016.

[32] Barandiaran, J. M., and J. Gutierrez, "Magnetoelastic Sensors Based on Soft Amorphous Magnetic Alloys," *Sensors and Actuators A: Physical*, Vol. 59, No. 1-3, April 1997, pp. 38–42.

[33] Bydzovsky, J., et al., "Strain Sensors Based on Stress-Annealed Co69Fe2Cr7Si8B14 Amorphous Ribbons," *Sensors and Actuators A: Physical*, Vol. 110, No. 1-3, February 2004, pp. 82–86.

[34] Alimohammadi, S., T. Meydan, and P. Williams, "Strain Sensing by Exploiting the Matteucci Effect in Amorphous Wire," *International Journal of Applied Electromagnetics and Mechanics*, Vol. 59, No. 1, 2019, pp. 115–121.

[35] Allue, A., et al., "Smart Composites with Embedded Magnetic Microwire Inclusions Allowing Non-Contact Stresses and Temperature Monitoring," *Composites Part A: Applied Science and Manufacturing*, Vol. 120, May 2019, pp. 12–20.

[36] Grimes, C. A., et al., "Theory, Instrumentation and Applications of Magnetoelastic Resonance Sensors: A Review," *Sensors*, Vol. 11, No. 3, March 2011, pp. 2809–2844.

[37] Garshelis, I. J., and C. A. Jones, "A Torque Transducer Based on Local Bands of Naturally Stabilized Remanent Circumferential Magnetization," *Journal of Applied Physics*, Vol. 85, No. 8, April 1999, pp. 5468–5470.

[38] Dahle, O., "The Ring Torductor—A Torque-Gauge, Without Slip Rings, for Industrial Measurement and Control," *ASEA Journal*, Vol. 33, No. 3, 1960.

[39] Beth, R. A., and W. W. Meeks, "Magnetic Measurement of Torque in a Rotating Shaft," *Review of Scientific Instruments*, Vol. 25, No. 6, 1954, pp. 603–607.

[40] Sasada, I., "Magnetostrictive Methods of Detecting Torque from Case-Hardened Steel Shafts," p. 231. *MRS Online Proceedings Library*, Vol. 360, 1994, pp. 231–242.

[41] Sendoh, I., and S. Kawahara, "Torque Meter," Japanese Patent Office, 1945.

[42] Garshelis, I. J., and C. R. Conto, "A Torque Transducer Utilizing 2 Oppositely Polarized Rings," *IEEE Transactions on Magnetics*, Vol. 30, No. 6, November 1994, pp. 4629–4631.

[43] Kari, R. J., et al., *Magnetoelastic Torquemeter System for LCAC Hovercraft Turboshaft Engine Monitoring & Control*, New York: American Society of Mechanical Engineers, 2012.

[44] Sahu, S., et al., "Development of an Optimised Magnetic Field Source for Flowmeter Applications," *Flow Measurement and Instrumentation*, Vol. 66, April 2019, pp. 190–199.

[45] Ripka, P., "Electric Current Sensors: A Review," *Measurement Science and Technology*, Vol. 21, No. 11, 2010.

[46] Ziegler, S., et al., "Current Sensing Techniques: A Review," *IEEE Sensors Journal*, Vol. 9, No. 4, April 2009, pp. 354–376.

[47] Iwansson, K., G. Sinapius, and W. Hoornaert, *Measuring Current, Voltage and Power*, New York: Elsevier, 1999.

[48] Chen, W. L., et al., "Wire-Positioning Algorithm for Coreless Hall Array Sensors in Current Measurement," *Measurement Science and Technology*, Vol. 29, No. 5, May 2018.

[49] Mlejnek, P., and P. Ripka, "AMR Yokeless Current Sensor with Improved Accuracy," *Proceedings of the 30th Anniversary Eurosensors Conference—Eurosensors 2016*, 2016, pp. 900–903.

[50] Weiss, R., et al., "Crosstalk in Circular Arrays of Magnetic Sensors for Current Measurement," *IEEE Transactions on Industrial Electronics*, Vol. 64, No. 6, June 2017, pp. 4903–4909.

[51] Snoeij, M. F., et al., "Integrated Fluxgate Magnetometer for Use in Isolated Current Sensing," *IEEE Journal of Solid-State Circuits*, Vol. 51, No. 7, July 2016, pp. 1684–1694.

[52] Bohnert, K., et al., "Fiber-Optic Current and Voltage Sensors for Electric Power Transmission Systems," *Fiber Optic Sensors and Applications XV, Proceedings of SPIE*, 2018.

[53] Cheng, S., et al., "Distributed Parameter Model for Characterizing Magnetic Crosstalk in a Fiber Optic Current Sensor," *Applied Optics*, Vol. 54, No. 34, December 2015, pp. 10009–10017.

[54] Nascimento, I. M., et al., "Novel Optical Current Sensor for Metering and Protection in High Power Applications," *Instrumentation Science & Technology*, Vol. 44, No. 2, March 2016, pp. 148–162.

[55] Draxler, K., and R. Styblikova, "Use of Nanocrystalline Materials for Current Transformer Construction," *Journal of Magnetism and Magnetic Materials*, Vol. 157, May 1996, pp. 447–448.

[56] Kondrath, N., and M. K. Kazimierczuk, "Bandwidth of Current Transformers," *IEEE Transactions on Instrumentation and Measurement*, Vol. 58, No. 6, June 2009, pp. 2008–2016.

[57] Draxler, K., and R. Styblikova, "Influence of Instrument Transformers on Quality of Electrical Power and Energy Measurement," *IEEE Intl. Symposium on Industrial Electronics*, 2007.

[58] Baccigalupi, A., and A. Liccardo, "Low-Cost Prototype for the Electronically Compensation of Current Transformers," *IEEE Sensors Journal*, Vol. 9, No. 5-6, May-June 2009, pp. 641–647.

[59] Miljanic, P. N., E. So, and W. J. M. Moore, "An Electronically Enhanced Magnetic Core for Current Transformers," *IEEE Transactions on Instrumentation and Measurement*, Vol. 40, No. 2, April 1991, pp. 410–414.

[60] Zachariades, C., et al., "Optimization of a High-Frequency Current Transformer Sensor for Partial Discharge Detection Using Finite-Element Analysis," *IEEE Sensors Journal*, Vol. 16, No. 20, October 2016, pp. 7526–7533.

[61] Gallo, D., C. Landi, and M. Luiso, "Compensation of Current Transformers by Means of Field Programmable Gate Array," *Metrology and Measurement Systems*, Vol. 16, No. 2, 2009, pp. 279–288.

[62] Mlejnek, P., and P. Kaspar, "Detection of Disturbance of Working Conditions of Current Transformer in Energy Meters for Reduction of Unauthorized Current Consumption," *International Conference on Power Electronics and Drive System (PEDS)*, December 2009.

[63] Mlejnek, P., P. Kaspar, and K. Draxler, "Measurement of Ratio Error and Phase Displacement of DC Tolerant Current Transformers," *Sensor Letters*, Vol. 5, No. 1, March 2007, pp. 289–292.

[64] Mlejnek, P., and P. Kaspar, "Drawback of Using Double Core Current Transformers in Static Watt-Hour Meters," *Sensor Letters*, Vol. 7, No. 3, June 2009, pp. 394–396.

[65] Draxler, K., and R. Styblikova, "Demagnetization of Instrument Transformers Before Calibration," *Journal of Electrical Engineering-Elektrotechnicky Casopis*, Vol. 69, No. 6, December 2018, pp. 426–430.

[66] Bauer, J., et al., "Demagnetization of Current Transformers Using PWM Burden," *IEEE Transactions on Magnetics*, Vol. 51, No. 1, 2015.

[67] Moore, W. J. M., and P. N. Miljanic, *The Current Comparator*, London, U.K.: Peter Peregrinus, 1968.

[68] Ponjavic, M. M., and R. M. Duric, "Nonlinear Modeling of the Self-Oscillating Fluxgate Current Sensor," *IEEE Sensors Journal*, Vol. 7, No. 11-12, November-December 2007, pp. 1546–1553.

[69] Belloy, E., et al., "A Hybrid Technology for Miniaturised Inductive Device Applications," *Sensors and Actuators A: Physical*, Vol. 85, No. 1-3, August 2000, pp. 304–309.

[70] O'Donnell, T., et al., "Planar Fluxgate Current Sensor Integrated in Printed Circuit Board," *Sensors and Actuators A: Physical*, Vol. 129, No. 1-2, May 2006, pp. 20–24.

[71] Veinovic, S., et al., "Low-Power Design for DC Current Transformer Using Class-D Compensating Amplifier," *IET Circuits Devices & Systems*, Vol. 12, No. 3, May 2018, pp. 215–220.

[72] Velasco-Quesada, G., et al., "Class H Power Amplifier for Power Saving in Fluxgate Current Transducers," *IEEE Sensors Journal*, Vol. 16, No. 8, April 2016, pp. 2322–2330.

[73] Callegaro, L., C. Cassiago, and E. Gasparotto, "On the Calibration of Direct-Current Current Transformers (DCCT)," *IEEE Transactions on Instrumentation and Measurement*, Vol. 64, No. 3, March 2015, pp. 723–727.

[74] Ripka, P., K. Draxler, and R. Styblíková, "DC-Compensated Current Transformer," *Sensors*, Vol. 16, 2016.

[75] Gotz, M., et al., "Improved Cryogenic Current Comparator Setup with Digital Current Sources," *IEEE Transactions on Instrumentation and Measurement*, Vol. 58, No. 4, April 2009, pp. 1176–1182.

[76] Unser, K. B., "The Parametric Current Transformer, A Beam Current Monitor Developed for LEP," *AIP Conference Proceedings*, 1992, pp. 266–275.

[77] Samimi, M. H., et al., "The Rogowski Coil Principles and Applications: A Review," *IEEE Sensors Journal*, Vol. 15, No. 2, February 2015, pp. 651–658.

[78] Draxler, K., and R. Styblikova, "Magnetic Shielding of Rogowski Coils," *2017 IEEE International Instrumentation and Measurement Technology Conference (I2MTC)*, 2017.

[79] Suomalainen, E. P., and J. K. Hallstrom, "Onsite Calibration of a Current Transformer Using a Rogowski Coil," *IEEE Transactions on Instrumentation and Measurement*, Vol. 58, No. 4, April 2009, pp. 1054–1058.

[80] Abdi-Ghaleh, R., "Dual-Channel Magnetic Field Sensors Based on Magnetophotonic Heterostructures," *Applied Optics*, Vol. 56, No. 5, February 2017, pp. 1561–1565.

[81] Eydan, A., et al., "Design and Fabrication of an Optimized Rogowski Coil for Plasma Current Sensing and the Operation Confidence of Alvand Tokamak," *Nuclear Engineering and Technology*, Vol. 52, No. 11, November 2020, pp. 2535–2542.

[82] Waeckerle, T., et al., "Upgrade Fe-50%Ni Alloys for Open-Loop DC Current Sensor: Design and Alloy-Potential Characteristics," *Journal of Magnetism and Magnetic Materials*, Vol. 304, No. 2, September 2006, pp. E850–E852.

[83] Xiang, Y. K., et al., "A Ferromagnetic Design for Current Sensor Temperature Characteristics Improvement," *IEEE Sensors Journal*, Vol. 18, No. 4, February 2018, pp. 1435–1441.

[84] Zhang, J., Y. M. Wen, and P. Li, "Nonintrusive Current Sensor for the Two-Wire Power Cords," *IEEE Transactions on Magnetics*, Vol. 51, No. 11, November 2015.

[85] Dalessandro, L., N. Karrer, and J. W. Kolar, "High-Performance Planar Isolated Current Sensor for Power Electronics Applications," *IEEE Transactions on Power Electronics*, Vol. 22, No. 5, September 2007, pp. 1682–1692.

[86] Popovic, R. S., P. M. Drljaca, and P. Kejik, "CMOS Magnetic Sensors with Integrated Ferromagnetic Parts," *Sensors and Actuators A: Physical*, Vol. 129, No. 1-2, May 2006, pp. 94–99.

[87] Blagojevic, M., et al., "Realization and Optimization of Bus Bar Current Transducers Based on Hall Effect Sensors," *Measurement Science and Technology*, Vol. 27, No. 6, June 2016.

[88] Blagojevic, M., et al., "Folded Bus Bar Current Transducer Based on Hall Effect Sensor," *Electrical Engineering*, Vol. 100, No. 2, June 2018, pp. 1243–1251.

[89] Ripka, P., and A. Chirtsov, "Influence of External Current on Yokeless Electric Current Transducers," *IEEE Transactions on Magnetics*, Vol. 53, No. 11, November 2017.

[90] Ripka, P., and A. Chirtsov, "Busbar Current Transducer with Suppression of External Fields and Gradients," *IEEE Transactions on Magnetics*, Vol. 54, No. 11, November 2018.

[91] Beltran, H., et al., "Modeling of Magnetoresistive-Based Electrical Current Sensors: A Technological Approach," *IEEE Sensors Journal*, Vol. 7, No. 11-12, November-December 2007, pp. 1532–1537.

[92] Itzke, A., R. Weiss, and R. Weigel, "Influence of the Conductor Position on a Circular Array of Hall Sensors for Current Measurement," *IEEE Transactions on Industrial Electronics*, Vol. 66, No. 1, January 2019, pp. 580–585.

[93] Frick, V., et al., "Electromagnetically Compatible CMOS Auto-Balanced Current Sensor

for Highly Integrated Power Control System-on-Chip," *International Journal of Electronics*, Vol. 94, No. 1, January 2007, pp. 9–22.

[94] Pastre, M., M. Kayal, and H. Blanchard, "A Hall Sensor Analog Front End for Current Measurement with Continuous Gain Calibration," *IEEE Sensors Journal*, Vol. 7, No. 5-6, May-June 2007, pp. 860–867.

[95] Jiang, J. F., and K. A. A. Makinwa, "A Hybrid Multi-Path CMOS Magnetic Sensor with 76 ppm/Degrees C Sensitivity Drift and Discrete-Time Ripple Reduction Loops," *IEEE Journal of Solid-State Circuits*, Vol. 52, No. 7, July 2017, pp. 1876–1884.

[96] Kim, H. G., G. B. Kang, and D. J. Nam, "Coreless Hall Current Sensor for Automotive Inverters Decoupling Cross-Coupled Field," *Journal of Power Electronics*, Vol. 9, No. 1, January 2009, pp. 68–73.

[97] Vieth, M., et al., "Contactless Current Detection with GMR Sensors Based on an Artificial Antiferromagnet (AAF) Subsystem," *Sensors and Actuators A: Physical*, Vol. 81, No. 1-3, April 2000, pp. 44–48.

[98] Pannetier-Lecoeur, M., et al., "Low Noise Magnetoresistive Sensors for Current Measurement and Compasses," *Journal of Magnetism and Magnetic Materials*, Vol. 316, No. 2, September 2007, pp. E246–E248.

[99] De Marcellis, A., et al., "Monolithic Integration of GMR Sensors for Standard CMOS-IC Current Sensing," *Solid-State Electronics*, Vol. 135, September 2017, pp. 100–104.

[100] Wang, N., et al., "Design and Characterization of a Low-Cost Self-Oscillating Fluxgate Transducer for Precision Measurement of High-Current," *IEEE Sensors Journal*, Vol. 16, No. 9, May 2016, pp. 2971–2981.

[101] Lee, D. W., et al., "Fabrication and Performance of Integrated Fluxgate for Current Sensing Applications," *IEEE Transactions on Magnetics*, Vol. 53, No. 11, November 2017.

[102] Ripka, P., et al., "Pulse Excitation of Micro-Fluxgate Sensors," *IEEE Transactions on Magnetics*, Vol. 37, No. 4, July 2001, pp. 1998–2000.

[103] Ripka, P., et al., "Rectangular Array Electric Current Transducer with Integrated Fluxgate Sensors," *Sensors*, Vol. 19, No. 22, November 2019.

[104] Ramboz, J. D., "A Highly Accurate, Hand-Held Clamp-On Current Transformer," *IEEE Transactions on Instrumentation and Measurement*, Vol. 45, No. 2, April 1996, pp. 445–448.

[105] So, E., and D. A. Bennett, "A Low-Current Multistage Clamp-On Current Transformer with Ratio Errors Below 50x10(-6)," *IEEE Transactions on Instrumentation and Measurement*, Vol. 46, No. 2, April 1997, pp. 454–458.

[106] Draxler, K., et al., "Use of a Nanocrystalline Core for a Precise Non-Invasive AC Current Measurement," *2016 Conference on Precision Electromagnetic Measurements (CPEM 2016)*, 2016.

[107] Takagi, S., et al., "DC Cable Sensors for Locating Underwater Telecommunication Cables," *Oceans '96 Mts/IEEE, Conference Proceedings, Vols. 1–3/Supplementary Proceedings: Coastal Ocean—Prospects for the 21st Century*, 1996, pp. 339–344.

[108] Szyrowski, T., et al., "Subsea Cable Tracking by an Unmanned Surface Vehicle," *Underwater Technology*, Vol. 32, No. 4, March 2015, pp. 217–229.

[109] Grim, V., et al., "Magnetometric Localization and Measurement of Hidden AC Currents," *2019 IEEE Sensors*, 2019.

[110] Campbell, W. H., and J. E. Zimmerman, "Induced Electric Currents in the Alaska Oil Pipeline Measured by Gradient Fluxgate and Squid Magnetometers," *IEEE Transactions on Geoscience and Remote Sensing*, Vol. 18, No. 3, 1980, pp. 244–250.

Acronyms and Abbreviations

A	core cross-sectional area
AC	alternating current
ADC	analog-to-digital converter
AMR	anisotropic magnetoresistance
AU	astronomical unit
B	magnetic field (T)
B_N	magnetic noise
B_{off}	offset induction
B_p	polarizing field
B_{res}	resultant field
B_0	magnetic field (flux density) in the open space (in air)
C	capacitance; pitch
CMR	colossal magnetoresistance
d	diameter
db	decibel
DAC	digital-to-analog converter
d_c	core diameter
DC	direct current
d_m	mean coil diameter
d_w	wire diameter
D	effective demagnetizing factor; dielectric displacement
DNP	dynamic nuclear polarization
DSP	digital signal processor
e	unit electrical charge
^{e}noise	noise voltage
$\mathbf{e}_n$	noise energy
$\mathbf{e}_r$	unity vector in the direction of r
E	electrical field strength; energy; energy sensitivity of SQUID; Young's modulus
E_H	Hall electric field
ESR	electronic spin resonance
f	frequency; correction factor

F	Faraday rotation; force
FFT	fast Fourier transform
f_L, f_h, f_1, f_c	low frequency, higher frequency, lower frequency, corner frequency
g	acceleration of gravity
G	geometric correction factor
g_m	transconductance
GMI	giant magnetoimpedance
GMR	giant magnetoresistance, also sensitivity of GMR magnetoresistor
h	height; Planck's constant
H	magnetic field intensity (A/m)
H_c	critical field
H_d	demagnetization field
H_{exc}	excitation field intensity
H_k	anisotropy field
H_m	maximum magnetic field intensity
H_o	characteristic field
H_0	intensity of the external field (in the open space) i, I current
HTS	high-temperature superconductor
I	intensity of light; moment of inertia
IC	integrated circuit
i_{EQ}	equivalent coil current
I_{exc}	excitation current
I_n, i_n	noise current
J	Coulomb's magnetic moment; polarization
J_c	current density
J_E	exchange coupling energy
j_z	longitudinal component of the current density
k	constant; wave factor
K	anisotropy constant
k_B	Boltzmann's constant
l, L	length
L	inductance; angular momentum
l_{eff}	effective coil length
L_0	arithmetic mean value $L_0 = \langle L(t) \rangle$
LF	low frequency
L_{G0}	geometric mean value of the pickup coil inductance
L_s	serial inductance
LTS	low-temperature superconductor

m	mass; magnetic moment; length/diameter ratio
M	magnetization
MBE	molecular beam epitaxy
m_e	mass of electron
M_s	spontaneous magnetization
m_w	mass of coil winding
n	multiple integer; carrier density
N	number of turns; number of atoms per cubic meter
NMR	nuclear magnetic resonance
N_{rms}	RMS level of the noise
N_Z	longitudinal demagnetization factor
PCB	printed circuit board
$P(f)$	power spectrum density of the noise
p-p	peak to peak
PSD	phase sensitive detector
q	elementary charge
Q	magnetic charge; current dipole strength
Q_e	electric charge
q_m	Bohr magneton
r	distance
R	resistance; radius
r_{Cu}	dc wire resistance
RF	radio frequency
R_H	Hall coefficient
rms	root mean square
R_s	serial resistance
S	sensitivity; shielding factor
S_A, S_I, S_V	absolute sensitivity, supply-current sensitivity, supply voltage-related sensitivity
SDT	spin-dependent tunneling
S/N	signal-to-noise ratio
SQUID	superconducting quantum interference device
SQUIF	superconducting quantum interference filter
t	time
T	period; torque; absolute temperature
T, t	thickness
T_1	spin-lattice relaxation constant
T_c	Curie temperature; critical (transition) temperature
TMR	tunneling magnetoresistance
U	magnetic voltage

v	speed
V	volume; voltage; Verdet constant
V_H	Hall voltage
V_I	induced voltage
v_n	noise voltage
w	width of the tape or strip; Weiss constant
W	energy per unit volume; equivalent volume
W_A	total anisotropy energy
W_C	magnetocrystalline anisotropy
W_D	shape anisotropy energy
Z	complex impedance; number of electrons per atom
Δ	change
Φ	magnetic flux
Φ_m, Φ_n	flux sensitivity
α	Gilbert's damping factor
β	linear birefringence; gradiometer balance
γ	density; gyromagnetic ratio
γ_p	gyromagnetic ratio of proton
δ	skin depth
ε	relative permittivity; strain
$\eta_{\max}$	GMI factor
λ	magnetostriction; relative change of the length; skin depth (also δ)
λ_s	saturation magnetostriction
μ	permeability (usually relative μ_r)
μ_a	apparent permeability
μ_p, μ_e	proton, electron magnetic moment
μ_n, μ_{Hn}	drift mobility of electrons, Hall mobility
μ_0	absolute permeability of open space ($= 4\pi \cdot 10^{-7}$ Hm^{-1})
ρ	resistivity (specific resistance)
ρ_e	electrical charge density
ρ_o, ρ_p	resistivity for J parallel, respectively, orthogonal to M_s
ρ_s	sheet resistance
σ	conductivity
τ	transmission coefficient
ν	Larmor resonance frequency
ω	angular frequency
Ω	angular rotation rate
∇	gradient operator

About the Editor

Pavel Ripka received an Ing. degree in 1984 and a CSc (equivalent to a Ph.D.) in 1989 at the Czech Technical University, Prague, Czech Republic. He works at the Department of Measurement, Faculty of Electrical Engineering, Czech Technical University as a professor. From 2011 to 2019, he served as a dean of the faculty. A stay at the Danish Technical University from 1991 to 1992 was a milestone is his scientific career. He also spent sabbaticals at the National University of Ireland in Galway, the Institute for the Protection and the Security of the Citizen, Ispra, Italy, and the National University of Singapore. His main research interests are magnetic measurements and magnetic sensors, especially fluxgate, magnetic position, and speed sensors and electric current sensors.

List of Contributors

[*]**Mario H. Acuña** earned an MSEE from the University of Tucuman, Argentina, in 1967 and a Ph.D. in space physics from the Catholic University of America, Washington, D.C., in 1974. From 1963 until 1967, he worked at the University of Tucuman as well as the Argentine National Space Research Commission. In 1967, he moved permanently to the United States, joining the Fairchile-Hiller Corporation in Germantown, Maryland, to provide engineering and scientific support to NASA. Since 1969, he has been associated with NASA's Goddard Space Flight Center in Greenbelt, Maryland, where his interests have centered around experimental investigations of the magnetic fields and plasmas in the solar system. As principal investigator, coinvestigator, instrument scientist, and project scientist, he has been part of many NASA missions.

James R. Biard was the chief scientist at Honeywell Sensing & Control, Richardson, Texas. He received a B.S. in 1954, an M.S. in 1956, and a Ph.D. in 1957 in electrical engineering from Texas A&M University. He is an inventor with 51 U.S. and foreign patents that include the GaAs LED, silicon MOS-ROM, Schottky clamped logic circuits, and a planar silicon vertical Hall element. He also served at Texas A&M University as an adjunct professor of electrical engineering. His major areas of interest were semiconductor device physics, semiconductor sensors, optoelectronic devices, and linear integrated circuit design.

Robert L. Fagaly received his BS in chemistry from San Jose State University in 1967, his PhD in physics from the University of Toledo in 1977, and an MBA from the University of San Diego in 1992. After scientific fellowships at the Illinois Institute of Technology and the Centre National de la Recherche Scientifique, Grenoble, France, Dr. Fagaly worked for Biomagnetic Technologies, General Atomics and Conductus, after which he cofounded Tristan Technologies. Subsequently, he was a senior program manager at Quasar Federal Systems and Honeywell. An IEEE Fellow, he chairs the IEEE Council on Superconductivity's Standards committee. He is also a member of the American Society of Hematology, the U.S. Department of Commerce's Technical Advisory Committee, and the International Electrotechnical Commission.

Ronald B. Foster received an M.S. in 1980 in physics from the University of Arkansas. From 1980 to 1983, he worked for Texas Instruments in the Circuit Design and Development Department. In 1983, he joined Honeywell and worked there as the manager of design for fabrication for several years and later as the

[*]Deceased.

manager of integrated circuit design and layout. He cofounded the MEMS company Axept, LLC. He was also the CEO of NanoWatt Design, Inc.

*__Ivan Garshelis__ was the president and founder of Magnova, Inc., Pittsfield, Massachusetts, and also Magnetoelastic Devices, Inc. His research was focused on magnetism, especially on magnetoelastic devices. He won the 1994 R&D 100 award for inventing the magnetoelastic torque sensor based on remanent circular magnetization and holds over 50 patents and has written numerous publications.

*__Hans Hauser__ received an Ing. degree in electrical engineering at the Technical University of Vienna in 1983. In 1988, he became a Doctor of Technical Sciences. In 1993, he became an IEEE fellow. He was a professor and the head of the Department at Technical University of Vienna, Austria. His main areas of interest were magnetism and magneto-optics.

Ryan Kari graduated from the University of Minnesota with a B.Sc. in mechanical engineering (magna cum laude honors) and from Stanford University with an M.Sc. in mechanical engineering with a focus on smart product design and systems identification. He has worked for MagCanica, located in San Diego, California, since 2002, and currently serves as the chief technical officer. His main area of focus is the development of magnetoelastic torque sensors. His research interests include the integration of new enabling technologies such as embedded systems and machine learning into magnetoelastic systems and devices with a focus on productization.

Ludek Kraus received an M.Sc. in solid state physics in 1968 from the Faculty of Nuclear and Technical Physics, Czech Technical University in Prague. In 1980, he defended his Ph.D. degree in experimental physics and acoustics at the Institute of Physics, Czech Academy of Sciences. He had since 1968 worked at the Institute of Physics, Czech Academy of Sciences in Prague and retired in 2010. Since then, he has been an emeritus scientist. His main areas of interest are the magnetism of amorphous and nanocrystalline materials and ferromagnetic resonance.

Roland Lammegger received a B.S. degree in physics in 2001 and a Ph.D. in experimental physics in 2006 from the Graz University of Technology, Graz, Austria. His research activities are devoted to the development of compact PT magnetometers and atomic clocks in earthbound and satellite applications. He now works for the Institute of Experimental Physics at Graz University of Technology.

Werner Magnes is the vice director and head of the magnetometer group at the Space Research Institute of the Austrian Academy of Sciences. He received a diploma in acoustics and electrical engineering in 1994 and a Ph.D. in electronics in 1999 from the Graz University of Technology. He has worked on the development, calibration, and operation of space-borne magnetometers since 1992. Dr. Magnes has been coinvestigator for a number of space magnetometers: Rosetta/Lander, Double Star, Venus Express, Solar Orbiter, BepiColombo, Magnetospheric Multiscale, JUICE, and Comet Interceptor. Furthermore, he gives lessons for the master courses “Space Sciences and Earth from Space,” and “Acoustics and Electrical Engineering” at the Graz University of Technology.

*Eugene Paperno** received an M.Sc. in electrical engineering from the Minsk Institute of Radio Engineering, Republic of Belarus, in 1983 and a Ph.D. (honors) in electrical engineering from the Ben-Gurion University of the Negev, Israel, in 1997. He worked at the Institute of Electronics, Belorussian Academy of Sciences from 1983 to 1991 and has worked at the Department of Electrical Engineering, the Ben-Gurion University of the Negev, Israel, since 1982. From 1997 to 1999, he was the Japan Society for the Promotion of Science (JSPS) Post-Doctoral Fellow at Kyushu University.

Radivoje S. Popovic obtained a Dipl. Ing. in applied physics from the University of Belgrade, Yugoslavia, in 1969, and an M.Sc. in 1974 and a Dr. Sc. In 1978, both in electronics, from the University of Nis, Yugoslavia. From 1969 to 1981, he worked for Elektronska Industrija Corporation, Nis, Yugoslavia. From 1982 to 1993, he worked for Landis & Gyr Corporation, Central R&D, Zug, Switzerland, as the vice president of Central R&D. From 1994 to 2010, he was a professor at the Swiss Federal Institute of Technology Lausanne (EPFL), Switzerland. He is currently a professor emeritus of EPFL and CTO of SENIS AG, Zug, Switzerland.

Ichiro Sasada received an M.S. of engineering in 1976 and Dr. of Engineering in electronic engineering in 1986, both from Kyushu University. He worked at the Department of Applied Science for Electronics and Materials, Kyushu University, Fukuoka, Japan. Dr. Sasada's research fields involve the development of magnetoelastic torque sensors, magnetic shieldings for biomagnetic measurements, magnetic imaging for nondestructive evaluation using eddy-current probes, and magnetic motion-capturing system.

Christian Schott received an M.Sc. in electrical engineering in 1992 and a Ph.D. on magnetic sensors from EPFL in 1999. He then joined the start-up Sentron in Switzerland where he led the development of integrated Hall sensors with magnetic concentrators. In 2004, he joined Melexis, holding different technical and management positions. In 2013, he founded and led a global intellectual property team and successfully managed various court litigations and license negotiations. Since 2018, he has worked as process and test architect and prepares the future of magnetic testing at Melexis. Dr. Schott holds over 30 patents and has published over 40 papers.

Ichiro Shibasaki received a B.Sc. in 1966 in physics from the Tokyo University of Science and an M.Sc. in 1968 and a Ph.D. in 1971 in theoretical physics from the Tokyo University of Education (now the University of Tsukuba), Japan. He began working for the Department of Physics, Tokyo University of Education and joined Asahi Chemical Industry in 1974. He developed the high-sensitivity InSb thin-film Hall sensors at Asahi Chemical Industry in 1975. He worked at the Asahi Kasei Corporation until 2008. In 2018, he received Yamazaki-Teiichi Prize. Currently, he serves as an advisor of The Noguchi Institute in Tokyo.

Mark Tondra received a B.S. in physics and mathematics, with honors, from the University of Wisconsin-Madison in 1989 and a Ph.D. in 1996 from the University of Minnesota in solid state physics. He currently works at Diagnostic Biosensors, Inc., in Minnesota, which he founded, to develop and commercialize magnetoresistance (MR) sensors for the biochemical detection market. He worked at NVE Corp (formerly NonVolatile Electronics Corp.).

Karel Závěta graduated in 1956 from the Charles University, Prague, and received a C.Sc. in physical sciences from the Czechoslovak Academy of Sciences in 1960. In 1966, he obtained an RNDr. from Charles University. He has been working since 1956 in the Institute of Physics of the Czechoslovak (since 1993, Czech) Academy of Sciences studying magnetic properties, in particular, relaxation in magnetically soft materials. He spent the school year 1968–1969 as a visiting professor at the University of Maryland. His interest was later centered on amorphous and nanocrystalline materials and in 1993–2009 he was the head of the Joint Laboratory of Mössbauer Spectroscopy located at the Mathematical-Physical Faculty of the Charles University.

Index

A

AC comparators, 361
AC/DC current clamps, 368
AC fluxgates, 85
AC measurements, 247–48
AC phase modulation, 273
Acronyms and abbreviations, this book, xiii–xvi
Active noise compensation systems, 321
Airborne magnetic surveys, 294
Air coils
  about, 30–31
  current output, 35–37
  design examples, 36
  distributed capacitances, 30
  equivalent circuit, 34
  frequency characteristics, 36
  geometry, 31
  high-frequency, 31
  inductance, estimating, 34
  parasitic capacitances and, 34–35
  shielding and grounding, 31
  short-circuited, 35–37
  thermal noise, 33–34
  tuning, 37
  use of, 30
  voltage output, 37
  voltage sensitivity, 32–33
  See also Induction sensors
Alkali metal vapor magnetometers
  about, 197–98
  classes, 197
  energy-level diagram, 198
  M_2 magnetometers, 199–200
  M_x magnetometers, 200–202
  special excitation principles, 202
Amorphous alloys, 21, 348
Amorphous magnetic materials, 63
Amorphous tapes and wires, xix
Ampère's law, 2, 363
Amplifier noise, 42–43
Amplitude permeability, 19
AMR magnetometers, 114–15
AMR sensors
  about, 100
  anisotropy in, 11
  crossfield sensitivity of, 112–13
  design examples, 110–12
  flipping, 113–14
  full-bridge, with high sensitivity, 111
  geometrical bias, 106
  layout, 109–12
  linearization and stabilization, 105–9
  longitudinal bias, 106
  magnetization and applied field and, 102–3
  magnetoresistance and, 100–103
  magnetoresistive films and, 103–5
  perpendicular bias, 106
  resistance and magnetization and, 100–102
  sensitivity and measuring range, 109–10
  theoretical analyses of, 100
  for weak fields, 111–12
  See also Magnetoresistive sensors
Angular rotation end-of-shaft sensor, 336–37
Anisotropic magnetoresistance sensors. *See* AMR sensors
Anisotropy
  in AMR sensors, 11
  creep-induced, 11
  field, 11
  induced, 9–12
  magnetic, 6–12
  in magnetic sensor materials, 11
  in magnetic wires, 12
  magnetocystalline, 7
  shape, 7–9
Annealing, 326–27
Antiferromagnetism, 5–6
Antiperiodical waveforms, 32
Antitheft systems, 289–90
Apparent permeability, 39
Applications
  automotive, 290
  biomagnetic measurements, 279–82
  geomagnetic measurements, 292–97
  magnetic marking and labeling, 292
  military and security, 287–90

navigation, 282–87
nondestructive testing, 290–92
space research, 297–306
SQUID, 243–50
Application-specific integrated circuits (ASICs), 66, 67
Audio MT (AMT), 250
Automotive applications, 290
Auto-oscillation magnetometers, 69
Axial magnetic shielding
with double-shell shields, 326
with single cylinders, 325
with single-shell shields, 324–26

B

Bandwidth, sensor, 26
Barber poles, 107–9
Basic laws, 2–3
Biological sensors, 274–75
Birds, magnetic orientation in, 274–75
Bi-SQUIDs, 224
Bloch wall, 15, 16
Broadband current-output fluxgate, 73–75, 76
BTi CryoSQUID, 240
Bulk magnetization, 17

C

Calibration coils
about, 313–14
for AC calibration, 319
Braunbek type, 318
four rectangular coils, 315–16
Helmholtz coils, 314, 315
ideal spherical coils, 318
large, 319
rules, 319
saddle coils, 317
scalar methods, 319
solenoids, 314–15
as sources of magnetic moment, 320
Cesium magnetometer, 199
Chemical sensors, 275
Circular arrays, 356
Closed-cycle refrigeration, 240
CMOS fluxgates, 82
CMOS Hall elements, 153–54
Coils for measurement, 46
Compact Spherical Coil (CSC) sensor, 80, 86, 87
Compass applications, 284–86
Cored coils
about, 37
absolute sensitivity, 40
apparent permeability, 39
current output, 42
demagnetization factors, 38
equivalent circuit, 41–42
geometry, 37
self-capacitance, 42
thermal noise, 41
voltage sensitivity, 37–41
Coreless current sensors
about, 366
based on fluxgate, 368
based on magnetoresistors, 367–68
Hall coreless current sensors, 366–67
Cost, sensor, 27
Creep-induced anisotropy, 11
Crossfield effect, 80, 114
Crossfield sensitivity, AMR sensors, 112–14
Cryogenic current comparators (CCC), 249–50
Current clamps, 368–69
Current contacts (CC), 153
Current output
air coils, 35–37
broadband, 73–75
contacts, 167
cored coils, 42
eddy, 336
Current output fluxgates. *See* Short-circuited fluxgates
Current-to-voltage (I/V) converter, 36
Current transformers
about, 357–58
electronically enhanced, 359–61
in electronic watt and energy meters, 360
Fe-based nanocrystalline allows and, 360–61
frequency-dependent errors of, 360
magnetizing inductance, 359

D

DC/AC current clamps, 368
DC comparators, 361, 362
DC SQUIDs
about, 222
block diagram, 221
electronics output, 240
minimum noise energy for, 226
RF SQUID versus, 220
white noise, 226
See also SQUID sensors
Deep quantum wells (DQW) Hall elements, 148–49
Deep-space magnetometry, 298–300
Demagnetization
accomplishing, 18–19
fluxgate sensors and, 59–62
magnetic shielding and, 327

by mechanical shock waves, 18–19
shape anisotropy and, 7–9
Demagnetization factors, 8, 9, 38
Dewars, 238–40, 241
Diamagnetism, 4
Differential permeability, 19
Differential variable inductance transducer (DVRT), 342
Digital fluxgate magnetometers, 65–67
Digital-to-analog converters (DACs), 65, 66–67
Direct current (DC) circuit, 3–4
Domain structures, 14–16
Domain walls, 15
Double-rod sensors, 56
Dual magnetometer method, 303, 304
Dynamic field compensation (DFC), 229

E

Earth's field vector components, 285
Earth's magnetic field, 293, 294
Eddy-current sensors
about, 345–46
ferrite core shapes, 339
ferromagnetic target, 336
inductive proximity, 340, 341
miniature, 338–39
pot core, 338
sensing coils, 336
sensor diameter, 337
target material, 338
use of, 339
See also Position sensors
Electric current sensors
about, 355–56
coreless current sensors, 366–68
current clamps, 368–69
current transformers, 357–61
feedback compensated, 365
fluxgate current sensors, 361–62
gapped core sensors, 364–66
hidden currents, measurement of, 369
magneto-optical current sensors, 356
Rogowski coils, 362–64
Electromagnetic compatibility (EMC), 333
Electronically enhanced current transformers, 359–61
Electronic noise cancellation, 236–38
Electron spin resonance (ESR), 182
Environmental noise, 240–43
Equilibrium state, 10
Exchange magnetostriction, 12
Excitation
alkali metal vapor magnetometers, 202
fluxgate, 69
integrated Hall sensor, 157–59
sinewave, 61–62

F

Faraday effect, 262–64
Faraday's induction law, 3
Fast Fourier Transform (FFT), 193
Ferrimagnetism, 5–6
Ferrite, 62
Ferromagnetic materials, 51, 99
Ferromagnetic sphere, 8
Ferromagnetism, 5–6
Fiber-optic magnetostriction field sensors, 270
Field compensation systems, 320–21
Field-programmable gate array (FPGA), 360
Finite-element modeling (FEM), 4
Flexible Rogowski coils, 363
Flipping pulses, 113–14
Flux concentrators, 124
Flux distribution, 326
Fluxgate compass, 284–85
Fluxgate current sensors, 361–62
Fluxgate gradiometers, 89–90
Fluxgate magnetometers
auto-oscillation, 69
designs of, 80–81
digital, 65–67
multi-axis, 85–89
nonselective detection methods, 67–69
offset from magnetometer electronics, 78–79
offset from other magnetometer sources, 79–80
portable and low-power, 80–81
principles of, 63–69
real-time, 66
relaxation-type, 68
sampling methods, 68–69
second-harmonic analog, 63–65
sensor zero stability and, 75
in space exploration, 302
station, 81
table of, 89
zero offset, 78–79
See also Magnetometers
Fluxgate sensors
about, 51–52
AC, 85
basic principle illustration, 53
coreless current sensors based on, 368
core materials, 62–63
crossfield effect, 80
demagnetization and, 59–62
in directional drilling, 295
excitation, 69

Fluxgate sensors *(Cont.)*
high sensitivity, 62
magnetic wires for, 12
miniature, 81–84
noise, 75–80
operation theory, 58–62
orthogonal-type, 52–55
output voltage, tuning, 69–72
parallel-type, 55–58
parallel waveforms, 53
parametric amplification, 70
racetrack, 71
ring-core, 71–72
short-circuited, 72–75
as solid-state devices, 51
space missions, 299
table of, 89
tuned oscillation circuits, 70
use of, 51, 52
Flux quantization, 213–14
Force and pressure sensors, 347–49
Fractional-turn SQUIDs, 223–24
Full-scale range, sensor, 23

G

GaAs Hall elements, 150
Gapped core, sensors with, 364–66
Geomagnetic measurements, 292–97
Geophysical SQUID applications
about, 250
active methods, 251
passive methods, 250–51
rock magnetometers, 251–52
See also SQUID applications
Geophysics, xviii
Giant magnetoimpedance (GMI)
of amorphous CoFeSIB wire, 266
applications, 267, 268
characterization, 265–66
curve, 267
effect, 267, 268, 269
magnetic wires for, 12
See also GMI sensors
Giant magnetoresistance (GMR)
AMR and, 120
bipolar magnetoresistive response, 125
bridge, 125
in commercial films, 121
cross-sections of structures, 117
effect basics, 117–22
as isotropic with current direction, 120
maximizing, 120
measured, 120–21
multilayer micromachined coils, 122
spin-dependent scattering, 119–21
spin values, 117–19
total, calculation of, 118
underpinned sandwich, 121
See also GMR sensors
Gifford-McMahon (GM) refrigerator, 240
GMI sensors
about, 268–69
magnetic multilayers and, 21
noise and offset stability, 269–70
off-diagonal, 269
See also Giant magnetoimpedance (GMI)
GMR sensors
about, 116
development of, 116
flux concentrators, 124
magnetic multilayers and, 21
multilayer bridge, 124
standard construction, 120
See also Giant magnetoresistance (GMR)
GMR/TMR sensors
applications, 127–28
bipolar structures, 125
cross-axis sensitivity, 127
design, 123–28
film deposition, 123
gradiometer, 126
material processing techniques, 123–24
micromagnetic design, 123
offset, 130
output of, 116
packaging, 127
patterning techniques, 123–24
sensor construction, 124–27
temperature characteristics, 126–27
trim sites, 127
Gradiometer nondestructive sensors, 89–90
Gradiometers
as compensated magnetometers, 235
first order, with noise cancellation channels, 237
fluxgate, 89–90
for noise reduction, 241–42
reference, 237
SQUID, 235–36

H

Hall coreless current sensors, 366–67
Hall devices with IMCs
about, 168–70
integrated current sensor and, 173
rotary sensor with, 170–71
stray-field robust gradiometric sensors and, 173–75
3-axis sensor with, 171–73

Hall effect
  about, 137–39
  basics, 136–43
  defined, 137
  in long samples of n-material, 136
Hall electric field, 138
Hall elements
  CMOS, 153–54
  commutation and, 156–57, 161
  cross-connected, 152
  DQW, 148–49
  dual, 154, 156
  epitaxial, 158–59
  fabrication of, 143
  GaAs, 150
  high electron mobility thin-film, 143–50
  InAs thin-film, by MBE, 146–48
  InSb, 144–46
  junction-isolated, 161
  low drift and, 153
  as N-type layer, 153–54
  placement, 151
  quad, 154–57
  resistance, 157
  vertical, 162
  voltage bias, 158
Hall mobility, 138, 158
Hall plates, 170
Hall sensors
  about, 135–36
  applicability of, 143
  basics of, 136–43
  characteristics of, 141–43
  current, 364, 366–67
  GaAs, 150, 151
  geometry, 140
  with IMCs, 168–75
  integrated, 135–36, 150–63
  material choice, 139
  noise, 143
  nonplate-like, 163–68
  offset, 142–43
  physical parameters, 135
  production statistics, 135
  relative size of contacts and, 140
  sensitivity, 141–42
  in shape of a plate, 137
  structure, 140
  temperature cross-sensitivity, 143
  2-D, 139
Hall voltage, 139, 142, 154, 158
Hard disk drive read-heads, 128
Hard magnetic materials, 22
Helmholtz coils, 314, 315, 318
Herring bones, 107
Hidden currents, measurement, 369
HTS materials, 219–20
HTS SQUIDs, 217, 231, 239–40
Humidity, 26
Hybrid 3-axial AMR magnetometers, 115
Hyperfine structure magnetometer, 200
Hysteresis
  magnetoresistive sensors, 130
  reducing effects of, 19
  as sensor specification, 23
Hysteresis loops, 10, 20, 21, 22, 46, 105

I

Ideal spherical coils, 318
Immunity, sensor, 27
InAs DQW Hall element, 149
InAs thin-film Hall elements, 146–48
Incremental permeability, 19
Induced anisotropy, 9–12
Induction magnetometers, 29
Induction sensors
  about, 29–30
  air coils, 30–37
  basic description of, 29
  coils for measurement, 46
  design examples, 43
  moving coils, 44–46
  noise matching, 42–43
  Rogowski-Chattock potentiometer, 46–47
  rotating coil magnetometers, 43–44
  search coils (ferromagnetic core), 37–42
  vibrating coils, 46
Inductive (eddy-current) proximity sensor, 340, 341
Inductive gear tooth sensor, 346, 348
Inductosyn, 343
In-flight calibration and coordinate systems, 305–6
Initial permeability, 19
InSb Hall elements, 144–46
Integrated Hall sensors
  about, 150–51
  amplification, 159
  applications and trends, 163
  CMOS Hall elements, 153–54
  cross-section view, 152
  excitation, 157–59
  Geometry considerations, 159–61
  historical perspective, 151–52
  junction-isolated Hall elements and, 161
  offset, 154–57
  packaging for, 162–63
  smart, 135–36
  spinning current sequence and, 155

temperature gradients, 155
types of, 150
vertical Hall elements, 162
See also Hall sensors
Integrated magnetic concentrators (IMCs)
deposition by electroplating, 174
electrical current sensor with, 172
Hall devices with, 168–75
passive signal amplification of, 173
rotary sensor with, 170–71
technology, 175
3-axis sensor with, 171–73
Intermagnet, 296
International association of Geomagnetism and Aeronomy (IAGA), 79

J

Josephson effect, 214–15, 216
Josephson junctions, 216
JPL Helium Magnetometer, 206
Junction-isolated Hall elements, 161

K

Kerr effect, magneto-optical, 264–65

L

Laboratory SQUID applications
about, 246
AC measurements, 247–48
current, 246
NMR, 248–49
SQUID susceptometers, 248
voltage, 246–47
Larmor frequency self-oscillating optical M_x magnetometer, 201
Lead frame technology, 155
LETI Overhauser magnetometer sensor, 195
Linearity, sensor, 23
Linear transformer sensors
Inductosyn, 343
LVDT, 341–42
PLCD sensor, 342–43
variable gap sensors, 342
See also Position sensors
Linear variable differential transformer (LVDT), 341–42
Longitudinal Kerr effect, 264
Long-term stability, sensor, 24
Lorentz-force magnetometers, 273–74
LTS CCCs, 250
LTS SQUIDs, 217, 219, 220, 231

M

M_2 magnetometers, 199–200
Magnetically shielded rooms (MSR), 243
Magnetic anisotropy
about, 6–7
induced, 9–12
in magnetic wires, 12
magnetocystalline, 7
shape, 7–9
torque sensors, 350–51
Magnetic anomaly detection (MAD), 250
Magnetic circuits, 3–4
Magnetic cleanliness, 302–5
Magnetic dust, 280–81
Magnetic fields
defined, 1
ferromagnetic sphere in, 8
magnitudes, 2
matter and, 3, 4–6
measurements, absolute reproducibility of, 181–82
Magnetic flowmeters, 355
Magnetic flux, 3, 29, 115, 212–16, 222, 231, 290
Magnetic flux concentrators, 163, 173
Magnetic flux density, 1, 137, 139, 165
Magnetic force microscope, 291
Magnetic load cells, 348–49
Magnetic marking and labeling, 292
Magnetic materials
about, 20
amorphous, 63
diamagnetic, 4
ferromagnetic, 51, 99
hard, 22
nonlinear, 30
paramagnetic, 5, 255
permeability, 267
polycrystalline, 351
polymer-bonded, 22
soft, 20–22, 46
Magnetic observatories, 296
Magnetic particle detection, 127
Magnetic particle imaging, 280
Magnetic polarization, 3
Magnetic reading heads, 128
Magnetic sensors
amorphous tapes and wires and, xix
hard magnetic materials for, 22
meanings of term, xviii
for nonmagnetic variables, 333–69
soft magnetic materials for, 20–22
specifications, 22–27

See also Applications; *specific types of sensors*
Magnetic shaking, 327–28
Magnetic shielding
about, 321–22
annealing, 326–27
axial, 324–26
coreless current sensors, 367
demagnetizing, 327
effectiveness, 322
enhancement by magnetic shaking, 327–28
flux distribution, 326
rooms, 328
SQUID, 242–43
theory, 322
three-layer, 322
transverse, 322–24
See also Testing and calibration instruments
Magnetic states, 4–6
Magnetic trackers, 345–46
Magnetic units, 1–2
Magnetic voltage, xv, 2
Magnetic wires, anisotropy in, 12
Magnetization
applied field and, 102–3
remanent, 297
resistance and, 100–102
saturation, 187
spontaneous, 101
Magnetization curves
illustrated, 18, 19
initial, 17
measuring, 19–20
nonlinearity of, 20
Magnetization process, 15–16
Magnetizing inductance, 359
Magnetocardiogram (MCG), 254
Magnetocardiography, 282
Magnetocystalline anisotropy, 7
Magnetoelastic field sensors
about, 270
fiber-optic magnetostriction, 270
magnetorestrictive-piezoelectric, 270–72
shear-wave, 272–73
Magnetoelastic phenomena, 12
Magnetoelastic resonance sensors, 349
Magnetoelastic torque sensors, 353–54
Magnetoelectric sensors, 270–72
Magnetoencephalogram (MEG), 254
Magnetoencephalography, 282
Magnetoimpedance and magnetoinductance
materials, 267–68
principle, 265–67
sensors, 268–70
Magnetometers
alkali metal vapor, 197–202
AMR, 114–15
auto-oscillation, 69
field sensitivity, 225
fluxgate, 63–69, 75, 78–81, 85–89, 302
induction, 29, 43–44
Lorentz-force, 273–74
meanings of term, xviii
optically pumped, 197–207
Overhauser effect, 193–97
proton-precession, 182–97
resonance, 26, 182–97
rock, 251–52, 297
rotating coil, 43–44
scalar, 300–301
shear-wave, 272–73, 274
SQUID, 248
3-axial, 328–29
vector, 301–2
See also Applications
Magneto-optical current sensors, 356
Magneto-optical sensors
about, 261
detection of polarization angle, 263–64
dual-quadrature, 263
Faraday effect and, 262–64
Kerr effect and, 264–65
Magnetopneumography, 280
Magnetoresistive films, 103–5
Magnetoresistive sensors
about, 99–100
AMR, 100–1115
applications, 127–28
commercially available, 131
electrical resistivity and, 99–100
field range and linearity, 129–30
GMR/TMR, 115–28
in hard disk drive read-heads, 128
hysteresis, 130
in magnetic particle detection, 127
in magnetic reading heads, 128
in memory, 128
noise, 128–29
offset, 130
offset drift, 130
operating parameters of, 128–31
in signal isolation, 128
use of, 99
Magnetoresistors, coreless current sensors based on, 367–68
Magnetorestrictive-piezoelectric sensors, 270–72
Magnetorestrictive position sensors, 344–45

Magnetostriction
about, 12–13
as anisotropic, 14
origin of, 13
saturation, 14
spontaneous, 12, 13
Magnetotactic bacteria, 274
Magnetotellurics (MT), 250
Magnetsrode, 321
MAGSAT satellite system, 88
Maximum permeability, 19
Maximum-variance processing, 305
Maxwell's equations, 213
Mechanical gyroscope
about, 182–83
coning rate, 184
illustrated, 182
mechanical torque, 184–85
rotation about skew axis, 183
spinning and coning, 184
spinning wheel, 183, 184
Medical SQUID applications
about, 253–55
magnetic measurements, 255
MCG, 254
MEG, 254
in research, 256
Meissner effect, 212–13
Metastable HE^4 magnetometer
about, 202–3
atom energy levels, 203
frequency determination, 204
general principle, 205
JPL, 206
light absorption, 205
M_2 mode, 204
omnidirectional, 207
sealed glass vessel, 202
Microfabricated fluxgates, 84
Microscopes, SQUID, 252–53
Military and security applications
about, 287
antitheft systems, 289–90
target detection and tracking, 289
unexploded ordinance (UXO), 287–89
Mineral prospecting, 292–97
Miniature fluxgates
about, 81–82
flat coil, 82–83
microfabricated solenoids, 84
PCB, 83–84
wire-wound sensors, 82
See also Fluxgate sensors
Mobile robots, navigation of, 287
Molecular beam epitaxy (MBE), 146–48
Mössbaur spectroscopy, 6
Moving coils, 44–46
Multi-axis magnetometers
about, 85
individually compensated sensors, 87–88
three-axial compensation systems, 86–87
two-axis compensated sensors, 85
Multilayer micromachined coils, xix
Multispacecraft measurements, 306
M_x magnetometers, 200–202

N

Nanocrystalline alloys, 21, 63, 360–61
Navigation applications, 282–87
Neel wall, 15–16
N-fold-shell shield, 323
Noise
about, 24–25
amplifier, 42–43
environmental, 240–43
fluxgate, 75–80
GMI sensors, 269–70
Hall sensors, 143
magnetoresistive sensors, 128–29
Nyquist, 233
1/*f* noise, 227–28
specification, 24–26
spectrum density, 25
SQUID, 224–28
thermal, 33–34, 41, 110, 223
white, 225–26
Noise matching, to an amplifier, 42–43
Noise reduction (environmental noise)
about, 240–41
gradiometers for, 241–42
magnetic shielding for, 242–43
shielded rooms for, 243
Nondestructive test and evaluation SQUID application, 252–53
Nondestructive testing applications, 290–92
Nonmagnetic variables, magnetic sensors for
electric current sensors, 355–69
force and pressure sensors, 347–49
magnetic flowmeters, 355
position sensors, 333–46
proximity and rotation detectors, 346–47
torque sensors, 349–55
Nonplate-like Hall sensors
about, 163–64
three-axis Hall devices, 167–68
two-axis vertical Hall device, 166–67
vertical Hall device, 164–66

See also Hall sensors
Nonselective detection methods, 67–69
Nuclear magnetic resonance (NMR)
defined, 179
spectral analysis routines, 193
SQUID and, 248–49
superparamagnetism and, 6
use of, 179–80
Nyquist noise, 233

O

Object location, 292–97
Off-diagonal GMI, 269
Offset
Hall sensor, 142–43
integrated Hall sensor, 154–57
magnetoresistive sensors, 130
as sensor specification, 24
zero, 78–79
Offset temperature coefficient, 24
1/*f* noise, 227–28, 230
Optically pumped magnetometers
alkali metal vapor magnetometers, 197–202
M_2 magnetometers, 197–202
metastable HE^4 magnetometer, 202–7
M_x magnetometers, 197–202
See also Resonance magnetometers
Optical pumping, 200
Orthogonal fluxgates
about, 52
gating mechanism, 52–54
illustrated, 54
mixed, 54–55
in unipolar fundamental mode, 54
See also Fluxgate sensors
Overhauser effect proton magnetometers
about, 193–94
DC-polarized free-precession, 195
LETI, 195
scalar, 194–95
signal-to-noise ratio, 196–97
See also Proton precession magnetometers

P

Packaging
GMR/TMR sensors, 127
integrated Hall sensors, 162–63
SQUID input circuit, 231
Parallel-type fluxgates
about, 55
double-rod sensors, 56
illustrated, 55
racetrack sensors, 57–58
ring-core sensors, 56–57, 58, 59, 60
single-rod sensors, 55
See also Fluxgate sensors
Paramagnetic materials, 5, 255
Paramagnetism, 5
Parasitic capacitances, air coils and, 34–35
Particle beam sensors, 362
PCB-based fluxgates, 83–84
PCB Rogowski coil, 364
Permalloy, 62
Permanent magnet, sensors with, 334–35
Permanent magnetic linear contactless displacement (PLCD) sensor, 342–43
Perming, sensor, 24
Phase-delay method, 67–68
Photo-sensitive detector (PSD), 63–64, 66, 79
Planar fluxgate compass sensor, 83
Planetary magnetometry, 298–300
Polar Kerr effect, 264
Polymer-bonded magnetic materials, 22
Position sensors
about, 333
eddy-current sensors, 335–41
linear transformer sensors, 341–43
magnetic trackers, 345–46
magnetorestrictive, 344–45
with permanent magnet, 334–35
rotational speed/incremental, 335
rotation transformer sensors, 343–44
Wiegand sensors, 345
See also Nonmagnetic variables, magnetic sensors for
Potentiometers, 46–47
Power, sensor, 27
Pressductors, 348–49
Printed circuit board (PCB) technology, 31, 83–84, 364
Proton-free precession magnetometer
amplified precision signal strength dependence, 191
continuously oscillating, 194
frequency measurement, 192
magnetization decay, 192
polarizing field, 190
proton magnetic moment and, 185, 186
rotation angle, 191
saturation magnetization, 187
Toroid, 188, 189
Proton magnetic moment, 185, 186
Proton precession magnetometers
mechanical gyroscope, 182–85
Overhauser effect, 193–97
proton-free, 185–93

Proton precession magnetometers *(Cont.)*
Toroid, 188, 189
See also Resonance magnetometers
Proximity and rotation detectors, 346, 348

R

Racetrack sensors, 57–58, 71, 90
Reed contacts, 346, 347
Refrigeration, SQUID
about, 238
closed-cycle, 240
dewars, 238–40
Relative permeability, 4, 5, 22
Relaxation-type magnetometer, 68
Reluctance method, 4
Remanent magnetization, 297
Resistance
Hall element, 157
magnetization and, 100–102
of mercury, 212
specification (environment), 25–26
specification (perpendicular field and field gradient), 26
Resolvers, 344
Resonance magnetometers
field gradients and, 26
magnetic resonance and, 179–82
optically pumped, 197–207
proton precession, 182–97
Reversible permeability, 19
RF SQUIDs
about, 221–22
DC SQUID versus, 220
white noise, 225–26
See also SQUID sensors
Ring-core sensors
about, 56–57
derivation of the pickup coil flux, 59
elements of, 57
fluxgate, 71–72
magnetization characteristics of the half-core, 58
model, 58, 59
use of, 56
waveforms, 60
See also Fluxgate sensors
RKKY (Ruderman-Kittel-Kasuya-Yosida) type, 116
Rock magnetometers, 251–52, 297
Rogowski-Chattock potentiometer, 46–47
Rogowski coils, 362–64
Room-temperature vulcanizing (RTV), 163
Rotary sensor with IMC, 170–71
Rotating coil magnetometers, 43–44
Rotational speed/incremental position sensors, 335
Rotation transformer sensors, 343–44

S

Saddle coils, 317
Satellite booms, magnetic sensors, 303
Saturation magnetization, 187
Saturation magnetostriction, 14
Scalar calibration of 3-axial magnetometers, 329
Scalar magnetometers, 300–301
Search coils (ferromagnetic core). *See* Cored coils
Sea turtles, inclination compass, 275
Second-harmonic analog magnetometers, 63–65
Self-compensation, 366
Semicircular potentiometers, 47
Semiconductor maagnetoresistors, 261
Semiconductor sensors, 27
Sensing contacts (SC), 153
Sensitivity
GMI sensors, 269–70
Hall sensor, 141–42
as sensor specification, 23
SQUID, 224–28, 232–33
Sensor specifications
about, 22–23
bandwidth, 26
cost, 27
full-scale range, 23
hysteresis, 23
immunity, 27
linearity, 23
long-term stability, 24
noise, 24–25
offset, 24
offset temperature coefficient, 24
perming, 24
power, 27
resistance (environment), 25–26
resistance (perpendicular field and field gradient), 26
sensitivity, 23
temperature coefficient, 23
Serial magnetic circuits, 3–4
Shaking efficiency, 327–28
Shape anisotropy, 7–9
Shear-wave magnetometers, 272–73, 274
Shielded rooms, 243
Short-circuited fluxgates
about, 72
broadband current-output, 73–75, 76

circuit diagram of, 73
resonance condition, 75
sensitivity of, 72
tuning, 75
See also Fluxgate sensors
Short-circuited induction coils, 35–37
Signal isolation, 128
Sinewave excitation, 61–62
Single-rod sensors, 55
SI units, 1, 2
Soft magnetic materials, 20–22, 46
Solenoids, 314–15
Spacecraft applications
in-flight calibration and coordinate systems, 305–6
magnetic cleanliness, 302–5
multispacecraft measurements, 306
Space magnetic instrumentation, 300–302
Space missions, 298
Space research applications
about, 297–98
deep-space and planetary magnetometry, 298–300
scalar magnetometers, 300–301
sensor environment exposure and, 298
spacecraft magnetic field measurements, 302–6
space magnetic instrumentation, 300–302
vector magnetometers, 301–2
See also Applications
Spin-dependent scattering, 119–21
Spinning spacecraft, 306
Spin values, GMR, 117–19
Spontaneous magnetostriction, 12, 13
SQIF, 222–23
SQUID applications
about, 243–45
configurations for, 244–45
cryogenic current comparators (CCC), 249–50
field sensitivities and bandwidths for, 244, 246
geophysical, 250–52
laboratory, 246–49
medical, 253–56
microscopes, 252–53
nondestructive test and evaluation, 252–53
product revenues, 243
SQUID array (SQA), 222
SQUID loop
decoupling into, 216
dual junction, 217
flux in, 214, 228
SQUID sensors
about, 217
basic parameters, 226
Bi, 224
as a black box, 231–32
block diagram, 221
configurations, 244–45
control electronics, 228–29
cooling, 227
DC, 222
design factors, 228
detection coils, 233–34, 248
differential measurements and, 229–30
dynamic field compensation (DFC), 229
electronic noise cancellation, 236–38
energy sensitivity versus frequency, 225
environmental noise, 240–43
external flux, 220
field dependence, 227
flux quantization and, 213–14
fractional-turn, 223–24
gradiometers, 235–36
HTS, 220, 231
humidity, 26
input circuits, 231–38
introduction to, 211–17
Josephson effect and, 214–15, 216
LTS, 217, 219, 220, 231
materials, 217–20
Meissner effect and, 212–13
noise and sensitivity, 224–28
1/*f* noise, 227–28, 230
operation, 220–24
packaging, 231
refrigeration, 238–40
RF, 221–22
RF versus DC, 220
sensitivity, 232–33
slew-rate limitations and, 230
SQIF, 222–23
superconductivity and, 211–12
technology limitations, 229–31
temperature dependence, 226–27
thermal environment for, 238
vector nature of, 230–31
white noise, 225–26
YBCO, 226, 231
SQUID susceptometers, 248
Stationary Rogowski coils, 363
Station fluxgate magnetometers, 81
Superconducting-insulator-superconducting (SIS) barrier, 214–15
Superconducting materials, properties of, 218
Superconducting-normal-superconducting (SNS) barrier, 215
Superconducting quantum interference filter (SQIF) devices, 216

Superconductivity, 4, 211–12
Superparamagnetism, 6
Surface magnetic mapping, 294
Synchros, 344

T

Target detection and tracking, 289
Temperature coefficient, sensor, 23
Temperature coefficient expansion (TCE), 162
Temperature range, 26
Tempone Nitroxide free radical, 196
Testing and calibration instruments
 calibration coils, 313–20
 calibration of 3-axial magnetometers, 328–29
 field compensation systems, 320–21
 magnetic shielding, 321–28
Thermal noise
 air coils, 33–34
 AMR sensors and, 110
 cored coils, 41
 fractional-turn SQUIDs and, 223
 See also Noise
Three-axial AMR magnetometers, 114–15
Three-axial compensation systems, 86–87
Three-axial magnetometers, 328–29
Three-axis Hall devices, 167–68
Three-axis sensor with IMC, 171–73
Torductors, 348–49
Toroid sensor, 188, 189
Torque sensors
 about, 349–50
 application categories, 349
 of axisymeetric structure, 353
 axisymmetric construction, 353
 low-profile pickup coils, 352
 magnetic anisotropy, 350–51
 magnetoelastic, 353–54
 magnetoelastically active ring, 353
 operation of, 350–55
 permeability-type, 351, 353
 principles of, 349–50
 ringed construction, 353, 354–55
 shaft as transducer, 354
 twist angle, 350
Transverse Kerr effect, 264
Transverse magnetic shielding, 322–24
Transverse shielding factor, 323–24
Tunnel magnetoresistance (TMR)
 about, 122–23
 advantages of, 122
 biased resistor, 126
 bipolar magnetoresistive response, 125
 GMR versus, 122–23
 magnetic multilayers and, 21
 See also GMR/TMR sensors
Two-axis vertical Hall device, 166–67

U

Unexploded ordinance (UXO), 287–89

V

Variable gap sensors, 342
Varian Associates alkali metal vapor magnetometer, 201
Variation stations, 292–97
Vector calibration of 3-axial magnetometers, 329
Vector magnetic sensors, 26
Vector magnetometers, 301–2
Vehicle magnetometer readings, 286
Vertical Hall device
 about, 164–65
 linearity, 165
 magnetic field measurement, 165–66
 matched, 166
 planar Hall effect, 165
 temperature sensitivity, 165
 See also Hall sensors
Vertical Hall elements, 162
Vibrating coils, 46
Voltage sensitivity
 air coils, 32–33
 cored coils, 37–41
 fluxgate operation and, 61
 frequency-normalized, 40

W

Wheatstone bridge, 107, 158
White noise, 25, 225–26
Wiegand sensors, 345
Wire materials, basic parameters of, 32

Y

YBCO SQUID, 226, 231

Z

Zero offset, 78–79